

2015
Gravitation
100 years after GR

Sponsored by

- . CNRS (Centre National de la Recherche Scientifique)
- . FNRS (Fond National de la Recherche Scientifique)
- . BSP (Belgian Science Policy)
- . ESA (European Space Agency)
- . CNES (Centre National d'Etudes Spatiales)
- . GRAM (Gravitation, Références, Astronomie, Métrologie)
- . Observatoire de Paris

50th Rencontres de Moriond

La Thuile, Aosta Valley, Italy – March 21-28, 2015

2015 Gravitation : 100 years after GR

© Published by ARISF, 2015

ISBN : 978-2-9546400-8-2



web

All rights reserved. This book, or parts thereof, may not be reproduced in any form or by any means, electronic or mechanical, including photocopying, recording or any information storage and retrieval system now known or to be invented, without written permission from the publisher.

Proceedings of the 50th RENCONTRES DE MORIOND

Gravitation : 100 years after GR

La Thuile, Aosta Valley Italy

March 21-28, 2015

2015
Gravitation
100 years after GR

edited by

**Etienne Augé,
Jacques Dumarchez
and
Jean Trân Thanh Vân**

The 50th Rencontres de Moriond
2015 Gravitation : 100 years after GR

was organized by :

Etienne Augé (LAL, Orsay)
Jacques Dumarchez (LPNHE, Paris)

with the active collaboration of :

P. Binétruy (Paris)
M.-A. Bizouard (Orsay)
L. Blanchet (Paris)
L. Cacciapuoti (Noordwijk)
F. Cavalier (Orsay)
M. Cruise (Birmingham)
P. Delva (Paris)
J. Dumarchez (Paris)
J.-M. Le Goff (Saclay)
S. Léon-Hirtz (Paris)
E. Rasel (Hannover)
S. Reynaud (Paris)
F. Ricci (Rome)
J.-Y. Vinet (Nice)

2015 RENCONTRES DE MORIOND

The 50th Rencontres de Moriond were held in La Thuile, Valle d'Aosta, Italy.

The first meeting took place at Moriond in the French Alps in 1966. There, experimental as well as theoretical physicists not only shared their scientific preoccupations, but also the household chores. The participants in the first meeting were mainly french physicists interested in electromagnetic interactions. In subsequent years, a session on high energy strong interactions was added.

The main purpose of these meetings is to discuss recent developments in contemporary physics and also to promote effective collaboration between experimentalists and theorists in the field of elementary particle physics. By bringing together a relatively small number of participants, the meeting helps develop better human relations as well as more thorough and detailed discussion of the contributions.

Our wish to develop and to experiment with new channels of communication and dialogue, which was the driving force behind the original Moriond meetings, led us to organize a parallel meeting of biologists on Cell Differentiation (1980) and to create the Moriond Astrophysics Meeting (1981). In the same spirit, we started a new series on Condensed Matter physics in January 1994. Meetings between biologists, astrophysicists, condensed matter physicists and high energy physicists are organized to study how the progress in one field can lead to new developments in the others. We trust that these conferences and lively discussions will lead to new analytical methods and new mathematical languages.

The 50th Rencontres de Moriond in 2014 comprised three physics sessions:

- March 14 - 21: "Electroweak Interactions and Unified Theories"
- March 21 - 28: "QCD and High Energy Hadronic Interactions"
- March 21 - 28: "Gravitation: 100 years after GR"

We thank the organizers of the 50th Rencontres de Moriond:

- A. Abada, E. Armengaud, J. Conrad, P. Fayet, J.-M. Frère, P. Hernandez, L. Iconomidou-Fayard, P. Janot, M. Knecht, J. P. Lees, S. Loucatos, F. Montanet, L. Okun, J. Orloff, A. Pich, S. Pokorski, V. Tisserand, D. Wood for the “Electroweak Interactions and Unified Theories” session,
- E. Augé, E. Berger, S. Bethke, A. Capella, A. Czarnecki, D. Denegri, N. Glover, B. Klima, M. Krawczyk, L. McLerran, B. Pietrzyk, L. Schoeffel, Chung-I Tan, J. Trần Thanh Vân, U. Wiedemann for the “QCD and High Energy Hadronic Interactions” session,
- P. Binétruy, M.-A. Bizouard, L. Blanchet, L. Cacciapuoti, F. Cavalier, M. Cruise, P. Delva, J. Dumarchez, J.-M. Le Goff, S. Léon-Hirtz, E. Rassel, S. Reynaud, F. Ricci, J.-Y. Vinet for the “Gravitation: 100 years after GR” session

and the conference secretariat and technical staff:

V. de Sá-Varanda and C. Bareille, I. Cossin, G. Dreneau, D. Fliegel, F. Legrand, G. Perrin, N. Ribet, S. Vydelingum.

We are also grateful to Giorgio Palmucci, Francesco Cante, Ida Liseno, Francesco Quinto and the Planibel Hotel staff who contributed through their hospitality and cooperation to the well-being of the participants, enabling them to work in a relaxed atmosphere.

The Rencontres were sponsored by the Centre National de la Recherche Scientifique, the Fonds de la Recherche Scientifique (FRS-FNRS) and the Belgium Science Policy. We would like to express our thanks for their encouraging support.

It is our sincere hope that a fruitful exchange and an efficient collaboration between the physicists and the astrophysicists will arise from these Rencontres as from previous ones.



The 50th edition of these Rencontres offered us the possibility to celebrate with dedicated talks by some of the pillars of Moriond, giving their personal recollections or panoramic views of the evolution of physics ideas along these 50 Rencontres. We would like to warmly thank D. Treille, G. Altarelli, E. Fischbach, M. Krawczyk, D. Goulianos, and B. Klima. This was also the occasion of renewing some long-standing traditions of Moriond, like the slalom: tens of participants of all ages skied down the track in all times and styles to eventually win ... a glass of mulled wine! And delving into the archives we have produced a list of the nearly 10000 participants of these 50 Rencontres, which has been put up as wallpaper along the corridor leading to the bar, resulting in persistent traffic jams!

E. Augé, J. Dumarchez and J. Trần Thanh Vân

Contents

1. Tests of GR and alternative theories

| | | |
|--|-----------------|----|
| What do we know about Lorentz Symmetry? | Q. Bailey | 3 |
| Lorentz violation in gravity | D. Blas | 11 |
| GINGER - A terrestrial experiment to verify the Lense-Thirring effect or possible deviations from General Relativity | A. Tartaglia | 15 |
| Aspects of massive gravity | S. Renaux-Petel | 19 |
| Consistent massive graviton on arbitrary background | L. Bernard | 23 |
| Nonlinear Cosmological Probes of Screening Mechanism in Modified Gravity | D. Mota | 27 |
| Basics of the Pressurion | O. Minazzoli | 31 |
| A dark matter superfluid | J. Khoury | 35 |
| Bimetric gravity and dark matter | L. Blanchet | 43 |
| GBAR status and goals | P. Perez | 53 |
| AEgIS experiment: goals and status | P. Nedelec | 59 |
| Gaia: astrometry and gravitation | S. Klioner | 65 |
| INPOP planetary ephemerides: Recent results in testing gravity | A. Fienga | 73 |
| An Autonomous Relativistic Positioning System | U. Koštić | 81 |
| Test of the gravitational redshift using Galileo satellites 5 and 6 | P. Delva | 89 |
| Probing deformed commutators with macroscopic harmonic oscillators | F. Marin | 97 |

2. Testing Fundamental Physics

| | | |
|--|-----------------|-----|
| The ACES Mission: Testing Fundamental Physics with Clocks in Space | L. Cacciapuoti | 103 |
| ACES MWL data analysis preparation status | F. Meynadier | 111 |
| Gravity experiments with ultracold neutrons and the q BOUNCE experiment | H. Abele | 115 |
| From precision spectroscopy to fundamental cosmology | C. Martins | 123 |
| Optimization of ESPRESSO Fundamental Physics Tests | A. C. Leite | 127 |
| An Equivalence Principle test in space on the way to launch | M. Rodrigues | 131 |
| The STE-QUEST M4 proposal | P. Wolf | 137 |
| Testing quantum physics in space using high-mass matter-wave interferometry | R. Kaltenbaek | 141 |
| Precision oscillator technology with application to testing fundamental physics, detecting high frequency gravitational waves, and quantum measurement | M. Tobar | 145 |
| Some cosmological consequences of a breaking of the Einstein equivalence principle | A. Hees | 149 |
| Ground Tests of Einstein's Equivalence Principle: From Lab-based to 10-m Atomic Fountains | E. Rasel | 153 |
| Matter-wave laser Interferometric Gravitation Antenna (MIGA): New perspectives for fundamental physics and geosciences | R. Geiger | 163 |
| Weak equivalence principle, Lorentz noninvariance, and nuclear decays | E. Fischbach | 173 |
| Dynamics, Relativity and the Equivalence Principle in the 'once-given' Universe | C. Unnikrishnan | 177 |
| A Joint Analysis of BICEP2/Keck Array and Planck Data | S. Galli | 181 |
| CORe+: mapping our cosmic origins | C. Martins | 185 |

3. Short range and Long range gravity

| | | |
|---|-----------------|-----|
| Neutrons and Gravity | V. Nesvizhevsky | 191 |
| Casimir effect and quantum reflection | G. Dufour | 197 |
| Atom interferometry test of short range gravity: recent progress in the FORCA-G experiment | M. Lopez | 205 |
| The Archimedes Experiment | E. Calloni | 213 |
| Investigating Dark Energy and Gravitation at cosmological scales with EUCLID | A. Blanchard | 217 |
| Backreaction Effects on the matter side of Einsteins Field Equations | U. Wiedemann | 225 |
| Disformal vectors and anisotropies on a warped brane | F. Urban | 229 |
| Constraints on Sterile Neutrino Dark Matter Candidate Mass by the Fermi Gamma-Ray Burst Monitor | R. Preece | 233 |
| Dark Matter: Connecting LHC searches to direct detection | A. Crivellin | 237 |

4. Gravitational wave detectors

| | | |
|--|--------------|----|
| The Status of the Advanced LIGO Gravitational-Wave Detectors | A. Staley | 24 |
| Advanced LIGO Input Optics | G. Ciani | 25 |
| Large-scale Cryogenic Gravitational wave Telescope: KAGRA | T. Tomaru | 25 |
| The CALVA facility for GW detector | D. Huet | 26 |
| Thermally Deformable Mirrors: a new Adaptive Optics scheme for Advanced Gravitational Wave Interferometers | M. Kasprzack | 26 |
| Dual readout of a Michelson interferometer for subtraction of stray light induced disturbances | M. Meinders | 27 |
| Next generation nonclassical light sources for gravitational wave detectors | S. Ast | 27 |
| Quantum Sensors in Space - Design Challenges for Spacecraft and Instruments | A. Heske | 27 |
| eLISA Optical Sensing Developments | C. Killow | 28 |
| Measurement of the Gravitational Redshift Effect with the RadioAstron satellite | V. Rudenko | 28 |

5. Search for gravitational waves

| | | |
|---|-------------------------|----|
| Gravitational Waves searches with advanced Ligo and advanced Virgo | C. Van Den Broeck | 29 |
| Multi-messenger searches: past results and future programs | G. Stratta | 30 |
| Observational perspectives with advanced gravitational wave detectors | A. Viceré | 31 |
| Planned search for LIGO/GBM coincidence in the LIGO O1 data run | J. Camp | 31 |
| Search for Joint sources of gravitational waves and high energy neutrinos with the LIGO-Virgo and ANTARES Detectors | B. Baret | 32 |
| Low latency search for compact binary coalescences using MBTA | T. Adams | 32 |
| On the possibility of GRB forecasting algorithm and alert system for future gravitational wave detectors | G. Debreczeni | 33 |
| Gravitational waves three-dimensional core collapse supernova simulations | H. Andresen | 33 |
| Post-Newtonian higher-order spin effects in inspiraling compact binaries | S. Marsat | 33 |
| High-order comparisons between post-Newtonian and perturbative self forces | G. Faye | 34 |
| Constraining the distance to inspiralling NS-NS with Einstein Telescope | I. Kowalska-Leszczynska | 34 |
| Relativistic stellar dynamics around a massive black hole in steady state | T. Alexander | 35 |

6. Posters

| | | |
|--|---------------|----|
| mSTAR: Testing Lorentz Invariance in Space Using High Performance Optical Frequency References | N. Gurlbeck | 35 |
| Gravity gradiometer using large momentum transfer beamsplitters | M. Langlois | 36 |
| Atom interferometry with ultra-cold strontium | N. Poli | 36 |
| Gravitational Wave Recoils in Non-head-on Collisions of Black Holes | I. D. Soares | 36 |
| Multimessengers from 3D Core-Collapse Supernovae | P. Marronetti | 36 |
| Study of a new generation spatio-temporal reference system based on inter-satellite links | E. Richard | 36 |
| Strong-field tests of $f(R)$ -gravity in binary pulsars | P. Dyadina | 37 |
| Inflationary and late universe tests for $\Lambda(H)$ cosmologies | L. Perico | 37 |
| Ensemble of galactic rotating neutron stars as a source of gravitational background for advanced Virgo, advanced LIGO and Einstein telescope detectors | D. Rosinska | 37 |
| Pure field physics of continuous charges without singularities | I. Bulzhenkov | 38 |
| Reviewing Grishchuk GW generator via Tokamak physics | A. Beckwith | 38 |

Authors Index 385

List of participants 395

1.
Tests of GR
&
Alternative Theories

What do we know about Lorentz Symmetry?

Q.G. Bailey

*Department of Physics, Embry-Riddle Aeronautical University, 3700 Willow Creek Road,
Prescott, AZ 86301, USA*



Precision tests of Lorentz symmetry have become increasingly of interest to the broader gravitational and high-energy physics communities. In this talk, recent work on violations of local Lorentz invariance in gravity is discussed, including recent analysis constraining Lorentz violation in a variety of gravitational tests. The arena of short-range tests of gravity is highlighted, demonstrating that such tests are sensitive to a broad class of unexplored signals that depend on sidereal time and the geometry of the experiment.

1 Overview

The Einstein equivalence principle is a crucial founding principle of General Relativity. The weak equivalence principle (WEP) and local Lorentz invariance (LLI) are two essential parts of this principle. The WEP states that gravity acts in a flavor independent manner, and local Lorentz invariance states that the local symmetries of nature include rotations and boosts. Strong experimental support for the WEP and LLI is necessary for developing a deep understanding of gravity.

Tests of the WEP are abundant, while tests of local Lorentz invariance have been largely limited to the matter sector.¹ Though the latter are primarily confined to the flat space-time limit, the breadth and scope of the current experimental tests of Lorentz invariance is impressive.² The motivation for the recent boom in Lorentz symmetry tests in the past two decades is due not only to the importance of this principle as a foundation of modern physics but also to the intriguing possibility that minuscule violations of Lorentz symmetry may occur in nature as a signal of Planck scale physics.^{3,4}

When definitive knowledge of the underlying physics is lacking, the method of effective field theory is a powerful tool for investigating physics at experimentally relevant scales. For studying local Lorentz invariance in gravity, effective field theory is particularly well suited. Using a Lagrange density containing the usual Einstein-Hilbert term, together with a series of observer scalar terms, each of which is constructed by contracting coefficient fields with gravitational field operators of increasing mass dimension d , one constructs the gravity sector of the effective field theory describing general local Lorentz violations for spacetime-based gravitation.⁵ One can

also consider a series of terms involving matter-gravity couplings where Lorentz-violating terms from the flat space-time scenario are coupled to gravity, thereby imparting observability to some lagrangian terms that are unobservable in flat space-time.⁶ To date, the so-called minimal sector of this framework, consisting of terms with operators of the lowest mass dimension $d = 4$, has been explored in experimental searches for local Lorentz violation and phenomenological studies in gravity related tests.^{7,8,9,10,11,12,13,14,15,16,17,18,19}

It is well known that Newtonian gravity and relativistic corrections from General Relativity accurately describe the dominant physics at the typical stellar system level. Experimental and observational searches for Lorentz violation within the general effective field framework described above have focused on observables at this level. However, it is currently unknown whether gravity obeys Newton's law of gravitation on small scales below about 10 microns. In fact, it is within the realm of possibility that forces vastly stronger than the usual Newtonian inverse-square law could exist. In a recent work, a systematic study of local Lorentz violation with $d > 4$ has been initiated.¹⁹ Lorentz-violating corrections to the Newtonian force law vary as $1/r^{d-2}$, since lagrangian terms constructed with operators of higher mass dimension d involve more derivatives. The sharpest sensitivities to effects from operators with $d > 4$ are therefore most likely to come from short-range tests of gravity. The phenomenology of such signals are discussed in this presentation.

2 Gravity Sector

It is known that explicit Lorentz violation is generically incompatible with Riemann geometry or is technically unnatural in spacetime theories of gravity, so we focus here on spontaneous violation of Lorentz symmetry.^{3,5,21} Spontaneous Lorentz violation occurs when an underlying local Lorentz invariant action involves gravitational couplings to tensor fields $k_{\alpha\beta\dots}$ that acquire nonzero background values $\bar{k}_{\alpha\beta\dots}$.²² The resulting phenomenology violates local Lorentz invariance due to the presence of nonzero backgrounds and so the backgrounds $\bar{k}_{\alpha\beta\dots}$ are called coefficients for Lorentz violation.²³ The massless Nambu-Goldstone and massive modes associated with spontaneous breaking are contained in the field fluctuations $\tilde{k}_{\alpha\beta\dots} \equiv k_{\alpha\beta\dots} - \bar{k}_{\alpha\beta\dots}$ and can potentially impact the physics.

The Lagrange density of the effective field theory action, focusing on pure gravitational and matter gravity couplings, can be written as the sum of four terms,

$$\mathcal{L} = \mathcal{L}_{\text{EH}} + \mathcal{L}_{\text{LV}} + \mathcal{L}_k + \mathcal{L}_M. \quad (1)$$

The first term is the usual Einstein-Hilbert term is $\mathcal{L}_{\text{EH}} = \sqrt{-g}R/16\pi G_N$, where G_N is Newton's gravitational constant, while the second term \mathcal{L}_{LV} contains the Lorentz-violating couplings. The dynamics of the coefficient fields triggering the spontaneous Lorentz violation are contained in \mathcal{L}_k . Finally, the matter is described by \mathcal{L}_M .

We can also include into the matter sector, the so-called matter-gravity couplings.⁶ These terms are determined from a general Lorentz-violating lagrangian series for Dirac fermions. For classical tests in which spin is irrelevant the physical effects can be shown to be equivalent to a classical action for point particles of the form

$$S_{\text{M,LV}} = - \int d\lambda \left(m \sqrt{-(g_{\mu\nu} + 2c_{\mu\nu})u^\mu u^\nu} - a_\mu u^\mu \right), \quad (2)$$

where $u^\mu = dx^\mu/d\lambda$ is the four velocity of the particle and $c_{\mu\nu}$ and a_μ are the species-dependent coefficients for Lorentz violation that also effectively violate the WEP. Observables for Lorentz violation from this action involve a variety of signals in terrestrial and space-based gravitational tests as well as solar system observations and beyond.⁴ In particular, experiments designed to test the WEP are ideally suited to measure the coefficients a_μ and $c_{\mu\nu}$.²⁰

In the pure-gravity sector, a series involving observer covariant gravitational operators comprise the term \mathcal{L}_{LV} :

$$\mathcal{L}_{LV} = \frac{\sqrt{-g}}{16\pi G_N} (\mathcal{L}_{LV}^{(4)} + \mathcal{L}_{LV}^{(5)} + \mathcal{L}_{LV}^{(6)} + \dots), \quad (3)$$

Each subsequent term involves higher mass dimension d and is formed by contracting covariant derivatives D_α and curvature tensors $R_{\alpha\beta\gamma\delta}$ with the coefficient fields $k_{\alpha\beta\dots}$. Though much of the discussion can be generalized to $d > 6$, here, we consider terms with $4 \leq d \leq 6$.

The first term in the series with $d = 4$ is known as the minimal term $\mathcal{L}_{LV}^{(4)}$ given by

$$\mathcal{L}_{LV}^{(4)} = (k^{(4)})_{\alpha\beta\gamma\delta} R^{\alpha\beta\gamma\delta}, \quad (4)$$

where the coefficient field $(k^{(4)})_{\alpha\beta\gamma\delta}$ is dimensionless.⁵ Due to the contraction with to the Riemann tensor, $(k^{(4)})_{\alpha\beta\gamma\delta}$ has the index symmetries of the Riemann tensor. In particular, the 20 independent coefficients can be decomposed into a traceless part $t_{\alpha\beta\gamma\delta}$ with 10 coefficients, a trace $s_{\alpha\beta}$ with 9 coefficients, and the double trace u .

In the linearized limit of gravity, assuming an origin in spontaneous symmetry breaking, the vacuum value of the coefficient \bar{u} acts as an unobservable rescaling of Newton's constant G_N . In contrast, many phenomenological effects are generated by the $\bar{s}_{\alpha\beta}$ coefficients.^{16,17,18,12} These coefficients have been constrained to various degrees to parts in 10^{10} by numerous analyses using including lunar laser ranging, atom interferometry, short-range tests, satellite ranging, light bending and orbital simulations, precession of orbiting gyroscopes, pulsar timing and spin precession, and solar system ephemeris.^{7,8,14,15,9,11,12,13,9} At leading order in the linearized gravity limit, the coefficients in $\bar{t}_{\alpha\beta\gamma\delta}$ are absent. The physical effects of these 10 independent coefficients remain unknown.³⁷

For the mass dimension 5 term, using covariant derivatives and curvature the general expression is

$$\mathcal{L}_{LV}^{(5)} = (k^{(5)})_{\alpha\beta\gamma\delta\kappa} D^\kappa R^{\alpha\beta\gamma\delta}. \quad (5)$$

The coefficient fields $(k^{(5)})_{\alpha\beta\gamma\delta\kappa}$ can be shown to contain 60 independent quantities by using the properties of the coupling with the covariant derivative and the Riemann tensor. Some features of this term can be determined from its space-time symmetries. Under the operational definition of the CPT transformation, the expression $D^\kappa R^{\alpha\beta\gamma\delta}$ is CPT odd⁵ This can have profound effects for phenomenology. For example, in the nonrelativistic limit the associated Newtonian gravitational force from $\mathcal{L}_{LV}^{(5)}$ would receive pseudovector contributions rather than conventional vector ones. Self accelerations of localized bodies would then occur due to these coefficients. In other sectors, some CPT-odd coefficients with similar issues are known.²⁴ For the higher mass dimension terms, the initial focus is on (stable) corrections to the Newtonian force and so the phenomenology of these coefficients, at higher post-newtonian order, remains an open issue.

For the mass dimension six terms, the coefficient fields are contracted with appropriate powers of curvatures and covariant derivatives, thus we write $\mathcal{L}_{LV}^{(6)}$ in the form

$$\mathcal{L}_{LV}^{(6)} = \frac{1}{2} (k_1^{(6)})_{\alpha\beta\gamma\delta\kappa\lambda} \{D^\kappa, D^\lambda\} R^{\alpha\beta\gamma\delta} + (k_2^{(6)})_{\alpha\beta\gamma\delta\kappa\lambda\mu\nu} R^{\kappa\lambda\mu\nu} R^{\alpha\beta\gamma\delta}. \quad (6)$$

In natural units, the coefficient fields $(k_1^{(6)})_{\alpha\beta\gamma\delta\kappa\lambda}$ and $(k_2^{(6)})_{\alpha\beta\gamma\delta\kappa\lambda\mu\nu}$ have dimensions of squared length, or squared inverse mass. Since the commutator of covariant derivatives is directly related to curvature the anticommutator of covariant derivatives suffices for generality in the first term. The first and last four indices on $(k_2^{(6)})_{\alpha\beta\gamma\delta\kappa\lambda\mu\nu}$ inherit the symmetries of the Riemann tensor as do the first four indices on $(k_1^{(6)})_{\alpha\beta\gamma\delta\kappa\lambda}$. A cyclic-sum condition of the form $\sum_{(\gamma\delta\kappa)} (k_1^{(6)})_{\alpha\beta\gamma\delta\kappa\lambda} = 0$ applies due to the Bianchi identities. These tensor symmetry conditions can be used to determine that there are 126 and 210 independent components in $(k_1^{(6)})_{\alpha\beta\gamma\delta\kappa\lambda}$ and $(k_2^{(6)})_{\alpha\beta\gamma\delta\kappa\lambda\mu\nu}$, respectively.

In an underlying theory, Lorentz-violating derivative couplings of fields to gravity could give rise to the coefficients $(k_1^{(6)})_{\alpha\beta\gamma\delta\kappa\lambda}$. It is straightforward to construct models that produce this type of coupling, although examples are currently unknown to us in the literature. On the hand, in many models specific forms of quadratic Lorentz-violating couplings occur as a result of integrating over fields in the underlying action that have Lorentz-violating couplings to gravity. General quadratic Lorentz-violating curvature couplings are represented by the coefficients $(k_2^{(6)})_{\alpha\beta\gamma\delta\kappa\lambda\mu\nu}$, thus including various models as special cases. For example, models of this type include the cardinal model, various types of bumblebee models, and Chern-Simons gravity.^{25,26,27,28,5} It is also useful to note the implications of introducing these higher derivative terms. It is well known that lagrangian terms with higher than two derivatives can suffer from stability issues. However, in the effective field theory formalism here, these terms with higher derivatives are to be considered only in the perturbative limit, thus they are considered small compared to the conventional terms with only two derivatives.

To extract the linearized modified Einstein equation resulting from the terms (6), we assume an asymptotically flat background metric $\eta_{\alpha\beta}$ as usual, and write the background coefficients as $(\bar{k}_1^{(6)})_{\alpha\beta\gamma\delta\kappa\lambda}$ and $(\bar{k}_2^{(6)})_{\alpha\beta\gamma\delta\kappa\lambda\mu\nu}$. The analysis is performed at linear order in the metric fluctuation $h_{\alpha\beta}$ and we seek results to leading order in the coefficients (assuming they are small). The coefficients are assumed constant in asymptotically flat coordinates. We can re-express the contributions of the fluctuations $\tilde{k}_{\alpha\beta\dots}$ in terms of the metric fluctuations and the background coefficients by imposing the underlying diffeomorphism invariance on the dynamics and that the conservations laws must hold (i.e., covariant conservation and symmetry of the energy-momentum tensor). This procedure yields a modified Einstein equation expressed in terms of $\bar{k}_{\alpha\beta\dots}$ and quantities involving $h_{\alpha\beta}$ such as the linearized curvature tensor. Similar procedures are detailed in the literature.^{16,6} To establish signals for local Lorentz violation in specific experiments, the phenomenology of the modified equation can be studied. An interesting feature of the coefficient fields $(k_2^{(6)})_{\alpha\beta\gamma\delta\kappa\lambda\mu\nu}$ is that for the linearization outlined above the coefficient fluctuations can be neglected because these contribute only at nonlinear order. This feature did not occur in the minimal, mass dimension 4 case.¹⁶

Following the procedure above the linearized modified Einstein equation can be obtained, after some calculation, and it can be written in the compact form

$$G_{\mu\nu} = 8\pi G_N (T_M)_{\mu\nu} - 2\widehat{s}^{\alpha\beta} G_{\alpha(\mu\nu)\beta} - \frac{1}{2}\widehat{u} G_{\mu\nu} + a(\bar{k}_1^{(6)})_{\alpha(\mu\nu)\beta\gamma\delta} \partial^\alpha \partial^\beta R^{\gamma\delta} + 4(\bar{k}_2^{(6)})_{\alpha\mu\nu\beta\gamma\delta\epsilon\zeta} \partial^\alpha \partial^\beta R^{\gamma\delta\epsilon\zeta}, \quad (7)$$

where double dual of the Riemann tensor is $G_{\alpha\beta\gamma\delta} \equiv \epsilon_{\alpha\beta\kappa\lambda} \epsilon_{\gamma\delta\mu\nu} R^{\kappa\lambda\mu\nu} / 4$ and the Einstein tensor is $G_{\alpha\beta} \equiv G^\gamma_{\alpha\gamma\beta}$. All gravitational tensors are understood to be linearized in $h_{\mu\nu}$ in Eq. (7). For notational convenience, the ‘‘hat’’ notation is used for the following operators:

$$\begin{aligned} \widehat{u} &= -2\bar{u} + (\bar{u}_1^{(6)})_{\alpha\beta} \partial^\alpha \partial^\beta, \\ \widehat{s}_{\alpha\beta} &= \frac{1}{2}\bar{s}_{\alpha\beta} + (\bar{s}_1^{(6)})_{\alpha\beta\gamma\delta} \partial^\gamma \partial^\delta, \end{aligned} \quad (8)$$

where $(\bar{u}_1^{(6)})_{\gamma\delta} \equiv (\bar{k}_1^{(6)})^{\alpha\beta}_{\alpha\beta\gamma\delta}$ and $(\bar{s}_1^{(6)})^\alpha_{\beta\gamma\delta} \equiv (\bar{k}_1^{(6)})^{\alpha\epsilon}_{\beta\epsilon\gamma\delta} - \delta^\alpha_\beta (\bar{u}_1^{(6)})_{\gamma\delta} / 4$. The factors in front of the \bar{u} and \bar{s} are chosen to match earlier work in the mass dimension 4 case. For the $d = 4$ Lorentz-violating term (4), the entire contribution is contained in \widehat{u} and $\widehat{s}_{\alpha\beta}$. There are also $d = 6$ terms contained in \widehat{u} and $\widehat{s}_{\alpha\beta}$. A model-dependent real number a remains in Eq. (7) that depends on the underlying dynamics specified by the Lagrange density \mathcal{L}_k . Furthermore, the quantity a may be measurable independently of the coefficients $(\bar{k}_1^{(6)})_{\alpha\beta\gamma\delta\kappa\lambda}$ and $(\bar{k}_2^{(6)})_{\alpha\beta\gamma\delta\kappa\lambda\mu\nu}$, revealing a way to extract information about the dynamics behind spontaneous Lorentz symmetry breaking, should it occur in nature.

Numerous phenomenological consequences both for relativistic effects, including gravitational waves, and effects in post-newtonian gravity are likely to be implied by the modified

Einstein equation (7). Since we expect the mass dimension 6 terms to be dominant on short distance scales, we consider the nonrelativistic limit and assume a source with mass density $\rho(\mathbf{r})$. In this limit, a modified Poisson equation is revealed:

$$-\bar{\nabla}^2 U = 4\pi G_N \rho + (\bar{k}_{\text{eff}})_{jk} \partial_j \partial_k U + (\bar{k}_{\text{eff}})_{jklm} \partial_j \partial_k \partial_l \partial_m U, \quad (9)$$

where the modified Newton gravitational potential is $U(\mathbf{r})$. The effective coefficients for Lorentz violation with totally symmetric indices in this equation are $(\bar{k}_{\text{eff}})_{jk}$ and $(\bar{k}_{\text{eff}})_{jklm}$. The former are associated with mass dimension 4 and are related to the \bar{s}_{00} , \bar{s}_{jk} and \bar{u} coefficients and are detailed in Ref. 16, while the latter depend on the mass dimension 6 coefficients and are the primary focus of more recent work. The effective coefficients $(\bar{k}_{\text{eff}})_{jklm}$ are linear combinations of the $d = 6$ coefficients $(k_1^{(6)})_{\alpha\beta\gamma\delta\kappa\lambda}$ and $(k_2^{(6)})_{\alpha\beta\gamma\delta\kappa\lambda\mu\nu}$. Since it is largely irrelevant for present purposes, we omit the explicit lengthy form of this relationship. Nonetheless it is important to note that many of the independent components $(k_1^{(6)})_{\alpha\beta\gamma\delta\kappa\lambda}$ and $(k_2^{(6)})_{\alpha\beta\gamma\delta\kappa\lambda\mu\nu}$ appear.

With the Lorentz-violating term assumed to generate a small correction to the usual Newtonian potential, we can adopt a perturbative approach to solve the modified Poisson equation (9). On the length scales of experimental interest, the $d = 6$ Lorentz-violating term (6) represents a perturbative correction to the Einstein-Hilbert action, thus the perturbative approach is consistent with this method of solution. Though it involves theoretical complexities that lie outside the present scope, the nonperturbative scenario with $\mathcal{L}_{\text{LV}}^{(6)}$ dominating the physics could in principle also be of interest.

The solution to the modified Poisson equation (9) for $d = 6$, within the perturbative assumption, is given by

$$U(\mathbf{r}) = G_N \int d^3 r' \frac{\rho(\mathbf{r}')}{|\mathbf{r} - \mathbf{r}'|} \left(1 + \frac{\bar{k}(\hat{\mathbf{R}})}{|\mathbf{r} - \mathbf{r}'|^2} \right) + \frac{4}{5} \pi G_N \rho(\mathbf{r}) (\bar{k}_{\text{eff}})_{jkjk}. \quad (10)$$

In addition to the conventional Newtonian potential, (10) contains a Lorentz-violating correction term that varies with the inverse cube of the distance. Adopting the convenient notation for the unit vector $\hat{\mathbf{R}} = (\mathbf{r} - \mathbf{r}')/|\mathbf{r} - \mathbf{r}'|$, the anisotropic combination of coefficients $\bar{k} = \bar{k}(\hat{\mathbf{r}})$ is a function of $\hat{\mathbf{r}}$ given by

$$\bar{k}(\hat{\mathbf{r}}) = \frac{3}{2} (\bar{k}_{\text{eff}})_{jkjk} - 9 (\bar{k}_{\text{eff}})_{jkil} \hat{r}^j \hat{r}^k + \frac{15}{2} (\bar{k}_{\text{eff}})_{jklm} \hat{r}^j \hat{r}^k \hat{r}^l \hat{r}^m. \quad (11)$$

In parallel with the usual dipole contact term in electrodynamics, the final piece in (10) is a contact term that becomes a delta function in the point-particle limit. Interestingly this last term is absent for the mass dimension 4 solution, showing up only starting at mass dimension 6. Via the Newtonian gravitational field $\mathbf{g} = \nabla U$, an inverse-quartic gravitational field results from the inverse-cube behavior of the potential^a. Short-range gravity tests measure the deviation from the Newton gravitational force between two masses, and the rapid growth of the force at small distances suggests that the best sensitivities to Lorentz violation could be achieved in experiments of this type.²⁹

3 Short-range gravity tests

Sensitivity to the coefficients $(\bar{k}_{\text{eff}})_{jklm}$ occurs instantaneously through the measurements of the force between two masses in an Earth-based laboratory frame. The Earth's rotation about its axis and revolution about the Sun induce variations of these coefficients with sidereal time T , since the laboratory frame is noninertial. The Sun-centered frame is the canonical frame adopted for reporting results from experimental searches for Lorentz violation^{2,30}. In this frame, \mathbf{Z} points

^aFor this analysis, we assume a conventional matter sector with the acceleration of test bodies being $\mathbf{a} = \mathbf{g}$. This can be generalized to include effects from other sectors.⁶

along the direction of the Earth's rotation and the X axis points towards the vernal equinox 2000. To relate the laboratory frame (x, y, z) to the Sun-centered frame (X, Y, Z) , a time-dependent rotation R^{jJ} is used if we neglect the Earth's boost (which is of order 10^{-4}), where $j = x, y, z$ and $J = X, Y, Z$. In terms of constant coefficients $(\bar{k}_{\text{eff}})_{JKLM}$ in the Sun-centered frame, the T -dependent coefficients $(\bar{k}_{\text{eff}})_{jklm}$ in the laboratory frame are given by

$$(\bar{k}_{\text{eff}})_{jklm} = R^{jJ} R^{kK} R^{lL} R^{mM} (\bar{k}_{\text{eff}})_{JKLM}. \quad (12)$$

One standard commonly adopted is to take the laboratory x axis pointing to local south, the z axis pointing to the local zenith. This convention yields the following rotation matrix:

$$R^{jJ} = \begin{pmatrix} \cos \chi \cos \omega_{\oplus} T & \cos \chi \sin \omega_{\oplus} T & -\sin \chi \\ -\sin \omega_{\oplus} T & \cos \omega_{\oplus} T & 0 \\ \sin \chi \cos \omega_{\oplus} T & \sin \chi \sin \omega_{\oplus} T & \cos \chi \end{pmatrix}. \quad (13)$$

The Earth's sidereal rotation frequency is $\omega_{\oplus} \simeq 2\pi/(23 \text{ h } 56 \text{ min})$ and the angle χ is the colatitude of the laboratory. The modified potential U and the force between two masses measured in the laboratory frame will vary with time T as a result of the sidereal variation of the laboratory-frame coefficients.

One simple application is the point-mass M modified potential. To extract the time dependence, Eq. (12) is used to express the combination $\bar{k}(\hat{\mathbf{r}}, T)$ in Eq. (11) in terms of coefficients $(\bar{k}_{\text{eff}})_{JKLM}$ in the Sun-centered frame. For points away from the origin, the potential then takes the form

$$U(\mathbf{r}, T) = \frac{G_N M}{r} \left(1 + \frac{\bar{k}(\hat{\mathbf{r}}, T)}{r^2} \right). \quad (14)$$

This contains novel signals in short-range experiments, where the modified force depends both on direction and sidereal time. In particular, the effective gravitational force between two bodies can be expected to vary with frequencies up to and including the fourth harmonic of ω_{\oplus} due to the time dependence in Eq. (12).

An asymmetric dependence of the signal on the shape of the bodies is implied by the direction dependence of the laboratory-frame coefficients $(\bar{k}_{\text{eff}})_{jklm}$. In conventional Newton gravity, the force on a test mass at any point above an infinite plane of uniform mass density is constant, and this result remains true for the potential (14). However, it is typically necessary to determine the potential and force via numerical integration for the finite bodies used in experiments. It turns out that shape and edge effects play an critical role in determining the sensitivity of the experiment to the coefficients for Lorentz violation, as suggested by some simple simulations for experimental configurations such as two finite planes or a plane and a sphere^{31,32,35}

An anisotropic inverse-cube correction to the usual Newtonian result is involved in the modified potential (14). Existing experimental limits on spherically symmetric inverse-cube potentials cannot be immediately converted into constraints on the coefficients $(\bar{k}_{\text{eff}})_{JKLM}$. This is due to the time and orientation dependence of the Lorentz-violating signal, whereas typical experiments collect data over an extended period and disregard the possibility of orientation-dependent effects. Thus new experimental analyses will be required for establishing definitive constraints on the coefficients $(\bar{k}_{\text{eff}})_{JKLM}$ for Lorentz violation.

It is useful to identify a measure of the reach of a given experiment, given the novel features of short-range tests of local Lorentz violation in gravity and the wide variety of experiments in the literature. Generally, a careful simulation of the experiment is required, but rough estimates can be obtained by comparing the Lorentz-violating potential with the potential modified by a two parameter (α, λ) Yukawa-like term, $U_{\text{Yukawa}} = G_N M (1 + \alpha e^{-r/\lambda})/r$, which is commonly used for experiments testing short-range gravity. Sensitivities to Lorentz violation of order $|\bar{k}(\hat{\mathbf{r}}, T)| \approx \alpha \lambda^2/e$ are indicated by comparing the Yukawa form with the potential (14) assuming distances $r \approx \lambda$. Thus using Eq. (11), the sensitivity to combinations of coefficients is approximately

$$|(\bar{k}_{\text{eff}})_{JKLM}| \approx \alpha \lambda^2/10. \quad (15)$$

Note that the experiment must be able to detect the usual Newtonian gravitational force in order to have sensitivity to the perturbative Lorentz violation considered here. This is the case for a subset of experiments reported in the literature. Also, distinct linear combinations of $(\bar{k}_{\text{eff}})_{JKLM}$ will be accessed by different experiments.

Experiments at small λ that are sensitive to the usual Newtonian force are the most interesting short-range experiments within this perspective. For example, eq. (15) gives the estimate $\alpha \simeq 10^{-3}$ at $\lambda \simeq 10^{-3}$ m for the Wuhan experiment which implies the sensitivity $|(\bar{k}_{\text{eff}})_{JKLM}| \simeq 10^{-10}$ m².³⁵ However, due to the geometry of this experiment, edge effects reduce the sensitivity by about a factor of 100 and the limits recently obtained are at the 10^{-8} m² level. The EötWash torsion pendulum experiment, which has been used to place limits on isotropic power law deviations from the inverse square law, achieves sensitivity of order $\alpha \simeq 10^{-2}$ at $\lambda \simeq 10^{-4}$ m.^{33,34} Thus suggests Lorentz violation can be measured at the level of $|(\bar{k}_{\text{eff}})_{JKLM}| \simeq 10^{-11}$ m², in agreement with the estimate from a simple simulation.¹⁹ Other experiments of interest include the Irvine experiment which achieved $\alpha \simeq 3 \times 10^{-3}$ at $\lambda \simeq 10^{-2}$ m, and should be able to obtain $|(\bar{k}_{\text{eff}})_{JKLM}| \simeq 3 \times 10^{-8}$ m².³⁶ Sitting on the cusp of the perturbative limit, the Indiana experiment achieves $\alpha \simeq 1$ at $\lambda \simeq 10^{-4}$ m. Naively, we would expect an estimated sensitivity of order $|(\bar{k}_{\text{eff}})_{JKLM}| \simeq 10^{-9}$ m².³¹ However, since this test uses flat plates, edge effects end up suppressing the sensitivity to the 10^{-7} m² level.¹⁴ There are also many other experiments that can potentially probe for the $(\bar{k}_{\text{eff}})_{JKLM}$ coefficients, including ones discussed at this conference.³⁸

Note that the predicted effects can be quite large while having escaped detection to date in some gravity theories with violations of Lorentz invariance.⁶ Because the Planck length $\simeq 10^{-35}$ m lies far below the length scale accessible to existing laboratory experiments on gravity, the above estimates suggest terms in the pure-gravity sector with $d > 4$ are interesting candidates for these “countershaded” effects. In any case, the Einstein equivalence principle for the gravity sector can be established on a firm and complete experimental footing with the types of analysis described here. In particular, short-range tests of gravity offer an excellent opportunity to search for local Lorentz violation involving operators of higher mass dimension.

Acknowledgements

Travel and housing to present this work was supported by the National Science Foundation under grant number PHY-1402890 and by the Moriond Conference Organizing Committee.

References

1. C.M. Will, *Liv. Rev. Rel.* **17**, 4 (2014).
2. V.A. Kostelecký and N. Russell, *Data Tables for Lorentz and CPT Violation*, 2015 edition, arXiv:0801.0287v8.
3. V.A. Kostelecký and S. Samuel, *Phys. Rev. D* **39**, 683 (1989).
4. J. Tasson, *Rep. Prog. Phys.* **77**, 062901 (2014).
5. V.A. Kostelecký, *Phys. Rev. D* **69**, 105009 (2004).
6. V.A. Kostelecký and J.D. Tasson, *Phys. Rev. Lett.* **102**, 010402 (2009); *Phys. Rev. D* **83**, 016013 (2011).
7. J.B.R. Battat, J.F. Chandler, and C.W. Stubbs, *Phys. Rev. Lett.* **99**, 241103 (2007).
8. H. Müller *et al.*, *Phys. Rev. Lett.* **100**, 031101 (2008); K.-Y. Chung *et al.*, *Phys. Rev. D* **80**, 016002 (2009).
9. L. Iorio, *Class. Quant. Grav.* **29**, 175007 (2012).
10. M.A. Hohensee *et al.*, *Phys. Rev. Lett.* **106**, 151102 (2011); *Phys. Rev. Lett.* **111**, 151102 (2013).

11. A. Hees *et al.*, in *Proceedings of the 13th Marcel Grossmann meeting*, edited by K. Rosquist, R.T. Jantzen and R. Ruffini (World Scientific, Singapore, 2015), arXiv:1301.1658v3.
12. Q.G. Bailey, R.D. Everett, and J.M. Overduin, *Phys. Rev. D* **88**, 102001 (2013).
13. L. Shao, *Phys. Rev. Lett.* **112**, 111103 (2014); *Phys. Rev. D* **90**, 122009 (2014).
14. J.C. Long and V.A. Kostelecký, *Phys. Rev. D* **91**, 092003 (2015).
15. C.-G. Shao *et al.*, arXiv:1504.03280.
16. Q.G. Bailey and V.A. Kostelecký, *Phys. Rev. D* **74**, 045001 (2006).
17. Q.G. Bailey, *Phys. Rev. D* **80**, 044004 (2009); *Phys. Rev. D* **82**, 065012 (2010).
18. R. Tso and Q.G. Bailey, *Phys. Rev. D* **84**, 085025 (2011).
19. Q.G. Bailey, V.A. Kostelecký, and R. Xu, *Phys. Rev. D* **91**, 022006 (2015).
20. S. Dimopoulos *et al.*, *Phys. Rev. Lett.* **98**, 111102 (2007); *Phys. Rev. D* **78**, 042003 (2008); A.M. Nobili *et al.*, *Exp. Astron.* **23**, 689 (2009); B. Altschul *et al.*, *Advances in Space Research* **55**, 501 (2015), M. Rodrigues, G. Tino, P. Wolf, these proceedings.
21. R. Bluhm, *Phys. Rev. D* **91**, 065034 (2015).
22. The tensor fields $k_{\alpha\beta\dots}$ can also include derivatives of scalars. See, for example, V.A. Kostelecký, R. Lehnert, and M.J. Perry, *Phys. Rev. D* **68**, 123511 (2003); N. Arkani-Hamed *et al.*, *JHEP* **0405**, 074 (2004).
23. D. Colladay and V.A. Kostelecký, *Phys. Rev. D* **55**, 6760 (1997); *Phys. Rev. D* **58**, 116002 (1998).
24. V.A. Kostelecký and M. Mewes, *Phys. Rev. D* **80**, 015020 (2009); *Phys. Rev. D* **85**, 096005 (2012); *Phys. Rev. D* **88**, 096006 (2013).
25. R. Jackiw and S.Y. Pi, *Phys. Rev. D* **68**, 104012 (2003).
26. S. Alexander and N. Yunes, *Phys. Rep.* **480**, 1 (2009).
27. V.A. Kostelecký and R. Potting, *Gen. Rel. Grav.* **37**, 1675 (2005); *Phys. Rev. D* **79**, 065018 (2009).
28. V.A. Kostelecký and S. Samuel, *Phys. Rev. D* **40**, 1886 (1989); C. Hernaski and H. Belich, *Phys. Rev. D* **89**, 104027 (2014); A.B. Balakin and J.P.S. Lemos, *Ann. Phys.* **350**, 454 (2014).
29. For reviews see, for example, J. Murata and S. Tanaka, arXiv:1408.3588; E. Fischbach and C. Talmadge, *The Search for Non-Newtonian Gravity*, Springer-Verlag, 1999.
30. V.A. Kostelecký and M. Mewes, *Phys. Rev. D* **66**, 056005 (2002); R. Bluhm *et al.*, *Phys. Rev. Lett.* **88**, 090801 (2002); *Phys. Rev. D* **68**, 125008 (2003).
31. J.C. Long *et al.*, *Nature* **421**, 922 (2003); H. Yan *et al.*, *Class. Quant. Grav.* **31**, 205007 (2014).
32. R.S. Decca *et al.*, *Phys. Rev. Lett.* **94**, 240401 (2005); Y.-J. Chen *et al.*, arXiv:1410.7267.
33. C.D. Hoyle *et al.*, *Phys. Rev. D* **70**, 042004 (2004); D.J. Kapner *et al.*, *Phys. Rev. Lett.* **98**, 021101 (2007).
34. E.G. Adelberger *et al.*, *Phys. Rev. Lett.* **98**, 131104 (2007).
35. L.C. Tu *et al.*, *Phys. Rev. Lett.* **98**, 201101 (2007); S.-Q. Yang *et al.*, *Phys. Rev. Lett.* **108**, 081101 (2012).
36. J.K. Hoskins *et al.*, *Phys. Rev. D* **32**, 3084 (1985).
37. Y. Bonder, arXiv:1506.03636.
38. V. Nesvizhevsky, M. Lopez, P. Hamilton, these proceedings.

Lorentz violation in gravity

Diego Blas

CERN, Theory Division, 1211 Geneva, Switzerland.

The study of gravitational theories without Lorentz invariance plays an important role to understand different aspects of gravitation. In this short contribution we will describe the construction, main advantages and some phenomenological considerations associated with the presence of a preferred time direction.

1 Introduction

One hundred years after its formulation, General Relativity (GR) is living a golden era of continuous verifications of its predictions, at many scales and in very different processes^{1,2,3}. The agreement of data with GR predictions is both astonishing (given the range of scales probed) and frustrating (since GR can not be a complete quantum theory, but we lack experimental guidance towards its completion)⁴.

Besides confirming the predictions of GR, the current data can also be used to constrain possible deviations. This is an important program from which we can learn about the robustness of the different properties of GR, the benefits of modifying them and the viability of the resulting alternative theories. This brief note is devoted to a particular modification suggested by theories of gravity with a better quantum behaviour than GR. To attain this, they abandon one of the principles of GR: Lorentz invariance. We will only discuss the case of a preferred frame defining a time direction at every point of space-time. After introducing the formalism and explaining its possible relation to quantum gravity, we will proceed to derive some of its phenomenological consequences. For further information, the reader can consult the recent review paper⁴.

2 Theoretical construction

We will consider metric theories where there is a local preferred time direction represented by a time-like vector field u^μ satisfying

$$u_\mu u^\mu = 1. \tag{1}$$

If this vector is otherwise generic, these theories are known as Einstein-aether theories⁵. Their relation to quantum gravity is not completely clear, but their study may be important for fundamental theories of gravity where Lorentz invariance is broken (spontaneously or fundamentally) by the selection of a preferred frame. A more concrete example of how this may happen is provided by Hořava gravity, which assumes the existence of a preferred foliation of space-time into space-like hypersurfaces⁶. This allows to construct a theory of gravity renormalizable by

⁴The existence of dark matter and dark energy is sometimes considered as a hint towards the construction of alternatives to GR. This motivation is certainly valid though the standard paradigm based on GR is consistent both theoretically and phenomenologically.

power-counting and close to GR at low-energies. In terms of the vector satisfying (1), the theory requires the existence of a field φ representing the foliation and

$$u_\mu \equiv \frac{\partial_\mu \varphi}{\sqrt{g^{\mu\nu} \partial_\mu \varphi \partial_\nu \varphi}}. \quad (2)$$

The generic theories defined with a vector of the form (2) are known as khronometric theories⁷. To construct the action we write the different operators including u^μ and $g^{\mu\nu}$, covariant under diffeomorphisms and organized in a derivative expansion (we also assume CPT),

$$S = -\frac{M_0^2}{2} \int d^4x \sqrt{-g} \left(R + K^{\alpha\beta}{}_{\mu\nu} \nabla_\alpha u^\mu \nabla_\beta u^\nu + \lambda(u^\mu u_\mu - 1) + \frac{\mathcal{O}^{n+2}}{M_\star^n} \right), \quad (3)$$

where g and R are the metric determinant and the Ricci scalar and

$$K^{\alpha\beta}{}_{\mu\nu} \equiv c_1 g^{\alpha\beta} g_{\mu\nu} + c_2 \delta_\mu^\alpha \delta_\nu^\beta + c_3 \delta_\nu^\alpha \delta_\mu^\beta + c_4 u^\alpha u^\beta g_{\mu\nu}, \quad (4)$$

We use the constant M_0 instead of M_P for the mass scale in front of the Einstein-Hilbert action to distinguish it from the quantity appearing in Newton's law⁴. By the last term in (3) we indicate the higher dimensional operators, which we assume to be suppressed by a common scale M_\star . We imposed the restriction (1) through a Lagrange multiplier λ . In the khronometric case, this is not necessary. Furthermore, the condition (2) implies that one of the terms in (4) can be expressed in terms of the others. One then absorbs the c_1 term into the other three terms by multiplying the second, third and fourth term respectively by the new couplings

$$\lambda \equiv c_2, \quad \beta \equiv c_3 + c_1, \quad \alpha \equiv c_4 + c_1. \quad (5)$$

For a reformulation of (3) in terms of geometrical quantities of the congruences of u^μ see⁸.

3 Short distance modifications

Let us first discuss the operators of (3) suppressed by the scale M_\star . Since we suppose that Lorentz invariance is broken in a regime where gravity is weakly coupled, one can start parameterizing the changes in gravitation by considering linear equations for the perturbations of the metric with Lorentz violating (LV) terms. Assuming that parity and time reversal are not violated and that the equations are at most second order in time derivatives, we can introduce the dispersion relations

$$\omega^2 = p^2 \left(1 + \sum_{n=1}^L \alpha_n \left(\frac{p}{M_\star^{g^w}} \right)^{2n} \right), \quad (6)$$

for the propagating degrees of freedom (e.g the graviton) and the modified Poisson's equation

$$p^2 \left(1 + \sum_{n=1}^L \beta_n \left(\frac{p}{M_\star^\phi} \right)^{2n} \right) \phi = -\frac{1}{2M_0^2} \tau_{00}, \quad (7)$$

for the potentials ϕ sourced by matter's energy, represented by τ_{00} . The mass scales M_\star^ϕ and $M_\star^{g^w}$ are kept independent, even if they are both related to M_\star .

Let us first discuss the modifications of the graviton's dispersion relation, Eq. (6). If the gravitational waves (GW) have the dispersion relation (6), this modifies the frequency dependence in the propagation of the wave-fronts, which may be observed by future detectors of GW. These effects will be very suppressed if we assume that $M_\star^{g^w} \approx M_\star^\phi$, given that the latter are constrained to be $M_\star^\phi < (\mu m)^{-1} \approx 10^{-2}$ eV (see below). They may still have an impact for the GWs generated in the primordial universe since in this case the typical energies during production may be almost as high as M_P . Thus, if primordial GWs are observed, the range of energies at which LV is tested (in fact any short-distance modification) will improve dramatically.

More is known about possible deviations of the potentials at high-energies, Eq. (7). Let us focus on the case relevant for the short distance behaviour of Hořava gravity where only $\beta_2 \neq 0$, and absorb its value into M_\star^ϕ ($M_\star^\phi \mapsto M_\star^\phi \beta_2^{1/4} 2^{1/8}$). Taking a point particle of mass m_{pp} at rest as a source, the solution of Eq. (7) away from the source is

$$\phi = -\frac{m_{pp}}{8\pi M_0^2 r} \left[1 - e^{-M_\star^\phi r} \cos(M_\star^\phi r) \right], \quad (8)$$

where r is the distance from the source. This potential regularises the divergent behaviour of Newton's potential at small distances. Furthermore, at scales where the deviations start to be important, it is similar to the potentials that have been considered to constrain the deviations from Newton's law at short distances¹⁰

$$\phi = -\frac{m_{pp}}{8\pi M_0^2 r} \left[1 + \tilde{\alpha} e^{-r/\tilde{\lambda}} \right]. \quad (9)$$

From these works, one concludes that a bound of the form $M_\star^\phi \lesssim (\mu m)^{-1}$ should apply. However, the differences between the potentials of Eq. (9) and (8) are important, e.g. the potentials in (9) are singular at short distances except for $\tilde{\alpha} = -1$ and they do not present the oscillatory behaviour of (8). Thus, a precise bound on M_\star^ϕ requires a reanalysis of the experimental data.

Finally, even though our previous discussion was organised around the modified equations (6) and (7), the effects of LV at short distances (high energies) may also be important for the background evolution in the primordial universe, see⁴ for the relevant references.

4 Long distance modifications

By long distance modifications we mean the theory whose gravitational action is given by (3) in the limit $M_\star \rightarrow \infty$. Independently of the coupling to matter, some bounds can be derived on the constants c_i from stability of perturbations around a Minkowski background and requiring the absence of gravitational Cherenkov radiation⁴. To find the phenomenological predictions of the theory we first need to understand how u^μ and $g_{\mu\nu}$ couple to matter. In principle, any coupling should be allowed. The generic consequence would be the presence of big deviations from Lorentz invariance also in the standard model of particle physics. These deviations are extremely small, cf.¹¹, which makes it natural to assume that, as long as gravitational test are concerned, matter is not coupled to u^μ at all. Explaining how this can happen in a natural way while keeping the other couplings to u^μ not too small remains an open challenge for the set-up. Different possibilities have been explored⁴, but no definite mechanism has been produced yet. Notice that for dark matter and dark energy one can keep these couplings arbitrary.

Bounds on the LV parameters in (3) come from different observations. Assuming that the preferred frame u^μ is aligned with the CMB, which is a reasonable supposition^{1,4}, one finds that the gravitational potential in the Solar System is modified by the presence of two post-Newtonian parameters α_1 and α_2 . These two parameters are functions of the LV parameters. For instance, for the khronometric parameters (5) they read

$$\alpha_1 = -4(\alpha - 2\beta), \quad \alpha_2 = \frac{(\alpha - 2\beta)(\alpha - \lambda - 3\beta)}{2(\lambda + \beta)}. \quad (10)$$

Current observations yield the bounds¹ $|\alpha_1| < 10^{-4}$ and $|\alpha_2| < 10^{-7}$.

Further bounds can be obtained from strongly gravitating bodies. In this case, even if matter is not coupled to u^μ , the gravitons in the body are, and for objects with large gravitational fields (very compact) the body as a whole will *effectively* feel the presence of u^μ . To parametrize this for the phenomena at large distances with respect to the size of the source, one can assume the action of the point particle to be

$$S_{pp\ A} = - \int ds_A \tilde{m}_A(\gamma_A), \quad (11)$$

where \tilde{m}_A is a function of $\gamma_A \equiv u_\mu v_A^\mu$ and v_A^μ is the four-velocity of the source (see¹² for similar descriptions in scalar-tensor theories). Finally, ds_A is the line element of the trajectory. If $\gamma_A \ll 1$, one can expand the action to second order in γ_A and describe the physics in terms of

$$\tilde{m}_A|_{\gamma_A=1}, \quad \sigma_A \equiv - \left. \frac{d \ln \tilde{m}_A(\gamma_A)}{d \ln \gamma_A} \right|_{\gamma_A=1}. \quad (12)$$

The parameters σ_A are called *sensitivities* and represent the effective coupling of the source to u^μ . The presence of these couplings introduces an extra force in the dynamics of binary systems, which precludes the conservation of the usual momentum sourcing gravitational waves⁹. This implies the emission of dipolar radiation, which is absent in GR. Since the latter is enhanced with respect to the quadrupolar radiation by a factors $(c/v)^2$, where v is the typical orbital velocity of the system, this means that even for very small σ_A (corresponding to neutron stars), one can get very tight bounds on the LV parameter space by observing the radiation damping of binary pulsars⁹. The same is also true for solitary pulsars, where the bounds come from changes in the spin-precession. For these bounds to relate to the fundamental parameters in (3) one needs to compute the numbers σ_A for different sources, which was done in⁹.

Finally, cosmological observations produce further bounds on the LV parameters. Remarkably, these also apply to the possible LV in the dark matter. The bounds come from different observations: first, the Friedmann equation is modified by a renormalization of Newton's constant depending on the LV parameters. This deviation can be constrained with the data from big bang nucleosynthesis, by the growth of structure (controlled by the local G_N) and CMB observations¹³. Furthermore, the existence of the vector field u^μ introduces a source of anisotropic stress present at many scales, and which can be constrained by CMB observations. Similarly, the possible coupling of dark matter to u^μ introduces an extra force in dark matter, which may violate the weak equivalence principle. This has consequences for the gravitational dynamics of dark matter¹³. The cosmological observations from the regimes where linearized cosmology is applicable imply bounds close to the percent level for all the previous couplings¹³. These bounds will improve once the consequences for non-linear scales (scales below 10 Mpc) are understood.

References

1. C. M. Will, arXiv:1409.7871 [gr-qc].
2. E. Berti, E. Barausse, V. Cardoso, L. Gualtieri, P. Pani, U. Sperhake, L. C. Stein and N. Wex *et al.*, arXiv:1501.07274 [gr-qc].
3. T. Clifton, P. G. Ferreira, A. Padilla and C. Skordis, Phys. Rept. **513** (2012) 1
4. D. Blas and E. Lim, Int. J. Mod. Phys. D **23** (2015) 13, 1443009
5. T. Jacobson and D. Mattingly, Phys. Rev. D **64** (2001) 024028
6. P. Horava, Phys. Rev. D **79** (2009) 084008
7. D. Blas, O. Pujolas and S. Sibiryakov, JHEP **1104** (2011) 018
8. T. Jacobson, Phys. Rev. D **89** (2014) 8, 081501
9. K. Yagi, D. Blas, E. Barausse and N. Yunes, Phys. Rev. D **89** (2014) 084067
10. D. J. Kapner, T. S. Cook, E. G. Adelberger, J. H. Gundlach, B. R. Heckel, C. D. Hoyle and H. E. Swanson, Phys. Rev. Lett. **98** (2007) 021101
11. S. Liberati, Class. Quant. Grav. **30** (2013) 133001
12. T. Damour and G. Esposito-Farese, Class. Quant. Grav. **9** (1992) 2093.
13. B. Audren, D. Blas, M. M. Ivanov, J. Lesgourgues and S. Sibiryakov, JCAP **1503** (2015) 03, 016

^bThere is still a conserved momentum associated with translation invariance, but it differs from the one of GR.

GINGER - A terrestrial experiment to verify the Lense-Thirring effect or possible deviations from General Relativity

A. TARTAGLIA

*Department of Applied Science and Technology, Politecnico di Torino, 24 Corso Duca degli Abruzzi,
10129 Torino, Italy*

After reviewing the signal to be expected from a ring laser of convenient size, located on earth, the project of a three-dimensional array of ring lasers named GINGER is presented. The sensitivity analysis is discussed, stressing that the available techniques for research lasers do allow for the detection of general relativistic effects originated by the mass and the angular momentum of the earth. The project is under development at the Gran Sasso National Laboratories of the INFN in Italy. Two intermediate instruments in the road towards the full GINGER have been built, one in Pisa (GP2) and one at the Gran Sasso (GINGERino). They are being used to validate the dynamical control of the geometry and to characterize the site allotted to the experiment.

1 Introduction

General Relativity (GR) is a most powerful and elegant theory, whose successes in describing the evolution of the universe and the behaviour of matter in strong gravitational fields are well established. Though there are reasons not to leave it as unchallenged and unperfectable. First there is the fundamental incompatibility with quantum mechanics, but, besides that, there is the requirement to allow for dark matter and dark energy in order to account for the behaviour of the universe on large enough scales. These remarks tell us that it is worthwhile to pursue the experimental verification of all predicted consequences of GR. The high energy or strong field domain pertains to cosmology and astrophysics, but the theory has also peculiar predictions in the domain of ultra-low energies. In particular it is useful and important to explore the relativistic effects of the motion, and especially the proper rotation, of masses producing gravity. Those effects are often qualified, altogether, as *gravito-magnetic*. The number of direct experiments in that area is limited and they have all been performed in space, facing various problems of averaging along the orbits and necessary knowledge of the gravito-electric (Newtonian) component of the gravitational field. ^{1,2,3,4,5,6}

Here I present a terrestrial experiment, based on ring laser technology, aimed to the detection of the GR effects associated with the rotation of the earth. The advantages of a ground based experiment are: lower cost with respect to experiments in space; hands on setting, allowing for immediate and direct intervention to amend configuration faults or to allow for real time changes of strategy; fixed position in the gravitational field of the earth allowing for point measurements, without averaging over different field configurations.

2 Small effects in General relativity

Considering a freely falling test particle, the equation of its geodetic space-time trajectory, in terms of the velocity four-vector u^μ and the Christoffel symbols $\Gamma_{\mu\nu}^\alpha$, may be written as

$$\frac{du^\alpha}{ds} + \Gamma_{00}^\alpha (u^0)^2 + 2\Gamma_{0i}^\alpha u^0 u^i + \Gamma_{ij}^\alpha u^i u^j = 0 \quad (1)$$

Two terms in the above formula depend on the space velocity of the test particle. It can be safely assumed that in most cases the velocity is much smaller than c . In other words, we may assume $u^0 \sim 1$ and $u^i \ll 1$. In a terrestrial non-rotating reference frame, the ratio of practical speeds to the speed of light is typically in the order of 10^{-6} . With such values, we may neglect the terms quadratic in the space velocities with respect to the linear ones. Finally we see that in non-relativistic (in the sense of 'low' velocity) approximation the four acceleration of a freely falling test particle is composed by a dominant term, independent from the velocity of the body, plus terms linearly depending on that velocity. The former term depends on the gravitational potential: we may say it to be due to the *gravito-electric* field. The latter terms are the analog of the Lorentz force of electromagnetism, and they are ascribed to the *gravito-magnetic* field.

As we have seen, the relevance of the gravito-magnetic effects is controlled by the Christoffels. The next step is to consider a static gravitational field, which is quite reasonable in the case of the earth. If so, all time derivatives in the Christoffels go to zero and we end with the explicit gravito-magnetic form

$$\Gamma_{0i}^\alpha = \frac{1}{2} g^{\alpha\beta} \left(\frac{\partial g_{0\beta}}{\partial x^i} - \frac{\partial g_{0i}}{\partial x^\beta} \right) = \frac{1}{2} g^{\alpha 0} \frac{\partial g_{00}}{\partial x^i} + \frac{1}{2} g^{\alpha j} \left(\frac{\partial g_{0j}}{\partial x^i} - \frac{\partial g_{0i}}{\partial x^j} \right) \quad (2)$$

The last terms in the round brackets looks like the k -th component of a three-dimensional curl. Interpreting the g_{0i} 's as the components of a three-dimensional vector potential, the bracket identifies the components of the corresponding gravito-magnetic axial field vector.

3 Asymmetric propagation in the field of a rotating mass

When the source of the gravitational field is a steadily rotating mass, the space-time assumes a chiral symmetry about the time axis of any reference frame centered on the main body. The line element may be written as:

$$ds^2 = g_{00} c^2 dt^2 + 2g_{0i} c dt dx^i + g_{ij} dx^i dx^j \quad (3)$$

Considering light, the interval is identically zero, so that it is possible to solve eq. (3) for dt :

$$dt = -\frac{g_{0i}}{cg_{00}} dx^i + \frac{1}{cg_{00}} \sqrt{(g_{0i} dx^i)^2 - g_{00} g_{ij} dx^i dx^j} \quad (4)$$

The sign in front of the square root could also be $-$ but we have chosen $+$ because we are interested in propagation towards the future.

Now let us assume that light follows a closed path in space. The parametric equation of the path, if its proper length is P , would be: $x^i(l) = x^i(l + P)$. The coordinated time interval (4) along the trajectory becomes

$$dt = -\frac{g_{0i}}{cg_{00}} \frac{dx^i}{dl} dl + \frac{1}{cg_{00}} \sqrt{(g_{0i} \frac{dx^i}{dl})^2 - g_{00} g_{ij} \frac{dx^i}{dl} \frac{dx^j}{dl}} |dl| \quad (5)$$

It is now possible to sum (integrate) along the loop, both to the right ($dl > 0$) and to the left ($dl < 0$), in order to obtain the time of flight for the round trip, getting two different results. Subtracting one result from the other and expressing the difference in terms of proper time τ of the laboratory, we get

$$\Delta\tau = \tau_+ - \tau_- = -\frac{2}{c}\sqrt{g_{00}} \oint \frac{g_{0i}}{g_{00}} \frac{dx^i}{dl} dl \quad (6)$$

The subscripts + and – stand for co- and respectively counter-rotating with the central mass.

$\Delta\tau$ differs from zero whenever it is $g_{0i} \neq 0$, which is the case for the space-time surrounding a rotating mass.

3.1 Ring lasers

Physically, a closed loop for light may be obtained using an optical fiber or three or more mirrors. In both solutions the source of light is the active cavity of a LASER so that the whole thing is called a ringlaser. The loop forms a resonating cavity within which standing light waves form. The stationarity condition converts the times of flight difference into a frequency difference for the right- and left-handed beams. The frequency difference, in turn, being the beams superposed, leads to a beat. Finally the beat frequency f_b is related to the proper time of flight difference by the formula

$$f_b = \frac{\Delta f}{2} = \frac{c^2}{2\lambda P} \Delta\tau \quad (7)$$

P is the proper length of the contour and λ is the wavelength of the laser.

When explicitly introducing the metric around the earth and expressing it to the lowest order of approximation in the angular momentum of the planet J_\oplus , in a reference frame originating in the center of the earth and rotating with it, the expected signal from a ring laser fixed to the ground will be⁷:

$$f_b = 2 \frac{A}{\lambda P} [\vec{\Omega} - 2 \frac{GM}{c^2 R} \Omega \sin\theta \hat{u}_\theta + \frac{GJ_\oplus}{c^2 R^3} (2\cos\theta \hat{u}_r + \sin\theta \hat{u}_\theta) \cdot \hat{u}_n] \quad (8)$$

A is the area enclosed by the loop; the factors multiplying the square bracket, altogether, are the *scale factor* of the ring; θ is the colatitude of the laboratory; the \hat{u} 's are unit vectors along the radial direction, along the local meridian, from the North to the South pole, along the perpendicular to the enclosed area of the ring. The angular velocity Ω coincides with the rotation speed of the earth.

The first term into the square brackets accounts for the kinematical Sagnac effect; the second term is the de Sitter precession, due to the coupling of the motion of the laboratory with the local gravito-electric field; the last term accounts for the gravito-magnetic frame dragging, originating from the angular momentum of the planet. The last two terms represent the GR effects, that should be measured.

4 GINGER

For an earth based laboratory, the two GR terms of (8) are approximately nine orders of magnitude smaller than the Sagnac effect; the de Sitter (or geodetic) term is a bit (less than one order of magnitude) smaller than the frame dragging (or Lense-Thirring) term. In order to perform an experiment, extremely stable and sensible instruments are needed, with a conveniently big scale factor. In order to see the LT term, a sensitivity better than 1 *prad/s* is required. The best existing research ring laser is G (Groß Ring), located in Wettzell, Bavaria⁸. G is a square ring (4 m side) whose sensitivity is now within one order of magnitude from the threshold of detectability of the GR effects.

We are presenting here GINGER (Gyroscopes IN General Relativity)⁹, designed to be a three-dimensional array made of three square mutually perpendicular rings (6 m side or more) assembled to form an octahedron (alternatively it could be a cube carrying six rings on its faces). The planned geometry control will be achieved dynamically using Fabry-Pérot cavities along the

main diagonal. The Fabry-Pérot will pilot piezoelectric actuators controlling the mirrors at the corners of the loops. The aim is to measure the GR terms and in particular the LT effect with an accuracy better than 1% (one year integration time). The location of GINGER will be the Gran Sasso National Laboratories in Italy, under more than 1400 m of rock. The underground location is needed in order to screen the apparatus from all rotational disturbances present on the surface of the earth (originating from wind, rain, pressure and temperature changes, moving masses in the vicinity etc.).

5 Intermediate steps on the GINGER roadmap

The full implementation of GINGER will require two or three years⁹. Meanwhile a couple of intermediate steps have been made. These are two rings already built and working. One is GP2, located in Pisa, destined to the test and calibration of the dynamic control process of the geometry using the main diagonals. GP2 is a square ring (1.6 m side) mounted on a granite table, oriented perpendicularly to the rotation axis of the earth, in order to maximize the Sagnac signal.

The second ring is GINGERino, located in a side tunnel of the Gran Sasso Laboratories. GINGERino is a square ring, 3.6 m side. The support is a granite cross, laid horizontally. GINGERino is used to characterise rotationally the underground site of the GS laboratories and to test various solutions for the control of the temperature and environmental conditions of the lab.

Work is steadily progressing, so that the goal of revealing general relativistic rotational effects on earth is now within reach in a reasonably short time.

The collaboration

The principal investigator of GINGER is Angela Di Virgilio of the INFN section in Pisa. The institutions wherefrom the members of the collaboration come, are: INFN-Pisa, Pisa University, Siena University, Padua University, LNL-INFN-Padua, INFN-Naples, CNR-SPIN Naples, Politecnico di Torino, INFN-Torino, National Gran Sasso Laboratory. Out of Italy, the collaboration includes the Technische Universität München (DE) and the University of Canterbury in Christchurch (NZ).

References

1. I. Ciufolini and C. Pavlis, *Nature* **431**, 958 (2004).
2. T.W. Murphy, K. Nordtvedt and S.G. Turyshev, *Phys. Rev. Lett.* **98**, 071102 (2007).
3. S.M. Kopeikin, *Phys. Rev. Lett.* **98**, 229001 (2007).
4. C.W.F. Everitt *et al*, *Phys. Rev. Lett.* **106**, 221101 (2011).
5. I. Ciufolini *et al*, *EPJ Plus* **126**, 1 (2011).
6. I. Ciufolini *et al*, *EPJ Plus* **127**, 127 (2012).
7. F. Bosi *et al*, *Phys. Rev. D* **84**, 122002 (2011).
8. K.U. Schreiber, J.-P.R. Wells, *Rev. Sci. Instrum.* **84**, 041101 (2013).
9. A. Di Virgilio *et al*, *Comptes Rendus Physique* **15**, 866 (2014).

ASPECTS OF MASSIVE GRAVITY

SEBASTIEN RENAUX-PETEL

*GRεCO Institut d'Astrophysique de Paris, UMR 7095, CNRS,
Sorbonne Universités UPMC Univ Paris 6, 98 bis boulevard Arago, 75014 Paris, France.*



We report here on two works on Lorentz invariant massive gravity. In the first part, we derive the decoupling limit of massive gravity on de Sitter, relying on embedding de Sitter into an higher dimensional Minkowski spacetime. This enables us to identify the unique candidate for a partially massless gravity theory, in which only four degrees of freedom propagate, although further work showed that this property does not hold beyond the decoupling limit. In the second part, we study the fate of the Vainshtein mechanism in the minimal model of massive gravity, in which we show the limits of the often used assumptions of staticity and spherical symmetry.

1 Introduction

Is it possible to give a mass to the graviton? While it can be motivated by a possible resolution of the old cosmological constant problem, this question is also theoretically interesting on its own right. It actually has a long and complex history, dating back from Fierz and Pauli¹ in 1939, passing from important works in the 70s, to recent breakthroughs in the past few years (see the reviews^{2,3}). In particular, de Rham, Gabadadze and Tolley recently identified the unique class of Lorentz-invariant massive gravity theories (henceforth dRGT)^{4,5} devoid of the so-called Boulware-Deser ghost, a fatal pathology that was present in all previous attempts. This class of theories, like any massive gravity theory, requires the introduction of a second metric beyond the “standard” one. This second, so-called reference metric, is usually chosen to be the one of Minkowski spacetime, but it can actually be arbitrary, and even dynamical⁶. However, the physical content of such enlarged class of theories is largely unknown. In section 3, we summarize a study of dRGT massive gravity on de Sitter spacetime⁷. This maximally symmetric set-up can be seen as the simplest extension of the theory around Minkowski, and is also motivated by cosmological reasons. Observational consistency of massive gravity theories requires that their additional degrees of freedom compared to General Relativity (GR) are hidden near dense sources, to conform for instance with gravity precision tests in the solar system. This non-trivial task is endorsed by the Vainshtein mechanism^{8,9,10}, in which non-linear effects render the new degrees of freedom strongly kinetically self-coupled, so that they almost do not propagate. In section 4, we report on a study of the fate of the Vainshtein mechanism in the minimal model

of massive gravity¹¹, in which we show the limits of the often used assumptions of staticity and spherical symmetry.

2 The action of dRGT massive gravity

The dRGT massive gravity action reads, in d spacetime dimensions⁵:

$$\mathcal{L}_{MG} = \frac{M_{\text{Pl}}^{d-2}}{2} \sqrt{-g} \left(R - \frac{m^2}{4} \mathcal{U}(g) \right), \quad (1)$$

where the first term is the Einstein-Hilbert action of GR, m will be identified with the mass of the graviton, and the most general potential \mathcal{U} is given by

$$\mathcal{U}(g) = -4 \sum_{n=2}^d \alpha_n \mathcal{L}_{\text{der}}^{(n)}(\mathcal{K}). \quad (2)$$

$$\text{with } \mathcal{L}_{\text{der}}^{(n)}(\mathcal{K}) = -\frac{1}{(d-n)!} \mathcal{E}^{\alpha_1 \dots \alpha_d} \mathcal{E}_{\beta_1 \dots \beta_n \alpha_{n+1} \dots \alpha_d} \mathcal{K}_{\alpha_1}^{\beta_1} \dots \mathcal{K}_{\alpha_n}^{\beta_n}, \quad (3)$$

where $\mathcal{E}^{\alpha_1 \dots \alpha_d}$ is the fully antisymmetric Levi-Cevita tensor and indices are raised and lowered using the metric $g_{\mu\nu}$. There, \mathcal{K}_ν^μ is defined as $\mathcal{K}_\nu^\mu = \delta_\nu^\mu - \sqrt{g^{\mu\alpha} \gamma_{\alpha\nu}}$, where $\gamma_{\mu\nu}$ is the reference metric, and we will only be concerned with cases in which $g_{\mu\nu}$ is close to $\gamma_{\mu\nu}$, so that $g^{\mu\alpha} \gamma_{\alpha\nu}$ is close to the identity matrix, and the matrix square root in \mathcal{K} is well defined in perturbation theory. For definiteness we will always choose $\alpha_2 = 1$ while the other coefficients α_n are arbitrary.

3 The decoupling limit of massive gravity on de Sitter

A theory of massive gravity free of the Boulware-Deser ghost propagates 5 degrees of freedom. Around Minkowski spacetime, this comprises two helicity-2 modes, like in GR, two helicity-1 modes and one helicity-0 mode. However, only around a maximally symmetric spacetime does it make sense to perform a helicity decomposition of a spin-2 field. Around an arbitrary reference metric, one no longer has a full Poincaré or equivalent group, and there is therefore no Poincaré representation to talk about. Since de Sitter (dS) spacetime is also a maximally symmetric manifold, the notion of a helicity decomposition around this spacetime is meaningful, but its identification requires additional work. The strategy we used is to embed d -dimensional dS into $d+1$ -dimensional Minkowski spacetime. There, the identification of the various helicity modes relies on the well known Stückelberg trick, in which the broken diffeomorphism invariance is restored while making the new degrees of freedom explicit¹². The subtlety then lies in their projection back into d -dimensional dS. Following this, we obtained the expression of the d -dimensional covariantized reference metric as

$$\tilde{\gamma}_{\mu\nu} = \gamma_{\mu\nu} - S_{\mu\nu} - S_{\nu\mu} + S_{\mu\alpha} \gamma^{\alpha\beta} S_{\nu\beta} + \frac{H^2}{1 - H^2 V^2} T_\mu T_\nu, \quad (4)$$

with

$$S_{\mu\nu} = \nabla_\mu V_\nu + \gamma_{\mu\nu} \left(1 - \sqrt{1 - H^2 V^2} \right), \quad T_\mu = \frac{1}{2} \partial_\mu V^2 - \sqrt{1 - H^2 V^2} V_\mu \quad (5)$$

and where $V^2 = \gamma_{\mu\nu} V^\mu V^\nu$, H^2 is proportional to the scalar curvature of dS spacetime $R = d(d-1)H^2$, and all the covariant derivatives are with respect to $\gamma_{\mu\nu}$. At this stage, we may split V_μ into $V_\mu = A_\mu + \partial_\mu \tilde{\pi}$, where at the linearized level, and in the decoupling limit that we will define below, A_μ describes the helicity-1 mode and is a vector field, while $\tilde{\pi}$ is a scalar field that successfully encodes the helicity-0 mode. From the above expression, it is straightforward to deduce the structure of the linearized fluctuations, and to recover the so-called Higuchi bound, namely that one should have $m^2 > (d-2)H^2$ to ensure that all fields have a positive kinetic energy¹³.

Beyond the free theory, the decoupling limit is constructed in such a way as to concentrate on the interactions arising at the lowest energy scale, and to disentangle them from the standard complications and non-linearities of GR. To achieve this, we simultaneously send $M_{\text{Pl}} \rightarrow \infty$ (effectively keeping the helicity-2 modes $\tilde{h}_{\mu\nu} = g_{\mu\nu} - \gamma_{\mu\nu}$ linear) and $m \rightarrow 0$, in such a way as to keep finite both the canonically normalized fields and the lowest energy scale of interactions of the helicity-0 mode, *i.e.*:

$$h_{\mu\nu} = M_{\text{Pl}}^{(d-2)/2} \tilde{h}_{\mu\nu} \rightarrow \text{finite}, \quad \pi = \Lambda^{(d+2)/2} \bar{\pi} \rightarrow \text{finite}, \quad \Lambda \equiv (m^2 M_{\text{Pl}}^{(d-2)/2})^{2/(d+2)} \rightarrow \text{finite} \quad (6)$$

To satisfy the Higuchi bound as $m \rightarrow 0$, we also send H to 0, and we keep the ratio $\beta \equiv H^2/m^2$ finite so as not to recover the flat space limit. In this decoupling limit, the helicity-1 mode always arises quadratically and can hence be consistently set to zero, which we do in the following. After a long and complicated calculation, one finds the decoupling limit Lagrangian:

$$\mathcal{L}_{\text{DL}} = -\frac{1}{4} \bar{h}^{\mu\nu} \hat{\mathcal{E}}^{\alpha\beta} \bar{h}_{\alpha\beta} + \frac{1}{2} \bar{h}^{\mu\nu} \sum_{n=3}^{d-1} (\alpha_n + (n+1)\alpha_{n+1}) \frac{X_{\mu\nu}^{(n)}}{\Lambda^{(d+2)(n-1)/2}} + \sum_{n=2}^{d+1} c_n \frac{\mathcal{L}_{\text{Gal}}^{(n)}}{\Lambda^{(d+2)(n-2)/2}}, \quad (7)$$

where one partially diagonalized the action by use of the transformation

$$h_{\mu\nu} = \bar{h}_{\mu\nu} + \frac{2}{d-2} \pi \eta_{\mu\nu} - \frac{1+3\alpha_3}{\Lambda^{(d+2)/2}} \partial_\mu \pi \partial_\nu \pi, \quad (8)$$

and the first term has the functional form of the linearized Einstein Hilbert action. The tensor $X_{\mu\nu}^{(n)}$ is a polynomial function of order n of the covariant second derivative $\Pi_{\mu\nu} = \nabla_\mu \nabla_\nu \pi$, the c_n 's are β and α_m 's dependent coefficients, and

$$\mathcal{L}_{\text{Gal}}^{(n)} = (\partial\pi)^2 \mathcal{L}_{\text{der}}^{(n-2)}(\Pi) \quad (9)$$

are the so-called Galileon Lagrangians, with $\mathcal{L}_{\text{der}}^{(0)} = 1$. The decoupling limit is hence qualitatively very similar to that on Minkowski, and the appearance of the Galileon terms testifies that we correctly identified the helicity-0 mode π , whose equations of motion are manifestly second-order.

When exploring this decoupling limit in more depth, we can unveil the existence of a very peculiar set of parameters: for the choice $\beta = 1/(d-2)$, $\alpha_3 = -\frac{1}{3} \frac{d-1}{d-2}$ and $\alpha_n = -\frac{1}{n} \alpha_{n-1}$ for $n \geq 4$, it turns out that the helicity-0 mode completely disappears from the decoupling limit Lagrangian! The corresponding model therefore represents the unique fully non-linear candidate theory of partially massless gravity, in which only 4 degrees of freedom would propagate. This important identification prompted an important number of further studies^{14,15,16,17,18}, which established the reappearance of the helicity-0 mode beyond the decoupling limit.

4 The Vainshtein mechanism beyond staticity and spherical symmetry

Any gravitational theory must conform with gravity precision tests in the solar system. In the context of massive gravity theories, the Vainshtein mechanism aims at screening the helicity 1- and 0-modes near dense sources to recover GR. In most studies, this amounts to establishing that in vacuum and static spherically symmetric (SSS) configurations, one can find a viable solution that interpolates between the Schwarzschild solution at sufficiently small radius from the source, and the expected Yukawa-type solution at large distances. Additionally, to gain some analytical insight, one often uses the decoupling limit approximation presented in the previous section. In this respect, the so-called minimal model is particularly interesting. It corresponds to a Minkowski reference metric and to the choice of parameters $\alpha_3 = -1/3$ and $\alpha_4 = 1/12$ in the potential (2). For this particular choice, the decoupling limit Lagrangian (7) simply describes a free theory! That is, no interactions arise at the energy scale $\Lambda = (m^2 M_{\text{Pl}})^{1/3}$, contrary to all other choices of parameters (note that the helicity-0 mode does appear though, but only through

its kinetic term). It can be tempting to infer from this absence of non-linear interactions at this scale that the Vainshtein mechanism is ineffective in this model¹⁹. However, it only testifies that the decoupling limit, which aims at concentrating on the lowest energy interaction, has not been correctly identified at this particular point in parameter space. Considering SSS configurations, we actually showed that all interactions below the Planck mass identically vanish in the helicity-2 and -0 sectors¹¹. This tantalizing fact does point towards an absence of Vainshtein mechanism in this set up, but does not prove it. For this reason, we resorted to the exact equations of motion in the metric formalism. We then showed completely generally that in all vacuum SSS configurations, there exists an obstruction that precludes any recovery of General Relativity.

While this could be seen as a proof that the minimal model is ruled out, we argue that this would be premature to reach this conclusion without further study. Indeed, we showed that in generic time-dependent or non-spherically symmetric configurations, interactions arbitrary close to the scale Λ reappear! Although it is hard to reach conclusions solely on these facts, one can thus wonder whether the small degree of spherical symmetry breaking in the solar system can be enough to lead to a successful Vainshtein mechanism in the minimal model. More generally, while screening mechanisms have been mostly studied in static/stationary spherically symmetric situations up to now (see however ref²⁰), our analysis leads us to question whether the high degree of symmetry of these configurations might miss some important physical phenomena that arise in nature in realistic circumstances.

Acknowledgments

This work was supported by French state funds managed by the ANR within the Investissements d'Avenir programme under reference ANR-11-IDEX-0004-02. I would like to thank the scientific committee of the Moriond conference for their financial support.

References

1. M. Fierz and W. Pauli, *Proc. Roy. Soc. Lond. A* **173**, 211 (1939).
2. K. Hinterbichler, *Rev. Mod. Phys.* **84** (2012) 671
3. C. de Rham, *Living Rev. Rel.* **17** (2014) 7
4. C. de Rham and G. Gabadadze, *Phys. Rev.* **D82**, 044020 (2010).
5. C. de Rham, G. Gabadadze and A. J. Tolley, *Phys. Rev. Lett.* **106**, **231101** (2011).
6. S. F. Hassan and R. A. Rosen, *JHEP* **1202** (2012) 126
7. C. de Rham and S. Renaux-Petel, *JCAP* **1301** (2013) 035
8. A. I. Vainshtein, *Phys. Lett. B* **39**, 393 (1972);
9. E. Babichev, C. Deffayet and R. Ziour, *Phys. Rev. Lett.* **103** (2009) 201102
10. E. Babichev and C. Deffayet, *Class. Quant. Grav.* **30** (2013) 184001
11. S. Renaux-Petel, *JCAP* **1403** (2014) 043
12. N. Arkani-Hamed, H. Georgi and M. D. Schwartz, *Annals Phys.* **305**, 96 (2003).
13. A. Higuchi, *Nucl. Phys. B* **282**, 397 (1987).
14. S. Deser, E. Joung and A. Waldron, *J. Phys. A* **46** (2013) 214019
15. S. F. Hassan, A. Schmidt-May and M. von Strauss, *Phys. Lett. B* **726**, (2013) 834
16. S. Deser, E. Joung and A. Waldron, *Phys. Rev. D* **86** (2012) 104004
17. S. Deser, M. Sandora and A. Waldron, *Phys. Rev. D* **87** (2013) 101501
18. C. de Rham, K. Hinterbichler, R. A. Rosen and A. J. Tolley, *Phys. Rev. D* **88** (2013) 024003
19. K. Koyama, G. Niz and G. Tasinato, *Phys. Rev. D* **84** (2011) 064033
20. E. Babichev, C. Deffayet and G. Esposito-Farese, *Phys. Rev. Lett.* **107** (2011) 251102

CONSISTENT MASSIVE GRAVITON ON ARBITRARY BACKGROUND

L. BERNARD

*Sorbonne Universités, UPMC et CNRS, UMR 7095,
Institut d'Astrophysique de Paris, GReCO, 98 bis bd Arago, 75014 Paris, France*

The only consistent linear theory for a massive spin-2 field on a flat space-time has been known for a long time as being the Fierz-Pauli theory. Its promotion to a non-linear theory, although essential, has long been thought impossible because of the appearance of the Boulware-Deser (BD) ghost. Recently de Rham Gabadadze and Tolley proposed a family of massive gravity theories, free of this ghost. We will present, for a particular subset of these theories, how to obtain the linearised field equations for a massive graviton propagating in a single arbitrary background. We will in particular focus on the derivation of the five covariant constraints, among which the scalar one removes the BD ghost.

1 Introduction

Lately there has been a renewal of interest in massive gravity with interesting applications to cosmology. One of the main motivations for massive gravity is to replace dark energy by a non-vanishing graviton mass, which is one of the simplest way to modify General Relativity in the Infra-Red. The only consistent linear theory for a massive spin-two field on a flat space-time has been known for a long time since the work of Fierz and Pauli¹. It propagates five degrees of freedom of positive energy, those of a transverse, traceless, symmetric, two times covariant tensor $h_{\mu\nu}$. It can easily be extended to an Einstein space-time background keeping the same number of propagating polarizations^{2,3}. However, a similar theory for an arbitrary background metric has not been written so far. A starting point to do so is the set of fully non linear theories formulated by de Rham, Gabadadze and Tolley (dRGT in the following)^{4,5}. Such a theory was shown to contain only five dynamical degrees of freedom^{5,6,7} and hence is devoid from a pathology long thought unavoidable: the presence of an extra ghost-like sixth degree of freedom in a generic non linear extension of Fierz-Pauli theory first discussed by Boulware and Deser⁸. However, the dRGT theory is formulated using two metrics, a dynamical one, called $g_{\mu\nu}$ in the following, and a non dynamical one, usually taken to be flat, called here $f_{\mu\nu}$. Hence, the expectation is that when one linearises the dRGT field equations one will obtain a theory for a massive graviton moving in a space-time endowed with two background metrics which has various drawbacks⁹. Moreover, it may not be easy to show that the obtained theory contains the correct number of degrees of freedom without using the elegant but involved proof obtained for the non linear theories⁶.

Here we will present a work^{10,11} in which we obtained from dRGT models a fully covariant theory for a massive graviton moving in a single, totally arbitrary, metric (hence eliminating the need for the non dynamical metric). In particular we will show how, for such a theory, one can obtain five covariant constraints, including the one which leads to the tracelessness of the graviton on flat space-time and removes the Boulware-Deser ghost.

2 Ghost-free Massive Gravity

Our starting point is the set of ghost-free massive gravity theories defined by the following action^{6,7}

$$S = M_g^2 \int d^4x \sqrt{|g|} \left[R(g) - 2m^2 \sum_{n=0}^3 \beta_n e_n(S) \right], \quad (1)$$

where the β_n are dimensionless parameters, S is a matrix square root defined by

$$S^\mu{}_\sigma S^\sigma{}_\nu = g^{\mu\sigma} f_{\sigma\nu}, \quad (2)$$

and $e_n(S)$ are the elementary symmetric polynomials of the matrix S . They can be expressed through a recursive formula, with $e_0 = 1$,

$$e_n(S) = -\frac{1}{n} \sum_{k=1}^n (-1)^k \text{Tr}[S^k] e_{n-k}, \quad n \geq 1. \quad (3)$$

The presence of the square-root matrix S makes the study of these theories more complicated. The field equations deriving from this action are given by

$$E_{\mu\nu} \equiv \mathcal{G}_{\mu\nu} + m^2 V_{\mu\nu} = 0, \quad (4)$$

where $\mathcal{G}_{\mu\nu} = R_{\mu\nu} - \frac{1}{2} R g_{\mu\nu}$ is the Einstein tensor and $V_{\mu\nu}$ is the interaction term given by

$$V_{\mu\nu} = g_{\mu\rho} \sum_{n=0}^3 \sum_{k=0}^n (-1)^{n+k} \beta_n [S^{n-k}]^\rho{}_\nu e_k(S). \quad (5)$$

3 Linearised field equations for generic ghost-free massive gravity

The next step in our derivation consists in linearising the field equations (4) around a background solution for the dynamical metric $g_{\mu\nu}$, calling $h_{\mu\nu}$ its small perturbation,

$$\delta E_{\mu\nu} \equiv \delta \mathcal{G}_{\mu\nu} + m^2 \delta V_{\mu\nu} = 0, \quad (6)$$

where $\delta \mathcal{G}_{\mu\nu} = \mathcal{E}_{\mu\nu}{}^{\rho\sigma} h_{\rho\sigma}$ is the linearised Einstein tensor and is easy to obtain. The difficult step consists in deriving the linearised interaction term $\delta V_{\mu\nu} = M_{\mu\nu}{}^{\rho\sigma} h_{\rho\sigma}$, because of the presence of the square-root matrix S . To tackle this difficulty we first notice that the variation of S , δS , satisfies to a particular matrix equation which enters in the mathematically well-known class of Sylvester equations¹²,

$$S^\mu{}_\nu (\delta S)^\nu{}_\sigma + (\delta S)^\mu{}_\nu S^\nu{}_\sigma = \delta[S^2]^\mu{}_\sigma. \quad (7)$$

The right-hand side of this equation is easy to get in terms of $h_{\mu\nu}$, as $[S^2]^\mu{}_\nu = g^{\mu\rho} f_{\rho\nu}$. It is a known mathematical result that this equation has a unique solution for δS if and only if the spectra of S and $-S$ do not intersect. In this case (which we will assume to be true from now) one can express the solution for δS linearly in terms of $\delta[S^2]$. Once this is done we insert it in the linearised mass term $M_{\mu\nu}{}^{\rho\sigma} h_{\rho\sigma}$. We thus derived the explicit and covariant expression of the linearised field equations in the general class of ghost-free massive gravity.

3.1 The β_1 model

We now consider the simple case where both β_2 and β_3 vanish but we keep otherwise β_0 , β_1 and $f_{\mu\nu}$ arbitrary. We call this model the " β_1 model". The field equations now reduce to

$$\mathcal{G}_{\mu\nu} + m^2 \left[\beta_0 g_{\mu\nu} + \beta_1 g_{\mu\rho} (e_1(S) \delta_\nu^\rho - S^\rho{}_\nu) \right] = 0. \quad (8)$$

Noting that the equations are now linear in S , one can obtain the expression of S as a function of the metric $g_{\mu\nu}$ and its curvature:

$$S^\rho{}_\nu = \frac{1}{\beta_1 m^2} \left[R^\rho{}_\nu - \frac{1}{6} \delta^\rho{}_\nu R - \frac{m^2 \beta_0}{3} \delta^\rho{}_\nu \right]. \quad (9)$$

This remarkable feature is unique to the β_1 model and only requires a non-vanishing β_1 . More precisely it means that in the linearised equations of motion we can eliminate any and all occurrences of the auxiliary metric $f_{\mu\nu}$ (or equivalently of S) in favour of the metric $g_{\mu\nu}$ and its curvature. It is important to notice that this is unique to the β_1 model and only requires a non-vanishing β_1 . Having carried out this elimination, we have now obtained the field equations of a massive graviton $h_{\mu\nu}$ propagating in a single arbitrary metric $g_{\mu\nu}$. We now consider these equations as our starting point, in particular the metric $g_{\mu\nu}$ is no more a solution of the background field equations.

4 The five covariant constraints

We will now show that the graviton $h_{\mu\nu}$ propagates at most five polarizations for a completely generic metric $g_{\mu\nu}$. The idea is to follow what can be done in the Fierz-Pauli theory, for a massive graviton on a flat space-time with metric $\eta_{\mu\nu}$. In this case by taking the divergence of the field equations, one gets four vector constraints,

$$\partial^\mu h_{\mu\nu} - \partial_\nu h = 0. \quad (10)$$

Taking another derivative of this equations and subtracting it from the trace of the field equations, one obtains the scalar constraint,

$$h = 0. \quad (11)$$

These are the five Lagrangian constraints (being at most first order in derivatives) required to remove five of the *a priori* ten dynamical degrees of freedom of $h_{\mu\nu}$.

We can try to do the same for the field equations (6). The first four vector constraints are easy to obtain. Indeed as a consequence of the Bianchi identities one has $\nabla^\mu \delta \mathcal{G}_{\mu\nu} \sim 0$, where here and henceforth two equations separated by the symbol " \sim " are equal off-shell up to terms containing no second or higher order derivatives. Hence the field equations yield the four vector constraints

$$\nabla^\mu \delta E_{\mu\nu} = 0. \quad (12)$$

Next we want to find the additional scalar constraint. Unfortunately it cannot be obtained, as in the Fierz-Pauli case, as a linear combination of the trace of the field equations and their double divergence. However we now have in hand two symmetric tensors which can be used to take traces, namely the metric $g_{\mu\nu}$ and its Ricci curvature $R_{\mu\nu}$. Equivalently we can use the tensor $S_{\mu\nu}$, trading $R_{\mu\nu}$ for $S_{\mu\nu}$ in the equations via Eq. (9). We stress that these two possibilities are strictly equivalent and do not impose any condition on the metric $g_{\mu\nu}$ because Eq. (9) can be considered as a definition for the tensor $S_{\mu\nu}$. We then define all possible scalars obtained by tracing the field equations and the derivative of its divergence with the tensor S , as it turns out to be more convenient,

$$\Phi_i \equiv [S^{\lambda\mu\nu}] \delta E_{\lambda\mu\nu}, \quad (13)$$

$$\Psi_i \equiv [S^{\lambda\mu\nu}] \nabla_\nu \nabla^\lambda \delta E_{\lambda\mu}. \quad (14)$$

An exhaustive set of linearly independent scalars is obtained by restricting i , $0 \leq i \leq 3$, due to the Cayley-Hamilton theorem. We are thus looking for a specific linear combination of these

eight scalars Φ_i and Ψ_i , $i = 0, \dots, 3$ with scalar coefficients $\{u_i, v_i\}$ to be determined, which would be free of second or higher order derivatives, such that

$$\sum_{i=0}^3 (u_i \Phi_i + v_i \Psi_i) \sim 0. \quad (15)$$

Computing explicitly the scalars Φ_i and Ψ_i , one obtains that, in these scalars, the second derivatives of $h_{\mu\nu}$ appear in the form of linear combinations (with S -dependent coefficients) of 26 different scalars \aleph_i made by contracting $\nabla_\mu \nabla_\nu h_{\rho\sigma}$ with powers of S in various ways, e.g. $\nabla_\rho \nabla_\sigma h^{\rho\sigma}$ and $[S^3]^{\rho\sigma} [S^3]^{\mu\nu} \nabla_\rho \nabla_\sigma h_{\mu\nu}$. We get *a priori* 26 equations for the seven unknowns $\{u_i, v_i\}$ (they only need to be determined up to an overall factor) by setting to zero each coefficient of the scalars \aleph_i which appears in (15). However, not all the scalars \aleph_i are independent thanks to identities between them, syzygies, that are obtained as a consequence of the second fundamental theorem of invariant theory¹³. These identities are just enough to reduce to seven the number of independent equations to be solved to fulfill (15). This yields a unique solution for the coefficients $\{u_i, v_i\}$ which translates into the scalar constraint

$$-\frac{m^2 \beta_1 \epsilon_4}{2} \Phi_0 - e_3 \Psi_0 + e_2 \Psi_1 - e_1 \Psi_2 + \Psi_3 = 0, \quad (16)$$

valid now for an arbitrary metric $g_{\mu\nu}$. In particular for flat or Einstein backgrounds this constraint reduces to $h = 0$ as expected, showing that the scalar constraint (16) is indeed independent from the four vector ones.

5 Summary

We obtained the linearised field equations for a massive graviton on an arbitrary background metric from dRGT theories. For a subset of this theories, the β_1 model, we were able to eliminate the non-dynamical metric $f_{\mu\nu}$ which appears in the formulation of dRGT theories. It results in a covariant theory for a massive graviton moving in a single, totally arbitrary, metric. For such a theory, we have shown that the massive graviton propagates at most five degrees of freedom, by exhibiting the fifth scalar constraint, which leads to the tracelessness of the graviton on flat space-time and removes the Boulware-Deser ghost.

Acknowledgments

L.B. thanks the organizing committee of the 50th Rencontres de Moriond for offering her the opportunity to attend the gravitation session and to give a talk there.

References

1. M. Fierz and W. Pauli, Proc. Roy. Soc. Lond. A **173**, 211 (1939).
2. A. Higuchi, Nucl. Phys. B **282**, 397 (1987).
3. I. Bengtsson, J. Math. Phys. **36**, 5805 (1995).
4. C. de Rham and G. Gabadadze, PRD **82**, 044020 (2010).
5. C. de Rham, G. Gabadadze and A. J. Tolley, PRL **106**, 231101 (2011).
6. S. F. Hassan and R. A. Rosen, PRL **108**, 041101 (2012).
7. S. F. Hassan, R. A. Rosen and A. Schmidt-May, JHEP **1202**, 026 (2012).
8. D. G. Boulware and S. Deser, PRD **6**, 3368 (1972).
9. C. Deffayet and T. Jacobson, Class. Quant. Grav. **29**, 065009 (2012).
10. L. Bernard, C. Deffayet and M. von Strauss, PRD **91**, 104013 (2015).
11. L. Bernard, C. Deffayet and M. von Strauss, arXiv:1504.04382 [hep-th].
12. Q. Hu and D. Cheng, App. Math. Lett. **19**, 9, 859 (2006).
13. C. Procesi, Advances in Mathematics **19**, 3, 306 (1976).

Nonlinear Cosmological Probes of Screening Mechanism in Modified Gravity

David F. Mota

Institute of Theoretical Astrophysics, University of Oslo, 0315 Oslo, Norway

We investigate the signatures induced by the Symmetron and a Chameleon $f(R)$ model in the peculiar velocity field using N -body simulations. By studying fifth force and halo velocity profiles we identify three general categories of effects found in screened modified gravity models: a fully screened regime where we recover ΛCDM to high precision, an unscreened regime where the fifth force is in full operation, and, a partially screened regime where screening occurs in the inner part of a halo, but the fifth force is active at larger radii. These three regimes can be pointed out very clearly by analyzing the deviation in the maximum cluster velocity. Observationally, the partially screened regime is of particular interest since an uniform increase of the gravitational force – as present in the unscreened regime – is degenerate with the (dynamical) halo mass estimate, and, thus, hard to detect.

1 Modified Gravity Models

In this work, we study the effect of screened-modified gravity theories on halo velocity profiles. To do this, we used the N -body code **ISIS**¹. The characteristic quantity of screened modified gravity models is the fifth force, $\mathbf{F}_{\text{Fifth}}$, which is an additional contribution to the (Newtonian) gravitational force and varies in space and time^{2,3,4,5}. In particular, screened modified gravity models are constructed so that $|\mathbf{F}_{\text{Fifth}}| \ll |\mathbf{F}_N|$ in the solar system to evade constraints from local gravity experiments. This variable gravitational force arises from an additional scalar field φ added to the Einstein-Hilbert action

$$S = \int d^4x \sqrt{-g} \left(\frac{M_{\text{Pl}}^2}{2} R - \frac{1}{2} \nabla_\mu \varphi \nabla^\mu \varphi - V(\varphi) \right) + \mathcal{S}_m(\psi^{(i)}, \tilde{g}_{\mu\nu}) \quad (1)$$

The evolution of the scalar field reads $\square\varphi = \frac{dV_{\text{eff}}}{d\varphi}$ where V_{eff} is the effective potential. In the Symmetron model⁷, the coupling function and the potential are given by

$$A(\varphi) = 1 + \frac{\varphi^2}{M^2} \quad V(\varphi) = -\frac{1}{2}\mu^2\varphi^2 + \frac{1}{4}\lambda\varphi^4. \quad (2)$$

With these definitions, the effective potential becomes

$$V_{\text{eff}} = \frac{1}{2} \left(\frac{\rho_m}{M^2} - \mu^2 \right) \varphi^2 + \frac{1}{4} \varphi^4 \quad (3)$$

We also consider the Hu-Sawicki model⁶ which incorporates a Chameleon screening. Through a conformal transformation $\tilde{g}_{\mu\nu} = A^2(\varphi)g_{\mu\nu}$ where $A(\varphi) = c^{\beta\varphi/M_{\text{Pl}}}$ with $\beta = 1/\sqrt{6}$ one can bring this $f(R)$ -action on the form of Eq. 1. The potential becomes

$$V(\varphi) = M_{\text{Pl}}^2 \frac{f_R R - f}{2(1 + f_R)^2}, \quad (4)$$

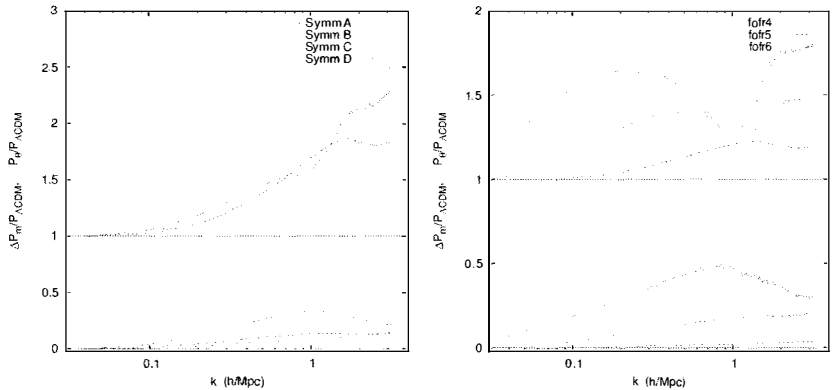


Figure 1 – The fractional difference of the velocity divergence (above) and matter (below) power-spectra with respect to Λ CDM for the Symmetron (left) and $f(R)$ (right) simulations.

where $f_R \equiv df/dR = \exp(-2\beta\varphi/M_{\text{Pl}}) - 1 \approx -\frac{2\beta\varphi}{M_{\text{Pl}}}$. We can then rewrite the potential as

$$V(\varphi) = \rho_\Lambda - \frac{n+1}{2n} M_{\text{Pl}}^2 R_0 |f_{R0}| \left(\frac{2\beta\varphi}{M_{\text{Pl}} |f_{R0}|} \right)^{\frac{n}{n+1}}. \quad (5)$$

2 Numerical Simulations

We will first present the global statistical properties of the velocity field that are described by the velocity divergence power spectrum. Normalizing the divergence of the velocity field $\vec{\nabla} \cdot \mathbf{v}$ with the Hubble parameter gives the dimensionless expansion scalar $\theta = \frac{1}{H} \vec{\nabla} \cdot \mathbf{v}$.

We compute the power-spectrum of θ from our simulations by using the Delaunay tessellation of the simulation volume. The velocity divergence field obtained this way gives us a field that is volume averaged rather than mass averaged. This yields an unbiased estimate for the power-spectrum which has better noise properties and is less sensitive to the details of the power-spectrum estimation. The velocity divergence is not the easiest quantity to measure in practice, but it is a useful diagnostic that can tell us to what degree the velocity field is affected by modified gravity.

To characterize this quantity, we study the relative particle velocity, which is simply defined as $v_{\text{rel}} = \sqrt{(\mathbf{v} - \mathbf{v}_H)^2}$, where \mathbf{v} and \mathbf{v}_H are the particles' velocity and its halo velocity, respectively. For the latter, we use the core velocity of the halo, i.e., the mean particles' velocity within 10% of the virial radius since this is expected to track the halo motion best. Furthermore, we investigate the quantity v_{max} which is defined to be the maximum relative particle velocity within R_{200} .

2.1 Velocity divergence power-spectrum

In Fig. 1 we show the fractional difference in the velocity divergence with respect to Λ CDM for both modified gravity models. For comparison we also show the matter power-spectrum. For our $f(R)$ simulations we find that the difference with respect to Λ CDM in the velocity divergence spectrum can be roughly two times as large as the difference in the matter power spectrum. For the Symmetron the difference can be much larger. For the `symm_C` model (which is the model with the largest value of the coupling strength β), we see that $(\Delta P/P)_m \approx 10\%$ at $k = 1h/Mpc$ while $(\Delta P/P)_\theta \approx 200\%$. The `symm_C` model has a fifth force in unscreened regions that is four

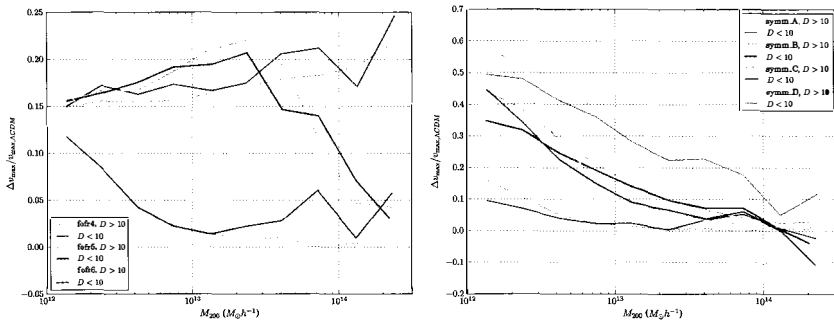


Figure 2 – The relative deviation in the maximum cluster velocity for the $f(R)$ model (LEFT) and for the Symmetron (RIGHT). Light and dark curves represent clusters located in under- and overdense regions, respectively.

times that of the other Symmetron models and this is likely the reason why we get this extreme signal.

2.2 Maximum cluster velocity

In Figs. 2-2 we show the deviation from Λ CDM of the maximum relative velocity found in a halo. For the fofr4 model v_{\max} is enhanced by 15 – 20% over the entire mass range. The fofr5 model shows an comparable boost for masses $M_{200} \leq 2 \times 10^{13} M_{\odot} h^{-1}$ but then the deviation drops sharply to $\leq 5\%$ at $2 \times 10^{14} M_{\odot} h^{-1}$. There is indication that the same happens for the fofr6 model but for a smaller cutoff mass. However, to reach a firm conclusion more simulations with a better mass resolution are necessary in order to resolve halos $M_{200} \leq 10^{12} M_{\odot} h^{-1}$.

We show the same quantity, $\Delta v_{\max}/v_{\max,\Lambda\text{CDM}}$, for the Symmetron model. Instead of a sharp cutoff we find a more gradual decline with halo mass. Overall, the v_{\max} deviation is larger which is expected from the Δv results. In both cases, we do find hardly any deviation which can be attributed clearly to environmental effects. The only exception are the Symmetron and fofr6 results for the smallest ($12 \leq \log_{10} M_{200} h/M_{\odot} \leq 13$) where the deviation for halos within underdense regions is always larger than in overdense regions.

3 Discussion

The velocity field in modified gravity simulations is found to be more affected by the presence of the fifth force than the density field for $f(R)$ -gravity. For the Symmetron model we found this to be even more apparent. A particular striking example of this – with boosts of up to $(\Delta P/P)_{\theta} \gtrsim 3$, whereas $(\Delta P/P)_m \sim 0.1$ – are our symm.C results. Here, the fact that the symm.C model possesses a maximum fifth force which is four times that value in the other Symmetron models is likely the reason for obtaining such an extreme signal. Support for this explanation can be seen in Fig. 2 where the maximum cluster velocity for small mass halos (which are more numerous in low-density regions) becomes greatest for the symm.C model.

The reason why generally, we have $(\Delta P/P)_{\theta} \gtrsim (\Delta P/P)_m$, is that the velocity divergence field is not mass-weighted in any way. Hence, low-density regions (voids) will contribute a large part of the signal in the velocity divergence power-spectrum (since voids contribute a large part of the volume in the Universe) which is not the case for the matter power-spectrum. Now the fifth-force is generally not screened in low-density regions so consequently velocities are boosted to significantly higher relative values (when compared with Λ CDM) in voids opposed to in clusters. This indicates that low-density regions like cosmic voids, as we would expect, is the place where the strongest signals of modified gravity can be found. Overall, we found that halo

velocity profiles are an excellent direct trace of the fifth force: large values of γ at a certain halo mass and radius, lead to large deviations in the relative velocity of particles at that point. Hereby, we could not detect any differences due to the halo environment. This suggests that for most halos considered are well within the self-screening mass range⁸, i.e., their own matter density dominates over that of the environment. This picture is supported by the fact that the only consistent discrepancy between the two environments can be found in the deviation of the maximum cluster velocity for $M_{200} \leq 10^{13} M_{\odot} h^{-1}$ in the Symmetron and the fofr6 results. Here, the halos residing in overdense regions show less deviations from Λ CDM compared to ones in underdense regions. This might indicate the transition to the *environmental-screening* mass range.

Although the theoretical nature of the two screening mechanisms is completely different, we found common features in the velocity properties. In particular, our findings suggest that one can group them into three general categories/regimes: (i) the fully screened regime where GR is recovered, (ii) an unscreened regime where the strength of the fifth force is large, and, (iii) a partially screened regime where screening occurs in the inner part of a halo, but the fifth force is active at larger radii.

These three regimes can be pointed out very clearly by analyzing the deviation in the maximum cluster velocity. Here, the fully screened regime corresponds to $\Delta v_{\max}/v_{\max, \Lambda\text{CDM}} \sim 0$, the unscreened regime to a constant upper limit in deviation, i.e., to $Y \equiv \Delta v_{\max}/v_{\max, \Lambda\text{CDM}} > 0$ with $dY/dM_{200} \sim 0$, and, the partially screened regime to the slope between (i) and (ii) (i.e., $Y > 0$ with $|dY/dM_{200}| > 0$).

This confirms the previously mentioned points. All considered halos in the fofr4 case are in the unscreened regime and in the fofr5 case halos with $M_{200} \leq 3 \times 10^{13} M_{\odot} h^{-1}$. To the contrary, the halos with $M_{200} \gtrsim 10^{13} M_{\odot} h^{-1}$ are in the fully screened regime in the fofr6 and symm_D parameters. For the other Symmetron models studied all the considered halos are in the partially screened regime.

References

1. C. Llinares, D. F. Mota and H. A. Winther, *Astron. Astrophys.* **562** (2014) A78
2. J. D. Barrow and D. F. Mota, *Class. Quant. Grav.* **20** (2003) 2045 [gr-qc/0212032].
3. B. Li, D. F. Mota and J. D. Barrow, *Astrophys. J.* **728** (2011) 109
4. D. F. Mota, D. J. Shaw and J. Silk, *Astrophys. J.* **675** (2008) 29
5. A. C. Davis, B. Li, D. F. Mota and H. A. Winther, *Astrophys. J.* **748** (2012) 61
6. W. Hu and I. Sawicki, *Phys. Rev. D* **76** (2007) 064004 [arXiv:0705.1158 [astro-ph]].
7. K. Hinterbichler and J. Khoury, *Phys. Rev. Lett.* **104** (2010) 231301
8. H. A. Winther, D. F. Mota and B. Li, *Astrophys. J.* **756** (2012) 166

BASICS OF THE PRESSURON

O. MINAZZOLI¹, A. HEES²

¹ *Centre Scientifique de Monaco, 8 Quai Antoine 1er, Monaco*

*UMR ARTEMIS, CNRS, University of Nice Sophia-Antipolis, Observatoire de la Côte d'Azur, BP4229,
06304, Nice Cedex 4, France*

² *Department of Mathematics, Rhodes University, Grahamstown 6140, South Africa*

The pressuron is a specific case of a dilaton-like field that leads to a decoupling of the scalar-field in the field equation for pressureless fluids. Hence, the pressuron recovers general relativity in the limit of weak pressure. Here we review its basics.

1 Introduction

Perturbative string theory predicts a scalar partner to the metric called dilaton. At tree-level, the dilaton couples multiplicatively to both the Ricci scalar and matter, and is massless¹. Hence, the dilaton should lead to a violation of the various flavours of the Einstein equivalence principle. But for the theory to be potentially valid, it must be able to satisfy the strong observational constraints existing on the equivalence principle. Unfortunately, perturbative string theory cannot predict the effective form of the dilaton couplings and therefore cannot explain how the dilaton is supposed to satisfy those constraints. A handful set of (bottom-up) solutions have been proposed. The pressuron is one of them — although its phenomenology could be studied independently of its speculative fundamental origin.

2 Decoupling in pressurless regimes

Assuming that one can factorize the scalar field contribution to the mass out — which can be either an approximation (see section 5), or come from a more fundamental (top-down) reason that would have to be understood^a — the action of the pressuron in the string frame can be written generally as

$$S = \frac{1}{c} \int d^4x \sqrt{-g} \frac{1}{2\kappa} (h^2 R - Z(h)(\partial h)^2 - V(h)) - c^2 \sum_A \int h m_A d\tau_A, \quad \text{with } \frac{dm_A}{d\tau_A} = 0, \quad (1)$$

where κ is the gravitational coupling constant, g is the determinant of the space-time metric $g_{\mu\nu}$, h is a scalar field, $Z(h)$ and $V(h)$ are arbitrary functions. Note that in this model all atom masses as well as the Planck mass are proportional to the pressuron field. We consider both massless and self-interacting cases to stay as general as possible. Considering the standard model of particles at low energies and in the chiral limit, one would have $m_A \sim AN\Lambda$, where Λ

^aNote for instance that in Bars, Steinhardt and Turok², local conformal symmetry in the particle sector implies that all masses are proportional to the non-minimally coupled scalar-field h — that is identified to the Higgs field in their fully Weyl invariant model of fundamental physics (ie. gravitation and particle physics).

is the quantum chromodynamics (QCD) renormalisation group invariant mass scale, N a pure number and A the atomic (mass) number of the considered atom³. The material part of the Lagrangian can be rewritten equivalently as follows:

$$\begin{aligned} S_m &= -\frac{1}{c} \int d^4x \sqrt{-g} h c^2 \rho, \quad \text{with } \nabla_\sigma(\rho U^\sigma) = 0, \\ \rho &= \sum_A (\sqrt{-g} U^0)^{-1} m_A \delta^{(3)}(x^\alpha - x_A^\alpha), \quad \text{and } U_A^\alpha \equiv \frac{dx^\alpha}{cd\tau_A}, \end{aligned} \quad (2)$$

where $\delta^{(3)}$ is the 3-Dirac delta function. It is obvious that one can rewrite action in Eq. 1 in the Einstein frame where the scalar field no-longer couples to neither the metric nor to the material fields

$$S = \frac{1}{c} \int d^4x \sqrt{-\bar{g}} \frac{1}{2\kappa} \left(\bar{R} - \bar{Z}(h)(\bar{\partial}h)^2 - \bar{V}(h) \right) - c^2 \sum_A \int m_A d\bar{\tau}_A, \quad \text{with } \bar{g}_{\mu\nu} = h^2 g_{\mu\nu}. \quad (3)$$

Therefore, as long as dust fields are considered, the theory is not different from general relativity. In other words, in the pressureless limit, the pressuron theory is nothing but a ‘‘Veiled’’ general relativity⁴. The question now is: what happens when material fields are pressureful?

3 From pressureless to pressureful fluids

One searches the Lagrangian \mathcal{L}_m suitable for pressureful perfect fluids — where one uses the following definition $S_m = 1/c \int d^4x \sqrt{-g} h \mathcal{L}_m$. In the pressureless case, Eq. 2 shows that $\mathcal{L}_m = -c^2 \rho$. One can show that the conservation equation $\nabla_\sigma(\rho U^\sigma) = 0$ — coming from the assumption that the pressuron field contribution to the mass can be factorized out (ie. $dm_A/d\tau_A = 0$ in Eq. 1) — induces a strict relation between the rest mass energy density variation and the metric field variation given by⁵ $\delta\rho = 1/2 \rho(g_{\mu\nu} + U_\mu U_\nu) \delta g^{\mu\nu}$. Using this relation, one can derive the following equation for the stress-energy tensor of a barotropic fluid:

$$T_{\mu\nu} \equiv \frac{2}{\sqrt{-g}} \frac{\partial(\sqrt{-g} \mathcal{L}_m)}{\partial g^{\mu\nu}} = -\rho \frac{d\mathcal{L}_m}{d\rho} U_\mu U_\nu + \left(\mathcal{L}_m - \rho \frac{d\mathcal{L}_m}{d\rho} \right) g_{\mu\nu}. \quad (4)$$

Since we want the Lagrangian \mathcal{L}_m of a perfect fluid, one simply has to equalize this equation to the stress-energy tensor of a perfect fluid $T_{\mu\nu} = (\epsilon + P)U_\mu U_\nu + P g_{\mu\nu}$, where ϵ is the total energy density of the fluid and P its pressure. This leads to a set of two first order linear equations whose solution when considering a barotropic fluid is⁶ $\mathcal{L}_m = -\epsilon(\rho)$. Therefore, the action considered in Eq. 1 for a barotropic perfect fluid becomes⁷

$$S = \frac{1}{c} \int d^4x \sqrt{-g} \left[\frac{1}{2\kappa} (h^2 R - Z(h)(\partial_\sigma h)^2 - V(h)) - h\epsilon \right], \quad \text{with } \epsilon(\rho) = c^2 \rho + \rho \int \frac{P(\rho)}{\rho^2} d\rho. \quad (5)$$

This way, one recovers the usual conservation equation for the total energy density $\nabla_\sigma(\epsilon U^\sigma) = -P \nabla_\sigma U^\sigma$. Note however that the equation of motion is unconventional: diffeomorphism invariance of action in Eq. (5) induces $\nabla_\sigma T^{\mu\sigma} = -(\epsilon g^{\mu\sigma} + T^{\mu\sigma}) \partial_\sigma \ln h$. Now, one can check that in comparison to the pressureless case, the scalar field in the Einstein frame action is no longer totally decoupled from matter because of a remaining pressure term. Hence the theory is no longer equivalent to general relativity when there is pressure. In some sense, pressure breaks the equivalence between the pressuron action and general relativity. Indeed, in both Einstein and string frames, the pressuron is sourced by pressure and not by energy density (i.e. roughly speaking, one has $\square h \propto P$ instead of $\square h \propto \epsilon$)^{7,8,9}. For instance, in the string frame, the scalar field equation reads

$$\square h + \frac{1}{h} \left[1 + \frac{h}{2} \frac{Z_{,h}(h)}{Z(h) + 6} \right] (\partial h)^2 = \frac{\kappa 3P}{Z(h) + 6} + \frac{V_{,h}(h)/2 - 2V(h)/h}{Z(h) + 6}. \quad (6)$$

Fortunately, in weak gravitational fields such as in the solar system, bodies pressure is orders of magnitude lower than their energy density (e.g. $P/(c^2\rho) \sim 10^{-6}$ for the Earth). Therefore, effects of the pressuron field are drastically reduced in low pressure regions such as in the solar system⁷ or during the cosmological matter era^{8,9}, whether the pressuron is massless or not. Hence, the pressuron is not constrained by current solar system gravitational tests as long as Z is not close to the singular value $Z = -6$. But as in usual Brans-Dicke theory, the singularity corresponds to an infinite coupling function in the Einstein frame such that it cannot be reached dynamically^{8,9}.

Note also that Z can be re-written in terms of the usual Brans-Dicke omega function via⁷ $Z(h) = 4\omega(h^2)$. On the other side, depending on the coupling function $Z(h)$, one can expect to see a pressuron's signature in strong field regimes, where pressure cannot be neglected. Hence, testing the theory in these regimes may be the only way to reasonably constrain it. In particular, it would be interesting to see whether or not a spontaneous scalarization can occur as in standard scalar-tensor theories for specific parameters¹⁰.

4 Cosmology

During the matter era the matter content of the universe is dominated by pressure-less fields. Therefore, the massless theory quickly converges towards a constant scalar field regardless the pressuron's value at the transition between the radiation and the matter era^{8,9}. For that reason, the pressuron cannot explain dark energy by itself and needs either a cosmological constant or a self-interaction potential — or some feedback effects — in order to explain the apparent acceleration of the expansion of the universe⁸. This may be seen as a drawback of the theory only if one believes that dilaton fields should also play the role of dark energy. However, there is no fundamental reason to believe so at the moment. Also because of the quick convergence of the pressuron during the matter era, the electromagnetic-pressuron coupling is not constrained by cosmological observations^{11,12} at low redshift.

The radiation era is more subtle when there is a multiplicative scalar-matter coupling because it is not obvious if the perfect fluid on-shell Lagrangian $\mathcal{L}_m = -\epsilon$ can still be used in this era. This subject is currently under investigation. However, it is expected that unlike in “standard” scalar-tensor theories¹³, the reduced scalar-field equation in the Einstein frame will keep a potential term during the radiation era, leading to a Damour and Nordtvedt dynamical decoupling mechanism¹³ during this period for a subclass of functions⁹ Z . In this scenario, Z would be dynamically driven toward a big value during the radiation era. But unlike in standard scalar-tensor theory, this mechanism is not mandatory in order to explain solar system observations since the pressuron is automatically already weakly coupled in regions with low pressure.

5 From universality to a more likely picture

In section 2, one assumes that the dilaton contribution can be factorized out of the particle masses at the level of the effective hadronic action. However, due to the complicated nature of the various contributions to the mass of nucleons, a more likely picture would be that the dilaton field cannot be fully factorized out, but that there would remain some functional dependencies of the masses with respect to the dilaton. In the action of Eq. 1, it would mean that one effectively has $m_A = m_A(h)$ and therefore $dm_A/d\tau \neq 0$.

However, since most of nucleons mass comes from the gluonic interaction, it is sufficient to suppose that the dilaton couples multiplicatively to the chiral limit of nucleons mass (ie. $\mathcal{L}_g \propto h\Lambda$, where Λ is the renormalisation group invariant QCD mass scale) to get a partial decoupling characterized by the fact that the main microscopic contribution to the particles mass (but not all contributions) will cancel out in the scalar-field equation. In that picture,

one would get deviations from general relativity, but weaker than for general dilaton fields. In addition, a linear coupling to the fermions mass as well can enhance this decoupling. In this optimistic scenario, only a few 0.1% of nucleons mass corresponding to the photons cloud could contribute to terms that violate the equivalence principle. In that case, one expects to get equivalence principle violating terms similar to those computed in Damour and Donoghue¹⁴, but with a decrease of about four orders of magnitude compared to the general dilaton case. A derivation of the actual numerical decoupling amplitudes in the chiral perturbation theory framework for various set of dilatonic parameters is on its way. Also, in this picture, one shall have to re-derive the fluid limit with $dm/d\tau \neq 0$. Indeed, let us recall that $\mathcal{L}_m = -\epsilon$ is solution of a set of equations that one expects to be modified when $dm/d\tau \neq 0$. Hence, it is likely that one will get a slightly different effective fluid Lagrangian, that nonetheless has to reduce to $\mathcal{L}_m = -\epsilon$ in the universal limit considered in sections 2 and 3 (ie. $dm/d\tau \rightarrow 0$). The question relative to the effective fluid description in this more likely picture is also under consideration.

6 Conclusion

It is often believed that a massless scalar field that would couple to both the Ricci and matter in the action necessarily leads to strong departures from what is observed in our solar system. However, we found a specific phenomenological example for which it is not the case. From a theoretical point of view, it would be interesting to see if one could imagine a top-down justification to the specific effective pressuron coupling, may it be in the string framework or not. From a phenomenological point of view, whether it is massless or not, one should try to derive the full pressuron phenomenology in order to find observational ways to constrain it.

Acknowledgments

The authors are really grateful to the organizers for having them get financial support to attend the conference. In addition, AH acknowledges support from “Fonds Spécial de Recherche” through a FSR-UCL grant.

References

1. T. Damour and A. M. Polyakov, *Nucl. Phys. B* **423**, 532 (1994).
2. I. Bars, P. Steinhardt, and N. Turok, *Phys. Rev. D* **89**, 043515 (2014).
3. J. Gasser and H. Leutwyler, *Physics Reports* **87**, 77 (1982).
4. N. Deruelle and M. Sasaki. *Cosmology, Quantum Vacuum and Zeta Functions*, Springer Proceedings in Physics page 247, 2011.
5. T. Harko, *Phys. Rev. D* **81**, 084050 (2010).
6. O. Minazzoli and T. Harko, *Phys. Rev. D* **86**, 087502 (2012).
7. O. Minazzoli and A. Hees, *Phys. Rev. D* **88**, 041504 (2013).
8. O. Minazzoli and A. Hees, *Phys. Rev. D* **90**, 023017 (2014).
9. O. Minazzoli, *Phys. Lett. B* **735**, 119 (2014).
10. T. Damour and G. Esposito-Farèse, *Phys. Rev. D* **54**, 1474 (1996).
11. A. Hees, O. Minazzoli, and J. Larena, *Phys. Rev. D* **90**, 124064 (2014).
12. A. Hees, O. Minazzoli, and J. Larena, *Gen. Rel. and Grav.* **47**, 9 (2015).
13. T. Damour and K. Nordtvedt, *Phys. Rev. D* **48**, 3436 (1993).
14. T. Damour and J. F. Donoghue, *Phys. Rev. D* **82**, 084033 (2010).

A DARK MATTER SUPERFLUID

Justin Khoury

*Center for Particle Cosmology, Department of Physics and Astronomy,
University of Pennsylvania, Philadelphia, PA 19104*



In this talk we present a novel framework that unifies the stunning success of MOND on galactic scales with the triumph of the Λ CDM model on cosmological scales. This is achieved through the rich and well-studied physics of superfluidity. The dark matter and MOND components have a common origin, representing different phases of a single underlying substance. In galaxies, dark matter thermalizes and condenses to form a superfluid phase. The superfluid phonons couple to baryonic matter particles and mediate a MOND-like force. Our framework naturally distinguishes between galaxies (where MOND is successful) and galaxy clusters (where MOND is not): dark matter has a higher temperature in clusters, and hence is in a mixture of superfluid and normal phase. The rich and well-studied physics of superfluidity leads to a number of striking observational signatures, which we briefly discuss. Remarkably the critical temperature and equation of state of the dark matter superfluid are similar to those of known cold atom systems. Identifying a precise cold atom analogue would give important insights on the microphysical interactions underlying DM superfluidity. Tantalizingly, it might open the possibility of simulating the properties and dynamics of galaxies in laboratory experiments.

1 Introduction

In the Λ -Cold-Dark-Matter (Λ CDM) standard model of cosmology, dark matter (DM) consists of collisionless particles. This model does exquisitely well at fitting a number of large-scale observations, from the background expansion history to the cosmic microwave background anisotropies to the linear growth of cosmic structures¹.

On the scales of galaxies, however, the situation is murkier. A number of challenges have emerged for the standard Λ CDM model in recent years, as observations and numerical simulations of galaxies have improved in tandem. For starters, galaxies in our universe are surprisingly regular, exhibiting striking correlations among their physical properties. For instance, disc galaxies display a remarkably tight correlation between the total baryonic mass (stellar + gas) and the asymptotic rotational velocity, $M_b \sim v_c^4$. This scaling relation, known as the Baryonic Tully-Fisher Relation (BTFR)^{2,3}, is unexplained in the standard model. In order to reproduce the BTFR on average, simulations must finely adjust many parameters that model complex baryonic processes. Given the stochastic nature of these processes, the predicted scatter around

the BTFR is much larger than the observed tight correlation⁴.

Another suite of puzzles comes from the distribution of dwarf satellite galaxies around the Milky Way (MW) and Andromeda galaxies. The Λ CDM model predicts hundreds of small DM halos orbiting MW-like galaxies, which are in principle good homes for dwarf galaxies, yet only $\sim 20 - 30$ dwarfs are observed around the MW and Andromeda. Recent attempts at matching the populations of simulated subhaloes and observed MW dwarf galaxies have revealed a “too big to fail” problem⁵: the most massive dark halos seen in the simulations are too dense to host the brightest MW satellites. Even more puzzling is the fact that the majority of the MW⁶ and Andromeda^{7,8} satellites lie within vast planar structures and are co-rotating within these planes. (Phase-space correlated dwarfs have also been found around galaxies beyond the Local Group⁹.) This suggests that dwarf satellites did not form independently, as predicted by the standard model, but may have been created through an entirely different mechanism^{6,10}.

A radical alternative is MODified Newtonian Dynamics (MOND)^{11,12}. MOND replaces DM with a modification to Newton’s gravitational force law that kicks in whenever the acceleration drops below a critical value a_0 . For large acceleration, $a \gg a_0$, the force law recovers Newtonian gravity: $a \simeq a_N$. At low acceleration, $a \ll a_0$, the force law is modified: $a \simeq \sqrt{a_N a_0}$. This simple empirical law has been remarkably successful at explaining a wide range of galactic phenomena¹³. In particular, asymptotically flat rotation curves and the BTFR are exact consequences of the force law.⁹ MOND does exquisitely well at fitting detailed galactic rotation curves, as shown in Fig. 1. There is a single parameter, the critical acceleration a_0 , whose best-fit value is intriguingly of order the speed of light c times the Hubble constant H_0 : $a_0 \simeq \frac{1}{6} c H_0 \simeq 1.2 \times 10^{-8} \text{ cm/s}^2$.

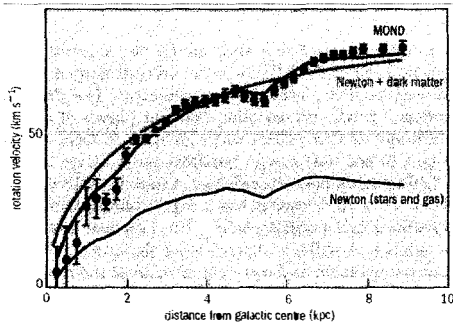


Figure 1 – Observed rotation curve for NGC1560 (blue points)¹⁴. The MOND curve (green)¹⁵ offers a much better fit to the data than the Λ CDM curve (blue)¹⁶. Reproduced from¹⁷.

However, the empirical success of MOND is limited to galaxies. The predicted X-ray temperature profile in massive clusters of galaxies is far from the observed approximately isothermal profile¹⁸. Relativistic extensions of MOND, *e.g.*¹⁹, fail to reproduce CMB anisotropies and large-scale clustering of galaxies²⁰. The “Bullet” Cluster^{21,22}, the aftermath of two colliding galaxy clusters, is also problematic for MOND²³.

2 Dark Matter Condensate

In this talk, based on two recent papers^{24,25}, we present a unified framework for the DM and MOND phenomena based on the rich and well-studied physics of superfluidity. The DM and

⁹Consider a test particle orbiting a galaxy of mass M_b , in the low acceleration regime. Equating the centripetal acceleration v^2/r to the MONDian acceleration $\sqrt{a_N a_0} = \sqrt{\frac{G_N M_b a_0}{r^2}}$, we obtain a velocity that is independent of distance, $v^2 = \sqrt{G_N M_b a_0}$, in agreement with the flat rotation curves of spiral galaxies. Squaring this gives the BTFR relation $M_b = \frac{v^4}{G_N a_0}$ as an exact prediction.

MOND components have a common origin, representing different phases of a single underlying substance. The central idea is that DM forms a superfluid inside galaxies, with a coherence length of galactic size.

As is familiar from liquid helium, a superfluid at finite temperature (but below the critical temperature) is best described phenomenologically as a mixture of two fluids^{26,27,28}: *i*) the superfluid, which by definition has vanishing viscosity and carries no entropy; *ii*) the “normal” component, comprised of massive particles, which is viscous and carries entropy. The fraction of particles in the condensate decreases with increasing temperature. Thus our framework naturally distinguishes between galaxies (where MOND is successful) and galaxy clusters (where MOND is not). Galaxy clusters have a higher velocity dispersion and correspondingly higher DM temperature. For $m \sim \text{eV}$ we will find that galaxies are almost entirely condensed, whereas galaxy clusters are either in a mixed phase or entirely in the normal phase.

As a back-of-the-envelope calculation, we can estimate the condition for the onset of superfluidity ignoring interactions among DM particles. With this simplifying approximation, the requirement for superfluidity amounts to demanding that the de Broglie wavelength $\lambda_{\text{dB}} \sim 1/mv$ of DM particles should be larger than the interparticle separation $\ell \sim (m/\rho)^{1/3}$. This implies an upper bound on the particle mass, $m \lesssim (\rho/v^3)^{1/4}$. Substituting the value of v and ρ at virialization, given by standard collapse theory, this translates to^{24,25}

$$m \lesssim 2.3 (1 + z_{\text{vir}})^{3/8} \left(\frac{M}{10^{12} h^{-1} M_{\odot}} \right)^{-1/4} \text{ eV}, \quad (1)$$

where M and z_{vir} are the mass and virialization redshift of the object. Hence light objects form a Bose-Einstein condensate (BEC) while heavy objects do not.

Another requirement for Bose-Einstein condensation is that DM thermalize within galaxies. We assume that DM particles interact through contact repulsive interactions. Demanding that the interaction rate be larger than the galactic dynamical time places a lower bound on the interaction cross-section. For $M = 10^{12} h^{-1} M_{\odot}$ and $z_{\text{vir}} = 2$, the result is^{24,25}

$$\frac{\sigma}{m} \gtrsim \left(\frac{m}{\text{eV}} \right)^4 \frac{\text{cm}^2}{\text{g}}. \quad (2)$$

With $m \lesssim \text{eV}$, this is just below the most recent constraint from galaxy cluster mergers²⁹, though such constraints should be carefully reanalyzed in the superfluid context.

Again ignoring interactions, the critical temperature for DM superfluidity is $T_c \sim \text{mK}$, which intriguingly is comparable to known critical temperatures for cold atom gases, *e.g.*, ${}^7\text{Li}$ atoms have $T_c \simeq 0.2 \text{ mK}$. Cold atoms might provide more than just a useful analogy — in many ways, our DM component behaves exactly like cold atoms. In cold atom experiments, atoms are trapped using magnetic fields; in our case, DM particles are attracted in galaxies by gravity.

3 Superfluid Phase

Instead of behaving as individual collisionless particles, the DM is more aptly described as collective excitations: phonons and massive quasi-particles. Phonons, in particular, play a key role by mediating a long-range force between ordinary matter particles. As a result, a test particle orbiting the galaxy is subject to two forces: the (Newtonian) gravitational force and the phonon-mediated force.

Specifically, it is well-known that the effective field theory (EFT) of superfluid phonon excitations at lowest order in derivatives is a $P(X)$ theory³⁰. Our postulate is that DM phonons are described by the non-relativistic MOND scalar action,

$$P(X) \sim \Lambda X \sqrt{|X|}; \quad X = \dot{\theta} - m\Phi - \frac{(\vec{\nabla}\theta)^2}{2m}. \quad (3)$$

where $\Lambda \sim \text{meV}$ to reproduce the MOND critical acceleration, and Φ is the gravitational potential. The fractional $3/2$ power would be strange if Eq. (3) described a fundamental scalar field. As a theory of phonons, however, it is not uncommon to encounter fractional powers in cold atom systems. For instance, the Unitary Fermi Gas (UFG)^{31,32}, which has generated much excitement recently in the cold atom community, describes a gas of cold fermionic atoms tuned at unitarity. The effective action for the UFG superfluid is uniquely fixed by 4d scale invariance at lowest-order in derivatives, $\mathcal{L}_{\text{UFG}}(X) \sim X^{5/2}$, which is also non-analytic³³.

To mediate a force between ordinary matter, θ must couple to the baryon density:

$$\mathcal{L}_{\text{int}} = -\alpha \frac{\Lambda}{M_{\text{Pl}}} \theta \rho_{\text{b}}, \quad (4)$$

where α is a dimensionless parameter. This term explicitly breaks the shift symmetry, but only at the $1/M_{\text{Pl}}$ level and is therefore technically natural. From the superfluid perspective, Eq. (4) can arise if baryonic matter couple to the vortex sector of the superfluid, giving rise to operators $\sim \cos \theta \rho_{\text{b}}$ that preserve a discrete subgroup of the continuous shift symmetry^{34,35,36}.

3.1 Properties of the Condensate and Phonons

The form of the phonon action uniquely fixes the properties of the condensate through standard thermodynamics arguments. At finite chemical potential, $\theta = \mu t$, ignoring phonon excitations and gravitational potential to zero, the pressure of the condensate is given as usual by the Lagrangian density,

$$P(\mu) = \frac{2\Lambda}{3} (2m\mu)^{3/2}. \quad (5)$$

This is the grand canonical equation of state, $P = P(\mu)$, for the condensate. Differentiating with respect to μ yields the number density of condensed particles:

$$n = \frac{\partial P}{\partial \mu} = \Lambda(2m)^{3/2} \mu^{1/2}. \quad (6)$$

Combining these expressions and using the non-relativistic relation $\rho = mn$, we find

$$P = \frac{\rho^3}{12\Lambda^2 m^6}. \quad (7)$$

This is a polytropic equation of state $P \sim \rho^{1+1/n}$ with index $n = 1/2$.

Including phonons excitations $\theta = \mu t + \phi$, the quadratic action for ϕ is

$$\mathcal{L}_{\text{quad}} = \frac{\Lambda(2m)^{3/2}}{4\mu^{1/2}} \left(\dot{\phi}^2 - \frac{2\mu}{m} (\vec{\nabla}\phi)^2 \right). \quad (8)$$

The sound speed can be immediately read off:

$$c_s = \sqrt{\frac{2\mu}{m}}. \quad (9)$$

3.2 Halo profile

Assuming hydrostatic equilibrium, we can compute the density profile of a spherically-symmetric DM condensate halo:

$$\frac{1}{\rho(r)} \frac{dP(r)}{dr} = -\frac{4\pi G_{\text{N}}}{r^2} \int_0^r dr' r'^2 \rho(r'). \quad (10)$$

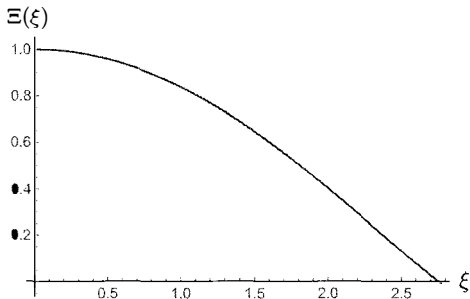


Figure 2 – Numerical solution of Lane-Emden equation, Eq. (11).

Substituting the equation of state given by Eq. (7), and introducing the dimensionless variables $\rho = \rho_0 \Xi$ and $r = \sqrt{\frac{\rho_0}{32\pi G_N \Lambda^2 m^6}} \xi$, with ρ_0 denoting the central density, Eq. (10) implies the Lane-Emden equation

$$\left(\xi^2 \Xi'\right)' = -\xi^2 \Xi^{1/2}, \quad (11)$$

where $' \equiv d/d\xi$. The numerical solution, with boundary conditions $\Xi(0) = 1$ and $\Xi'(0) = 0$, is shown in Fig. 2. The superfluid density profile is cored, not surprisingly, and therefore avoids the cusp problem of CDM.

The density is found to vanish at $\xi_1 \simeq 2.75$, which defines the halo size: $R = \sqrt{\frac{\rho_0}{32\pi G_N \Lambda^2 m^6}} \xi_1$. Meanwhile the central density is related to the halo mass as³⁷ $\rho_0 = \frac{3M}{4\pi R^3 |\Xi'(\xi_1)|}$, with $\Xi'(\xi_1) \simeq -0.5$. Combining these results, it is straightforward to solve for ρ_0 and R :

$$\begin{aligned} \rho_0 &\simeq \left(\frac{M_{\text{DM}}}{10^{12} M_\odot}\right)^{2/5} \left(\frac{m}{\text{eV}}\right)^{18/5} \left(\frac{\Lambda}{\text{meV}}\right)^{6/5} 7 \times 10^{-25} \text{ g/cm}^3; \\ R &\simeq \left(\frac{M_{\text{DM}}}{10^{12} M_\odot}\right)^{1/5} \left(\frac{m}{\text{eV}}\right)^{-6/5} \left(\frac{\Lambda}{\text{meV}}\right)^{-2/5} 36 \text{ kpc}. \end{aligned} \quad (12)$$

Remarkably, for $m \sim \text{eV}$ and $\Lambda \sim \text{meV}$ we obtain DM halos of realistic size! In the standard CDM picture a halo of mass $M_{\text{DM}} = 10^{12} M_\odot$ has a virial radius of ~ 200 kpc. In our framework, the condensate radius can in principle be considerably smaller or larger depending on parameter values. For concreteness, in the remainder of the analysis we will choose as fiducial values

$$m = 0.6 \text{ eV}; \quad \Lambda = 0.2 \text{ meV}. \quad (13)$$

This implies a condensate radius of ~ 125 kpc for a halo of mass $M_{\text{DM}} = 10^{12} M_\odot$.

4 Phonon-Mediated MONDian Force

Next we derive the phonon profile in galaxies, modeling the baryons as a static, spherically-symmetric localized source for simplicity. We first focus on the zero-temperature analysis, where the Lagrangian is given by the sum of Eqs. (3) and (4). In the static spherically-symmetric approximation, $\theta = \mu t + \phi(r)$, the equation of motion reduces to

$$\vec{\nabla} \cdot \left(\sqrt{2m|X|} \vec{\nabla} \phi \right) = \frac{\alpha \rho_b(r)}{2M_{\text{Pl}}}, \quad (14)$$

where $X(r) = \mu - m\Phi(r) - \frac{\phi'^2(r)}{2m}$. This can be readily integrated:

$$\sqrt{2m|X|} \phi' = \frac{\alpha M_b(r)}{8\pi M_{\text{Pl}} r^2} \equiv \kappa(r). \quad (15)$$

There are two branches of solutions, depending on the sign of X . We focus on the MOND branch (with $X < 0$):

$$\phi'(r) = \sqrt{m} \left(\hat{\mu} + \sqrt{\hat{\mu}^2 + \kappa^2/m^2} \right)^{1/2}, \quad (16)$$

where $\hat{\mu} \equiv \mu - m\Phi$. Indeed, for $\kappa/m \gg \hat{\mu}$ we have

$$\phi'(r) \simeq \sqrt{\kappa(r)}. \quad (17)$$

In this limit the scalar acceleration on an ordinary matter particle is

$$a_\phi(r) = \alpha \frac{\Lambda}{M_{\text{Pl}}} \phi' \simeq \sqrt{\frac{\alpha^3 \Lambda^2 G_N M_b(r)}{M_{\text{Pl}} r^2}}. \quad (18)$$

To reproduce the MONDian result $a_{\text{MOND}} = \sqrt{a_0 \frac{G_N M_b(r)}{r^2}}$, we are therefore led to identify

$$\alpha^{3/2} \Lambda = \sqrt{a_0 M_{\text{Pl}}} \simeq 0.8 \text{ meV} \implies \alpha \simeq 0.86 \left(\frac{\Lambda}{\text{meV}} \right)^{-2/3}, \quad (19)$$

which fixes α in terms of Λ through the critical acceleration. For the fiducial value $\Lambda = 0.2 \text{ meV}$, we obtain $\alpha \simeq 2.5$.

As it stands, however, the $X < 0$ solution is unstable. It leads to unphysical halos, with growing DM density profiles^{24,25}. The instability can be seen by expanding Eq. (3) to quadratic order in phonon perturbations $\varphi = \phi - \bar{\phi}(r)$,

$$\mathcal{L}_{\text{quad}} = \text{sign}(\bar{X}) \frac{\Lambda (2m)^{3/2}}{4\sqrt{|\bar{X}|}} \left(\dot{\varphi}^2 - 2 \frac{\bar{\phi}'}{m} \varphi' \dot{\varphi} - 2 \frac{\varphi'^2}{m} \left(\bar{X} - \frac{\bar{\phi}^{\prime 2}}{2m} \right) - \frac{2\bar{X}}{mr^2} (\partial_\Omega \varphi)^2 \right). \quad (20)$$

The kinetic term $\dot{\varphi}^2$ has the wrong sign for $\bar{X} < 0$. (The $X > 0$ branch, meanwhile, is stable but does not admit a MOND regime^{24,25}.)

Since the DM condensate in actual galactic halos has non-zero temperature, however, we expect that the zero-temperature Lagrangian (Eq. (3)) to receive finite-temperature corrections in galaxies. At finite sub-critical temperature, the system is described phenomenologically by Landau's two-fluid model: an admixture of a superfluid component and a normal component. The finite-temperature effective Lagrangian is a function of three scalars³⁸: $\mathcal{L}_{T \neq 0} = F(X, B, Y)$. The scalar X , already defined in Eq. (3), describes the phonon excitations. The remaining scalars are defined in terms of the three Lagrangian coordinates $\psi^I(\vec{x}, t)$, $I = 1, 2, 3$ of the normal fluid:

$$\begin{aligned} B &\equiv \sqrt{\det \partial_\mu \psi^I \partial^\mu \psi^J}; \\ Y &\equiv u^\mu \left(\partial_\mu \theta + m \delta_\mu^0 \right) - m \simeq \mu - m\Phi + \dot{\phi} + \vec{v} \cdot \vec{\nabla} \phi, \end{aligned} \quad (21)$$

where $u^\mu = \frac{1}{6\sqrt{B}} \epsilon^{\mu\alpha\beta\gamma} \epsilon_{IJK} \partial_\alpha \psi^I \partial_\beta \psi^J \partial_\gamma \psi^K$ is the unit 4-velocity vector, and in the last step for Y we have taken the non-relativistic limit $u^\mu \simeq (1 - \Phi, \vec{v})$. By construction, these scalars respect the internal symmetries: *i*) $\psi^I \rightarrow \psi^I + c^I$ (translations); *ii*) $\psi^I \rightarrow R^I_J \psi^J$ (rotations); *iii*) $\psi^I \rightarrow \xi^I(\psi)$, with $\det \frac{\partial \xi^I}{\partial \psi^J} = 1$ (volume-preserving reparametrizations).

There is much freedom in specifying finite-temperature operators that stabilize the MOND profile. The simplest possibility is to supplement Eq. (3) with the two-derivative operator

$$\Delta \mathcal{L} = M^2 Y^2 = M^2 (\dot{\mu} + \dot{\phi})^2, \quad (22)$$

where we have specialized to the rest frame of the normal fluid, $\vec{v} = 0$. This leaves the static profile given by Eq. (16) unchanged, but modifies the quadratic Lagrangian by $M^2 \dot{\phi}^2$, restoring stability for sufficiently large M . Specifically this is the case for

$$M \gtrsim \frac{\Lambda m^{3/2}}{\sqrt{|\bar{X}|}} \sim 0.5 \left(\frac{10^{11} M_\odot}{M_b} \right)^{1/4} \left(\frac{\Lambda}{\text{meV}} \right)^{1/2} \left(\frac{r}{10 \text{ kpc}} \right)^{1/2} m, \quad (23)$$

which, remarkably, is of order eV! Hence, for quite natural values of M , this two-derivative operator can restore stability. Furthermore, this operator gives a contribution $\Delta P = M^2 \mu^2$ to the condensate pressure, which obliterates the unwanted growth in the DM density profile. Instead, the pressure is positive far from the baryons, resulting in localized, finite-mass halos^{24,25}.

5 Observational Implications

We conclude with some astrophysical implications of our DM superfluid.

Gravitational Lensing: In TeVeS¹⁹ the complete absence of DM requires introducing a time-like vector field A_μ , as well as a complicated coupling between ϕ , A_μ and baryons in order to reproduce lensing observations. In our case, there is no need to introduce an extra vector, as the normal fluid already provides a time-like vector u^μ . Moreover, our DM contributes to lensing, so we are free to generalize the TeVeS coupling^{24,25}.

Vortices: When spun faster than a critical velocity, a superfluid develops vortices. The typical angular velocity of halos is well above critical^{24,25}, giving rise to an array of DM vortices permeating the disc³⁹. It will be interesting to see whether these vortices can be detected through substructure lensing, *e.g.*, with ALMA⁴⁰.

Galaxy mergers: A key difference with Λ CDM is the merger rate of galaxies. Applying Landau's criterion, we find two possible outcomes. If the infall velocity v_{inf} is less than the phonon sound speed c_s (of order the viral velocity^{24,25}), then halos will pass through each other with negligible dissipation, resulting in multiple encounters and a longer merger time. If $v_{\text{inf}} \gtrsim c_s$, however, the encounter will excite DM particles out of the condensate, resulting in dynamical friction and rapid merger.

Bullet Cluster: For merging galaxy clusters, the outcome also depends on the relative fraction of superfluid vs normal components in the clusters. For subsonic mergers, the superfluid cores should pass through each other with negligible friction (consistent with the Bullet Cluster), while the normal components should be slowed down by self interactions. Remarkably this picture is consistent with the lensing map of the Abell 520 "train wreck"^{41,42,43,44}, which show lensing peaks coincident with galaxies (superfluid components), as well as peaks coincident with the X-ray luminosity peaks (normal components).

Dark-bright solitons: Galaxies in the process of merging should exhibit interference patterns (so-called dark-bright solitons) that have been observed in BECs counterflowing at super-critical velocities⁴⁵. This can potentially offer an alternative mechanism to generate the spectacular shells seen around elliptical galaxies⁴⁶.

Globular clusters: Globular clusters are well-known to contain negligible amount of DM, and as such pose a problem for MOND⁴⁷. In our case the presence of a significant DM component is necessary for MOND. If whatever mechanism responsible for DM removal in Λ CDM is also effective here, our model would predict DM-free (and hence MOND-free) globular clusters.

Acknowledgments

I wish to thank Lasha Berezhiani for a stimulating collaboration. I also want to warmly thank the organizers and participants of the 2015 Rencontres de Moriond for an inspiring and most enjoyable conference. This work is supported in part by NSF CAREER Award PHY-1145525 and NASA ATP grant NNX11AI95G.

References

1. P. A. R. Ade *et al.* [Planck Collaboration], *Astron. Astrophys.* **571**, A16 (2014).
2. S. S. McGaugh, J. M. Schombert, G. D. Bothun and W. J. G. de Blok, *Astrophys. J.* **533**, L99 (2000).
3. S. S. McGaugh, *Astrophys. J.* **632**, 859 (2005).
4. M. Vogelsberger *et al.*, *MNRAS* **444**, 1518 (2014).
5. M. Boylan-Kolchin, J. S. Bullock and M. Kaplinghat, *MNRAS* **415**, L40 (2011).
6. M. S. Pawlowski, J. Pflamm-Altenburg and P. Kroupa, *MNRAS* **423**, 1109 (2012).
7. R. A. Ibata *et al.*, *Nature* **493**, 62 (2013).
8. R. A. Ibata *et al.*, *Astrophys. J.* **784**, L6 (2014).
9. N. G. Ibata, R. A. Ibata, B. Famaey and G. F. Lewis, *Nature* **511**, 563 (2014).
10. H. Zhao, B. Famaey, F. Lghausen and P. Kroupa, *Astron. Astrophys.* **557**, L3 (2013).
11. M. Milgrom, *Astrophys. J.* **270**, 365 (1983).
12. R. H. Sanders and S. S. McGaugh, *Ann. Rev. Astron. Astrophys.* **40**, 263 (2002).
13. B. Famaey and S. McGaugh, *Living Rev. Rel.* **15**, 10 (2012).
14. A. H. Broeils, *Astron. and Astrophys.* **256**, 19 (1992).
15. K. G. Begeman, A. H. Broeils and R. H. Sanders, *MNRAS* **249**, 523 (1991).
16. J. A. Sellwood and S. S. McGaugh, *Astrophys. J.* **634**, 70 (2005).
17. M. Milgrom, arXiv:0908.3842 [astro-ph.CO].
18. A. Aguirre, J. Schaye and E. Quataert, *Astrophys. J.* **561**, 550 (2001).
19. J. D. Bekenstein, *Phys. Rev. D* **70**, 083509 (2004) [Erratum-ibid. *D* **71**, 069901 (2005)].
20. C. Skordis, D. F. Mota, P. G. Ferreira and C. Boehm, *Phys. Rev. Lett.* **96**, 011301 (2006).
21. D. Clowe, A. Gonzalez and M. Markevitch, *Astrophys. J.* **604**, 596 (2004).
22. D. Clowe *et al.*, *Astrophys. J.* **648**, L109 (2006).
23. G. W. Angus, B. Famaey and H. Zhao, *MNRAS* **371**, 138 (2006).
24. L. Berezhiani and J. Khoury, arXiv:1506.07877 [astro-ph.CO].
25. L. Berezhiani and J. Khoury, arXiv:1507.01019 [astro-ph.CO].
26. L. Tisza, *C. R. Acad. Sci.* **207**, 1035 (1938); **207**, 1186 (1938).
27. F. London, *Phys. Rev.* **54**, 947 (1938).
28. L. D. Landau, *J. Phys. (USSR)* **5**, 71 (1941); **11**, 91 (1947).
29. D. Harvey *et al.*, *Science* **347**, no. 6229, 1462 (2015).
30. D. T. Son, hep-ph/0204199.
31. W. Zwerger, ed. *The BCS-BEC Crossover and the Unitary Fermi Gas*, Lecture Notes in Physics, Vol. 836 (Springer-Verlag, Berlin Heidelberg, 2012).
32. S. Giorgini, L. P. Pitaevskii and S. Stringari, *Rev. Mod. Phys.* **80**, 1215 (2008).
33. D. T. Son and M. Wingate, *Annals Phys.* **321**, 197 (2006).
34. J. Villain, *J. Phys. (France)* **36**, 581 (1975).
35. J. V. José, L. P. Kadanoff, S. Fitzpatrick and D. R. Nelson, *Phys. Rev. B* **16**, 1217 (1977).
36. R. D. Kamien, HUTP-89/A025.
37. S. Chandrasekhar, "An introduction to the study of stellar structure," Dover Publications, New York (1957).
38. A. Nicolis, arXiv:1108.2513 [hep-th].
39. M. P. Silverman and R. L. Mallett, *Gen. Rel. Grav.* **34**, 633 (2002).
40. Y. Hezavehvet *et al.*, *Astrophys. J.* **767**, 9 (2013).
41. A. Mahdavi *et al.*, *Astrophys. J.* **668**, 806 (2007).
42. M. J. Jee *et al.*, *Astrophys. J.* **747**, 96 (2012).
43. D. Clowe *et al.*, *Astrophys. J.* **758**, 128 (2012).
44. M. J. Jee *et al.*, *Astrophys. J.* **783**, 78 (2014).
45. C. Hamner, J. J. Chang, P. Engels and M. A. Hoefler, *Phys. Rev. Lett.* **106**, 065302 (2011).
46. A. P. Cooper *et al.*, *Astrophys. J. Lett.* **743**, L21 (2011).
47. R. Ibata *et al.*, *Astrophys. J.* **738**, 186 (2011).

BIMETRIC GRAVITY AND DARK MATTER

Laura BERNARD and Luc BLANCHET

*GRεCO Institut d'Astrophysique de Paris, UMR 7095, CNRS,
Sorbonne Universités & UPMC Univ Paris 6, 98^{bis} boulevard Arago, 75014 Paris, France*

Lavinia HEISENBERG

*Nordita, KTH Royal Institute of Technology and Stockholm University,
Roslagstullsbacken 23, 10691 Stockholm, Sweden, and
Department of Physics & The Oskar Klein Centre,
AlbaNova University Centre, 10691 Stockholm, Sweden*

We review some recent proposals for relativistic models of dark matter in the context of bimetric gravity. The aim is to solve the problems of cold dark matter (CDM) at galactic scales, and to reproduce the phenomenology of the modified Newtonian dynamics (MOND), while still being in agreement with the standard cosmological model Λ -CDM at large scales. In this context a promising alternative is dipolar dark matter (DDM) in which two different species of dark matter particles are separately coupled to the two metrics of bigravity and are linked together by an internal vector field. The phenomenology of MOND then results from a mechanism of gravitational polarization. Probably the best formulation of the model is within the framework of recently developed massive bigravity theories. Then the gravitational sector of the model is safe by construction, but a ghostly degree of freedom in the decoupling limit is still present in the dark matter sector. Future work should analyze the cosmological solutions of the model and check the post-Newtonian parameters in the solar system.

1 Introduction and motivation

1.1 Problem of dark matter at galactic scales

The standard model of cosmology Λ -CDM is widely held to be an excellent description of reality at large cosmological scales. Impressive observational successes of this model include the fit of the anisotropies of the cosmic microwave background (CMB), the baryon acoustic oscillations, the formation of large scale structures and the accelerated expansion of the Universe. However some fundamental issues remain: (i) The measured value of the cosmological constant Λ looks unnatural from a quantum field perspective; (ii) The weakly interacting particles envisaged as candidates for the cold dark matter (CDM) are still undetected in the laboratory; (iii) The model Λ -CDM falls short in explaining the observed regularities in the properties of dark matter halos around galaxies.

Regarding point (iii) we have in mind the baryonic Tully-Fisher relation between the observed luminous mass and the asymptotic rotation velocity of spiral galaxies¹, the analogous Faber-Jackson relation for elliptical galaxies², and, very important, the tight correlation between the mass discrepancy (i.e. the presence of dark matter) and the involved acceleration scale³. In the prevailing view⁴, these issues should be resolved once we understand the complicated baryonic processes (e.g. supernova winds and outflows from a central supermassive black hole) that affect galaxy formation and evolution. Note that with such foreseen explanation, conclusive tests of

the Λ -CDM model become difficult since any new failure can be attributed to some further unknown aspect of baryonic physics. More importantly, this explanation is challenged by the fact that galactic data are — mysteriously enough — in excellent agreement with the MOND (MODified Newtonian Dynamics) empirical non relativistic formula^{5,6,7}.

A relativistic MOND theory is required to address issues concerning cosmology and gravitational lensing. Many relativistic extensions for MOND have been proposed, including a tensor-vector-scalar (TeVeS) theory^{8,9}, a bimetric theory¹⁰, non-canonical Einstein-Æther theories^{11,12}, a Galileon theory¹³, a Khronon theory¹⁴, a modified dark matter theory^{15,16,17}. Most theories have difficulties at reproducing the cosmological observations, notably the full spectrum of CMB anisotropies. An exception is the modified dark matter approach^{15,16,17} which agrees with the model Λ -CDM at first order cosmological perturbations. This approach, also called dipolar dark matter (DDM), is motivated by the dielectric analogy of MOND — that MOND represents the gravitational analogue of the Gauss law of electrostatics in dielectric non-linear materials^{18,19}. A natural formulation of the model is based on a bimetric extension of general relativity (GR)²⁰, where two species of dark matter particles are respectively coupled to the two metrics, and are linked by an internal vector field generated by the mass of these particles. In this model the phenomenology of MOND emerges naturally and elegantly from a mechanism of gravitational polarization.

1.2 Bimetric massive gravity theories

Bimetric theories have been extensively investigated in the quest of a consistent massive gravity theory. From a theoretical point of view, the existence of a graviton mass is a very important fundamental question. At the linear level, there is a unique mass term which ensures the absence of ghosts in the theory, namely the Fierz-Pauli action²¹. Even though theoretically consistent, this linear theory suffers from the van Dam-Veltman-Zakharov (vDVZ) discontinuity^{22,23}, which reflects the fact that one does not recover GR in the limit of vanishing graviton mass. In other words, this discontinuity can be traced to the coupling of the additional longitudinal graviton to the matter field in the mass going to zero limit. Vainshtein very soon realized that the nonlinearities of the theory become actually stronger in the vanishing mass limit²⁴, pointing that these nonlinearities might cure the vDVZ discontinuity, which required the non-linear completion of the Fierz-Pauli theory. Unfortunately, this task seemed to face the inevitable problem of reintroducing the ghost-like instability²⁵.

Recent joint effort to construct a consistent ghost-free non-linear theory for massive gravity gave fruitful results^{26,27,28,29}, which have initiated a revival of interests. The theory can be further generalized to bigravity³⁰, or multigravity³¹, by the inclusion of the corresponding additional kinetic terms. Another fundamental question in the context of massive gravity is the consistent coupling to the matter fields. If one couples the matter fields in a naive way additively to both metrics simultaneously, this immediately reintroduces the Boulware-Deser (BD) ghost^{32,33}. Moreover, quantum corrections at one loop dictate that the only consistent way of coupling the matter sector to the two metrics is either through a minimal coupling to just one metric (which preserves the technical naturalness of the theory^{34,35,36}), or through a composite effective metric built out of both metrics in a very specific way^{32,36,37}. An important consequence of the coupling through the effective metric is a possible way out of the no-go result for the flat Friedmann-Lemaître-Robertson-Walker (FLRW) metric together with the propagation of the five physical degrees of freedom of the graviton sector without introducing ghost and gradient instabilities³⁸.

Massive gravity is replete of phenomenology. Especially, its potential application in cosmology received much attention. Even if the decoupling limit of the theory admits self-accelerating solutions³⁹, the full theory with Minkowski reference metric suffers from the no-go result for flat FLRW solution⁴⁰. The cosmology of the bigravity theory has more freedom and features due to the dynamics of the reference metric^{41,42,43}. Assuming that the matter fields couple minimally

to one metric and further assuming that the mass of the graviton is of the same order as the Hubble parameter today, the theory admits several interesting branches of solutions.

1.3 Content and summary

In Sec. 2 of this paper we shall review the initial bimetric model²⁰ and the broad range of phenomenology it is able to predict. On the bad side of this model, we shall also discuss, in Sec. 2.3, with the help notably of the minisuperspace of the model, the likely presence of ghost instabilities. This will motivate the redefinition, in Sec. 3, of the gravitational sector of the model²⁰ in a way to make it consistent with the beautiful framework of massive bigravity theories^{44,45}. Gladly, this move will substantially simplify the model. On the other hand, the dark matter sector will essentially remain the same as in²⁰. The mechanism of gravitational polarization, and recovery of the MOND equation, checked in Sec. 3.2, thus appear as a natural consequence of massive bigravity theory for this type of matter. Concerning ghosts, the new model is safe in the gravitational sector (by construction), but a ghostly degree of freedom in the decoupling limit is reintroduced in the dark matter sector⁴⁵. A crucial question to address in future work is whether the polarization mechanism can be realized in absence of ghosts.

2 Bimetric theory with two dark matter species

2.1 Relativistic action

A relativistic model involving, in addition to the ordinary matter simply described by baryons, two species of dark matter particles, was proposed in²⁰. A vector field \mathcal{A}_μ is sourced by the mass currents of dark matter and dubbed *graviphoton*. This vector field is crucial in order to ensure the stability of the dipolar medium. The gravitational sector is composed of two dynamical Lorentzian metrics $g_{\mu\nu}$ and $f_{\mu\nu}$. The baryons (representing in fact the full standard model of particle physics) are coupled in the usual way to the metric $g_{\mu\nu}$. The two species of dark matter particles are respectively coupled to the two metrics $g_{\mu\nu}$ and $f_{\mu\nu}$. The gravitational-plus-matter action of the model²⁰ reads (in geometrical units $G = c = 1$)

$$S = \int d^4x \left\{ \sqrt{-g} \left(\frac{R_g - 2\lambda_g}{32\pi} - \rho_{\text{bar}} - \rho_g \right) + \sqrt{-f} \left(\frac{R_f - 2\lambda_f}{32\pi} - \rho_f \right) + \sqrt{-G_{\text{eff}}} \left[\frac{\mathcal{R}_{\text{eff}} - 2\lambda_{\text{eff}}}{16\pi\varepsilon} + (\mathcal{J}_g^\mu - \mathcal{J}_f^\mu) \mathcal{A}_\mu + \frac{a_0^2}{8\pi} \mathcal{W}(\mathcal{X}) \right] \right\}. \quad (1)$$

Here R_g , R_f and \mathcal{R}_{eff} are the Ricci scalars of the g and f metrics, and of an effective composite metric $G_{\mu\nu}^{\text{eff}}$ defined non-perturbatively from $g_{\mu\nu}$ and $f_{\mu\nu}$ by^a

$$G_{\mu\nu}^{\text{eff}} = g_{\mu\rho} X_\nu^\rho = f_{\mu\rho} Y_\nu^\rho, \quad (2)$$

where the square root matrix is defined by $X = \sqrt{g^{-1}f}$, together with its inverse $Y = \sqrt{f^{-1}g}$. Notice that $G_{\mu\nu}^{\text{eff}}$ can be shown to be automatically symmetric^{46,47}. The dimensionless coupling constant ε measures the strength of the interaction between the two sectors g and f . We inserted three different cosmological constants λ_g , λ_f and λ_{eff} in the g , f and interaction sectors. They will be ultimately related to the observed cosmological constant Λ .

Baryons and dark matter particles are described by pressureless fluids with conserved scalar densities ρ_{bar} , ρ_g and ρ_f . In addition \mathcal{J}_g^μ and \mathcal{J}_f^μ stand for the mass currents of the two types

^aActually the effective composite metric was defined in²⁰ by the different condition

$$G_{\mu\nu}^{\text{eff}} = G_{\text{eff}}^{\rho\sigma} g_{\rho\mu} f_{\nu\sigma} = G_{\text{eff}}^{\rho\sigma} g_{\rho\nu} f_{\mu\sigma}.$$

It has been shown⁴⁴ that this condition is equivalent to the requirement (2).

of dark matter particles, defined by

$$\sqrt{-\mathcal{G}_{\text{eff}}}J_g^\mu = \sqrt{-g}J_g^\mu, \quad \sqrt{-\mathcal{G}_{\text{eff}}}J_f^\mu = \sqrt{-f}J_f^\mu, \quad (3)$$

where $J_g^\mu = \rho_g u_g^\mu$ and $J_f^\mu = \rho_f u_f^\mu$ are the conserved dark matter currents associated with the respective metrics g and f , thus obeying $\nabla_\mu^g J_g^\mu = 0$ and $\nabla_\mu^f J_f^\mu = 0$.

The vector field \mathcal{A}_μ obeys a non-canonical kinetic term $\mathcal{W}(\mathcal{X})$ where

$$\mathcal{X} = -\frac{\mathcal{G}_{\text{eff}}^{\mu\rho}\mathcal{G}_{\text{eff}}^{\nu\sigma}\mathcal{F}_{\mu\nu}\mathcal{F}_{\rho\sigma}}{2a_0^2}, \quad (4)$$

with $\mathcal{F}_{\mu\nu} = \partial_\mu\mathcal{A}_\nu - \partial_\nu\mathcal{A}_\mu$. Note that the vector field strength in (4) has been rescaled by the MOND acceleration $a_0 \simeq 1.2 \cdot 10^{-10} \text{ m/s}^2$. The function $\mathcal{W}(\mathcal{X})$ is determined phenomenologically, but in principle it should be interpreted within some more fundamental theory. In the limit $\mathcal{X} \ll 1$, which corresponds to the MOND weak-acceleration regime below a_0 , we impose

$$\mathcal{W}(\mathcal{X}) = \mathcal{X} - \frac{2}{3}\mathcal{X}^{3/2} + \mathcal{O}(\mathcal{X}^2). \quad (5)$$

On the other hand we also impose that when $\mathcal{X} \gg 1$, corresponding to the strong-acceleration regime much above a_0 ,

$$\mathcal{W}(\mathcal{X}) = A + \frac{B}{\mathcal{X}^b} + o\left(\frac{1}{\mathcal{X}^b}\right), \quad (6)$$

where A and B are constants and $b > 0$.

2.2 Phenomenological predictions

We now review the rich phenomenology of this model, which is quite successful at different scales and in different regimes. We refer to²⁰ for the details.

- *Cosmology.* We study the cosmology of the model by expanding the two metrics around two homogeneous and isotropic FLRW background metrics,

$$ds_g^2 = a_g^2 [-d\eta^2 + \gamma_{ij} dx^i dx^j], \quad (7a)$$

$$ds_f^2 = a_f^2 [-d\eta^2 + \gamma_{ij} dx^i dx^j], \quad (7b)$$

where η is the conformal time and a_g and a_f are the two different scale factors. We show that the consistency of the equations in the background, where the two metrics superpose, is ensured provided that the background densities obey,

$$\bar{\rho}_b = \frac{(\alpha - 1)(\varepsilon - 1)}{\alpha + \varepsilon} \bar{\rho}, \quad (8)$$

where $\alpha = a_g/a_f$ is constant, and $\bar{\rho}$ is the common density of the two dark matter fluids in the background. The cosmological constants should also be related to the observed cosmological constant Λ , through the relations,

$$\lambda_g = \Lambda, \quad \lambda_f = \alpha^2 \Lambda, \quad \lambda_{\text{eff}} = \alpha \Lambda. \quad (9)$$

Then, at first order cosmological perturbations around the FLRW metrics, we define the g -sector as being the observable one because it is where the baryons live and light propagates, and all observations take place. We thus study the perturbation equations in this sector. We define some effective dark matter quantities that modify the g -type dark matter particles taking into account their interaction with the other sector. Using these new variables we find that the perturbation equations in the g sector take exactly the same form as those of the Λ -CDM model. Thus the model turns out to be indistinguishable from Λ -CDM up to first order perturbation, and is then fully consistent with the observed fluctuations of the CMB.

- *MOND*. At galactic scales, in a regime of small accelerations $a \ll a_0$, the potential function \mathcal{W} takes the form (5). Based on a particular solution for the equation of the vector field \mathcal{A}_μ , the two dark matter fluids can be described as a polarizable dipolar medium. The MOND equation is then recovered as a result of a mechanism of gravitational polarization which appears as a natural consequence of the model. Moreover the dipolar dark matter medium undergoes stable plasma-like oscillations. We shall give some more details of this polarization mechanism in Sec. 3.2 at the occasion of the next model based on massive bigravity. However note that the next model has essentially the same predictions with regards to MOND phenomenology as the model²⁰. There is though a difference, in that in the model²⁰ we have to assume that the coupling constant ε in the action (1) tends to zero, while no particular requirement will be necessary in the next model.
- *Solar System*. As we modify GR we have to check the post-Newtonian limit in the Solar System, for which the potential function \mathcal{W} in the action takes the form (6). We have shown that when we expand the model at first post-Newtonian order, the parametrized post-Newtonian (PPN) parameters are exactly the same as in GR. A crucial point for this test is a non-linear effect present in our definition of the effective metric (2) and which permits to recover the correct value for the parameter measuring the amount of non-linearity, $\beta^{\text{PPN}} = 1$. Thus the model passes the Solar System tests and is viable.

2.3 Minisuperspace and ghosts

Unfortunately, the previous model proposed in²⁰ suffers from an harmful ghost instability. The source of its origin is multifaceted. First of all, the presence of the square root of the determinant of \mathcal{G}_{eff} in the action (1) corresponds to ghostly potential interactions,

$$\sqrt{-\mathcal{G}_{\text{eff}}} = \sqrt{\sqrt{-g}\sqrt{-f}}. \quad (10)$$

Already at the linear order around a flat background, posing $g_{\mu\nu} = (\eta_{\mu\nu} + h_{\mu\nu})^2$ and $f_{\mu\nu} = (\eta_{\mu\nu} + \ell_{\mu\nu})^2$, these potential interactions do not preserve the Fierz-Pauli tuning, with $[\dots]$ denoting the trace as usual,

$$\begin{aligned} \sqrt{-\mathcal{G}_{\text{eff}}} &= 1 + \frac{1}{2}[h + \ell] + \frac{1}{8}\left([h + \ell]^2 - 2[h^2 + \ell^2]\right) \\ &\quad + \frac{1}{48}\left([h + \ell]^3 - 6[h + \ell][h^2 + \ell^2] + 8[h^3 + \ell^3]\right) + \dots, \end{aligned} \quad (11)$$

yielding a linear ghost instability already present at the scale

$$m^2 M_{\text{Pl}}^2 \sqrt{-\mathcal{G}_{\text{eff}}} \sim \frac{m^2 M_{\text{Pl}}^2 (\Box\pi)^2}{\Lambda_3^6} = \frac{(\Box\pi)^2}{m^2}, \quad (12)$$

where $\Lambda_3 = (M_{\text{Pl}} m^2)^{1/3}$ and π encodes the helicity-0 degree of freedom of the massive graviton with mass m . The ghost corresponds to a very light degree of freedom, and hence the theory cannot be used as an effective field theory. The other source of ghostly interactions in the model²⁰ is originated in the presence of three kinetic terms. Studying the theory in the minisuperspace immediately reveals the ghostly interactions of the considered kinetic terms. The dangerous sub-Lagrangian due to kinetic interactions is given by

$$\mathcal{L}_{\text{kin}}^{\text{eff}} = \frac{M_{\text{Pl}}^2}{2} \sqrt{-g} R_g + \frac{M_{\text{eff}}^2}{2} \sqrt{-\mathcal{G}_{\text{eff}}} \mathcal{R}_{\text{eff}}. \quad (13)$$

As a first diagnostic, we can assume the two metrics to be of the mini-superspace form

$$ds_g^2 = g_{\mu\nu} dx^\mu dx^\nu = -n_g^2 dt^2 + a_g^2 dx^2, \quad (14a)$$

$$ds_f^2 = f_{\mu\nu} dx^\mu dx^\nu = -n_f^2 dt^2 + a_f^2 dx^2, \quad (14b)$$

where n_g, n_f are the lapse functions and a_g, a_f are the scale factors of the respective metrics. The effective metric \mathcal{G}_{eff} in the mini-superspace becomes

$$ds_{\mathcal{G}_{\text{eff}}}^2 = \mathcal{G}_{\mu\nu}^{\text{eff}} dx^\mu dx^\nu = -n_{\text{eff}}^2 dt^2 + a_{\text{eff}}^2 dx^2, \quad (15)$$

where the effective lapse and effective scale factor correspond to $n_{\text{eff}} = \sqrt{n_g n_f}$ and $a_{\text{eff}} = \sqrt{a_g a_f}$. We compute the conjugate momenta for the scale factors and get

$$\begin{aligned} p_g &= -6M_{\text{Pl}}^2 a_g^2 H_g - \frac{3}{2} M_{\text{eff}}^2 a_f \frac{a_{\text{eff}}}{n_{\text{eff}}} (H_g n_g + H_f n_f), \\ p_f &= -\frac{3}{2} M_{\text{eff}}^2 a_g \frac{a_{\text{eff}}}{n_{\text{eff}}} (H_g n_g + H_f n_f), \end{aligned} \quad (16)$$

with the conformal Hubble factors $H_g = \frac{\dot{a}_g}{a_g n_g}$ and $H_f = \frac{\dot{a}_f}{a_f n_f}$ respectively. After performing the Legendre transformation we obtain the Hamiltonian in the mini-superspace:

$$\mathcal{H}_{\text{kin}}^{\text{eff}} = -\frac{(p_g a_g - p_f a_f)^2 n_g}{12M_{\text{Pl}}^2 a_g^3} - \frac{p_f^2 a_g a_{\text{eff}} n_{\text{eff}}}{3M_{\text{eff}}^2 a_g^3}. \quad (17)$$

As one can see immediately, the Hamiltonian is highly non-linear in the lapses n_g and n_f , signalling the presence of the BD ghost degree of freedom already in the mini-superspace. Summarising, the model proposed in²⁰ cannot represent a consistent theory for dipolar dark matter in bigravity due to the ghostly contribution in form of the cosmological constant for \mathcal{G}_{eff} , and the kinetic term $\sqrt{-\mathcal{G}_{\text{eff}}}\mathcal{R}_{\text{eff}}$.

3 Model based on massive bigravity theory

3.1 Covariant theory

The previous model²⁰ is plagued by harmful ghosts, but it remains that the phenomenology, especially at galactic scales (i.e. MOND), calls for a more fundamental theory. We now look for a consistent coupling of the dark matter particles within the framework of massive bigravity theory and the restrictions made in^{32,36,37} concerning matter fields. We thus propose a new model, whose dark matter sector is essentially the same as in the previous model²⁰, but whose gravitational sector is now based on ghost-free massive bigravity theory. As bigravity theory represents essentially a unique consistent deformation of GR, we think that the new model could represent an important step toward a more fundamental theory of dark matter *à la* MOND in galactic scales.

The model is based on the bigravity-plus-matter action^{44,45}

$$\begin{aligned} S &= \int d^4x \left\{ \sqrt{-g} \left(\frac{M_g^2}{2} R_g - \rho_{\text{bar}} - \rho_g \right) + \sqrt{-f} \left(\frac{M_f^2}{2} R_f - \rho_f \right) \right. \\ &\quad \left. + \sqrt{-g_{\text{eff}}} \left[\frac{m^2}{4\pi} + \mathcal{A}_\mu \left(j_g^\mu - \frac{\alpha}{\beta} j_f^\mu \right) + \frac{a_0^2}{8\pi} \mathcal{W}(X) \right] \right\}, \end{aligned} \quad (18)$$

where M_g and M_f are two coupling constants, and m is the mass of the graviton. The ghost-free potential interactions between the two metrics g and f take the particular form of the square root of the determinant of the effective metric^{32,48},

$$g_{\mu\nu}^{\text{eff}} = \alpha^2 g_{\mu\nu} + 2\alpha\beta \mathcal{G}_{\mu\nu}^{\text{eff}} + \beta^2 f_{\mu\nu}, \quad (19)$$

where α and β are arbitrary constants, which can always be restricted in the model (18) to satisfy $\alpha + \beta = 1$, and $\mathcal{G}_{\mu\nu}^{\text{eff}}$ denotes the effective metric of the previous model as defined by (2)

in terms of $X = \sqrt{g^{-1}f}$ and $Y = \sqrt{f^{-1}g}$. The square root of the determinant of this effective metric admits a closed-form expression,

$$\sqrt{-g_{\text{eff}}} = \sqrt{-g} \det(\alpha \mathbb{1} + \beta X) = \sqrt{-f} \det(\beta \mathbb{1} + \alpha Y), \quad (20)$$

and can also be written with the help of the usual elementary symmetric polynomials $e_n(X)$ and $e_n(Y)$ of the square root matrices X or Y as

$$\sqrt{-g_{\text{eff}}} = \sqrt{-g} \sum_{n=0}^4 \alpha^{4-n} \beta^n e_n(X) = \sqrt{-f} \sum_{n=0}^4 \alpha^n \beta^{4-n} e_n(Y). \quad (21)$$

We see that (20)–(21) corresponds to the right form of the acceptable potential interactions between the metrics g and f . To recover the usual Newtonian limit for the motion of baryons with respect to the ordinary metric g we must impose

$$M_g^2 + \frac{\alpha^2}{\beta^2} M_f^2 = \frac{1}{8\pi}. \quad (22)$$

Finally the vector field \mathcal{A}_μ is now coupled to the metric $g_{\mu\nu}^{\text{eff}}$ rather than to $\mathcal{G}_{\mu\nu}^{\text{eff}}$, thus

$$X = -\frac{g_{\text{eff}}^{\mu\rho} g_{\text{eff}}^{\nu\sigma} \mathcal{F}_{\mu\nu} \mathcal{F}_{\rho\sigma}}{2a_0^2}. \quad (23)$$

However the functional form of the non-canonical kinetic term \mathcal{W} in the MOND regime is the same as in the previous model, see (5), and we could also impose (6). Finally the mass currents to which is coupled the vector field in (18) are defined by

$$\sqrt{-g_{\text{eff}}} j_g^\mu = \sqrt{-g} J_g^\mu, \quad \sqrt{-g_{\text{eff}}} j_f^\mu = \sqrt{-f} J_f^\mu, \quad (24)$$

where, as before, $J_g^\mu = \rho_g u_g^\mu$ and $J_f^\mu = \rho_f u_f^\mu$. However, notice the presence of the factor α/β in the interaction term between \mathcal{A}_μ and the current j_f^μ in (18). This factor can be interpreted as a ratio between the gravitational charge and the inertial mass of the f particles when measured with respect to the g metric.

3.2 Gravitational polarization & MOND

We now discuss the main point of this model, which is to allow a mechanism of gravitational polarization that permits to recover in a straightforward way the phenomenology of dark matter at galactic scales (MOND). In this respect the predictions of the new model are essentially the same as those of the previous model²⁰.

For this purpose we are mainly interested to that particular combination of the two metrics g and f which is massless⁴⁷. Working in the non-relativistic limit $c \rightarrow \infty$, we find that the massless combination reduces to an ordinary Poisson equation for the Newtonian potentials U_g and U_f associated with the two metrics, namely

$$\Delta \left(\frac{2M_g^2}{\alpha} U_g - \frac{2M_f^2}{\beta} U_f \right) = -\frac{1}{\alpha} (\rho_{\text{bar}}^* + \rho_g^*) + \frac{1}{\beta} \rho_f^*, \quad (25)$$

where ρ_{bar}^* , ρ_g^* and ρ_f^* denote the ordinary Newtonian densities of the matter fluids. However, with massive (bi-)gravity the two sectors associated with the metrics g and f do not evolve independently but are linked together by a constraint equation which comes from the Bianchi identities. We find that this constraint reduces in the non-relativistic limit to

$$\nabla(\alpha U_g + \beta U_f) = 0. \quad (26)$$

Combining (25)–(26) and using (22) we readily obtain the following Poisson equation for the Newtonian potential in the ordinary sector,

$$\Delta U_g = -4\pi \left(\rho_{\text{bar}}^* + \rho_g^* - \frac{\alpha}{\beta} \rho_f^* \right). \quad (27)$$

Similarly we find that the equation governing the vector field, obtained by varying the action (18) with respect to \mathcal{A}_μ , reduces in the non-relativistic limit to a single Coulomb type equation,

$$\nabla \cdot \left[\mathcal{W}_X \nabla \phi \right] = 4\pi \left(\rho_g^* - \frac{\alpha}{\beta} \rho_f^* \right), \quad (28)$$

where \mathcal{W}_X is the derivative of \mathcal{W} with respect to its argument X . Finally we have also at our disposal the equations of motion of the baryons and the dark matter particles. We look for explicit solutions of the equations of motion of dark matter in the form of plasma-like oscillations around some equilibrium configuration. Thanks to the constraint equation (26) we find that an equilibrium is possible, i.e. the dark matter particles are at rest, when the Coulomb force annihilates the gravitational force, namely

$$\nabla U_g + \nabla \phi = 0. \quad (29)$$

At equilibrium we shall grasp a mechanism of gravitational polarization, i.e. we can define a polarization field which will be aligned with the gravitational field. Away from equilibrium we find that the polarization field undergoes stable plasma like oscillations (see ⁴⁵ for details). Finally, combining the three equations (27), (28) and (29) we easily deduce that the equation for the ordinary potential U_g takes exactly the Bekenstein-Milgrom form ⁴⁹,

$$\nabla \cdot \left[(1 - \mathcal{W}_X) \nabla U_g \right] = -4\pi \rho_{\text{bar}}^*, \quad (30)$$

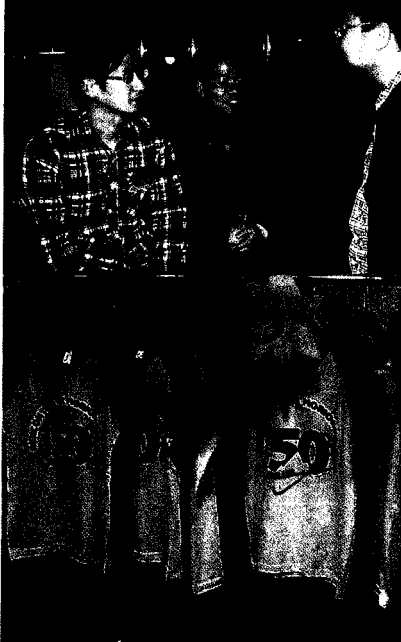
with MOND interpolating function $\mu = 1 - \mathcal{W}_X$. Furthermore, thanks to the postulated form (5) of the function $\mathcal{W}(X)$ we recover the correct deep MOND regime when $X \rightarrow 0$. We refer to ^{19,20,45} for more details about this way of recovering the MOND phenomenology, which is of course reminiscent of the dielectric analogy of MOND.

Let us emphasize that gravitational polarization & MOND appear as natural consequences of this model, and are made possible by the constraint equation (26) linking together the two metrics of massive bigravity theory. Furthermore this requires that the gravitational force can be annihilated by some internal non-gravitational force, here chosen to be a vector field. This implies the existence of a coupling between the two species of dark matter particles living in the g and f sectors. Unfortunately, as has been shown in ⁴⁵, the latter coupling is problematic as it yields a ghostly degree of freedom in the dark matter sector. Further work is needed to determine the exact mass of the ghost and see whether the required polarization mechanism and the ghost absence are compatible. On the phenomenology side, the cosmological implications of the model and the post-Newtonian parameters in the Solar System should be investigated in great details, as it has been done for the previous model ²⁰.

References

1. S. S. McGaugh. *Phys. Rev. Lett.*, 106:121303, 2011.
2. R.H. Sanders. *Mon. Not. Roy. Astron. Soc.*, 407:1128–1134, 2010.
3. B. Famaey and S. McGaugh. *Living Rev. Rel.*, 15:10, 2012.
4. J. Silk and G. Mamon. *Research in Astron. Astrophys.*, 12:917–946, 2012.
5. M. Milgrom. *Astrophys. J.*, 270:365, 1983.
6. M. Milgrom. *Astrophys. J.*, 270:371, 1983.
7. M. Milgrom. *Astrophys. J.*, 270:384, 1983.

8. J.D. Bekenstein. *Phys. Rev. D*, 70:083509, 2004.
9. R.H. Sanders. *Mon. Not. Roy. Astron. Soc.*, 363:459, 2005.
10. M. Milgrom. *Phys. Rev. D*, 80:123536, 2009.
11. T. G. Zlosnik, P. G. Ferreira, and G. D. Starkman. *Phys. Rev. D*, 75:044017, 2007.
12. A. Halle, H. S. Zhao, and B. Li. *Astrophys. J. Suppl.*, 177:1, 2008.
13. E. Babichev, C. Deffayet, and G. Esposito-Farèse. *Phys. Rev. D*, 84:061502(R), 2011.
14. L. Blanchet and S. Marsat. *Phys. Rev. D*, 84:044056, 2011.
15. L. Blanchet and A. Le Tiec. *Phys. Rev. D*, 78:024031, 2008.
16. L. Blanchet and A. Le Tiec. *Phys. Rev. D*, 80:023524, 2009.
17. L. Blanchet, D. Langlois, A. Le Tiec, and S. Marsat. *J. Cosm. Astropart.*, 22:1302, 2013.
18. L. Blanchet. *Class. Quant. Grav.*, 24:3529, 2007.
19. L. Blanchet and L. Bernard. 2014. In the proceedings of the second Workshop on Antimatter and Gravity (WAG 2013).
20. L. Bernard and L. Blanchet. *Phys. Rev. D*, 91:103536, 2015.
21. M. Fierz and W. Pauli. *Proc. Roy. Soc. Lond.*, A173:211–232, 1939.
22. H. van Dam and M.J.G. Veltman. *Nucl. Phys.*, B22:397–411, 1970.
23. V.I. Zakharov. *J. Exp. Th. Phys. Lett.*, 12:312, 1970.
24. A.I. Vainshtein. *Phys. Lett.*, B39:393–394, 1972.
25. D.G. Boulware and S. Deser. *Phys. Rev.*, D6:3368–3382, 1972.
26. C. de Rham and G. Gabadadze. *Phys. Rev.*, D82:044020, 2010.
27. C. de Rham, G. Gabadadze, and A. J. Tolley. *Phys. Rev. Lett.*, 106:231101, 2011.
28. S.F. Hassan and R. A. Rosen. *J. High Energy Phys.*, 1107:009, 2011.
29. S.F. Hassan and R. A. Rosen. *Phys. Rev. Lett.*, 108:041101, 2012.
30. S.F. Hassan and R. A. Rosen. *J. High Energy Phys.*, 1202:126, 2012.
31. K. Hinterbichler and R.A. Rosen. *J. High Energy Phys.*, 1207:47, 2012.
32. C. de Rham, L. Heisenberg, and R.H. Ribeiro. *Class. Quantum Grav.*, 32:035022, 2015.
33. Y. Yamashita, A. De Felice, and T. Tanaka. *Int. J. Mod. Phys.*, D23:1443003, 2014.
34. C. de Rham, G. Gabadadze, L. Heisenberg, and D. Pirtskhalava. *Phys. Rev.*, D87, 2012.
35. C. de Rham, L. Heisenberg, and R. H. Ribeiro. *Phys. Rev.*, D88:084058, 2013.
36. L. Heisenberg. *Class. Quant. Grav.*, 32(10):105011, 2015.
37. C. de Rham, L. Heisenberg, and R.H. Ribeiro. *Phys. Rev. D*, 90:124042, 2014.
38. A. E. Gümürükçüoğlu, L. Heisenberg, and S. Mukohyama. *J. Cosm. Astropart.*, 1502:022, 2015.
39. C. de Rham, G. Gabadadze, L. Heisenberg, and D. Pirtskhalava. *Phys. Rev. D*, 83:103516, 2011.
40. G. D’Amico, C. de Rham, S. Dubovsky, G. Gabadadze, D. Pirtskhalava, and A. J. Tolley. *Phys. Rev. D*, 84:124046, Dec 2011.
41. M. S. Volkov. *J. High Energy Phys.*, 1201:035, 2012.
42. M. von Strauss, A. Schmidt-May, J. Enander, E. Mortsell, and S.F. Hassan. *J. Cosm. Astropart.*, 1203:042, 2012.
43. D. Comelli, M. Crisostomi, F. Nesti, and L. Pilo. *J. High Energy Phys.*, 1203:067, 2012.
44. L. Blanchet and L. Heisenberg. *Phys. Rev.*, D91:103518, 2015.
45. L. Blanchet and L. Heisenberg. 2015. Submitted to *J. Cosmo. Astropart.*
46. V. Baccetti, P. Martin-Moruno, and M. Visser. *J. High Energy Phys.*, 1208:148, 2012.
47. S.F. Hassan, A. Schmidt-May, and M. von Strauss. *J. High Energy Phys.*, 1305:086, 2013.
48. J. Noller and S. Melville. *J. Cosmo. Astropart.*, 1501:003, 2015.
49. J.D. Bekenstein and M. Milgrom. *Astrophys. J.*, 286:7, 1984.



GBAR STATUS AND GOALS

P. PEREZ

*IRFU, Service de Physique des Particules, CEN Saclay,
91191 Gif-sur-Yvette, France*

The GBAR experiment (Gravitational Behaviour of Anti hydrogen at Rest) at CERN, aims to measure the free fall acceleration of ultracold neutral anti hydrogen atoms in the gravity field of the Earth. Anti hydrogen ions (one antiproton and two positrons) are produced in the interaction of antiprotons and positronium in two subsequent charge exchange reactions. These ions will be sympathetically cooled with Be^+ ions to less than $10 \mu\text{K}$. The ultracold ions will then be photo-ionized just above threshold, and the free fall time over a known distance measured.

1 Introduction

The aim of the GBAR experiment at CERN is to measure the free fall of antihydrogen atoms in order to test the Equivalence Principle in a direct way with antimatter. There are already indirect constraints on this subject coming either from matter experiments¹ or from measurements on antiprotons². A direct constraint may be obtained from the arrival times of neutrinos and antineutrinos that were observed from supernova 1987a³. However, this result is based on a single event classified at only 90% CL as having originated from a neutrino interaction, and is not guaranteed to be reproducible in the near future. A first direct experiment was performed by the ALPHA collaboration at CERN⁴ that set a constraint on the ratio of the gravitational to inertial mass of antihydrogen to be less than about 100. The first phase of GBAR is to obtain a precision of 1% on the acceleration of these antiatoms in the terrestrial gravity field. A brief description of the methods and techniques that we are preparing for this experiment are given below.

2 Principle of the method

It is necessary to obtain atoms at very low velocities in order to perform a free fall measurement. The AEGIS⁵ experiment has chosen to cool first the antiprotons in order to produce cold antihydrogen atoms after combination with positrons. We chose a different path⁶ based on an idea first suggested by Walz and Hänisch⁷ that uses an antihydrogen ion, the antimatter counterpart of H^- , i.e. composed of an antiproton and two positrons, that we denote $\bar{\text{H}}^+$. In the experiments that already produced antihydrogen, a three-body interaction where an antiproton interacts with two positrons efficiently produces the antihydrogen atoms, although in a highly excited state. For GBAR we will use two charge exchange reactions with positronium (Ps):



followed by



The first reaction with an antiproton is also a three-body process, but since Ps is a bound state, the cross-section is much higher. The second reaction between the previously produced antiatom and Ps produces the anti-ion. Note also that the binding energy of H^- being 0.75 eV is also the energy level of the third excited state of Ps. We may thus expect an enhancement of the cross section if Ps is excited. These cross-sections have been calculated recently⁸, including excitation of Ps, and show that the cross-section is maximal for \bar{p} energies in the keV range (Fig. 1). Still, given the expected number of around $5 \cdot 10^6$ low energy antiprotons available per burst at CERN, a high density of 10^{12}cm^{-2} Ps is necessary to produce one \bar{H}^+ . This anti-ion can be sympathetically cooled with laser cooled matter ions such as Be^+ to temperatures of less than $10 \mu\text{K}$. The extra positron may then be photo-detached by a laser pulse, with an energy only a few μeV above threshold, in order to obtain an ultra cold antiatom. The measurement of the time of flight of the resulting free fall allows to extract the acceleration due to the Earth's gravity.

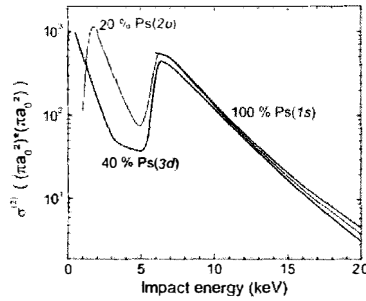


Figure 1 – \bar{H}^+ production cross-sections from⁸ for \bar{p} impinging on a Ps cloud. The black curve represents the case without Ps excitation. The red and blue curves are for 2P and 3D level excitation that correspond to the 243 or 410 nm lasers in Fig. 2. The 410 nm laser will be used in a 2 photon excitation.

3 Apparatus

The different parts of the apparatus that are presently in preparation and their status are briefly described in the following sections. They follow the experimental proposal that was approved by CERN in 2012⁹. An overall scheme is shown in figure 2.

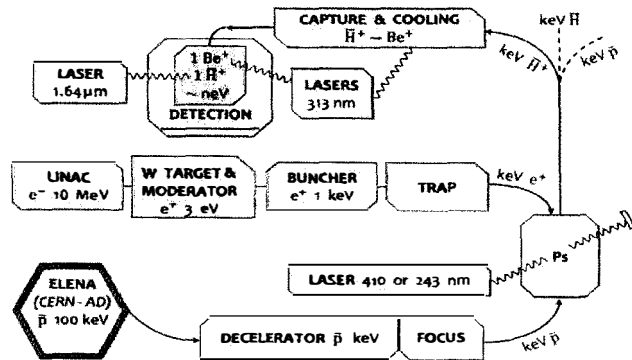


Figure 2 – Overall scheme of the GBAR experiment.

3.1 Antiprotons

The Antiproton Decelerator at CERN that currently produces 5 MeV antiprotons will be complemented by a decelerator ring called ELENA to bring the antiprotons to 100 keV kinetic energy¹⁰. In order to optimise production (see Sect. 2), we must further decelerate in the range from 1-10 keV. To this aim, the CSNSM team in Orsay is preparing a system of electrodes that first reduce the energy by applying a high voltage. In order to keep the rest of the apparatus grounded, while the antiprotons traverse a drift tube long enough to contain the pulse, its voltage is quickly dropped using a fast switch (see Fig. 3). However, the emittance of the beam is thus increased by the ratio of the square root of the input to output energies. A set of electrostatic lenses ensures a 30% efficiency for the beam to pass through a 1 mm x 1 mm x 2 cm tube corresponding to the Ps target geometry, according to simulations.

The dispersion in longitudinal momentum of the antiproton beam from ELENA is too large for an efficient capture of the anti ions. Modifications to the drift tube scheme (see Fig. 3) are under study.

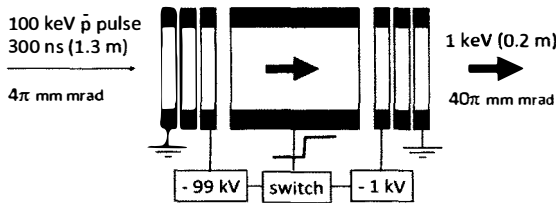


Figure 3 – Sketch of the drift tube for antiproton deceleration.

3.2 Ps target

The positronium target will be made in the form of a cylinder of 1 mm x 1mm cross section and 2 cm long. The four plates making this cylinder will be coated with a porous silica film developed at Saclay. This film was shown to convert 30 to 40% of the incident positrons into ortho positronium that return from this surface into vacuum¹¹. It was recently shown by Crivelli¹², that a 30 nm thick Si₃N₄ window inserted into one of these plates allows the positrons to impinge onto the silica target from the side (see figure 4) with no loss if the energy is above a few keV, i.e. in the efficient range to be converted into Ps. The coating has a negative work function for Ps, so that once produced inside the tube it may bounce without being annihilated, thus forming a dense cloud. This cloud can also be excited with laser beams (see figure 4). The Kastler-Brossel laboratory (LKB) in Paris has developed a 410 nm two-photon laser system to excite the 3D level of orthopositronium¹³, and is preparing also a 243 nm one photon laser to excite the 2P level (see Fig. 1). The 3D laser is presently being used to prepare a fluorescence detector using a Cs vapour to mimic the conditions that will be available with the positronium setup being installed at Saclay.

3.3 Positron production and accumulation

In order to produce one anti-ion per ELENA pulse every 110 s, the flux of slow positrons must be $3 \times 10^8 \text{s}^{-1}$. For this purpose an electron beam will produce the positrons by pair production in a tungsten target. A 10 MeV electron linac with 0.2 mA average current and repetition rate of 300 Hz will be built by the NCBJ group in Swierck (Poland). Positrons are then moderated in a tungsten mesh moderator placed close to the primary target. Presently positron production and accumulation are being tested using a demonstrator setup at Saclay (see Fig. 5). It consists

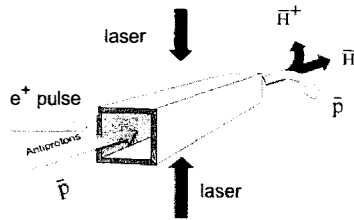


Figure 4 – Sketch of the Ps target formed of 4 faces internally coated with porous silica and of the directions of incoming and outgoing beams.

of a small 4.3 MeV, 0.12 mA accelerator producing 3×10^6 slow e^+s^{-1} . A positron beam line allows transport of the positrons to a Penning-Malmberg trap. The trapping mechanism being tested is based on electron cooling rather than the standard Greaves-Surko buffer-gas technique. This technique has been pioneered by N. Oshima at RIKEN with the same trap¹⁴. In the Saclay setup, we are taking advantage of the pulsed structure of the beam¹⁵ to increase efficiency. First trials showed accumulation only when the preloaded electron plasma is present¹⁶. Work is going on to increase the accumulation rate.

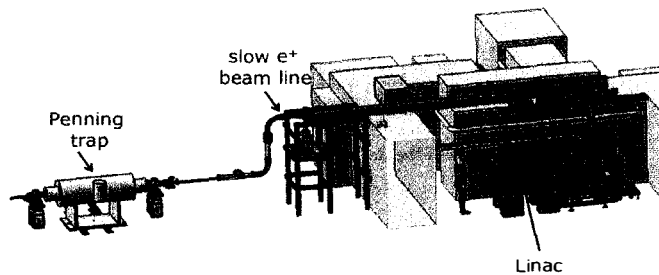


Figure 5 – Picture of the demonstration setup for positron production and accumulation at Saclay.

3.4 \bar{H}^+ trapping and cooling

The antiprotons have keV energies as well as tens of eV energy spread. The anti-ions will keep the kinematic phase space from their parent antiprotons. Although the task to reach the required neV energies seems formidable, a scheme involving two cooling steps has been outlined¹⁷. In the first step, the keV antimatter ions are captured in a linear RF trap where they are sympathetically cooled by Coulomb interaction with a laser cooled crystal of more than 10000 Be^+ ions. To avoid photodetachment by the cooling laser light near 313 nm, it is necessary to obtain a short cooling time. Detailed simulations¹⁷ showed that the mechanical coupling between Be^+ and \bar{H}^+ is not optimal with a 9 to 1 mass ratio. Instead, adding HD^+ ions to the Be^+ cloud allows better coupling leading to a cooling time of the order of 1 ms to reach a temperature in the mK range. For the second cooling step, the \bar{H}^+ ions are separated from the Be crystal, extracted and injected in a precision trap to form a Be^+ / \bar{H}^+ ion pair on which ground state Raman side band cooling can be performed to the ground state of vibration at the Heisenberg limit $\Delta p \times \Delta x = \hbar/2$. This will be followed by an adiabatic expansion of the trap potential to improve on the momentum uncertainty further, reaching average velocities of $1ms^{-1}$. The precision trap is being prepared in the QUANTUM group at Mainz University where the first tests will be made with $^{40}Ca^+$ and Be^+ ions (mass ratio of 4.4 to 1). The catching trap and first cooling trap are under construction at LKB Paris and will be tested with H_2^+ ions and protons (mass ratios of 9 to 2 and to 1).

3.5 Free fall detection

After photodetachment of the ion, the free fall of the neutral atom will take place in a vacuum vessel surrounded by a tracking detector and plastic scintillator plates. The tracker will serve to reject background events such as cosmic rays. An annihilation event has an average of three charged pions produced with each 0.3 GeV/c. Such particles easily traverse the vacuum chamber vessel and leave straight tracks by ionising the gas of the detector. Reconstruction of these track segments allows determination of the annihilation vertex with a topology much different from that of a typical cosmic ray. The technology envisaged by ETH Zurich for this tracking detector is the so-called bulk microMegas in the form of a set of three double planes of $0.5\text{ m} \times 0.5\text{ m}$ dimensions. Five such sets will surround the vacuum vessel. The low event rate also allows multiplexing the readout channels¹⁸. A cryogenic vacuum environment will lower the pressure such that no residual gas annihilation may take place. The time of flight of the free fall will be measured from the difference in the timing signals given on one hand by the photodetachment laser and on the other hand by the plastic scintillators.

3.6 Vertical velocity selection

The spread of the distribution of the reconstructed acceleration of the antihydrogen atoms will be dominated by the initial velocity dispersion, exceeding 40% (r.m.s.). In a recent publication¹⁹, some of our collaborators proposed to reduce the initial vertical velocity dispersion by adding two small disks above and below the launch point. The high velocity atoms annihilate on such disks whilst those at lower energies bounce off on them taking advantage of the effect of quantum reflection. Even though the measured event statistics are reduced by a factor 40, the spread of the reconstructed acceleration is lowered to 1.4% (r.m.s.). In order to obtain the same 1% precision on the acceleration of antimatter as in the case where no such disks are present, the number of produced $\bar{\text{H}}^+$ ions needed is reduced by a factor of 10.

4 Outlook

The GBAR collaboration is now composed of 15 institutes gathering 50 researchers from 8 countries. Installation at CERN should start by the end of 2015 in order to be ready to accept the protons and H^- ions during ELENA commissioning in 2016 and the first run of antiprotons during 2017.

Acknowledgments

Part of the preparation work is funded through the following grants: ANR-SOPHI (ANR-05-BLAN-0380-01), ANR-POSITRAP (ANR-10-BLAN-0420-02), ANR-ANTION (ANR-14-CE33-0008), ANR/DFG-BESCOOL (ANR-13-IS04-0002). A large part of this text is taken from a presentation at the EXA 2014 conference that is to be published in *Hyperfine Interactions*.

References

1. E.G. Adelberger et al., *Phys. Rev. Lett.* **66**, 850 (1991); T. Goldman et al., *Phys. Rev. Lett.* **67**, 1048 (1991).
2. G. Gabrielse et al., *Phys. Rev. Lett.* **82**, 3198 (1999).
3. S. Pakvasa, W. A. Simmons, and T. J. Weiler, *Phys. Rev. D* **39**, 1761 (1989).
4. C. Amole et al., *Nature Communications* **4**, 1785 (2013).
5. See talk by P. Nedelec at this conference; A. Kellerbauer et al., *Nucl. Instrum. Methods B* **266**, 351 (2008).
6. P. Pérez and A. Rosowsky, *Nucl. Instrum. Methods A* **545**, 20 (2005).
7. J. Walz and T. Hänsch, *General Relativity and Gravitation*, **36**, 561 (2004).

8. P. Comini and P-A. Hervieux, *New J. Phys.*, **15**, 095022 (2013); P. Comini et al., *Hyp. Int.*, **228**, 159 (2014).
9. G. Chardin et al., CERN-SPSC-P-342, 30/09/2011.
10. C. Carli, *Hyp. Int.*, **229**, 105 (2014).
11. D. B. Cassidy et al., *Phys. Rev. A* **81**, 012715 (2010); P. Crivelli et al., *Phys. Rev. A* **81**, 052703 (2010).
12. P. Crivelli et al., *Int. J. Mod. Phys. Conf. Ser.*, **30**, 1460257 (2014).
13. Pauline Comini, PhD thesis, Université Paris 6, <https://tel.archives-ouvertes.fr/tel-01150446>.
14. N. Oshima et al., *Phys. Rev. Lett.* **93**, 195001 (2004).
15. P. Dupré, *AIP Conf. Proc.* **1521**, 113 (2013).
16. P. Grandemange et al., *J. Phys.: Conf. Ser.*, **505**, 012035 (2014)
17. L. Hilico et al., *Int. J. Mod. Phys: Conf. Ser.*, **30**, 1460269 (2014)
18. S. Procureur et al., *Nucl. Instrum. Methods A* **729**, 888 (2013).
19. G. Dufour et al., *Eur. Phys. J. C*, **74**, 2731 (2014).

AEGIS experiment: goals and status

P. NEDELEC^a

*Institut de Physique Nucléaire de Lyon, Department of Physics, University Lyon 1, 4 rue E. Fermi,
69100 Villeurbanne, France*



The gravitational interaction of matter with matter is a well known interaction well tested experimentally and well described by the theory of general relativity. The weak equivalence principle (WEP) is telling us that any kind of matter will fall in a unique way in a gravitational field. But what about the gravitational behaviour of antimatter in a matter field? This is the question the AEGIS experiment at CERN, is addressing ; It has been designed to the measurement of the gravitational free fall of anti-hydrogen in the Earth gravitational field. In this paper we will remind antiatom production mechanisms, we will describe the AEGIS experiment and report on the first achievements.

1 Introduction

Antimatter is born in the 30's from a the theoretical unification of special relativity and quantum mechanics as developed by P.A.M. Dirac¹. Experimentally, the discovery of the "positive electron" by C. D. Anderson² opened the field of antiparticles, of antimatter. This remains a very hot topic in Modern Physics. Experimental comparisons between matter and antimatter properties was a tremendous way to reveal fundamental symmetry properties, namely symmetry violations, like the C, P or CP symmetries. Precision spectroscopy measurements on antimatter are considered to be an important test of the CPT theorem³. In fact, a possible violation of the CPT theorem is considered in some extensions of the Standard Model⁴. Another issue concerns the gravitational interaction of antimatter. The weak equivalence principle (WEP) tells us that the free falling of a body in an external gravitational field is not affected by its composition, but depends only on its initial position and velocity. Careful measurements verified WEP at 10^{-13} level for ordinary matter⁵. Testing WEP for antimatter was performed with charged antimatter. But this is very complicated, owing to the overwhelming effect of residual electromagnetic forces⁶. On the theoretical side, some attempts to formulate quantum theories of gravity, or to unify gravity with the other forces⁷ consider the possibility of a non-identical gravitational interaction between matter and antimatter, which could even repel each other, in spite of being self-attractive⁸. A possible gravitational repulsion between matter and antimatter could

^afor the AEGIS collaboration: <http://aegis.web.cern.ch>

be consistent with the standard formulation of the general relativity and would not imply any modification of the theory⁹. A good way to investigate the gravitational interaction is to test it with neutral antimatter, i.e. antiatoms. The only antiatom which can be reasonably created and manipulated is the anti-hydrogen $\bar{\text{H}}$, an antiproton associated with a positron. A measurement of the Earth gravitational acceleration g on $\bar{\text{H}}$, at a few percent precision would sound scientifically relevant, as it would represent the first direct measurement of the gravitational interaction between matter and antimatter.

2 The AEGIS experiment

The AEGIS (Antimatter Experiment: gravity, Interferometry, Spectroscopy) experiment as been designed to study fundamental physics with anti-hydrogen atoms. The primary goal is to measure the gravitational acceleration g on $\bar{\text{H}}$. In a first step of the AEGIS experiment will produce $\bar{\text{H}}$ with energy in the 0.1 meV range and measure the Earth gravitational free fall with a precision of 1%. As far as the gravity measurement is concerned, a beam of cold $\bar{\text{H}}$ will be formed and sent to a moiré deflectometer where a vertical displacement should be recorded.

2.1 $\bar{\text{H}}$ production

The different steps to produce cold $\bar{\text{H}}$, as well as to measure its gravity acceleration are summarized in the following and shown on figure 1): 1) Capture and accumulation of anti-protons coming from the Antiproton Deceleration (AD) facility at CERN in a Penning-Marlberg trap; 2) Cooling of \bar{p} to sub-K temperatures; 3) Production of positrons and storage into an accumulator; 4) Production and emission in vacuum of cold (<150 K) positronium Ps formed from impinging a positron bunch on a suitable nano-porous target; 5) Excitation of ortho-positronium oPs in a Rydberg state (Ps*) by means of suitable laser pulses; 6) Formation of cold Rydberg $\bar{\text{H}}^*$ from a charge-exchange reaction (see equation1) between antiprotons and Ps*; 7) Extraction of $\bar{\text{H}}^*$ atoms by means of inhomogeneous electric fields (Stark acceleration technique); 8) Measurement of their vertical deflection due to gravitational acceleration using a moiré deflectometer coupled to a position sensitive detector.

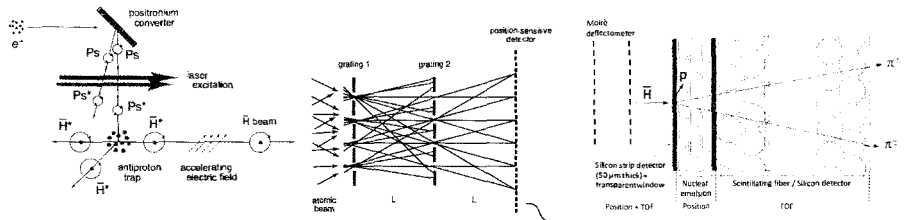


Figure 1 - (Left) Sketch of $\bar{\text{H}}$ production in the AEGIS experiment. (Right) Position sensitive $\bar{\text{H}}$ detection scheme.

2.2 AEGIS overview

The main apparatus (see figure 2) consists of two magnets: a 5T magnet, where field strength is important in maximizing the trapping efficiency for antiprotons delivered from the AD. It is followed by a 1T magnet in which the anti-hydrogen beam will be produced and where the magnetic field homogeneity is important in obtaining very low-temperature antiprotons. The custom design integrates the super-conducting magnets and their cryostats with the dilution refrigerator and its cryostats, as well as allowing access from the two sides (antiproton and positron injection on the upstream side and antihydrogen beam extraction on the downstream side) and in the region between the two magnets (cabling for the electrodes and diagnostics).

Laser light for positronium excitation is injected in the central region and transported to the anti-hydrogen production region via glass fibers and reflecting prisms. Positrons are produced and accumulated in a structure straddling the antiproton injection line, and then transferred through a transfer beam line into the 5T magnet trap. A series of detectors, including the central scintillating fiber vertex detector (FACT), provide diagnostics for the particle detection and manipulations.

2.3 AEGIS commissioning

The AEGIS experiment is in a well advanced phase of commissioning and antiproton data have been already recorded¹⁰ in 2014 and 2015. Antiprotons are delivered by the antiproton decelerator (AD) with an energy of 5.3 MeV. They pass through a degrader (a stack of Al foils, with variable thicknesses) and the low momentum part (<10 keV) is caught in a trap placed in the 5 T magnet. Preloaded electrons provide electron cooling of \bar{p} . Then, \bar{p} are transferred into the 1 T region for further cooling, taking advantage of a dilution refrigerator as well as a resistive active-feedback cooling system. The possibility of sympathetic cooling with La^- or Os^- ions is also under study. The final design envisages a cloud of 10^5 \bar{p} at equivalent temperature of ~ 0.1 K;

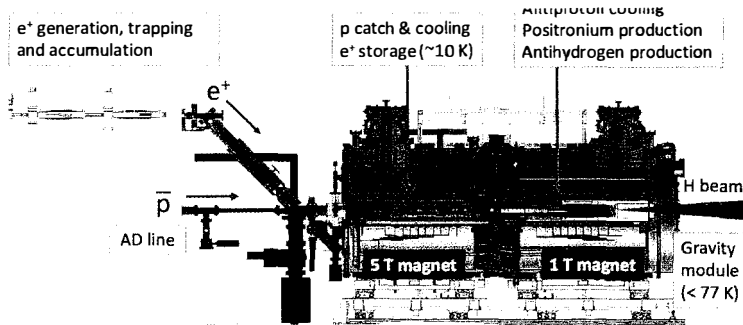


Figure 2 – Schematic drawing of the main components of the AEGIS experiment.

Positrons are generated by a ^{22}Na source (activity ~ 740 MBq) and then monochromated through a solid Ne moderator and then captured in a Surko-type trap¹¹. Afterwards, they are dumped to an accumulator, able to stack up to 10^8 e^+ in 200 s, corresponding to the \bar{p} delivering time from AD. Then, positrons are magnetically guided to the 1 T region to impinge on a porous target where cold^b (Ps) will be produced. A fraction of the oPs formed inside the target is re-emitted in vacuum at low energies (corresponding to a temperature < 150 K). After a two stages laser excitation free oPs become Rydberg excited positronium oPs*. They will interact with the cold \bar{p} cloud stored in the 1T trap to produce anti-hydrogen states $\bar{\text{H}}^*$ according to the charge-exchange reaction:



It is worth noting the consequence of the reaction 1 the $\bar{\text{H}}$ will be formed in a Rydberg state. This allows a Stark acceleration of the antiatom in an inhomogeneous electric field. By means of a time varying electric field, $\bar{\text{H}}^*$ will reach a velocity around 500 m/s; this technique, already tested with H^{12} , will let the antiatoms to be sent to the gravity measurement module. This one,

^bPs is a e^+e^- bounded states. The singlet state, parapositronium (pPs), has a short 125ps lifetime, while the triplet state, orthopositronium (oPs), has a long lifetime of 142 ns in vacuum.

a moiré deflectometer, consists of two identical gratings, normal to the trajectory of \bar{H} , having a $40 \mu\text{m}$ periodicity, placed at a distance $L = 50 \text{ cm}$ from each other¹³ followed by a detection plane located at the same distance L . The time of flight T ($\sim 10^{-3} \text{ s}$) will be measured from the time span between the Stark acceleration time and the arrival time at the detection plane.

Among the particles impinging the two gratings only those ones having well defined trajectories are selected and produce a fringe pattern in a third plane. This pattern is shifted in the presence of a vertical force; in the case of (anti)gravity the shift δ depends on both T and g : $\delta = -gT^2$. Therefore, g can be obtained by fitting the shift versus the time of flight on an event-by-event basis. The data will be obtained by means of a hybrid detector placed in the third plane. The detector is formed by a thin foil of silicon, where annihilation events will take place and which separates the UHV region from the region containing a stack of nuclear emulsion films. Behind the emulsions are two planes of scintillating fibres; both the fibres and the silicon foil will measure the time of flight T of each annihilation event. The production of \bar{H} atoms and the formation of an anti-hydrogen beam are critical issues, which require a careful diagnostic system. To this purpose, a detector has been designed, working in challenging conditions; indeed, it must operate at 4 K, inside a 1 T magnetic field, in vacuum conditions (10^{-6} mbar) within a cylindrical volume surrounding the region of \bar{H} formation. The power dissipation should be as low as possible ($< 10 \text{ W}$) not to perturb the cryogenic environment. Last but not least, the detector must be fast enough to identify annihilations occurring during the time interval (1 ms) of pulsed \bar{H} production. Such a Fast Annihilation Cryogenic Detector (FACT)¹⁴ consists of four layers of 1 mm diameter multi-clad scintillating fibres coupled to clear fibres which have the task of transferring the optical signal from the cryogenic region onto an array of multi-pixel-photon-counters. Reconstruction of the position of the annihilation vertex along the axis of the anti-hydrogen beam will allow us to measure both production and temperature of the beam. A resolution of 2.1 mm is expected.

3 First AEgIS Results

The catching of the \bar{p} in The Penning-Malmberg trap located in the cold (7 K) 5 T magnet can trap about $1.3 \cdot 10^5 \bar{p}$ per AD bunch (every 110 s) with a lifetimes $>$ of 600 s. The more complex trap system in the 5T magnet, includes four Penning-Malmberg traps. Manipulation of different kind of particles (e^- , e^+ and \bar{p}) in both 5T and 1T traps was performed. Different diagnostic devices (Faraday cups and MCP based detector) are used to measure and visualize the trap contents.

The design of the moiré deflectometer will take advantage from the experience gained on a compact prototype device, working with antiprotons¹⁵. It is formed by two parallel gratings (distance 25 mm from each other) and an emulsion detector at a distance 25 mm from the second grating. A beam of particles passing through the deflectometer produces a fringe pattern on the detector, which is shifted in the presence of a force. To infer the force, a comparison with a near-field interference pattern produced by light is carried out. An additional transmission grating in direct contact with the emulsion is illuminated simultaneously to the moiré deflectometer, with antiprotons as well as with light. This provides a reference for alignment, since the pattern behind the contact grating cannot show any dependence on a force. The results show a shift in the moiré pattern with respect to the interference pattern due to the light, which corresponds to a force acting on \bar{p} of about 530 aN.

4 Conclusion

The AEgIS experiment is designed to look for the free fall measurement of anti-hydrogen in the gravitational field. The Collaboration starting to use the apparatus to perform experiments with antihydrogen. First antiprotons run were performed last two runs, showing good performances of

the apparatus. The catching of antiprotons and the production of excited Rydberg positronium have been demonstrated. We are now preparing the mixing of both species to produce anti-hydrogen atoms. Manipulation of $\bar{\text{H}}$ atoms has been demonstrated with protons. We have also demonstrated with antiprotons the capability of the moiré defectometer and we are working on final version.

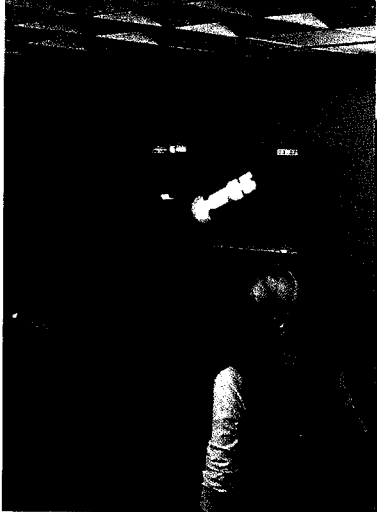
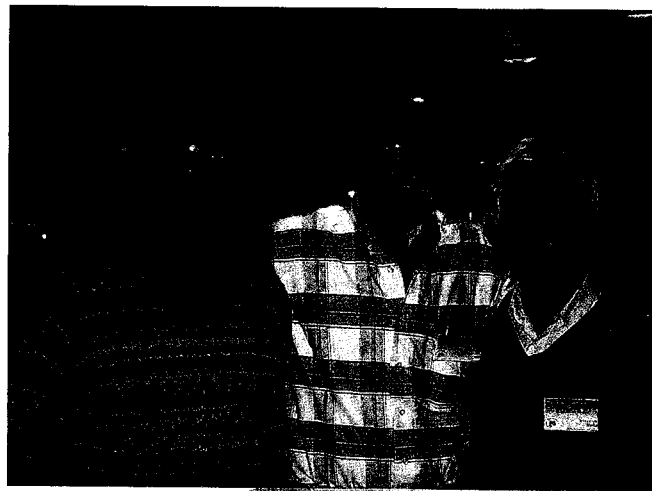
The current experiment is limited by the amount of \bar{p} we can store. In 2017 the ELENA (Extra Low ENergy Antiproton) stage will be added to the AD, producing further deceleration to \bar{p} down to 100keV. Two orders of magnitude are expected on the \bar{p} flux, opening new perspectives in the field of antimatter physics.

Acknowledgments

I would like to thank the quite patient organizers for giving me the opportunity to participate at the Conference.

References

1. P.A.M. Dirac, *Proc. Royal Soc. A* **117**, 661 (1928)
2. C. D. Anderson, *Phys. Rev.* **43**, 491 (1933)
3. N.F. Ramsey, *Physica Scripta* **T59**, 323 (1995).
4. D. Colladay and V.A. Kostelecky, *Phys. Rev.* **D55**, 6760 (1997)
5. E. G. Adelberger et al., *Prog. Part. Nucl. Physics* **62**, 102 (2009)
6. T.W. Darling et al., *Rev. Mod. Phys.* **64**, 237 (1992)
7. J. Barrow and R. Scherrer, *Phys. Rev.* **D 70**, 103515 (2004)
8. G.J. Ni, in: *Relativity, Gravitation, Cosmology*, edited by V.V. Dvoeglazov and A.A. Espinoza Garrido (Nova Science Publications) , 123 (2004)
9. M. Villata, *Europhys. Lett.* **94**, 20001 (2011)
10. A. Kellerbauer et al., *Nuclear Instrum. and Methods in Phys. Research B* **266**, 351 (2008)
11. R.G. Greaves and C.M. Surko, *Phys. Plasmas* **4**, 1528 (1997)
12. E. Vliegen, S. D. Hogan, H. Schmutz, and F. Merkt, *Phys. Rev.* **A 76**, 023405 (2007)
13. M.K. Oberthaler, S. Bennet, E.M. Rasel, J. Schniedmayer and A. Zeilinger, *Phys. Rev.* **A 54**, 3165 (1996)
14. J. Storey et al., *Nucl. Instr. & Meth.* **A 732**, 437 (2013)
15. S. Aghion et al., *Nature Comm.* **5**, 4538 (2014)



Gaia: astrometry and gravitation

S.A. KLIONER

Lohrmann Observatory, Technische Universität Dresden, 01062 Dresden, Germany

Gaia is an ESA space mission launched on 19 December 2013 with the main goal to provide astrometric and spectro-photometric measurements of over one billion celestial objects. The accuracy of the astrometric parameters at the end of the mission (at least 5 years of observations) should reach the level of about 10 microarcseconds for stars of optimal brightness. This level of accuracy allows one to realize a bundle of relativistic tests in the weak-field regime of the solar system as well as to provide a number of results relevant for strong-field tests of general relativity. An overview of Gaia modelling and results is provided here with the emphasis on the complications that one faces when measuring the PPN parameter γ using space astrometry mission like Gaia.

1 Gaia

Gaia is an ESA L-class mission launched on 19 December 2013. After more than half a year of testing and commissioning Gaia has started its science operations in July 2014. The main goal of Gaia is to deliver astrometric and spectro-photometric observations of over one billion celestial objects up to a certain magnitude limit (approximately, 20 mag). Celestial objects observed by Gaia include stars of our Galaxy, minor bodies of the solar system, bright objects of nearby galaxies, QSOs, etc. Astrometric accuracy of Gaia is expected to reach a level of about 10 microarcseconds for well-behaving stars of optimal brightness. Gaia is based on the same principle of scanning astrometric observations as the first ESA space astrometry mission called Hipparcos. Gaia instrument and mission concept are optimized to give highest possible astrometric performance:

- two telescopes with main mirrors of $1.45\text{ m} \times 0.5\text{ m}$ and the focal length of 35 m mounted in the same mechanical structure (the angle between two telescopes is called “basic angle”, has the nominal value of $\Gamma = 106.5^\circ$, should be as constant as possible, and is monitored on board using laser interferometry); two telescopes are needed to obtain absolute parallaxes;
- high thermo-mechanical stability of the instrument (e.g., no moving parts, main elements made of SiC);
- the orbit (a Lissajous orbit around the Lagrange point L_2 of the Earth-Sun system) and the satellite design ensure highly stable thermal environment for the science instrument;
- quasi-continuous observations with minimal dead time (e.g., the CCDs in the focal plane work in the so-called Time Delay Integration (TDI) mode allowing uninterrupted observations from rotating satellite);
- specially designed “scanning law” of Gaia provides astrometric observations that can be optimally used to measure astrometric parameters of each source (position, proper motion and parallaxes);
- automatic on-board recognition of celestial objects (those which are brighter than some pre-programmed limit);

- automatic on-board initial data processing: only those CCD pixels that may contain useful scientific information are downloaded to the ground (Gaia has the largest CCD assembly ever operated in space – about 1 Gpixel in 106 CCDs; a waste majority of the pixels at some moment of time contains only noise and are automatically ignored).

Gaia data processing is one of the most ambitious computational tasks in the history of astronomy. Gaia is expected to produce approximately 1 PB of data and most of those data must be processed simultaneously to obtain the global astrometric solution – a solution of a slightly non-linear optimization problem with about 10^{12} observations and about 10^{10} unknowns.

The scientific goals of Gaia include stellar physics, structure and history of our Galaxy, census of non-single stars in our Galaxy, exoplanetary science, solar system studies, fundamental reference frame and physics of QSOs in the optical, and, finally, certain aspects of fundamental physics. More details on Gaia, its principal ideas, mission design etc. can be found in the Gaia White Book ¹ and the associated publications ². Recent after-launch estimates of the expected astrometric and photometric performance of Gaia can be found at <http://www.cosmos.esa.int/web/gaia/science-performance>. The results of the data processing will be published in several steps that include a number of preliminary data releases and the final release in about 2022. The first preliminary release is expected in 2016.

2 Relativistic Modelling for Gaia

Before all above-mentioned scientific questions can be considered in a meaningful way one needs to model the observations in the framework of general relativity. The corresponding model has been constructed ^{4,5,6} and involves:

- the relativistic astronomical reference systems BCRS and GCRS ³ as the basis of the modelling of all auxiliary data (solar system ephemerides, time synchronization observations, Gaia ephemeris etc.),
- local reference system of the satellite as the basis for the model of observables and internal physical processes in the instrument ⁵,
- relativistic definitions of the observables (e.g. aberration treated via Lorentz transformations in compact form) and satellite attitude,
- the theory of light propagation in the solar system (post-Newtonian and enhanced post-post-Newtonian terms, effects due to translational motion of the deflecting bodies, quadrupole light bending),
- relativistic definitions of astrometric parameters as coordinate quantities in the BCRS.

3 Tests of General Relativity with Gaia

From the very beginning of the project development it was clear that the unprecedented accuracy of Gaia observations allows one to test certain aspects of fundamental physics and, first of all, high-accuracy tests of general relativity in the weak-field regime of the solar system. The results of Gaia relevant for fundamental physics and cosmology include weighing the invisible components of binary stellar systems with black hole candidates (e.g. Cyg X1), upper estimates of the energy flux of gravitational waves in a certain wave-band, etc. Several reviews of the tests planned with Gaia were published ^{7,8,9} and should not be duplicated here. Below the most obvious test of general relativity that is expected from high-accuracy astrometry – the determination of the amplitude of the light-bending effect – is discussed in more detail.

4 Determination of the PPN γ from space astrometry data

The determination of the PPN parameter γ is one of the most accurate tests of general relativity expected from Gaia. The sensitivity of Gaia observations to γ comes from the light-bending effect

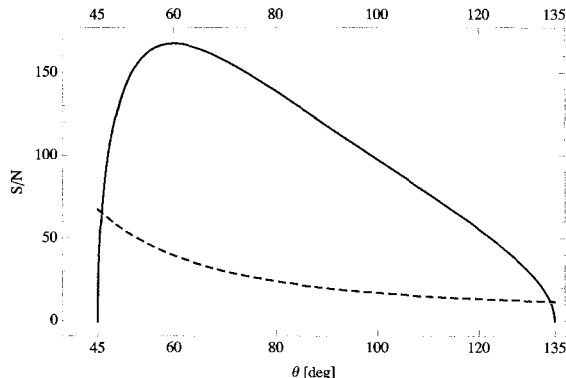


Figure 1 – Signal-to-noise (s/n) ratio of the light bending due to the Sun for one single transit: 10 subsequent observations of a source with 10 adjacent CCDs on the focal plane. The s/n ratio is shown for a star of magnitude optimal for Gaia as function of the angular distance θ to the Sun and the direction of observation: along-scan observations (solid line) and across-scan observations (dashed line). Gaia is designed to observe in the range $45^\circ \leq \theta \leq 135^\circ$. Across-scan observations cannot be used for scientific results since this information is almost completely used to determine certain calibration parameters.

in the gravitational field of the solar system (mostly, the Sun). Fig. 1 shows the signal-to-noise ratio of the light bending due to the Sun for one single transit for a star of magnitude optimal for Gaia accuracy. One transit through the focal plane gives a set of (up to) 10 subsequent CCD observations of a source by 10 adjacent CCDs. The signal-to-noise ratio varies with the angular distance between the Sun and the source and is different depending on the direction of observation (along-scan observations are more accurate than across-scan observations) and depends on the angular distance from the Sun. The across-scan observations cannot be used for scientific results since this information is almost completely used to determine certain nuisance and calibration parameters (e.g., the attitude of the satellite). One sees that under optimal conditions Gaia is in principle able to determine the PPN γ with a precision of $\sigma_\gamma \approx \frac{2}{170} \approx 0.012$ from a single transit of an optimal source. Each source has approximately 80 transits distributed over five years of observations and one expects approximately 10^9 sources observed by Gaia. One should take into account that the observations are performed at different angular distances θ to the Sun and that the sources have different brightnesses (the distribution of the stellar magnitudes can be obtained using some realistic model of our Galaxy). One could naively think that it is sufficient to use the statistical $N^{-1/2}$ law and thus arrive at unrealistically good uncertainties of γ . In reality, one has to cope with a number of complications and sources of systematic errors, which are discussed below.

4.1 Correlation between γ and the parallax zero point

The signal-to-noise ratio shown on Fig. 1 can be directly interpreted as uncertainty of γ only if all other parameters influencing the observations are perfectly known. This assumption is of course not justified and the correlations between γ and other parameters should be taken into account. The simplest case which is known for decades is the relatively strong correlations between γ and the parallax zero point ϖ_0 (that is, a constant that is simultaneously added to the parallaxes of all sources). This case can be treated analytically^{10,11}.

The geometry of the positional shifts of a source due to the light deflection and the parallax are shown on Fig. 2. The magnitude of the shifts $\delta\theta_1$ and $\delta\theta_2$ depend on the angular distance θ between the source and the Sun:

$$\delta\theta_1 = \varpi R \sin \theta, \quad (1)$$

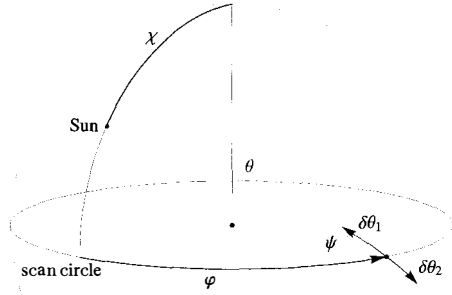


Figure 2 – Geometry of the positional shifts of a source due to the light deflection and the parallax. Here χ is the solar aspect angle ($\chi \approx 45^\circ$ for Gaia), φ is the heliotropic phase angle of the field of view under consideration, θ is the angular distance between the source and the Sun, $\delta\theta_1$ is the parallactic shift, $\delta\theta_2$ is the shift due to the light deflection (see text).

$$\delta\theta_2 = (1 + \gamma) \frac{GM_\odot}{c^2 r} \cot \frac{\theta}{2}, \quad (2)$$

where ϖ is the parallax of the source, r is the *heliocentric* distance of the observer, while R is the *barycentric* distance of the observer expressed in astronomical units (1 au = 149597870700 m). Here we neglect the fact that the parallactic shift is directed towards the solar system *barycentre*, while the light-bending shift due to the Sun increases the angular distance to the Sun. We, thus, neglect the difference between the position of the Sun and that of the solar system barycentre as seen from Gaia (see below). For a scanning satellite like Gaia observables are the projections of the shifts on the scanning direction. Considering the direction of the shifts and the spherical triangle “source – Sun – the projection of the Sun on the scan circle” one gets:

$$\delta\varphi_1 = -\delta\theta_1 \cos \psi = -\varpi R \sin \theta \cos \psi = -\varpi R \sin \chi \sin \varphi, \quad (3)$$

$$\begin{aligned} \delta\varphi_2 &= \delta\theta_2 \cos \psi = (1 + \gamma) \frac{GM_\odot}{c^2 r} \cot \frac{\theta}{2} \cos \psi \\ &= (1 + \gamma) \frac{GM_\odot}{c^2 r} \frac{\sin \theta \cos \psi}{1 - \cos \theta} = (1 + \gamma) \frac{GM_\odot}{c^2 r} \frac{\sin \chi \sin \varphi}{1 - \sin \chi \cos \varphi}. \end{aligned} \quad (4)$$

Here χ is the solar aspect angle and φ is the heliotropic phase angle of the field of view under consideration (see Fig. 2). Our goal now is to compute the correlation between the observable shifts $\delta\varphi_1$ and $\delta\varphi_2$. Here we ignore the time dependence of r and R (see below) and it is therefore possible to ignore positive factors ϖR and $(1 + \gamma) \frac{GM_\odot}{c^2 r}$, which don’t influence the correlation. Therefore, the signals read:

$$f_\varpi(\varphi) = -\sin \chi \sin \varphi, \quad (5)$$

$$f_\gamma(\varphi) = \frac{\sin \chi \sin \varphi}{1 - \sin \chi \cos \varphi}. \quad (6)$$

It is natural to assume that observations are homogeneously distributed with respect to φ . Direct calculations show that the correlation between $\delta\varphi_1$ and $\delta\varphi_2$ read:

$$\rho_{\gamma\varpi}^{\text{abs}} = -\sqrt{\frac{2}{1 + \sec \chi}}. \quad (7)$$

For Gaia, $\chi \approx 45^\circ$ and one gets $\rho_{\gamma\varpi}^{\text{abs}} \approx -0.910$.

The discussion above is valid for each individual source. One often considers a common additive change of all parallaxes ϖ_0 called “parallax zero point”: for each source $\varpi' = \varpi + \varpi_0$. Then parameter ϖ_0 and its correlation with γ does not depend on the source. There are several small effect which decorrelate γ and ϖ_0 : (1) the fact that the parallactic effect depends on the direction and distance to the solar system barycentre, while the light-bending effect is related to the direction and distance from the observer to the Sun, (2) finite size of the field of view (in the calculation above we assumed that the field of view of the telescope is infinitely small), (3) light deflection due to other bodies of the solar system (first of all, Jupiter). These effects are, however, small. Dedicated numerical simulations show that the correlation between γ and the parallax zero point is $\rho_{\gamma\varpi_0}^{\text{num}} \approx -0.900$. In particular it means that the formal uncertainty of γ from the simultaneous fit of γ and the parallax zero point ϖ_0 is by a factor of

$$\frac{\sigma_{\gamma}^{\text{with } \varpi_0}}{\sigma_{\gamma}^{\text{alone}}} = \left(1 - \left(\rho_{\gamma\varpi_0}^{\text{num}}\right)^2\right)^{-1/2} \approx 2.294 \quad (8)$$

larger than the formal error of γ when fitted alone.

One can argue that a part of the information from along-scan observations is also used to determine some nuisance and calibration parameters. In particular, the along-scan observations are used to determine the along-scan attitude of the satellite as function of time. One can show that the only information directly available for scientific parameters (astrometric source parameters as well as physical parameters like the PPN γ) is the difference of the along-scan observation obtained in two different fields of view. This changes¹² the correlation between γ and ϖ (or ϖ_0). To compute the correlation in this situation one has to consider the following signals instead of (5)–(6):

$$g_{\varpi}(\varphi) = f_{\varpi}(\varphi + \Gamma) - f_{\varpi}(\varphi), \quad (9)$$

$$g_{\gamma}(\varphi) = f_{\gamma}(\varphi + \Gamma) - f_{\gamma}(\varphi). \quad (10)$$

Here Γ is the basic angle between two telescopes. It is easy to demonstrate that the correlation between these two signals reads:

$$\rho_{\gamma\varpi}^{\text{diff}} = -\frac{2}{1 + \cos \chi} \sqrt{\cos \chi \left(\sin^2 \frac{\Gamma}{2} + \cos^2 \frac{\Gamma}{2} \cos^2 \chi \right)}. \quad (11)$$

Note that since f_{ϖ} and f_{γ} are 2π -periodic the same result is true also if one defines $g_{\dots}(\varphi) = f_{\dots}(\varphi + \Gamma/2) - f_{\dots}(\varphi - \Gamma/2)$. For Gaia $\Gamma \approx 106.5^\circ$ and, therefore, $\rho_{\gamma\varpi}^{\text{diff}} \approx -0.893$. In principle, this correlation better characterizes Gaia astrometric solution than $\rho_{\gamma\varpi}^{\text{abs}}$. However, Eq. (11) still describes an idealized artificial situation: only γ , ϖ_0 and (a simplified model for) along-scan attitude are fitted. A more realistic discussion is given in the next Section.

4.2 Correlations between γ and other source and attitude parameters

One can expect that the correlation with the parallax zero point is the largest correlation between γ and other parameters that are fitted from the same observational data. However, other correlations cannot be neglected especially in the view of the number of those parameters. Here we consider only source (astrometric) parameters – positions, proper motions and parallaxes – of the sources as well as the parameters describing the attitude of the satellite.

As we mentioned above, the astrometric solution of Gaia involves approximately 10^{10} parameters and represents a robust version of the least squares fit where the outliers are automatically identified and correspondingly down-weighted. Clearly, it is not possible to make this enormous fit in a usual way of computing the normal matrix, etc. For this reason, one uses a highly optimized iterative solution that uses many properties of mission design. This is called Astrometric

Global Iterative Solution (AGIS) ¹³. This approach makes the computation of the astrometric solution possible. However, since the solution is block-iterative, one never computes full normal matrix and, therefore, one never sees the correlations between all the parameters. Special methods should be used to investigate those correlations and the uncertainties in the resulting parameters.

Given the complexity of the data properties and the size of the fitting process, it is not known how to treat the problem of correlations analytically. The only available method to estimate the effects of the correlations between γ and all other parameters is to perform statistical bootstrapping using the software that simulates the iterative astrometric solution for Gaia. This can be done using AGISLab – a highly sophisticated software created by the AGIS team ¹⁰. AGISLab allows one to generate true and noisy observational data using all relevant properties of Gaia and perform iterative astrometric solution starting from some initial values of parameters. AGISLab has an important possibility to down-scale the astrometric fit so that less parameters can be used while preserving many important statistical properties of the solution. This allows one to compute an astrometric solution within a reasonable time and thus makes it possible to perform a large number of simulations.

If one uses simulated true (noiseless) observations, all the parameters – astrometric source parameters, attitude parameters as well as any global parameters used to generate those true observations – converge to their true values. In this situation, the errors of all parameters are negligibly small and come from numerical round-off errors only. If one adds observational noise, the parameters converge to some values, the errors of which are defined both by the particular realization of the observational noise and by the statistical properties of the astrometric solution (in particular, by the correlations between the parameters). Using different realizations of observational noise with given statistical properties (defined by the best available model for the observational noise of Gaia) one can analyze statistics of the errors of any involved parameters. In particular, the realistic statistical uncertainty of the PPN γ can be determined. This realistic uncertainty of γ reflects all correlations between parameters of the solutions and the observational noise of Gaia and agrees with the uncertainty that would be obtained from an explicit non-iterative least-squares fit of all parameters simultaneously. Obviously, this “realistic” uncertainty does not reflect possible systematic errors in the real Gaia data (that is, possible deficiencies of the model used to described Gaia data). Such systematic errors should be discussed separately.

Two sets of numerical experiments were performed. First, we consider solutions where only source parameters and γ are fitted. Approximately 550 such solutions with different realizations of the observational noise were performed. Computing the standard deviation from the set of obtained estimates of γ one sees that the ratio of the uncertainty σ_γ^S when fitting γ together with the source parameters and the uncertainty $\sigma_\gamma^{\text{alone}}$ when γ is fitted alone reads:

$$\frac{\sigma_\gamma^S}{\sigma_\gamma^{\text{alone}}} = 2.529 \pm 0.077. \quad (12)$$

This results should be compared to (8) where only the correlation between γ and the parallax zero point ϖ_0 is considered in some approximation. Expectedly, other source parameters increases the uncertainty of γ compared to (8). In particular, one sees that other source parameters increase the uncertainty of γ as $\sigma_\gamma^S/\sigma_\gamma^{\text{with } \varpi_0} = 1.102 \pm 0.033$.

The second sort of numerical experiments with AGISLab is to fit γ together with all source and attitude parameters. Approximately 1000 of such experiments were performed and showed that the ratio of the uncertainty $\sigma_\gamma^{\text{SA}}$ when fitting γ together the source and attitude parameters and the uncertainty $\sigma_\gamma^{\text{alone}}$ when γ is fitted alone can be estimated as:

$$\frac{\sigma_\gamma^{\text{SA}}}{\sigma_\gamma^{\text{alone}}} = 3.335 \pm 0.075. \quad (13)$$

This means that a combination of the source and attitude parameters increases the uncertainty of γ by $\sigma_\gamma^{\text{SA}}/\sigma_\gamma^{\text{with } \varpi_0} = 1.454 \pm 0.033$.

Since $\sigma_\gamma^{\text{alone}}$ can be easily determined from the AGIS, Eq. (13) allows one to determine the realistic statistical uncertainty of γ .

4.3 The expected uncertainties of γ

Combining all the aspects mentioned above one can arrive to an estimate of the accuracy, with which Gaia can determine the PPN γ . Depending on which part of the sources can be used for the estimate one gets:

- 1) $\sigma_\gamma > 1.3 \times 10^{-6}$ if all stars with $G \leq 20$ can be used,
- 2) $\sigma_\gamma > 2.5 \times 10^{-6}$ if only faint stars with $15 \leq G \leq 20$ are used.

Here G is the Gaia magnitude that takes into account spectral sensitivity of Gaia astrometric CCDs. The sign “>” is used here to stress that systematic errors may potentially ruin this promise.

4.4 Instabilities of the basic angle as a systematic error

An important source of systematic errors is an uncalibrated (unknown) variation of the basic angle Γ between the two fields of view. One can show that in principle, if one neglects small second-order effects due to the finite size of the Gaia fields of view, a certain specially designed variation of the basic angle combined with a certain variation of the attitude cannot be distinguished from a constant change in the PPN γ . In the Gaia data processing the attitude is an unknown function of time fitted from the same astrometric data. Therefore, if such a variation of Γ is present in the data, it would be impossible to distinguish it from a shift of the PPN γ .

Given arbitrary along-scan shifts in the two fields of view one can argue that half of the sum of these effects is equivalent to a rotation of the instrument as a whole in the along-scan direction while the difference is equivalent to a change of the basic angle. Let us define the heliotropic phase Ω of the satellite as the heliotropic phase of the direction exactly bisecting the directions of the two fields of view. The heliotropic phase angle of the preceding field of view is $\phi_p = \Omega + \Gamma/2$ and that of the following field of view is $\phi_f = \Omega - \Gamma/2$. Using the light-bending effect (4) written for these two values of ϕ and computing the difference one gets the basic-angle variation $\delta\Gamma_\gamma$ equivalent to a change $\delta\gamma$ of the PPN γ :

$$\delta\Gamma_\gamma = \delta\gamma \frac{2GM_\odot}{c^2 r} \frac{a + b \cos \Omega}{c + d \cos \Omega + \cos^2 \Omega}, \quad (14)$$

$$a = \frac{1}{2} \sin \Gamma, \quad b = -\csc \chi \sin \frac{\Gamma}{2}, \quad c = \csc^2 \chi - \sin^2 \frac{\Gamma}{2}, \quad d = -2 \csc \chi \cos \frac{\Gamma}{2}. \quad (15)$$

Using $\chi = 45^\circ$, $\Gamma = 106.5^\circ$ and the orbital parameters for Gaia one gets

$$\delta\Gamma_\gamma = 4.03 \text{ mas} \frac{0.47941 - 1.13314 \cos \Omega}{1.35799 - 1.69232 \cos \Omega + \cos^2 \Omega} \delta\gamma. \quad (16)$$

Hence, a certain variation of the basic angle with an amplitude of 4 mas can mimic a shift of γ of the order of unity (see Fig. 3). Fortunately, the basic angle of Gaia is measured by the Basic Angle Monitor. In addition, the usual considerations of plausibility should be used: there is no physical reason for the basic angle to have a variation with such a “fancy” profile. One can hope that the available information together with a detailed modelling of all parts of the satellite will allow one to calibrate the basic angle to the desired level of accuracy.

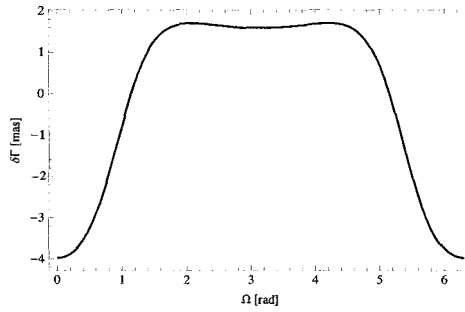


Figure 3 – The basic-angle variation equivalent to a shift of the PPN γ given by Eq. (16) as function of the heliotropic phase Ω of the satellite. The amplitude is given for $\delta\gamma = 1$.

Acknowledgments

This review is based on the work of many people involved in Gaia. The use of AGISLab created by Lennart Lindgren, Berry Holl, David Hobbs, Daniel Michalik and Alex Bombrun is gratefully acknowledged. Hagen Steidelmüller implemented the Generic Global Update, which was used, in particular, in the study of γ , and made it possible to automatically create AGISLab runs for the bootstrapping. This work was partially supported by the BMWi grant 50QG1402 awarded by the Deutsche Zentrum für Luft- und Raumfahrt e.V. (DLR).

References

1. Gaia: Composition, Formation and Evolution of the Galaxy, the Gaia Concept and Technology Study Report (CTSR), compiled by Gaia Science Advisory Group, ESA-SCI(2000)4.
2. M.A.C. Perryman *et al.*, *A&A* **369**, 339 (2001).
3. M. Soffel *et al.*, *Astron. J.* **126**, 2687 (2003).
4. S.A. Klioner, *Astron.J.* **125**, 1580 (2003).
5. S.A. Klioner, *Phys. Rev. D* **69**, 124001 (2004).
6. S.A. Klioner, S. Zschocke, *Class.Quantum Grav.* **27**, 075015 (2010).
7. S.A. Klioner in *Lasers, Clocks and Drag-Free: Exploration of Relativistic Gravity in Space*, ed. H. Dittus, C. Lämmerzahl, S. G. Turyshev (Berlin: Springer, Berlin, 2007).
8. F. Mignard, S. Klioner in *Relativity in Fundamental Astronomy*, ed. S. Klioner, K. Seidelmann, M. Soffel (Cambridge University Press, Cambridge, 2010).
9. S.A. Klioner in *The Milky Way Unravalled by Gaia*, ed. C. Soubiran, F. Figueras, N. Walton, (Les Ulis, EDP Sciences, 2015).
10. D. Hobbs *et al.* in *Relativity in Fundamental Astronomy*, ed. S. Klioner, K. Seidelmann, M. Soffel (Cambridge, Cambridge University Press, 2010).
11. F. Mignard in *Gaia: a European Space Project*, ed. O. Bienaymé, C. Turon (Les Ulis, EDP Sciences, 2002).
12. L. Lindgren, *private communication*, 2008.
13. L. Lindgren *et al.*, *A&A* **538**, A78 (2012).

INPOP planetary ephemerides: Recent results in testing gravity

A. Fienga¹, J. Laskar², P. Exertier¹, H. Manche², M. Gastineau²

¹*GéoAzur, Observatoire de la Côte d'Azur, France* ² *IMCCE, Observatoire de Paris, France*

In this paper, are given numerical estimations of the sensitivity of the latest version of the INPOP planetary ephemerides (INPOP13c) to GR parameters: the PPN parameters β , γ , the flattening of the sun J_2^\odot but also to time variations of the gravitational mass of the sun μ . A first estimation is obtained by fitting these parameters with the classic method of least squares to planetary observations together with other parameters used for planetary ephemeris construction. A second approach is investigated by a new method of construction of alternative ephemerides based on the same dynamical modeling and observational samples but in a non-GR framework by considering non-zero or non-unity GR parameters. Some alternative ephemerides are found to be close to INPOP13c and acceptable intervals of GR parameters are then defined at the light of the present INPOP13c accuracy. These intervals are compared with the one obtained with the direct least square estimations and with those extracted from the literature. Based on these results and comparisons, no violation of GR is at this point noticeable.

1 INPOP13c

1.1 Description

By the use of the tracking data of the MESSENGER mission, INPOP13a becomes an interesting tool for testing GR close to the Sun¹. The MESSENGER mission was indeed the first mission dedicated to the study of Mercury. The spacecraft orbits the smallest and closest to the sun planet of the solar system since 2011. In¹ are described the methods and procedures used for the analysis of the MESSENGER Doppler and range data included in the construction of the Mercury improved ephemerides, INPOP13a as well as the determination of acceptable intervals of non-unity values for the PPN β and γ .

INPOP13c⁵ is an upgraded version of INPOP13a, fitted to LLR observations, and including new observables of Mars and Venus deduced from MEX, Mars Odyssey and VEX tracking data^{2,3,4}.

Together with the eight planets and the Moon initial conditions, the INPOP13c adjustment also includes the gravitational mass of the sun as recommended by the IAU resolution B2 as well as the sun oblateness (J_2^\odot), the ratio between the mass of the earth and the mass of the moon (EMRAT) and the mass of the Earth-Moon barycenter. Perturbations of 290 individual asteroids are taken into account in the dynamical modeling as well as perturbations induced by an asteroid ring at 3.15 AU. The mass of this ring as well as 290 individual asteroid masses are also fitted to observations.

1.2 Comparisons to other planetary ephemerides

A classical approach to estimate planetary ephemerides uncertainties is to make comparisons between different ephemerides: the JPL DE430⁶, the IAA EPM2011⁷ and INPOP13c. These

three ephemerides differ in their dynamical modeling mainly in the modeling of the asteroid perturbations but are adjusted with approximatively the same sample of observations. DE430 fits an important number (343) of objects with a priori values and uncertainties when EPM2011 fits a more limited number of objects (21) in association with more global estimations such as main belt and TNO rings and mean taxonomic densities. INPOP13c is an intermediate approach combining numerous individual fit (290) with a global main belt ring. The orbit differences between the ephemerides do not only picture the differences in the modeling and fitting strategy. They also include differences in the weighting scheme used for the construction of the ephemerides. Comparisons between the orbits of the planets provided by these ephemerides give the present uncertainties on the planetary orbits.

Knowing these uncertainties, it is then possible to consider alternative planetary orbits built on the basis of the INPOP13c ephemerides with different values of GR parameters and to compare these ephemerides to INPOP13c, DE430 and EPM2011. An acceptable alternative theory will be the one with differences to INPOP13c smaller or comparable to differences between INPOP13c, DE430 and EPM2011. These figures will be used as limits for considering an alternative ephemerides as acceptable at the light of the present ephemeris differences. Important differences for Mercury and Saturn are induced by independant spacecraft navigation analysis done by JPL and INPOP teams. Such thresholds can be scaled by the maximum residuals of INPOP13c for the fit dataset and besides the Messenger case, the maximum differences between INPOP13c and DE430 are below or about 50% of the maximum residuals of INPOP13c. EPM2011 does not include Messenger and Cassini tracking data. This explains the important differences for Mercury and Saturn. Furthermore, other data for Mars and Venus are also not included in EPM2011 but in DE430 and INPOP13c. Here again, for INPOP13c and EPM2011 common periods (before 2011), the differences stay below 50 % of the maximum postfit residuals of INPOP13c. The threshold of 50 % of the maximum INPOP13c postfit residuals for the maximum differences between ephemerides is adopted as a possible threshold for defining *close enough* ephemerides.

2 GR tests with INPOP

2.1 Implementation

Since INPOP10a, regular estimations of possible non-unity values for PPN parameters β and γ are regularly done with INPOP. For this work, we add to the INPOP dynamical modeling the possibility of constraining variations of the gravitational mass of the sun, μ , considering a variation of the mass of the sun noted \dot{M}_{\odot} and a variation of the gravitational constant \dot{G} . At each step t of the numerical integration of the INPOP equations of motion, we then estimate :

$$M_{\odot}(t) = M_{\odot}(J2000) + (t - J2000) \times \dot{M}_{\odot} \quad (1)$$

$$G(t) = G(J2000) + (t - J2000) \times \dot{G} \quad (2)$$

$$\mu(t) = G(t) \times M_{\odot}(t) \quad (3)$$

$\dot{\mu}/\mu$ is also updated in the computation of the Shapiro delay of the observables (see⁸). We use for $M_{\odot}(J2000)$ the fitted mass of the sun and for $G(J2000)$ the Newtonian gravitation constant as defined by the IAU⁹. We then deduce values of \dot{G}/G by considering a fixed value for the Sun total mass loss. We choose for this work the¹⁰ total solar mass loss updated with the¹¹ mean mass loss from wind emission of charged particules during the 11-year solar cycle. This update leads to an interval of values of about $\frac{\dot{M}_{\odot}}{M_{\odot}} = (-0.92 \pm 0.46) \times 10^{-13} \text{ yr}^{-1}$. This value is used in the following section for deducing \dot{G}/G from the estimated $\dot{\mu}/\mu$ gathered in Table 1.

Table 1: Results compared to values found in the literature. For least square determinations (LS), uncertainties are given at $3\text{-}\sigma$. Each line gives the results obtained after the fit including 60 (*Limited*) or 290 asteroid masses (*Full*), spacecraft bias (SC) and observational station bias (DSN), defined in section 2.2. The Monte Carlo uncertainties give the length of the acceptable interval of violation as defined in the text. For the MC and LS estimations of \dot{G}/G , the values are deduced from the estimated values of μ/μ and in considering $\frac{M_{\odot}}{M_{\oplus}} = (-0.92 \pm 0.46) \times 10^{-13} \text{ yr}^{-1}$.

| Method | PPN $\beta - 1$ $\times 10^5$ | PPN $\gamma - 1$ $\times 10^5$ | \dot{G}/G $\times 10^{13} \text{ yr}^{-1}$ | J_2^{\odot} $\times 10^7$ |
|--|----------------------------------|-----------------------------------|---|--------------------------------|
| Least squares (LS) | | | | |
| Limited | -12.8 ± 6.7 | 10.2 ± 0.8 | 1.12 ± 0.47 | 2.23 ± 0.2 |
| Limited + SC + DSN | -2.3 ± 8.4 | 3.1 ± 2.2 | 0.94 ± 0.48 | 2.23 ± 0.2 |
| Full | -4.9 ± 6.4 | -2.0 ± 6.4 | -0.58 ± 0.63 | 2.27 ± 0.3 |
| Full + SC + DSN | -6.7 ± 6.9 | -0.81 ± 5.7 | 0.42 ± 0.75 | 2.27 ± 0.25 |
| Monte Carlo (MC) | | | | |
| MC + GA 50 % | -0.49 ± 6.31 | -1.19 ± 4.43 | 0.36 ± 1.22 | 2.26 ± 0.11 |
| MC + GA 25 % | -1.06 ± 4.46 | -0.75 ± 3.23 | 0.41 ± 1.00 | 2.28 ± 0.08 |
| MC + GA χ^2 H _{iter} | 0.34 ± 6.91 | -1.67 ± 5.12 | 0.51 ± 1.18 | 2.218 ± 0.135 |
| MC + GA χ^2 H1 | 0.11 ± 7.07 | -1.62 ± 5.10 | 0.52 ± 1.18 | 2.220 ± 0.135 |
| MC + GA χ^2 H2 | 0.05 ± 7.12 | -1.62 ± 5.17 | 0.53 ± 1.20 | 2.221 ± 0.137 |
| MC + GA χ^2 H3 | -0.01 ± 7.10 | -1.67 ± 5.25 | 0.55 ± 1.22 | 2.220 ± 0.14 |
| MC + GA (50 % + χ^2) | 0.0 ± 6.90 | -1.55 ± 5.01 | 0.494 ± 1.20 | 2.224 ± 0.131 |
| Planetary ephemerides | | | | |
| DE ²⁷ | 4 ± 24 | fixed to (2.1 ± 2.3) | 0.0 | fixed to 1.8 |
| | fixed | 18 ± 26 | 0.0 | fixed to 1.8 |
| | 0.0 | 0.0 | $1.02 \pm 2.06^*$ | fixed to 1.8 |
| DE ¹³ | 0.0 | 0.0 | 0.0 | 2.1 ± 0.70 |
| EPM ¹⁴ | -2 ± 3 | 4 ± 6 | $0.29 \pm 0.89^*$ | 2.0 ± 0.2 |
| INPOP13a ¹ | 0.2 ± 2.5 | -0.3 ± 2.5 | 0.0 | 2.40 ± 0.20 |
| INPOP10a ¹⁵ | -4.1 ± 7.8 | -6.2 ± 8.1 | 0.0 | 2.40 ± 0.25 |
| INPOP08 ¹⁶ | 7.5 ± 12.5 | 0.0 | 0.0 | 1.82 ± 0.47 |
| LLR | | | | |
| ¹⁷ | 12 ± 11 | fixed to (2.1 ± 2.3) | | |
| ¹⁸ | 0.0 | | ± 3 | |
| ¹⁹ | 0.0 | 0.0 | -0.7 ± 3.8 | |
| | 3 ± 13 | fixed to (2.1 ± 2.3) | 0.0 | |
| Other technics | | | | |
| Cassini ²⁰ | 0.0 | 2.1 ± 2.3 | 0.0 | NC |
| VLBI ²¹ | 0.0 | -8 ± 12 | 0.0 | fixed |
| Planck + Brans-Dicke ²² | | | -1.315 ± 2.375 | |
| Binary pulsar ²⁴ | | | 40 ± 50 | |
| Big Bang nucleosynthesis ²³ | | | 0 ± 4 | |
| Heliosismo ^{25,26} | | | | 2.206 ± 0.05 |

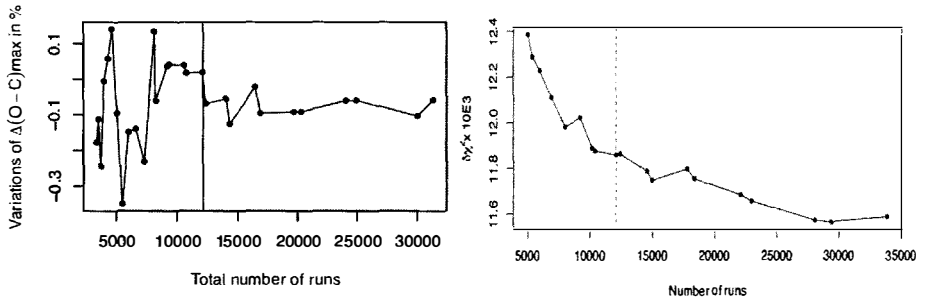


Figure 1 – Evolution of the number of selected ephemerides based on the two $\Delta(O-C)_{max}$ criteria (left) and the four H3 χ^2 criteria (right) described in the text.

2.2 Direct Least square estimations

In using INPOP13c as a reference ephemeris, least square adjustments of GR parameters together with regular planetary ephemeris adjusted parameters were done considering i) the impact of the asteroid perturbations on the dynamical modeling with two different fits (one with a limited number of fitted asteroid masses (60) and one with 290 fitted asteroid masses) and ii) the observational bias induced either by systematic effects related to the spacecraft itself (electronic degradation, mismodeling of the spacecraft macromodel) either by calibration uncertainties at the DSN stations. Table 1 gathers the fitted GR parameter values and uncertainties deduced from the different least squares.

These results are globally consistent with previous analysis done by²⁷ or²⁸ which stress the limitation due to the asteroid perturbations on the determination of $\dot{\mu}/\mu$, J_2^\odot and β .²⁹ also point out the importance of asteroid perturbations for J_2^\odot determinations. Observational bias play also a role especially in the case of the limited modeling, stressing the importance of the asteroid perturbations on the GR tests which can be done with planetary ephemerides.

Finally, the χ^2 obtained with the full modeling fit including the estimation of the spacecraft bias is still very close to the one without bias χ^2 : the difference between the two χ^2 is below 1 %. For the limited modeling, the differences between the χ^2 obtained with and without observational bias are more important indicating again a better robustness of the full modeling in comparison to the limited one.

2.3 Monte Carlo optimized estimations

Besides such computations, theoreticians often ask if some GR violations can be possible in the frame of some specific modeling of the solar system. In order to answer to this type of questions, one can introduce possible violations of GR through PPN parameters and time variation of G in the planetary ephemerides and to fit such ephemerides by comparison to observations. Acceptable intervals of GR violations can then be defined such as inducing fitted planetary ephemerides with small differences (relative to planetary ephemeris uncertainties) in comparison to a GR planetary ephemeris, in our case INPOP13c, built with $\beta = \gamma = 1$, $\dot{\mu}/\mu = 0$ and $J_2^\odot = 2.3 \times 10^{-7}$.

In order to investigate a wide range of possible values for GR parameters, we set up an algorithm based on a genetic combination of PPN β , γ , J_2^\odot and $\dot{\mu}/\mu$. For each combination of GR parameters, we built a fitted planetary ephemeris that we test by considering two criteria: one based on the maximum differences in postfit residuals relative to INPOP13c and one based on the χ^2 differences. These tests say if the planetary ephemeris is *close enough* to INPOP13c by limiting the differences in $\Delta(O-C)_{max}$ (criteria 1) or the differences in $\delta\chi^2$ (criteria 2).

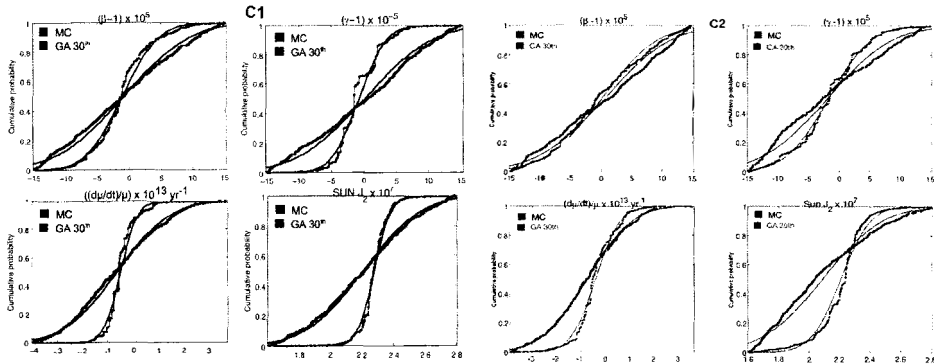


Figure 2 – Cumulative histogram of (PPN β , PPN γ , J_2^{\odot} , $\dot{\mu}/\mu$) for the generation 0 of ephemerides selected with the $\Delta(O - C)_{max}$ criteria (left) and the H3 χ^2 criteria (right, noted MC and colored in black) and for the final generation noted GA 30th and colored in red also selected with the $\Delta(O - C)_{max}$ criteria (left) and the H3 χ^2 criteria(right). The full lines are the corresponding cumulative histograms for the normal distribution fitted on the distributions of the first generation and the 30th generation.

In order to test the sensitivity of the algorithm to these thresholds, we consider two values for the $\Delta(O - C)_{max}$ limits (25% and 50% as noticed by the INPOP13c, DE430 and EMP2011 differences) and four values of the $\delta\chi^2$ criteria: H_{iter} for ephemerides with $\delta\chi^2 < 0.5\%$, H1 for ephemerides with $\delta\chi^2 < 1\%$, H2 for ephemerides with $\delta\chi^2 < 2\%$ and finally H3 with $\delta\chi^2 < 3\%$. These limits are consistent with $\delta\chi^2$ values experienced during the least squares estimations of GR parameters presented in section 2.2.

If two fitted planetary ephemerides are selected by one of the two criteria (both being selected by the same criteria), the corresponding GR parameters are recombined using a two crossover algorithm associated with a mutation probability of 10%. A new set of GR parameters of then obtained and a new planetary ephemeris is created and fitted and the same testing procedure is applied and new sets of GR parameters are selected (constituting a new generation of parameters) before a new recombination is done.

A total of 35800 runs spread over 30 generations were computed on the MesoPSL computer center of Paris Science et Lettres (www.mesops1.fr). We stop the generational process until the average change in the maximum differences of postfit residuals $\Delta(O - C)_{max}$ or in $\delta\chi^2$ are stable. As one can see on Figure 1, these differences stabilized at about 12 000 runs corresponding to the 18th generation. The selected samples of GR parameters with which produced ephemerides are selected based on the $\Delta(O - C)_{max}$ or on the χ^2 criteria constitute gaussian samples from which one can define mean and 1- σ . The gaussianity of the selected samples is improving with the number of runs as one can see on Figure 2 as well as the dispersion of the selected parameters is decreasing with the number of runs (see Figure 3).

3 Discussion

Table 1 gathers the results obtained with this work as well as very diverse estimations found in the literature. The first values presented in Table 1 are those estimated by direct least square procedures described in section 2.2. As discussed in this section, GR parameters estimated directly from a global fit of planetary ephemerides are sensitive to the dynamical modeling but also to observational bias. However, the full modeling adjustment presents a better robustness in comparison to the limited modeling. The values of GR parameters deduced from the full modeling tend to have consistent values at 3- σ with or without observational bias when higher

variations are noticeable for the limited modeling. Greater variations in the χ^2 values are also present for the limited modeling. Considering results obtained with the MC simulations and more specifically the χ^2 criteria, one can note the consistency of the deduce intervals for the four criteria of selections, stressing the robustness of the method. Intervals deduced from the $\Delta(O - C)_{max}$ criteria appear to have greater variations but always in keeping consistent intervals. In this context, in order to exhibit one single set of values of acceptable intervals for the four parameters randomly modified in this work, one can consider the mean values of the most numerous MC+GA selection presented in Table 1, gathering values of (PPN β , PPN γ , J_2^\odot , $\dot{\mu}/\mu$) inducing ephemerides with $\Delta(O - C)_{max} < 50\%$ and ephemerides selected with the four χ^2 criteria. We then obtain the values labeled MC + GA (50 % + χ^2) in Table 1.

As noticed in ¹ the interval of possible violations for the PPN parameters β and γ with no time variation of the Newtonian gravitational constant G and in fixing the value of the Sun flattening is as accurate as the reference values obtained with the Cassini experiment²⁰. However by adding the variations of $\dot{\mu}/\mu$ and J_2^\odot , we have enlarged the possible interval of violations for the four parameters as given in line MC + GA (50 % + χ^2) of Table 1.

Furthermore, by selecting non GR ephemerides with $\Delta(O - C)_{max}$ smaller than the present uncertainty of planetary ephemerides (see section 1.2) and with $\Delta\chi^2$ compatible with the differences in χ^2 of the same order as the increase of the number of fitted asteroid masses or by the addition of observational bias (see section 2.2), we have obtained a selection of ephemerides compatible with the actual estimations of uncertainties induced either by the dynamical modeling (differences between DE430, EPM2011 and INPOP13c, various numbers of fitted asteroid masses) or the observational accuracy (addition of observational bias). From this selection are deduced the intervals of parameters presented in Table 1 which by construction include uncertainties induced by the differences in dynamical modeling and adjustment procedures (through $\Delta(O - C)_{max}$ and $\Delta\chi^2$ thresholds). An example is the estimation of the acceptable interval of $\dot{\mu}/\mu$ and \dot{G}/G obtained with MC simulations which is twice larger than the one obtained by LS. This increase of the interval is consistent with the important variability of the $\dot{\mu}/\mu$ LS determination due to significant correlations with asteroid masses. More generally, in comparisons to other values found in the literature, the LS uncertainties are compatible with those given by²⁷, LLR¹⁹ and VLBI²¹ estimations. When these comparable values are estimated with one or more GR parameters kept fixed in the fit, but only EPM values are obtained in a global fit as the one done with INPOP. The EPM uncertainties are generally smaller than the LS or MC ones. They are also not balanced as for INPOP LS or MC determinations: EPM determinations show smaller uncertainties for β and greater error bars for γ when LS and MC values face the opposite. LS and EPM uncertainties on $\dot{\mu}/\mu$ are quite compatible. MC interval of $\dot{\mu}/\mu$ is larger than the EPM values but still compatible at 3σ . One can also note the differences in the Sun flattening determinations between EPM and LS, MC estimations, the EPM value being smaller (2.0 ± 0.2) than the MC and LS mean value ($(2.255 \pm 0.146) \times 10^{-7}$). The Lense-Thirring effect, inducing variations in J_2^\odot up to 10%, was not included in the LS and MC estimations, but it is not clear if it was taken into account in the EPM determinations. However the determinations of the Sun flattening by LS or MC without Lense-Thirring effect give values very close to the one obtained with helioseismology. Finally, values of \dot{G}/G obtained by astrophysical technics such as pulsar timing analysis give larger intervals than those obtained in the solar system.

4 Conclusions

In this work we have estimated in using two methods possible violations of general relativity with the PPN parameters β , γ in considering in the same time time variations of the gravitational constant G and values of the sun flattening.

We first made an global adjustment of the GR parameters together with parameters usually considered for the construction of planetary ephemerides such as INPOP. Important variations

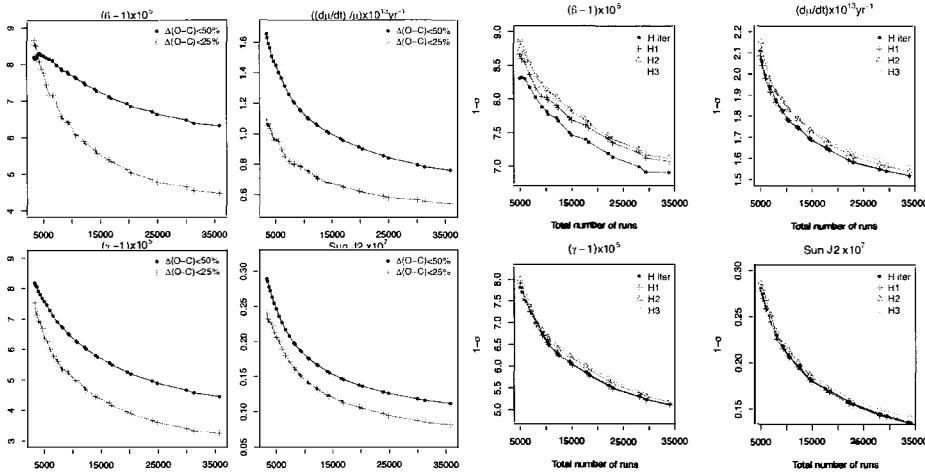


Figure 3 – Evolution with the number of selected runs of the 1- σ of the gaussian distribution of the PPN β , PPN γ , J_2^\odot , and $\dot{\mu}/\mu$ parameters corresponding to the ephemerides selected with the $\Delta(O - C)_{max}$ criteria (left) and χ^2 criteria (right).

(up to the factor 3) in the fitted values but also in the obtained uncertainties were then obtained depending the number of fitted asteroid masses (from 60 to 190) and the observational bias considered in the fit (s/c delay and station calibration bias). However, in considering the most complete modeling, no violation of GR is then statistically detectable at the level of 1×10^{-4} for β and γ , and $2 \times 10^{-13} \text{yr}^{-1}$ for \dot{G}/G and the sun flattening is found to be compatible with other values found in the literature with an uncertainty of about 4×10^{-8} .

Such variability of the least square results leads us to consider another approach based on random selections of GR parameters. We then used Monte Carlo simulations and genetic algorithm procedures for producing more than 35000 planetary ephemerides fitted to observations and compared to INPOP13c. Using a χ^2 selection and postfit residual procedures based on planetary ephemerides uncertainty analysis (see section 1.2), we have identified intervals of parameters inducing the smallest modifications to the planetary dynamics relative to their current uncertainty (estimated for INPOP13c in section 1.2).

We have reduced the uncertainty of the estimation of the sun flattening by a factor 2 (up to 1.2×10^{-8}) in comparison to the previous estimations so far and we have explored a wide range of possible combination of parameters (35000 runs). Considering all the given figures of Table 1 one should conclude that no deviation to general relativity is noticeable for the four GR parameters modified simultaneously at the level of 7×10^{-5} for β , 5×10^{-5} for γ , and $2 \times 10^{-13} \text{yr}^{-1}$ for \dot{G}/G .

New tests will be implemented such as the addition of supplementary terms in the equation of motions of the planets as proposed by alternative theories^{31, 32, 33}. Tests of the equivalence principal can also be proposed for Monte Carlo simulations and genetic algorithm procedures. In the case of the planetary orbits, one would have to consider one ratio of gravitational and inertial masses for each planet which would multiply the number of runs by an important scale.

References

1. A. K. Verma, A. Fienga, J. Laskar, H. Manche, and M. Gastineau, *A&A*, 5 (6)1:A115, 2014.
2. T. Morley. Private communication, 2012.

3. T. Morley. Private communication, 2013.
4. J.-C. Marty. Private communication, 2013.
5. A. Fienga, H. Manche, J. Laskar, M. Gastineau, and A. Verma, <http://www.imcce.fr/inpop>, 2014.
6. W.B. Folkner, J.G. Williams, D.H. Boggs, R.S. Park, P. Kuchynka, http://ipnpr.jpl.nasa.gov/progress_report/42-196/196C.pdf, 2014.
7. Pitjev, N. P., & Pitjeva, E. V., *Astronomy Letters*, 39, 141, 2013.
8. T.D. Moyer. Monography of DEEP SPACE COMMUNICATIONS AND NAVIGATION SERIES 2, JPL, 2000.
9. B. Luzum, N. Capitaine, A. Fienga, W. Folkner, T. Fukushima, J. Hilton, C. Hohenkerk, G. Krasinsky, G. Petit, E. Pitjeva, M. Soffel, and P. Wallace. *Celestial Mechanics and Dynamical Astronomy*, 110:293–304, August 2011.
10. E. V. Pitjeva and N. P. Pitjev. *Solar System Research*, 46:78–87, February 2012.
11. R. F. Pinto, A. S. Brun, L. Jouve, and R. Grappin. *Astrophys. J.*, 737:72, August 2011.
12. A. S. Konopliv, S. W. Asmar, W. M. Folkner, Ö. Karatekin, D. C. Nunes, S. E. Smrekar, C. F. Yoder, and M. T. Zuber. *Icarus*, 211:401–428, January 2011.
13. W. M. Folkner, J. G. Williams, D. H. Boggs, R. S. Park, and P. Kuchynka. *Interplanetary Network Progress Report*, 196:C1, February 2014.
14. E. V. Pitjeva and N. P. Pitjev. *MNRAS*, 432:3431–3437, July 2013.
15. A. Fienga, J. Laskar, H. Manche, P. Kuchynka, G. Desvignes, . Gastineau, M, I. Cognard, and G. Thereau. *Celestial Mechanics and Dynamical Astronomy*, 111:363–+, 2011.
16. A. Fienga, J. Laskar, T. Morley, H. Manche, P. Kuchynka, C. Le Poncin-Lafitte, F. Budnik, M. Gastineau, and L. Somenzi. *AAP*, 507:1675–1686, December 2009.
17. J. G. Williams, S. G. Turyshev, and D. H. Boggs. *International Journal of Modern Physics D*, 18:1129–1175, 2009.
18. J. G. Williams and W. M. Folkner. In *IAU Symposium #261, American Astronomical Society*, volume 261, page 801, May 2009.
19. F. Hofmann, J. Müller, and L. Biskupek. *AAP*, 522:L5, November 2010.
20. B. Bertotti, L. Iess, and P. Tortora, *Nature*, 425:374, 2003.
21. S. B. Lambert and C. Le Poncin-Lafitte. *AAP*, 499:331–335, May 2009.
22. Y.-C. Li, F.-Q. Wu, and X. Chen. *Phys. Rev. D*, 88(8):084053, October 2013.
23. C. Bambi, M. Giannotti, and F. L. Villante. *Phys. Rev. D*, 71:123524, 2005.
24. V. M. Kaspi, J. H. Taylor, and M. F. Ryba. *Astrophys. J.*, 428:713, 1994.
25. J. Armstrong and J. R. Kuhn. *Astrophys. J.*, 525:533–538, November 1999.
26. R. Mecheri, T. Abdelatif, A. Irbah, J. Provost, and G. Berthomieu. *Solphys*, 222:191–197, August 2004.
27. A. S. Konopliv, S. W. Asmar, W. M. Folkner, Ö. Karatekin, D. C. Nunes, S. E. Smrekar, C. F. Yoder, and M. T. Zuber. *Icarus*, 211:401–428, January 2011.
28. N. Ashby, P. L. Bender, and J. M. Wahr. *Phys. Rev. D*, 75(2):022001, January 2007.
29. L. Iorio, H. I. M. Lichtenegger, M. L. Ruggiero, and C. Corda. *APSS*, 331:351–395, February 2011.
30. V. Magnin. PhD in electronics, University Lille 1, 1998.
31. L. Blanchet and J. Novak. *MNRAS*, 412:2530–2542, April 2011.
32. A. Hees, W. M. Folkner, R. A. Jacobson, and R. S. Park. *Phys. Rev. D*, 89(10):102002, May 2014.
33. M.-T. Jaekel and S. Reynaud. *Mass, Inertia, and Gravitation*, pages 491–530. 2011.

AN AUTONOMOUS RELATIVISTIC POSITIONING SYSTEM

UROŠ KOSTIČ, MARTIN HORVAT, JAN BOHINEC, ANDREJA GOMBOC

University of Ljubljana

Faculty of Mathematics and Physics

Jadranska 19, 1000 Ljubljana, Slovenia

Email: uros.kostic@fmf.uni-lj.si

Current GNSS systems rely on reference frames fixed to the Earth (via the ground stations) so their precision and stability in time are limited by our knowledge of the Earth dynamics. To avoid these drawbacks, the constellation of satellites should have the possibility of constituting by itself a primary and autonomous positioning system, without any a priori realization of a terrestrial reference frame. We constructed such a system, an Autonomous Basis of Coordinates, via emission coordinates. Here we present the idea of the Autonomous Basis of Coordinates and its implementation in the perturbed space-time of Earth, where the motion of satellites, light propagation, and gravitational perturbations are treated in the formalism of general relativity.

1 Introduction

The classical concept of a positioning system for a Global navigation satellite system (GNSS) would work ideally if all satellites and a receiver were at rest in an inertial reference frame. But at the level of precision provided by a GNSS, one has to take into account curvature and relativistic inertial effects of spacetime, which are far from being negligible. These effects are most consistently and elegantly dealt with in a relativistic positioning system based on emission coordinates^{1,2,3,4,5}. They depend on the set of four satellites and their dynamics, and can be linked to a terrestrial reference frame. Consequently, the difficulty no longer lies in the conception of the primary reference frame but in its link with terrestrial reference frames⁴. This allows to control much more precisely all the perturbations that limit the accuracy and the stability of the primary reference frame, if the dynamics of the GNSS satellites, described by their orbital parameters, is known sufficiently well.

Our previous work shows that it is possible to construct such a system and do the positioning within it: the orbital parameters of the GNSS satellites can be determined and checked internally by the GNSS system itself through inter-satellite links⁶. In this way, we can construct a reference system called Autonomous Basis of Coordinates (ABC), which is independent of any Earth based coordinate system. Its reference frame consists of the GNSS satellites. The system is self-assembled from continuous exchange of proper times between the satellites, which enables us to determine the parameters of the ABC system with great accuracy.

Here we present the results of our recent work, where we have further developed relativistic positioning and the ABC by including all relevant gravitational perturbations, such as the Earth multipoles (up to the 6th), the Earth solid and ocean tides, the Sun, the Moon, Jupiter, Venus, and the Kerr effect. Furthermore, we show that in addition to precise positioning, ABC also offers a possibility to measure the space-time with unprecedented accuracy.

2 Relativistic Positioning System

To model a relativistic positioning system, we simulate a constellation of four satellites moving along their time-like geodesics in perturbed Shwarzschild space-time, where the initial orbital parameters $(Q^\mu(0), P_\mu(0))$ of the geodesics are known^{4,5,7,8}.

At every time-step of the simulation, each satellite emits a signal and a user on Earth receives signals from all satellites – the signals are the proper times of satellites at their emission events and constitute the emission coordinates of the user. The emission coordinates determine the user’s “position” in this particular relativistic reference frame defined by the four satellites and allow him to calculate his position and time in the more customary Schwarzschild coordinates. In order to simulate the positioning system, two main algorithms have to be implemented: (1) determination of the emission coordinates, and (2) calculation of the Schwarzschild coordinates.

Determination of the emission coordinates The satellites’ trajectories are parametrized by their true anomaly λ . The event $\mathcal{P}_o = (t_o, x_o, y_o, z_o)$ marks user’s Schwarzschild coordinates at the moment of reception of the signals from four satellites. These were emitted at events $\mathcal{P}_i = (t_i, x_i, y_i, z_i)$ corresponding to λ_i with index $i = 1, \dots, 4$ labeling satellites. The emission coordinates of the user at \mathcal{P}_o are, therefore, the proper times $\tau_i(\lambda_i)$ of the satellites at \mathcal{P}_i . Taking into account that the events \mathcal{P}_o and \mathcal{P}_i are connected with a light-like geodesic^a we calculate λ_i at the emission point \mathcal{P}_i using the equation

$$t_o - t_i(\lambda_i | Q^\mu(\tau_i), P_\mu(\tau_i)) = T_{\vec{r}_i}(\vec{R}_i(\lambda_i | Q^\mu(\tau_i), P_\mu(\tau_i)), \vec{R}_o), \quad (1)$$

where $\vec{R}_i = (x_i, y_i, z_i)$ and $\vec{R}_o = (x_o, y_o, z_o)$ are the spatial vectors of the satellites and the user, respectively. The function $T_{\vec{r}_i}$ represents the time-of-flight of photons between \mathcal{P}_o and \mathcal{P}_i as shown in⁹ and⁴. The equation (1) is actually a system of four equations for four unknown λ_i – once the values of λ_i are determined, it is straightforward to calculate τ_i for each satellite and thus obtain user’s emission coordinates at $\mathcal{P}_o = (\tau_1, \tau_2, \tau_3, \tau_4)$.

Calculation of the Schwarzschild coordinates Here we solve the inverse problem of calculating Schwarzschild coordinates of the event \mathcal{P}_o from proper times $(\tau_1, \tau_2, \tau_3, \tau_4)$ sent by the four satellites. We do this in the following way: For each satellite, we numerically solve the equation

$$\tau(\lambda_i | Q^\mu(\tau_i), P_\mu(\tau_i)) = \tau_i, \quad (2)$$

to obtain λ_i , where $\tau(\lambda | Q^\mu(\tau), P_\mu(\tau))$ is a known function for proper time on time-like geodesics⁷. The Schwarzschild coordinates of the satellites are then calculated from λ_i using the solutions of the orbit equation. With the satellites’ coordinates known, we can take the geometrical approach presented in⁴ to calculate the Schwarzschild coordinates of the user. The final step in this method requires us again to solve (1), however, this time it is treated as a system of 4 equations for 4 unknown user coordinates, i.e., solving it, gives (t_o, x_o, y_o, z_o) .

The accuracy of this algorithm has been tested for satellites with the following initial orbital parameters: for all satellites $\Omega = 0^\circ$, $a = 30000$ km, $\varepsilon = 0.007$, $t_a = 0$, for satellites 1 and 2 the inclination is $\iota = 45^\circ$, while for satellites 3 and 4 it is $\iota = 135^\circ$. The arguments of the apoapsis are $\omega_1 = 270$, $\omega_2 = 315$, $\omega_3 = 275$, $\omega_4 = 320$ for satellites 1, 2, 3, and 4, respectively. The user’s coordinates $r_o = 6371$ km, $\theta_o = 43.97^\circ$, $\phi_o = 14.5^\circ$ remain constant during the simulation. Our algorithms show, that the relative errors, defined as

$$\epsilon_t = \frac{t_o - t_o^e}{t_o}, \quad \epsilon_j = \frac{(\vec{R}_o - \vec{R}_o^e)_j}{(\vec{R}_o)_j} \quad \text{for } j = x, y, z, \quad (3)$$

^aThe light-like geodesics are calculated in Schwarzschild space-time without perturbations, because the effects of perturbations on light propagation are negligible.

are of the order $10^{-32} - 10^{-30}$ for coordinate t , and $10^{-28} - 10^{-26}$ for x , y , and z ; here t_o^e and \vec{R}_o^e are user time and coordinates as calculated from the emission coordinates. Using a laptop^b for calculations, the user's position (with such errors) was determined in 0.04 s, where we assumed that (1) in real applications of the positioning the true values of orbital parameters would be transmitted to the user together with the emission coordinates, so to account for this in our simulations, we calculated the evolution of parameters from their initial values before starting the positioning, and (2) the position of the user is completely unknown, i.e., we do not start from the last known position. If we did, the times for calculating the position would be even shorter.

3 Autonomous Basis of Coordinates

To construct an autonomous coordinate system, we apply the idea of the Autonomous Basis of Coordinates (ABC) presented in⁶ to a perturbed satellite system⁸, i.e., we simulate the motion of a pair of satellites along their perturbed orbits.

At each time-step of the simulation, both satellites exchange emission coordinates as shown in Fig. 1 left, where, for clarity, only communication from satellite 1 to satellite 2 is plotted. These events of emission at proper time τ of the first satellite and reception at $\bar{\tau}$ of the second

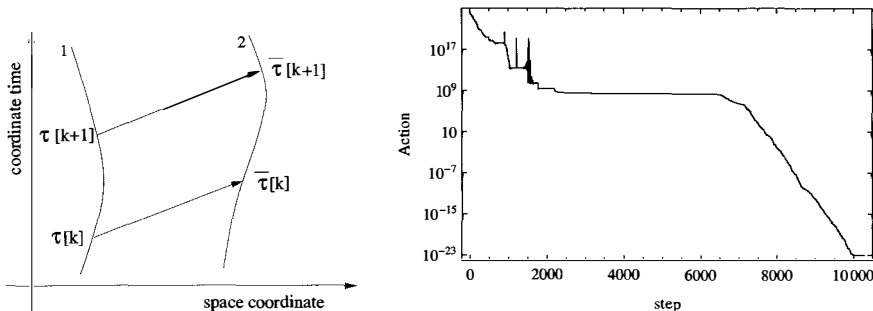


Figure 1 – Left: A pair of satellites exchanging their proper times. At every time-step k , the satellite 1 sends the proper time of emission $\tau[k]$ to the satellite 2, which receives it at the time of reception $\bar{\tau}[k]$. The emission and reception event pairs are connected with a light-like geodesic. Right: The action $S(Q^\mu(0), P_\mu(0))$ during the minimization process. The first stage takes 1765 steps and the second one takes 8513 steps.

satellite are connected with a light-like geodesic, i.e., the difference between the coordinate times of emission $t_1(\tau)$ and reception $t_2(\bar{\tau})$ must be equal to the time of flight of a photon between the two satellites (cf. (1))

$$T_{\bar{t}} = t_2(\bar{\tau}) - t_1(\tau) , \quad (4)$$

where $T_{\bar{t}}$ depends on the positions of both satellites.

When constructing the relativistic positioning system, it is reasonable to assume that the initial orbital parameters $(Q^\mu(0), P_\mu(0))$ are not known very precisely. To improve their values, we sum the differences between the right-hand side and the left-hand side of (4) for all communication events into an action

$$S(Q^\mu(0), P_\mu(0)) = \sum_k \left(t_{2,k} - t_{1,k} - T_{\bar{t}}(\vec{R}_{1,k}, \vec{R}_{2,k}) \right)^2 \quad (5)$$

^bConfiguration: Intel[®] Core[™] i7-3610QM CPU @ 2.30GHz, 8GB RAM.

expressed via auxiliary symbols

$$\begin{aligned} t_{1,k} &= t_1(\tau[k]|Q^\mu(\tau[k]), P_\mu(\tau[k])), \\ t_{2,k} &= t_2(\bar{\tau}[k]|Q^\mu(\bar{\tau}[k]), P_\mu(\bar{\tau}[k])), \\ \bar{R}_{1,k} &= \bar{R}_1(\tau[k]|Q^\mu(\tau[k]), P_\mu(\tau[k])), \\ \bar{R}_{2,k} &= \bar{R}_2(\bar{\tau}[k]|Q^\mu(\bar{\tau}[k]), P_\mu(\bar{\tau}[k])), \end{aligned}$$

The action S has a minimum value (close to zero) for the true initial values of orbital parameters, i.e., the 2×6 orbital parameters^c. The search for the correct initial orbital parameters becomes a minimization problem in 12 dimensions. Because the orbital parameters depend on time, their time evolution has to be recalculated at every step of the minimization, which makes the minimization process very slow.

The minimization was done in two stages. In the first stage, we use the PRAXIS minimization method¹⁰ implemented in the NLOPT library¹¹ to determine the parameters within double precision. The resulting values are then used as initial values for the second stage, where we use the simplex method to “polish” the parameters within 128-bit precision.^d In Fig. 1 right, we plot the values of the action during the minimization process; the first stage takes 1765 steps, while the second one takes 8513 steps.

The number of time-steps along the orbits was large enough ($k = 1 \dots 433$) to cover approximately two orbital times. The initial values of the orbital parameters used as starting point in the minimization differ from the true values by an amount which induces the error of $\sim 2-3$ km in the satellites’ positions. At the beginning of the minimization, the value of the action is $S \approx 10^{24}(r_g/c)^2$, at the end of the first stage it is $2 \times 10^{10}(r_g/c)^2$, and at the end of the second stage it drops to $8 \times 10^{-24}(r_g/c)^{2e}$. The relative errors of the orbital parameters ($Q^\mu(0), P_\mu(0)$) after the minimization are of the order of 10^{-22} .

By repeating the minimization procedure for all possible pairs of satellites, we can reconstruct the orbital parameters of every satellite in the system. This method thus gives the possibility to obtain an autonomous coordinate system without tracking the satellites from Earth.

3.1 Degeneracies

We investigate possible degeneracies in the solutions for orbital parameters by scanning the values of action S around its true minimum: we take two satellites on orbits with known initial orbital parameters and calculate the action by varying two of them (one for the first satellite and one for the second) around their true values. In case of no degeneracy between these two orbital parameters, we expect to find one well defined minimum of S . In case of a degeneracy, we expect to get more than one point in which S reaches minimum, i.e., S has a minimum for different values of these two orbital parameters, therefore the solutions are degenerate.

First, we considered unperturbed Schwarzschild metric, which is spherically symmetric. True orbital parameters of both satellites were:

- satellite 1: $\Omega_1 = 20^\circ, \omega_1 = 120^\circ, \iota_1 = 40^\circ, a_1 = 30025$ km, $\varepsilon = 0.008, t_{a,1} = 7.04$ h, $\tau_{a,1} = 0$,
- satellite 2: $\Omega_2 = 20^\circ, \omega_2 = 120^\circ, \iota_2 = 80^\circ, a_2 = 30025$ km, $\varepsilon_2 = 0.008, t_{a,2} = 7.04$ h, $\tau_{a,2} = 0$.

The action S was calculated for one orbit.

We find that the action S in the planes (ι_1, ι_2) , (Ω_1, Ω_2) and $(t_{a,1}, t_{a,2})$ depends only on the difference between the parameters $\iota_1 - \iota_2$, $\Omega_1 - \Omega_2$, and $t_{a,1} - t_{a,2}$, respectively. In the scanning region

^c $(Q^\mu(0), P_\mu(0))$ for both satellites, excluding (Q^0, P_0) , since these can be calculated from the constraint $H = -\frac{1}{2}$.

^dThe quadruple-precision is required because cancellation effects become significant in case of quasi-circular orbits.

^eThe gravitational radius r_g is defined as $r_g = GM/c^2 \approx 4.4$ mm, where M is the Earth mass.

in the vicinity of their true values, the action S has a shape of a "valley" (see Fig. 2), which is understandable considering the spherical symmetry of the Schwarzschild metric. Changing ι and Ω of both satellites' orbital planes by the same amount, i.e. keeping the same orientation of one satellite with respect to the other, means moving along one of the Hessian matrix eigenvector direction (see Fig. 2) and does not make a difference in the action S . The same applies also if t_a of both satellites are changed by the same amount.

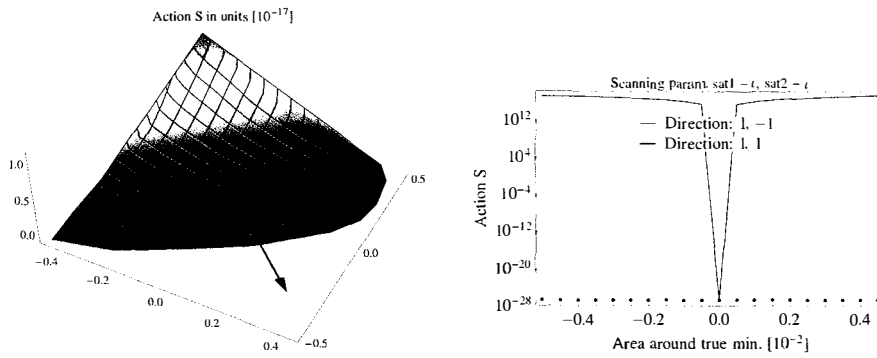


Figure 2 – Left: 2D scan of action S for t_1 - t_2 pairs in case of unperturbed Schwarzschild metric. Blue arrows show the direction of eigenvectors of the Hessian matrix. Right: Section of action S along the eigenvector directions for t_1 - t_2 pairs. It is evident that there is a degeneracy along the direction marked '1,1'. ' ± 0.5 ' on horizontal axes corresponds to ± 0.01 rad.

Next, we repeated our analysis for perturbed metric. In Fig. 3 we show the results where only the Earth multipoles, Earth tides and ocean tides were included as perturbations. Since the metric is no longer spherically symmetric, the degeneracies disappear.

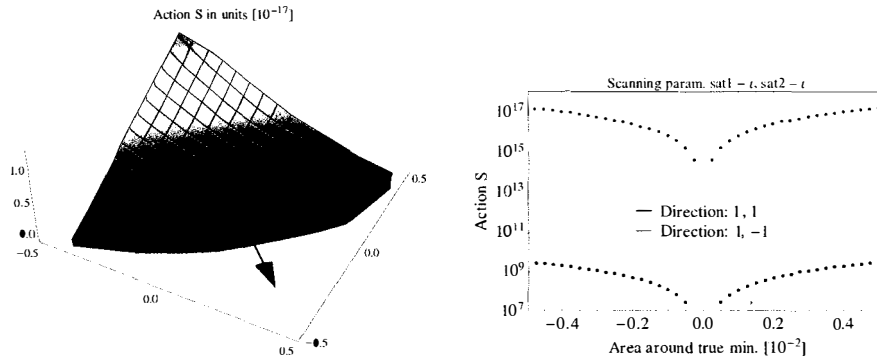


Figure 3 – Left: 2D scan of action S for t_1 - t_2 pairs in case of metric perturbed by Earth multipoles, Earth tides and ocean tides. Blue arrows show the direction of eigenvectors of the Hessian matrix. Right: Section of action S along the eigenvector directions for t_1 - t_2 pairs. It is evident that there is no degeneracy. ' ± 0.5 ' on horizontal axes corresponds to ± 0.01 rad.

To sum up, when determining the orbital parameters which preserve the relative orientation of the two satellites, the solutions are degenerate in case of spherically symmetric Earth. As soon as perturbations are present (Earth multipoles etc.), the spherical symmetry is broken, therefore the degeneracies disappear.

Table 1: Influence of gravitational parameter variation on the action S and satellite's position. Columns are: gravitational parameter, its relative change, corresponding value of action S and change in satellite's position ΔL , order of magnitude of the knee value.

| parameter P | $\frac{\Delta P}{P}$ | $S [(\frac{r_E}{c})^2]$ | ΔL [m] | $(\frac{\Delta P}{P})_{\text{knee}}$ |
|-------------------|----------------------|-------------------------|--------------------|--------------------------------------|
| Ω_{δ} | $1.4 \cdot 10^{-8}$ | $1.1 \cdot 10^{-6}$ | 0.00048 | 10^{-21} |
| $M_{2,0}$ | $7 \cdot 10^{-8}$ | 1.5 | 0.1 | $7 \cdot 10^{-23}$ |
| Re $M_{2,1}$ | $5 \cdot 10^{-21}$ | $1 \cdot 10^{-31}$ | $8 \cdot 10^{-24}$ | $> 5 \cdot 10^{-18}$ |
| Im $M_{2,1}$ | $8 \cdot 10^{-22}$ | $1 \cdot 10^{-31}$ | $4 \cdot 10^{-21}$ | $> 8 \cdot 10^{-19}$ |
| Re $M_{2,2}$ | 0.00002 | 10 | 0.38 | $2 \cdot 10^{-20}$ |
| Im $M_{2,2}$ | 0.00004 | 12 | 0.002 | $4 \cdot 10^{-20}$ |

3.2 Mapping the Space-time

When the satellites exchange communication, they actually scan the space-time around Earth, as sketched in Fig. 4. Such a mapping can be used to measure the properties of the sources responsible for the space-time curvature.

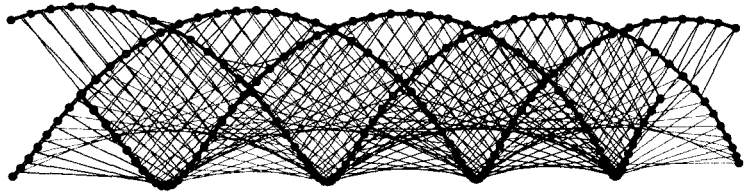


Figure 4 – Mapping the space-time with three satellites.

To check whether an RPS could be used to determine the values of gravitational parameters, e.g. Earth multipoles, we simulate a constellation of satellites with inter-satellite links and assume that in addition to initial values of orbital parameters, also gravitational perturbation coefficients are known only with limited accuracy. We find that the action (5) has a well defined minimum also in this case. We vary 2×6 orbital parameters + 14 gravitational parameters and investigate to which level of accuracy it would be possible to refine values of gravitational parameters by this method. For this purpose, we calculate the action S as a function of a relative offset of the gravitational parameter from its true value. In Fig. 5 we show the results for the Earth's angular velocity: the action stays more or less constant to some relative offset, and after it, it starts increasing. The position of this “knee” determines, how accurately it is possible to determine a given gravitational parameter with this method, namely, for offsets below the knee value, this method is not sensitive.^f The results for other gravitational parameters are in Table 1.

In addition, we checked the effects of clock noise on determination of gravitational parameters. It turns out that the clock noise increases the minimum value of action S and moves the “knee” towards higher values (see Fig. 5). This means that even in presence of clock noise, the ABC system is stable and can be used to measure the space-time, although with reduced accuracy.

Although in our work we focused on gravitational perturbations, we also modelled the effects of Solar radiation pressure. The results show that, regardless of its non-gravitational nature, the solar radiation pressure contribution can be divided into an oscillating and a secular term,

^fWe note that these numbers represent the accuracy of the numerical methods used. In a real system, the accuracy would be much lower due to numerous effects, e.g. non-gravitational perturbations, atmospheric effects, clock errors...

similarly as gravitational perturbations¹². Furthermore, the action has a well defined minimum for the true values of the radiation pressure model parameters. We expect that the same would hold also for the perturbations due to Solar wind. The collisions with micrometeorites are stochastic in nature, and as such they contribute to the overall noise⁴, therefore, their effect on the action would be similar as of the clock noise – the orbital parameters and the properties of the space-time could still be determined, only the accuracy would be lower.

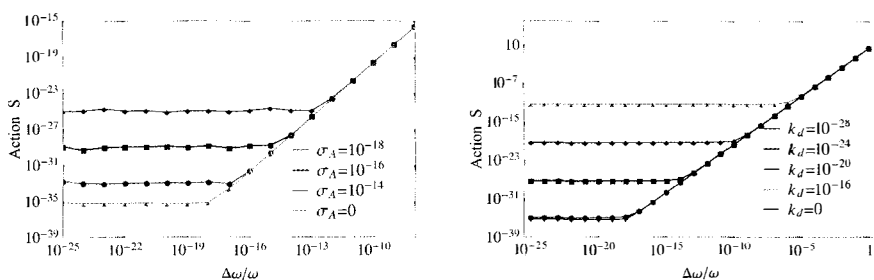


Figure 5 – Action (5) as a function of relative error in Earth angular frequency. The clock random noise is included; different plots correspond to different values of Allan deviation (left) and frequency drift (right).

4 Conclusions

In this contribution we have shown how to construct an Autonomous Basis of Coordinates (ABC) for relativistic GNSS in a perturbed Schwarzschild space-time.

The ABC concept establishes a local inertial frame, which is based solely on dynamics of GNSS satellites and is thus completely independent of a terrestrial reference. General relativity was used to calculate the dynamics of the GNSS satellites and the gravitational perturbations affecting the dynamics (Earth multipoles, Earth solid and ocean tides, the Sun, the Moon, Jupiter, Venus, and the Kerr effect), as well as the inter-satellite communication, which actually makes possible for construction of the whole system. The numerical codes for positioning determine all four coordinates in 40 ms with 25-30 digit accuracy, showing that general relativistic treatment presents no technical obstacles for current GPS devices.

Because the system does not rely on Earth based reference frames and is constructed only through proper time exchange between satellites, it offers unprecedented accuracy and stability. In fact, present technology, planned to be used in the Galileo system, should be able to routinely reach millimetre accuracy with respect to an absolute local inertial frame defined independently of Earth based coordinates. At this level of accuracy it seems necessary to decouple the local inertial frame from the geodetic Earth frame, and allow the comparison of the two, to tell us fine details about Earth rotation, gravitational potential and dynamics of Earth crust. ABC can measure such details despite noise. Last but not least, tracking of satellites with ground stations is necessary only to link the relativistic positioning system to a terrestrial frame, although this link can also be obtained by placing several receivers at the known terrestrial positions.

Acknowledgments

The authors acknowledge financial support from ESA PECS project *Relativistic Global Navigation System*.

References

1. Bartolomé Coll and Juan Antonio Morales. Symmetric frames on Lorentzian spaces. *Journal of Mathematical Physics*, 32(9):2450, 1991.
2. C. Rovelli. GPS observables in general relativity. *Phys. Rev. D*, 65(4):044017–+, February 2002.
3. M. Blagojević, J. Garecki, F. W. Hehl, and Y. N. Obukhov. Real null coframes in general relativity and GPS type coordinates. *Phys. Rev. D*, 65(4):044018–+, February 2002.
4. Andrej Čadež, Uroš Kostić, and Pacôme Delva. Mapping the spacetime metric with a global navigation satellite system, european space agency, the advanced concepts team, ariadna final report (09/1301). Technical report, European Space Agency, 2010.
5. Pacôme Delva, Uroš Kostić, and Andrej Čadež. Numerical modeling of a Global Navigation Satellite System in a general relativistic framework. *Advances in Space Research*, 47:370–379, January 2011.
6. Andrej Čadež, Uroš Kostić, and Pacôme Delva. Mapping the spacetime metric with a global navigation satellite system-extension study: Recovery of orbital constants using intersatellite links, european space agency, the advanced concepts team, ariadna final report (09/1301 ccn). Technical report, European Space Agency, 2011.
7. U. Kostić. Analytical time-like geodesics in Schwarzschild space-time. *General Relativity and Gravitation*, 44:1057–1072, April 2012.
8. A. Gomboc, M. Horvat, and U. Kostić. Relativistic gnss – final report (pecs contract no. 4000103741/11/nl/kml). Technical report, European Space Agency, 2014.
9. A. Čadež and U. Kostić. Optics in the Schwarzschild spacetime. *Phys. Rev. D*, 72(10):104024–+, November 2005.
10. R.P. Brent. *Algorithms for Minimization Without Derivatives*. Dover Books on Mathematics. Dover Publications, 1973.
11. S.G. Johnson. *The NLOpt nonlinear-optimization package*, 2013. <http://ab-initio.mit.edu/nlopt>.
12. J Bohinec. Degeneration of solutions for gravitational parameters of a relativistic positioning system. Master’s thesis, University of Ljubljana, Faculty of Mathematics and Physics, 2015.

TEST OF THE GRAVITATIONAL REDSHIFT USING GALILEO SATELLITES 5 AND 6

P. DELVA¹, A. HEES², S. BERTONE³, E. RICHARD¹ AND P. WOLF¹

¹ *SYRTE, Observatoire de Paris, PSL Research University, CNRS, Sorbonne Universités, UPMC Univ. Paris 06, LNE, 61 avenue de l'Observatoire, 75014 Paris, France*

² *Department of Mathematics, Rhodes University, 6140 Grahamstown, South Africa*

³ *Astronomical Institute, University of Bern, Sidlerstrasse 5 CH-3012 Bern, Switzerland*

In this paper we propose to use satellites Galileo 5 and 6 to perform a test of the gravitational redshift. The best test to date was performed with the Gravity Probe A experiment (1976) with an accuracy of 1.4×10^{-4} . Here we show that considering a realistic clock noise and thanks to a highly eccentric orbit, it is possible to improve the GP-A limit with an accuracy around 3×10^{-5} after one year of integration of Galileo 5 and 6 data.

1 Introduction

The classical theory of General Relativity (GR) is the current paradigm to describe the gravitational interaction. Since its creation in 1915, GR has been confirmed by experimental observations. Although very successful so far, it is nowadays commonly admitted that GR is not the ultimate theory of gravitation. First of all, GR is a classical theory in the sense that it does not include quantum effects. A quantum theory of gravitation is required to understand processes happening in very strong gravitational fields like in the very early universe or around black holes. Moreover, most physicists believe that GR and the Standard Model of particle physics are only approximations of a more fundamental unified theory. Several attempts to develop such a theory have been proposed so far like e.g. string theory or loop quantum gravity. Most of these theories produce some violations with respect to GR and/or to the Standard Model of particle physics. It is therefore crucial to search for such violations and to constrain them.

GR is built upon two fundamental principles. The first principle is the Einstein Equivalence Principle (EEP) which gives to gravitation a geometric nature. More precisely, the EEP implies that gravitation can be identified to space-time curvature which is mathematically described by a space-time metric $g_{\mu\nu}$. If the EEP postulates the existence of a metric, the second principle of GR specifies the form of this metric. In GR, the metric tensor is determined by solving the Einstein field equations which can be derived from the Einstein-Hilbert action.

From a phenomenological point of view, three aspects of the EEP can be tested¹: (i) the Universality of Free Fall (UFF), (ii) the Local Lorentz Invariance (LLI) and (iii) the Local Position Invariance (LPI). The UFF stipulates that the motion of a test body is independent of its composition. It has been tested experimentally at the very impressive level of 10^{-13} with torsion balances (see e.g. ^{2,3}) and with Lunar Laser Ranging measurements^{4,5}. The LLI stipulates that the outcome of any local non-gravitational experiment is independent of the velocity of the freely-falling reference frame in which it is performed¹. One way to test the LLI is to search for anisotropies in the speed of electromagnetic interactions usually parametrized with the c^2 -formalism¹. Amongst all the measurements performed to test the LLI (for a review,

see⁶), it is interesting to mention that GPS data have provided a good test of the LLI⁷. Let us also mention that a wide framework called “Standard Model Extension” (SME) has been developed to parametrize systematically possible violations of the Lorentz symmetry (see for example^{8,9}). The last part of the EEP, the LPI stipulates that the outcome of any local non-gravitational experiment is independent of where and when in the universe it is performed¹. This part of the EEP is tested by searching for space-time variations of the constants of Nature (see e.g.^{10,11,12,13}) or by redshift tests^{14,15,16}.

In addition to the EEP tests, the second principle of GR (the form of the metric) is thoroughly tested by different observations in the Solar System: deflection of light¹⁷, planetary ephemerides^{18,19}, radioscience tracking data of spacecraft^{20,21,22}, etc (for a larger review, see^{1,6}).

As mentioned above, a gravitational redshift experiment tests the LPI¹. Historically, the first gravitational redshift test was performed by Pound-Rebka-Snider^{23,24}: they measured the frequency shift of gamma-ray photons from ⁵⁷Fe in the Earth potential. The accuracy of this test was around 10^{-1} . The most precise test of the gravitational redshift to date has been realized with the Vessot-Levine rocket experiment in 1976, also named the Gravity Probe A (GP-A) experiment^{14,15,16}. The frequency differences between a spaceborne hydrogen maser clock and ground hydrogen masers were measured thanks to a continuous two-way microwave link. The duration of the experiment was limited to one parabola of the rocket trajectory. The gravitational redshift was verified to 1.4×10^{-4} accuracy¹⁶. The future Atomic Clock Ensemble in Space (ACES) experiment, an ESA/CNES mission, planned to fly on the ISS in 2017, will test the gravitational redshift to around $2 - 3 \times 10^{-6}$ accuracy²⁵. Furthermore, other projects like STE-QUEST²⁶ propose to test the gravitational redshift at the level of 10^{-7} .

In this paper, we will show how clocks onboard GNSS satellites can be used to perform an improved test of the gravitational redshift if they are placed on an elliptical orbit around Earth. As an application, we will consider the case of the satellites Galileo 5 and 6. These satellites were launched on August, 30th 2014. Because of a technical problem, the launcher brought them on a wrong, elliptic orbit. In GNSS data processing, the well-known frequency shift between the satellite clock and a ground clock is a combination of the gravitational redshift and of the second order Doppler effect, both predicted within the framework of general relativity. For a Keplerian orbit, this frequency shift can be separated as a constant shift which depends on the semi-major axis of the satellite orbit, and a periodic term that depends on its eccentricity (sometimes called the eccentricity correction)²⁷. The measurement of the constant shift requires an accurate clock. This can be done with standard GNSS satellites only to around 1% relative accuracy⁶, as their clocks have poor accuracy.

However, GNSS clocks (and Galileo in particular) have a good stability, so that it is possible to test the periodic part of the gravitational redshift (whose amplitude grows with the satellite eccentricity) to a very good level. The Galileo 5 and 6 satellites, with their large eccentricity, are hence perfect candidates to perform this test. Contrary to the GP-A experiment, it is possible to integrate the signal on a long duration, therefore improving the statistics. In this paper, we assess the sensitivity of the gravitational redshift test that can be performed with Galileo satellites 5 and 6. To do so, we use a Monte Carlo approach, where we simulate typical noise of clock solutions for in flight GPS and Galileo clocks. We then use the simulated solutions to fit a phenomenological model for a violation of the general relativistic gravitational redshift, and use the statistics of the outcomes to determine the limits we expect to obtain on such a violation from Galileo 5 and 6.

In section 2, we describe the experimental data needed in order to perform the test with Galileo satellites. Then, we introduce in section 3 the simulation of the satellites orbits, clocks and signal. Finally, in section 4 we estimate the test sensitivity with two different statistical methods to estimate the averaging of random noise in the signal. We very briefly mention systematic effects in section 5, but we leave a detailed discussion of those to an upcoming publication.

2 Experimental data

The experiment proposed here requires an accurate knowledge of the frequency of the satellite clock as it orbits the Earth. These data are made available by several analysis centers (ACs) in the framework of the International GNSS service (IGS)²⁸. Currently, ten ACs produce the IGS products, which are: precise ephemerides and clocks of all active GPS and GLONASS satellites; Earth rotation parameters (ERPs), as polar motion and length of day; IGS tracking station coordinates, velocities, and clock corrections; global ionosphere maps (GIMs); and finally IGS tracking station troposphere zenith path delays.

Even if initially intended for the processing of GPS and (some years later) GLONASS data, the IGS has recently adapted to the introduction of several new GNSS (Galileo, Beidou) and regional services (eg. QZSS for Japan). As a result, the IGS launched the Multi-GNSS-EXperiment (MGEX,²⁹), which applies the standard IGS processing chain to the new systems. All active Galileo satellites orbits, clock corrections, and inter-system biases are then currently available for public use through the MGEX product directory at the IGS data center CDDIS, which is updated on a regular basis.

Since each AC is following a different strategy, as an example we shall focus on the processing performed at the CODE (Center for Orbit Determination in Europe) analysis center³⁰ and in the framework of the MGEX. In this particular case, the whole solution is based on a two steps process. First, orbits are determined using a double difference network solution. This technique allows to eliminate or reduce several biases by combining observations among a pair of receivers and a pair of satellites. All clock errors are eliminated in the combination while the remaining parameters (including ephemerides, atmospheric and antenna parameters, etc...) are estimated for all stations and satellites involved. The latter are then used as a framework for the clock solution, which is based on a zero-difference processing. For more general information about the IGS and its products and data centers, the reader can refer to²⁸.

We propose to use the MGEX products detailed above in order to perform a test of the gravitational redshift. The orbit solution of Galileo 5 and 6 satellites would be used to calculate the behaviour of the onboard clocks and the gravitational redshift as predicted by GR⁶. The latter would then be compared to the clock solution from the IGS processing to recover any violation of the LPI, as detailed in section 4.

Several conditions need to be satisfied by the data to assure the success of the experiment. The availability of continuous orbit and clock parameters is paramount and is assured by the IGS guidelines for the clock and orbit products. Orbits and station coordinates need not to be affected by an eventual violation of the gravitational redshift. This is assured as a result of the processing outlined above, since both are derived by a double-difference solution which eliminates all clock parameters. Also, the reference clock has to be unaffected by an eventual LPI violation, which would not be the case if it is a satellite clock. Even if it is in principle possible, reference clocks are in practice always chosen among ground station H-maser clocks since these are more stable and less affected by orbit modeling errors³¹.

3 Simulation: orbits, clocks and signal

Orbital parameters of Galileo satellites 5 and 6 used for this paper are summarized in table 1. Their orbits have been recently circularized, from eccentricity $e = 0.22$ to $e = 0.16$. However, we will consider both the initial and the final orbits, in order to compare the sensitivity of the redshift test to different eccentricities. Orbits are calculated by solving the Kepler equation for a duration of two years. This method gives the best numerical stability of the solution with time compared to other methods.

We use the clock solutions provided by CODE to simulate a realistic random noise for Galileo satellite clocks. Fig. 1 (left) shows the Modified Allan Deviations (MDEVs) for several GPS and Galileo clocks³² around Day Of Year (DOY) 100/2013, as well as the MDEV of the simulated

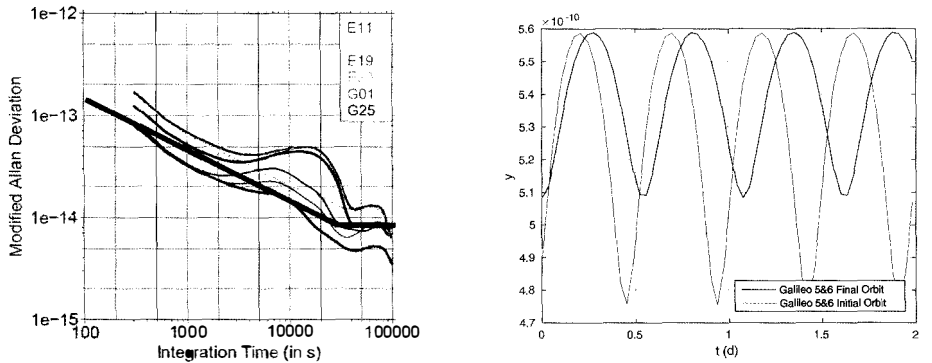


Figure 1 – (left) MDEV for Galileo In-Orbit Validation (IOV) (PRN E11-12-19-20) and for GPS Block II-F (PRN G01-25), figure from³². Superimposed in blue is the MDEV of the simulated clock noise; (right) Gravitational redshift signal with $\alpha = 0$.

clock noise (in blue). For an integration time of 1000 s, the MDEVs are between 3×10^{-14} and 7×10^{-14} , and the MDEV of the simulated clock noise is around 5×10^{-14} . The MDEVs decrease like $\tau^{-1/2}$, which is a characteristic of white frequency noise. There is a bump at about 20000 s, which will be analysed in a subsequent paper focusing on systematic effects. Moreover, we add a flicker noise in the simulated clock noise at 8×10^{-15} in the MDEV (flat part of the blue curve on Fig. 1 (left)).

The ideal signal y is the gravitational part of the frequency difference between a ground clock g and the satellite clock s :

$$y = \frac{GM}{c^2} \left(\frac{1}{r_g} - \frac{1}{r_s} \right), \quad (1)$$

where GM is the standard gravitational parameter of Earth, c is the speed of light in vacuum, and r_g and r_s are respectively the norm of the position vectors of the ground clock and of the onboard clock. We neglect the noise coming from the ground clock, and we are interested only in the variable part of y . Therefore one can remove the first term in (1), which is constant. We use a simple phenomenological model for a possible violation of the gravitational redshift, characterised by a parameter α which is zero in general relativity^{1,6}:

$$\tilde{y}(\alpha) = -(1 + \alpha) \frac{GM}{c^2 r_s}. \quad (2)$$

The GP-A limit corresponds¹⁶ to $\sigma_\alpha < 1.4 \times 10^{-4}$, where σ_α is the estimated uncertainty of the determination of the parameter α .

The simulated signal y is shown in fig. 1 (right). Its amplitude is around twice larger for Galileo satellites 5&6 initial orbits than for Galileo 5&6 final orbits. The asymmetry between the upper part and the bottom part of the curves is a characteristic of the elliptical orbit.

| Name | e | a (km) | i ($^\circ$) |
|---------------------------|--------|----------|------------------|
| Galileo 5&6 Final Orbit | 0.1561 | 27977 | 49.7212 |
| Galileo 5&6 Initial Orbit | 0.2330 | 26192 | 49.7740 |

Table 1: Orbital parameters of satellites Galileo 5 and 6. Their orbits were circularized so that they can be used for positioning. Both orbits are now very similar.

4 Estimation of the statistical sensitivity of the test

We study the sensitivity of the gravitational redshift test performed with Galileo 5 and 6 through two very different methods: the Fast Fourier Transform (FFT) method and the Linear Least-Square (LSQ) method.

The sensitivity of the gravitational redshift test can be calculated as the inverse of the Signal-to-Noise Ratio (SNR) ρ . The SNR can be maximized with matched filtering, i.e. by using a filter optimized for the searched signal and the considered noise. Then the SNR is given by³³:

$$\rho^2 = \int_{-\infty}^{+\infty} \frac{|\mathcal{F}[y](f)|^2}{S_\epsilon(f)} df, \quad (3)$$

where y and ϵ are respectively the gravitational redshift signal and the clock noise, $\mathcal{F}[y]$ is the Fourier transform of y and S_ϵ is the PSD of the clock noise. We implemented a numerical version of this method, with the following steps: first we generate 100 different sequences of clock noise; we calculate the PSD of each sequence using a fast Fourier transform algorithm and average the 100 different PSD; finally we compute the SNR (3) with the mean PSD of the clock noise, by integrating in the frequency domain $[-F_s/2, F_s/2]$, where F_s is the sampling rate of the signal. This is done for several different duration of the experiment.

The second method implemented consists in using a linear least-square (LSQ) fit combined with a Monte-Carlo method, where we find the minimum of the merit function χ^2 with respect to α and A :

$$\chi^2 = \sum_{i=1}^N [(y(t_i) + \epsilon_i) - (\tilde{y}(\alpha; t_i) + A)],^2 \quad (4)$$

where N is the number of simulated observables, A is a constant to be estimated and $(\epsilon_i)_{i=1..N}$ is one sequence of simulated clock noise, while $(y(t_i) + \epsilon_i)$ corresponds to the simulated observable at time t_i . The constant A is introduced to remove a constant frequency bias which cannot be measured accurately. Instead of fitting A , it is also possible to remove the mean of $\tilde{y}(\alpha)$ from the model, so that the fitted model has a zero mean, like the noise ϵ . We implemented a numerical version of this method, with the following steps: we generate 100 different sequences of clock noise (we take the same ones as for the FFT method); we estimate α for each clock noise sequence with the linear LSQ method, for different duration of the experiment; finally, for each duration, we calculate the mean of the 100 obtained values of α and their standard deviation σ_α . The standard deviation corresponds approximately to 68% of the obtained values around the mean.

Using³⁴, it can be shown that for high SNR and in the case of a one parameter determination, the inverse of the SNR found with matched filtering method is equal to the standard deviation of α found with the LSQ method, i.e. $\sigma_\alpha = \rho^{-1}$. We have verified that this is the case, thus giving us strong confidence in our estimation of the test sensitivity. Fig. 2 shows the statistical sensitivity of the gravitational redshift test, σ_α , with respect to the duration of the experiment for the two different methods presented above and for the final and initial orbits of Galileo satellites 5 & 6.

This result is very promising, as it can be seen that even with the less eccentric orbit, the Gravity Probe A limit could be attained in less than a month. However, this result has to be tempered with a study of systematic effects.

5 Systematic effects

The bump in the Allan deviation (see Fig. 1 (left)) is coming from systematic effects entering the orbit modeling, acting on the frequency of the reference ground clock and of the space clocks and on the electromagnetic links³⁵. These systematics may induce a bias in the estimation of α and need to be considered properly in our sensitivity analysis. A preliminary analysis shows that

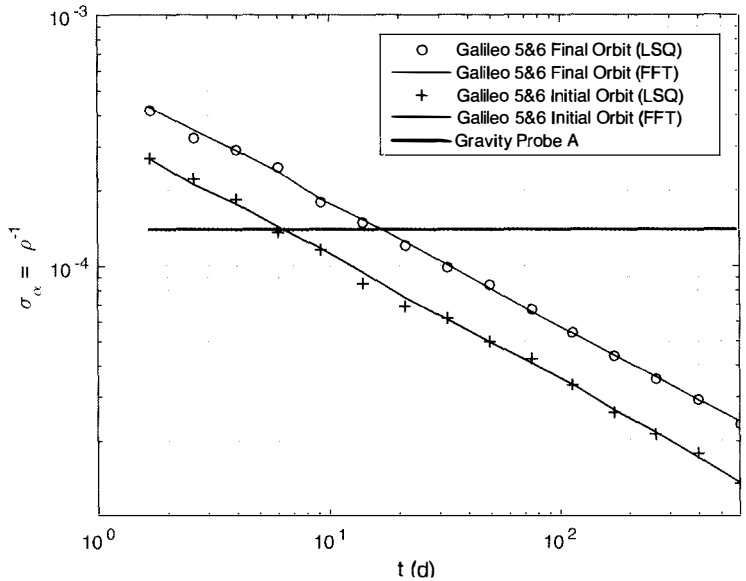


Figure 2 – Statistical sensitivity of the gravitational redshift test with respect to the duration of the experiment. We show the results for the two methods FFT and LSQ, and for the initial and final orbits of Galileo satellites 5&6. In green is the accuracy of the Gravity Probe A experiment for reference.

they will limit the experiment in the low 10^{-5} , provided at least one year of data is available. This minimum duration is required in order to partially decorrelate some of the systematic effects from the signal, the former being mainly around diurnal frequency, the latter around sidereal frequency. The corresponding study is still ongoing and detailed results will be presented in an upcoming publication.

6 Conclusion

We have shown that it is possible to improve on the GP-A (1976) limit on the gravitational redshift test, down to an accuracy of 3×10^{-5} with at least one year of data. These tests are of high scientific relevance, as many alternative theories of gravitation predicts violations of the Einstein Equivalence Principle at some level of accuracy (see for example^{36,37,38,39}).

In this contribution, a detailed analysis of the stochastic noise is presented. However, systematic effects will induce a bias in the estimation of α which can limit the accuracy of the estimation. We have done a preliminary analysis that shows that for systematic effects that depend on the Sun direction (solar radiation pressure, onboard temperature effects, ...), these effects can be decorrelated from the gravitational redshift signal with (at least) one year of data. These results will be presented in a subsequent paper.

Acknowledgments

AH acknowledges support from “Fonds Spécial de Recherche” through a FSR-UCL grant. PD acknowledges support from GPhys/Observatoire de Paris.

References

1. C. M. Will. *Theory and Experiment in Gravitational Physics*. Cambridge University Press, 1993.
2. S. Schlamminger, K.-Y. Choi, T. A. Wagner, J. H. Gundlach, and E. G. Adelberger. Test of the equivalence principle using a rotating torsion balance. *Phys. Rev. Lett.*, 100(4):041101, 2008.
3. E. G. Adelberger, J. H. Gundlach, B. R. Heckel, S. Hoedl, and S. Schlamminger. Torsion balance experiments: A low-energy frontier of particle physics. *Prog. Part. Nucl. Phys.*, 62:102–134, 2009.
4. J. G. Williams, S. G. Turyshev, and D. H. Boggs. Lunar laser ranging tests of the equivalence principle with the earth and moon. *Int. J. Mod. Phys. D*, 18:1129–1175, 2009.
5. J. G. Williams, S. G. Turyshev, and D. Boggs. Lunar laser ranging tests of the equivalence principle. *Class. Quantum Gravity*, 29(18):184004, 2012.
6. C. M. Will. The confrontation between general relativity and experiment. *Living Reviews in Relativity*, 17:4, 2014.
7. P. Wolf and G. Petit. Satellite test of special relativity using the global positioning system. *Phys Rev A*, 56:4405–4409, 1997.
8. D. Colladay and V. A. Kostelecký. CPT violation and the standard model. *Phys Rev D*, 55:6760–6774, 1997.
9. D. Colladay and V. A. Kostelecký. Lorentz-violating extension of the standard model. *Phys Rev D*, 58(11):116002, 1998.
10. T. Rosenband, D. B. Hume, P. O. Schmidt, C. W. Chou, A. Brusch, L. Lorini, W. H. Oskay, R. E. Drullinger, T. M. Fortier, J. E. Stalnaker, S. A. Diddams, W. C. Swann, N. R. Newbury, W. M. Itano, D. J. Wineland, and J. C. Bergquist. Frequency ratio of al^+ and hg^+ single-ion optical clocks; metrology at the 17th decimal place. *Science*, 319:1808–, 2008.
11. J.-P. Uzan. Varying constants, gravitation and cosmology. *Living Rev. Relativ.*, 14(2), 2011.
12. J. Guéna, M. Abgrall, D. Rovera, P. Rosenbusch, M. E. Tobar, P. Laurent, A. Clairon, and S. Bize. Improved tests of local position invariance using rb87 and cs133 fountains. *Phys. Rev. Lett.*, 109(8):080801, 2012.
13. A. Hees, O. Minazzoli, and J. Larena. Breaking of the equivalence principle in the electromagnetic sector and its cosmological signatures. *Phys Rev D*, 90(12):124064, 2014.
14. R. F. C. Vessot and M. W. Levine. A test of the equivalence principle using a space-borne clock. *Gen. Relativ. Gravit.*, 10:181–204, 1979.
15. R. F. C. Vessot, M. W. Levine, E. M. Mattison, E. L. Blomberg, T. E. Hoffman, G. U. Nystrom, B. F. Farrel, R. Decher, P. B. Eby, and C. R. Baugher. Test of relativistic gravitation with a space-borne hydrogen maser. *Phys. Rev. Lett.*, 45:2081–2084, 1980.
16. R. F. C. Vessot. Clocks and spaceborne tests of relativistic gravitation. *Adv. Space Res.*, 9:21–28, 1989.
17. S. B. Lambert and C. Le Poncin-Lafitte. Determining the relativistic parameter gamma using very long baseline interferometry. *A&A*, 499:331–335, 2009.
18. A. K. Verma, A. Fienga, J. Laskar, H. Manche, and M. Gastineau. Use of MESSENGER radioscience data to improve planetary ephemeris and to test general relativity. *A&A*, 561:A115, 2014.
19. E. V. Pitjeva and N. P. Pitjev. Development of planetary ephemerides EPM and their applications. *Celest. Mech. Dyn. Astron.*, 119:237–256, 2014.
20. B. Bertotti, L. Iess, and P. Tortora. A test of general relativity using radio links with the cassini spacecraft. *Nature*, 425:374–376, 2003.
21. A. Hees, W. M. Folkner, R. A. Jacobson, and R. S. Park. Constraints on modified

- newtonian dynamics theories from radio tracking data of the cassini spacecraft. *Phys Rev D*, 89(10):102002, 2014.
22. A. Hees, B. Lamine, S. Reynaud, M.-T. Jaekel, C. Le Poncin-Lafitte, V. Lainey, A. Füzfa, J.-M. Courty, V. Dehant, and P. Wolf. Radioscience simulations in general relativity and in alternative theories of gravity. *Classical and Quantum Gravity*, 29(23):235027, December 2012.
 23. R. V. Pound and G. A. Rebka. Apparent weight of photons. *Phys Rev Lett*, 4(7):337–341, 1960.
 24. R. V. Pound and J. L. Snider. Effect of gravity on gamma radiation. *Phys Rev*, 140:788–803, 1965.
 25. L. Cacciapuoti and Ch. Salomon. Space clocks and fundamental tests: The ACES experiment. *Eur. Phys. J. - Spec. Top.*, 172(1):57–68, 2009. 10.1140/epjst/e2009-01041-7.
 26. B. Altschul, Q. G. Bailey, L. Blanchet, K. Bongs, P. Bouyer, L. Cacciapuoti, S. Capozziello, N. Gaaloul, D. Giulini, J. Hartwig, L. Iess, P. Jetzer, A. Landragin, E. Rasel, S. Reynaud, S. Schiller, C. Schubert, F. Sorrentino, U. Sterr, J. D. Tasson, G. M. Tino, P. Tuckey, and P. Wolf. Quantum tests of the einstein equivalence principle with the STE-QUEST space mission. *Adv. Space Res.*, 55:501–524, 2015.
 27. N. Ashby. Relativity in the global positioning system. *Living Rev. Relativ.*, 6:1, 2003.
 28. J. M. Dow, R. E. Neilan, and C. Rizos. The international GNSS service in a changing landscape of global navigation satellite systems. *J. Geod.*, 83:191–198, 2009.
 29. O. Montenbruck, C. Rizos, R. Weber, G. Weber, R.E. Neilan, and U. Hugentobler. Getting a grip on multi-GNSS: The international GNSS service MGEX campaign. *GPS World*, 24(7):44–49, 2013.
 30. R. Dach, S. Schaer, S. Lutz, M. Meindl, H. Bock, E. Orliac, D. Thaller L. Prange, L. Mer-
vart, A. J. äggi, G. Beutler, E. Brockmann, D. Ineichen, A. Wiget, G. Weber, H. Habrich,
J. Ihde, P. Steigenberger, and U. Hugentobler. Center for orbit determination in europe
(CODE). Technical report, International GNSS Service: Technical Report 2012, 2013.
edited by R. Dach and Y. Jean (AIUB), IGS Central Bureau.
 31. H. Bock, R. Dach, A. Jäggi, and G. Beutler. High-rate GPS clock corrections from CODE:
support of 1 hz applications. *J. Geod.*, 83:1083–1094, 2009.
 32. L. Prange, R. Dach, S. Lutz, S. Schaer, and A. Jäggi. The CODE MGEX orbit and clock
solution. In P Willis, editor, *IAG Potsdam 2013 Proceedings*. Springer, International
Association of Geodesy Symposia, 2014. accepted for publication.
 33. W. A. Gardner. *Introduction to Random Processes: with applications to signals and
systems*, volume 31. McGraw-Hill New York, 1990.
 34. K. G. Arun, B. R. Iyer, B. S. Sathyaprakash, and P. A. Sundararajan. Parameter estima-
tion of inspiralling compact binaries using 3.5 post-newtonian gravitational wave phasing:
The nonspinning case. *Phys. Rev. D*, 71(8):084008, 2005.
 35. O. Montenbruck, P. Steigenberger, and U. Hugentobler. Enhanced solar radiation pressure
modeling for galileo satellites. *J. Geod.*, 2014.
 36. T. Damour and A. M. Polyakov. The string dilation and a least coupling principle. *Nucl.
Phys. B*, 423:532–558, 1994.
 37. T. Damour and J. F. Donoghue. Equivalence principle violations and couplings of a light
dilaton. *Phys Rev D*, 82(8):084033, 2010.
 38. T. Damour. Theoretical aspects of the equivalence principle. *Class. Quantum Gravity*,
29(18):184001, 2012.
 39. O. Minazzoli and A. Hees. Intrinsic solar system decoupling of a scalar-tensor theory with
a universal coupling between the scalar field and the matter lagrangian. *Phys Rev D*,
88(4):041504, 2013.

PROBING DEFORMED COMMUTATORS WITH MACROSCOPIC HARMONIC OSCILLATORS

MATEUSZ BAWAJ^{1,2}, CIRO BIANCOFIORE^{1,2}, MICHELE BONALDI^{3,4}, FEDERICA BONFIGLI^{1,2}, ANTONIO BORRIELLI^{3,4}, GIOVANNI DI GIUSEPPE^{1,2}, LORENZO MARCONI⁵, FRANCESCO MARINO^{6,7}, RICCARDO NATALI^{1,2}, ANTONIO PONTIN^{5,6}, GIOVANNI A. PRODI^{4,8}, ENRICO SERRA^{4,8,9,10}, DAVID VITALI^{1,2}, FRANCESCO MARIN^{5,6,11,*}

¹ *School of Science and Technology, Physics Division, University of Camerino, via Madonna delle Carceri, 9, I-62032 Camerino (MC), Italy*

² *Istituto Nazionale di Fisica Nucleare (INFN), Sezione di Perugia, Italy*

³ *Institute of Materials for Electronics and Magnetism, Nanoscience-Trento-FBK Division, I-38123 Povo (TN), Italy*

⁴ *INFN, Trento Institute for Fundamental Physics and Application, I-38123 Povo (TN), Italy*

⁵ *Dipartimento di Fisica e Astronomia, Università di Firenze, Via Sansone 1, I-50019 Sesto Fiorentino (FI), Italy*

⁶ *INFN, Sezione di Firenze, Via Sansone 1, I-50019 Sesto Fiorentino (FI), Italy*

⁷ *CNR-Istituto Nazionale di Ottica, Largo E. Fermi 6, I-50125 Firenze, Italy*

⁸ *Dipartimento di Fisica, Università di Trento, I-38123 Povo (TN), Italy*

⁹ *Centre for Materials and Microsystem, Fondazione Bruno Kessler, I-38123 Povo (TN), Italy*

¹⁰ *Dept. of Microelectronics and Computer/ECTM/DIMES Technology Centre, Delft University of Technology, Feldmanweg 17, 2628 CT Delft, PO Box 5053, 2600 GB Delft, The Netherlands*

¹¹ *European Laboratory for Non-Linear Spectroscopy (LENs), Via Carrara 1, I-50019 Sesto Fiorentino (FI), Italy*
e-mail: marin@fi.infn.it

According to different quantum gravity models, gravitational effects at the Planck scale appear in the form of generalized commutation relations. In this framework, the dynamics of an isolated harmonic oscillator becomes intrinsically nonlinear and shows a dependence of the oscillation frequency on the amplitude. Here we analyze the free decay of micro and nano-oscillators, to place new upper limits to the parameters quantifying the commutator deformation.

1 Introduction and model

General relativity and quantum physics are expected to merge at the Planck scale, defined by distances of the order of $L_P = 1.6 \times 10^{-35}$ m and/or extremely high energies of the order of $E_P = 1.2 \times 10^{19}$ GeV. Since the study of particles collisions around the Planck energy is well beyond the possibilities of current and foreseeable accelerators, high-energy astronomical events (e.g. γ -ray bursts) have been considered as the privileged natural system to unveil quantum gravitational effects. This common view has been enriched in the last years thanks to a number of studies proposing that signatures of the Planck-scale physics could manifest also at low energies¹⁻⁵. It is indeed widely accepted that, when gravity is taken into account, deviations from standard quantum mechanics are expected. Such deviations are likely to be derived from a deformed canonical commutator between position q and momentum p , that in its most common

form is written as⁶⁻⁸:

$$[q, p] = i\hbar \left(1 + \beta_0 \left(\frac{L_P p}{\hbar} \right)^2 \right). \quad (1)$$

Here we describe an experiment conceived to test this hypothesis, and set limits to the deformation parameter β_0 . Our work is based on two assumptions. First, we suppose that Eq. (1) holds for the operator q describing a measured position in a macroscopic harmonic oscillator, and its conjugate momentum p . In terms of the usually normalized operators, $Q = q/\sqrt{\hbar/(m\omega_0)}$ and $P = p/\sqrt{\hbar m\omega_0}$, defined for an oscillator with mass m and resonance angular frequency ω_0 , the commutation relations are therefore

$$[Q, P] = i(1 + \beta P^2), \quad (2)$$

where $\beta = \beta_0 (\hbar m\omega_0/m_P^2 c^2)$ ($m_P = E_P/c^2$ is the Planck mass) is a further dimensionless parameter that we assume to be small ($\beta \ll 1$). Such assumption will be shown to be consistent with the experimental results. The second hypothesis is the validity of the Heisenberg equations for the temporal evolution of an operator \hat{O} , i.e. $d\hat{O}/dt = [\hat{O}, H]/i\hbar$, where H is the Hamiltonian $H = \frac{\hbar\omega_0}{2}(Q^2 + P^2)$.

In particular, the standard Heisenberg evolution equations are applied to the operators P and Q . The solution is

$$Q = Q_0 \left[\sin(\tilde{\omega}t) + \frac{\beta}{8} Q_0^2 \sin(3\tilde{\omega}t) \right], \quad (3)$$

where

$$\tilde{\omega} = \left(1 + \frac{\beta}{2} Q_0^2 \right) \omega_0. \quad (4)$$

It is valid at the first order in βQ_0^2 , and implies two relevant effects with respect to the harmonic oscillator: the appearance of the third harmonic and, less obvious, a quadratic dependence of the frequency shift on the oscillation amplitude. In case of small damping with relaxation time τ , the dynamics is described by a modified version of Eq. (3) with the replacements $\tilde{\omega}t \rightarrow \Phi(t)$, implying $\tilde{\omega}(t) = d\Phi/dt$, and $Q_0 \rightarrow Q_0 \exp(-t/\tau)$.

2 Experiment

We have exploited three kinds of oscillators, spanning a wide range of masses around the Planck mass $m_P = 22\mu\text{g}$. The measurements are performed by exciting an oscillation mode and monitoring a possible dependence of the oscillation frequency and of the third harmonic distortion on the oscillation amplitude, during the free decay. The first device is a ‘‘double paddle oscillator’’ (DPO)⁹ made from a $300\mu\text{m}$ thick silicon plate. Thanks to its shape, for two particular balanced oscillation modes, the oscillator is supported by the outer frame with negligible energy dissipation and it can therefore be considered as isolated from the background¹⁰. The sample is kept in a temperature stabilized vacuum chamber and vibrations are excited and detected capacitively. We have monitored the mode oscillating at frequency of 5636 Hz with a mechanical quality factor of 1.18×10^5 (at room temperature) and mass $m = 0.033\text{g}$.

For the measurements at intermediate mass we have used a silicon wheel oscillator, made on the $70\mu\text{m}$ thick device layer of a SOI wafer and composed of a central disk kept by structured beams¹¹, balanced by four counterweights on the beams joints that so become nodal points (Fig. 1b)¹². On the surface of the central disk, a multilayer $\text{SiO}_2/\text{Ta}_2\text{O}_5$ dielectric coating forms an high reflectivity mirror. The design strategy allows to obtain a balanced oscillating mode (its resonance frequency is 141 797 Hz), with a planar motion of the central mass (significantly reducing the contribution of the optical coating to the structural dissipation) and a strong isolation from the frame. The oscillator is mechanically excited using a piezoelectric ceramic glued on the sample mount. The surface of the core of the device works as end mirror in one arm of a stabilized Michelson interferometer, that allows to measure its displacement. The

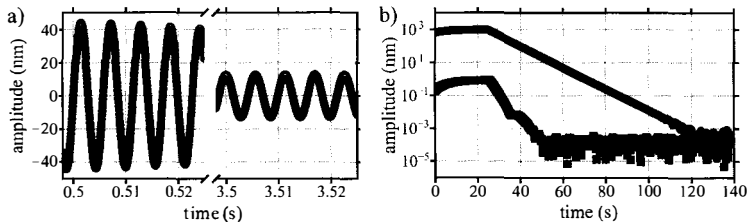


Figure 1 – a) Example of the decaying oscillation of the wheel oscillator, down shifted to ~ 200 Hz by a lock-in amplifier, fitted with the theoretical model including the possibility of a parabolic dependence of the oscillation frequency on the amplitude. b) Simultaneous detection of the first and third harmonic in the decay of the DPO oscillator.

quality factor surpasses 10^6 at the temperature of 4.3 K, kept during the measurements. The meaningful mass is $m = 20 \mu\text{g}$. Finally, the lighter oscillator is a $L = 0.5$ mm side, 30 nm thick, square membrane of stoichiometric silicon nitride, grown on a $5 \text{ mm} \times 5 \text{ mm}$, $200 \mu\text{m}$ thick silicon substrate¹³. The physical mass of the membrane is 20 ng. We have performed the measurements in a cryostat at the temperature of 65 K and pressure of 10^{-4} Pa, where the oscillation frequency is 747 kHz and the quality factor is 8.6×10^5 . Excitation and readout are performed as in the experiment with the wheel oscillators.

The frequency shift of the oscillation as function of the amplitude is obtained both by directly fitting the exponentially decaying oscillation with the expected expression, in some cases after a preliminary frequency down-conversion performed with a lock-in amplifier (see Fig. 1a for an example), and by completely frequency down-converting the oscillating signal (down to dc) with hardware and software lock-in amplifiers, then calculating the frequency as first derivative of the residual phase. Similarly, the third harmonic content is deduced both from the fit of time series, and by simultaneous recording of first and third harmonic of the signal with two separated lock-in amplifiers (Fig. 1b). For both indicators, the two methods give comparable results.

Table 1: Maximum relative frequency shifts measured for different oscillators, and corresponding oscillation amplitudes.

| Mass (kg) | Frequency (Hz) | Max. ampl. (nm) | $1/Q$ | Max. $\Delta\omega/\omega_0$ |
|----------------------|--------------------|-----------------|----------------------|------------------------------|
| 3.3×10^{-5} | 5.64×10^3 | 600 | 8×10^{-6} | 4×10^{-7} |
| 2×10^{-8} | 1.42×10^5 | 55 | 1×10^{-6} | 6×10^{-8} |
| 2×10^{-11} | 7.47×10^5 | 47 | 1.2×10^{-6} | 3×10^{-6} |

We remark that the frequency stability of the oscillating signal is typically significantly better than the linewidth, as shown in Table 1. We note that $\Delta\omega/\omega_0 \ll 1$ is required in order for the model to be valid (indeed, it implies $\beta Q_0^2 \ll 1$). In all cases, for large enough excitation, the frequency shows indeed a parabolic dependence on the oscillation amplitude. This feature can be attributed to structural nonlinearity which is intrinsic in all the oscillators. The parabolic coefficients (with its uncertainty) can be used to determine upper limits to the deformation parameters β and, actually, β_0 .

3 Results and discussion

Our results are summarized in Fig. 2, where we also report some previously existing limits to the deformation parameter β_0 . In our experiments we have considered a wide range of masses around the Planck mass. We believe our analysis to be particularly meaningful in this regime, as strong deviations from classical Newtonian mechanics arise as soon as the momentum

is of the order of m_{pc} . This is not only true for planetary motion, but even for Kg-scale mechanical oscillators. In relation to this point, we remark that the present approach involves just the expectation values of position and momentum operators. A more powerful route to the search of quantum gravitational effects should focus on specific quantum features of a system. For instance, quantum fluctuations of the spacetime metric and/or spacetime discreteness are expected to significantly affect the evolution of higher order momenta. This motivates a future experiment, based on quantum macroscopic oscillators.

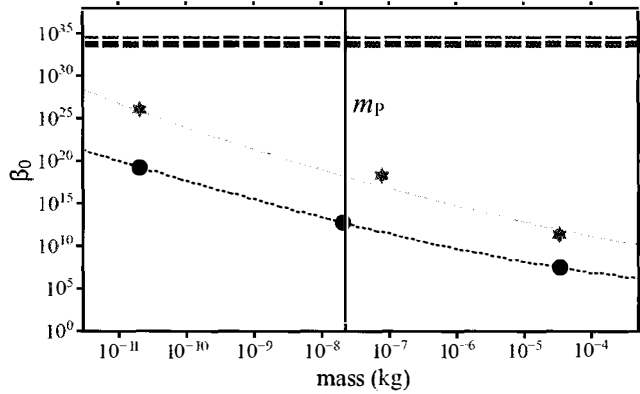


Figure 2 – The parameter β_0 quantifies the deformation to the standard commutator between position and momentum, or the scale $\sqrt{\beta_0}L_P$ below which new physics could come into play. Full symbols report its upper limits obtained in this work, as a function of the mass. Blue dots: from the amplitude-dependence of the oscillation frequency; red stars: from the third harmonic distortion. Dotted lines are guides for the eyes. Dashed lines reports some previously estimated upper limits, obtained in mass ranges outside this graph. At lower mass, in green: from high resolution spectroscopy on the hydrogen atom, considering the ground state Lamb shift (upper line)² and the 1S-2S level difference (lower line)¹. At higher mass, in magenta: from the AURIGA detector^{4,5}, in yellow: from the lack of violation of the equivalence principle¹⁴.

References

1. C. Quesne, and V.M. Tkachuk, *Phys. Rev. A* **81**, 012106 (2010).
2. A.F. Ali, S. Das, and E.C. Vagenas, *Phys. Rev. D* **84**, 044013 (2011).
3. I. Pikovski *et al.*, *Nature Phys.* **8**, 393 (2012).
4. F. Marin *et al.*, *Nature Phys.* **9**, 71 (2013).
5. F. Marin *et al.*, *New J. Phys.* **16**, 085012 (2014).
6. D. Amati, M. Ciafaloni, and G. Veneziano, *Phys. Lett. B* **197**, 81 (1987).
7. D.J. Gross, and P.F. Mende, *Nucl. Phys. B* **303**, 407 (1988).
8. L.G. Garay, *Int. J. Mod. Phys. A* **10**, 145 (1995).
9. C.L. Spiel, R.O. Pohl, and A.T. Zehnder, *Rev. Sci. Instr.* **72**, 1482 (2001).
10. A. Borrielli *et al.*, *J. Micromech. Microeng.* **21**, 065019 (2011).
11. E. Serra *et al.*, *Appl. Phys. Lett.* **101**, 071101 (2012).
12. A. Borrielli *et al.*, *Microsyst. Technol.* **20**, 907 (2014).
13. J.D. Thompson *et al.* *Nature* **452**, 72 (2008).
14. S. Ghosh, *Class. Quantum Grav.* **31**, 025025 (2014).

2. Testing Fundamental Physics

TESTING FUNDAMENTAL PHYSICS WITH CLOCKS IN SPACE: THE ACES MISSION

L. Cacciapuoti^a, P. Laurent^b, D. Massonnet^c, C. Salomon^d

^aEuropean Space Agency, Keplerlaan 1, 2200 AG Noordwijk ZH - The Netherlands
Luigi.Cacciapuoti@esa.int

^bSYRTE, CNRS UMR 8630, Observatoire de Paris, LNE, UPMC, 61 Av. de l'Observatoire, 75014 Paris - France

^cCNES, Centre Spatial de Toulouse, 18 Avenue Edouard Belin, 31401 Toulouse - France

^dLaboratoire Kastler Brossel, ENS-PSL Research University, CNRS, UPMC, Collège de France, 24 rue Lhomond, 75005, Paris - France

Atomic clocks and high-performance links are used to measure time and frequency to accuracy levels never reached before. When operated in a space-based laboratory, the large variations of the gravitational potential, the large velocities and velocity variations, as well as the worldwide access to ground clocks become key ingredients to measure tiny deformations in space-time that might bring the signature of new physics and new fundamental constituents. From the International Space Station, the ACES payload will distribute a clock signal with fractional frequency stability and accuracy of $1 \cdot 10^{-16}$. The comparison of distant clocks via ACES will be used to test Einstein's theory of general relativity. The ACES mission elements are now close to flight maturity. The flight model of the cold cesium clock PHARAO has been tested and delivered for integration in the ACES payload. Tests on the active hydrogen maser SHM and the microwave link MWL have been completed and manufacturing of the flight models is ongoing. The time transfer optical link ELT is also well advanced. This paper presents the progress of the ACES mission elements.

1 ACES Mission Elements

Clocks and interferometers based on samples of ultracold atoms are today state-of-the-art instruments for the measurement of time and frequency, accelerations, rotations, and faint forces. The sensitivity of these devices increases as the interaction time of the atomic sample with the probing electromagnetic field increases. In many of these instruments, e.g. fountain clocks and atom interferometers, atoms interrogation takes place during the free evolution of the sample in the gravity field. The most severe constraint to their performance is therefore imposed by gravity, which limits the maximum free fall time of the atoms in the limited volume of the apparatus. Operating these instruments in space becomes very attractive for the long interaction times that can be achieved in a freely falling laboratory.

Proposed to the European Space Agency in 1997, the *Atomic Clock Ensemble in Space* (ACES) mission relies on PHARAO, a clock based on laser-cooled caesium atoms, to generate a high stability and accuracy time reference in space^{1,2}. The free fall conditions are crucial for PHARAO to reach or even surpass the performance of the best atomic fountain clocks on ground, while keeping a very compact volume, small mass, and power consumption. Installed onboard the International Space Station (ISS), at the external payload facility of the Columbus module, the ACES payload distributes its time scale to ground clocks by using two independent time & frequency transfer links, a link operating in the microwave domain (MWL) and the ELT (European Laser Timing) optical link. On the ground, a network of MWL ground terminal and satellite laser ranging stations

provides the physical interface between the ACES clock ensemble and atomic clocks on ground.

The ACES payload is shown in Figure 1. It has a volume of about 1 m^3 , for a mass of 230 kg and a power consumption of 450 W. The main onboard instruments are the cesium clock PHARAO and the active hydrogen maser SHM. The PHARAO clock reaches a fractional frequency stability of $1 \cdot 10^{13}/\sqrt{\tau}$, where τ is the integration time expressed in seconds, and an accuracy of a few parts in 10^{16} . SHM is the ACES flywheel oscillator, also providing the frequency reference needed for the onboard characterization of the PHARAO clock accuracy. PHARAO and SHM 100 MHz signals are compared in the phase comparator FCDP, which also distributes the ACES frequency reference to MWL electronics. MWL is the ACES metrology link: coherently with the ACES clock signal, it generates the ACES time scale and compares it with the time scales locally generated by atomic clocks on the ground; furthermore, it stamps the arrival of the electrical pulses generated by the ELT detector in the onboard time. Finally, a GNSS receiver, tracking GPS, GALILEO and GLONASS signals, provides precise orbit data of the ACES clocks.

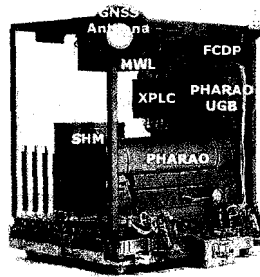


Figure 1 – The ACES payload has a volume of 1 m^3 , for a mass of 230 kg, and a power consumption of 450 W.

Figure 2 shows the ACES network of MWL ground terminals. Seven fixed units will be deployed around the world, at the best institutes for time & frequency metrology: two in the US, JPL (Pasadena) and NIST (Boulder), three in Europe, at SYRTE (Paris, FR), PTB (Braunschweig, DE), and NPL (Teddington, UK), one in Japan, NICT (Tokyo), and one in the southern hemisphere, at UWA (Perth, AU). Furthermore, one transportable MWL station will be located in Europe and shared by other institutes, including the Wettzell geodetic observatory (Wettzell, DE), INRIM (Torino, IT), and METAS (Bern, CH); a second transportable station will be dedicated to the calibration of MWL fixed terminals for time transfer experiments and for comparisons with the laser link ELT. As shown in Figure 2, space-to-ground comparisons will occur over 4 continents, at the same time enabling ground-to-ground comparisons over intercontinental distances by using ACES as a relay satellite.

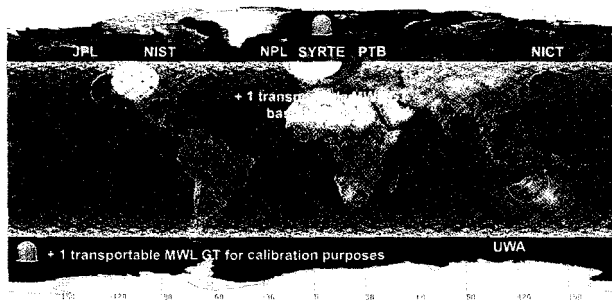


Figure 2 – The ACES network of MWL ground terminals and typical ground tracks of the ISS orbit.

Combined with the growing network of regional links using compensated optical fibers, which have already demonstrated frequency comparison capability at $1 \cdot 10^{-19}$ resolution, clock comparisons at the level of $1 \cdot 10^{-17}$ or better will soon be available with ACES on a worldwide scale. Such performance represents one to two orders of magnitude improvement over the currently used TW-STFT and GPS time transfer systems. Several institutes, such as PTB and SYRTE, are already interconnected by a fiber link and additional links will be operational by the time of the ACES mission. Furthermore, the fiber links between NIST and JILA (Boulder, US) as well as between NICT, NMIJ (Tsukuba, JP), and RIKEN (Tokyo, JP) will connect additional institutes sensibly enlarging the ensemble of ground clocks contributing to ACES.

The ground clocks connected to the ACES network are based on different atoms and ions, with transitions both in the microwave and in the optical domain. Microwave fountain clocks are today mature instruments, with fractional frequency stability and accuracy of a few parts in 10^{-16} , able to run on a very high duty cycle ($> 95\%$)^{4,3}. They will be compared over the whole mission duration with the ACES clocks. Following the advances in optical frequency measurements using frequency combs, clocks based on the optical transitions of atoms and ions have made spectacular progress in the last years. Several optical clocks have demonstrated a stability of $3 \cdot 10^{-16}$ at 1s, down to $2 \cdot 10^{-18}$ after 20000s, and an accuracy in the 10^{-18} range^{5,6,7,8,9,10}. These clocks are not yet as reliable as microwave fountain clocks, but with ACES they will be compared over intercontinental distances at 10^{-17} frequency resolution during dedicated measurement campaigns.

ACES is scheduled for launch with Space X in the first half of 2017. The ISS has a nearly circular orbit around the Earth with a mean elevation of 400 km, an orbital period of 5400 s, and an inclination of 51.6° . The first 6 months of operations will be devoted to the characterization and performance evaluation of the ACES clocks and links. In microgravity, it will be possible to optimize the interaction time of cesium atoms in the PHARAO clock and tune the linewidth of the atomic resonance by two orders of magnitude. After the clocks optimization, performance in the 10^{16} range both in frequency stability and accuracy are expected. In parallel, the ACES metrology links will be calibrated and characterized. During the second part of the mission (12 months, possibly extended to 30 months), the ACES clocks will be routinely compared to ground clocks operating both in the microwave and in the optical domain.

2 Scientific Objectives

2.1 Testing General Relativity with ACES

According to Einstein's theory of general relativity, identical clocks placed in different gravitational fields experience a frequency shift that depends on the difference between the Newtonian potentials at the clock positions. The comparison between the ACES clocks and ground-based atomic clocks will measure the frequency variation due to the gravitational redshift with a 35-fold improvement on the GP-A experiment¹¹, testing Einsteins prediction at the 2 ppm uncertainty level.

Time variations of fundamental constants can be measured by comparing clocks based on different atomic species and transitions^{12,13}. Indeed, the energy of an atomic transition can be expressed in terms of the fine structure constant α and the two dimensionless constants m_q/Λ_{QCD} and m_e/Λ_{QCD} , depending on the quark mass m_q , the electron mass m_e , and the QCD mass scale Λ_{QCD} ^{14,15}. ACES will perform crossed comparisons of ground clocks both in the microwave and in the optical domain with a frequency resolution of $1 \cdot 10^{-17}$ in a few days of integration time. These comparisons will impose strong and unambiguous constraints on the time variations of the three fundamental constants reaching an uncertainty of $1 \cdot 10^{-17}/\text{yr}$ after one year, down to $3 \cdot 10^{-18}/\text{yr}$ after three years.

The foundations of special relativity lie on the hypothesis of Local Lorentz Invariance (LLI). According to this principle, the outcome of any local test experiment is independent of the velocity of the freely falling apparatus. In 1997, LLI tests based on the measurement of the round-trip speed of light have been performed by comparing clocks onboard GPS satellites to ground hydrogen masers¹⁶. In such experiments, LLI violations would appear as variations of the speed of light c

with the line-of-sight direction and the relative velocity of the clocks. ACES will perform a similar experiment by measuring relative variations of the speed of light at the 10^{-10} uncertainty level.

2.2 Applications

ACES will also demonstrate a new technique to map the Earth gravitational potential. It relies on a precision measurement of the Einstein's gravitational redshift between two clocks to determine the corresponding difference in the local gravitational potentials. The possibility of performing comparisons of ground clocks to the 10^{-17} frequency uncertainty level will allow ACES to resolve geopotential differences down to 10 cm on the geoid height.

A dedicated GNSS receiver onboard the ACES payload will ensure orbit determination of the space clocks. The receiver will be connected to the ACES clock signal, opening the possibility of using the GNSS network for space-to-ground clock comparisons.

The simultaneous operation of MWL and ELT will allow to cross calibrate the two links. Optical versus dual-frequency microwave measurements will provide useful data for the study of atmospheric propagation delays and for the construction of atmosphere mapping functions in S-band, Ku-band, and at optical frequencies. The ACES links will also deliver absolute ranging measurements, both in the microwave and in the optical domain.

3 ACES Status

The development status of the ACES clocks and links is discussed in the following.

3.1 PHARAO

PHARAO is a primary frequency standard based on laser cooled cesium atoms developed by LNE-SYRTE, LKB, and CNES. Its concept is very similar to ground-based atomic fountains. Atoms, launched in free flight along the PHARAO tube, cross a resonant cavity composed of two spatially separated interrogation zones where they interact with a microwave field tuned on the transition between the two hyperfine levels of the cesium ground state (9.192631770 GHz, from the SI definition of the second). In microgravity, the velocity of the atoms is constant and it can be continuously changed over almost two orders of magnitude (5 to 500cm/s), allowing the detection of atomic signals down to sub-Hz linewidth.

All PHARAO subsystems have passed the qualification tests: random vibration level of 10 grms and 30 g at 30Hz; storage temperature from -32°C to $+40^{\circ}\text{C}$ and operating temperature from $+10^{\circ}\text{C}$ to $+33^{\circ}\text{C}$. Figure 3 shows the PHARAO flight model assembled on the ACES baseplate at CNES premises in Toulouse. During ground tests, PHARAO is operated under vacuum with the cesium tube aligned vertically and the atoms launched upwards at a velocity of 3.56 m/s. The space environment is emulated by changing the temperature at the clock baseplate and the magnetic field via large external Helmholtz coils. The clock performance tests lasted 4 months and ended in summer 2014. The capture, cooling, launch, and detection of cold atoms have been optimized. The frequency stability and the largest systematic frequency shifts of the clock have been measured. A short summary of the main results is given below.

$5 \cdot 10^8$ atoms are typically collected in the PHARAO optical molasses for a laser power of 13 mW/beam and a loading time of 1.5 s. During ground operation, this number is reduced to about $5 \cdot 10^7$ (laser power 5 mW per beam, loading time 200ms) to avoid saturation of the detection signal. The PHARAO Ramsey fringes are in full agreement with numerical simulations. The central fringe has a linewidth of 5.6 Hz corresponding to an interaction time of 90 ms. In microgravity, the linewidth can be reduced to 0.12 Hz at a launch velocity of 50 mm/s.

The PHARAO frequency stability (see Figure 4) has been measured as a function of the integration time τ by comparing the clock to the SYRTE mobile fountain FOM¹⁷. PHARAO Allan deviation is $3.15 \cdot 10^{-13}/\sqrt{\tau}$, while FOM is contributing with $1.3 \cdot 10^{-13}/\sqrt{\tau}$. The clock model predicts a frequency stability of $1.1 \cdot 10^{-13}/\sqrt{\tau}$ in microgravity. PHARAO and FOM frequencies agree to better than $2 \cdot 10^{-15}$.

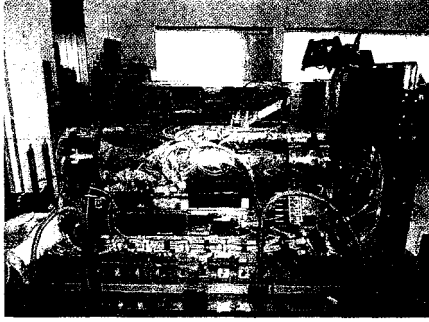


Figure 3 – The flight model of the PHARAO clock integrated on the ACES baseplate.

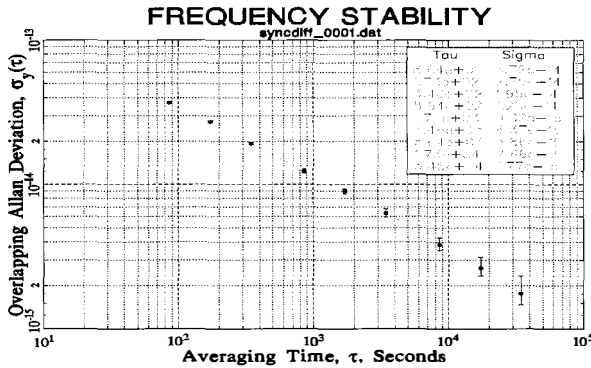


Figure 4 – PHARAO frequency stability on the ground measured against the mobile fountain clock FOM.

The frequency accuracy of the PHARAO clock has been analyzed and systematic frequency shifts are summarized in Table 1. The dominant frequency shift results from the second-order Zeeman effect. The high-contrast Ramsey profile obtained on the transition between $m=1$ Zeeman sub-levels corresponds to a magnetic field homogeneity better than $\delta B/B \sim 10^{-3}$ ($B=1$ mG) along the atomic trajectories. The orbital variations of the Earth magnetic field ($\pm 40 \mu\text{T}$) remain an important issue as the overall attenuations factor of 270000 provided by the PHARAO μ -metal shields and the active compensation is not sufficient to control the corresponding frequency variations ($2 \cdot 10^{-16}$). Therefore, the magnetic field experienced by the atoms is periodically measured at a rate of 2 mHz by using the high sensitivity of the $m=1$ hyperfine resonance. The measurement lasts 10 seconds and has negligible influence on the overall clock stability. In this way, an uncertainty at the 10^{-17} level can be reached. The second main systematic effect is the black-body radiation shift¹⁸. The thermal behaviour of the cesium tube has been modeled using finite element analysis and its accuracy has been verified during thermal balance tests by using calibrated platinum resistors. The error on the temperature seen by the atomic ensemble is estimated to 56 mK, corresponding to a $1.5 \cdot 10^{-17}$ contribution of the black-body radiation shift to the clock accuracy. The cold collisions shift depends on the relative energy of colliding atoms and on the local density. The effect is measured by operating the clock with different atom numbers and densities and extrapolating the frequency shift to the zero-density limit. The number of atoms is varied by changing the frequency of the preparation cavity with optimized power to ensure that atomic densities are proportional to the atom numbers to better than 1%. On ground, the uncertainty is mainly limited by the measurement duration. In space, with typical velocities of 300 mm/s, a frequency shift of $1.5 \cdot 10^{-15}$ is expected. Measurements will be performed during

Table 1: Main systematic frequency shifts and uncertainties of PHARAO tested on ground.

| Effect | Correction (10^{-15}) | Uncertainty (10^{-16}) |
|-----------------------------|---------------------------|----------------------------|
| Magnetic field | 181 | < 1 |
| Black-body shift | -17.6 | < 1 |
| Collisions | -7 | 12 |
| Longitudinal phase gradient | 3 | 6 |
| Microwave recoil/lensing | 0.12 | < 1 |
| Phase transients | < 1 | < 1 |
| Total | 160.55 | 14 |

the whole mission duration to reach an uncertainty of $5 \cdot 10^{-17}$. The residual Doppler effect resulting from the inhomogeneous phase distribution of the microwave field inside the cavity has been calculated by numerical simulations and verified by measurements. On the ground, the longitudinal phase gradient is amplified by the atomic deceleration between the first and the second Ramsey interaction regions, producing a frequency shift of $3 \cdot 10^{-15}$. In space, a frequency shift of $3 \cdot 10^{-17}$ is expected for typical operating conditions. This effect is linear with the atomic velocity, but it remains coupled to the collisional shift. By varying both the launch velocity and the density over two orders of magnitude, we expect to reach an uncertainty of $5 \cdot 10^{-17}$ for the combined contribution. The effect of the transverse phase gradient in the cavity has been evaluated in collaboration with K. Gibble^{3,4}, who is also estimating the recoil shift produced by microwave photons (microwave lensing)¹⁹. The frequency shift is of the order of $1 \cdot 10^{-16}$ and it depends on the size of the atomic wave function and on the geometry of the cesium tube. In summary, the PHARAO clock is expected to have an accuracy of $1 - 3 \cdot 10^{-16}$ when operated in microgravity.

PHARAO is now in the ACES integration room at ADS premises in Friedrichshafen.

3.2 SHM

SHM is an active H-maser operating on the hyperfine transition of atomic hydrogen at 1.420405751 GHz. Developed by SpectraTime, SHM provides ACES with a stable fly-wheel oscillator. SHM is designed to fit into a volume of $390 \times 390 \times 590$ mm³ and a mass of 42 kg, while still providing the frequency stability performance of a ground maser. To this purpose, the number of thermal shields has been reduced and a dedicated Automatic Cavity Tuning (ACT) system has been implemented to steer the resonance frequency of the maser cavity against thermal drifts. SHM ACT injects two tones, symmetrically placed around the H-maser signal. The two tones are coherently detected and the unbalance between their power levels is used to close a feedback loop acting on the cavity varactor and stabilizing the resonance frequency of the microwave cavity against temperature variations. This method allows SHM to reach fractional frequency stabilities down to $1.5 \cdot 10^{-15}$ at 10^4 s of integration time. Figure 5 shown the Allan deviation of the clock measured under stable laboratory conditions against a ground H-maser.

The SHM sensitivity to temperature and magnetic field variations has been measured. The thermal sensitivity can be counteracted by a fast servo of the ACES baseplate temperature (< 600 s time constant) and by the natural filtering of frequency fluctuations introduced by the thermal inertia of the instrument. In addition, SHM frequency variations can be calibrated as a function of temperature. SHM sensitivity to magnetic fields has been measured to about $8 \cdot 10^{-14}$ /G. At this level, the magnetic field variations along the ISS orbit (± 0.4 G) are expected to introduce a degradation to the H-maser stability of $1 - 2 \cdot 10^{-14}$. These frequency fluctuations will be corrected by the ACES servo loops. In addition, magnetic field perturbations are suppressed to high degree when taking the difference over 100 s time intervals, as needed for the PHARAO accuracy evaluation. Tests will be performed to better characterize the H-maser sensitivity to external B-fields.

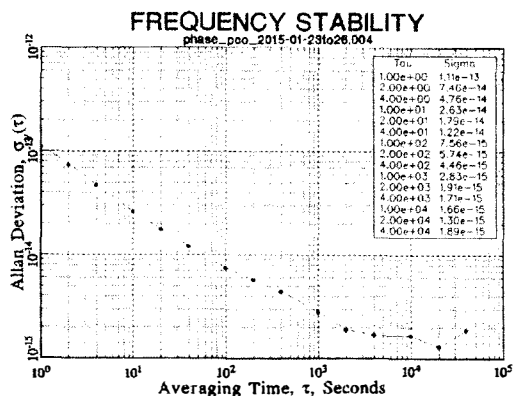


Figure 5 – SHM frequency stability measured against a ground H-maser.

The SHM flight model is under completion. Its delivery for integration in the ACES baseplate is expected in the first months of 2016.

3.3 MWL

The ACES microwave link is developed by ADS, TIMETECH, TZR, and EREMS. The proposed MWL concept is an upgraded version of the Vessot two-way technique used for the GP-A experiment in 1976¹¹ and the PRARE geodesy instrument. The system operates continuously with a carrier frequency in the Ku-band. The high carrier frequencies of the up and down links (13.5 GHz and 14.7 GHz respectively) allow for a noticeable reduction of the ionospheric delay. A third frequency in the S-band (2.2 GHz) is used to determine the Total Electron Content (TEC) and correct for the ionospheric time delay. A PN-code modulation (100 Mchip/s) on the carrier removes the phase ambiguity between successive comparison sessions separated by large dead times. The system is designed for multiple access capability, allowing up to 4 simultaneous ground users distinguished by the different PN-codes and Doppler shifts.

The engineering model of the flight segment electronic unit has been completed and tested in end-to-end configuration with the ground terminal electronics in the presence of signal dynamics (attenuation and Doppler frequency variations as predicted along the ISS orbit). MWL long-term stability is ensured by the continuous calibration of the receiver channels provided by a built-in test-loop translator. For shorter durations (<300 s), the time stability is driven by the noise performance of the Ku-band transmitter and receiver and the DLL (Delay-Locked Loop) boards. The 100 MHz chip rate allows to reach a time stability at the 5 ps level already with code measurements. However, the ultimate performance is achieved with the carrier phase measurements, whose time stability is at the level 200 fs at about 100 s of integration time in the presence of signal dynamics. The thermal sensitivity of the system has been calibrated. The sensitivity to a series of key parameters such as clock input power, received signal-to-noise density ratios, supply voltage, Doppler, and Doppler rate has also been measured.

MWL ground terminal (GT) electronics are similar to the MWL flight hardware, symmetry being important in a two-way system to reduce instrumental errors. The electronic unit of the MWL GT has been rigidly attached to the antenna unit to reduce phase instabilities due to the tracking motion. The Ku-band signal is delivered to the antenna feeder via a waveguide; a high stability RF cable is used for the S-band. The antenna is a 60 cm offset reflector with a dual-band feed system automatically pointed in azimuth and elevation by a steering mechanism. A computer controls the steering unit based on ISS orbit prediction files, collects telemetry and science data both from the local clocks and the MWL GT electronics, and it interfaces directly with the ACES Users Support and Operation Center (USOC). The system is housed below a protective radome

cover, which also allows to stabilize the temperature of the enclosed volume by an air conditioning system, part of a separate service pallet. The thermal design allows to operate the MWL GT for an external temperature between -30°C and $+45^{\circ}\text{C}$.

The MWL flight model is under assembly and board level tests have already started. The delivery of MWL flight segment electronics for integration in the ACES payload is expected by end 2015. The deployment of the ACES MWL ground terminals will start in the fall of 2015.

3.4 ELT

ELT, acronym for European Laser Timing, is an optical link based on picosecond laser pulses exchanged between Satellite Laser Ranging (SLR) stations on ground and the ACES payload. The onboard hardware consists of a corner cube reflector, a Single-Photon Avalanche Diode (SPAD), and an event timer board connected to the ACES time scale. Laser pulses fired towards the ISS are detected by the SPAD diode and stamped in the ACES scale. At the same time, the ELT reflector re-directs the laser pulses towards the ground station. The measurement of the start and return times on ground and of the detection time in space is then used to determine the desynchronization between space and ground clocks as well as the range.

Developed by the Technical University of Prague and CSRC, the SPAD diode has been tested in conjunction with a laboratory time tagging board providing sub-picosecond resolution. The time deviation of the combined system has a floor slightly below 200 fs. Peak-to-peak time fluctuations amount to a few picoseconds over several days of measurement. The detector is extremely robust against stray light and temperature variations. The temperature sensitivity has been measured between -60°C and $+70^{\circ}\text{C}$ showing a mean slope as low as 0.48 ps/K.

The flight model of the detector is expected to be delivered after this summer. The corner cube reflector is already integrated.

Acknowledgments

The development of the ACES mission is a collective effort and the authors would like to thank all participants, in particular the ACES Investigators Working Group (IWG), the ACES project team at ESA and ADS, the PHARAO team at CNES, SYRTE, LKB, TAS, Sodern, Eremis, CS, the SHM team at SpectraTime, the University of Prague team, the Technical University of Munich team, and the data analysis team at SYRTE for their contributions. This work is supported by ESA, CNES, and CNRS.

References

1. C. Salomon *et al*, C. R. Acad. Sci. Paris **t.2 Séries 4**, 1313 (2001).
2. L. Cacciapuoti and C. Salomon, Eur. Phys. J. Special topics **172**, 57 (2009).
3. R. Li *et al*, Metrologia **48**, 283 (2011).
4. J. Guéna *et al*, Phys. Rev. Lett **106**, 130801 (2011).
5. T. Rosenband *et al*, Science **319**, 1808 (2008).
6. A.D. Ludlow *et al*, Science **319**, 1805 (2008).
7. N. Hinkley *et al*, Science **341**, 1215 (2013).
8. B.J. Bloom *et al*, Nature **506**, 71 (2014).
9. I. Ushijima *et al*, Nature Photonics **9**, 185 (2015).
10. T.L. Nicholson *et al*, Nature **6**, 6896 (2015).
11. R.F.C. Vessot *et al*, Phys. Rev. Lett. **45**, 2081 (1980).
12. N. Huntermann *et al*, Phys. Rev. Lett. **113**, 210802 (2014).
13. R.M. Godun *et al*, Phys. Rev. Lett. **113**, 210801 (2014).
14. V.V. Flambaum *et al*, Phys. Rev. D **69**, 115006 (2004).
15. V.V. Flambaum *et al*, Phys. Rev. C **73**, 055501 (2006).
16. P. Wolf and G. Petit, Phys. Rev. A **56**, 4405 (1999).
17. J. Guéna *et al*, IEEE Trans. Ultrason. Ferroelec. Freq. Contr. **59**, 391 (2012).
18. W. Itano *et al*, Phys Rev. A **25**, 1233 (1981).
19. K. Gibble, Phys. Rev. A **90**, 015601 (2014).

ACES MWL DATA ANALYSIS PREPARATION STATUS

F. MEYNADIER¹, P. DELVA¹, C. GUERLIN², C. LE PONCIN-LAFITTE¹, P. LAURENT¹,
P. WOLF¹

¹ *LNE-SYRTE, Observatoire de Paris, CNRS, UPMC, LNE,
61 avenue de l'Observatoire 75014 Paris, France*

² *Laboratoire Kastler-Brossel, ENS, CNRS, UPMC,
24 rue Lohmond, 75005 Paris, France*

We present the current state of development of the ACES Microwave link data analysis software at Syrte.

1 Introduction

The ACES-PHARAO mission is an ESA space mission aiming at realizing a time scale of high stability and accuracy on board the International Space Station (ISS), and perform time and frequency transfer between the payload and ground stations during the flight. A description of its setup and main objectives may be found in reference¹. The SYRTE laboratory has been heavily involved in the design and development of the PHARAO cold atom clock (Laurent *et al.*, 2014)² as well as the data analysis software that will generate the mission's scientific products. This paper focusses on the current status of the data analysis.

2 The ACES experiment setup

In order to compare their local timescales to the ACES timescale, several metrology institutes will host a ACES Ground Terminal (GT), which will enable them to perform a two-way time transfer through microwave signals. ISS visibility will only last 300 to 500 seconds for a given station, with common-view configurations being possible if two GTs are close enough. Collected data on ground and in space is centralized at CADMOS (see fig. 1).

The MWL core data consists in 3 series of one-way time comparisons for each pass : 13.475 GHz uplink, 14.7 GHz Ku-band downlink, 2.24 GHz downlink. Combining the first two signals allows to perform a two-way time transfer, while combining the last two signals allows to determine the delay due to the ionosphere traversal³.

Time transfer data is determined either by determining the phase of the incoming carrier (dubbed "carrier" data), or by matching an encoded pattern at 100Mchips rate (dubbed "code" data). Code data is unambiguous, but coarse (20 ps resolution). Carrier data can theoretically achieve 1ps resolution, but suffers from phase ambiguity (any measurement will only be able to give a modulo- 2π phase). Combining both measurements correctly is key to optimal performance of the MWL.

Auxiliary data needed for data processing will also be contributed to the archive : instrumental calibrations, ISS orbitography, ground station positions and atmospheric parameters, etc.

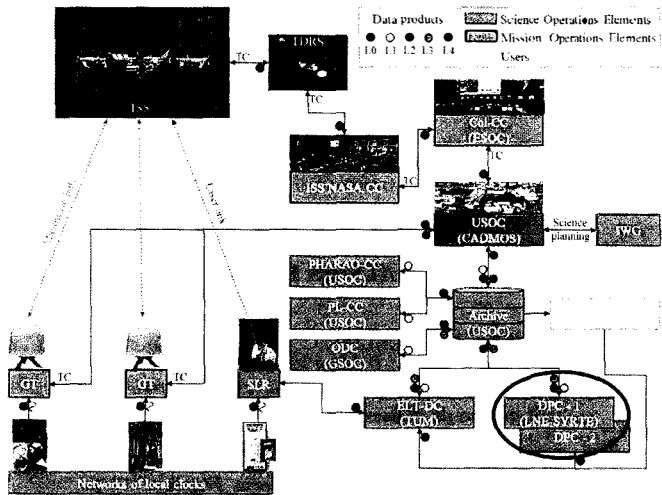


Figure 1 – Data processing flowchart for ACES-PHARAO data. L0 to L4 data levels correspond to various levels of processing from raw data to scientifically usable measurements. The red ellipse indicates the situation of LNE-SYRTE data processing center, at the interface between partially processed data in the archive, and users.

2.1 Two-way microwave link

The basic principle of such a link has been presented in Delva *et al.* (2012)³. In summary : sending a timestamp from clock *A* to clock *B* while sending a timestamp the other way, from clock *B* to clock *A*, allows (at the first order) to cancel the signal’s propagation time between the two clocks, thus allowing the calculation of the desynchronisation without precise knowledge of this time of flight. However, we remain sensitive to the variation of this value between the uplink and downlink measurement : ISS orbitography and ground station positioning allow us to model this effect to the required level.

As ISS positionnal uncertainty has been found to be a major source of error, we minimize its influence by interpolating signals so that uplink arrival time matches downlink departure time, thus making the “same” error on both trips, which cancels out well (Λ configuration³).

2.2 Software development

SYRTE has developed a data processing and analysis software, designed to extract scientific products from (nearly) raw ACES data. To test this software and experiment we also developed a simulation software that generates raw data in the format specified by ACES Ground Segment ICD, aiming at including all relevant effects in the calculation.

Care has been taken to separate as much as possible the development of both softwares : different developers, different languages (Python + Numpy for the processing software, Matlab for the simulation), different approaches are used in order to avoid common interpretation mistakes.

3 Current status

Figure 2 is the output of the tool we have designed for validating our software during its coding: as much as possible, each effect is isolated during the process and compared to its theoretical value (i.e. the value we can calculate from simulation’s input parameters).

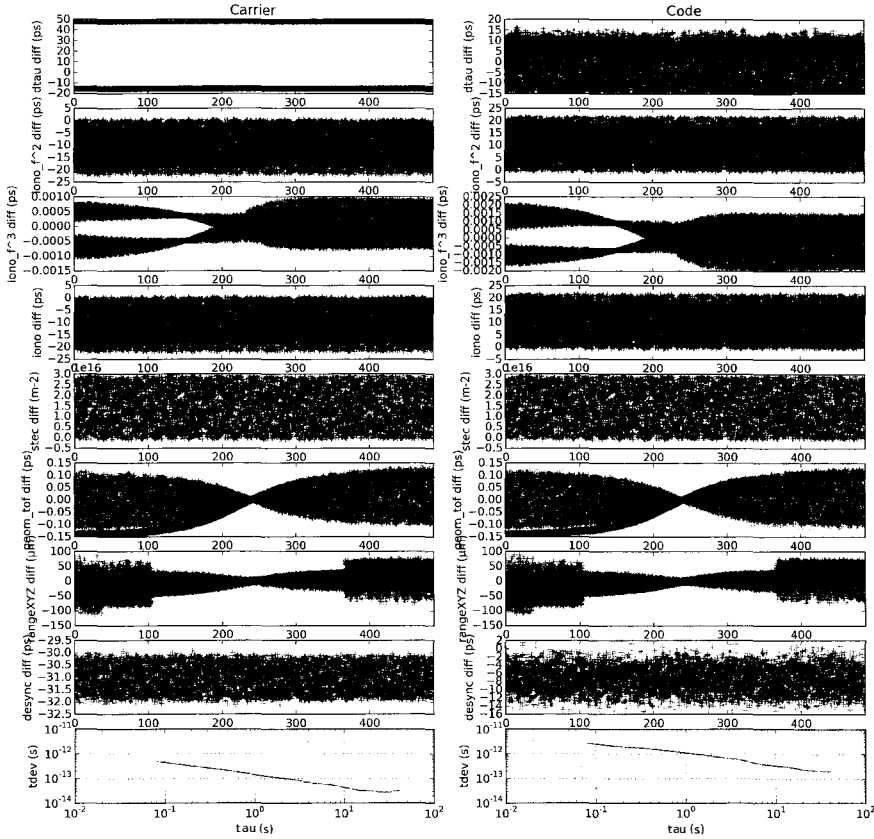


Figure 2 – Typical output from a comparison between the input data (i.e. theoretical values calculated by the simulation), and intermediate/final results calculated by the processing software. In this example, the simulated data includes a keplerian orbit for the ISS, earth rotation, atmospheric delays with variable parameters (troposphere + ionosphere), initial desynchronisation between the clock equal to 0.1 ms, frequency drifts due to velocity and gravitational potential for ground and space. Each point is the difference between the expected data at this date (known from the simulation’s scenario), and the data actually calculated by the processing software for the same coordinate time. Ideally we should therefore get values close to zero + noise. Blue points refer to uplink (f1) signals, green points refer to downlink (f2) signals, and red points refer to desynchronisation (which combines both signals). Left column contains result for carrier-phase data, and right column for code-phase data. Sampling period is 80 ms. See text for a description of the lines.

Preprocessing (1st line of fig 2) This module transforms raw data into pseudo-ranges, which is the expected input for our algorithms (see Delva *et al.* 2012³).

The 20 ps spread on code data is expected : it is a direct consequence of the 10 ns resolution of the raw data. Carrier data is affected by an offset of a few 10 ps, which we are currently investigating.

Tropospheric delays (2nd line of fig 2) Tropospheric delay is a (mainly) non-dispersive effect that can reach several hundred nanosecond on each signal. Two-way measurement cancel

it to a large extent, but we want to evaluate it as well as possible at higher orders. Some dispersive, second order effects have been studied by Hobiger, Piester and Baron (2013)⁴ and will be implemented in the future.

Ionospheric delays (3rd, 4th and 5th lines of fig 2) These are due to the dispersive nature of the ionosphere, and therefore affect differently frequencies f_1 and f_2 . We separated those in 2 terms, one that is proportional to $1/f^2$, the other that is proportional to $1/f^3$. Slight differences may be seen in the latter case : these have been identified as results of the difference between the model used for Earth's magnetic field in the simulation and in the processing software, and remain largely below detection threshold. STEC (Slanted Total Electron Content) is an intermediate result of this calculation and will be issued as a by-product.

Geometrical time of flight and range (6th and 7th lines of fig 2) Geometrical time of flight is the "classical, atmosphere-free" coordinate time interval between emission and reception of a given signal : As both stations move with respect to a geocentric non-rotating reference frame (GCRF), this calculation needs iterations or Taylor series developments to converge.

Range is the instantaneous distance between the two stations at a given coordinate time. This is calculated from the ISS orbitography files and the ground station coordinates, after conversion to GCRF.

Desynchronisation and associated time deviation (8th and 9th lines of fig 2) This is the end result of the processing : residual spreads are consistent with those of the pseudo ranges (first line), which is expected. The offset for carrier-phase data is the mean between the offsets on pseudo-ranges, it is a direct consequence of the offsets on pseudo-ranges which should disappear once those are removed.

Apart from this offset, no visible effects are noticed throughout the pass, showing that all other effects were correctly removed.

4 Conclusion

Our analysis software now implements the core functionalities that will be needed to perform ACES data analysis. Although some important points still need to be elucidated, we are confident that this software will be operational on schedule, with an ACES launch foreseen in early 2017.

Acknowledgements

FM acknowledges support from Centre National d'Études Spatiales for his participation to the Rencontres de Moriond 2015.

References

1. C. Salomon, L. Cacciapuoti, and N. Dimarcq. Atomic Clock Ensemble in Space: An Update. *International Journal of Modern Physics D*, 16:2511–2523, 2007.
2. Laurent, P. et al. PHARAO : The first primary frequency standard using cold atoms for space applications. *Revue française de métrologie*, 34, 2014.
3. P. Delva, F. Meynadier, P. Wolf, C. Le Poncin-Lafitte, and P. Laurent. Time and frequency transfer with a microwave link in the ACES/PHARAO mission. In *Proceedings of the European Frequency and Time Forum (EFTF) 2012 held in Gothenburg, Sweden, April 2012*, June 2012.
4. T Hobiger, D Piester, and P Baron. A correction model of dispersive troposphere delays for the aces microwave link. *Radio Science*, 48(2):131–142, 2013.

GRAVITY EXPERIMENTS WITH ULTRACOLD NEUTRONS AND THE *q*BOUNCE EXPERIMENT

T. Jenke, G. Cronenberg, M. Thalhammer, T. Reichberger, P. Geltenbort, H. Abele
Atominstytut, Technische Universität Wien, Stadionallee 2, 1020 Vienna, Austria

Institut Laue Langevin, 71 avenue des Martyrs, 38000 Grenoble, France

This work focuses on the control and understanding of a gravitationally interacting elementary quantum system. It offers a new way of looking at gravitation based on quantum interference: an ultracold neutron, a quantum particle, as an object and as a tool. The ultracold neutron as a tool reflects from a mirror in well-defined quantum states in the gravity potential of the earth allowing to apply the concept of gravity resonance spectroscopy (GRS). GRS relies on frequency measurements, which provide a spectacular sensitivity.

1 Introduction

We present the quantum bouncing ball: a neutron falling in the gravity potential of the earth and reflecting from a mirror for ultracold neutrons. As typical for bound quantum systems, neutrons have discrete energy eigenstates, and we find them in a coherent superposition of particular levels. The discrete energy levels occur due to the combined confinement of the matter waves by the mirror and the gravitational field. For neutrons the lowest discrete states are in the range of several pico-eVs, opening the way to a new technique for gravity experiments and measurements of fundamental properties. The energy levels together with the neutron density distribution are shown in Fig. 1. As Gea-Banacloche¹ has pointed out, the eigenfunctions for this problem are pieces of the same Airy function in the sense that they are shifted in each case in order to be zero at $z = 0$ and cut for $z < 0$, see section 2.

One task is a precise measurement of the energy levels by a resonance spectroscopy technique called Gravity Resonance Spectroscopy (GRS), see section 3. Quantum mechanical transitions with a characteristic energy exchange between an externally driven modulator and the energy levels are observed on resonance. An essential novelty of this kind of spectroscopy is the fact that the quantum mechanical transition is mechanically driven by an oscillating mirror and is not a consequence of a direct coupling of an electromagnetic charge or moment to an electro-magnetic field. The concept is related to Rabi's magnetic resonance technique for the measurements of nuclear magnetic moments.

The other task is to study the dynamics of such a quantum bouncing ball, i.e. the measurement of the time evolution of such a superposition of quantum states interpreted as reflections, when they come close to the mirror, see section 4. A quantum mechanical description of UCNs of mass m moving in the gravitational field above a mirror is essentially a one-dimensional (1D) problem. The corresponding gravitational potential is usually given in linear form by mgz , where g is the gravitational acceleration and z the distance above the mirror, respectively. The mirror, frequently made of glass, with its surface at $z = 0$ is represented by a constant potential V_{mirror} for $z < 0$. The potential V_{mirror} is essentially real because of the small absorption cross section of glass and is about 100 neV high, which is large compared to the neutron energy E perpendicular to the surface of the mirror. Therefore it is justified to assume that the mirror is a hard boundary for neutrons

at $z = 0$. Our tasks offer a new way of looking at gravitation based on quantum interference: an ultracold neutron, a quantum particle, as an object and as a tool. This unique system – systematic effects are extremely small – allows to map aspects of gravitation including the dark energy and dark matter searches.

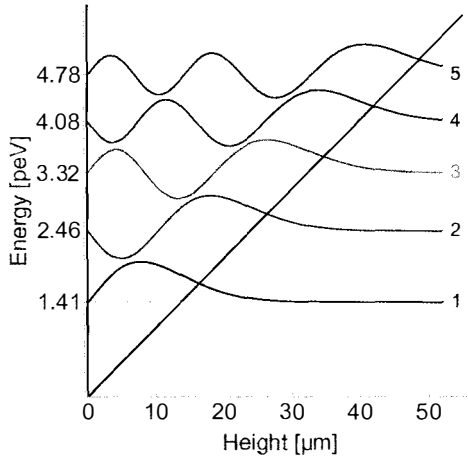


Figure 1 – The vertical wave function of the first five eigen states in the gravity potential with their eigen energies. The black lines indicate the potential composed from the neutron mirror and gravity.

2 Experiments with Quantum States of Ultracold Neutrons in the gravity field

Ultracold neutrons (UCN) bridge the gap between gravity experiments at short distances and the precise measurement techniques of quantum mechanics: These neutrons are so slow, that their corresponding wave length is much larger than interatomic distances of matter. Hence, they are totally reflected under any angle of incidence (why they are referred to as ultracold), and may bounce on a flat, polished glass mirror. The measurements take place at the Institut Laue-Langevin which houses the worlds most intense steady-mode neutron source. For UCN with a tiny vertical velocity component, quantum mechanics comes into play: Schrödinger’s equation with the linear gravity potential tells us, that bound states ψ_k of these UCN with macroscopic size should exist:

$$\left(-\frac{\hbar^2}{2m_i} \frac{\partial^2}{\partial z^2} + m_g g z\right) \psi_k = i\hbar \frac{\partial}{\partial t} \psi_k. \quad (1)$$

Here, m_i and m_g are the inertial and gravitational mass of the neutron, g corresponds to the local acceleration of the earth, and z denotes the height over the glass mirror. The equation can be transformed in order to be dimensionless using a substitution $z \rightarrow z/z_0$, $E \rightarrow E/E_0$, and $t \rightarrow t/t_0$. The corresponding scaling factors read

$$z_0 = \sqrt[3]{\frac{\hbar^2}{2m_i m_g}} \approx 5.9 \text{ } \mu\text{m}, \quad E_0 = m_g g z_0 \approx 0.6 \text{ peV}, \quad t_0 = \frac{\hbar}{E_0} \approx 1.1 \text{ ms}. \quad (2)$$

The scaling factors define the typical distance and energy scale of any experiment with gravitationally bound UCN.

The solutions of Schrödinger’s equation are the well-known Airy-functions. In Fig. 1, the first five states are shown. The eigen energies depend solely on the neutron’s inertial and gravitational mass, Planck’s constant, the zeros of the Airy function and the local acceleration of the earth.

Their actual values are in the pico-eV range. Typical sizes of the states are in the range of a few ten microns. Their detection using position-sensitive detectors is feasible.

In order to perform quantum experiments with these states, a state preparation mechanism is needed. One possibility is the introduction of a second neutron mirror with a rough mirror surface, which acts as a boundary condition from top. This new boundary condition has two effects: On the one hand, it influences the shape and eigen energies of the quantum states. On the other hand, it effectively removes higher states from the system, because higher states have a significantly larger overlap with the rough mirror surface, and are in this way scattered off the experiment and absorbed. In fact, quantum states were observed in that way by measuring the surviving neutrons as a function of height of top mirror in a transmission experiment^{2,3,4}. These earlier experiments with neutrons are presented in a review⁵.

In this article, we present two different kind of experiments with well-prepared wave packets of gravitationally bound quantum states: one might imagine to detect the states itself using a position-sensitive detector with micron-resolution. For this purpose, a well-defined wave packet is dropped a step of a few ten microns. This converts the originally prepared wave packet into a super-position of higher states, which evolve with different timing $e^{-iE_k/\hbar t}$. The time evolution of this so-called Quantum Bouncing Ball (QBB) is shown in Fig. 2. It can be monitored using

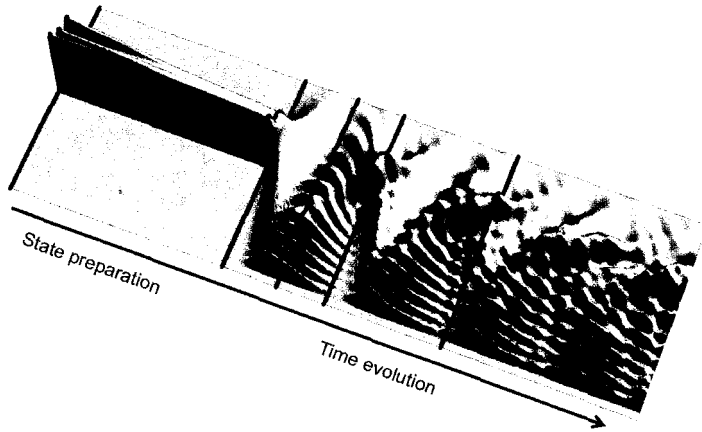


Figure 2 – The simulated so-called quantum carpet shows the time-evolution of the wave function of the neutron after falling down the step.

position-sensitive detectors. First results of our measurements in 2014 will be presented in section 4.

A second approach takes advantage of the fact that the eigen energies of the states are not equidistant. In fact, the difference in energy of any two states is unique, which allows to treat any two state as effective two-level-system. This principally allows for the implementation of the powerful measuring techniques of quantum physics - resonance spectroscopy. Here, one prepares a wave packet of state $|p\rangle$. Then, one exposes the system to a periodic perturbation with an oscillation frequency ω and oscillation strength a . Using an appropriate oscillation strength, the system will be driven into state $|q\rangle$ close to the resonance condition $E_q - E_p \approx \hbar\omega$. As a third step, the wave packet is analysed with respect to state $|p\rangle$ using the same mechanism as for the preparation process. The rate of neutrons is recorded versus the oscillation frequency and amplitude. The method converts the measurement of an unknown quantity of energy into a frequency measurement, which can be done with incredibly high precision. In contrast to all other resonance spectroscopy experi-

ments, the described resonance method is not linked to any electro-magnetic force as the transition is induced by mechanical oscillations. However, other groups pursue also electro-magnetically induced transitions⁶. We refer to this method as gravity resonance spectroscopy (GRS). The expected sensitivity was outlined in⁷.

3 Progress on Gravity Resonance Spectroscopy

Last Moriond conference, we reported on the first realization of the second experimental technique described in section 2, realized in a simplified setup^{8,9}: Here, the state preparation, transition and analysis took place simultaneously. As was shown¹⁰, this simplified setup leads to the same set of Rabi's differential equations, complicated with damping terms. Moreover, the system had to be treated as an effective three-level system, because the transitions $|1\rangle \leftrightarrow |2\rangle$ and $|2\rangle \leftrightarrow |3\rangle$ were close due to the second boundary condition from the rough top mirror. The advantage was a very simple and easy-to-control experimental setup, which is crucial for a successful first-time realization of an experiment.

As these measurements were still statistically limited, they were repeated in two different experiments. The results are shown in Fig. 3 and published and described in¹¹. In these measurements,

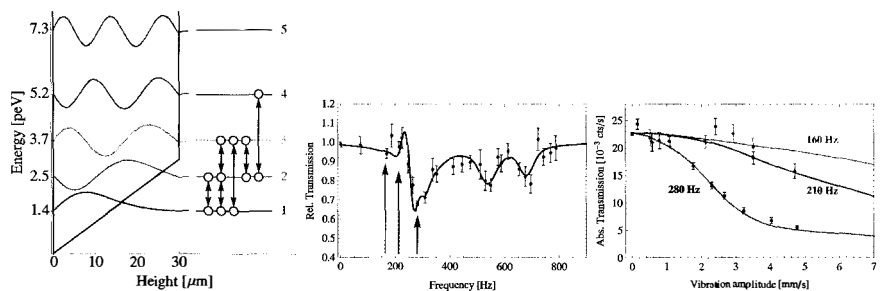


Figure 3 – *Left*: The first five wave functions of a neutron confined by a mirror at the bottom and on top separated by 30 μm . The many transitions that were driven are indicated by arrows. *Middle*: The transmission at the detector is shown in dependency of the oscillation frequency applied to the system. The rich structure due to the effective three-level system can be seen. The coloured arrow indicate the frequencies which are shown in the sub-figure to the *right*. *Right*: The transmission decreases with the oscillation amplitude for frequencies close to resonance. Due to the damping in the system no state revival is observed.

the transitions $|1\rangle \leftrightarrow |3\rangle$, $|2\rangle \leftrightarrow |4\rangle$, and the three-state cascade system $|1\rangle \leftrightarrow |2\rangle \leftrightarrow |3\rangle$ are identified. Moreover, damped Rabi oscillations for the cascade system were studied. The neutron flux dropped close to the resonance condition ($\omega/2\pi \approx 280\text{Hz}$) with respect to the oscillation strength. On the opposite, the flux remained high, when the resonance condition was not fulfilled.

A careful analysis of systematic effects was carried out. The main effect arises due to the rough surface of the upper glass mirror and its influence to the neutrons and its quantum states. While the surface roughness can be measured, its influence on the quantum states is more difficult to predict. The measurements on the roughness were performed using secondary emission microscopy and a mechanical surface roughness scanner, which gave similar results. The influence on the transition frequencies was deduced by large numerical simulations on a super computer.

As a result, we concluded that all systematic effects due to the roughness are well below the 10^{-14} eV level, which was the level of precision of the experiment. Therefore, we were able to set experimental constraints on the existence of hypothetical Non-Newtonian short-range forces. The experimental limit for the existence of hypothetical chameleon scalar fields improved the existing limit by five orders of magnitude and was the reason for the community of atom interferometry to build dedicated experiments to search for such mechanisms, too. A first result was presented in this Moriond conference¹².

The next generation GRS experiment we employed, used a three part realisation of Rabis method (see figure 4). The three steps preparation, excitation and analysis are now implemented in three physically distinct regions. The major difference is that in the second region where the excitation between the different quantum levels takes place, no upper mirror confines the neutron from above. Compared to the one-part setup, no additional energy shift of the states dependant on the slit height occurs, such that the energy of the states only depends on the values mentioned in section two. This opens up the possibility to determine the inertial and the gravitational mass of the neutron at the same time with the current generation of the experiment¹³.

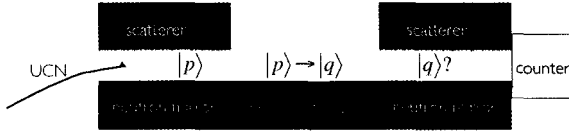


Figure 4 – A GRS setup realisation with its three regions for preparation, excitation and analysis. The neutron travels through the setup from left to right and if it survives the setup, it is detected at the neutron counter. Ideally, first the neutron is prepared in the state $|p\rangle$, then the transition to state $|q\rangle$ can be controlled. Finally only the state $|q\rangle$ is which leads to a count-rate drop upon successful transition. In the middle region no upper mirror is present.

The move to a three part setup came at the cost of increased experimental complexity as more mirrors were used and their alignment to each other needed to be guaranteed. With improved methods we were able to keep gaps and steps at a level without any influence on the experiment.

Figure 5 shows all measurement performed in a 2D contour plot. The theoretical transmission curve with the parameters obtained by a fit for the transitions $|1\rangle \leftrightarrow |3\rangle$ and $|1\rangle \leftrightarrow |4\rangle$ is plotted as contour. The dips of the transmission are visible and correspond to successful excitations into the higher state. The frequencies of the transitions $|1\rangle \leftrightarrow |3\rangle$ and $|1\rangle \leftrightarrow |4\rangle$ were found at $464.1_{-1.1}^{+1.1}$ Hz and $648.8_{-1.6}^{+1.5}$ Hz respectively. Again, the experiment was statistically limited.

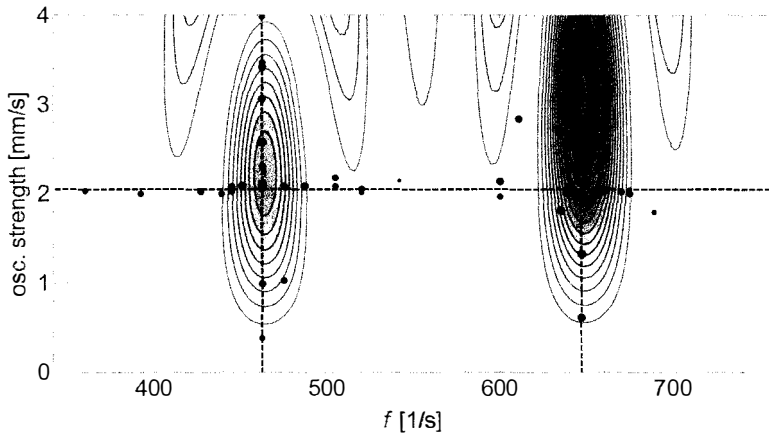


Figure 5 – Contour plot of the transmission signal as a function of the oscillation strength and frequency f . The coloured dots show the parameters used in the measurements. The colouring of the contour plot show the dips in the transmissions from the transitions $|1\rangle \leftrightarrow |3\rangle$ and $|1\rangle \leftrightarrow |4\rangle$ at 464.1 Hz and 648.8 Hz respectively as obtained by the theory with fitted parameters. The measurements were mainly performed around the same oscillation strength of 2 mm/s. The transitions $|1\rangle \leftrightarrow |3\rangle$ and $|1\rangle \leftrightarrow |4\rangle$ have been also mapped out for varying oscillation strength.

From the measured data, improved limits on the hypothetical chameleon field are expected by two orders of magnitude compared to the previous generation.

4 Realization of a Quantum Bouncing Ball

Gravity resonance spectroscopy offers the possibility to perform very sensitive measurements, because they rely on frequency measurements. These experiments are still strongly limited by statistics, and an improvement by several orders of magnitude seems feasible. Nevertheless, measurements with track detectors are desired, too. The reason is, that GRS measurements probe the energy scale E_0 , while measurements of the spatial probability distribution of the wave packet have access to the distance scale z_0 . As can be seen in Eq. 2, these scales have a different dependence on the inertial and gravitational mass of the neutron. Therefore, the knowledge of z_0 and E_0 allows for a test of the weak equivalence principle (WEP) in the quantum regime, which is conceptionally different from ordinary tests. Here, only one quantum particle is used. Moreover, the experiments offer the possibility to study quantum phenomena like quasi-stationary structures in the time evolution of wave packets, so-called quantum carpets, as well as quantum phenomena without classical analoga like collapses and revivals of the wave function. Other so far unobserved aspects of the QBB like collapse and revival of the wave function are presented in¹⁴.

These measurements are challenging, because position-sensitive detectors with high efficiency, very low background and a spatial resolution of approx. 1 μm are needed. Currently, we use nuclear track detectors with a converter layer of $^{10}\text{Boron}$ ¹⁵. First quantum states measurements with time evolution of a coherent superposition are presented in^{16,17}. There are several projects^{18,19,20} under development in order to build "online" detectors, which have the advantage to see the results immediately. A measurement of a neutron spatial density distribution using nuclear track detectors with uranium coating can be found in²¹.

A second challenging point is the implementation of a step between two mirrors, which is precisely known and stable on a level of much less than a micron for a few days, the typical time to take one snapshot. We solve the problem of stability by mounting the mirrors on two nanopositioning tables, that are working in closed-loop operation. The step is measured by capacitive sensors, which directly monitor the mirror surfaces (which are coated with aluminium for that purpose). The sensors are moved over the surfaces using another micropositioning table and monitor the step in this way. The positioning errors of this micropositioning table (roll-, pitch- and yaw angle) would directly affect the measurement of the step. Therefore, the movement of the table is measured using three additional capacitive sensors that measure the distance to a large measurement plane, which consists of another glass mirror coated with aluminium. In this way, the step was controlled on a stability level of 10 nm.

In 2014, the actual measurements were again carried out at the beam position PF2 at the ILL. Nine snapshots of the Quantum Bouncing Ball were taken within 75 days of beam time. Here, we present the first two snapshots, see Fig. 6. An experimental scheme of the experiment can be found in the top figure. Neutrons traverse the setup from left to right. They are prepared into a wave packet of the lowest states in a 30 μm wide slit of a flat glass mirror on bottom and a rough one on top. The step was adjusted to either 20 or 30 μm . In order to realize different evolution times, the length of the second mirror was adapted. The figure in the middle shows the height profile of the neutrons directly after the preparation process. It verifies, that the neutrons form wave packets containing only the lower states. The lower figure shows one snapshot of the Quantum Bouncing Ball, taken with a step size of 20 μm and a mirror length of the second mirror of 51 mm. This is the position where the expectation value in height should reach its minimum, and the quantum wiggles of the quantum carpet should be at maximal visibility. Indeed, the quantum carpet reaches a contrast of approx. 50%.

Clearly, the microscope calibration enters the result of the extracted value for the distance scale z_0 directly. Currently, the microscope is calibrated to an accuracy of 1%. The statistical error on the common data set is well below this value. Therefore, the data evaluation process and microscope calibration is currently on-going.

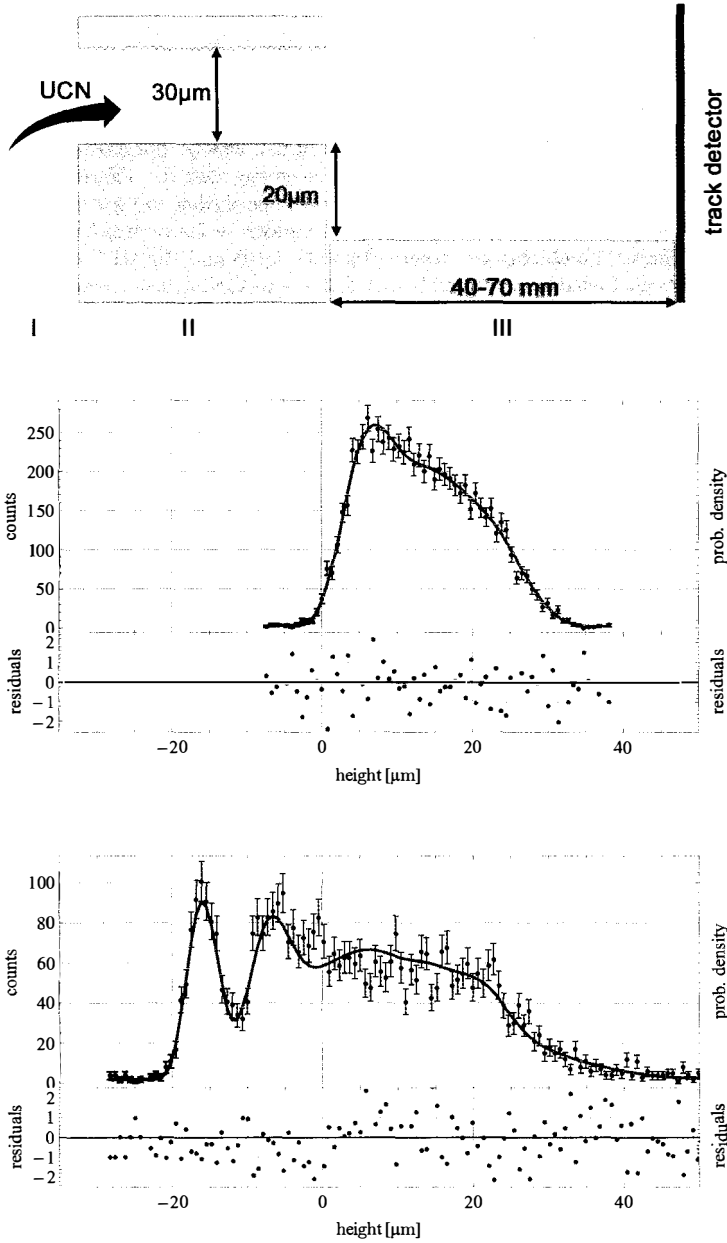


Figure 6 – Top: Experimental Scheme. The neutrons pass through the setup from left to right. After a preparation into a superposition of the lowest states, the wave packet is dropped a step of 20 microns and evolves in time. The probability density is recorded using track detectors. Middle/bottom: The spatial probability distribution measured directly at the step and in a distance of 51 mm behind the step. The measurements agree well with the theoretical prediction, a coherent superposition of the gravitationally bound quantum states.

5 Outlook

It is quite natural to follow the path of history and extend GRS currently using Rabi's method with Ramsey's method of separate oscillating fields⁷. An additional region of state evolution between two oscillating regions will steepen the transmission signal and thus enhance the energy sensitivity of the setup. This can be used to search for a plethora of new effects. For example a hypothetical electric charge of the neutron might be detectable by the energy shift the different states obtain in an external electric field²². The QBB with improved spatial resolution and systematically rigorous experiments with sufficient count-rate statistic will demonstrate fascinating and simultaneously simple quantum effects. Combining the results from the QBB and the GRS measurements will allow to test the Weak Equivalence Principle as GRS probes the intrinsic energy scale E_0 of the system while QBB measures the length scale z_0 .

The continuous improvement of the qBounce experiments, both the Quantum Bouncing Ball and Gravity Resonance Spectroscopy show promising potential to tackle the questions about new Fifth Forces.

Acknowledgments

We thank D. Seiler (TU München) for preparing the spatial resolution detectors and R. Stadler (Univ. of Heidelberg) for preparing the rough mirror surface. We thank T. Brenner (ILL) for technical support. We gratefully acknowledge support from the Austrian Fonds zur Förderung der Wissenschaftlichen Forschung (FWF) under Contract No. I529-N20, and No. I531-N20, No. P26781-N20, and the German Research Foundation (DFG) as part of the Priority Programme (SPP) 1491. We also gratefully acknowledge support from the French Agence Nationale de la Recherche (ANR) under Contract No. ANR-2011-ISO4-007-02 and FWF No. I862-N20, Programme Blanc International – SIMI4-Physique.

References

1. J. Gea-Banacloche, *American Journal of Physics* **67**, 776 (1999).
2. V.V. Nesvizhevsky, *et al.*, *Nature* **415**, 297 (2002).
3. H. Abele, *2003 Gravitational Waves and Experimental Gravity*, ed. J. T. Vân, C. Barthelemy (2003).
4. A. Westphal *et al.*, *The European Physical Journal C* **51**, 367 (2007).
5. H. Abele, *Prog. Part. Nucl. Phys.* **60**, 1 (2008).
6. G. Pignol, *Advances in High Energy Physics* **1**, 628125 (2014).
7. Abele H *et al.* *Phys. Rev. D* **81**, 065019 (2010).
8. T. Jenke *et al.*, *Nature Physics* **7**, 468 (2011).
9. T. Jenke *et al.* in *2011 Gravitational Waves and Experimental Gravity*, ed. E. Aug e *et al.* (Th e Gioi, Vietnam, 2011).
10. T. Jenke, qBounce - vom Quantum Bouncer zur Gravitationsresonanzspektroskopie, *Dissertation* (2011).
11. T. Jenke *et al.*, *Phys. Rev. Lett.* **112**, 151105 (2014).
12. P. Hamilton *et al.*, arxiv , 1502.03888 (2015).
13. E. Kajari, *et al.*, *Applied Physics B* **100**, 1 (2010).
14. H. Abele, H. Leeb, *New Journal of Physics* **14**, 055010 (2012).
15. T. Jenke *et al.*, *Nucl. Instr. and Meth. A* **732**, 1 (2013).
16. H. Abele *et al.*, *Nuclear Physics A* **827**, 593c (2009).
17. T. Jenke *et al.*, *Nucl. Instrum. Methods A* **611**, 318 (2009).
18. J. Jakubek, *et al.*, *Nucl. Instrum. Methods A* **600**, 651 (2009).
19. Th. Lauer, *et al.*, *The European Physical Journal A* **47**, 150 (2011).
20. Y. Kamiya, *et al.*, *Advances in High Energy Physics* **2014**, 859241 (2014).
21. V.V. Nesvizhevsky, *et al.*, *The European Physical Journal C* **40**, 479 (2005).
22. K. Durstberger-Rennhofer, T. Jenke, H. Abele, *Phys. Rev. D* **84**, 036004 (2011).

FROM PRECISION SPECTROSCOPY TO FUNDAMENTAL COSMOLOGY

C.J.A.P. MARTINS, M.C. FERREIRA, A.C.O. LEITE, A.M.M. PINHO, S.M. JOÃO, P.M.M. LEAL,
I.S.A.B. MOTA, L.B. VENTURA, P.M.T. VIANEZ and P.E. VIELZEUF
*Centro de Astrofísica da Universidade do Porto and IA-Porto,
Rua das Estrelas S/N, 4150-762 Porto, Portugal*

We discuss the importance of astrophysical tests of the stability of fundamental couplings such as the fine-structure constant α and the proton-to-electron mass ratio μ as direct and optimal probes of fundamental physics and cosmology. We present a short overview of the current state-of-the-art in the field, highlighting the contributions of the CAUP Dark Side team. We also briefly outline the opportunities for significantly tighter tests afforded by forthcoming facilities such as ESPRESSO and ELT-HIRES.

1 Introduction

We now know that fundamental scalar fields are part of Nature's building blocks. An obvious follow-up question is then whether the Higgs has a cosmological counterpart. Even though the answer to this question is at present unknown, scalar fields already play a key role in most paradigms of modern cosmology, having been invoked to yield, *inter alia*

- A period of exponential expansion of the early universe (inflation)
- Cosmological phase transitions and their relics (cosmic defects)
- The dynamical dark energy powering current acceleration phase
- Spacetime variations of Nature's fundamental couplings

Even more important than each of these is the fact that they don't come alone. Whenever a dynamical scalar field is responsible for one of these paradigms, it will generically also manifest itself through some of the others. This will provide us with key consistency tests.

This contribution highlights this point by focusing on tests of the stability of fundamental couplings and their relation to dynamical dark energy. It's well known that fundamental couplings run with energy, and in many (or indeed most) models they will equally naturally roll in time and ramble in space (meaning that they may depend on the local environment). Therefore astrophysical (as well as local) tests of their stability provide us with optimal probes of fundamental cosmology. In what follows we will present the state-of-the-art astrophysical measurements, and highlight some of their implications.

2 The UVES Large Program and consistency tests

Recent work of Webb *et al.*¹ has led to the suggestion of a spatial dipole on the value of the fine-structure constant α , with a few parts-per-million (ppm) amplitude and in the approximate redshift range $0.5 < z < 4.0$. The statistical significance is more than four standard deviations

(although the data is too sparse to distinguish between a pure spatial dipole and a dependence on lookback time), and the obvious question is whether this is a sign of new physics or a manifestation of hidden systematics. One reason for caution is that the results were obtained with archival data, which was taken for other purposes and is not optimised for the present one. Improving the sensitivity of these tests is a key driver for future instruments.

Meanwhile, an international collaboration is carrying out a dedicated 40-night UVES Large Program, with similar goals. This is the only large program dedicated to varying couplings, using an optimised sample and methodology. Among other improvements the calibration lamps are attached to science exposures (we don't reset the cross-disperser encoding the position for each exposure) and we observe bright (mag 9-11) asteroids at twilight (to monitor radial velocity accuracy of UVES and the optical alignments). Our sample selection criteria included multiple absorption systems, brightness (S/N), high redshift (due to the presence of the sensitive FeII 1608 transition), simplicity, narrow components at sensitive wavelengths, and no line broadening/saturation. Our data has $R \sim 60000$, $S/N \sim 100$ per pixel and a potential accuracy of 1-2ppm per system, where photon noise and calibration errors are comparable. Our goal is to reach 2ppm per system, and 0.5ppm for the full sample. All active observational groups are involved and we have been comparing and optimising different analysis pipelines; we have also introduced blind analysis techniques.

The first results of this effort have already been reported^{2,3,4}. So far our focus has been on understanding the data and optimising data reduction pipelines. We have identified³ wavelength-dependent velocity drifts (corrected with bright asteroid data) and intra-order ($\delta \sim 200m/s$) and long-range distortions on UVES (which were also identified in HARPS and Keck-HIRES). We have also shown⁴ that directly comparing spectra (from the world's 3 largest optical telescopes) and 'super-calibrating' with asteroid and iodine-cell tests allows removal of long-range distortions. Our currently published results are compatible both with the null result and with the dipole^{2,4}. The full sample analysis is ongoing, and more results should be appearing soon.

Measurements of α and μ can be obtained in the UV/optical; in the radio/mm band one can usually measure combinations of them. Parts per million sensitivity is nominally easier to reach in the radio, but usually at significantly lower redshift—the arrival of ALMA may however change this. Key consistency tests between optical and radio measurements are now possible^{5,6}, and suggest slight discrepancies. The radio sensitivity is even better within the Galaxy (i.e., at $z = 0$), where one can search for environmental dependencies. For α no variation is seen at the 0.1 ppm level⁷ (previously reported constraints⁸ were based on nonphysical assumptions), while for μ no variation is seen at 0.05 ppm level⁹.

These precision spectroscopy tests are akin to finding exoplanets, except much harder: the sources are much fainter, and only a few lines are clean. Indeed these tests require observing procedures—and instruments—beyond current facilities. One needs customised data reduction pipelines, including careful wavelength calibration procedures, and ideally must calibrate with laser frequency combs, not ThAr lamps or I2 cells. A new generation of high-resolution, ultra-stable spectrographs will have these measurements as key driver and is expected to significantly improve on current tests. Notable among these are ESPRESSO at the VLT (whose commissioning is currently foreseen for late 2016, and able to work both in 1UT and in 4 UT mode) and ELT-HIRES at the E-ELT (in the mid to late 2020s).

3 Cosmological constraints

The Universe seems dominated by component whose gravitational behaviour is similar to that of a cosmological constant. This may indeed turn out to be the explanation, but a dynamical scalar field is (arguably) more likely. Such a field must be slow-rolling (which is mandatory for a negative pressure) and be dominating the dynamics around the present day (which provides it with a rough normalisation). One can then show¹⁰ that couplings of this field will lead to po-

tentially observable long-range forces and varying fundamental couplings. These measurements (whether they are detections of null results) will constrain fundamental physics and cosmology, and this ensures a 'minimum guaranteed science'.

The entire zoo of possible varying α models can be split into just two physically different classes. Class I models stem from the 'minimal' assumption that the same degree of freedom is responsible for dark energy and varying α ; in this case the latter's evolution is parametrically determined. For this class of models a joint analysis¹¹ of current QSO, atomic Clock and Cosmological (type Ia supernova and Hubble parameter) data leads to the following marginalised constraints for the coupling of the scalar field to the electromagnetic sector

$$|\zeta| < 5 \times 10^{-6} \quad (2 \text{ sigma}) \quad (1)$$

and for the dark energy equation of state

$$|1 + w_0| < 0.06 \quad (3 \text{ sigma}) \quad (2)$$

This assumed a fiducial model with a constant dark energy equation of state, but this turns out to be a good assumption¹² since the current constraints are dominated by the atomic clocks constraint, and this is only sensitive to the value of the dark energy equation of state today.

Moreover, constraints on ζ can be expressed as constraints on the Eotvos parameter quantifying violations of the Weak Equivalence Principle^{13,14}. We find¹²

$$\eta < 3 \times 10^{-14} \quad (2 \text{ sigma}) \quad (3)$$

This is about one order of magnitude stronger than current direct bounds from torsion balance and lunar laser ranging experiments. However, it is testable by MICROSCOPE whose expected sensitivity is $\eta \sim 10^{-15}$; should it find violations at a level higher than the above constraint, this would exclude this class of models (or alternatively point to systematics in some of the data used in the analysis). The expected η sensitivities of future high-resolution ultra-stable spectrographs are $\text{few} \times 10^{-16}$ for ESPRESSO and 10^{-18} (comparable to STEP) for ELT-HIRES.

It is well known¹⁵ that standard cosmological probes (SNe, etc) are of limited use as dark energy probes: since the field is slow-rolling when dynamically important, a convincing detection of $w(z) \neq -1$ will be tough at low redshifts. We must probe the deep matter era regime, where the dynamics of the hypothetical scalar field is fastest. Fundamental couplings ideally probe scalar field dynamics beyond the domination regime^{16,17,18}, and ALMA, ESPRESSO and ELT-HIRES will map the dark side out to $z \sim 4$. (This is further discussed in Ana Catarina Leite's contribution in these proceedings) Key synergies with other probes, such as Euclid¹⁹ and redshift drift^{20,21} are also noteworthy (and have been quantified), and a roadmap for the field has been outlined elsewhere²².

Class II models are the ones where, contrary to natural theoretical expectations, the dynamical degree of freedom leading to the α variation does not provide all the dark energy (in which case the aforementioned link to dark energy is lost). Models in this class can be identified via $w(z)$ consistency tests, and redshift drift measurements are ideal for this²⁰. Examples of models in this class that have been recently constrained include BSBM toy models²³ and string-inspired Runaway dilaton models²⁴. For the former, the current α measurements lead to the bound

$$\eta < 5 \times 10^{-14}. \quad (4)$$

Note that even if this degree of freedom does not dominate at low redshift it can bias cosmological parameter estimations. For example, if α varies with redshift then the peak luminosity of type Ia supernovae will be redshift-dependent. This issue has been recently studied in the Euclid consortium context¹⁹, and although the effect is relatively small for ppm-level variations of α it could be measured by future supernova surveys.

4 Conclusions

The observational evidence for the acceleration of the universe demonstrates that our canonical theories of cosmology and particle physics are incomplete, if not incorrect. Tests of the stability of fundamental couplings are a direct, optimal probe of this new physics. At present it is clear that nothing is varying at the 10^{-5} level, which is already a very significant constraint (stronger than the Cassini bound, for example) and excludes a number of otherwise cosmologically viable models. At the ppm level things are less clear, but there's a very strong growth of activity and interest in the field.

Improvements in sensitivity of 2 or even 3 orders of magnitude are foreseen, but it is also clear that doing things properly is tough (and requires dedicated, optimised calibration and data reduction procedures). Moreover, dedicated instruments are also coming, leading to a new generation of precision consistency tests. These will be the ideal complement to other cosmological and local (Equivalence Principle) tests as well as to entirely new observational probes (most notably the redshift drift). There are also important synergies with other facilities, including ALMA, Euclid and the SKA, which are currently being explored.

Acknowledgements

This work was done in the context of project PTDC/FIS/111725/2009 (FCT, Portugal). CJM is also supported by an FCT Research Professorship, contract reference IF/00064/2012, funded by FCT/MCTES (Portugal) and POPH/FSE (EC). ACL is also supported by the Gulbenkian Foundation through *Programa de Estímulo à Investigação 2014*, grant number 2148613525.

References

1. J.K. Webb *et al.*, *Phys. Rev. Lett.* **107**, 191101 (2011).
2. P. Molaro *et al.*, *A. & A.* **555**, A68 (2013).
3. H. Rahmani *et al.*, *M.N.R.A.S.* **435**, 861 (2013).
4. T.M. Evans *et al.*, *M.N.R.A.S.* **445**, 128 (2014).
5. M.C. Ferreira *et al.*, *Phys. Rev. D* **89**, 083011 (2014).
6. M.C. Ferreira & C.J.A.P. Martins, submitted (2015).
7. S.M. João, C.J.A.P. Martins, I.S.A.B. Mota & P.M.T. Vianez, submitted (2015).
8. S. Truppe *et al.*, *Nature Comm.* **4**, 2600 (2013).
9. S.A. Levshakov *et al.*, *A. & A.* **559**, A91 (2013).
10. S.M. Carroll, *Phys. Rev. Lett.* **81**, 3067 (1998).
11. C.J.A.P. Martins & A.M.M. Pinho, *Phys. Rev. D* **91**, 103501 (2015).
12. C.J.A.P. Martins *et al.*, submitted (2015).
13. G.R. Dvali & M. Zaldarriaga, *Phys. Rev. Lett.* **88**, 091303 (2002).
14. T. Chiba & K. Kohri, *Prog.Theor.Phys.* **107**, 631 (2002).
15. I. Maor, R. Brustein, J. McMahon & P.J. Steinhardt, *Phys. Rev. D* **65**, 123003 (2002).
16. L. Amendola *et al.*, *Phys. Rev. D* **86**, 063515 (2012).
17. A.C.O. Leite, C.J.A.P. Martins, P.O.J. Pedrosa & N.J. Nunes, *Phys. Rev. D* **90**, 063519 (2014).
18. A.C.O. Leite & C.J.A.P. Martins, *Phys. Rev. D* **91**, in press (2015).
19. E. Calabrese *et al.*, *Phys. Rev. D* **89**, 083509 (2014).
20. P.E. Vielzeuf & C.J.A.P. Martins, *Phys. Rev. D* **85**, 087301 (2012).
21. M. Martinelli, S. Pandolfi, C.J.A.P. Martins & P.E. Vielzeuf, *Phys. Rev. D* **86**, 123001 (2012).
22. C.J.A.P. Martins, *Gen.Rel.Grav.* **47**, 1 (2015).
23. P.M.M. Leal, C.J.A.P. Martins & L.B. Ventura, *Phys. Rev. D* **90**, 027305 (2014).
24. C.J.A.P. Martins *et al.*, *Phys. Lett. B* **743**, 377 (2015).

OPTIMIZATION OF ESPRESSO FUNDAMENTAL PHYSICS TESTS

A. C. O. LEITE and C. J. A. P. MARTINS

Centro de Astrofísica, Universidade do Porto, Rua das Estrelas, 4150-762 Porto, Portugal

ESPRESSO is a high-resolution-ultra-stable spectrograph for the VLT, whose commissioning is expected in late 2016. One of its key science drivers is to test the stability of fundamental couplings such as the fine structure constant with unprecedented accuracy and control of possible systematics. The criteria for selecting an optimal target list for the Consortium's GTO is an ongoing work and the present forecasts of the impact that this sample will have on fundamental physics and cosmology is discussed. In particular, we discuss how these measurements and future supernova datasets will constrain the behaviour of dark energy deep in the matter era (i.e., in the redshift range $1.5 < z < 2.5$).

1 Current Data Sets and ESPRESSO

ESPRESSO is a high-resolution-ultra-stable spectrograph for the VLT, that will contribute to test the stability of fundamental couplings¹. In order to choose the most suitable targets that can achieve higher constrains on the variation of the fine structure constant, α , we will have to define the characteristics of a good system, and then in particular for ESPRESSO selection, take into account the effect of the shorter wavelength coverage compared with previous measurements from UVES and Keck spectrographs^{2,3,4,5,6,7,8,9,10}.

The combined existing datasets are represented in the Figure 1, measurements that loose some transitions are represented in red crosses. Its visible a redshift coverage degradation due to this effect.

These type of measurements are important by themselves for testing the stability of α , but can also be used to constrain dark energy. In the next section we will describe how astrophysical measurements of nature's dimensionless fundamental coupling constants can be used to study the properties of Dark Energy¹¹ and the formalism used in order to do forecasts to future programs.

2 Formalism and Forecasts

Our formalism is described in Amendola et al.¹², to which we refer the reader for further details. Here we will simply provide a brief summary of the features that will be relevant for our subsequent comparison with data.

One can divide the relevant redshift range into N bins such that in bin i the equation of state parameter takes the value w_i . The precision on the measurement of w_i can be inferred from the Fisher matrix of the parameters w_i . If the Fisher matrix is diagonalized, it defines a new basis in which the new coefficients α_i are uncorrelated. In this processes one also obtains the eigenvalues λ_i (ordered from largest to smallest) and the variance of the new parameters, $\sigma_i^2 = 1/\lambda_i$.

We consider models for which the variation of α is linearly proportional to the displacement of a scalar field, and further assume that this field is a quintessence type field, i.e. responsible

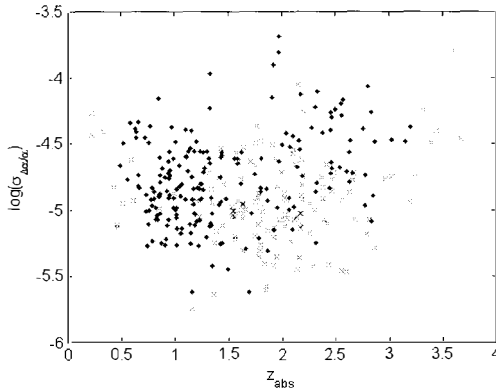


Figure 1 – Compilation of current datasets of the variation of the fine structure constant measurements, represented in the figure are the uncertainties and the respective redshifts. In red crosses are represented the data that loose some transitions in the ESPRESSO wavelength range and in blue dots the ones that don't.

for the current acceleration of the Universe. We take the coupling between the scalar field and electromagnetism to be:

$$\mathcal{L}_{\phi F} = -\frac{1}{4}B_F(\phi)F_{\mu\nu}F^{\mu\nu}, \quad (1)$$

where the gauge kinetic function $B_F(\phi) = 1 - \zeta(\phi - \phi_0)$, $\kappa^2 = 8\pi G$ and ζ is a constant to be marginalized over. This can be seen as the first term of a Taylor expansion, and should be a good approximation if the field is slowly varying at low redshift. Then, the evolution of α is given by

$$\frac{\Delta\alpha}{\alpha} \equiv \frac{\alpha - \alpha_0}{\alpha_0} = \zeta\kappa(\phi - \phi_0). \quad (2)$$

For a flat Friedmann-Lemaître-Robertson-Walker Universe with a canonical scalar field, $\dot{\phi}^2 = (1 + w(z))\rho_\phi$, hence, for a given dependence of the equation of state parameter $w(z)$ with redshift, the scalar field evolves as

$$\phi(z) - \phi_0 = \frac{\sqrt{3}}{\kappa} \int_0^z \sqrt{1 + w(z)} \left(1 + \frac{\rho_m}{\rho_\phi}\right)^{-1/2} \frac{dz}{1 + z}. \quad (3)$$

where we have chosen the positive root of the solution.

From this, one can calculate the Fisher matrix using standard techniques, as discussed in Amendola et al.¹². We will consider two fiducial forms, presented in that same work, for the equation of state parameter: $w_c(z) = -0.9$ and $w_s(z) = -0.5 + 0.5\tanh(z - 1.5)$. In what follows we will refer to these cases as the constant and step fiducial models.

2.1 Future Data and Results

We will consider three datasets for Type Ia supernovas and two for the fine-structure constant measurements. The detailed information of this datasets, analysis and results are described in detail in Leite and Martins¹⁴ and summarized below.

For Type Ia supernovas we will consider the following datasets: **LOW**: A low-redshift sample, of 3000 supernovas uniformly distributed in the redshift range $0 < z < 1.7$, with an uncertainty on the magnitude of $\sigma_m = 0.11$; **MID**: An intermediate redshift sample, of 1700 supernovas uniformly distributed in the redshift range $0.75 < z < 1.5$ and the same σ_m as

before; **ELT** and **TMT**: A high-redshift sample of supernovas identified by JWST NIRCam imaging and then characterized by extremely large telescopes on the ground such as the E-ELT and the TMT. Based on their respective Phase A studies we assume a sample of 50 supernovas in the range $1 < z < 5$ for the E-ELT and a sample of 250 supernovas in the range $1 < z < 3$ for the TMT. We assume a uniform distribution in the respective redshift ranges and the same σ_m as before.

For the fine-structure constant measurements we will focus on the ESPRESSO (ESP) and its successor ELT-HIRES (HRS) for the E-ELT¹⁵. We explored in Leite and Martins¹⁴ two scenarios: **Baseline**, in which we assumed measurements in 30 systems with uncertainty $\sigma_{\Delta\alpha/\alpha} = 6 \times 10^7$ for ESPRESSO and 100 systems with $\sigma_{\Delta\alpha/\alpha} = 1 \times 10^7$ for ELT-HIRES, uniformly distributed in the redshift range $0.5 < z < 4$. This is meant to represent what we can confidently expect to achieve from each spectrograph; **Ideal** scenario, in which we assumed 100 systems with $\sigma_{\Delta\alpha/\alpha} = 2 \times 10^7$ for ESPRESSO and 150 systems with $\sigma_{\Delta\alpha/\alpha} = 3 \times 10^8$ for ELT-HIRES. This is optimistic both in the uncertainty of individual measurements and in the number of measurements.

For our PCA analysis we will in general assume 30 redshift bins in the range $0 \leq z \leq 4$. In the case where ELT supernovas are used, the last bin is extended until $z = 5$. In order to quantify gains in sensitivity for each case using the PCA, we used a ‘figure of merit’ defined as the inverse of the product of the uncertainties of the two best determined modes, $FoM = 1/(\sigma_1\sigma_2)$. We will adopt this to compare gains of different scenarios.

The ‘figures of merit’ for the ideal case of α measurements are shown in Table 1, for the Constant(c) and Step(s) equation of state of dark energy. Here we present the table for the ideal scenarios because the differences from case to case are more noticeable, but information on the baseline scenario and further exploitation of the different cases are presented in Leite and Martins¹⁴.

We note that the gains in sensitivity to the dark energy equation of state due to ESPRESSO measurements are significant (up to about a factor of 2) in the Ideal case. ELT-HIRES, will lead to dramatic improvements (sometimes more than a factor of 50). Its also noteworthy that judging by this ‘figure of merit’ diagnostic the impact of the E-ELT supernovas is always greater than that of the TMT supernovas. Note that for the case of supernovas only, the 50 ELT supernovas (uniformly distributed in the range $1 < z < 5$) would not only be more constraining than the 250 TMT supernovas (in the range $1 < z < 3$) but also more constraining than the 1700 MID supernovas (in the range $0.75 < z < 1.5$). The results of this comparison do highlight the importance of the redshift lever arm in characterizing dynamical dark energy.

3 Conclusions

The ESPRESSO target selection for the GTO has to be very meticulous, since the limited time dedicated to test the stability of fundamental constants. Its impact on cosmology as here presented by the PCA-based forecasts can be achieved with a beyond GTO program. The limited wavelength coverage of ESPRESSO make the ideal range of the measurements to be between 1.0 and 2.5.

We have used previously available PCA-based forecast techniques to quantify the gains in sensitivity expected from constraints on the behaviour of dark energy enabled by forthcoming ground and space-based astronomical facilities. Specifically, we have focused on the reconstruction of the dark energy equation of state, using both future space-based supernova surveys in combination with high-resolution spectroscopic measurements of the fine-structure constant expected from ESPRESSO and the high-resolution ultra-stable spectrograph planned for the E-ELT.

Our results quantitatively confirm that the combination of these two types of measurements, leads to a more complete and robust mapping of the evolution of the equation of state, and that

Table 1: Figures of merit for the dark energy equation of state, assuming the ideal scenario for measurements and 30 redshift bins. For each pair of entries, the top and bottom lines correspond, respectively, to the constant and step fiducial models.

| | Sne only | Sne + ESP | Sne + HRS |
|---------------------|----------|-----------|-----------|
| LOW (c) | 409 | 996 | 58684 |
| LOW (s) | 404 | 554 | 11228 |
| LOW + MID (c) | 839 | 1352 | 58737 |
| LOW + MID (s) | 831 | 955 | 11295 |
| LOW + ELT (c) | 881 | 1515 | 79431 |
| LOW + ELT (s) | 881 | 1064 | 18176 |
| LOW + MID + ELT (c) | 1973 | 2357 | 79639 |
| LOW + MID + ELT (s) | 1971 | 2133 | 18652 |
| LOW + TMT (c) | 631 | 1089 | 58740 |
| LOW + TMT (s) | 634 | 712 | 11335 |
| LOW + MID + TMT (c) | 1253 | 1443 | 58846 |
| LOW + MID + TMT (s) | 1260 | 1328 | 11514 |

a detailed reconstruction between redshift 0 and 2 is within the reach of forthcoming facilities. The combination of the two data sets leads to ‘figure of merit’ improvements that are typically a factor of a few, and more than 50 in ideal circumstances.

Acknowledgments

We are grateful to Luca Amendola, Nelson Nunes and Pedro Pedrosa for many interesting discussions and suggestions in the early stages of this project. This work was done in the context of grant PTDC/FIS/111725/2009 from FCT (Portugal). A.C.L. is supported by the Gulbenkian Foundation through *Programa de Estímulo à Investigação 2014*, grant number 2148613525. C.J.M. is also supported by an FCT Research Professorship, contract reference IF/00064/2012, funded by FCT/MCTES (Portugal) and POPH/FSE (EC).

References

1. F. Pepe et al., *The Messenger* 153, 6 (2013).
2. J. A. King, PhD Thesis (UNSW, 2011), arXiv:1202.6366.
3. M. T. Murphy, Ph.D. Thesis, University of New South Wales (2002).
4. H. Chand, R. Srianand, P. Petitjean & B. Aracil, *Astron. Astrophys.*, 417, 853 (2004).
5. H. Chand, P. Petitjean, R. Srianand & B. Aracil, *Astron. Astrophys.*, 430, 47 (2005).
6. H. Chand, R. Srianand, P. Petitjean, et al., *Astron. Astrophys.*, 451, 45 (2006).
7. S. A. Levshakov, P. Molaro, S. Lopez, et al., *Astron. Astrophys.*, 466, 1077 (2007).
8. P. Molaro, D. Reimers, I. I. Agafonova & S. A. Levshakov, *European Physical Journal Special Topics*, 163, 173 (2008).
9. P. Molaro, M. Centurión, J. B. Whitmore, et al., *Astron. Astrophys.*, 555, A68 (2013).
10. P. Bonifacio, H. Rahmani, J. B. Whitmore, et al., *Astronomische Nachrichten*, 335, 83 (2014).
11. N. J. Nunes and J. E. Lidsey, *Phys. Rev. D* 69, 123511 (2004).
12. L. Amendola et al., *Phys. Rev. D* 86, 063515 (2012).
13. A. C. O. Leite et al., *Phys. Rev. D* 90, 063519 (2014).
14. A. C. O. Leite and C. J. A. P. Martins, *Phys. Rev. D* 91, 103519 (2015).
15. J. Liske et al., Document ESO 204697 Version 1 (2014).

AN EQUIVALENCE PRINCIPLE TEST IN SPACE ON THE WAY TO LAUNCH

MANUEL RODRIGUES*, PIERRE TOUBOUL[◊], QUENTIN BAGHI*, RATANA CHHUN*

* ONERA, 29 avenue de la Division Leclerc, 92320 Chatillon, France

◊ ONERA, Chemin de la Humière, 91123 Palaiseau, France



In 2016, the Microscope satellite should be launched from Kourou by Soyouz and conclude 20 years of instrumental development in order to test the Equivalence Principle at levels of 10^{-15} . The instrument is composed of two differential accelerometers which compare the accelerations of two pairs of body in “free-fall” at 710 km altitude. As a founding principle of the Einstein’s theory of gravitation (General Relativity), the Equivalence Principle verification is a challenging target for most of the alternatives theory: quantum loops, string theory, dilatons, ...

This paper presents the current development status of the mission. It underlines also some specific results obtained from the qualification phase and the on-going development of the data process that should exhibit the mission performance objective.

1 Overview of the mission

The Equivalence Principle (EP) expressed by Einstein as a basis of its theory of General Relativity stipulates that all bodies, independently of their mass or intrinsic composition acquire the same acceleration in the same uniform gravity field. It was tested throughout the years by ground-based experiments with an increasing accuracy which reaches a few 10^{-13} by the Eöt-Wash Group¹. The accuracy of this ground experiment is in particular limited by the local gravity gradients and its fluctuations, by the temperature and the magnetic field variations. The two papers in reference describe some clues for order of magnitude improvement in the future. The currently obtained best results are the following:

Table 1: The best experimental results for testing the EP

| <i>Tests</i> | <i>Ref</i> |
|---|------------|
| Torsion balance: $(\Delta a/a)_{BeTi} = (0.3 \pm 1.8) \times 10^{-13}$ $(\Delta a/a)_{BeAl} = (-0.7 \pm 1.3) \times 10^{-13}$ | 1 |
| Lunar Laser Ranging: $(\Delta a/a)_{EarthMoon} = (-0.8 \pm 1.3) \times 10^{-13}$ | 2 |

In papers ^{3,4}, authors explain how these values constrain the alternative standard models as the dilaton string theory and underline the necessity to go further. This is the motivation of the space MICROSCOPE mission that should improve by two orders of magnitude the best already performed tests. Increasing the accuracy to the ranges predicted by some alternative theories to the General Relativity is therefore crucial to confirm or infrim the equivalence between inertial and gravitational masses at the heart of the metric theories.

Going to space helps to reduce the environment disturbances of the experience, linked to the local gravity fluctuations. By using a drag-free satellite, the instrument is orbiting along a quasi-geodesic trajectory. The drag-free system controls also the torques that helps to finely tune the attitude motion of the satellite against gravity or magnetic torques.

Placed at 710 km of altitude during a mission period of 2 years, the satellite will fly in inertial pointing on Sun synchronous, quasi-polar orbit most of the time as depicted in Figure 1. The Earth constitutes the gravitational source of the experiment. For one measuring axis in the orbital plane, the Earths gravity source has a relative cyclic effect (at orbital frequency, i.e 1.68×10^{-4} Hz). A rotation about the orbital plane axis can be applied to the satellite in order to increase the measurement frequency to 7.59×10^{-4} Hz or 9.27×10^{-4} Hz. These rotations give different conditions of operation with respect to potential systematic error sources: thermal behaviour, pointing stability, magnetic effects...

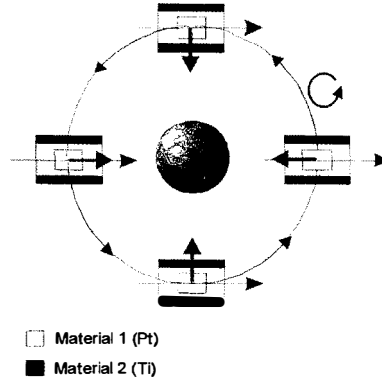


Figure 1 – MICROSCOPE experiment concept: the two masses fall around the Earth, controlled along the same orbit, either in inertial pointing or spinning around the normal to the orbit. The difference of electrostatic accelerations actuated by the servo-control along the axial cylindrical direction to maintain the masses motionless (straight black arrows) is accurately measured to detect any EP violation signal along the Earth monopole gravity field (grey arrows).

MICROSCOPE is in fact a test of the universality of free-fall. Indeed, two bodies of different material (Platinum Rhodium-10% alloy versus Titanium alloy) are servo-controlled by electrostatic forces to be motionless with respect to the instrument frame. The difference of the accelerations needed to control the two bodies on the same orbit should be null if the Equivalence Principle is true. MICROSCOPE accurately measures the Eötvös parameter:

$$\eta = \frac{a1 - a2}{\frac{1}{2}(a1 + a2)} = \frac{\frac{mg1}{mi1} - \frac{mg2}{mi2}}{\frac{1}{2}\left(\frac{mg1}{mi1} + \frac{mg2}{mi2}\right)}$$

Where $a1$ and $a2$ are the accelerations of the two tested bodies, $mg1$ and $mg2$ their respective gravitational masses, $mi1$ and $mi2$ their respective inertial masses. In the frame of General Relativity, η is assumed null as a fundamental principle of the theory leading to the universality of free-fall in a uniform gravity field: i.e. $g = a$.

The two test bodies constitute the test-masses of two inertial sensors or accelerometers accurately centered to feel the same gravitational field. The mean output of the accelerometers gives the mean acceleration of the satellite. It is used by the servo-loop of the drag compensation control system

to accelerate the satellite against the residual air drag or the radiation pressure with the help of gas micro-thrusters. As the test-mass are controlled along their 6 degrees of freedom, the accelerometers also deliver the angular accelerations that are combined with the star sensors to finely control the satellite angular motion and pointing.

The 320 kg satellite uses cold gas thrusters adapted from the developed technology for the ESA GAIA mission to fulfil the required thrust range and noise, $300\mu N$ & $0.001\mu N.Hz^{-1/2}$.

The payload is placed in a thermal case enabling mK stability at EP frequency (in inertial pointing or satellite rotating mode). It contains the sensor core of the accelerometers (including the inertial test-masses) and the Front-End Electronics with all reference voltages and pick-up measurements circuits. The digital electronics unit embarking the test-masses control law (ICUME on Figure 2) is placed on a wall of the satellite with other service equipment.

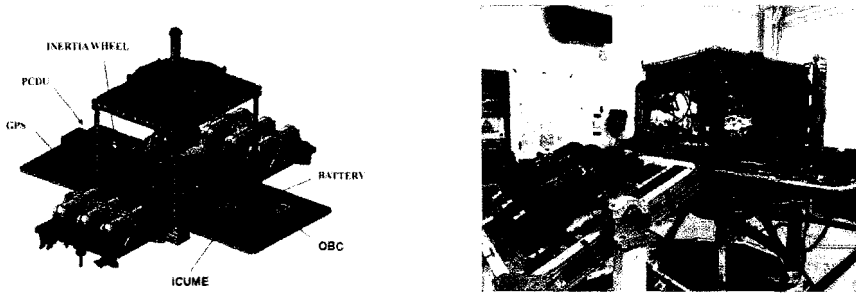


Figure 2 – Schema of the opened satellite and picture taken during integration (credits CNES)

2 The instrument description

The instrument comprises two sensor units (see Figure 3). In each sensor unit, two cylindrical test-masses are servo-controlled to remain concentric in order to be submitted to the same gravity field. By construction the concentricity of the two test-masses is achieved at $20\mu m$ accuracy and calibrated in orbit at $0.1\mu m$ in order to reject the gravity gradient effect at EP frequency.

The relative alignment of the two test-masses is also required to a fraction of 1milirad in order to minimize the projection of the angular motion or the gravity gradient from the radial axis: the measurement of the differential acceleration due to an possible violation is performed along the cylinder axis direction (Figure1). To achieve these accuracies of centering and alignment, all the parts have been machined to less than 3 to $5\mu m$ accuracy and controlled to $1\mu m$ accuracy. The integration of all parts has been realized with different controls of the partially assembled instrument with the use of a 3D machine control up to $1\mu m$ accuracy. At last, once integrated, the capacitive measurements of all electrodes surrounding the test-masses allow confirming the electrical geometry and assessing all the accuracies.

One sensor unit is composed of two test-masses with the same material (Pt-Rh10) for which no differential acceleration is expected unless noise and systematic errors: this is for demonstration of the experiment accuracy. The other sensor unit embarks a pair of test-masses made of Pt-Rh10 and Ti alloy which are dedicated to the EP violation detection. Both sensor units will be submitted to the same orbital conditions, calibration and data processes. The metrology of the parts associated to the measured characteristics of the flight model electronics have been considered to establish a budget evaluation of noise and systematic error sources: in the order of $10^{-12}ms^{-2}Hz^{-1/2}$ for the acceleration noise measurement and a few $10^{-15}ms^{-2}$ for the sum of systematics perturbations due essentially to the thermal variations of either the sensor mechanics or the electronics unit (respectively passively limited to 1mK and 5mK at EP frequency) and also to the S/C pointing stability ($< 10\mu$ rad at one and three times EP frequencies).

When considering the different S/C pointings and in orbit environment, and with no correlation

between the major error sources, the detectability of any violation signal of EP should be 10^{-15} . The payload was delivered to CNES in October 2014 and has been integrated in the satellite which will undergo the qualification environment tests in the summer of 2015: chocks, vibrations and thermal vacuum tests. The flight is being scheduled to April 2016.

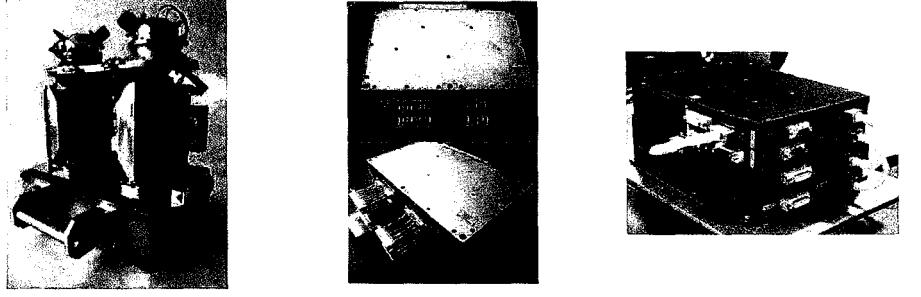


Figure 3 – T-SAGE flight model payload (Twin Space Accelerometer for Gravitation Experiment): on the left, the two sensor units (SU) aligned with optical cube; on the middle, the two front-end high stable electronics, each one measuring one SU; on the right, the ICUME, the digital controller of the test-mass servo-loops and data interface with the S/C.

3 The data process

Beyond the development of the payload and the mission definition, ONERA and OCA (Observatoire de la Côte d'Azur, Nice, France) have been developing the Science Mission Center located in ONERA premises. This center is in charge of the definition of the mission scenario and its update during the two years⁸ mission. Actually, every day of the in orbit flight, this Mission Centre analyses the data coming from the payload for the diagnostic of any anomaly. Every week, in addition to the payload data, mission data are collected to establish the validity of the passed scenario and the necessity to update the future one to be sent to CNES for implementation in the S/C scheduling. All this operational loop needs the development of software tools which survey the behavior of the major on board subsystems. The scenario will be also led by the Science Working Group of the mission in a monthly time loop to optimize the scientific return of the space experiment.

| | |
|---|---|
| $\Gamma_{mes,dx} = \frac{1}{2} K_{1cx} \cdot \eta \cdot g_{x/sat}$ $+ \frac{1}{2} \begin{bmatrix} K_{1cx} \\ \eta_{cz} + \theta_{cz} \\ \eta_{cy} - \theta_{cy} \end{bmatrix}^t \cdot [T - In] \cdot \begin{bmatrix} \Delta_x \\ \Delta_y \\ \Delta_z \end{bmatrix}$ $+ \begin{bmatrix} K_{1dx} \\ \eta_{dz} + \theta_{dz} \\ \eta_{dy} - \theta_{dy} \end{bmatrix}^t \cdot (\vec{\Gamma}_{resdf} + \vec{C})$ $+ 2 \cdot K_{2cxx} \cdot (\Gamma_{app,dx} + b_{1dx}) \cdot (\Gamma_{resdf,x} + C_x - b_{0cx})$ $+ K_{2dxx} \cdot ((\Gamma_{resdf,x} + C_x - b_{0cx})^2 + (\Gamma_{app,dx} + b_{1dx})^2)$ $+ noise$ | <p>EP searched signal</p> <p>Impact of gravity gradients (T) and S/C angular motion (In)</p> <p>Impact of residual acceleration in presence of drag compensation (C)</p> <p>Impact of nonlinear terms</p> <p>Noise of the instrument</p> |
|---|---|

Table 2: $g_{x/sat}$ is the local gravity; K_{1cx} the common mode scale factor, K_{1dx} the differential mode scale factor; Θ stands for misalignment ('c index' with respect to S/C reference frame, 'd index' test-mass relative misalignment); K_2 quadratic term of the scale factor, b_0 and b_1 are instrument bias components (c or d index precise common or differential).

⁸During eclipse phase, the payload is switched off. Some days are also lost during S/C maneuvers in order to avoid the star sensors to be dazzled by the Moon light. At the end, the useful duration is 500 days.

Concerning the measurement equation, let us consider the two measured accelerations, each one by inertial sensor (linked to each mass), and subtracted to form a differential measurement. As the accurate measurement is realized along the cylinder axes (noted X here), only the X component of the differential acceleration is first considered at EP frequency. In the following equation, the measurement is expressed in the test-mass reference frame and shows the main disturbing sources, that may affect the signal of the EP violation.

During the mission, dedicated sessions are used to calibrate the instrument. Calibration sessions consist of amplifying the disturbing acceleration by applying larger reference signals. For instance K_{1dx} is estimated by biasing the S/C (common) acceleration along x with a sine signal of $10^{-8}ms^{-2}$ at a few $10^{-3}Hz$, observing or not residue. The equation of measure is then corrected as follows:

$$\begin{aligned}
\Gamma_{mes,dx} &= \frac{1}{2} K_{1cx} \cdot \eta \cdot g_{x/sat} \\
&+ \frac{1}{2} \begin{bmatrix} K_{1cx} \\ \eta_{cz} + \theta_{cz} \\ \eta_{cy} - \theta_{cy} \end{bmatrix}^t \cdot [T - In] \cdot \begin{bmatrix} \Delta_x \\ \Delta_y \\ \Delta_z \end{bmatrix} - \frac{1}{2} \begin{bmatrix} K_{1cx} \\ \eta_{cz} + \theta_{cz} \\ \eta_{cy} - \theta_{cy} \end{bmatrix}_{calibrated}^t \cdot [T]_{computed} \cdot \begin{bmatrix} \Delta_x \\ \Delta_y \\ \Delta_z \end{bmatrix}_{calibrated} \\
&+ \begin{bmatrix} K_{1dx} \\ \eta_{dz} + \theta_{dz} \\ \eta_{dy} - \theta_{dy} \end{bmatrix}^t \cdot (\vec{\Gamma}_{resaf} + \vec{C}) - \begin{bmatrix} K_{1dx} \\ \eta_{dz} + \theta_{dz} \\ \eta_{dy} - \theta_{dy} \end{bmatrix}_{calibrated}^t \cdot (\vec{\Gamma}_{mes,c}) \\
&+ 2 \cdot K_{2cxx} \cdot (\Gamma_{app,dx} + b_{1dx}) \cdot (\Gamma_{resaf,x} + C_x - b_{0cx}) \\
&+ K_{2dxx} \cdot ((\Gamma_{resaf,x} + C_x - b_{0cx})^2 + (\Gamma_{app,dx} + b_{1dx})^2) \\
&+ Noise
\end{aligned}$$

In case of no interruption in the telemetry, the integration of the measurement signal can be performed over at least 20 orbits reducing the impact of the stochastic error (in particular, the instrument noise) and the required performance for all the subsystems (instrument, star sensors, S/C thermal environment, S/C self-gravity, GPS,...) is sufficient to achieve the mission performance objective of 10^{-15} .

Unfortunately, the quality of data could be affected by the loss of telemetry or more frequently by micro-disturbances due to micro-meteorites that will saturate the acceleration measurement (range of $2.5 \times 10^{-7}m/s^2$). In this last case, the data will be affected during several seconds after the choc generated by the micro-meteorites and must be eliminated. Unfortunately, the measurement power spectrum is dramatically modified and out of the specifications of the processing, even with few holes due to telemetry defects or micrometeorites. Several processes have been studied to cope with these missing data. In⁵ it is shown that a simple ordinary least square (OLS) is not sufficient: the mission performance is reduced by a factor 10 with only 5 holes per orbit (at 4Hz frequency sampling, it corresponds to about 0.08% of loss).

To overpass this difficulty, the authors of the paper^{5,6} developed two methods^{5,6}. The first one relies on fitting the signal PSD with a high order autoregressive model using the Burg's algorithm adapted to missing data. The inversion of the system is performed with a process based on a Kalman filter algorithm that gives at the end the eventual EP parameter, but also the other unknown, the miss-centering of the test-mass and the noise parameters. This method is called KARMA (for Kalman-AR model analysis). The results of this method are satisfactory with respect to the specifications and can be used to reconstruct the data in the missing interval as shown in Figure 4. Another method⁶ derived from the Impainting method⁷ has been developed and gives equivalent results. This last method uses the fact that the mask of missing data is known and tries to recover the real temporal data with the minimum of coefficient.

4 Conclusion

The MICROSCOPE space mission will test the Equivalence Principle with a 10^{-15} accuracy, i.e two orders of magnitude better than current experiments. The payload has been qualified and delivered

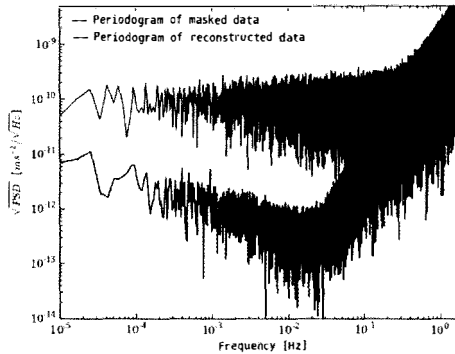


Figure 4 – Spectral density of the signal with missing data (black line) in the worst case of the mission and of the corrected data (blue line) with KARMA method; Karma recovers the initial noise spectrum of the instrument with quite no additional residue while the black line shows how the colored spectrum is affected when missing data are considered.

in October 2014 to the CNES satellite team. The payload is now integrated in the satellite that will be submitted to the environmental tests before the launch scheduled to early April 2016. A lot of effort has been paid to develop the Science Mission Center and in particular to cope with missing data or saturated data that should be eliminated. Two processing methods have been developed to allow processing the scientific data with these defects. They give good results in accordance to the required objectives.

Acknowledgements

The authors want to acknowledge the CNES for their support and funding to develop the payload, OCA (Nice, France) for their contribution to the mission analysis and performance, the PTB for their contribution through DLR to the development of the flight model test-masses, the ZARM for their contribution to the qualification and acceptance tests of the payload in free-fall. Part of the work is also funded by ONERA.

References

1. T.A.Wagner,S.Schlaminger, J.H.Gundlach and E. G.Adelberger, Class. Quantum Grav. **29** 184002, *Torsion-balance tests of the weak equivalence principle*.
2. James G. Williams, Slava G. Turyshev, and Dale Boggs, Class. Quantum Grav. **29** 184004, *Lunar laser ranging tests of the equivalence principle*.
3. T Damour and J F Donoghue. Equivalence principle violations and couplings of a light dilaton. Phys. Rev., **82**:084033, 2010
4. T. Damour, Theoretical, arXiv:1202.6311, Aspects of the Equivalence Principle
5. Baghi, Q., G. Mtris, J. Berg, B. Christophe, P. Touboul, and M. Rodrigues (2015). *Phys. Rev. D* **91**, 062003, *Regression analysis with missing data and unknown colored noise: Application to the MICROSCOPE space mission*.
6. Berge, J., S. Pires, Q. Baghi, et al., in preparation; *Correcting for missing data in colored noise: An Inpainting application to the MICROSCOPE space mission* (<https://hal.archives-ouvertes.fr/hal-01070586/document>)
7. S. Pires, S. Mathur, R. A. Garcia, J. Ballot, D. Stello, and K. Sato, ArXiv e-prints (2014), arXiv:1410.6088 [astro-ph.SR].

The STE-QUEST M4 proposal

K. Bongs, P. Bouyer, C. Braxmaier, D. Calonico, M. Cruise, N. Gaaloul, L. Iess, P. Jetzer, W. von Klitzing, S. Lecomte, E. Rasel, M. Rothacher, S. Schiller, C. Soppuerta, G.M. Tino, P. Tuckey, P. Wolf¹, M. Zelan

¹*LNE-SYRTE, Observatoire de Paris, CNRS, UPMC, France*

We summarise the Space-Time Explorer and QUantum Equivalence Space Test (STE-QUEST) space mission, as proposed to ESA in 2015 in response to the Cosmic Vision M4 call. STE-QUEST carries out tests of different aspects of the Einstein Equivalence Principle using atomic clocks, matter wave interferometry, and long distance time/frequency links. We emphasize the specific strong interest of performing equivalence principle tests in the quantum regime, *i.e.* using quantum atomic wave interferometry. Although STE-QUEST was not selected in M4 because of budgetary and technological reasons, we are looking forward to future opportunities with hopefully better outcomes for the fascinating science of STE-QUEST at the interface between quantum mechanics and gravitation.

1 Introduction

This paper is based on ¹ that describes in detail the initial STE-QUEST M3 proposal science case, and the reader is referred to that publication for more details. Here we point out the main differences and evolutions between the M3 and M4 proposals, the main change being that all optional science was dropped in order to fit the much more stringent financial conditions of the M4 call. Additionally the orbit was modified and the mission duration reduced, with a re-evaluation of the science performance within this new scenario.

Einstein's theory of general relativity (GR) is a cornerstone of our current description of the physical world. It is used to understand the flow of time in presence of gravity, the motion of bodies from satellites to galaxy clusters, the propagation of electromagnetic waves in the presence of massive bodies, the evolution of stars, and the dynamics of the Universe as a whole. Although very successful so far, general relativity as well as numerous other alternative or more general theories of gravitation are classical theories. As such, they are fundamentally incomplete, because they do not include quantum effects. A theory solving this problem would represent a crucial step towards the unification of all fundamental forces of Nature. Several concepts have been proposed and are currently under investigation (e.g. string theory, quantum gravity, extra spatial dimensions) to bridge this gap and most of them lead to tiny violations of the basic principles of GR. Therefore, a full understanding of gravity will require observations or experiments able to determine the relationship of gravity with the quantum world. This topic is a prominent field of activity with repercussions covering the complete range of physical phenomena, from particle and nuclear physics to galaxies and the Universe as a whole including dark matter and dark energy.

STE-QUEST will address the most fundamental corner stone of GR, the Einstein Equivalence Principle in all its aspects, and for doing so will use state of the art quantum technology (atomic clocks and atom interferometers), thereby also exploring the relationship between gravitation and the quantum world. The on board dual species atom interferometer will use ⁴¹K and ⁸⁷Rb atoms in quantum degenerate gases (Bose-Einstein Condensates) and in quantum states that have no classical analogues *i.e.* coherent superposition states with macroscopic separations (≤ 24 cm) which are up

to two orders of magnitude larger than the sizes of the individual wave-packets. Additionally STE-QUEST also provides a wealth of legacy science for other fields like time and frequency metrology, realization of space-time reference frames, and geodesy, thereby bridging the gap between fundamental physics and applications like studies of climate change, sea level rise or geophysics. The table below summarises the STE-QUEST M4 mission and its main science goals.

| SCIENTIFIC OBJECTIVES | | | | | | |
|---|---|--|--------------|--|------------|-------|
| Test Einstein Equivalence Principle to high precision and search for new fundamental constituents and interactions in the Universe through: | | | | | | |
| Weak Equivalence Principle Tests | | | | | | |
| Free fall of quantum matter-waves | Test of the universality of free fall of quantum matter waves to an uncertainty in the Eötvös ratio lower than $2 \cdot 10^{-15}$. | | | | | |
| Tests of Local Position Invariance | | | | | | |
| Sun field | Sun gravitational red-shift test to a fractional uncertainty of $2 \cdot 10^{-6}$. | | | | | |
| Moon field | Moon gravitational red-shift test to a fractional uncertainty of $4 \cdot 10^{-4}$. | | | | | |
| Local Lorentz Invariance and CPT Tests | | | | | | |
| LLI and CPT | Provide significant improvements on the determination of several parameters of the Lorentz and CPT symmetry violating Standard Model Extension. | | | | | |
| Legacy Science | | | | | | |
| Intercontinental clock comparison below 10^{-18} in fractional frequency | Unification of reference frames at sub-cm level | Clock based geodesy. Determination of ΔU to $< 0.1 \text{ m}^2/\text{s}^2$ | | | | |
| REFERENCE PAYLOAD | | | | | | |
| Instrument | Performance | | | | | |
| | Instability (Allan deviation) | | | Inaccuracy | | |
| ^{41}K , ^{87}Rb atom interferometer | $(1 \cdot 10^{-11} \text{ m/s}^2)/\sqrt{\tau}$, for $20 \text{ s} \leq \tau \leq 3.5 \cdot 10^6 \text{ s}$ | | | $< 2 \cdot 10^{-15}$ | | |
| Payload Complement | Performance | | | | | |
| Microwave link (MWL) 2-way, 3-frequency | Ground-to-ground clock comparisons | | | | | |
| | Instability (modified Allan deviation, $1 \text{ s} \leq \tau \leq 7 \cdot 10^3 \text{ s}$): $< \sqrt{(5.0 \cdot 10^{-13}/\tau^{3/2})^2 + (1.6 \cdot 10^{-13}/\tau)^2 + (5.9 \cdot 10^{-17}/\tau^{1/2})^2 + (5.0 \cdot 10^{-19})^2}$ Inaccuracy: $< 5 \cdot 10^{-19}$ | | | | | |
| GNSS receiver | Requirement: 3 m position error in post-processing | | | Requirement: 0.3 mm/s velocity error in post-processing | | |
| MISSION PROFILE | | | | | | |
| Launcher | Soyuz Fregat from Kourou; launch window available all year. | | | | | |
| Orbit | Elliptical GTO-type orbit around the Earth (~2500 km perigee, ~33600 km apogee) with 10.6 h period; optimized in terms of visibility at the selected ground terminals locations. | | | | | |
| Mission duration | 3.5 years: 6 months of on-orbit commissioning and calibration; 3 years of routine science phase. | | | | | |
| SPACECRAFT | | | | | | |
| Spacecraft bus | Based on the two design solutions proposed in M3 assessment study, but adapted for reduced payload mass and power, modified orbit, and propulsion requirements. | | | | | |
| AOCS | Cold gas / reaction wheel architecture for low acceleration and microvibration environment | | | | | |
| Pointing | Angular velocity averaged over the time interval T between consecutive pulses in the atom interferometer sequence within $[-10^{-6}, +10^{-6}] \text{ rad/s}$ | | | | | |
| | Payload module | Service module | Margin (20%) | Adapter/Harness | Propellant | Total |
| Mass (kg) | 422 | 552 | 195 | 86 | 103 | 1358 |
| Power | 1290 W total consumption | | | | | |
| GROUND SEGMENT | | | | | | |
| 3 microwave terminals connected to atomic clocks; baseline locations: Boulder (US), Torino (IT), Tokyo (JP). | | | | | | |
| Ground clocks performance | Instability (Allan deviation) | | | $< 2.5 \cdot 10^{-16}/\sqrt{\tau}$, for $1 \text{ s} \leq \tau \leq 2.5 \cdot 10^5 \text{ s}$ | | |
| | Inaccuracy | | | $< 1 \cdot 10^{-18}$ | | |
| Satellite Laser Ranging | Sub-cm orbit determination, to support legacy science objectives | | | | | |
| VLBI | VLBI observations of MWL X-band signal, to support legacy science objectives | | | | | |

The previous STE-QUEST M3 mission² was designed around a core payload consisting of the Atom Interferometer (ATI) and the MicroWave Link (MWL), and two optional payload elements, the Atomic Clock (ATC) and the Optical Link (OL). The rationale for M4 is to limit STE-QUEST to the core payload only (55% of the total payload mass), and optimize the spacecraft accordingly in terms of mass accommodation and power requirements. Furthermore, the orbit is optimized for the core science objectives, which are unchanged, without provision for options. Another change is specific to the ATI, as it is modified from the ^{85}Rb - ^{87}Rb differential accelerometer to a ^{87}Rb - ^{41}K one. The main reasons for this change are recent developments on ground³, in zero-g parabolic flights⁴, in the Bremen Drop tower⁵, and in sounding rocket experiments that use Rb-K. Thus the Rb-K choice provides more synergy with ongoing ground and zero-g experiments leading to enhanced TRL in the short term. Additionally, the Rb-K combination is more sensitive to a WEP violation in certain scenarios (Dilaton, SME) at similar 2×10^{-15} performance. Finally the M4 scenario also simplifies the development of the MWL, as the apogee is reduced to 33600 km allowing for smaller antennas (direct re-use of ACES ground antennas), and MWL operation is only required in

apogee phases, which saves the low gain antenna on board, and reduces complexity due to strongly reduced Doppler and Doppler rate. Both, ATI and MWL are presently undergoing TRL (Technical Readiness Level) raising activities under national and ESA contracts that will ensure TRL 5-6 by 2018.

2 STE-QUEST Test of the Weak Equivalence Principle

Quantum tests of the Equivalence Principle differ from classical ones because classical and quantum descriptions of motion are fundamentally different. In particular, the Universality of Free Fall (or WEP) has a clear significance in the classical context where it means that space-time trajectories of test particles do not depend on the composition of these particles. How UFF/WEP is to be understood in Quantum Mechanics is a much more delicate point. More generally, considering quantum phenomena in the context of gravity poses many conceptual and fundamental difficulties as discussed e.g. in¹. Although not all of these are directly explored by STE-QUEST, they provide a broad picture of the limits of our knowledge in this domain and thus the interest of experiments like STE-QUEST that lie at the frontier between QM and GR. In that respect STE-QUEST offers outstanding possibilities. The atoms are cooled to temperatures below the critical temperature (few nK) for Bose-Einstein Condensation (BEC), which allows operation of the interferometer with degenerate quantum gases (BECs). This together with the large coherent splitting of the wave packets in the interferometers produces highly non-classical states for long periods of time lasting up to 10 s.

UFF/WEP tests are generally quantified by the Eötvös ratio $\eta_{AB} = 2(a_A - a_B)/(a_A + a_B)$ for the gravitational accelerations of two test objects A and B and a specified source mass of the gravitational field. Note that for a same experiment the data can be interpreted with respect to different source masses⁶ with corresponding different results for η , and the analysis can be further refined in a model dependent way when searching violations linked to particular types of mass-energy (see¹ for more details).

Numerical simulations (as described in¹ but applied to the M4 scenario) show that the STE-QUEST WEP/UFF test reaches an uncertainty of 2×10^{-15} in the Eötvös ratio after 1.2 years of integration. Meanwhile, systematic effects are estimated to be below the 2×10^{-15} level once calibrated, with the possibility of carrying out some of the calibrations during the rest of the orbit (away from perigee) thus not impacting the useful measurement time. This uncertainty can be compared to present and upcoming tests, as shown in Table 1.

Table 1: Present and expected limits from WEP/UFF tests. (CC = corner cube)

| Type | Elements | Limits on η | Reference(year) | Comments |
|-------------|-----------------------------------|---------------------|-------------------|--------------------|
| Macroscopic | Be - Ti | 2×10^{-13} | Schlaminger(2008) | Best present limit |
| | Pt - Ti | 10^{-15} | 2016+ | Microscope mission |
| Quantum vs. | Cs - CC | 7×10^{-9} | Peters(1999) | Co-located |
| Macroscopic | Rb - CC | 7×10^{-9} | Merlet(2010) | gravimeters |
| Pure | $^{87}\text{Rb} - ^{85}\text{Rb}$ | 2×10^{-7} | Fray(2004) | Sequential meas. |
| | $^{87}\text{Rb} - ^{85}\text{Rb}$ | 5×10^{-7} | Bonnin(2014) | Simultaneous meas. |
| | $^{88}\text{Sr} - ^{87}\text{Sr}$ | 2×10^{-7} | Tarallo(2014) | Boson vs. Fermion |
| | $^{39}\text{K} - ^{87}\text{Rb}$ | 6×10^{-7} | Schlippert(2014) | Simultaneous meas. |
| | $^{41}\text{K} - ^{87}\text{Rb}$ | 2×10^{-15} | 2025+ | STE-QUEST |

The STE-QUEST UFF/WEP test represents an improvement by impressive 8 orders of magnitude over the best present quantum tests. Even when comparing to macroscopic tests, with best present ground tests from the Eöt-Wash group at the 2×10^{-13} level, STE-QUEST still represents an improvement by two orders of magnitude. However, it is important to stress here that the STE-QUEST measurement is truly quantum in nature.

Ground tests using coherent matter waves are also likely to improve within the STE-QUEST

time frame. However, they are not expected to reach performances comparable to those of STE-QUEST because of the inherent limits of the ground laboratory environment (short free fall times, gravity gradients, perturbed laboratory environment, etc.), which will ultimately limit tests on ground. This is somewhat akin to classical tests where the next significant improvement is expected from going into space with the MICROSCOPE mission.

3 STE-QUEST Test of Local Position Invariance

In the baseline configuration, STE-QUEST will be able to compare ground clocks over intercontinental distances using the microwave link (MWL) in common-view mode, during the apogee phase of the orbit. In the framework discussed in ^{1,7}, with the Sun as the source of the anomalous gravitational coupling, the measured frequency ratio of the two clocks can be written as

$$\frac{\nu_T}{\nu_B} = 1 - \frac{1}{c^2} \left[(U_B - U_T) + \frac{v_B^2 - v_T^2}{2} + (\alpha_B U_B - \alpha_T U_T) \right] + \Delta, \quad (1)$$

where U_B and U_T are the solar Newtonian gravitational potentials at the locations of the ground clocks and v_B and v_T are the corresponding velocities in a solar system barycentric reference frame. The LPI violating parameters α_B and α_T depend on the type of transition used in the respective clocks, and Δ represents all corrections due to the other solar system bodies (including the Earth) assumed to behave normally, as well as higher order correction terms.

As is well known, in the absence of an LPI violation ($\alpha_B = \alpha_T = 0$) the leading part in (1) is equal to zero (up to small tidal correction terms in Δ and constant terms from the Earth field) ⁷. This is a direct consequence of the EEP, as the Earth is freely falling in the Sun field. The LPI test in the Sun field is thus verifying whether the measured frequency ratio is equal to the expected value, i.e. $1 + \Delta$ in this example.

The experiment will measure the time evolution of the ratio ν_T/ν_B , which again should be zero in GR (up to correction terms), but will evolve in time if the LPI violating parameters are non-vanishing because of the time evolution of $U_B - U_T$, mainly related to the rotation of the Earth. The determination of the LPI parameters then boils down to a search of a periodic signal with known frequency and phase in the clock comparison data. A Monte-Carlo simulation taking into account the measurement uncertainties of the MWL and clocks, the orbit, and the baseline ground station locations, shows that any value of $|\alpha| \geq 2 \times 10^{-6}$ will be detected, which represents an improvement on best existing limits ⁸ by about 4 orders of magnitude. The procedure for the LPI test in the Moon field is identical to the Sun field test described above. The difference is that the frequency and phase of the signal that one searches for are different and that the sensitivity is decreased by a factor ~ 175 ¹.

4 Conclusion

We have summarized the main scientific aspects of the STE-QUEST M4 mission, together with the main changes with respect to the M3 proposal. For lack of space we could not discuss other, equally important, science objectives like tests of Lorentz invariance and CPT symmetry, time/frequency metrology, reference frames, and geodesy. For more details the reader is referred to ¹.

References

1. B. Altschul *et al*, *Advances in Space Research*, **55**, 501 - 524 (2015).
2. D. N. Aguilera *et al*, *Class. Quantum Grav.* **31** 115010 (2014).
3. Schlippert D. *et al*, *Phys. Rev. Lett.*, **112**, 203002 (2014).
4. Geiger R. *et al*, *Nat. Comm.* **2**, 474 (2011).
5. Rudolph J. *et al*, accepted in *NJP*, arXiv:1501.00403, (2015).
6. Schlamminger S. *et al*, *Phys. Rev. Lett.* **100**, 041101 (2008).
7. P. Wolf & L. Blanchet, in preparation (2015).
8. LoPresto J.C. *et al*, *Astrophys. J.* **376**, 757 (1991).

TESTING QUANTUM PHYSICS IN SPACE USING HIGH-MASS MATTER-WAVE INTERFEROMETRY

R. KALTENBAEK

*Vienna Center for Quantum Science and Technology, Faculty of Physics, University of Vienna,
Boltzmannngasse 5, 1090 Vienna, Austria*

Quantum superposition is central to quantum theory but challenges our concepts of reality and spacetime when applied to macroscopic objects like Schrödinger's cat. For that reason, it has been a long-standing question whether quantum physics remains valid unmodified even for truly macroscopic objects. By now, the predictions of quantum theory have been confirmed via matter-wave interferometry for massive objects up to 10^4 atomic mass units (amu). The rapid development of new technologies promises to soon allow tests of quantum theory for significantly higher test masses by using novel techniques of quantum optomechanics and high-mass matter-wave interferometry. Such experiments may yield novel insights into the foundations of quantum theory, pose stringent limits on alternative theoretical models or even uncover deviations from quantum physics. However, performing experiments of this type on Earth may soon face principal limitations due to requirements of long times of flight, ultra-low vibrations, and extremely high vacuum. Here, we present a short overview of recent developments towards the implementation of the proposed space-mission MAQRO, which promises to overcome those limitations and to perform matter-wave interferometry in a parameter regime orders of magnitude beyond state-of-the-art.

1 Introduction

Some of the central concepts of quantum physics have been a topic of discussion from the start. In particular, quantum superposition in the case of macroscopic objects like Schrödinger's cat¹ challenges our concepts of reality. For massive particles with a mass up to 10^4 atomic mass units (amu), the predictions of quantum theory have been confirmed experimentally². While this is still far from the mass of Schrödinger's cat, experiments may soon be able to prepare quantum superpositions of objects visible to the naked eye. Various alternative theoretical models (collapse models) predict observable deviations from quantum theory in that context^{3,4}. Independent of whether any of those models are correct or not, achieving quantum control over sufficiently macroscopic physical systems will mark a milestone towards systematically exploring an entirely new parameter regime. Eventually, high-mass matter-wave interferometry may allow testing deviations from quantum theory due to metric fluctuations due to quantum gravity⁵ or gravitational-wave background^{6,7} or, in the presence of a gravitational field, decoherence due to time dilation⁸. Recently, it has been suggested that high-mass matter-wave interferometry may even be sensitive to certain types of dark matter^{9,10}.

2 Limitations in ground-based experiments

To enable matter-wave interferometry for masses beyond current experiments, novel techniques are being developed, like optical time-domain ionizing matter-wave (OTIMA) interferometry^{11,12}

or using optically trapped particles for far-field¹³ or near-field interferometry¹⁴. These approaches may allow achieving tests of quantum theory for test masses up to 10^6 amu or even 10^8 amu over the next years. Beyond that, ground-based experiments may face principal limitations due to limited free-fall times as well as limited quality of vacuum and micro-gravity^{15,16}. Given this mass limit, ground-based experiments may eventually allow decisive tests^{12,13} of the continuous spontaneous localization (CSL) model¹⁷ and the quantum-gravity (QG) model of Ellis et al¹⁸. Testing quantum physics for higher masses, and testing other collapse models like that of Károlyházy¹⁹ or Diósi-Penrose²⁰ seems to be beyond ground-based experiments. The same holds true for more ambitious tests of metric fluctuations, time-dilation or dark matter.

It is conceivable that some of those limitations can be overcome by using magnetic levitation of superconducting spheres²¹. Still, this approach has to be investigated in more detail to assure its applicability for testing quantum physics under realistic conditions (i.e., in the presence of field fluctuations, vibrations, material inhomogeneities, etc.).

Given the rapid development of space technology, e.g., in the context of LISA Pathfinder²², using a space environment for quantum experiments is becoming an attractive alternative. For this reason, in 2010, we proposed a medium-sized space mission MAQRO to perform high-mass matter-wave interferometry in space¹⁵. Here, we present an short overview of the MAQRO mission proposal and its current status.

3 The MAQRO mission proposal

The goal of MAQRO is to perform decisive tests of quantum physics by optimally harnessing the unique opportunities offered by a space platform, i.e., microgravity, and the possible low temperatures and ultra-high vacuum outside the spacecraft. In particular, MAQRO will take full advantage of the rich heritage of several missions and mission proposals. It will use the same spacecraft, carrier and orbit as LISA Pathfinder (LPF)²², microthrusters as used in GAIA, LPF and Microscope²³, and Onera inertial sensors based on established technology used in missions like Microscope and GOCE²⁴. The experiments performed in MAQRO will be matter-wave interferometry with high-mass test particles: dielectric nanospheres of different radii and materials to quantitatively test quantum physics over a wide range of parameters. Compared to the present mass record of 10^4 amu², MAQRO aims at testing quantum physics with test masses up to several 10^{10} amu.

Achieving this goal and the corresponding requirements of ~ 100 s coherence time will require extremely low vacuum levels of $\sim 10^{13}$ Pa and temperatures of $\lesssim 20$ K for the environment and $\lesssim 25$ K¹⁶. In the original proposal of MAQRO¹⁵, we suggested to achieve the ultra-high vacuum level and low environment temperature by using a platform outside the spacecraft.

3.1 Mission configuration

The central component of MAQRO is an optical bench mounted outside the spacecraft and isolated from the hot spacecraft via a structure of three thermal shields¹⁵. The design of the heat-shield structure and the optical bench was optimized in two thermal studies^{25,26}. In particular, we showed that the vacuum achievable on the optical bench should only be limited by interplanetary vacuum in a Lissajous orbit around the Earth-Sun Lagrange point L1 (or L2)¹⁵, compatible with the requirements of MAQRO¹⁶. Our thermal studies showed that the environment temperature achievable via passive cooling is ~ 25 K for the optical bench and down to ~ 12 K for a small test volume around the experimental region – the “test volume”. This is achieved by placing only the absolute minimum of optical components and dissipative elements on the optical bench, and by optimizing the coating of optical elements and the optical bench. Using reflective instead of refractive optics for the on-bench imaging system allowed reducing the temperature of the test volume from ~ 16 K to ~ 12 K.

The thermal-shield structure will be mounted outside the spacecraft and always pointing to deep space with the spacecraft in a sun-synchronous orbit around L1 (or L2). The orbit was chosen for several reasons: (1) the high thermal stability achievable¹⁵, (2) the ultra-high interplanetary vacuum, (3) the low temperature achievable via passive cooling, (4) the low gravitational field gradients, and (5) the technological heritage of LPF.

We choose a nominal mission life-time of two years with possible extension in order to allow for the accumulation of a sufficient amount of data to achieve the scientific goals. The spacecraft, launcher and orbit were chosen identical to LPF apart from larger fuel tanks to accommodate the longer mission lifetime.

3.2 *The experiment*

In contrast to the original MAQRO proposal¹⁵, which was based on double-slit-type far-field matter-wave interference using a novel form of quantum state preparation, the updated mission proposal¹⁶, takes advantage of established matter-wave-interferometry techniques to perform near-field interferometry¹⁴.

The central approach remains the same: (1) optically trap a dielectric particle, (2) cool its center-of-mass motion close to the quantum ground-state using optomechanical techniques, (3) release the particle and let the wavefunction expand for a time t_1 , (4) prepare a non-classical state of motion of the particle, (5) let the wavefunction freely evolve for a time t_2 , (5) measure the position of the test particle. This procedure is then repeated many times to gather enough statistics to determine the interference visibility. In order to test the predictions of quantum theory, such experimental runs are repeated for different materials and different particle sizes.

In contrast to the original proposal, we have $t_1 \approx t_2$, and step (4) is the application of a phase grating of UV light with a wavelength of ~ 200 nm. Central advantages of the new approach are that the total measurement time $t_1 + t_2$ is shorter, that the experiment relies on laser wavelengths that are already available in space (1064 nm) or may be soon (~ 200 nm CW on the mW level) with a manageable amount of delta development, and that the matter-wave interference visibility to be expected can be very high.

MAQRO will use a combination of ion and optical trapping to provide a reliable source of high-mass test particles for the experiment. They will be guided via hollow-core fibre from inside the spacecraft to the optical bench outside. Buffer gas in the hollow-core fibres will ensure that the temperature of the test particles will only be slightly above the environment temperature. Before loading the test particle into the experimental region, we plan to discharge using UV radiation¹⁶. We will also aim at minimizing the time of optical trapping of the particle in order to keep it cool. Moreover, a different particle will be used for each experimental run.

4 Outlook

In the near future, we will further improve and detail the MAQRO mission design, perform preliminary experiments on ground, extend and intensify our international collaboration for realizing MAQRO, and we will prepare for the submission of an improved mission proposal for the next mission opportunity.

5 Conclusions

We presented a short overview of the current status of the proposal MAQRO of a medium-sized space mission for testing the foundations of quantum physics – its goals, the mission outline and the next steps towards implementing that mission.

Acknowledgements

We acknowledge support from the FFG Austrian Research Promotion Agency (MAQROsteps, project no. 3589434).

References

1. E. Schrödinger, *Die Naturwissenschaften* **23**, 807 (1935).
2. Sandra Eibenberger, Stefan Gerlich, Markus Arndt, Marcel Mayor and Jens Tüxen, *Phys. chem. chem. phys.*: PCCP **15**, 14696 (2013).
3. Stephen L Adler and Angelo Bassi, *Science* **325**, 275 (2009).
4. Angelo Bassi, Kinjalk Lochan, Seema Satin, Tejinder P. Singh and Hendrik Ulbricht, *Rev. Mod. Phys.* **85**, 471 (2013).
5. H.-P. Breuer, E. Göekli and C. Lämmerzahl, *Class. Quantum Grav.* **26**, 105012 (2009).
6. Marc-Thierry Jaekel and Serge Reynaud, *Phys. Lett. A* **185**, 143 (1994).
7. Brahim Lamine, Rémy Hervé, Astrid Lambrecht and Serge Reynaud, *Phys. Rev. Lett.* **96**, 050405, February 2006.
8. Igor Pikovski, Magdalena Zych, Fabio Costa and Časlav Brukner, arXiv:1311.1095 (2013).
9. C. J. Riedel, *Phys. Rev. D* **88**, 116005 (2013).
10. J. Bateman, I. McHardy, A. Merle, T. R. Morris and H. Ulbricht, *Sci. Rep.* **5**, 8058 (2015).
11. Stefan Nimmrichter, Philipp Haslinger, Klaus Hornberger and Markus Arndt, *New J. Phys.* **13**, 075002 (2011).
12. Stefan Nimmrichter, Klaus Hornberger, Philipp Haslinger and Markus Arndt, *Phys. Rev. A* **83**, 043621 (2011).
13. O. Romero-Isart, A. C. Pflanzer, F. Blaser, R. Kaltenbaek, N. Kiesel, M. Aspelmeyer and J. I. Cirac, *Phys. Rev. Lett.* **107**, 020405 (2011).
14. James Bateman, Stefan Nimmrichter, Klaus Hornberger and Hendrik Ulbricht, *Nature comm.* **5**, 4788 (2014).
15. Rainer Kaltenbaek, Gerald Hechenblaikner, Nikolai Kiesel, Oriol Romero-Isart, Keith C. Schwab, Ulrich Johann and Markus Aspelmeyer, *Exp. Astron.* **34**, 123 (2012).
16. Rainer Kaltenbaek *et al* arXiv:1503.02640 (2015).
17. Gian Carlo Ghirardi, Philip Pearle and Alberto Rimini, *Phys. Rev. A* **42**, 78 (1990).
18. J. Ellis, S. Mohanty and D. V. Nanopoulos, *Phys. Lett. B* **221**, 113 (1989).
19. F. Károlyházy, *Nuovo Cimento A* **52**, 390 (1966).
20. Lajos Diósi, *Phys. Rev. A* **78**, 021801(R) (2008).
21. O. Romero-Isart, L. Clemente, C. Navau, A. Sanchez and J. I. Cirac, *Phys. Rev. Lett.* **109**, 147205 (2012).
22. M. Armano *et al*, *Class. Quantum Grav.* **26**, 094001 (2009).
23. F. Liorzou, D. Boulanger, M. Rodrigues, P. Touboul and H. Selig, *Adv. Space Res.* **54**, 1119 (2014).
24. J.-P. Marque, B. Christophe and B. Foulon, In *61st Int. Astronaut. Congress* **6**, IAC-10.B1.3.1, Prague, CZ (2010).
25. Gerald Hechenblaikner, Fabian Hufgard, Johannes Burkhardt, Nikolai Kiesel, Ulrich Johann, Markus Aspelmeyer and Rainer Kaltenbaek, *New J. Phys.* **16**, 013058 (2014).
26. André Pilan-Zanoni, Johannes Burkhardt, Ulrich Johann, M. Aspelmeyer, Rainer Kaltenbaek and Gerald Hechenblaikner, in preparation (2015).

PRECISION OSCILLATOR TECHNOLOGY WITH APPLICATION TO TESTING FUNDAMENTAL PHYSICS, DETECTING HIGH FREQUENCY GRAVITATIONAL WAVES, AND QUANTUM MEASUREMENT

M.E. TOBAR

*ARC Centre of Excellence for Engineered Quantum Systems, M013, School of Physics,
The University of Western Australia 35 Stirling Hwy, 6009, Crawley, Australia*



This paper summarises research programs at The University of Western Australia to develop precision oscillator technology based on cryogenic sapphire whispering gallery mode resonators and cryogenic quartz bulk acoustic wave oscillators. Research programs include precision tests of fundamental physics, experiments to detect high frequency gravitational waves and cosmic dark sector particles, as well as quantum measurement, and in particular to measure large mass harmonic oscillators at the ground state.

1 Oscillator Technology

1.1 *Cryogenic Sapphire Oscillators based on Whispering Gallery Modes*

At the University of Western Australia we have built the most stable and precise electromagnetic oscillator, the Cryogenic Sapphire Oscillator (CSO) at microwave frequencies with parts in 10^{16} frequency instabilities¹. At the heart of any CSO is a cylindrical sapphire dielectric resonator with its rotational axis aligned with the crystal axis in which high-Q Whispering Gallery (WG) modes are excited.

Recently, characterization of the power to frequency conversion in the CSO has shown that fluctuations of power incident on the resonator is the primary limiting factor contributing to the frequency instabilities in the oscillator. At such high levels of precision the task of further optimisation to improve the CSO sets a challenge. The way forward is to lower the noise floor of the power control scheme. As outlined in² there are a few strategies to be followed. 1) To undertake a thorough search of noise in detectors (the limiting component) our calculations show that the radiation pressure noise floor can be reduced to a part in 10^{17} at 1 second of fluctuations. 2) A power versus frequency turning point may be engineered as spin resonance effects of impurities have opposite effect to radiation pressure, this would reduce the requirement of the power control. 3) Adaption of novel low-noise power detection using interferometer technology³. Any improvement in this technology will not only improve the oscillator performance, but the tests of fundamental physics through the application of this technology

Phonon-trapping Bulk Acoustic Wave (BAW) cavity resonator technology shows great potential for use in applications that require precision control, measurement, and sensing at the quantum limit. This is mainly due to the relatively high mechanical frequencies and extremely high Q-factors achievable at cryogenic temperatures ($Q \approx 10^{10}$) for frequencies ranging from a MHz to a GHz, beyond the capability of any other competing technology compared in⁴. This uniqueness has been perfected for decades for precision room temperature oscillators and related devices, culminating in $Q \times f$ products as high 2×10^{13} Hz, and in a collaboration with FEMTO-ST in Besancon, only recently has been extended to cryogenic temperatures attaining $Q \times f$ products as high 2×10^{18} Hz⁵. Thus, further improvement of BAW oscillators can only be achieved by cooling the resonators and reducing the resonator flicker phase self-noise, since this is the dominant noise source both at cryogenic and room temperature. The influence on the frequency stability of high-performance quartz oscillators on time scales of order 150 s is well-documented and it has been observed that the flicker self-noise decreases with decreasing power of the incident signal, and our recent results confirm that the resonators are thermal noise limited, and flicker free without the carrier⁶. Thus, the noise in the quartz oscillator is dependent on power, with the white noise floor decreasing with power, while the flicker noise increases. The best quartz typically has frequency instabilities of better than 10^{-13} limited by flicker fluctuations. However at cryogenic temperatures the white noise floor is reduced by 40 dB, allowing a much lower oscillator power and a large reduction of the flicker noise so the increased Q-factor may be exploited. Assuming the typical phase noise of -130 dBc/Hz at 1 Hz limited by the resonator self noise, the increase in Q-factor at 4K should see frequency instabilities as low as 2×10^{-16} through the development of Cryogenic Quartz Oscillators (CQO), and if this can be pushed down further due to power optimisations it is strongly feasible to push the stability into the 10^{-17} regime⁷.

2 Precision Tests of Local Lorentz Invariance Violations

The broad experimental research for Lorentz Invariance Violations LIV is successfully bundled by test theories, such as the Standard Model Extension (SME)⁸ and Robertson-Mansouri-Sexl theory^{9,10}, which enable the comparison and exchange of experimental results by collective efforts to put bounds to a number of test parameters. Experimental tests for LIV are performed across almost all sectors of physics (proton, neutron, electron and photons), LIV in the photon sector refers to scenarios where the velocity of light depends slightly on direction in space, boost velocity, and/or frequency, we undertake these experiments with rotating cryogenic sapphire oscillators¹¹. Our most recent experiment in collaboration with Humboldt University of Berlin¹¹ (known as a modern Michelson-Morley experiment) put bounds on LIV of order 10^{-18} . This result is just into the range, which is able to falsify LIV in the photon sector beyond the electroweak transition, to push beyond this regime, better sensitivity is necessary and with improvements in CSO technology should see an order of magnitude improvement in the future.

In collaboration with UC Berkeley we have implemented room temperature quartz oscillators to set limit in the neutron sector⁷. This experiment was based on rotating commercial room temperature oscillators with 10^{-12} fractional frequency instabilities. The physical setup is that of a Modern Michelson Morley experiment, but tests phonon oscillations rather than photon oscillations and tests the spatial invariance of phonons to a part in 10^{15} with 120 hours worth of data⁷. CQOs have the possibility to improve this to parts in 10^{-19} if they perform as calculated with a fractional frequency instability of 10^{-16} .

3 Precision Tests to Detect High Frequency Gravitational Waves

There are a number of theoretical predictions for astrophysical and cosmological objects, which emit high frequency ($10^6 - 10^9$ Hz) Gravitational Waves (GW) or contribute somehow to the stochastic high frequency GW background⁶. We propose a new sensitive detector in this frequency band⁶, which is based on existing cryogenic ultra-high quality factor quartz Bulk Acoustic Wave cavity technology^{17,18,19}, coupled to near-quantum-limited SQUID amplifiers at 20 mK⁶. We show that spectral strain sensitivities reaching 10^{-22} per $\sqrt{\text{Hz}}$ per mode is possible, which in principle can cover the frequency range with multiple (> 100) modes with quality factors varying between $10^6 - 10^{10}$ allowing wide bandwidth detection. Due to its compactness and well established manufacturing process, the system is easily scalable into arrays and distributed networks that can also impact the overall sensitivity and introduce coincidence analysis to ensure no false detections.

4 Precision Tests to Detect Dark Sector Particles

The axion is a hypothetical bosonic particle that was first proposed^{20,21} as a consequence of Peccei and Quinns solution to the strong CP problem²². It is a particle with non-zero mass that interacts gravitationally and via a weak coupling to Standard Model particles; as such it belongs to a family called the Weakly Interacting Sub-eV Particles (WISPs). These properties make it both a very compelling dark matter candidate and extremely difficult to detect. In particular, axions with masses in the range of micro-eV to milli-eV could account for cold dark matter in galactic halos. Axions provide explanations for many cosmological observations, including the formation of caustic rings; they are an elegant and natural solution to many problems in physics.

Recently, Beck reported on a possible axion dark matter signal²³. Beck postulates that a flux of dark matter axions would induce certain signals in Josephson junctions without the application of an external microwave field. This theory explains a previously reported anomalous signal in Josephson junctions²⁴ as being caused by the presence of axions with a mass of $110 \pm 2 \text{micro-eV}$ (26.6 GHz) and a local axion dark matter density of $0.05 \text{ GeV}/\text{cm}^3$. Such a claim further compels full investigation over the possible range of masses. At UWA we are constructing an experiment to target this precise mass range, which will allow for verification or rejection of this claim. This first experiment will also serve as the pathfinder project for an expanded search over the 15 - 30 GHz mass range.

Similar cavity experiments to detect dark photons have been conducted in our laboratories. These experiments are generate and detect experiments and take the form of a light shining through the wall experiment^{25,26,27}. More recently we developed a new experiment that uses the coupling of photons and axions to create a frequency shift between two microwave oscillator cavities²⁸, which has the potential to improve these experiments by more than one order of magnitude.

5 Applications to Quantum Measurement

We are undertaking two experiments at the University of Western Australia with the goal to read out electromechanical systems in the ground state. The first is using quartz BAW resonators of order gram scale, which have the highest $Q \times f$ produce of any acoustic system by a few orders of magnitude, with the acoustic motion detected through the piezo-electric effect^{29,30}. Motion has already been detected, which should be high enough in frequency that the quantum fluctuations of motion can be directly detected^{31,18}. The second is through a high-Q acoustic sapphire dumbbell of order kg scale coupled parametrically through high-Q whispering gallery modes due to the strain dependent permittivity³². This experiment will need to make use of parametric cooling to reach this goal.

Acknowledgments

This work was funded by the Australian Research Council grant numbers CE110001013 and DP130100205.

References

1. C.R. Locke, E.N. Ivanov, J.G. Hartnett, P.L. Stanwix, M.E. Tobar, *Rev. Sci. Instrum.*, **79**, 051301, (2008).
2. N.R. Nand, S.R. Parker, E.N. Ivanov, J.-M. le Floch, J.G. Hartnett, M.E. Tobar, *Appl. Phys. Lett.*, **103**, 043502, (2013).
3. EN Ivanov, ME Tobar, *Rev. Sci. Instrum.*, **80**, 044701, 2009.
4. M. Aspelmeyer, T. Kippenberg, F. Marquardt, *Rev. Mod. Phys.*, **86**, 1391, (2014).
5. S. Galliou, M. Goryachev, R. Bourquin, P. Abbe, J.-P. Aubry, M.E. Tobar, *Sci. Rep.*, **3**, 2132, 2013.
6. M. Goryachev, E.N. Ivanov, F. van Kann, S. Galliou, M.E. Tobar, *Appl. Phys. Lett.*, **105**, 153505, (2014).
7. A. Lo, P. Haslinger, E. Mizrachi, L. Anderegg, H. Mller, M. Hohensee, M. Goryachev, M.E. Tobar, *arXiv:1412.2142 [gr-qc]*, (2014).
8. D. Colladay, V.A. Kostelecky, *Phys. Rev. D* **58**, 23 (1998)
9. H. Robertson, *Rev. Mod. Phys.*, **J1**, 378, (1949).
10. R. Mansouri, R.U. Sexl, *GRG*, **8**, 497, (1977).
11. M. Nagel, S.R. Parker, E.V. Kovalchuk, P.L. Stanwix, J.G. Hartnett, E.N. Ivanov, A. Peters, M.E. Tobar, *arXiv:1412.6954 [hep-ph]*, (2014).
12. M.E. Tobar, P.L. Stanwix, J.J. McFerran, J. Guena, M. Abgrall, S. Bize, A. Clairon, Ph. Laurent, P. Rosenbusch, D. Rovera, G. Santarelli, *Phys. Rev. D* **87**, 122004 (2013)
13. S.R. Parker, M. Mewes, P.L. Stanwix, M.E. Tobar, *Phys. Rev. Lett.* **106**, 180401 (2011)
14. M.A. Hohensee, P.L. Stanwix, M.E. Tobar, S.R. Parker, D.F. Phillips, R.L. Walsworth, *Phys. Rev. D* **82**, 076001 (2010)
15. M.E. Tobar, P. Wolf, S. Bize, G. Santarelli, V.V. Flambaum, *Phys. Rev. D* **81**, 022003 (2010)
16. M. Goryachev and M.E. Tobar *Phys. Rev. D* **90**, 102005 (2014).
17. M. Goryachev, D.L. Creedon, E.N. Ivanov, S. Galliou, R. Bourquin, M.E. Tobar, *Appl. Phys. Lett.*, **100**, 243504, (2012).
18. M. Goryachev, D.L. Creedon, S. Galliou, M.E. Tobar, *Phys. Rev. Lett.* **111**, 085502 (2013)
19. M. Goryachev, W.G. Farr, E.N. Ivanov, M.E. Tobar, *J. Appl. Phys.*, **114**, 094506, 2013.
20. F. Wilczek, *Phys. Rev. Lett.* **40**, 279 (1978)
21. R.D. Peccei, H.R. Quinn, *Phys. Rev. Lett.* **38**, 1440 (1977)
22. J. Ipser, P. Sikivie, *Phys. Rev. Lett.* **50**, 925 (1983)
23. C. Beck, *Phys. Rev. Lett.* **111**, 231801 (2013)
24. C. Hoffmann, F. Le Floch, M. Sanquer, B. Pannetier, *Phys. Rev. B*, **70**, 180503(R), (2004).
25. S.R. Parker, J.G. Hartnett, R.G. Povey, M.E. Tobar, *Phys. Rev. D* **88**, 112004 (2013)
26. R.G. Povey, J.G. Hartnett, M.E. Tobar, *Phys. Rev. D* **84**, 055023 (2011)
27. R.G. Povey, J.G. Hartnett, M.E. Tobar, *Phys. Rev. D* **82**, 052003 (2010)
28. S.R. Parker, G. Rybka, M.E. Tobar, *Phys. Rev. D* **87**, 115008 (2013)
29. R. Bara-Maillet, M. Goryachev, D. Creedon, J.-M. Le Floch, M.E. Tobar, *IEEE Trans. on IM*, **63**(3), 628, (2014).
30. M. Goryachev, W.G. Farr, S. Galliou, M.E. Tobar, *Appl. Phys. Lett.*, **105**, 063501, (2014).
31. M. Goryachev, M.E. Tobar, *New J. Phys.*, **16**, 083007, (2014).
32. J. Bourhill, E.N. Ivanov, M.E. Tobar, *arXiv:1502.07155 [physics.ins-det]*, (2015).

SOME COSMOLOGICAL CONSEQUENCES OF A BREAKING OF THE EINSTEIN EQUIVALENCE PRINCIPLE

A. HEES¹, O. MINAZZOLI², J. LARENA¹

¹ *Department of Mathematics, Rhodes University, 6139 Grahamstown, South Africa*

² *Centre Scientifique de Monaco – UMR ARTEMIS, CNRS, University of Nice Sophia-Antipolis, France*

In this communication, we consider a wide class of extensions to General Relativity that break explicitly the Einstein Equivalence Principle by introducing a multiplicative coupling between a scalar field and the electromagnetic Lagrangian. In these theories, we show that 4 cosmological observables are intimately related to each other: a temporal variation of the fine structure constant, a violation of the distance-duality relation, the evolution of the cosmic microwave background (CMB) temperature and CMB spectral distortions. This enables one to put very stringent constraints on possible violations of the distance-duality relation, on the evolution of the CMB temperature and on admissible CMB spectral distortions using current constraints on the fine structure constant. Alternatively, this offers interesting possibilities to test a wide range of theories of gravity by analyzing several datasets concurrently.

1 Introduction

The theory of General Relativity (GR) is based upon two fundamental principles: the Einstein Equivalence Principle (EEP) which gives to gravitation its geometrical nature and the Einstein field equations that specify the form of the space-time geometry. All GR extensions (in 4 dimensions) produce a deviation from at least one of these principles and it is therefore highly important to test and to constrain them (see¹ and references therein for a review of the tests of GR). From a theoretical point of view, the EEP implies the existence of a space-time metric $g_{\mu\nu}$ to which the matter Lagrangian is minimally coupled to¹. Phenomenologically, three aspects of the EEP can be tested¹: (i) the Universality of Free Fall, (ii) the Local Lorentz Invariance and (iii) the Local Position Invariance.

A way to break the EEP in tensor-scalar theory is to introduce a multiplicative coupling between the scalar field and the matter Lagrangian. This kind of coupling appears naturally in string-inspired theories^{2,3}, in theories with a varying fine structure constant^{4,5} or in the so-called *pressurion* phenomenology^{6,7}.

In this communication, we will focus on the cosmological implications of such coupling in the electromagnetic sector

$$S_{\text{EM}} = -\frac{1}{4} \int d^4x \sqrt{-g} e^{-2\varphi} F^{\mu\nu} F_{\mu\nu} + q_p \int A_\mu dx^\mu, \quad (1)$$

where g is the determinant of the space-time metric $g_{\mu\nu}$, φ is a scalar field whose action is unspecified, $F_{\mu\nu} = \partial_\mu A_\nu - \partial_\nu A_\mu$ is the standard Faraday tensor, A_μ is the 4-potential and q_p is the electric charge of a particle interacting with the electromagnetic field. It is important to point out that in order to preserve the $U(1)$ gauge invariance, the interaction part of the electromagnetic Lagrangian can not include a contribution from the scalar field^{4,8}. The coupling introduced breaks explicitly the EEP (in particular, it can not be absorbed through a conformal

transformation). Implications of this kind of couplings on the universality of free fall and on variations of fundamental constants have been studied for instance in ^{2,3,9}. In addition to these effects, we will show that four cosmological observables are modified (with respect to GR) and are intimately related to each other in this class of theory ¹⁰: (i) temporal variation of the fine structure constant, (ii) violation of the distance-duality relation, (iii) modification of the evolution of the CMB temperature and (iv) CMB spectral distortions.

2 Modification of cosmological observables

The coupling introduced in Eq. 1 leads to a modification of four cosmological observables. Details concerning the theoretical derivations of these observables can be found in ¹⁰. It is worth to insist on the fact that the derivation relies only on the matter part of the action and not on the gravitational part. This means that our results apply to a very wide class of gravitation theories. In a Friedman-Lemaître-Robertson-Walker space-time, the expressions of the four observables are given by the following expressions:

1. temporal variation of the fine structure constant. A straightforward identification in the action leads to ¹¹ $\Delta\alpha/\alpha = (\alpha(z) - \alpha_0)/\alpha_0 = e^{2(\varphi - \varphi_0)} - 1 \approx 2(\varphi - \varphi_0)$, where z is the redshift and subscripts 0 refer to $z = 0$.
2. violation of the cosmic distance-duality relation. The optic geometric limit of the modified Maxwell equations shows that photons propagate on null geodesics but their number is not conserved due to an exchange with the scalar field. Therefore, the expression of the angular diameter distance (D_A) is the same as in GR but this leads to a modification of the distance-luminosity expression (D_L) ⁷ and hence to a violation of the cosmic distance-duality relation: $\eta(z) = D_L(z)/(D_A(z)(1+z)^2) = e^{(\varphi - \varphi_0)} \approx 1 + (\varphi - \varphi_0)$.
3. modification of the evolution of the CMB temperature. Considering the CMB as a gaz of photons described by a distribution function solution of a relativistic Boltzman equation and using the geometric optic approximation of the modified Maxwell equation lead to a modification of the CMB temperature evolution:

$$T(z) = T_0(1+z) \left[1 + 0.12 \left(e^{2(\varphi - \varphi_{CMB})} - e^{2(\varphi_0 - \varphi_{CMB})} \right) \right] \approx T_0(1+z) [1 + 0.24(\varphi - \varphi_0)].$$

4. spectral distortion of the CMB. Using the same approach as the one sketched in the last item, one gets an expression for the chemical potential of the CMB radiation at current epoch $\mu = 0.47 \left(e^{2(\varphi_{CMB} - \varphi_0)} - 1 \right) \approx 0.94 (\varphi_{CMB} - \varphi_0)$.

To summarize, the coupling introduced in Eq. 1 implies that the four observables are intimately linked to each other through the relations

$$\varphi(z) - \varphi_0 = \frac{1}{2} \frac{\Delta\alpha(z)}{\alpha} = \eta(z) - 1 = 4.17 \left(\frac{T(z)}{T_0(1+z)} - 1 \right) \quad (2)$$

$$\mu = 0.47 \frac{\Delta\alpha(z_{CMB})}{\alpha} = 0.94 (\eta(z_{CMB}) - 1) = 3.92 \left(\frac{T(z_{CMB})}{T_0(1+z_{CMB})} - 1 \right). \quad (3)$$

3 Transformation of experimental constraints assuming a multiplicative coupling

Assuming that the theory of gravitation is described by the multiplicative coupling introduced in Eq. 1 (which is a large class of theory including GR), we can use Eq. 2 to transform observational constraints on one type of observations into constraints on another type. In this communication, we use three datasets of α measurements: precise clocks measurements of variations of α providing the constraint ^{12,13} $\dot{\alpha}/\alpha = (-1.6 \pm 2.3) \times 10^{-17} \text{yr}^{-1}$, 154 quasar absorption lines

observed at the VLT¹⁴ and 128 quasar absorption lines observed at the Keck observatory¹⁵. Using separately these three datasets and Eq. 2, we constrain the parameters η_i , ε and β that enter standard parametrizations of $\eta(z)$ and $T(z)$:

$$\begin{aligned} \eta(z) &= 1 + \eta_0, & \eta(z) &= 1 + \eta_2 \frac{z}{1+z}, & \eta(z) &= (1+z)^\varepsilon, \\ \eta(z) &= 1 + \eta_1 z, & \eta(z) &= 1 + \eta_3 \ln(1+z), & T(z) &= (1+z)^{1-\beta}. \end{aligned}$$

A Bayesian inversion of the three datasets lead to estimations of the η_i , ε and β parameters given in Tab. 1. The constraints derived from clocks measurements rely only on one observation and is valid only if no screening mechanism occurs around Earth. The obtained constraints improve by 5 orders of magnitude direct observations of η or of the CMB temperature¹⁶ but are valid only under the assumption that the coupling given by Eq. 1 is valid.

Table 1: Estimation of the parameters entering standard parametrizations of $\eta(z)$ and $T(z)$ using Eq. 2 and measurements of α from three different datasets.

| Parameter | Estimation [$\times 10^{-7}$] | | |
|---------------|---------------------------------|---------------|----------------|
| | VLT | Keck | Clocks |
| η_0 | 10 ± 6 | -29 ± 10 | - |
| η_1 | 8.4 ± 3.5 | -16 ± 6 | 1.0 ± 1.4 |
| η_2 | 20 ± 10 | -49 ± 17 | 1.0 ± 1.4 |
| η_3 | 14 ± 6 | -30 ± 11 | 1.0 ± 1.4 |
| ε | 14 ± 6 | -30 ± 11 | 1.0 ± 1.4 |
| β | -3.3 ± 1.5 | 7.2 ± 2.5 | -0.3 ± 0.3 |

4 Test of the multiplicative coupling using Gaussian processes

We can also use the different types of observations to assess the validity of the coupling introduced in Eq. 1. Indeed, if different types of observations indicate a violation of Eqs. 2-3, this would be an indication of a departure from a multiplicative coupling. Here, we transform separately observations on $\Delta\alpha/\alpha$, on $\eta(z)$ and on the CMB temperature into an estimation of the evolution of $\varphi - \varphi_0$ using Eq. 2. Then, we compare the different evolutions of the scalar field estimated from the different types of observations to see if they are compatible. The analysis is done using Gaussian processes¹⁷ in order to provide a model independent analysis. More details on the analysis can be found in¹⁰.

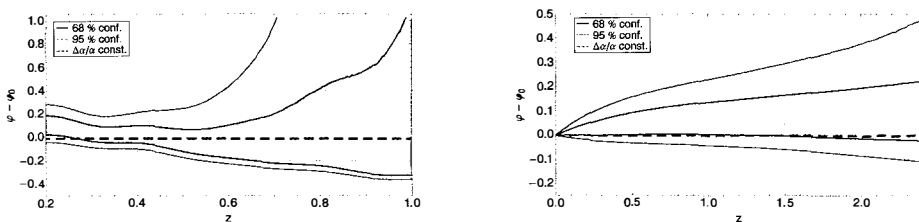


Figure 1 – Estimation of the evolution of $\varphi - \varphi_0$ from observations of $\Delta\alpha/\alpha$ (green dashed lines), from observations of angular and luminosity distance (left) and from observations of CMB temperature (right) using Eq. 2.

On Fig. 1 is represented the evolution of the scalar field estimated from observations of $\Delta\alpha/\alpha$ (dashed green lines), from observations of angular and luminosity distance^{18,19} (on the left of the figure) and from observations of the CMB temperature²⁰ (on the right of the figure). The comparison of the three different evolutions does not show any incoherence. Therefore, current

data are consistent with the coupling considered in Eq. 1. One limitation for this test comes from angular distance measurements. We estimate that EUCLID and the SKA will improve this test by one order of magnitude by measuring the BAO at different redshifts¹⁰.

5 Conclusion

A multiplicative coupling between a scalar field and the electromagnetic Lagrangian produces a violation of the EEP. Amongst others, it is known that this type of coupling leads to a violation of the universality of the free fall^{2,3,9} and to variations of the “constants” of Nature^{11,9}. In this communication, we show that this type of coupling has also some cosmological implications. In particular, it will produce four cosmological deviations with respect to GR at the cosmological scales: temporal variation of α , violation of the distance-duality relation, modification of the evolution of the CMB temperature and CMB spectral distortions. Therefore, in this class of models, these cosmological observations are complementary to local constraints on the EEP.

In addition, we have shown that in this class of theory, there are unambiguous relations between these four observables. These relations allow one to transform measurements of $\Delta\alpha/\alpha$ on constraints on $\eta(z)$ and on the evolution of the CMB temperature. Using current data, this results in an improvement by 5 orders of magnitude in the estimation of the parameters entering standard expressions of $\eta(z)$ and CMB temperature evolution. This improvement is only valid under the assumption that the coupling introduced in Eq. 1 holds.

Finally, a comparison between the different types of observations leads to a test of the multiplicative coupling introduced in Eq. 1. Current data are compatible with this coupling.

Acknowledgments

AH and OM thank the organizers for financial support to attend the conference. In addition, AH acknowledges support from “Fonds Spécial de Recherche” through a FSR-UCL grant. JL is supported by the National Research Foundation (South Africa).

References

1. C. M. Will, *LRR* **17**, 4 (2014).
2. T. Damour and A. M. Polyakov, *Nucl. Phys. B* **423**, 532 (1994).
3. T. Damour and J. F. Donoghue, *Phys. Rev. D* **82**, 084033 (2010).
4. J. D. Bekenstein, *Phys. Rev. D* **25**, 1527 (1982).
5. H. B. Sandvik *et al*, *Phys. Rev. Lett.* **88**, 031302 (2002).
6. O. Minazzoli and A. Hees, *Phys. Rev. D* **88**, 041504 (2013).
7. O. Minazzoli and A. Hees, *Phys. Rev. D* **90**, 023017 (2014).
8. A. Hees *et al*, *Gen. Rel. and Grav.* **47**, 9 (2015).
9. T. Damour, *Class. and Quantum Grav.* **29**, 184001 (2012).
10. A. Hees *et al*, *Phys. Rev. D* **90**, 124064 (2014).
11. J.-P. Uzan, *LRR* **14**, 2 (2011).
12. T. Rosenband *et al*, *Science* **319**, 1808 (2008).
13. J. Guéna *et al*, *Phys. Rev. Lett.* **109**, 080801 (2012).
14. J. A. King *et al*, *MNRAS* **422**, 3370 (2012).
15. M. T. Murphy *et al*, *MNRAS* **345**, 609 (2003).
16. Planck Collaboration, *arXiv* **1502.01589**, (2015).
17. M. Seikel *et al*, *J. Cosmology Astropart. Phys.* **6**, 36 (2012).
18. M. Bonamente *et al*, *ApJ* **647**, 25 (2006).
19. E. De Filippis *et al*, *ApJ* **625**, 108 (2005).
20. A. Saro *et al*, *MNRAS* **440**, 2610 (2014).

Ground Tests of Einstein’s Equivalence Principle: From Lab-based to 10-m Atomic Fountains

D. Schlippert, H. Albers, L. L. Richardson, D. Nath, H. Heine, C. Meiners, É. Wodey, A. Billon,
J. Hartwig, C. Schubert, N. Gaaloul, W. Ertmer, E. M. Rasel

*Institut für Quantenoptik and Centre for Quantum Engineering and Space-Time Research (QUEST),
Leibniz Universität Hannover, Welfengarten 1, D-30167 Hannover, Germany*

To date, no framework combining quantum field theory and general relativity and hence unifying all four fundamental interactions, exists. Violations of the Einstein’s equivalence principle (EEP), being the foundation of general relativity, may hold the key to a theory of “quantum gravity”. The universality of free fall (UFF), which is one of the three pillars of the EEP, has been extensively tested with classical bodies. Quantum tests of the UFF, e.g. by exploiting matter wave interferometry, allow for complementary sets of test masses, orders of magnitude larger test mass coherence lengths and investigation of spin-gravity coupling. We review our recent work towards highly sensitive matter wave tests of the UFF on ground. In this scope, the first quantum test of the UFF utilizing two different chemical elements, ^{87}Rb and ^{39}K , yielding an Eötvös ratio $\eta_{\text{Rb,K}} = (0.3 \pm 5.4) \times 10^{-7}$ has been performed. We assess systematic effects currently limiting the measurement at a level of parts in 10^8 and finally present our strategies to improve the current state-of-the-art with a test comparing the free fall of rubidium and ytterbium in a very long baseline atom interferometry setup. Here, a 10 m baseline combined with a precise control of systematic effects will enable a determination of the Eötvös ratio at a level of parts in 10^{13} and beyond, thus reaching and overcoming the performance limit of the best classical tests.

1 Introduction

With the great success of the grand unification theory¹ the question arose whether the remaining fourth interaction, gravitation, could be unified with the other three yielding a “theory of everything”. However, all approaches trying to merge quantum field theory and general relativity to a “quantum gravity” framework consistent over all energy scales have failed so far². Hence, in spite of both theories being confirmed at outstanding precision on their own, extensions of at least one of them, e.g. additional fields, are necessary in order to resolve their incompatibility. General relativity is fully based on the postulates constituting Einstein’s equivalence principle (EEP). Next to local position invariance and local Lorentz invariance, the EEP comprises the universality of free fall (UFF), which states that in absence of other forces all bodies located at the same space-time point experience the same acceleration in a gravitational field independently of their composition when neglecting self-gravity. While scrutinizing the EEP, it moreover was identified that under certain circumstances the UFF can be treated as direct empirical foundation for EEP³. Hence, tests of the UFF are a promising candidate in order to further investigate possible extensions of our understanding of gravity compatible with a theory of “quantum gravity”.

A validity of the UFF implies the equality of inertial mass m_{in} and gravitational mass m_{gr} of any test body. In 1884, Hertz described the fact that gravity, unlike any other interaction, acts identically on all bodies independently of their gravitational charge as a “wonderful mystery”⁴.

The so called Eötvös ratio

$$\eta_{A,B} \equiv 2 \frac{g_A - g_B}{g_A + g_B} = 2 \frac{\left(\frac{m_{gr}}{m_{in}}\right)_A - \left(\frac{m_{gr}}{m_{in}}\right)_B}{\left(\frac{m_{gr}}{m_{in}}\right)_A + \left(\frac{m_{gr}}{m_{in}}\right)_B}, \quad (1)$$

where g_i is the gravitational acceleration of test body $i = A, B$ is a comprehensive figure of merit when testing the UFF and is non-zero in case of a violation of the UFF.

Tests of the UFF emerged from Galilei's thought experiment in the 16th century of comparing the free fall of different cannon balls dropped from the leaning tower of Pisa, commonly referred to as Galilean tests⁵. A demonstration test of this kind was performed during the Apollo 15 mission in 1971 by dropping a hammer and a feather on the Moon⁶. The most accurate measurements of the Eötvös ratio were performed by i) monitoring the distance between Earth and Moon in free fall around the Sun by means of laser ranging^{7,8}, yielding $\eta_{\text{Earth,Moon}} = (-0.8 \pm 1.3) \times 10^{-13}$ and ii) employing a torsion balance⁹ with beryllium and titanium test masses¹⁰ yielding $\eta_{\text{Be,Ti}} = (0.3 \pm 1.8) \times 10^{-13}$. The best Galilean test used a laser interferometer to read out the differential free fall motion of copper and uranium test masses¹¹ and found $\eta_{\text{Cu,U}} = (1.3 \pm 5.0) \times 10^{-10}$.

The aforementioned tests employ classical, macroscopic bodies as test masses. In a complementary approach, the UFF can also be tested with quantum objects by observing the interference of massive particles such as neutrons or atoms under the influence of gravity. As first demonstrated in 1973 by Colella, Overhauser, and Werner¹², the gravitationally induced phase shift imprinted on a particle's wave function is either compared to a classical gravimeter or to a second quantum object.

Quantum tests of the UFF differ from their classical counterparts in various aspects. Matter wave tests extend the set of test masses by allowing to employ any laser-coolable species. Furthermore, use of cold atoms add the spin as a degree of freedom and enables investigation of spin-gravity coupling², and the accessible ultracold temperatures are inherently linked to macroscopic coherence lengths¹³ which stands in fundamental contrast to classical test masses.

Quantum tests of the UFF that have been performed in the past can be classified in three categories: i) semi-classical tests, comparing an atom interferometer to a classical gravimeter^{14,15} and reaching accuracies on the ppb-level; ii) quantum tests at a level of parts in 10^7 comparing the free fall of rubidium^{16,17,18} or strontium¹⁹ isotopes; iii) quantum tests comparing the free fall of two different chemical elements²⁰.

Analyzing a test mass pair in a given framework, e.g. a test theory²¹ or a parametrization²², allows to quantify the influence of a violation of the UFF ruled out with a given test mass pair. In general, a well-suited test mass pair fulfills $m_A \gg m_B$ or vice versa, making different chemical elements generally interesting test pairs. Accordingly, with their naturally low relative mass difference comparisons of heavier isotopes suffer from lower sensitivity to violations. On the other hand, however, they benefit from strong rejection of noise sources¹⁷ and systematic errors^{23,24}.

This article is organized as follows: In section 2, we provide a brief overview on the underlying theory of dual species matter wave interferometry and summarize the first quantum test of the UFF using two different chemical elements, ⁸⁷Rb and ³⁹K. We furthermore discuss an assessment of the systematic biases influencing our measurement. Section 3 focuses on our strategies aiming towards a state-of-the-art test of the UFF comparing the free fall of ytterbium and rubidium in a 10 m very long base line atom interferometry setup. This article closes with an outlook into the future of matter wave tests of the UFF and a conclusion in section 4.

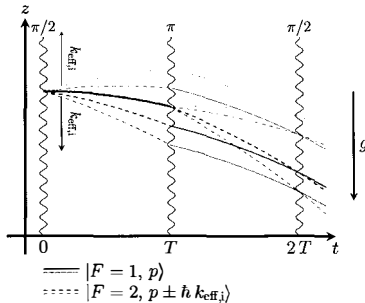


Figure 1 – Space-time diagram of a dual-species Mach-Zehnder matter wave interferometer in a constant gravitational field for the downward (thick lines) and upward (thin lines) direction of momentum transfer. Stimulated Raman transitions at times 0 , T , and $2T$ couple the states $|F_i = 1, p\rangle$ and $|F_i = 2, p \pm \hbar k_{\text{eff},i}\rangle$, where i stands for Rb (blue lines) or K (red lines). The velocity change induced by the Raman pulses is not to scale with respect to the gravitational acceleration.

2 Quantum test of the universality of free fall of ^{87}Rb and ^{39}K

In order to observe the gravitational acceleration acting on ^{87}Rb and ^{39}K , we employ the Mach-Zehnder-type matter wave interferometer geometry²⁵ realized with stimulated Raman transitions coupling the states $|F_i = 1, p\rangle$ and $|F_i = 2, p \pm \hbar k_{\text{eff},i}\rangle$ as displayed in fig. 1. In this configuration, we make use of an effective wavefront acceleration $\frac{\alpha}{k_{\text{eff}}}$ caused by a linear frequency ramp α of the beam splitting light frequency difference with effective wave vector k_{eff} . This acceleration enters the leading order phase shift as (throughout this Section, i is Rb or K)

$$\Delta\phi_i = \left(g_i - \frac{\alpha_i}{k_{\text{eff},i}}\right) \cdot k_{\text{eff},i} \cdot T^2. \quad (2)$$

An experimental cycle starts by collecting 8×10^8 atoms of ^{87}Rb and 3×10^7 atoms of ^{39}K from a transversely cooled atomic beam within 1 s in a three-dimensional magneto-optical trap. The ensembles are subsequently cooled down to sub-Doppler temperatures utilizing the techniques described in Refs.^{26,27,28} yielding temperatures $T_{\text{Rb}} = 27 \mu\text{K}$ and $T_{\text{K}} = 32 \mu\text{K}$. Optical pumping is utilized to prepare the atoms in the $|F_i = 1\rangle$ Zeeman manifold. By switching off all cooling light fields, the atoms are subsequently released into free fall.

A sequence of three Raman light pulses separated by the time T is employed to form a Mach-Zehnder-type interferometer while applying a linear chirp α on the Raman laser difference frequency causing an acceleration of the wavefronts of the beam splitters. Afterwards, the exit ports of the interferometer are selectively read out by optical pumping and detection of fluorescence driving the $|F_i = 2\rangle \rightarrow |F'_i = 3\rangle$ transition. A single experimental cycle takes ≈ 1.6 s.

By varying the the effective wavefront acceleration, a global phase minimum appears independently of the free evolution time T where $g - \frac{\alpha}{k_{\text{eff}}} = 0$ and thus allows to determine g . Figure 2 shows the determination of gravitational acceleration $a_i^{(\pm)}(g)$ of ^{87}Rb and ^{39}K for the upward and downward direction of momentum transfer. Here, observation of the phase shift for both directions allows to strongly suppress systematic phase shifts that do not invert their sign when changing directions of momentum transfer by computing the half difference signal^{29,30}.

2.1 Data analysis

For testing the universality of free fall, the global phase minimum positions $a_i^{(\pm)}(g)$ in fig. 2 are monitored continuously over ≈ 4 h by tuning the effective acceleration of the Raman wavefronts $\alpha_i^{(\pm)}/k_{\text{eff},i}$ around $a_i^{(\pm)}(g)$ in 10 steps per direction of momentum transfer with pulse separation

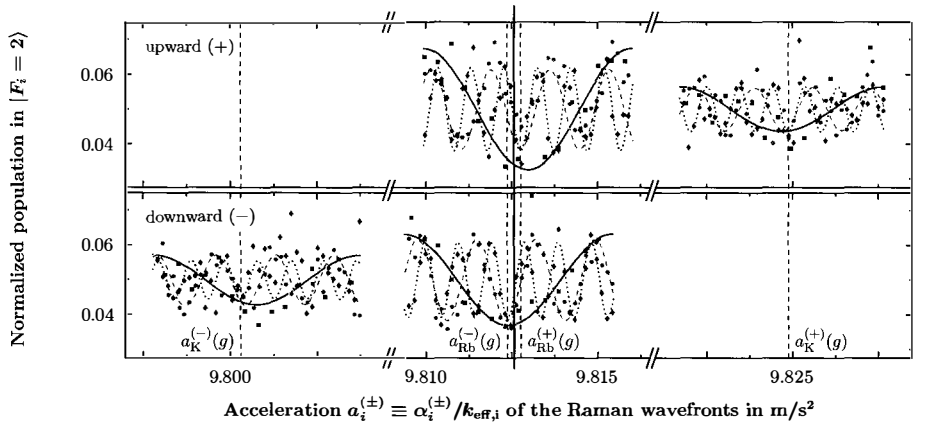


Figure 2 – Determination of the differential gravitational acceleration of rubidium and potassium. Typical fringe signals and sinusoidal fit functions are plotted in dependence of the effective Raman wavefront acceleration for pulse separation times $T = 8$ ms (black squares and solid black line), $T = 15$ ms (red circles and dashed red line), and $T = 20$ ms (blue diamonds and dotted blue line) for upward (+) and downward (-) direction of momentum transfer. The central fringe positions $a_i^{(\pm)}(g)$ (dashed vertical lines), where i is Rb or K, are shifted symmetrically around $g_i = [a_i^{(+)}(g) - a_i^{(-)}(g)]/2$ (solid vertical line). The data sets are corrected for slow linear drifts and offsets.

Table 1: Overview systematic biases $\Delta\eta$ and comparison of the current uncertainties $\delta\eta$ of the Eötvös ratio to the improved uncertainties $\delta\eta^{\text{adv}}$ achieved by using an optical dipole trap. The uncertainties are treated to be uncorrelated at the level of inaccuracy.

| Contribution | $\Delta\eta$ | $\delta\eta$ | $\delta\eta^{\text{adv}}$ |
|------------------------------|-----------------------|-----------------------|---------------------------|
| Second-order Zeeman effect | -5.8×10^{-8} | 2.6×10^{-8} | 3.0×10^{-9} |
| Wavefront aberration | 0 | 1.2×10^{-8} | 3.0×10^{-9} |
| Coriolis force | 0 | 9.1×10^{-9} | 1.0×10^{-11} |
| Two-photon light shift | 4.1×10^{-9} | 8.2×10^{-11} | 8.2×10^{-11} |
| Effective wave vector | 0 | 1.3×10^{-9} | 1.3×10^{-9} |
| First-order gravity gradient | 0 | 9.5×10^{-11} | 1.0×10^{-12} |
| Total | -5.4×10^{-8} | 3.1×10^{-8} | 4.4×10^{-9} |

time $T = 20$ ms. Accordingly, the acquisition of $g_i = [a_i^{(+)}(g) - a_i^{(-)}(g)]/2$ takes 32 s in total and yields one data point for the Eötvös ratio (eq. (1)). The statistical uncertainty of the Eötvös ratio measurement after 4096 s of integration is $\sigma_\eta = 5.4 \times 10^{-7}$, dominated by technical noise of the potassium interferometer.

In Table 1 we list systematic effects influencing our measurement with overall bias of $\Delta\eta_{\text{tot}} = -5.4 \times 10^{-8}$ and an uncertainty $\delta\eta_{\text{tot}} = 3.1 \times 10^{-8}$. A third column $\delta\eta^{\text{adv}}$ shows expected improved uncertainties at an overall level of parts per billion when using a dual-species optical dipole trap³¹ as a common source which allows to precisely collocate the ensembles and to control their differential center of mass motion and expansion.

2.2 Summary

Taking into account the statistical uncertainty σ_η and the bias $\Delta\eta_{\text{tot}}$, the Eötvös ratio can be determined to $\eta_{\text{Rb,K}} = (0.3 \pm 5.4) \times 10^{-7}$. At the current stage, the experiment is solely limited by technical noise dominating the short-term instability of the potassium interferometer. Hence,

in the quadratic sum the statistical uncertainty fully overrules our systematic uncertainty. By reducing technical noise sources common mode noise rejection³² between the interferometers will allow to push the experiment towards its limit posed by systematic uncertainty.

3 Very long baseline atom interferometry

3.1 Experimental setup

As shown in section 2 for a Mach-Zehnder-type geometry, the sensitivity to accelerations of an atom interferometer scales with the square of the pulse separation time T^2 . A natural way to improve this sensitivity is to increase the free-fall time of the atoms enabling longer pulse separation times. This is the main driver for ground-based very long baseline devices and micro-gravity experiments. The latter feature free-fall times up to several seconds (droptower, parabolic flights), minutes (sounding rockets), or even days (space stations, satellites) in a small and thus well characterized volume. The practical and technological challenges combined with the high costs limit, however, the use of such platforms. In this section, we report about an on-going project of a ground-based very long baseline atom interferometer (VLBAI) device that will extend the baseline of the apparatus described in section 2 from 30 cm to more than 10 m, allowing atoms to experience free-fall times up to $2T \sim 1.3$ s in drop mode or up to $2T \sim 2.6$ s in fountain mode. Together with our choice of species described below, we expect to reach an inaccuracy of $7 \cdot 10^{-13}$ in the Eötvös ratio in the near future³³.

As a device targeting a quantum test of the UFF, the proposed apparatus is designed as a dual-species gravimeter using ultra-cold mixtures of rubidium and ytterbium. The relevance of this species choice is motivated by the constraints possible to put on UFF violating theories, such as the dilaton scenario²¹ and the standard model extension²² (SME). In particular, an analysis in the SME framework shows that the Rb-Yb test pair choice is complementary to the Rb-K pair which was chosen for the previously described project, the QUANTUS/MAIUS/PRIMUS micro-gravity experiments^{34,35,36} and the STE-QUEST^{37,23} M4 satellite proposal.

The extended size of the apparatus triggers specific engineering challenges to reach the UFF test performance announced above. As already demonstrated in other precision atom interferometers, a rotation compensation^{38,39,40} of the inertial reference mirror at rates of $\sim \mu\text{rad s}^{-1}$ is required in order to mitigate the systematic uncertainty linked to the Coriolis effect. Moreover, the use of rubidium atoms with magnetic susceptibility⁴¹ of 57.5 GHz T^{-2} requires magnetic shielding of a factor at least 1×10^4 along the entire interferometry region. In this case, it extends over more than 10 m. Finally, the reduced diameter of the vacuum tube (for efficient magnetic shielding) limits its conductance and makes its evacuation down to 1×10^{-10} mbar challenging.

3.2 Atomic sources

In order to fully take advantage of the long baseline without severe systematics limiting the performance, the size of the clouds during their free-fall must be kept as small as possible. This can be achieved by delta-kick collimation (DKC) techniques^{42,43} already demonstrated in the scope of micro-gravity experiments⁴⁴ or very-long-baseline atom fountains⁴⁵. In the current design, we plan for a mixture of rubidium and ytterbium with $2 \cdot 10^5$ and $1 \cdot 10^5$ atoms, respectively. Preliminary estimations show that with a DKC pulsed at few tens of milliseconds, it is possible to keep the radius of the mixture at around 2 mm after 1.5 s of free evolution time. Within this regime, the leading systematics effects are not expected to deteriorate the uncertainty of the UFF test³³.

Furthermore, the preparation time of such an ultra-cold mixture should not exceed 10 s in order to enable sufficient repetition rates for reaching a statistical error of $7 \cdot 10^{-13}$ after one day

of averaging. This cycling rates should be within reach in view of recent development in the production of high-flux sources of degenerate gases³⁴.

3.3 Dual-species launch for precision tests

The initial collocation and differential velocity of the two atomic clouds need to be kept small and very well characterized. Indeed, gravity gradients couple to the initial spatial offset and differential velocity inducing detrimental phase shifts at the output ports of the dual-interferometer²⁴. More precisely, the desired accuracy for a UFF test implies a maximum offset between the two clouds of about 10 nm and a maximum relative velocity of about 10 nm s^{-1} derived in previous work³³. Beyond these limits, the characterization of the gravity gradients becomes extremely challenging. In the condensed regime, the interactions play a crucial role in defining the symmetry of the ground state of the mixture. For a large overlap between the two test species, the choice of isotopes has to be restricted to miscible pairs. In a previous study³³, we showed that the isotopes ^{168}Yb and ^{170}Yb can be good candidates to mix with ^{87}Rb thanks to their scattering length properties. Their natural abundances of 3% and 0.1%, respectively, increase, however, the challenge for a high-flux source of suitable cold ytterbium atoms. The collocation requirement implies the use of a common trap for both species. Since the ground state of bosonic ytterbium cannot be magnetically trapped, a mid-infrared dipole trap will be used for this purpose. In order to fully unfold the potential of the baseline in terms of achievable free fall time, a fountain launch is necessary. Due to the very small differential velocity allowed here, molasses launch is not sufficiently accurate. In a recent proposal⁴⁶, it was shown that a single lattice cannot drive atoms with different masses to the same velocity after an acceleration ramp. The use of two lattices to control each species is not possible due to crosstalks between the atoms transitions and the two light frequencies. It was rather suggested in the latter proposal to utilize two lattices at *tune-out* or *zero-magic* frequencies of one atom each. For rubidium, light frequencies for which the contribution of the D₁ and D₂ lines to the dipole potential balance, were recently precisely measured⁴⁷ to an uncertainty below 1 pm. Concerning ytterbium, there are, to our knowledge, no experimental data available but only theoretical calculations⁴⁸ predicting tune-out wavelengths at 358.78 nm and 553.06 nm with a large uncertainty of a fraction of a nanometer. It is therefore highly interesting to experimentally determine these wavelength for fundamental as well as practical reasons. Once this is done, it is possible to engineer a selective lattice launch accelerating the two atomic species to equal velocities up to few nm/s as suggested⁴⁶ for rubidium and potassium.

The baseline presented in this section, would in this case close the precision gap between classical and quantum UFF tests utilizing interferometers with free fall times of up to 2.8 s.

4 Outlook & Conclusion

Matter wave interferometers are a new tool with fascinating prospects for future investigations of gravity, its relation to quantum mechanics and related open questions^{49,50}. We demonstrated a test of the UFF with the two different chemical elements Rb and K to a level of $5 \cdot 10^{-7}$. With the same apparatus we anticipate an improvement by two orders of magnitude with the implementation of an optical dipole trap. We are setting up a large scale experiment with increased free fall time, targeting a UFF test with Rb and Yb to the level of $7 \cdot 10^{-13}$ competitive with classical tests. Pursuing tests of the universality of free fall is a very promising strategy to find the missing piece for a self-consistent “quantum gravity” framework valid over all energy scales and complementary to Galilean tests in space⁵¹. Matter wave interferometry is not only enlarging the choice of test materials, but also allows to probe gravity with new states of matter such as entangled atoms or even Schrödinger cats.

Acknowledgments

We are grateful to W. P. Schleich, A. Roura, and H. Ahlers for fruitful discussions.

This work was funded by the German Research Foundation (DFG) via the Sonderforschungsbereich (SFB) 1128 Relativistic Geodesy and Gravimetry with Quantum Sensors (geo-Q) and the Cluster of Excellence Centre for Quantum Engineering and Space-Time Research (QUEST). It is also supported by the German Space Agency (DLR) with funds provided by the Federal Ministry for Economic Affairs and Energy (BMWi) due to an enactment of the German Bundestag under grant numbers DLR 50WM1131-1137 (QUANTUS-III) and DLR 50WM1142 (PRIMUS-II).

References

1. H. Georgi and S. L. Glashow. Unity of all elementary-particle forces. *Phys. Rev. Lett.*, 32(8):438–441, 1974.
2. C. Lämmerzahl. The search for quantum gravity effects i. *Appl. Phys. B*, 84(4):551–562–, 2006.
3. C. M. Will. The confrontation between general relativity and experiment. *Living Rev. Relativity*, 17(4), 2014.
4. H. Hertz. *Die Constitution der Materie: Eine Vorlesung über die Grundlagen der Physik aus dem Jahre 1884*. Springer, Berlin, 1999.
5. D. Stillman. *Galileo at work : his scientific biography*. Mineola (N.Y.): Dover publ., 2003.
6. Manned Spacecraft Center NASA. Apollo 15 preliminary science report. *NASA SP*, 289, 1972.
7. J. G. Williams, S. G. Turyshev, and D. H. Boggs. Progress in lunar laser ranging tests of relativistic gravity. *Phys. Rev. Lett.*, 93(26):261101–, 2004.
8. J. Müller, F. Hofmann, and L. Biskupek. Testing various facets of the equivalence principle using lunar laser ranging. *Classical and Quantum Gravity*, 29(18):184006–, 2012.
9. L. Eötvös. über die anziehung der erde auf verschiedene substanzen. *Mathematische und naturwissenschaftliche Berichte aus Ungarn*, 8:65–, 1889.
10. S. Schlamminger, K.-Y. Choi, T. A. Wagner, J. H. Gundlach, and E. G. Adelberger. Test of the equivalence principle using a rotating torsion balance. *Phys. Rev. Lett.*, 100(4):041101–, 2008.
11. T. M. Niebauer, M. P. McHugh, and J. E. Faller. Galilean test for the fifth force. *Phys. Rev. Lett.*, 59:609–612, 1987.
12. R. Colella, A. W. Overhauser, and S. A. Werner. Observation of gravitationally induced quantum interference. *Phys. Rev. Lett.*, 34(23):1472–1474, 1975.
13. E. Göklü and C. Lämmerzahl. Metric fluctuations and the weak equivalence principle. *Classical Quantum Gravity*, 25(10):105012–, 2008.
14. A. Peters, K.-Y. Chung, and S. Chu. Measurement of gravitational acceleration by dropping atoms. *Nature (London)*, 400(6747):849–852, 1999.
15. S. Merlet, Q. Bodart, N. Malossi, A. Landragin, F. Pereira Dos Santos, O. Gitlein, and L. Timmen. Comparison between two mobile absolute gravimeters: optical versus atomic interferometers. *Metrologia*, 47(4):L9–, 2010.
16. S. Fray, C. A. Diez, T. W. Hänsch, and M. Weitz. Atomic interferometer with amplitude gratings of light and its applications to atom based tests of the equivalence principle. *Phys. Rev. Lett.*, 93(24):240404–, 2004.
17. A. Bonnin, N. Zahzam, Y. Bidel, and A. Bresson. Simultaneous dual-species matter-wave accelerometer. *Phys. Rev. A*, 88(4):043615–, 2013.
18. L. Zhou, S. Long, B. Tang, X. Chen, F. Gao, W. Peng, W. Duan, J. Zhong, Z. Xiong, J. Wang, Y. Zhang, and M. Zhan. Test of equivalence principle at 10^{-8} level by a dual-species double-diffraction raman atom interferometer. arXiv:1503.00401.

19. M. G. Tarallo, T. Mazzoni, N. Poli, D. V. Sutyryn, X. Zhang, and G. M. Tino. Test of einstein equivalence principle for 0-spin and half-integer-spin atoms: Search for spin-gravity coupling effects. *Phys. Rev. Lett.*, 113(2):023005–, 2014.
20. D. Schlippert, J. Hartwig, H. Albers, L. L. Richardson, C. Schubert, A. Roura, W. P. Schleich, W. Ertmer, and E. M. Rasel. Quantum test of the universality of free fall. *Phys. Rev. Lett.*, 112:203002, 2014.
21. T. Damour. Theoretical aspects of the equivalence principle. *Classical Quantum Gravity*, 29(18):184001–, 2012.
22. M. A. Hohensee, H. Müller, and R. B. Wiringa. Equivalence principle and bound kinetic energy. *Phys. Rev. Lett.*, 111(15):151102–, 2013.
23. D. Aguilera et al. Ste-quest - test of the universality of free fall using cold atom interferometry. *Classical and Quantum Gravity*, 31(11):115010–, 2014.
24. J. M. Hogan, D. M. S. Johnson, and M. A. Kasevich. Light-pulse atom interferometry. arXiv:0806.3261.
25. M. Kasevich and S. Chu. Atomic interferometry using stimulated raman transitions. *Phys. Rev. Lett.*, 67(2):181–184, 1991.
26. M. Landini, S. Roy, L. Carcagnì, D. Trypogeorgos, M. Fattori, M. Inguscio, and G. Modugno. Sub-doppler laser cooling of potassium atoms. *Phys. Rev. A*, 84(4):043432–, 2011.
27. S. Chu. Nobel lecture: The manipulation of neutral particles. *Rev. Mod. Phys.*, 70(3):685–706, 1998.
28. W. D. Phillips. Nobel Lecture: Laser cooling and trapping of neutral atoms. *Rev. Mod. Phys.*, 70(3):721–741, Jul 1998.
29. J. M. McGuirk, G. T. Foster, J. B. Fixler, M. J. Snadden, and M. A. Kasevich. Sensitive absolute-gravity gradiometry using atom interferometry. *Phys. Rev. A*, 65(3):033608–, 2002.
30. A. Louchet-Chauvet, T. Farah, Q. Bodart, A. Clairon, A. Landragin, S. Merlet, and F. Pereira Dos Santos. The influence of transverse motion within an atomic gravimeter. *New J. Phys.*, 13(6):065025–, 2011.
31. M. Zaiser, J. Hartwig, D. Schlippert, U. Velte, N. Winter, V. Lebedev, W. Ertmer, and E. M. Rasel. Simple method for generating bose-einstein condensates in a weak hybrid trap. *Phys. Rev. A*, 83:035601, 2011.
32. B. Barrett, L. Antoni-Micollier, L. Chichet, B. Battelier, P.-A. Gominet, A. Bertoldi, P. Bouyer, and A. Landragin. Correlative methods for dual-species quantum tests of the weak equivalence principle. arXiv:1503.08423.
33. J. Hartwig, S. Abend, C. Schubert, D. Schlippert, H. Ahlers, K. Posso-Trujillo, N. Gaaloul, W. Ertmer, and E. M. Rasel. Testing the universality of free fall with rubidium and ytterbium in a very large baseline atom interferometer. *New J. Phys.*, 17(3):035011–, 2015.
34. J. Rudolph et al. A high-flux bec source for mobile atom interferometers. *New Journal of Physics*, 17(6):065001–, 2015.
35. S. T. Seidel, N. Gaaloul, and E. M. Rasel. Maius - a rocket-born test of an atom interferometer with a chip-based atom laser. *Proceedings of the 63rd International Astronautical Congress 2012*, 3:801, 2013.
36. S. Herrmann, H. Dittus, and C. Lämmerzahl. Testing the equivalence principle with atomic interferometry. *Classical and Quantum Gravity*, 29(18):184003–, 2012.
37. C. Schubert et al. Differential atom interferometry with ^{87}Rb and ^{85}Rb for testing the uff in ste-quest. arXiv:1312.5963.
38. S.-Y. Lan, P.-C. Kuan, B. Estey, P. Haslinger, and H. Müller. Influence of the coriolis force in atom interferometry. *Phys. Rev. Lett.*, 108(9):090402–, 2012.
39. A. Sugarbaker, S. M. Dickerson, J. M. Hogan, D. M. S. Johnson, and M. A. Kasevich.

- Enhanced atom interferometer readout through the application of phase shear. *Phys. Rev. Lett.*, 111(11):113002–, 2013.
40. S. M. Dickerson, J. M. Hogan, A. Sugarbaker, D. M. S. Johnson, and M. A. Kasevich. Multi-axis inertial sensing with long-time point source atom interferometry. *Phys. Rev. Lett.*, 111(8):083001–, 2013.
 41. D. A. Steck. Rubidium 87 D Line Data, rev. 2.1.4. 2010.
 42. S Chu, A Ashkin Bjorkholm, P Gordon, and LW Hollberg. Proposal for optically cooling atoms to temperatures of the order of 10^{-6} K. *Opt. Lett.*, 11:73, 1986.
 43. Hubert Ammann and Nelson Christensen. Delta kick cooling: A new method for cooling atoms. *Phys. Rev. Lett.*, 78:2088–2091, Mar 1997.
 44. H. Müntinga, H. Ahlers, M. Krutzik, A. Wenzlawski, S. Arnold, D. Becker, K. Bongs, H. Dittus, H. Duncker, N. Gaaloul, C. Gherasim, E. Giese, C. Grzeschik, T. W. Hänsch, O. Hellmig, W. Herr, S. Herrmann, E. Kajari, S. Kleinert, C. Lämmerzahl, W. Lewoczko-Adamczyk, J. Malcolm, N. Meyer, R. Nolte, A. Peters, M. Popp, J. Reichel, A. Roura, J. Rudolph, M. Schiemanck, M. Schneider, S. T. Seidel, K. Sengstock, V. Tamma, T. Valenzuela, A. Vogel, R. Walser, T. Wendrich, P. Windpassinger, W. Zeller, T. van Zoest, W. Ertmer, W. P. Schleich, and E. M. Rasel. Interferometry with bose-einstein condensates in microgravity. *Phys. Rev. Lett.*, 110:093602, Feb 2013.
 45. Tim Kovachy, Jason M. Hogan, Alex Sugarbaker, Susannah M. Dickerson, Christine A. Donnelly, Chris Overstreet, and Mark A. Kasevich. Matter wave lensing to picokelvin temperatures. *Phys. Rev. Lett.*, 114:143004, Apr 2015.
 46. R. Chamakhi. Species-selective lattice launch for precision atom interferometry. *to be published*, 2015.
 47. C. D. Herold, V. D. Vaidya, X. Li, S. L. Rolston, J. V. Porto, and M. S. Safronova. Precision measurement of transition matrix elements via light shift cancellation. *Phys. Rev. Lett.*, 109:243003, Dec 2012.
 48. Yongjun Cheng, Jun Jiang, and J. Mitroy. Tune-out wavelengths for the alkaline-earth-metal atoms. *Phys. Rev. A*, 88:022511, Aug 2013.
 49. P. Hamilton, M. Jaffe, J. M. Brown, L. Maisenbacher, B. Estey, and H. Müller. Atom interferometry in an optical cavity. *Phys. Rev. Lett.*, 114(10):100405–, March 2015.
 50. P. Hamilton, M. Jaffe, P. Haslinger, Q. Simmons, H. Müller, and J. Khoury. Atom-interferometry constraints on dark energy. arXiv:1502.03888.
 51. P. Touboul, G. Métris, V. Lebat, and A. Robert. The microscope experiment, ready for the in-orbit test of the equivalence principle. *Classical Quantum Gravity*, 29(18):184010–, 2012.



Matter-wave laser Interferometric Gravitation Antenna (MIGA): New perspectives for fundamental physics and geosciences

R. Geiger¹, L. Amand¹, A. Bertoldi², B. Canuel², W. Chaibi⁴, C. Danquigny^{5,6}, I. Dutta¹, B. Fang¹, S. Gaffet³, J. Gillot², D. Holleville¹, A. Landragin¹, M. Merzougui⁴, I. Riou², D. Savoie¹ and P. Bouyer²

¹*SYRTE, Observatoire de Paris, PSL Research University, CNRS, Sorbonne Universités, UPMC Univ. Paris 06, LNE, 61 avenue de l'Observatoire, 75014 Paris, France*

²*LP2N, Laboratoire de Photonique Numérique et Nanosciences, Institut d'Optique Graduate School IOA, Rue Francois Mitterrand, 33400 Talence, France*

³*LSBB, UMS UNS, UAPV, CNRS, 84400 Rustrel, France*

⁴*ARTEMIS Observatoire de la Côte d'Azur, Boulevard de l'Observatoire CS 34229, 06304 Nice Cedex 04, France*

⁵*UAPV, UMR1114 EMMAH, F-84000 Avignon, France*

⁶*INRA, UMR1114 EMMAH, F-84914 Avignon, France*

The MIGA project aims at demonstrating precision measurements of gravity with cold atom sensors in a large scale instrument and at studying the associated powerful applications in geosciences and fundamental physics. The first stage of the project (2013-2018) will consist in building a 300-meter long optical cavity to interrogate atom interferometers and will be based at the low noise underground laboratory LSBB based in Rustrel, France. The second stage of the project (2018-2023) will be dedicated to science runs and data analyses in order to probe the spatio-temporal structure of the local gravity field of the LSBB region, which represents a generic site of hydrological interest. MIGA will also assess future potential applications of atom interferometry to gravitational wave detection in the frequency band $\sim 0.1 - 10$ Hz hardly covered by future long baseline optical interferometers. This paper presents the main objectives of the project, the status of the construction of the instrument and the motivation for the applications of MIGA in geosciences. Important results on new atom interferometry techniques developed at SYRTE in the context of MIGA and paving the way to precision gravity measurements are also reported.

1 Introduction

After more than 20 years of fundamental research, atom interferometers have reached sensitivity and accuracy levels competing with or beating inertial sensors based on different technologies. Atom interferometers offer interesting applications in geophysics (gravimetry, gradiometry, Earth rotation rate measurements), inertial sensing (submarine or aircraft autonomous positioning), metrology (new definition of the kilogram) and fundamental physics (tests of the standard model, tests of general relativity). Atom interferometers already contributed significantly to fundamental physics by, for example, providing stringent constraints on quantum-electrodynamics through measurements of the hyperfine structure constant¹, testing the Equivalence Principle with cold atoms², or providing new measurements for the Newtonian gravitational constant³.

Cold atom sensors have moreover been established as key instruments in metrology for the new definition of the kilogram⁴ or through international comparisons of gravimeters⁵. The field of atom interferometry (AI) is now entering a new phase where very high sensitivity levels must be demonstrated, in order to enlarge the potential applications outside atomic physics laboratories. These applications range from gravitational wave (GW) detection in the [0.1 – 10 Hz] frequency band to next generation ground and space-based Earth gravity field studies to precision gyroscopes and accelerometers.

The Matter-wave laser Interferometric Gravitation Antenna (MIGA) project will explore the use of AI techniques to build a large-scale matter-wave sensor which will open new applications in geoscience and fundamental physics. The MIGA consortium gathers 15 expert French laboratories and companies in atomic physics, metrology, optics, geosciences and gravitational physics, with the aim to build a large-scale underground atom-interferometer instrument by 2018 and operate it till at least 2023. In this paper, we present the main objectives of the project, the status of the construction of the instrument and the motivation for the applications of MIGA in geosciences. Important results on new atom interferometry techniques developed at SYRTE in the context of MIGA and paving the way to precision gravity measurements are also reported.

2 MIGA principle and sensitivity

The AI geometry of MIGA is similar to the one of a Mach-Zehnder Interferometer for optical waves. The geometry is described in Fig. 1a) where matter waves are manipulated by a set of counter-propagating laser pulses. At the input of the interferometer, a $\pi/2$ pulse creates an equiprobable coherent superposition of two different momentum states of the atom. The matter-waves are then deflected by the use of π pulse before being recombined with a second $\pi/2$ pulse. To realize these beam-splitters and mirror pulses, MIGA will make use of Bragg diffraction of matter-waves on light standing waves⁶. Conservation of energy-momentum during this process imposes to couple only atomic states of momentum $|+\hbar k\rangle$ to state $|-\hbar k\rangle$ where $k = 2\pi\nu_0/c$ is the wave vector of the interrogation field. At the output of the interferometer, the transition probability between these states is obtained by a two waves interference formula $P = \frac{1}{2}(1 + \cos\phi)$. The atom phase shift ϕ depends on the phase difference between the two counterpropagating lasers which is imprinted on the diffracted matter-wave during the light pulse. MIGA will make use of a set of such AIs interrogated by the resonant field of an optical cavity as described in Fig. 1b). In this configuration, each AI will measure the inertial effects $s_X(X_i)$ along the cavity axis at position X_i together with GW effects associated to the cavity propagation of the interrogation laser. Spurious effects such as fluctuations of the cavity mirror position $x_1(t)$ and $x_2(t)$ or laser frequency noise $\delta\nu(t)$ also affect the AI signal. Taking into account these different effects, the atom phase shift $\phi(X_i)$ measured by the AI at position X_i reads:

$$\phi(X_i) = 2ks_{x_2} + 2k \left(\frac{s_{\delta\nu}}{\nu_0} + \frac{s_h}{2} \right) (X_i - L) + 2ks_X(X_i) \quad (1)$$

where h is the GW strain amplitude, L is the mean cavity length and s_u accounts for the convolution of the time-fluctuations of effect $u(t)$ by the AI sensitivity function $s(t)$ ⁷. The last term in Eq. (1) accounts for the acceleration of the center of mass of the free falling atom cloud which depends on the local position of the AI because of the non-homogeneous gravitational field. Common mode rejection between the AI signals at different positions will enable to cancel out most of the contribution of cavity mirror position fluctuations s_{x_2} . The influence of laser frequency noise will be kept negligible in the first version of the MIGA instrument (till 2023) by using state-of-the-art ultra stable laser techniques, yielding relative stabilities better than $\delta\nu/\nu_0 \sim 10^{-15}$. Eq. (1) thus shows that the instrument can be used for local monitoring of mass motion encoded in the last term s_X and, in the future, for GW detection without being affected by position noise of the optics.

The last term of Eq. (1) can be written as $\phi(X) = 2ka(X)T^2$ where $a(X)$ is the local acceleration of gravity of the atoms at position X and T is the time between the light pulses in a 3 light pulse geometry (see Fig. 1a)). For two AI separated by the baseline $L = X_2 - X_1$ and assuming a constant gravity gradient γ , the gradiometer sensitivity of the instrument is given by $\sigma_\gamma = \sigma_\phi / (2kLT^2\sqrt{\tau})$ where σ_ϕ is the AI phase sensitivity and τ the integration time. For $L = 100$ m, a shot-noise limited AI with 10^6 atoms (1 mrad phase sensitivity) and $T = 0.5$ s yields a gradiometer sensitivity of 2.4×10^{-13} s $^{-2}$ after $\tau = 100$ s of measurement time, which corresponds to a mass anomaly of few tons (of water) in a 100 meter region around the instrument. Combining the different measurements provided by the different AIs of the array allows better positioning the mass anomaly and potentially following its motion.

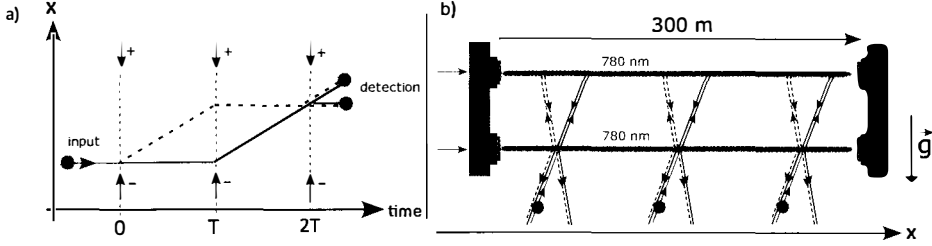


Figure 1 – MIGA geometry. a) Schematic of the 3 pulse atom interferometer. Two laser beams propagating in opposite directions are used to split and recombine the matter waves. The atoms are detected at the output using fluorescence detection. b) Sketch of the MIGA baseline: 3 atom interferometers are interrogated by the 780 nm laser beams resonating inside two optical cavities and operating in parallel.

3 MIGA subsystems

3.1 Cold atom source

The atom source unit delivers cold atom clouds which will be interrogated by the MIGA cavity Bragg beams to form the atom interferometer (AI). The general design of the unit is presented in Fig. 2. Its main functions are (i) the loading and laser cooling of ^{87}Rb atoms, (ii) the launching of the atomic cloud along a quasi-vertical trajectory and the control of the angle of the trajectory with respect to the cavity beams, (iii) the preparation of the cold atom source before it enters the interferometer, and (iv) the detection of the atoms at the interferometer output.

In order to optimize the contrast of the atom interferometer, the quantum state of the atoms is prepared on their way up, before the interrogation region. A first counter-propagating velocity-selective Raman pulse (bottom red beam in Fig. 2) is used to select the atoms in the $m_F = 0$ Zeeman sub-level of the $F = 2$ hyperfine state, with a relatively narrow velocity class (width of 1 photon recoil, corresponding to a temperature of ≈ 400 nK in the direction of the Raman lasers). The unselected atoms are then pushed by a laser tuned on resonance with the cycling transition. This Raman/push procedure is repeated a second time to clean the remaining unwanted atoms produced by spontaneous emission on the first Raman selection pulse. For this purpose, we use the Raman 2 beam (top big red beam) with the approximately same duration and Rabi frequency as the Raman 1 beam to transfer the atoms back to the $F = 2$ state. The remaining atoms in the $F = 1$ state are pushed with an orthogonal push beam tuned on the $F = 1 \rightarrow F' = 0$ transition (gray beam at the top). The angle of the Raman beams can be tuned by few degrees around zero in order to introduce a Doppler effect which allows lifting the degeneracy between the $|p\rangle \rightarrow |p + 2\hbar k\rangle$ and $|p\rangle \rightarrow |p - 2\hbar k\rangle$ transitions. In this way, the atoms will enter the interferometer in a well-defined momentum state. Moreover, the Raman beam angle enables to control the angle of the trajectory with respect to the vertical direction, i.e. the Bragg angle. After this all-optical preparation steps, the atoms enter the interferometer in the

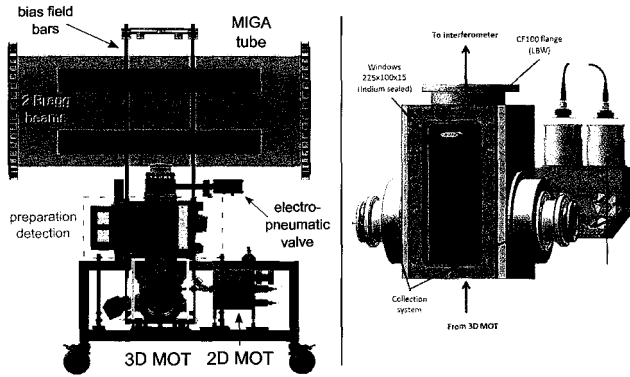


Figure 2 – Left: Global view of the cold atom source unit. Right: technical drawing of the cold atom preparation and detection region.

$|F = 2, m_F = 0\rangle$ internal state, with a relatively narrow velocity distribution in the longitudinal direction of the Bragg interrogation beams and with a well-controlled trajectory.

After their interrogation by the Bragg beams in the atom interferometer, the two different momentum states $|\pm \hbar k\rangle$ of the atoms are labelled to two different internal states with the Raman 2 laser. More precisely, the velocity selective feature of the Raman transition is used to transfer the $|F = 2, \hbar k\rangle$ atoms to the $F = 1$ internal state, while the $|F = 2, -\hbar k\rangle$ atoms remain in the $F = 2$ internal state. The atoms can then be resolved with common fluorescence techniques. Detection of the atoms labelled in $F = 2$ is first realized with a light sheet beam (see Fig. 2) tuned on resonance on the $F = 2 \rightarrow F' = 3$ transition. The beam is partially blocked at the retroreflection mirror so that the atoms acquire a net momentum in the beam direction and will therefore not be resonant with the following light beams. The $F = 1$ atoms are re-pumped to the $F = 2$ state using a thinner intermediate light sheet, before these $F = 2$ atoms enter the third light sheet. The fluorescence light of the two light sheets is collected by a 2% collection efficiency lens and imaged on a two-quadrant photodiode, one quadrant recording the fluorescence associated with one detection zone. The fluorescence signal is used to reconstruct the normalized atomic populations and then the transition probability, yielding the atom interferometer phase.

3.2 Laser System.

The different lasers used to cool and manipulate the atoms are delivered from an all-fibered laser module developed by the company muQuans⁸. The laser architecture is based on frequency doubled telecom lasers, as already described in various publications, see e.g. Refs.⁹. A Master laser is locked using a Rubidium 85 saturated absorption spectroscopy signal and references 3 slave diodes which are respectively used for the 2D MOT cooling laser, the 3D MOT cooling/Raman 2 laser, and the 3D MOT repumper/Raman 1 laser. The 3 slave diodes are all phase locked to the Master laser. The repumping light for the 2D MOT is generated from a fiber electro-optic phase modulator at 1560 nm fed with the appropriate microwave frequency.

After amplification in Erbium doped fiber amplifiers and second harmonic generation in PPLN waveguide crystals, the 780 nm light is sent to optical splitters and guided to the experiment chamber in several optical fibers. The laser module nominally delivers 170 mW total power for the 2D MOT (fiber outputs), 150 mW total power for the 3D MOT, and 100 + 75 mW in each of the two Raman beams used for the preparation stage and the detection. The power and polarization fluctuations at the fiber outputs are close to the one percent level. The phase

lock signals are controlled by various radio-and-microwave frequency sources all referenced to a stable 100 MHz oscillator. The full laser system is hosted in a $1.7 \times 0.5 \times 0.5 \text{ m}^3$ transportable rack.

3.3 Optical cavity setup

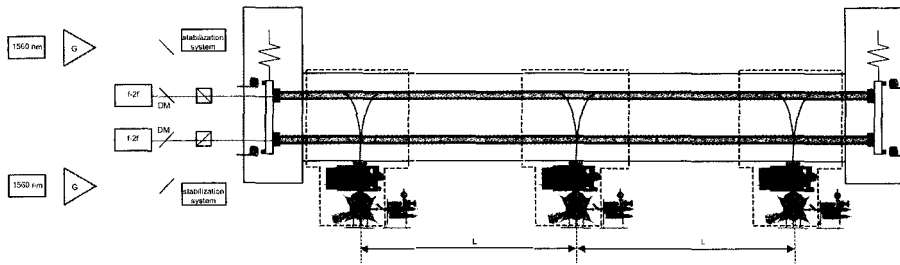


Figure 3 – **Overview of the MIGA cavity with the main sub-systems.** The three atomic heads separated by a distance L launch atomic clouds in an almost vertical parabolic flight. The atoms are manipulated in the upper part of the parabola with a Bragg interferometric sequence by way of radiation pulses at 780 nm (red lines) resonant with two horizontal cavities. The resonance condition for the interrogation light relies on generating the 780 nm via frequency doubling of a 1560 nm laser (yellow lines) locked to one of the two cavities, and using stabilized, common payloads for the mirrors on each side of the cavities to avoid relative length fluctuations of the two resonators. The Ultra High Vacuum system encompassing the optical cavities, the mirror payloads and their stabilization system is represented with gray solid lines; to it are connected the atomic source units. Each interferometric region and most of the related atomic head are enclosed in a mu-metal shield, represented in dashed violet lines. The control system of the experimental setup and the laser systems dedicated to each atomic head are not represented in the plot.

The intensity of the Bragg pulses is enhanced thanks to two cavities, one for the splitting and projection $\pi/2$ pulses, and one at the trajectories' apogee for the π pulse. The solution adopted to have the 780 nm interrogation pulses at resonance with the cavities relies on obtaining the probe radiation via frequency doubling of a telecom laser at 1560 nm continuously locked to one of the two resonators to track its length variations. The servo system is used also to control the payload tilts and rotations so as to maintain the phase coherence between the two cavities. The Bragg pulses are shaped with acousto-optic modulators (AOMs) on the two beams at 780 nm before their injection in the cavities. The telecom laser is phase modulated and locked to the cavity on one frequency sideband, and the modulation frequency Ω is chosen so as to have the doubled component of the carrier resonant with the resonator. Ω has to account for the different cavity length at 780 nm and 1560 nm, because of the refraction index of the two coatings on the mirrors, as well as for the frequency shift imposed by the AOM used to pulse the interrogation beams. The LP2N laboratory is currently developing a prototype system using low power laser sources (100 mW at 1560 nm, and 1 W at 780 nm). The CELIA laboratory at Bordeaux 1 University is developing a high power solution, which targets 100 W of radiation at 780 nm before the injection in the cavity.

The two cavities share a common payload on each side to hold the mirrors, placed at a vertical distance of $\approx 30.6 \text{ cm}$ to have an interrogation time $T = 250 \text{ ms}$. The impact of ground seismic noise on the position of the cavity mirrors will be reduced by way of an antivibration system, which must limit the related phase noise contribution on each atom interferometer. Two different approaches are being considered: a passive system of mechanical filters to suspend each payload, and an active stabilization of each mirror position using piezoelectric actuators. The main constraints on the system are set by the level of the seismic noise at the installation site

(LSBB), and the response function of the atom interferometers to mirror acceleration noise, as in Eq. (1).

4 High sensitivity atom interferometry techniques

The performance of the MIGA antenna will rely on the possibility to achieve high sensitivity gravito-inertial measurements. Moreover, future applications to gravitational wave detection will require higher bandwidth (~ 10 Hz) cold atom interferometers than what is currently obtained in laboratories (about 1 Hz for long T AIs). In this section, we briefly present two results obtained at the SYRTE laboratory on an atom interferometer which geometry is similar to the fountain-like architecture of the MIGA sensors.

First, we demonstrated a new method to interrogate several clouds of cold atoms simultaneously in the interferometer in a so-called joint interrogation scheme¹⁰ (the principle of the joint interrogation is represented in Fig. 4, left panel). Conventional cold atom interferometers run in sequential mode: after laser cooling, the cold atoms are injected in the interferometer where the inertial effects are measured. Thus, the sensor does not operate continuously. Information on signals varying during the cold atom source preparation is lost, which is a major drawback for various applications. Moreover, the aliasing effect of the vibration noise associated with the dead time results in a degradation of the short term sensitivity. To circumvent this problem, the joint interrogation solution compatible with the MIGA fountain geometry allows interrogating the atoms in the interferometer region, while another cold atom cloud is being prepared simultaneously. This leads to a zero-dead time gyroscope. Moreover, if the different atom clouds share common (Bragg) interrogation pulses, the vibration noise is correlated between the successive measurements, which leads to a faster averaging of the vibration noise. We demonstrated a multiple joint operation in which up to five clouds of atoms were interrogated simultaneously in a single fountain with $2T = 800$ ms interrogation time¹⁰. The essential feature of the multiple joint operation, which we demonstrated for a micro-wave Ramsey interrogation is currently being generalized to the inertial sensor operation. The multiple joint operation gives access to high-frequency components while maintaining high sensitivity linked to long interaction times achievable with cold atom sensors.

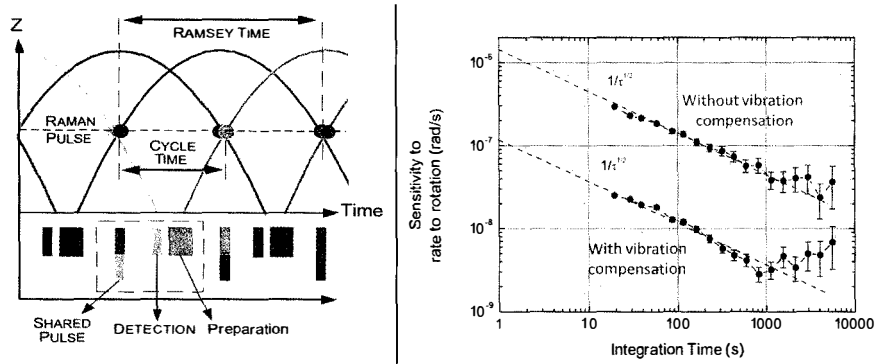


Figure 4 – **New atom interferometry techniques for high precision inertial measurements.** Left: schematic of the joint interrogation technique allowing the interrogation of several clouds of atoms simultaneously in the interferometer and rejection of vibration noise aliasing due to dead times. From Ref.¹⁰. Right: SYRTE cold atom gyroscope with a 3 nrad/s after 1000 s of integration time using a Sagnac matter-wave interferometer of 2.4cm^2 area^{11,12}.

A second key feature of MIGA will be to operate an atom interferometer with a long inter-

rogation time, $2T = 500$ ms, yielding a high accelerometer scale factor $2kT^2$. In this regime, the effect of vibrations from the payload results in several radians of AI phase noise and must be managed to keep it below the targeted phase sensitivity level (ideally below the atom shot noise of ~ 1 mrad). While vibration noise is common to the different AIs in the gradiometer configuration of MIGA, the extraction of the AI phase still requires the Atom interferometer to be operated in its linear range, i.e. $[0 - \pi]$. Moreover, being able to extract the individual AI phase yields the absolute local gravity field (in the direction of the Bragg beams) and therefore provides additional information to the gravity gradient and its curvature. To this end, we demonstrated in the SYRTE experiment the possibility to reject the vibration noise with a factor up to 20 using classical accelerometers in an interferometer with $2T = 800$ ms interrogation time. This noise rejection was performed in a gyroscope configuration where the AI mainly senses rotation rates, allowing us to demonstrate a gyroscope with 3 nrad/s long term stability (see Fig. 4, right panel). These results strongly support the possibility to obtain high sensitivity gravity measurements with the MIGA interferometers.

5 MIGA: new perspectives in geosciences

5.1 Hydrological interest of the Fontaine de Vaucluse/LSBB site

Almost a quarter of the world population obtains its drinking water from karst hydrosystems¹³ (see Fig. 5 for a schematic). Efficient protection and sustainable management of such resources require appropriate tools and strategies to be developed¹⁴. The numerical modelling of karst aquifers is probably the major stumbling block in developing such tools. Karst remains aside from other hydrosystems, because the paroxysmal¹⁵ and self-organized¹⁶ heterogeneity of that medium limits the relevance of classical hydrogeological tools, such as physically-based and gridded flow models, and because of the difficulty of characterisation of this heterogeneity. Hopefully, recent improvements of computing power and computational techniques in the one hand and geophysical measurement techniques in the other hand¹⁷ enable considering now the applicability of physically-based and gridded flow models to karst hydrodynamics. However the Holy Grail to achieve developing and fitting such tools remains acquiring 4D hydro-geo-physical data (water content, flux and velocities, ...) at different scales.

In south-eastern France, the Fontaine-de-Vaucluse karst hydrosystem is one of the biggest karst watershed in the world: its catchment area is around 1115 km² and composed of a nearly 1500 m thick massive and continuous limestone^{18,19} from Nocomanian marls to upper Aptian marls. The Fontaine-de-Vaucluse spring is quite the only outlet of this hydrosystem and the biggest karst spring in Europe with an average outlet discharge of 19 m³/s between 1877 and 2004²⁰. Within this peculiar karst hydrosystem, LSBB (Low Noise Underground Research Laboratory) is an almost horizontal tunnel coming across the karst medium and intersecting arbitrarily faults, karst networks and flowpaths at depths between 0 and 519 m. All these elements make the Fontaine-de-Vaucluse and LSBB sites a relevant multi-scales observatory to develop physically-based and gridded flow models to karst hydrodynamics based on innovative 4D hydro-geo-physical data acquisition.

5.2 Methods

Whereas recent developments of geophysical methods enable to expect better characterization of complex hydrosystems¹⁷, their application to karst remains not obvious²¹. Nevertheless, various conventional techniques and instruments are currently applied to karst hydrogeology such as Electrical Resistivity Tomography (ERT) and 2D Ground Penetration Radar (GPR). One of the important questions is to have enough resolution and depth of investigation all at once to detail all the features controlling the groundwater circulation and storage from matrix porosity or micro-fracturing to major faults and karst conduits. On the other hand, estimating

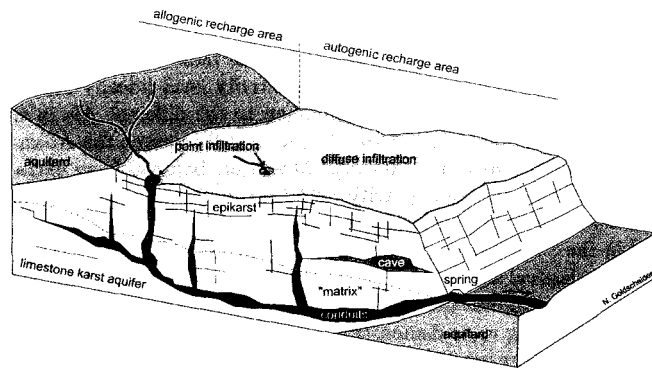


Figure 5 – Block diagram illustrating the hydrogeological functioning of a karst aquifer, from N Goldscheider, D Drew (2007), *Methods in Karst Hydrogeology*, Taylor et Francis, <http://www.agu.kit.edu/english/3851.php>.

the variation of water mass requires the use of integrating methods directly or indirectly related to water content such as seismic, ERT, Magnetic Resonance Sounding (MRS) or Gravimetry. For instance, as shown in Ref. ²², GPR results supply a near surface high resolution (~ 10 cm) imaging and thus can provide relevant geological information such as stratifications and fractures. However, GPR's investigation depth remains limited to around 12 meters. ERT surveys shows strong lateral and vertical variations which can inform on general geological structuring and feature orientation. ERT is able to prospect down to 40 meters but is a low resolution integrative technique. Finally, active seismic reflection imaging or transmission tomography (at frequencies $\sim 10 - 500$ Hz) allows measuring the ground seismic velocities and probing the rock elasticity and porosity, yielding information on the rock structure and fractures ²³. The corresponding resolution is ~ 10 m with accessible depth ~ 100 m.

In contrast to these techniques requiring an inversion model, Atom Interferometry can provide direct measurements of the surrounding mass distribution and thus represents an interesting complementary method. Moreover, long-term (years) measurements of the gravity field can be obtained thanks to the long term stability of cold atom sensors. In this context, MIGA will provide non-invasive long-term (years) measurements of the gravity field on a ~ 1 km-long baseline. As discussed in section 2, the typical gradiometer sensitivity of MIGA will be $\sim 10^{-13} \text{ s}^{-2}$ after 100 s of measurement time, with a maximum sensitivity in the direction of the baseline. Such gravity gradients typically correspond to water masses of 1 ton at 100 meter from the instrument. If the source mass producing such gravity gradients moves in time, the AI antenna signal will vary accordingly. The spatial resolution of the antenna will depend on the number of atom interferometers and their relative distance (3 units separated by 100 m in the first version of MIGA) and the targeted confidence level for the positioning of the source mass. Tuning the AI geometry (inter-pulse duration T , more light pulses, etc.) allows changing the response of the sensor to the source mass thus yielding more information.

6 Conclusion and perspectives

The MIGA instrument will use long baseline (300 m) optical and matter-wave interferometry for high precision gravity field measurements, in order to monitor subsurface mass transfers in the LSBB region, which represents a unique site of hydrological interest. Combining conventional instruments and methods from hydrogeology with cold atom gravitation sensor measurements will allow better modelling of karst aquifers, for which only very few (3+1)-dimensional data are currently available to constrain the models. MIGA will also investigate the applications of

atom interferometry to extend the sensitivity of future GW detectors at frequencies below 10 Hz.

The first cold atom source unit has been characterized and will be installed at LP2N (Talence) in June 2015, where the first experiments on AI in the 1 meter optical cavity will be performed. A 6 meter AI gradiometer prototype based at LP2N is currently under design and will allow testing at a reduced scale the measurement strategy for mass monitoring at LSBB. Digging of the galleries at LSBB is planned for the beginning of 2016, with an installation of the 300 meter long vacuum cavity and the three AI units in 2017. Following the final optimizations of the instrument, the operation phase should start in 2018.

The MIGA Equipex aims at being the first step to a larger, more ambitious program that may lead to a future European infrastructure. The development, the scientific operation and the technical implementation of this first version of the gravitational antenna will pave the way to a more sensitive version that will take advantage of the current fundamental research in advanced atom interferometry. The MIGA instrument and its envisioned evolution will ensure France and Europe's position at the forefront of subterranean instrumentation and a leadership in key quantum technologies. Beyond the development of this equipment, the results of the MIGA project can be anticipated for use in future gravitational wave detectors in order to enhance their low frequency sensitivity.

Acknowledgments

The MIGA Equipex is funded by ANR under the programme *Investissement d'Avenir* (ANR-11-EQPX-0028). We also thank funding from the city of Paris (Emergence project HSENS-MWGRAV), Délégation Générale pour l'Armement (DGA) and CNES.

References

1. Rym Bouchendira and et al. New determination of the fine structure constant and test of the quantum electrodynamics. *Phys. Rev. Lett.*, 106:080801, Feb 2011.
2. D. Schlippert and et al. Quantum test of the universality of free fall. *Phys. Rev. Lett.*, 112:203002, May 2014.
3. G. Rosi and et al. Precision measurement of the newtonian gravitational constant using cold atoms. *Nature*, 510(7506):518–521, June 2014.
4. M. Thomas and et al. First determination of the planck constant using the lne watt balance. *Metrologia*, 52(2):433, 2015.
5. P. Gillot and et al. Stability comparison of two absolute gravimeters: optical versus atomic interferometers. *Metrologia*, 51(5):L15, 2014.
6. Peter J. Martin, Bruce G. Oldaker, Andrew H. Miklich, and David E. Pritchard. Bragg scattering of atoms from a standing light wave. *Phys. Rev. Lett.*, 60:515–518, Feb 1988.
7. P. Cheinet and et al. Measurement of the sensitivity function in time-domain atomic interferometer. *IEEE Trans. on Instrum. Meas*, 57:1141, 2008.
8. <http://www.muquans.com/>.
9. V. Ménotet and et al. Dual-wavelength laser source for onboard atom interferometry. *Opt. Lett.*, 36(21):4128–4130, Nov 2011.
10. M. Meunier, I. Dutta, and et al. Stability enhancement by joint phase measurements in a single cold atomic fountain. *Phys. Rev. A*, 90:063633, Dec 2014.
11. I. Dutta, D. Savoie, B. Fang, R. Geiger, A. Landragin, in preparation.
12. Brynle Barrett and et al. The sagnac effect: 20 years of development in matter-wave interferometry. *Comptes Rendus Physique*, 15(10):875–883, December 2014.
13. D. C. Ford and P. W. Williams. *Karst hydrogeology and geomorphology*. John Wiley & Sons, Chichester., 2007.
14. M. Mudarra, B. Andreo, and J. Mudry. Hydrochemical heterogeneity in the discharge

- zone of a karstic aquifer. In Environmental Earth Sciences, pages 163–168. Springer Berlin Heidelberg, 2010.
15. de Marsily, M. Methodes et domaines d'application de la mécanique des fluides en milieux poreux et fissurés. Annales des Mines, 1984, 5-6, 5-10 (1984).
 16. S.R.H. Worthington and D.C. Ford. Self-organized permeability in carbonate aquifers. Ground Water, 47(3):326–336, 2009.
 17. Brian Berkowitz. Characterizing flow and transport in fractured geological media: A review. Advances in Water Resources, 25(8):861–884, August 2002.
 18. Masse, J.P. 1969. Contribution à l'étude de l'Urgonien (Barrmien - Bdoulien) des Monts de vacluse et du Luberon. Bureau de Recherches Géologiques et Minières, Orlan, 59 p.
 19. Masse, J.P. 1976. Les calcaires urgoniens de Provence ; Valanginien - Aptien inférieur ; Tome 1 : Stratigraphie - Paléontologie ; Tome 2 : Les paléoenvironnements et leur évolution. Thesis: Univ. d'Aix-Marseille, 445 p.
 20. Cognard-Plancq, A. L., C. Gevaudan, and C. Emblanch. 2006. Historical monthly rainfall-runoff database on Fontaine de Vaucluse karst system : review and lessons. Proceedings of 3rd international symposium on karst "Groundwater in the Mediterranean Countries", Malaga, Spain, IGME Publications, vol 18, pp 465-475.
 21. Konstantinos Chalikakis and et al. Contribution of geophysical methods to karst-system exploration: an overview. Hydrogeology Journal, 19:1169–1180, 2011.
 22. Simon D. Carrière and et al. Combining electrical resistivity tomography and ground penetrating radar to study geological structuring of karst unsaturated zone. Journal of Applied Geophysics, 94(0):31–41, July 2013.
 23. Emeline Maufroy et al, Travel time inversion from ground level to gallery: protocol for the characterization of P-wave seismic signature in a fractured-porous Urgonian platform at hectometric scale, Near Surface Geophysics Vol 12, No 6, December 2014 pp. 697 - 708.

WEAK EQUIVALENCE PRINCIPLE, LORENTZ NONINVARIANCE, AND NUCLEAR DECAYS

E. FISCHBACH^{1*}, V. E. BARNES¹, J. M. HEIM¹, D. E. KRAUSE^{2,1}, J. M. NISTOR¹

¹*Department of Physics and Astronomy, Purdue University
West Lafayette, IN, 47906 United States*

²*Physics Department, Wabash College, Crawfordsville, IN 47933 United States*

We consider three possible manifestations of physics beyond the Standard Model, and the relations among them. These are Lorentz non-invariance (LNI), violations of the Weak Equivalence Principle (WEP), and indications of time-varying nuclear decay constants. We present preliminary results from a new experiment indicating the presence of annual and subannual periodicities in decay data, and discuss their implications for physics beyond the Standard Model.

Although the recent discovery of the Higgs boson has reaffirmed our belief in the Standard Model of particle physics, it has also provided a stimulus to search for new physics beyond the Standard Model. In what follows we discuss possible connections among tests of Lorentz Non-Invariance (LNI), violations of the Weak Equivalence Principle (WEP), and recent evidence for time-varying nuclear decay constants. In particular we will suggest that evidence for new physics in any of these areas may also imply new physics in the others. As we will note, mounting evidence that nuclear decay rates can be influenced by ambient neutrinos may also be pointing to new physics arising from the preferred frame defined by these neutrinos.

To illustrate the connection between LNI and WEP violation, we consider two models as examples. In the Nielsen-Picek model¹ LNI effects are introduced by adding to the usual covariant metric tensor $g_{\mu\nu}(x)$ a constant tensor $\chi_{\mu\nu} = \alpha \text{diag}(1/3, 1/3, 1/3, -1)$, where α is a constant. [Here we assume $g_{\mu\nu} = \delta_{\mu\nu}$, $x^\mu = (\vec{x}, x_4 \equiv ix^0)$ and $c = 1$.] For $\alpha \neq 0$ the usual relativistic dispersion relation for a particle of mass m and 4-momentum $p^\mu = (\vec{p}, ip^0)$,

$$-g_{\mu\nu}p^\mu p^\nu = m^2, \quad (1)$$

becomes

$$-(g_{\mu\nu} + \chi_{\mu\nu})p^\mu p^\nu = m^2 - \chi_{\mu\nu}p^\mu p^\nu = m^2 - \alpha \left(\frac{1}{3}\vec{p}^2 + p_0^2 \right). \quad (2)$$

If we assume that the hypothesized LNI effects in Eq. (2) arise only in weak interactions through a modification of the W^\pm and Z^0 propagators, then the total inertial mass of a test body M can be written as²

$$M = M_0 + \alpha B_w \left(1 + \frac{4}{3}\vec{v}^2 \right), \quad (3)$$

where M_0 is the total Lorentz invariant portion of the mass, \vec{v} is its velocity, and αB_w is the Lorentz non-invariant model-dependent contribution to the mass of each sample. Using energy

*ephraim@purdue.edu

conservation it is then straightforward to show that the acceleration a of a test mass falling towards the Earth is given by²

$$a \simeq \left(1 - \frac{11}{3} \frac{\alpha B_w}{M_0}\right) g, \quad (4)$$

where g is the acceleration due to gravity. It follows from Eq. (4) that the difference in acceleration between two test masses #1 and #2 is

$$\frac{\Delta a}{g} = \frac{a_1 - a_2}{g} = -\alpha \frac{11}{3} \left(\frac{B_{w1}}{M_{01}} - \frac{B_{w2}}{M_{02}} \right). \quad (5)$$

This establishes the connection between LNI effects ($\alpha \neq 0$) and WEP violation ($\Delta a/g \neq 0$).

As a second example we consider a modified dispersion relation³ for a particle of mass m and momentum \vec{p} ,

$$E^2 = m^2 + \vec{p}^2 + \frac{\vec{p}^4}{\mu^2}, \quad (6)$$

where μ is a model-dependent constant. If the particle is non-relativistic and in the Earth's gravitational field g at height z above the ground level, its energy can be written as

$$E \simeq m + \frac{\vec{p}^2}{2m} - \frac{\vec{p}^4}{8m^3} + \frac{\vec{p}^4}{2m\mu^2} + mgz. \quad (7)$$

Then for two different particles #1 and #2 falling in the gravitational field, one can show that the LNI effects arising from the presence of the term proportional to $1/\mu^2$ lead to a WEP-violating acceleration difference of the form

$$\frac{\Delta a}{g} = \frac{a_1 - a_2}{g} \simeq 6\bar{v}^2 \left(\frac{m_1^2}{\mu_1^2} - \frac{m_2^2}{\mu_2^2} \right), \quad (8)$$

where \bar{v} is the particle's velocity. Hence in this model $\Delta a/g \neq 0$ can arise even when $\mu_1 = \mu_2$ (i.e., the interaction is composition-independent) provided $m_1 \neq m_2$.

Having established the connection between WEP violation and LNI effects, we next ask whether there is any evidence for LNI effects. Although there is no direct evidence at present, there is both direct and indirect evidence that ambient solar and cosmic neutrinos are in fact interacting with our detection systems. Since cosmic neutrinos (i.e., relic big-bang neutrinos) define a preferred coordinate frame with respect to which the Earth is moving, LNI effects could in principle arise if these neutrinos interact with local experiments. The same is also true for solar neutrinos which have been detected in terrestrial experiments.⁴ Here we focus on the possibility that recent observations of time-dependent nuclear decay parameters could also arise from interactions between background neutrinos and terrestrial detectors. If so, these effects could represent evidence for LNI contributions, and by extension, WEP violations as well.

In Table 1 of Ref.⁵ a summary is presented of earlier results indicating time-varying nuclear decay rates. Although the most common periodic signals seen in those data are annual variations, the most significant are those associated with solar rotation⁶, and with solar storms⁷, since these cannot reasonably be attributed to seasonal variations in the efficiencies of the detectors in the respective experiments. Further support for the inference that the time varying effects are not simply variations in detector efficiencies comes from experiments in which dissimilar variations were seen in the decays of different isotopes being recorded by the same detectors.^{8,9,10}

Here we present preliminary results from a repetition by our group of the original BNL experiment⁸ which measured the half-life of ^{32}Si using ^{36}Cl as a comparison standard. Our experiment utilized both the same samples and the same sample-changing system as in the original experiment, but included an updated detector and electronics. As in the original experiment, data were taken in alternating half-hour runs on the ^{32}Si and ^{36}Cl samples. This insured that the same long term variations in detector efficiencies would be present in the daily count rates of

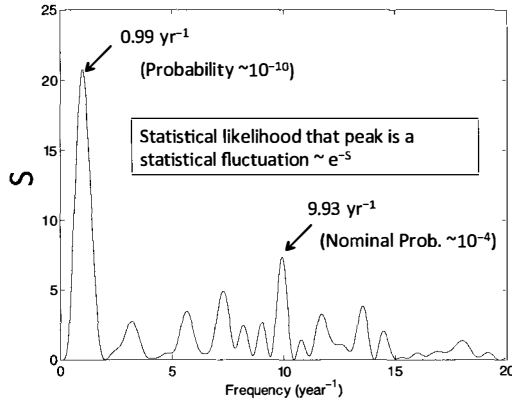


Figure 1 – Power spectrum analysis of time series of $^{32}\text{Si}/^{36}\text{Cl}$ data showing evidence of 1-year and 0.1-year periods. As noted in the text, the latter cannot be attributed to any known environmental effect on our detection system, and has been observed in other decay experiments.

each isotope, and would thus cancel when the $^{32}\text{Si}/^{36}\text{Cl}$ ratio was determined daily. In contrast to the original experiment, which acquired data for only a few days each month for a period of 4 years, our experiment has run continuously for a period of 2 years in an environment where the influences of variations in temperature, pressure, humidity, and magnetic fields have been controlled and monitored.

Figure 1 presents a power spectrum analysis of the time series of data formed by taking the daily ratios of the $^{32}\text{Si}/^{36}\text{Cl}$ data. We see immediately a strong annual signal along with a signal with a frequency of $\sim 10/\text{year}$ similar to the signals found in other decay experiments.¹¹ These signals cannot be attributed to any known environmental effect on our detection system.

A possible explanation for these decay anomalies suggested by the observed frequencies and correlations with solar storms could be an interaction involving solar or relic neutrinos.¹² A possible interaction shown in Fig. 2(a) involves a solar neutrino scattering off the electron anti-neutrino emitted in a beta decay, which would lead to a modification of the decay rate. If such a process existed, then there would also be a similar scattering off a virtual neutrino found in the 2-neutrino-exchange interaction between nucleons as shown in Fig. 2(b). Such an interaction would lead to a composition-dependent force and apparent violations of the WEP in gravity experiments.¹³ Such WEP violations could show up in the forthcoming space-based MICROSCOPE experiment, scheduled to be launched in 2016.¹⁴

Figure 3 summarizes the principal conclusions of this paper. Lorentz non-invariance (LNI) almost inevitably leads to violations of the Weak Equivalence Principle (WEP). The background of solar and relic neutrinos yields preferred directions in space that could produce interactions leading to apparent LNI, and to variations in nuclear decay rates. Such interactions would inevitably produce composition-dependent interactions that could appear in experiments testing the WEP. Hence, anomalies observed in any one of these three areas has consequences for the others.

Acknowledgments

The authors wish to thank J. Jenkins, D. Koltick, T. Mohsinally, J. Scargle, and G. Steinitz for helpful discussions, and to P. A. Sturrock for the spectral analysis leading to Figure 1. We are deeply indebted to D.E. Alburger, and G. Harbottle for making their samples and detection systems available to us.

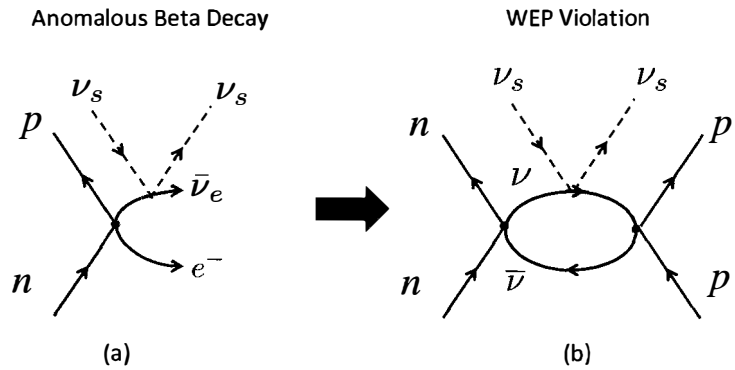


Figure 2 – (a) Feynman diagram of an anomalous beta decay of a neutron, where the emitted electron anti-neutrino ($\bar{\nu}_e$) interacts with a solar neutrino (ν_s). (b) The corresponding diagram of a solar neutrino interacting with a virtual neutrino in a nucleus, leading to a violation of the WEP.

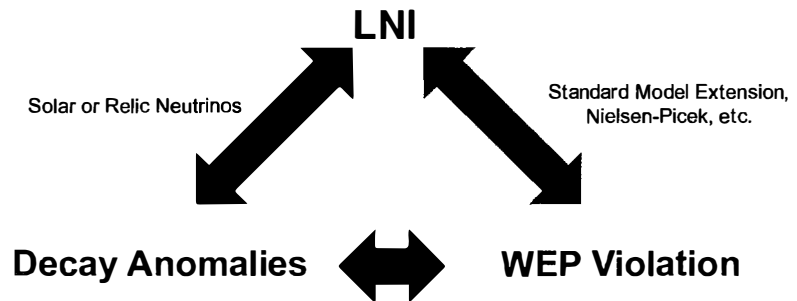


Figure 3 – The relationships among Lorentz non-invariance, WEP violation, and decay anomalies.

References

1. H. B. Nielsen and I. Picek, *Phys. Lett. B* **114**, 141 (1982); *Nucl. Phys. B* **211**, 269 (1983).
2. E. Fischbach, M. P. Haugan, D. Tadić, and H. -Y. Cheng, *Phys. Rev. D* **32**, 154 (1985).
3. D. Mattingly, *Living Rev. Relativity* **8**, 5 (2005).
4. J. Yoo, et al., *Phys. Rev. D* **68**, 092002 (2003).
5. D. O’Keefe, et al., *Astrophys. Space Sci.* **344**, 297 (2013).
6. P. A. Sturrock, et al., *Solar Phys.* **267**, 251 (2010).
7. J. H. Jenkins and E. Fischbach, *Astroparticle Physics* **31**, 407 (2009).
8. D.E. Alburger, G. Harbottle, and E.F. Norton, *Earth Planet Sci. Lett.* **78**, 68 (1986).
9. K. J. Ellis, *Phys. Med. Biol.* **35**, 1079 (1990).
10. A. G. Parkhomov, arXiv:1012.4174v1; arXiv:1004.1761v1.
11. P. A. Sturrock, A. G. Parkhomov, E. Fischbach, and J. H. Jenkins, *Astropart. Phys.* **35**, 755 (2012).
12. E. Fischbach, et al., *Space Sci. Rev.* **145**, 285 (2009).
13. E. Fischbach, D. E. Krause, C. Talmadge, and D. Tadić, *Phys. Rev. D* **52**, 5417 (1995).
14. P. Touboul and M. Rodrigues, *Class. Quantum Grav.* **18**, 2487 (2001).

DYNAMICS, RELATIVITY AND THE EQUIVALENCE PRINCIPLE IN THE 'ONCE-GIVEN' UNIVERSE

C. S. UNNIKRISHNAN

Tata Institute of Fundamental Reserch, Homi Bhabha Road, Mumbai 400005, India (unni@tifr.res.in)



I discuss the main results and experimental support of the paradigm of Cosmic Relativity in which all of dynamics and relativistic effects are gravitational effects of the matter-energy in the universe. The large gravito-magnetic effect of the matter in the universe, in relative motion to the laboratory observer, is directly demonstrated in an experiment. These results lead us to the Centenary Einstein Equation, with cosmic gravity included as its integral element.

1 Introduction and the Core Paradigm

All fundamental theories of physics were formulated well before we gained any knowledge about the real universe. In particular, theories of dynamics, relativity and quantum mechanics were formulated explicitly with empty space as their arena. However, all experimental tests in physics are unavoidably in the presence of cosmic matter and its gravity. Hence, an empirically and logically rigorous reconsideration becomes essential by examining the gravitational effects of the matter in the universe on bodies in motion relative to the cosmic frame. The results of such a study is staggering, to say the least, pointing to a fundamentally new paradigm for dynamics and relativity with several new predictions.^{1,2} The resulting theory, called Cosmic Relativity, has the matter filled cosmic frame and its gravity defining a preferred absolute frame and the universal and monotonically decreasing temperature of the cosmic microwave background radiation defining the absolute time. All relativistic physical effects are then gravitational effects due to the motion relative to the single preferred frame of the matter-filled universe. Of course, only the Galilean transformations (GT) are consistent with such an absolute frame because motion relative to the cosmic frame causes large matter currents and the relevant metric becomes anisotropic. However, GT correctly reproduces all the essential relativistic effects, like time dilation, with the velocity relative to the cosmic frame as the relevant parameter, instead of relative velocities between observer frames. This new paradigm has the strength that it is fully consistent with all known experiments and has significant new predictions. Law of dynamics and the equivalence principle follow as consequences.³ Since gravity of the real 'once-given' universe determines all dynamical and relativistic effects without added postulates, there is no more freedom in the theory or its parameters. It then demands a significant modification of the

Einstein's equation because the equation (as all other equations of dynamics and fields in physics) is operative and tested in the eternal presence of cosmic gravity. The resulting 'Centenary Einstein's Equation' encodes the gravitational presence of cosmic matter by including its energy momentum tensor as an integral non-removable part. We now examine the key results and tests, including a direct demonstration of the large gravitational effect of cosmic matter on the dynamics of a gravitational current loop.

2 Main results

Description of fundamental physical quantities by observers in motion is characterized by the metric of space and time. Empty space and its metric remains homogenous and isotropic in every moving frame and the only coordinate transformation that is consistent with this feature is the Lorentz transformation (LT). The metric $diag \{-1, 1, 1, 1\}$ goes to $diag \{-1, 1, 1, 1\}$ under LT. This is the very basis of the special theory of relativity. However, in reality, space is filled with the charge of gravity, or mass-energy, nearly at the critical density in our spatially flat universe. Motion results in a large gravitational current, thus generating anisotropy of order v/c . To reflect this, the metric should also become anisotropic, which is impossible with Lorentz transformations. Therefore, the real universe is maximally Lorentz violating in the sense of the anisotropy due to the motion-induced vector-like gravitational potential. The Doppler dipole anisotropy of the temperature of the cosmic microwave background enables fairly precise determination of one's motion relative to the cosmic frame. A uniform current of gravitational mass generates a gravitational vector potential (which is in fact a part of the full 10-component symmetric tensor), $A_i/c = g_{0i} = v_i/c$. The fact that there are no locally measurable physical effects of a constant vector potential field is then the statement of the principle of relativity and it is strongly tied to the observed homogeneity of the matter-energy distribution. Surprisingly, the Galilean transformations correctly gives us, along with the observed anisotropy, the most important relativistic feature of motion – time dilation! To illustrate this we work with a limited version of the actual Robertson-Walker metric, ignoring the very slow time evolution. Under GT, the metric coefficients transform from $\{g_{00} = -1, g_{0i} = g_{i0} = 0, g_{ii} = 1\}$ to $\{g_{00} = -(1 - v^2/c^2), g_{0i} = g_{i0} = v/c, g_{ii} = 1\}$. Nonzero g_{i0} , a gravito-magnetic potential, gives the observed anisotropy.

The constant c is the absolute velocity of light in the cosmic frame. One may verify that the spatial metric and the correct length contraction also follows from this. I also mention that an experiment that compares the genuine one-way velocity of light relative to a slowly moving observer indeed shows that light behaves as Galilean as familiar waves like sound, with first order relative velocity $c \pm v$.¹

This can also be treated in the language of gravitational potentials. It is well known that the Newtonian gravitational potential Φ_u at a point in this universe of size Hubble radius or so, evaluated using the observed matter-energy density, is numerically close to c^2 . Hence, even a phenomenological claim that all relativistic effects and due to the gravity of the universe with motional relativistic factor $1/\gamma = (1 - v^2/\Phi_u)$ is empirically accurate. In moving frames, the relativistic potential will have velocity dependent 'vector potential' component

$$A_i = \frac{v_i \Phi_u}{c} \left(1 - v^2/c^2\right)^{-1/2} = \gamma \frac{v_i \Phi_u}{c} \quad (1)$$

leading to several large gravito-magnetic effects.

The gravitational consequences of the cosmic matter and its current for the physics of moving bodies is enlightening. Though g_{i0} is homogeneous in a uniformly moving frame, which implies the principle of relativity, if there an acceleration g_{i0} becomes time dependent and the physical effect is a reactive force on the accelerated system,

$$F_i = -m_g \frac{dA_i}{cdt} = -\frac{m_g \Phi_u}{c^2} \left(\gamma a_i + \gamma^3 v_i (\vec{v} \cdot \vec{a}) \right) \quad (2)$$

Another way of writing this is to note that the vector potential modifies the momentum (enabling generalizing to quantum theory) as $p' = p - m_g A_i$. We see that accelerating a body requires overcoming this cosmic gravito-magnetic reaction and hence a force F_i which is the full relativistic form of Newton's law of dynamics and the conventional inertial mass is just $m_i = m_g \Phi_u / c^2$.

Hence the ratio m_i/m_g is universal. The equivalence principle is a necessary implication of cosmic gravity. Therefore, Newton's law of dynamics and the equivalence principle have the same physical content and one implies the other through their cosmic gravity connection.³ Newton's law is a relativistic gravito-magnetic consequence of cosmic matter and the analogue in electrodynamics is the Lenz's law.

Needless to emphasize that both the centrifugal and the Coriolis forces follow as consequences of cosmic gravity, as had been speculated by E. Mach. Also, the Sagnac phase Φ_S turns out to be a gravitational phase, independent of the shape of the loop, similar to the electromagnetic Aharonov-Bohm phase.

$$\Phi_S = \frac{m_g}{\hbar} \oint A_g \cdot dx = \frac{m_g (\nabla \times \vec{v}) \cdot d\vec{S}}{\hbar} = \frac{2m_g \vec{\Omega} \cdot \vec{S}}{\hbar} \quad (3)$$

The large cosmic gravito-magnetic field in every rotating frame, amounting to $B_g = c\nabla \times g_{0i} = 2\Omega$ becomes very important for spin physics because spin (the fundamental gravito-magnetic moment) couples to a gravito-magnetic field with energy $s \cdot B_g/2$. Cosmic relativity takes the view that since spin is the current of gravitational charge, all spin-dependent effects in fundamental physics should be traceable to the gravitational interaction. This turns out to be crucial for a variety of physical phenomena including spin-statistics connection, hyperfine spectra, spin transport in chiral biomolecules and the fractional quantum Hall effect.^{4,5}

The 'gravitational field' F_i generated in an accelerated frame is fundamentally different from the usual Newtonian field $F_N = -\nabla\Phi$ because F_i appears only during motion relative to the cosmic frame. The 'weightlessness' during free fall is a force balance determined by

$$\nabla\Phi = -\frac{dA_i}{dt} \quad (4)$$

This has the important consequence that in an accelerated frame the motional gravitational field from time dependent g_{0i} does not lead to gravitational time dilation. Hence, the redshift in an accelerated frame is a Galilean consequence of the preferred frame and Galilean relative velocity, and not the gravitational time dilation.

3 Demonstrable experimental evidence

The enormous relativistic gravitational effect of cosmic gravity can be directly demonstrated in a simple, yet immensely important, experiment analogous to Ampere's experiment on current-current interaction. The interaction of a small loop of electrodynamic current i with a another larger loop of current I with effective magnetic field B can be written as $E = \mu \cdot B$ where $\mu = \pi i r^2$. The electromagnetic torque on the test current loop is $\tau = \mu \times B$. With even a slight angle between μ and B this torque will flip the loop if the direction of the current I is opposite to that in the test loop. The physical effect is the same when the small current loop is inside a rotating charged sphere.

It is easy to generate a current loop of the charge of gravity by rotating a small massive disc (gyrodisk) with $L = m\vec{v}_d \vec{r}_d$. It is equally easy to generate a large gravitational current and a gravito-magnetic field by rotating the laboratory relative to all the matter in the universe, if Cosmic Relativity is fundamentally correct. The amazing result is there to verify easily – the rotating disk flips when the external cosmic gravitational current is flipped in sign by changing the direction of the rotation of the laboratory, acted upon by real force; there is indeed a large torque, $\tau = cL \times (\nabla \times g_{0i})/2 = L \times \Omega$, that promptly flips the disk when the two currents are in

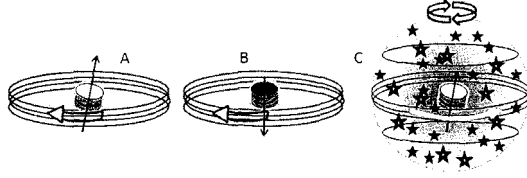


Figure 1 – Panels A and B indicate how a small current loop or magnet flips its direction when the current in the larger loop is in a direction opposite to that of the test loop current. Panel C: When a spinning disk is taken into a frame slowly rotating relative to the matter in the universe (indicated by dual arrows on top), the spinning disk flips due to the large gravitomagnetic force, when the current of the cosmic matter in the frame is in the same direction as the current in the spinning disk.

the same direction (in contrast to opposite currents in electrodynamics). It is most important to note that the physical flips can happen only with a transfer of energy and angular momentum from an external source through one of the two long range interactions known to physics. Since we have an electrically neutral spinning disk, it has to be gravity! The force arises from the interaction of the gravitational current in the disk i_d and the relativistic cosmic current generated I_c by rotating the frame. Quantitatively, the maximum force is

$$F_I = \frac{G i_d I_c}{c^2 R^2} \simeq \frac{G m_d \bar{v}_d M_u (\Omega R_u)}{c^2 R_u^2} = \frac{\Phi_u L}{c^2 \bar{r}_d} \Omega \quad (5)$$

from which the torque $\tau = L \times \Omega$ follows when the cosmic gravitational potential $\Phi_u \simeq c^2$. There is no escape from this conclusion.

Conventional physics has the experiment in the Schwartzchild metric of the earth, a solution of the vacuum Einstein equation $R_{ik} = 0$, where the gravito-magnetic effects are way too small to detect. This experiment falsifies the conventional picture and decisively demands the need to rewrite the paradigm to include the real physical effect of cosmic gravity. This can be done only by modifying the Einstein equation itself, with cosmic relativity as the new basis. Fortunately this is easy, maintaining the Bianchi identities and the consistency with all known experimental tests. The resulting Centenary Einstein's equation is

$$R_{ik} - \frac{1}{2} g_{ik} R + \Lambda_{g_{ik}} - \frac{8\pi G}{c^2} T_{ik(U)} = \frac{8\pi G}{c^2} T_{ik} \quad (6)$$

The extra piece on the left is the energy momentum tensor of the universe, included as the non-removable integral part of the equation itself.

In conclusion, new experimental tests in a variety of situations involving motion of massive bodies relative to the matter-filled universe demands a paradigm change in the fundamental theories of dynamics and relativity. This is answered by Cosmic Relativity, in which all relativistic effects and the law of dynamics are demonstrably identified as cosmic gravitational effects.

References

1. C. S. Unnikrishnan, *Physics in the 'once-given' universe*, in Recent Developments in Theoretical Physics, p 99, (Eds. Subir Ghosh and Guruprasad Kar, World Scientific, 2010).
2. C. S. Unnikrishnan, *Cosmic Relativity: The fundamental theory of relativity, its implications and experimental tests*, arXiv:gr-qc/0406023.
3. C. S. Unnikrishnan, Int. J. Mod. Phys (Conf. series) 30, 1460267 (2014).
4. C. S. Unnikrishnan, *Spin-Statistics connection and the gravity of the Universe*, arXiv:gr-qc/0406046.
5. C. S. Unnikrishnan, *Cosmic Relativity: Dynamics and relativity in the once-given universe*, Monograph in preparation (2015).

A Joint Analysis of BICEP2/Keck Array and Planck Data

S. Galli

*Kaoli Institute for Cosmological Physics, University of Chicago,
Chicago, IL 60637, USA*

1 Introduction

In March 2014, the BICEP2 collaboration claimed the detection of an excess in the B-mode polarization power spectrum over the lensed- Λ CDM expected signal at multipoles $\ell = 30 - 150$ ¹. If interpreted as a signal due to a background of primordial gravitational waves produced during the epoch of inflation, this detection led to a constraint on the tensor-to-scalar ratio of $r = 0.2_{-0.05}^{+0.07}$ prior to foreground subtraction, with $r = 0$ disfavoured at 7σ .

Based on the data available at the time of this claim (including preliminary unpublished results from the Planck collaboration)^a, the BICEP2 collaboration estimated the foreground contamination to be considerably smaller than the observed signal.

Taking foregrounds into account, they estimated the tensor to scalar ratio to be $r = 0.16_{-0.05}^{+0.06}$, corresponding to a 5.9σ detection above zero.

Shortly after this claim, in May 2014 Mortonson & Seljak⁵ and Flauger et al.⁶ remarked the fact that dust emission could potentially account for the BICEP2 signal. Furthermore, the Planck collaboration published a first study about the characteristics of galactic dust emission at intermediate galactic latitudes, not including the region observed by BICEP2³. This study showed that previous estimates had underestimated the dust polarization fraction. Finally, in September 2014, the Planck collaboration published a study of galactic dust emission at high galactic latitudes², including the BICEP2 region. In particular, extrapolating the polarized galactic emission observed by Planck at 353GHz (the highest Planck polarized frequency) down to the frequency of observation of BICEP2 at 150GHz, the Planck collaboration showed that a substantial part (possibly all) of the BICEP2 signal could be attributed to dust, as shown in Fig. 1.

These findings stimulated the BICEP2-Keck and Planck collaborations to perform a joint analysis, using the data from the second Planck data release (made available in 2015⁷), the BICEP-2 data at 150GHz, and the data from the Keck-array at 150GHz

2 The Planck, BICEP2 and Keck-Array experiments

The Planck and the BICEP2/Keck telescopes are two different kinds of CMB experiments.

^a[//www.rssd.esa.int/SA/PLANCK/docs/eslab47/Session07_Galactic_Science/47ESLAB_April_04_11_25_Bernard.pdf](http://www.rssd.esa.int/SA/PLANCK/docs/eslab47/Session07_Galactic_Science/47ESLAB_April_04_11_25_Bernard.pdf)

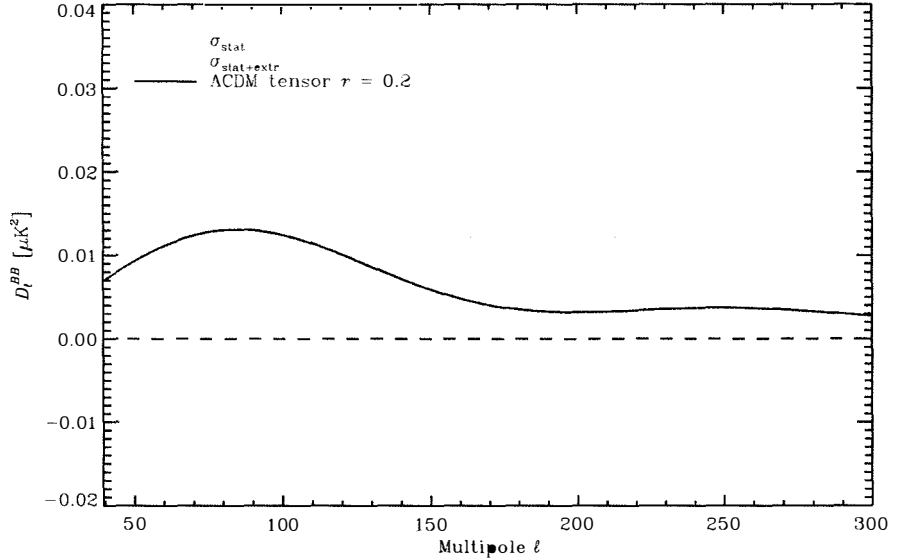


Figure 1 – Planck 353 GHz BB angular power spectrum computed on a region of the sky that includes the BICEP2 patch and extrapolated to 150 GHz (box centres). The shaded boxes represent the $\pm\sigma$ uncertainties: blue for the statistical uncertainties from noise; and red adding in quadrature the uncertainty from the extrapolation to 150 GHz. The Planck 2013 best-fit Λ CDM BB CMB model based on temperature anisotropies, with a tensor amplitude fixed at $r = 0.2$, is overplotted as a black line. Reproduced from².

Planck is an ESA satellite that operated between 2009-2013. It has a large number of scientific goals, which are achieved by observing the CMB anisotropies in temperature and polarization on the full sky. It observed the sky in 9 frequency bands between 30-857GHz, in order to efficiently disentangle CMB emission from foregrounds, with the 7 channels between 30-353GHz being also sensitive to polarization.

BICEP2 is a ground-based experiment in the South Pole, that operated between 2010-2012. Its main scientific goal is the search for a primordial B-mode polarization signal. In order to achieve this, BICEP2 observed a very small patch of the sky ($f_{sky} \sim 1\%$), that allowed to produce deep maps of the CMB polarization with the lowest instrumental noise to date. It observed the sky in only one frequency channel at 150GHz

Finally, the Keck-array is an advanced version of the BICEP2 telescope. It observed the sky at 150 GHz since 2012, and started observing the sky also at 100GHz in 2013. The BICEP2-Keck (from here on, BK) collaboration found a good agreement between the observations of BICEP2 and Keck, so that the data coming from the two telescopes could be combined together. The combination of the Keck and BICEP2 data provides the most sensitive CMB polarization maps to date, at the level of 57 nK – deg².

3 The Planck-BICEP2/Keck joint analysis

The Planck, BICEP2 and Keck joint analysis used the Planck data between 30 and 353GHz and the BICEP2 and Keck data at 150GHz, in the multipole range $\ell = 20-200$. They first performed a cross-correlation between all the Planck and the BK channels. The BK-150GHz \times Planck-353GHz cross-correlation power spectrum showed a clear excess. Since galactic dust dominates the signal at 353GHz, this suggested that at least a large part of the BK signal was contaminated

by dust. Furthermore, the absence of a clear excess in the BK-150GHz×Planck-30GHz suggested that synchrotron emission is negligible in the BK channel.

Using these data, the following fiducial analysis was then performed in order to constrain the tensor-to-scalar ratio. A lensed- Λ CDM model with a free tensor-to-scalar ratio r was assumed, with a pivot scale $k_{pivot} = 0.05\text{Mpc}^{-1}$ and spectral index $n_T = 0$. In addition to that, the dust contribution was modelled as a power-law with an angular power spectrum $C_\ell = l^{-2.4}$ and frequency emission following a modified black body spectrum $BB(\nu, T_d) \nu^\beta$, where the $T_d = 19.6\text{K}$ is the effective temperature of the dust^{3,2}. The dust spectrum parameter β is measured to be $\beta = 1.59 \pm 0.11$ ^{3,2}. The fiducial analysis used all the cross and auto frequency B-mode power spectra of BK150, P217 and P353. It let free to vary the amplitude of the dust power spectrum at $\ell = 80$ at 353GHz, the tensor-to-scalar ratio, and the index β with a tight gaussian prior, while all other cosmological parameters were fixed to the Planck 2013 best-fit model. This analysis led to a constraint on the tensor-to scalar-ratio of $r = 0.048_{-0.032}^{+0.035}$, corresponding to an upper limit of $r < 0.12$ at 95%C.L., with no significant detection over zero. Furthermore, the dust amplitude was detected with a significance of 5.1σ , as shown in Fig. 2.

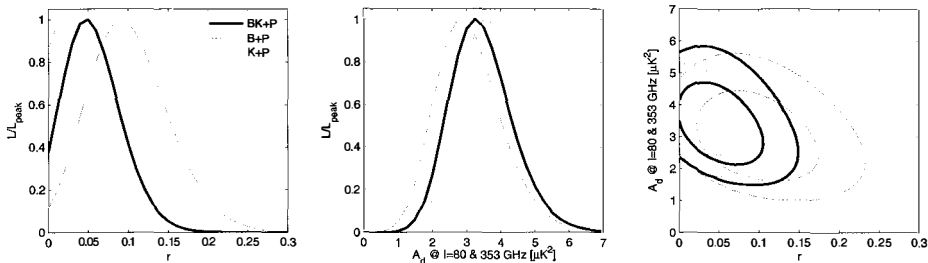


Figure 2 – Likelihood results from a basic lensed- Λ CDM+r+dust model, fitting BB auto- and cross-spectra taken between maps at 150GHz, 217, and 353GHz. The 217 and 353GHz maps come from Planck. The primary results (heavy black) use the 150GHz combined maps from BICEP2/Keck. Alternate curves (light blue and red) show how the results vary when the BICEP2 and Keck Array only maps are used. In all cases, a gaussian prior is placed on the dust frequency spectrum parameter $\beta = 1.59 \pm 0.11$. In the right panel the two dimensional contours enclose 68% and 95% of the total likelihood. Reproduced from⁴.

Several tests have been performed to assess the robustness of this analysis. None of them change substantially the conclusions.

Finally, a further analysis was performed to assess the significance at which the B-modes produced by the weak gravitational lensing of E-mode polarization were detected. In order to do this, an additional parameter A_L , that multiplies the fixed Λ CDM lensing B-mode template, is added to the fiducial analysis settings. This results in a constraint on $A_L = 1.13 \pm 0.18$, corresponding to a 7σ detection of lensing B-mode polarization, the best-to-date.

References

1. Ade, P. A. R., Aikin, R. W., Barkats, D., et al. 2014, Physical Review Letters, 112, 241101
2. Planck Collaboration, Adam, R., Ade, P. A. R., et al. 2014, arXiv:1409.5738
3. Planck Collaboration, Ade, P. A. R., Alves, M. I. R., et al. 2015, AAP, 576, A107
4. BICEP2/Keck and Planck Collaborations, Ade, P. A. R., Aghanim, N., et al. 2015, Physical Review Letters, 114, 101301
5. Mortonson, M. J., & Seljak, U. 2014, JCAP, 10, 035
6. Flauger, R., Hill, J. C., & Spergel, D. N. 2014, JCAP, 8, 039
7. Planck Collaboration, Adam, R., Ade, P. A. R., et al. 2015, arXiv:1502.01582



CORe+: MAPPING OUR COSMIC ORIGINS

C.J.A.P. MARTINS, on behalf of the CORe+ COLLABORATION
*Centro de Astrofísica da Universidade do Porto and IA-Porto,
Rua das Estrelas, 4150-762 Porto, Portugal*

We discuss *CORe+* (Cosmic Origins Explorer +) a proposal for an ESA M4 space mission to investigate Cosmic Origins through high sensitivity, full-sky observations of the polarized microwave and sub-millimeter sky between 60 and 600 GHz. With these observations we will explore our Cosmic Origins, from the origin of stars and cosmic structures on large scales to that of the Universe itself.

1 Introduction

These are exciting times for cosmology. Dramatic observational and experimental progress in the last two decades led to the consolidation of the ‘concordance cosmology’ model, which beautifully fits the available data with a minimal six-parameter model. The latest results of the Planck mission¹ (see also Silvia Galli’s contribution to these proceedings) provides a good illustration.

However, concordance does not imply correctness. The universe seems dominated by a dark sector whose underlying physics remains to be characterized, and many key questions remain. What are these dark matter and dark energy, that we have discovered mathematically, but not yet in the laboratory (as LeVerrier mathematically discovered Neptune before it was discovered on the sky)? Did inflation really occur, and if so when, and what new degrees of freedom were responsible for it?

In an attempt to tackle these and other questions, the European CMB community (together with colleagues from elsewhere) has been, for about a decade, developing the concept of a post-Planck CMB mission. This started out by having a relatively low resolution, limited frequency coverage and focusing on primary CMB B-modes, and gradually matured towards increased sensitivity and more comprehensive science cases (including spectroscopy, sub-mm astronomy, astrophysical cosmology). The more ambitious among these was the PRISM proposal². In what follows we briefly summarize the recent CORe+ proposal; a more detailed description can be found elsewhere³.

2 Primary Science

The primary science goal of CORe+ is to investigate the physics of the very early Universe, which is the source of the entire cosmic web we observe today. The energy scale for this new physics is around 10^{16} GeV, more than 12 orders of magnitude beyond the energy scales accessible to the Large Hadron Collider (LHC) at CERN, and it will be probed by ultra-precise observations of the B-mode polarization of the CMB radiation. This is also the energy scale where quantum gravity effects start to become relevant. B-mode observations will detect or set an upper bound on the primordial gravitational waves (tensor mode fluctuations) as predicted by theories of

Cosmic Inflation. Such long wavelength gravity waves have not yet been detected, despite a vigorous sub-orbital observation programme that has been actively pursued for more than a decade.

Cosmic inflation does not provide a unique prediction for the amplitude of the primordial tensor mode, parameterized by the ‘tensor-to-scalar ratio’ r . A precise measurement of, or upper bound on, r is essential for constraining inflationary physics. Knowledge of r will substantially restrict the field of inflationary models allowed by current observations. Present constraints on these models rely mainly on measurements of the primordial scalar mode power spectrum, which is well measured by Planck and ground-based CMB experiments and unlikely to improve substantially in the future. Because of the uncertainty in the expected value of r it is not possible to predict which CMB polarization experiment will deliver a first statistically significant detection of primordial tensor modes. However, the comprehensive study of CMB polarization is a scientific imperative that requires observations by a space mission with exquisite sensitivity, matching control of systematic errors and broad frequency coverage. Any tentative detection by a suborbital experiment will require a confirmation from space because of uncertainties in the removal of galactic foreground contamination. Compared to proposed experiments with a lower budget and faster schedule, CORe+ is designed as the ultimate experiment for probing inflation from CMB polarization observations, an objective that cannot be achieved by any other means.

Despite the uncertainty in the expectation for r , a generic class of inflationary models known as ‘large-field’ models predicts $r \sim 10^{-1}$. A value of r this large is detectable by ground-based experiments but is already disfavored by the current Planck data¹. Should such a large-field model turn out to be correct, CORe+ observations will provide precision constraints on the shape of the B-mode power spectrum and thus test with exquisite precision the expected near-scale invariance of the primordial tensor modes. Under this scenario, CORe+ will also provide the best possible full-sky, signal-dominated maps of CMB E and B mode polarization anisotropies, to be further studied for statistical anomalies similar to those detected in WMAP or Planck CMB intensity maps. These apparent anomalies constitute one of the main puzzles in current CMB observations. It is presently unclear whether they are statistical flukes or a sign of new physics.

At the time of writing a more plausible scenario is $r \sim 2 \times 10^{-3}$ which, even for ambitious experiments from the ground or from stratospheric balloons, would be very challenging to detect convincingly if not altogether out of reach. CORe+, on the other hand, is designed to provide the best possible detection and characterization of the primordial B mode polarization for any value of r larger than 0.001 and even in the presence of complex polarized foregrounds. This ultimate measurement is possible only from space and requires a mission that will map the CMB B-mode polarization over most of the sky with an angular resolution of a few arcminutes and with a polarization sensitivity better than $2.5\mu K$ per square arcminute pixel after foreground removal (20 times better than the aggregated CMB polarization sensitivity of the Planck HFI polarized detectors at 100, 143 and 217 GHz). This mission will collect virtually all the information about the Early Universe encoded in the CMB polarization.

3 Ancillary Science

CORe+ also addresses a broad range of other questions of prime scientific importance that cannot be answered by any other means. It will probe the distribution of clustered mass in the Universe through the observation of the lensing of CMB polarization due to dark matter structures between our telescopes and the last scattering surface. The reconstruction of the CMB lensing potential will provide high signal-to-noise- ratio maps of the distribution of dark matter at redshifts $z = 1 - 3$ without recourse to biased baryonic tracers. In addition to providing a map of the dark matter integrated along the line of sight up to high redshift, this measurement, combined with cosmological constraints from Euclid, will constrain the sum of the three light

neutrino masses with a statistical error of 3 meV, 5 times better than any single cosmological probe alone and sufficient to distinguish unambiguously between the standard neutrino hierarchy, with a minimum mass sum of about 60 meV, and the inverted hierarchy, with a minimum mass sum of about 100 meV.

COrE+ will also probe the distribution of hot gas up to redshifts $z = 2 - 3$ by measuring the thermal Sunyaev-Zel'dovich effect, the inverse Compton scattering of CMB photons by energetic electrons. It will detect about 10^5 galaxy clusters extending to high redshift and part of the hot baryons in the cosmic web. Combined with high resolution (2-3') ground-based CMB data in atmospheric windows between 90 and 250 GHz, COrE+ will extend this number, and also detect the individual peculiar motions of about 30000 galaxy clusters, thus directly measuring the cosmic velocity field at large redshift, a measurement that cannot be performed by any other means.

At frequencies above 350 GHz, where sky signals are dominated by emission from thermal dust and point sources, COrE+ will for the first time provide full-sky, high quality polarization maps. These maps will provide astrophysicists with the most detailed view yet of the Galactic magnetic field, unveiling its role in creating the filamentary web-like structures where stars form. Magneto-hydrodynamical turbulence will be revealed, with unprecedented statistical information characterizing the energy injection and energy transfer down to dissipation scales. The spectral dependence of the polarized signal from dust will be measured with high accuracy across the sky, furthering our understanding of the nature of interstellar dust. Moreover, together with the corresponding high sensitivity intensity maps, these observations will discover and characterize a large number of new galactic and extragalactic point sources and also measure their polarization properties.

4 What space mission?

The proposed COrE+ baseline mission reaches the high CMB sensitivity required to achieve its science goals with an array of 2410 cryogenically cooled, linearly polarized detectors at the focus of a 1.5 meter aperture Gregorian telescope. The entire sky will be surveyed with 19 frequency bands spanning the range from 60 to 600 GHz. The spacecraft will be located in a large Lissajous orbit around the Sun-Earth L2 Lagrange point to avoid far sidelobe contamination. The combination of three rotations of the spacecraft at different timescales provides an observation pattern such that each sky pixel is crossed frequently along many different directions. This scan strategy provides for a strong mitigation of systematic effects and will thus ensure optimal use of the inherent high sensitivity, especially for extracting large angular scale signals. The COrE+ instrument builds on the success of Planck and Herschel, re-utilizing many of the subsystems and methods developed by the mm/submm community.

Achieving the COrE+ cosmological science programme will require accurate separation of the many astrophysical foregrounds as well as exquisite control and assessment of systematic errors. COrE+ is designed to generate all the data required for this assessment by including, in particular, a large number of closely packed spectral bands. Using all presently available information as summarized in the Planck Sky Model, we carried out simulations and analyzed them using state-of-the-art component separation algorithms. These simulations show that COrE+ will achieve its science objectives and that the design includes redundancy and margin for error³.

The COrE+ ultra-high sensitivity maps of the three Stokes parameters I, Q, and U in 19 frequency bands will establish a long-standing legacy and a reference dataset for the microwave and submillimeter emission in both intensity and polarization over the full sky. Astrophysicists will mine these maps for decades. In addition to the compelling science deliverables we know of today, even more exciting are all the discoveries buried in these maps, and that we cannot yet imagine, nor describe.

5 Outlook

It is clear that a space mission is the only way to extract *all* the essential information from the CMB polarization. This is true both for primordial gravitational waves and for the exploitation of CMB lensing. The CORe+ concept is optimized for these objectives, which can't be reached by any means short of it—in other words, regardless of any progress from the ground or from modest space missions, a mission such as CORe+ mission is a scientific necessity. Doing this will automatically bring along a vast amount of extra science that will serve a broad community.

Acknowledgements

I'm grateful to Jacques Delabrouille, Paolo de Bernardis and the rest of the CORe+ Collaboration for their help in the preparation of this contribution. The author is supported by an FCT Research Professorship, contract reference IF/00064/2012, funded by FCT/MCTES (Portugal) and POPH/FSE (EC).

References

1. P. A. R. Ade *et al.* [Planck Collaboration], Planck 2015 results. XIII. Cosmological parameters, arXiv:1502.01589 [astro-ph.CO].
2. P. André *et al.* [PRISM Collaboration], PRISM (Polarized Radiation Imaging and Spectroscopy Mission): An Extended White Paper, JCAP **1402**, 006 (2014) [arXiv:1310.1554 [astro-ph.CO]].
3. CORe+ Collaboration, to appear (2015).

3.
Short range
&
Long range gravity

Neutrons and Gravity

V. V. Nesvizhevsky
Institut Max von Laue - Paul Langevin
71 avenue des Martyrs, Grenoble, France, F-38042



Neutrons not only fall classically in the gravitational field of the Earth as potatoes and other normal objects do; at certain conditions, they reveal quantum behavior, or even form well-defined gravitational quantum states. Due to the relative simplicity of quantum mechanical rules for solving this problem, we could predict analytically the motion of a neutron in a gravitational field in the vicinity of a reflecting surface. Such a bouncing neutron can have only certain, discrete values of energy. These extremely small energy values turn out to be very sensitive probes to the presence of even tiny extra interactions, in particular those between the neutron and the mirror. Moreover, several emerging fields of research profit from experience and knowledge gained in the recent experimental observation of gravitational quantum states of ultracold neutrons, and extend the developed methods to atoms and anti-atoms, to whispering-gallery effect and other domains, thus providing more and more application for the method. Quantum bouncing particles could play their role in quantum tests of the equivalence principle, in explorations of gravitational properties of antimatter, in searching for new fundamental short-range and other interactions beyond the Standard Model of particle physics, in surface and thin-layer physics, in chemistry, and so on. In this short note we mention results of a few previous years and project nearest developments..

1 Introduction

Results presented in this talk have been published in detailed publications, and related references are given below. More information could also be found in reviews^{1,2}, (and in references therein), in particular in proceedings of GRANIT workshops^{4,5}, which take place every fourth “Olympic” year and cover the topics, which are very close to the subject of this short note. Luckily, precisely during the days of the “Rencontres de Moriond 50” conference, our textbook⁵ was published, which analyses all relevant topics; therefore we only list the main results briefly, and refer the reader to original publications.

2 Quantum bouncing

A particular feature of a falling quantum particle is that its “fall” depends on its mass. In order words, in contradiction to a naively interpreted classical equivalence principle, the probability

to observe a quantum particle as a function of time and height does depend on the value of the particle mass. This conclusion follows from the fact that the neutron mass(es) cannot be reduced from the corresponding Schrödinger equation $(-\frac{\hbar^2}{2m} \frac{d^2}{dz^2} + Mgz)\varphi(z) = E\varphi(z)$, where \hbar is the reduced Planck constant, m is the inertial mass of the particle, M is the gravitational mass of the particle, g is the gravitational acceleration, $\varphi(z)$ is the wave function, and E is the energy of the particle. In order to estimate the importance of quantum effects, it is useful to introduce two scales: the spatial scale $l_0 = \sqrt[3]{\frac{\hbar^2}{2mMg}}$ and the energy scale $\varepsilon - 0 = \sqrt[3]{\frac{\hbar^2 M^2 g^2}{2m}}$.

For a particle with the mass equal to that of neutron, hydrogen or anti-hydrogen atom, these values are equal to 6μ and $0.6peV$ respectively. As far the raising height of such a particle in the gravitational field above a mirror is approaching 6μ , or as far as the energy of such a particle is approaching $0.6peV$, quantum effects could not be ignored. In the limit of minimum raising heights (energies) the particle is found in pure gravitational quantum states. An evident equation $t_0 = \frac{\hbar}{\varepsilon_0} = \sqrt[3]{\frac{2m\hbar}{M^2 g^2}}$ relates the energy scale to the time scale; it is the time interval needed to form a low quantum state. Another relation $T_0 = \frac{2}{3k}\varepsilon_0$, where k is the Boltzmann constant, allows us to estimate that the effective temperature T_0 of such a particle is equal $4.6nK$, much lower than the temperature of a macroscopic experimental setup you could achieve!

3 Observations

Gravitational quantum states of neutrons^{6,7,8} were observed experimentally^{9,10,11,12} at ILL; analogous states of anti-hydrogen atoms^{13,14,15} are going to be observed by GBAR collaboration in CERN^{16,17,18}. For a much lighter particle, say positronium, the length scale will be much larger and the energy scale will be much smaller¹⁹; in contrast, for heavier particles, like heavier atoms or nanoparticles, energies are larger and distances are smaller²⁰. We consider theoretically a variety of such options, and concluded that corresponding experiments are not completely unrealistic. Although a gravitational field provides an extraordinary stable wall for the potential well, which forms quantum states²¹, it is not automatically the case for the opposite wall of the quantum well that corresponds to the bottom mirror. In order to make an experiment realistic, the bottom mirror should represent a uniform potential barrier with no internal structure, and the particles should reflect elastically from the mirror. We selected ultra-cold neutrons (UCNs)^{22,23,24} for first experiments, because the mentioned conditions are met for UCNs with good accuracy. This is so essentially due to the fact the UCN wavelengths are much larger than interatomic distances, and thus UCNs interact coherently with many atoms (nuclei) simultaneously, like with a uniform mean repulsive potential wall²⁵. However, UCNs seem not to be the only object for observing gravitational quantum states, because many particles with sufficiently large wavelength would reflect elastically from the surface due to so-called quantum reflection^{26,27,28,29}; in fact, counterintuitively, an attractive van der Waals/Casimir-Polder potential repulses an atom because its range is shorter than the atom wavelength – just as it is the case in a simple quantum-mechanical problem of the reflection of a slow particle from a deep and sharp negative potential step. In accordance to the equivalence principle, motion of a mirror with the acceleration g (in the absence of the gravitational field) is equivalent to its rest in the presence of the gravitational field; both these situations are also equivalent to the whispering-gallery motion of a particle along a concave cylindrical mirror. Such whispering-gallery quantum states were observed with neutrons^{30,31,32}, and could be also observed with antiatoms^{33,34} and atoms in the future.

4 Applications

Soon after the first experimental observation of gravitational quantum states of neutrons, we analyzed some applications and developments in the field, and proposed experimental methods

for their realization³⁵. Presently these studies are carried out by several independent research groups, with the aim of application of these phenomena for various problems in fundamental and applied physics. Thus new results on gravitational quantum states of UCNs are available from qBounce^{36,37,38} and Tokyo^{39,40} collaborations. A dedicated facility GRANIT^{41,42} for precision experiments with gravitational quantum states of neutrons and related topics is under commissioning at ILL. Applications of gravitational and whispering-gallery quantum states of neutrons, atoms and antiatoms include constraints for fundamental short-range forces of different nature, exploration of physics beyond the Standard Model, non-commutative quantum mechanics, studies of nature of gravity, precision surface-physics methods, studies of quantum phenomena^{43–56}, (to give a non-exhaustive list of examples). The absolute precision of measurements is a common key parameter in most cases; an optimum sensitivity to a certain range of characteristic distances is another key parameter in many studies. The application of methods of gravitational and whispering-gallery quantum spectroscopy and interferometry provides in some cases crucial advantages. To give some examples: 1) precision interference methods, long observation time and optimized sensitivity as a function of interaction range provide the best constraints for fundamental short-range forces in the range of ten(s) nanometers^{31,50}; 2) precision spectroscopic methods, long observation times localization of antiatoms in space and energy provide smaller systematic effects and lower costs for direct measurements of gravitational fall of antimatter, thus the most precise method under discussion for direct measurements of gravitational fall of antimatter^{14,15}.

5 Prospects

The method of gravitational quantum states is rapidly gaining attention and support of broad scientific community that is a good sign, which means that the method is powerful and “eas” for implementation. Neutron, and neutron-related, constraints for fundamental short-range forces are steadily improving due to the efforts of different groups using different methods. All these activities are efficient in terms of the ratio results/resources. There are no reasons to doubt that these tendencies will continue for the observable future.

Acknowledgment

As real authors of this note are all people participating in the original works overviewed above, and also as they could not be co-authors of this short note, we give full references to their work to underline their names.

References

1. Baessler, S. Gravitationally bound quantum states of ultracold neutrons and their applications. *J. Phys. G.* **36** (2009) 104005.
2. Nesvizhevsky, V.V. Near-surface quantum states of neutrons in the gravitational and centrifugal potentials. *Physics-Uspekhi.* **53** (2010) 645.
3. Antoniadis, I., Baessler, S., Bertolami, O., Dubbers, D., Meyerovich, A., Nesvizhevsky, V., Protasov, K., and Reynaud, S. Workshop GRANIT-2010, 14-19 February 2010, Les Houches, France. *Compt. Rend. Phys.* **12** (2011) 703.
4. Nesvizhevsky, V.V., Antoniadis, I., Baessler, S., and Pignol, G. Quantum Gravitational Spectroscopy. *Adv. High En. Phys.* (2015) in press.
5. Nesvizhevsky, V.V., and Voronin, A.Yu. Surprising Quantum Bouncing. London, UK : Imperial College Press, 2015.
6. Goldman, I.I., Krivchenkov, V.D., Kogan, V.I., and Galitski, V.M. Problems in Quantum Mechanics. Ney York, NY, USA : Academic Press, 1960.

7. Sakurai, J.J. Modern Quantum Mechanics. Menlo Park, Calif, USA : Benjamin/Cummings, 1985.
8. Luschikov, V.I., and Frank, A.I. Quantum effects occurring when ultracold neutrons are stored on a plane. *JETP Lett.* **28** (1978) 559.
9. Nesvizhevsky, V.V., Boerner, H., Gagarski, A.M., Petrov, G.A., Petukhov, A.K., Abele, H., Baessler, S., Stoferle, T., and Soloviev, S.M. Search for quantum states of the neutron in a gravitational field: gravitational levels. *Nucl. Instr. Meth. A.* **440** (2000) 754.
10. Nesvizhevsky, V.V., Boerner, H.G., Petukhov, A.K., Abele, H., Baessler, S., Ruess, F.J., Stoferle, T., Westphal, A., Gagarski, A.M., Petrov, G.A., and Strelkov, A.V. Quantum states of neutrons in the Earth's gravitational field. *Nature.* **415** (2002) 297.
11. Nesvizhevsky, V.V., Boerner, H.G., Gagarski, A.M., Petukhov, A.K., Petrov, G.A., Abele, H., Baessler, S., Divcovic, G., Ruess, F.J., Stoferle, T., Westphal, A., Strelkov, A.V., Protasov, K.V., and Voronin, A.Yu. Measurement of quantum states of neutrons in the Earth's gravitational field. *Phys. Rev. D.* **67** (2003) 102002.
12. Nesvizhevsky, V.V., Petukhov, A.K., Boerner, H.G., Baranova, T.A., Gagarski, A.M., Petrov, G.A., Protasov, K.V., Voronin, A.Yu., Baessler, S., Abele, H., Westphal, A., and Lucovac, L. Study of the neutron quantum states in the gravity field. *Europ. Phys. J. C.* **40** (2005) 479.
13. Voronin, A.Yu., Froelich, P., and Nesvizhevsky, V.V. Gravitational quantum states of antihydrogen. *Phys. Rev. A.* **83** (2011) 032903.
14. Dufour, G., Debu, P., Lambrecht, A., Nesvizhevsky, V.V., Reynaud, S., and Voronin, A.Yu. Shaping the distribution of vertical velocities of antihydrogen in GBAR. *Europ. Phys. J. C.* **74** (2014) 2731.
15. Voronin, A.Yu., Nesvizhevsky, V.V., Dalkarov, O.D., Kupriyanova, E.A., and Froelich, P. Resonance spectroscopy of gravitational states of antihydrogen. *Hyperf. Inter.* **228** (2014) 133.
16. Debu, P. GBAR, gravitational behaviour of antihydrogen at rest. *Hyperf. Inter.* **212** (2011) 51.
17. Perez, P., and Sacquin, Y. The GBAR experiment: gravitational behaviour of antihydrogen at rest. *Class. Quant. Grav.* **29** (2012) 184008.
18. Indelicato, P., Chardin, G., Grandemange, P., Lunney, D., Manea, V., Badertscher, A., Crivelli, P., Curioni, A., Marchionni, A., Rossi, B., Rubbia, A., Nesvizhevsky, V.V., Brook-Roberge, D., Comini, P., Debu, P., Dupre, P., Liskay, L., et al (56 names). The Gbar project, or how does antimatter fall? *Hyperf. Inter.* **228** (2014) 141.
19. Crivelli, P., Nesvizhevsky, V.V., and Voronin, A.Yu. Can we observe the gravitational quantum states of positronium. *Adv. High En. Phys.* (2015) in press.
20. Bertolami, O., and Rosa, J.G. Quantum and classical divide: the gravitational case. *Phys. Lett. B.* **633** (2006) 111.
21. Pignol, G., Protasov, K.V., and Nesvizhevsky, V.V. A note on spontaneous emission of gravitons by a quantum bouncer. *Class. Quant. Grav.* **24** (2007) 2439.
22. Zeldovich, Y.B. Storage of cold neutrons. *Sov. Phys. JETP.* **9** (1959) 1389.
23. Luschikov, V.I., Pokotilo, Y.N., Strelkov, A.V., and Shapiro, F.L. Observation of ultracold neutrons. *JETP Lett.* **9** (1969) 23.
24. Steyerl, A. Measurements of total cross section for very slow neutrons with velocities from 100 m/s to 5 m/s. *Phys. Lett. B.* **29** (1969) 33.
25. Fermi, E., and Marshall, L. Interference phenomena of slow neutrons. *Phys. Rev.* **71** (1947) 666.
26. Friedrich, H., Jacoby, G., and Meister, C.G. Quantum reflection by Casimir / van der Waals potential tails. *Phys. Rev. A.* **65**(1997) 032902.
27. Voronin, A.Yu., Froelich, P., and Zygelman, B. Interaction of ultracold antihydrogen with a conducting wall. *Phys. Rev. A.* **72** (2005) 062903.

28. Dufour, G., Gerardin, A., Guerout, R., Lambrecht, A., Nesvizhevsky, V.V., Reynaud, S., and Voronin, A.Yu. Quantum reflection of antihydrogen from the Casimir potential above matter slabs. *Phys. Rev. A.* **87** (2013) 012901.
29. Dufour, G., Guerout, R., Lambrecht, A., Nesvizhevsky, V.V., Reynaud, S., and Voronin, A.Yu. Quantum reflection of antihydrogen from nanoporous media. *Phys. Rev. A.* **87** (2013) 022506.
30. Nesvizhevsky, V.V., Petukhov, A.K., Protasov, K.V., and Voronin, A.Yu. Centrifugal quantum states of neutrons. *Phys. Rev. A.* **78** (2008) 033616.
31. Nesvizhevsky, V.V., Voronin, A.Yu., Cubitt, R., and Protasov, K.V. Neutron whispering gallery. *Nature Phys.* **6** (2010) 114.
32. Nesvizhevsky, V.V., Cubitt, R., Protasov, K.V., Voronin, A.Yu. The whispering gallery effect in neutron scattering. *New J. Phys.* **12** (2010) 113050.
33. Voronin, A.Yu., Nesvizhevsky, V.V., and Reynaud, S. Whispering-gallery states of antihydrogen near a curved surface. *Phys. Rev. A.* **85** (2012) 014902.
34. Voronin, A.Yu., Nesvizhevsky, V.V., and Reynaud, S. Interference of the whispering gallery states of antihydrogen. *J. Phys. B.* **45** (2012) 165007.
35. Nesvizhevsky, V.V., and Protasov, K.V. Quantum states of neutrons in the Earth's gravitational field: state of the art . Trends in Quantum Gravity Research. New York, USA : NOVA Scie. Publ., 2006.
36. Abele, H., Jenke, T., Stadler, D., and Geltenbort, P. QuBounce: the dynamics of ultracold neutrons falling in the gravity potential of the Earth. *Nucl. Phys. A.* **827** (2009) 593C.
37. Jenke, T., Stadler, D., Abele, H., and Geltenbort, P. Q-BOUNCE-experiments with quantum bouncing ultracold neutrons. *Nucl. Instr. Meth. A.* **611** (2009) 318.
38. Jenke, T., Geltenbort, P., Lemmel, H., and Abele, H. Realization of a gravity-resonance-spectroscopy technique. *Nature Phys.* **7** (2011) 468.
39. Kamiya, Y., Ichikawa, G., and Komamiya. Precision measurement of the position-space wave functions of gravitationally bound ultracold neutrons. *Adv. High En. Phys.* (2014) 859241.
40. Ichikawa, G., Komamiya, S., Kamiya, Y., Minami, Y., Tani, M., Geltenbort, P., Yamamura, K., Nagano, M., Sanuki, T., Kawasaki, S., Hino, M., and Kitaguchi, M. Observation of the spatial distribution of gravitationally bound quantum states of ultracold neutrons and its derivation using the Wigner function. *Phys. Rev. Lett.* **112** (2014) 071101.
41. Baessler, S., Beau, M., Kreuz, M., Kurlov, V.N., Nesvizhevsky, V.V., Pignol, G., Protasov, K.V., Vezzu, F., and Voronin, A.Yu. The GRANIT spectrometer. *Compt. Rend. Phys.* **12** (2011) 707.
42. Roullet, D., Vezzu, F., Baessler, S., Clement, B., Morton, D., Nesvizhevsky, V., Pignol, G., and Rebreyend, D. Status of the GRANIT facility. *Adv. High En. Phys.* (2015) in press.
43. Robinett, R.W. Quantum wave packet revivals. *Phys. Rep.* **392** (2004) 1.
44. Bertolami, O., Rosa, J.G., de Aragao, C.L.M., Castorina, P., and Zappala, D. Noncommutative gravitational quantum well. *Phys. Rev. D.* **72** (2005) 025010.
45. Brau, F., and Buisseret, F. Minimal length uncertainty relation and gravitational quantum well. *Phys. Rev. D.* **74** (2006) 036002.
46. Baessler, S., Nesvizhevsky, V.V., Protasov, K.V., and Voronin, A.Yu. Constraint on the coupling of axionlike particles to matter via an ultracold neutron gravitational experiment. *Phys. Rev. D.* **75** (2007) 075006.
47. Romera, E., and de los Santos, F. Identifying wave-packet fractional revivals by means of information entropy. *Phys. Rev. Lett.* **99** (2007) 263601.
48. Nesvizhevsky, V.V., Pignol, G., and Protasov, K.V. Neutron scattering and extra-short-range interactions. *Phys. Rev. D.* **77** (2008) 034020.

49. Nozari, K., and Pedram, P. Minimal length and bouncing-particle spectrum. *Europ. Phys. Lett.* **92** (2010) 50013.
50. Antoniadis, I., Baessler, S., Buechner, M., Fedorov, V.V., Hoedl, S., Lambrecht, A., Nsvizhevsky, V.V., Pignol, G., Protasov, K.V., Reynaud, S., and Sobolev, Yu. Short-range fundamental forces. *Compt. Rend. Phys.* **12** (2011) 755.
51. Brax, P., and Pignol, G. Strongly coupled chameleons and the neutronic quantum bouncer. *Phys. Rev. Lett.* **107** (2011) 111301.
52. Jenke, T., Cronenberg, G., Burgdorfer, J., Chizhova, L.A., Geltenbort, P., Ivanov, A.N., Lauer, T., Lins, T., Rotter, S., Saul, H., Schmidt, U., and Abele, H. Gravity resonance spectroscopy constraints dark energy and dark matter scenarios. *Phys. Rev. Lett.* **112** (2015) 151105.
53. Chang, L.N., Lewis, Z., Minic, D., and Takeuchi, T. On the minimal length uncertainty relation and the foundations of string theory. *Adv. High En. Phys.* (2011) 493514.
54. Kobakhidze, A. Gravity is not an entropic force. *Phys. Rev. D.* **83** (2011) 021502.
55. Onofrio, R. On weak interactions as short-range manifestations of gravity. *Mod. Phys. Lett. A* **28** (2013) 1350022.
56. Brax, P., Pignol, G., and Roulier, D. Probing strongly coupled chameleons with slow neutrons. *Phys. Rev. D.* **88** (2013) 083004.

CASIMIR EFFECT AND QUANTUM REFLECTION

G. DUFOUR, R. GUÉROUT, A. LAMBRECHT, S. REYNAUD

*Laboratoire Kastler Brossel, UPMC-Sorbonne Universités, CNRS, ENS-PSL Research University,
Collège de France, Campus Jussieu, F-75252 Paris, France.*

The GBAR experiment will time the free fall of cold antihydrogen atoms dropped onto an annihilation plate to test the universality of free fall on antimatter. In this contribution, we study the quantum reflection of the anti-atom resulting from the Casimir-Polder attraction to the plate. We evaluate the Casimir-Polder potential and the associated quantum reflection amplitudes and find that reflection is enhanced for weaker potentials. A Liouville transformation of the Schrödinger equation is used to map the quantum reflection problem onto an equivalent problem of scattering on a barrier, leading to an intuitive understanding of the phenomenon.

Introduction

The universality of free fall is tested with ever increasing precision both for macroscopic test masses¹ and atoms^{2,3}. However, a precise direct measurement of the free fall of antimatter is still lacking. The current experimental bound on the gravitational acceleration \bar{g} of antihydrogen was obtained by the ALPHA collaboration⁴: $-65g \leq \bar{g} \leq +110g$. Several experiments built around the CERN Antiproton Decelerator and the new deceleration ring ELENA will attempt to reduce this bound to the percent level in the coming years^{5,6}. In particular, the GBAR experiment (Gravitational Behavior of Antihydrogen at Rest) will time the free fall of cold antihydrogen ($\bar{\text{H}}$) atoms^{7,8}. Following the method proposed in⁹, a cold $\bar{\text{H}}$ will be obtained by photo-detaching the excess positron of an $\bar{\text{H}}^+$ ion that has been previously cooled down to the lowest quantum state in a Paul trap. The neutral $\bar{\text{H}}$ then falls in the Earth's gravity field with an acceleration $\bar{g} = Mg/m$, where M is the gravitational mass of $\bar{\text{H}}$, m its inertial mass and g the local gravity field. Annihilation of the anti-atom on a material plate placed at a height h below the ion trap marks the end of the free fall. Assuming no initial velocity, the value of \bar{g} can be inferred from the time between the photo-detachment pulse and the detection signal: $T = \sqrt{2h/\bar{g}}$. A more detailed description of the quantum wavepacket's motion gives the arrival time distribution around this mean value¹⁰.

The above program assumes that no force other than gravity is acting on the anti-atom during the free-fall. Yet Casimir and Polder have shown^{11,12} that neutral atoms in the vicinity of a material medium experience an attractive force because quantum fluctuations of the electromagnetic field couple the atomic induced dipole to induced dipoles in the medium. Within experimental accuracy, the Casimir-Polder (CP) force does not modify the free fall time. However, despite its attractive nature, it causes quantum reflection of atoms at low energies^{13,14,15}.

Such classically forbidden reflection from an attractive potential is a manifestation of the wave-like behavior of quantum matter and it occurs when the potential varies rapidly on the scale of the de Broglie wavelength^{17,18,13}. Experiments have observed quantum reflection on the CP potential near liquid He^{19,20,21} and solid surfaces^{22,23,24}, as well as rough or mi-

cro/nanostructured surfaces^{25,26,27}.

Theory^{18,28} and experiments^{25,26} have shown that the reflection probability increases when the energy is reduced, but also when the absolute magnitude of the potential is decreased. For example, it is larger for atoms falling onto a silica mirror than onto silicon or metallic mirrors²⁹ and it is even larger for nanoporous silica³⁰ which couples extremely weakly to the electromagnetic field. We give an intuitive explanation of this paradoxical effect by mapping the quantum reflection problem into a problem of reflection on a repulsive barrier by means of a Liouville transformation of the Schrödinger equation. Liouville transformations are exact mappings of Schrödinger equations onto one another which have the remarkable property of preserving scattering amplitudes.

In this contribution, we will first sketch how the scattering approach to Casimir forces^{31,32} can be used to accurately calculate the interaction of \bar{H} with various types of surfaces. We then compute the associated quantum reflection, seen as the exchange between counter-propagating WKB waves. In section 3 we introduce Liouville transformations of the Schrödinger equation and show how a specific choice of coordinate maps scattering on an attractive well onto reflection from a repulsive wall. We finish by looking into the high reflection limit of low energies and weak potentials and discuss its relevance to high precision tests of the Equivalence Principle.

1 The Casimir-Polder potential

In the scattering approach to Casimir forces, the interaction energy between two arbitrary objects in vacuum is written in terms of the reflection operators $\mathcal{R}_1, \mathcal{R}_2$ for electromagnetic waves on each object³¹. For distances z between the objects below the thermal wavelength ($\sim 1 \mu\text{m}$ at 300 K), one can use the zero-temperature expression:

$$V(z) = \hbar \int_0^\infty \frac{d\xi}{2\pi} \text{Tr} \log (1 - \mathcal{R}_1 e^{-\kappa z} \mathcal{R}_2 e^{-\kappa z}) . \quad (1)$$

This formula is obtained after a Wick rotation to imaginary frequencies $\omega = i\xi$, which transforms the oscillating terms $e^{ik_z z}$ describing translation from one object to the other into decaying exponentials $e^{-\kappa z}$, $\kappa = \sqrt{\vec{k}_\perp^2 + \xi^2/c^2}$. In these formulas, $\vec{k} = \vec{k}_\perp \pm k_z \vec{e}_z$ is the wavevector of the electromagnetic radiation. The trace runs over the transverse wavevector \vec{k}_\perp and the polarizations TE, TM.

We now specialize to the case of an atom above a plane. The reflection operator on the plane is diagonal in the plane wave basis where it is given by the Fresnel reflection amplitudes $\rho^{\text{TE}}, \rho^{\text{TM}}$. These reflection coefficients depend on the material properties of the medium through its relative dielectric function $\varepsilon(\omega)$. We treat the atom in the dipolar approximation, so its reflection operator depends on the dynamic polarizability $\alpha(\omega)$, which is supposed to be the same as that of (ground state) hydrogen. Finally we neglect multiple reflections on the atom by expanding the logarithm in (1) to first order and find^{33,29}:

$$V(z) = \frac{\hbar}{c^2} \int_0^\infty d\xi \xi^2 \alpha(i\xi) \int \frac{d^2 \vec{k}_\perp}{(2\pi)^2} \frac{e^{-2\kappa z}}{\kappa} \left[\rho^{\text{TE}} - \left(1 + \frac{2c^2 k_\perp^2}{\xi^2} \right) \rho^{\text{TM}} \right] . \quad (2)$$

This formalism allows an easy inclusion of realistic optical response properties for the atom and for all types of mirrors. Those used in this work are detailed in Ref.²⁹.

The typical wavelength λ characterizing the optical response of the atom and plane defines a transition between two asymptotic behaviors of the CP potential. For a thick mirror:

$$V(z) \xrightarrow{z \ll \lambda} -\frac{C_3}{z^3} , \quad V(z) \xrightarrow{z \gg \lambda} -\frac{C_4}{z^4} . \quad (3)$$

The short distance limit is the well known van der Waals potential; whereas the large separation limit is referred to as the *retarded* CP interaction since it takes into account the finiteness of the speed of light^{11,12}.

In the left panel of Fig. 1 we plot the exact CP potentials between an \bar{H} atom and a perfectly reflective mirror and bulk mirrors made of intrinsic silicon and amorphous silica. The inset shows the ratios $V(z)/V^*(z)$ to the retarded CP limit calculated for an ideal mirror: $V^*(z) = -C_4^*/z^4$, with $C_4^* = (3\hbar c/8\pi)(\alpha(0)/4\pi\epsilon_0) = 1.57 \times 10^{-7}$ neV.nm⁴ for \bar{H} . These ratios tend to constant values $C_4/C_4^* \leq 1$ at large distances and linear variations C_3z/C_4^* at small distances. The less reflective for the electromagnetic field a material is, the weaker the CP potential, from perfectly reflective to silicon and silica mirrors.

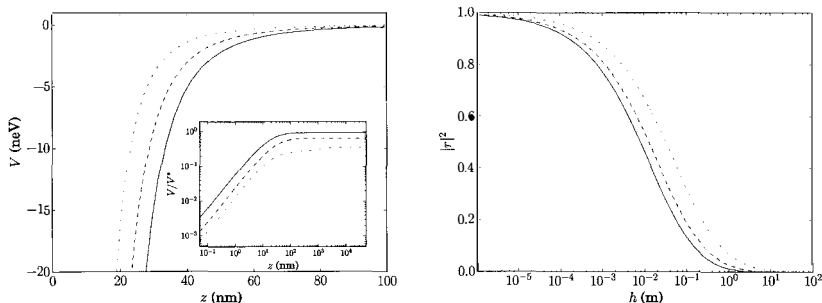


Figure 1 – Left panel: Casimir-Polder potential for \bar{H} near a conducting surface (full blue line), a silicon bulk (dashed green line) and a silica bulk (dash-dot red line). The inset shows the ratio $V(z)/V^*(z)$ to the retarded potential for an ideal mirror (see text). Right panel: Quantum reflection probability for \bar{H} on the same surfaces (same line styles as the left panel), as a function of the drop height $h = E/mg$.

2 Quantum reflection of \bar{H}

The physical problem addressed in this work involves three distinct length scales:

- the free fall height of \bar{H} : $h \approx 10$ cm,
- the scale at which quantization of energy levels in the gravitational scale becomes important: $\ell_{grav} = (\hbar^2/2m^2\bar{g})^{1/3} \approx 6$ μm for \bar{H} , assuming $\bar{g} = g$,
- the typical range of the Casimir-Polder potential : $\ell_{CP} = \sqrt{2mC_4}/\hbar \approx 30$ nm.

The hierarchy between these lengths scales $\ell_{CP} \ll \ell_{grav} \ll h$ allows to decouple free fall and scattering on the CP potential. Therefore, we will solve the Schrödinger equation in the CP potential only, with an energy $E > 0$ corresponding to the kinetic energy of the atom before it reaches the CP potential:

$$\psi''(z) + F(z)\psi(z) = 0, \quad F(z) = \frac{2m}{\hbar^2} (E - V(z)). \quad (4)$$

Primes denote differentiation with respect to the function's argument. To make the connection with the free-fall problem, we will often use the free fall height h as a measure of the energy $E = mgh = 102.5$ neV/m $\times h$.

The function $F(z)$ is the square of the de Broglie wave-vector $k_{dB}(z)$ associated with the classical momentum $p = \pm\hbar k_{dB}$. Since the potential is attractive, the classical momentum never changes sign: the particle has no classical turning point. In particular, a classical particle moving towards the medium is increasingly accelerated until it hits the surface. This classical behavior is mimicked by the WKB wavefunctions which each propagate in a well defined direction:

$$\psi_{\text{WKB}}^{\pm}(z) = \frac{1}{\sqrt{k_{dB}(z)}} e^{\pm i\phi_{dB}(z)}, \quad \phi_{dB}(z) = \int_{z_0}^z k_{dB}(z') dz', \quad (5)$$

The WKB phase $\phi_{\text{dB}}(z)$ is proportional to Hamilton's characteristic function associated with the classical trajectory with energy E joining z_0 and z . We fix the freedom associated with the choice of a reference point z_0 by enforcing $\phi_{\text{dB}}(z) \approx \sqrt{2mE}z/\hbar$ at $z \rightarrow \infty$.

In contrast to this semiclassical approximation, the exact wavefunction undergoes quantum reflection. To underline this effect we write the wavefunction in the basis of WKB waves with z -dependent coefficients:

$$\psi(z) = b_+(z)\psi_{\text{WKB}}^+(z) + b_-(z)\psi_{\text{WKB}}^-(z). \quad (6)$$

Introducing this ansatz in Eq. (4) we obtain coupled first-order equations for the amplitudes $b_{\pm}(z)$, which describe the conversion of an incident wave into a reflected wave^{16,17}.

In the case of the CP potential, b_{\pm} go to constant values as $z \rightarrow 0$ or ∞ , so that quantum reflection only occurs in an intermediate region. The ratio of the amplitudes $b_+(z)$ and $b_-(z)$ as z goes to infinity is the quantum reflection amplitude r . Because \bar{H} annihilates if it touches the wall, there can be no outgoing wave immediately above the material surface. This enforces a full absorption boundary condition $b_+(z=0) = 0$.

The right panel of Fig. 1 shows the reflection probability $|r|^2$ as a function of the energy for each of the potentials calculated in the previous section. While the reflection probability vanishes in the classical limit $E \rightarrow \infty$, it goes to unity in the purely quantum limit. If not properly accounted for, this energy dependence will bias the detection statistics of GBAR in favor of higher energy atoms. For an intermediate energy $E = mg \times 10$ cm typical of GBAR the reflection probability is significant: 14% on a perfectly reflective mirror, 19% on bulk silicon and 33% on bulk silica. Surprisingly, these numbers show that the reflection probability is larger for weaker CP interactions. We look into this apparent paradox in more detail in the next section.

3 Liouville transformations

A Liouville transformation of the Schrödinger equation (4) consists in a smooth change of coordinate $z \rightarrow \tilde{z}$ (with $\tilde{z}'(z) > 0$) and an associated rescaling of the wavefunction: $\tilde{\psi}(\tilde{z}) = \sqrt{\tilde{z}'(z)}\psi(z)$. Equation (4) for ψ is thereby transformed into an equivalent equation for $\tilde{\psi}$ ³⁶:

$$\tilde{\psi}''(\tilde{z}) + \tilde{F}(\tilde{z})\tilde{\psi}(\tilde{z}) = 0, \quad \tilde{F}(\tilde{z}) = \frac{F(z) - \frac{1}{2}\{\tilde{z}, z\}}{\tilde{z}'(z)^2} = z'(\tilde{z})^2 F(z) + \frac{1}{2}\{z, \tilde{z}\}, \quad (7)$$

where the curly braces denote the Schwarzian derivative of the coordinate transformation:

$$\{\tilde{z}, z\} = \frac{\tilde{z}'''(z)}{\tilde{z}'(z)} - \frac{3}{2} \frac{\tilde{z}''(z)^2}{\tilde{z}'(z)^2}. \quad (8)$$

Cayley's identity for the Schwarzian derivatives

$$\{\hat{z}, z\} = (\tilde{z}'(z))^2 \{\hat{z}, \tilde{z}\} + \{\tilde{z}, z\} \quad (9)$$

ensures that the composition of two transformations $z \rightarrow \tilde{z}$ and $\tilde{z} \rightarrow \hat{z}$ is also a transformation $z \rightarrow \hat{z}$. The inverse transformation, used for writing the last equality in (7), is obtained by applying (9) to the case $\hat{z} = z$. The group of Liouville transformations has the remarkable property of preserving the Wronskian of two solutions ψ_1, ψ_2 of the Schrödinger equation:

$$\mathcal{W}(\psi_1, \psi_2) = \psi_1(z)\psi_2'(z) - \psi_1'(z)\psi_2(z) = \tilde{\psi}_1(\tilde{z})\tilde{\psi}_2'(\tilde{z}) - \tilde{\psi}_1'(\tilde{z})\tilde{\psi}_2(\tilde{z}) = \tilde{\mathcal{W}}(\tilde{\psi}_1, \tilde{\psi}_2). \quad (10)$$

In particular, the reflection and transmission amplitudes r and t can be written in terms of Wronskians of solutions which match incoming and outgoing WKB waves³⁷, so they are invariant under the transformation. The probability density current $j = \hbar\mathcal{W}(\psi^*, \psi)/2im$ is also preserved.

We now consider a specific Liouville transformation, where the WKB phase is used as coordinate: $z = \phi_{\text{dB}}(z)$. We use boldfacing to identify quantities related to this coordinate choice. In particular the transformed function (7) can be expressed in terms of a dimensionless energy $\mathbf{E} = 1$ and potential $\mathbf{V}(z)$ given by the “badlands” function $Q(z)$:

$$\mathbf{F}(z) = \mathbf{E} - \mathbf{V}(z), \quad \mathbf{E} = 1, \quad \mathbf{V}(z) = Q(z), \quad (11)$$

$$Q(z) = \frac{1}{2F(z)} \{\phi_{\text{dB}}, z\} = \frac{F''(z)}{4F(z)^2} - \frac{5F'(z)^2}{16F(z)^3}. \quad (12)$$

In regions where $Q(z) \approx 0$, the WKB wavefunctions are solutions of the Schrödinger equation and there is no reflection. Conversely, the WKB approximation breaks down in regions where $Q(z)$ takes values of order one^{17,34,35,13}, hence the name “badlands”.

In the case of the CP potential, $Q(z)$ is a peaked function which vanishes far from the surface where the potential goes to zero but also at the surface, where the classical momentum becomes very large. The original problem of quantum reflection on a potential well which diverges at one end of the domain $z \in]0, \infty[$ is therefore mapped onto an equivalent problem where a particle of unit energy scatters on a potential barrier which vanishes at both ends of the transformed domain $z \in]-\infty, \infty[$. The transformed problem is thus a well-defined scattering problem with no interaction in the asymptotic input and output states. Moreover the transformed problem can have classical turning points where $\mathbf{F} = 0$ or $\mathbf{E} = \mathbf{V}$, in which case it corresponds to a radically different semiclassical picture from the original.

We illustrate this striking fact in Figs. 2 and 3 where we show the result of the Liouville transformation for various energies and the potentials presented in section 1. The original quantum reflection problem on an attractive well is now intuitively understood as reflection on a wall, with the same scattering properties. The height of the barrier grows both when the energy is reduced and when the potential is weakened, which entails a larger reflection probability since the “energy” $\mathbf{E} = 1$ is fixed.

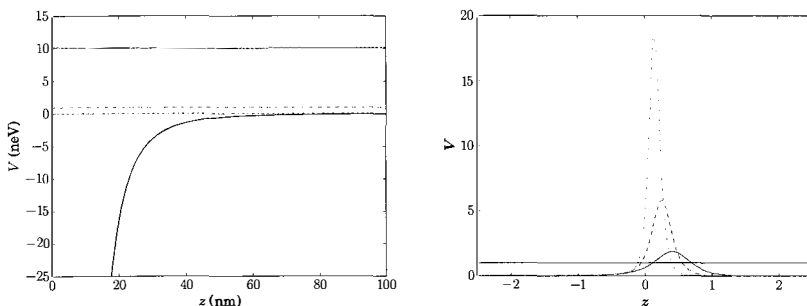


Figure 2 – Original (left panel) and Liouville-transformed (right panel) energies and potentials for $\bar{\text{H}}$ scattering on a silica bulk with energy $E = m.g \times 10$ cm (full blue line), 1 cm (dashed green line) and 0.1 cm (dash-dot red line).

4 Enhancing quantum reflection

We have seen that a precise evaluation of quantum reflection probabilities is necessary to interpret correctly the results of the GBAR experiment. Beyond this, a good control of quantum reflection opens exciting perspectives for trapping and manipulating antimatter near matter surfaces. For example, the precision of the GBAR experiment is limited by the large initial velocity spread of atoms. This velocity distribution could be tailored by bouncing the atoms on a mirror above which an absorber is placed to eliminate the faster atoms¹⁰.

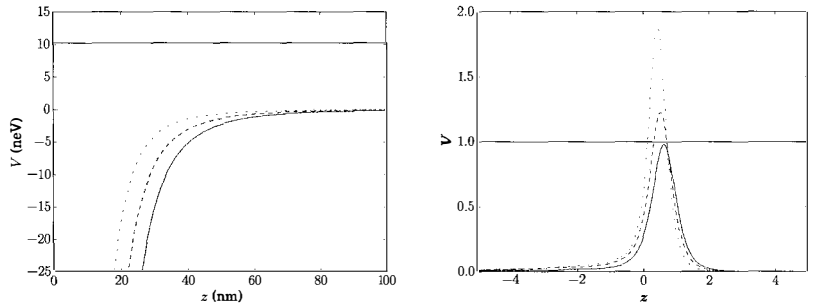


Figure 3 – Original (left panel) and Liouville-transformed (right panel) energies and potentials for \bar{H} impinging with energy $E = mg \times 10$ cm on conducting (full blue line), silicon (dashed green line) and silica (dash-dot red line) bulks.

In the light of the previous section's results, efficient quantum reflection is obtained for low energies and weak CP interactions. At low energies, quantization of the energy levels in the gravitational potential field becomes important. The solutions of the Schrödinger equation in the linear gravitational potential $V(z) = m\bar{g}z$ are expressed with the Airy function:

$$\psi(z) \propto \text{Ai} \left(\frac{z}{\ell_{grav}} - \frac{E}{m\bar{g}\ell_{grav}} \right), \quad \ell_{grav} = \left(\frac{\hbar^2}{2m^2\bar{g}} \right)^{1/3} \quad (13)$$

For an impenetrable mirror the wavefunction vanishes on the surface so the energies E_n of the gravitationally bound states (GBS) are such that $-E_n/m\bar{g}\ell_{grav}$ is a zero of Ai. For a real surface, the low energy interaction of \bar{H} with the surface is described by a complex scattering length $a = \lim_{E \rightarrow 0} -\hbar \log(-r)/2i\sqrt{2mE}^{14,15}$. This has the effect of displacing the eigen-energies: $E_n \rightarrow E_n + m\bar{g}a$ which pick up an imaginary part. The GBS therefore acquire a finite lifetime $\tau = \hbar/2m\bar{g}|\text{Im}(a)|$ associated with the small probability of \bar{H} being transmitted through the badlands and annihilated on the surface.

Low CP interaction can be achieved by removing matter from the mirror, so as to reduce its coupling to the electromagnetic field. Nanoporous materials such as silica aerogels incorporate a large fraction of gas or vacuum in 1-10 nm sized pores. For processes involving scales larger than the size of these inhomogeneities, such materials can be described by the Bruggeman effective medium theory^{38,30}. At the energies of the low-lying GBS, the badlands peak is located $\gtrsim 100$ nm from the surface so \bar{H} is reflected far enough from the medium for the effective description to be valid.

The lifetimes of GBS above various bulk and porous media are given in Tab. 1. In consequence of their weaker CP interaction, the lifetime increases dramatically for porous materials compared with bulk materials, reaching several seconds for silica aerogel. Spectroscopy of these long lived GBS could lead to orders of magnitude improvements on the determination of \bar{g} ³⁹.

Table 1: Lifetime in seconds of the first gravitationally bound states of \bar{H} above various material surfaces.

| mirror | perfectly reflective | bulk silicon | bulk silica | silica aerogel (50% porosity) | silica aerogel (90% porosity) | silica aerogel (98% porosity) |
|--------------|----------------------|--------------|-------------|-------------------------------|-------------------------------|-------------------------------|
| lifetime (s) | 0.11 | 0.14 | 0.22 | 0.32 | 1.07 | 4.64 |

Conclusion

We have obtained a realistic estimate of the CP potential between \bar{H} and a variety of material mirrors using the scattering approach to Casimir forces. Quantum reflection on such potentials is the result of a breakdown of the WKB approximation in the so-called badlands region. This is highlighted by performing a Liouville transformation of the Schrödinger equation, which maps quantum reflection to scattering on a barrier given by the badlands function. In this new picture, the increase of the reflection probability when the energy is lowered or the potential weakened is simply interpreted as reflection on a higher peak. Low energy particles can therefore be trapped from above by gravity and from below by quantum reflection. These gravitationally bound states are exceptionally long-lived above nanoporous mirrors and they could be used for highly precise tests of the Equivalence Principle for antimatter.

Acknowledgments

The authors wish to thank V. V. Nesvizhevsky, A. Yu. Voronin and the GBAR (gbar.in2p3.fr) and GRANIT collaborations for insightful discussions.

References

1. T. A. Wagner, S. Schlamminger, J. H. Gundlach and E. G. Adelberger. *Classical Quant. Grav.* **29**, 184002 (2012).
2. S. Fray, C. A. Diez, T. W. Hänsch, M. Weitz. *Phys. Rev. Lett.* **93**, 240404 (2004).
3. D. Schlippert, J. Hartwig, H. Albers, L. L. Richardson, C. Schubert, A. Roura, W. P. Schleich, W. Ertmer, E. M. Rasel. *Phys. Rev. Lett.* **112**, 203002 (2014).
4. The ALPHA Collaboration. *Nature Comm.* **4**, 1785 (2013).
5. A. Knecht *et al.* *Hyperfine Interact.* **228**, 121 (2014).
6. P. Hamilton, A. Zhmoginov, F. Robicheaux, J. Fajans, J. S. Wurtele and H. Müller. *Phys. Rev. Lett.* **112**, 121102 (2014).
7. G. Chardin *et al.* Technical Report CERN-SPSC-2011-029. SPSC-P-342, CERN, Geneva (2011).
8. P. Indelicato *et al.* *Hyperfine Interact.* **228**, 141 (2014).
9. J. Walz and T. W. Hänsch. *Gen. Relat. Gravit.* **36**, 561 (2004).
10. G. Dufour, P. Debu, A. Lambrecht, V. V. Nesvizhevsky, S. Reynaud and A. Y. Voronin. *Eur. Phys. J. C* **74**, 2731 (2014).
11. H. B. G. Casimir and D. Polder. *Nature* **158**, 787 (1946).
12. H. B. G. Casimir. *Proc. K. Ned. Akad. Wet* **51**, 793 (1948).
13. H. Friedrich, G. Jacoby and C. G. Meister. *Phys. Rev. A* **65**, 032902 (2002).
14. A. Y. Voronin, P. Froelich and B. Zygelman. *Phys. Rev. A* **72**, 062903 (2005).
15. A. Y. Voronin and P. Froelich. *J. Phys. B* **38**, L301 (2005).
16. E. C. Kemble. *Phys. Rev.* **48**, 549 (1935).
17. M. V. Berry and K. E. Mount. *Rep. Prog. Phys.* **35**, 315 (1972).
18. A. Mody, M. Haggerty, J. M. Doyle and E. J. Heller. *Phys. Rev. B* **64**, 085418 (2001).
19. V. U. Nayak, D. O. Edwards and N. Masuhara. *Phys. Rev. Lett.* **50**, 990 (1983).
20. J. J. Berkhout, O. J. Luiten, I. D. Setija, T. W. Hijmans, T. Mizusaki and J. T. M. Walraven. *Phys. Rev. Lett.* **63**, 1689 (1989).
21. I. A. Yu, J. M. Doyle, J. C. Sandberg, C. L. Cesar, D. Kleppner and T. J. Greytak. *Phys. Rev. Lett.* **71**, 1589 (1993).
22. F. Shimizu. *Phys. Rev. Lett.* **86**, 987 (2001).
23. V. Druzhinina and M. DeKieviet. *Phys. Rev. Lett.* **91**, 193202 (2003).
24. T. A. Pasquini, Y. Shin, C. Sanner, M. Saba, A. Schirotzek, D. E. Pritchard and W. Ketterle. *Phys. Rev. Lett.* **93**, 223201 (2004).

25. F. Shimizu and J.-i. Fujita. *J. Phys. Soc. Jpn.* **71**, 5 (2002).
26. T. A. Pasquini, M. Saba, G.-B. Jo, Y. Shin, W. Ketterle, D. E. Pritchard, T. A. Savas and N. Mulders. *Phys. Rev. Lett.* **97**, 093201 (2006).
27. B. S. Zhao, H. C. Schewe, G. Meijer and W. Schoellkopf. *Phys. Rev. Lett.* **105**, 133203 (2010).
28. T. E. Judd, R. G. Scott, A. M. Martin, B. Kaczmarek and T. M. Fromhold. *New J. Phys.* **13**, 083020 (2011).
29. G. Dufour, A. Gérardin, R. Guérout, A. Lambrecht, V. V. Nesvizhevsky, S. Reynaud and A. Y. Voronin. *Phys. Rev. A* **87**, 012901 (2013).
30. G. Dufour, R. Guérout, A. Lambrecht, V. V. Nesvizhevsky, S. Reynaud and A. Y. Voronin. *Phys. Rev. A* **87**, 022506 (2013).
31. A. Lambrecht, P. A. Maia Neto and S. Reynaud. *New J. Phys.* **8**, 243 (2006).
32. T. Emig, N. Graham, R. L. Jaffe and M. Kardar. *Phys. Rev. Lett.* **99**, 170403 (2007).
33. R. Messina, D. A. R. Dalvit, P. A. M. Neto, A. Lambrecht and S. Reynaud. *Phys. Rev. A* **80**, 022119 (2009).
34. N. T. Maitra and E. J. Heller. *Phys. Rev. A* **54**, 4763 (1996).
35. R. Côté, H. Friedrich and J. Trost. *Phys. Rev. A* **56**, 1781 (1997).
36. F. Olver. *Asymptotics and Special Functions*. Taylor & Francis (1997).
37. W. Whitton and J. Connor. *Mol. Phys.* **26**, 1511 (1973).
38. D. A. G. Bruggeman. *Ann. Phys. Berlin* **416**, 636 (1935).
39. A. Y. Voronin, P. Froelich and V. V. Nesvizhevsky. *Phys. Rev. A* **83**, 032903 (2011).

ATOM INTERFEROMETRY TEST OF SHORT RANGE GRAVITY : RECENT PROGRESS IN THE FORCA-G EXPERIMENT

Matthias Lopez, Cyrille Solaro & Franck Pereira

SYRTE, Observatoire de Paris, PSL Research University, CNRS, Sorbonne Universités, UPMC Univ. Paris 06, LNE, 61 avenue de l'Observatoire, 75014 Paris, France



In this paper we describe ForCa-G, an experiment that aims at measuring short range forces between a surface and particles in its vicinity. Using atoms trapped in a vertical standing wave, we perform a measurement of the local gravitational potential using atom interferometry techniques.

1 Introduction

Measuring short range forces is one of the new experimental challenges of modern physics. While electromagnetic, strong and weak forces are very well unified within the standard model, gravity remains elusive and stands on its own within general relativity. A great variety of unifying conjecture a deviation to Newton's law on small scales^{1,2,3,4}, some even picture Lorentz violation at those scales⁵. They however predict neither range nor magnitude, and must hence be trialed and constrained by experiments.

Originally proposed in 2007⁶, the ForCa-G experiment has advanced a great deal since then and is now able to measure local potentials with great resolution^{7,8,9,10}. We present here the principle of the experiment and give stability measurements for the local gravitational field we probe. We also put forth novel phenomena arising from the necessary developments in our apparatus.

2 Measuring local forces

Our experiment is an atomic interferometer that performs local measurements of vertical potentials. For atoms far from any surface, we only measure the local earth gravitational field. This potential is used to trial test the performances of our apparatus.

In order to do so, we trap ⁸⁷Rb atoms in an optical vertical lattice. The dynamic on their

external degree of freedom is described by the following Hamiltonian :

$$\hat{H} = \underbrace{\frac{\hat{p}^2}{2m}}_{\text{Kinetic energy}} + \underbrace{\frac{U_0}{2} (1 - \cos(k_l \hat{z}))}_{\text{Lattice potential}} + \underbrace{mg\hat{z}}_{\text{Gravitational potential}}, \quad (1)$$

where m is the mass of the ^{87}Rb atom, U_0 the depth of the lattice, k_l the lattice wave-number and g the earth acceleration constant.

Such a Hamiltonian naturally bears as solutions the Wannier-Stark eigenstates $|W_m\rangle$, where m is the lattice well index. Such states are localised in space. This feature can be interpreted as the translational-symmetry breaking of the Bloch states by tilting the lattice — there is no longer constructive interference site to site. The eigenvalues E_m possess an interesting property, they are separated by multiples of the Bloch energy:

$$E_{m+\Delta m} = E_m + \Delta m \times \underbrace{mg\lambda_l}_{\text{Bloch energy}}, \quad (2)$$

where λ_l is the lattice period. This very naturally yields the Bloch frequency $h\nu_B = mg\lambda_l$ ($\nu_B = 568.505$ Hz in our experiment). It is important at this point to understand that measuring the ν_B is equivalent to measuring the local earth gravitational acceleration constant g . The endgame of our experiment revolves around measuring this frequency and extracting the information contained within.

The internal atomic state is approximated by a two-level system : the hyperfine structure of Rb, where $|g\rangle = |5^2S_{1/2}, F = 1, m_F = 0\rangle$ and $|e\rangle = |5^2P_{3/2}, F = 2, m_F = 0\rangle$. These states are long-lived and separated in energy by $h\nu_{\text{HFS}}$ ($\nu_{\text{HFS}} = 6.835$ GHz in our experiment).

A recap of all these energetic features, internal or external, can be found on figure 1.

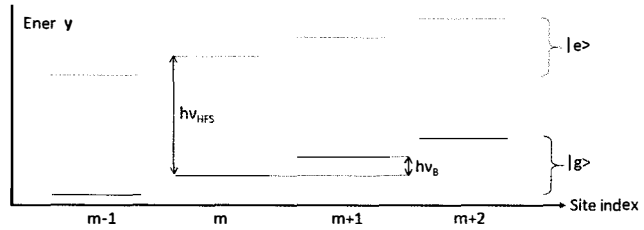


Figure 1 - Energy levels of a two-level particle trapped in a vertical (tilted by gravity) lattice. The index m can be seen as the lattice site at the centre of the wave function.

3 Experimental Setup

Our experiment consists of cooling ^{87}Rb atoms and trapping them in a shallow vertical optical lattice (figure 2). Once trapped, atomic interferometry is performed to measure the Bloch frequency.

3.1 Cooling atoms

A standard 3 dimensional Magneto-Optical Trap (MOT) loaded from a 2 dimensional MOT¹⁶ is systematically used as first stage cooling. Properly tuned, a few millions atoms are brought to a $2 \mu\text{K}$ temperature within 1 second. From this stage atoms are transferred in the vertical lattice.

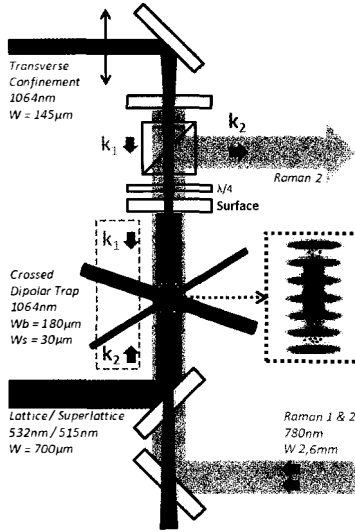


Figure 2 – Scheme of the experiment. Proper use of dichroic mirrors allows for superposition of beams with different wave-lengths.

3.2 The MixTrap

The lattice is created by using a back-reflected 532 nm laser. To yield exploitable depths and reduce position-induced jitter, the waist is set to 700 μm . The power sits around 7W. The depths brought forth by such values are typically of 3 to $4E_r$ (kinetic energy gained/lost by the absorption/emission of one photon on the ^{87}Rb D2 transition traditionally called "recoil energy").

The lattice beam being blue-detuned, Rb atoms are repelled by the maximums of light intensity. In the axial direction this naturally creates the lattice. However, in the radial direction, the atoms eventually fall out. To avoid this deleterious effect and to constrain the atoms on the maximum intensity of the lattice, we superimpose a thinner red-detuned 1064nm beam with a 145 μm waist.

The combination of those two beams is referred to as the MixTrap.

3.3 Measuring the Bloch frequency ν_B with atomic Ramsey-Raman spectroscopy

The atoms being trapped in the MixTrap, their wave-functions are naturally described by Wannier-Stark states, energetically separated by $h\nu_B$. Let $|m, i\rangle$ describe the state of an atom, where $m \in \mathbb{Z}$ is the site index of the Wannier-Stark wave-function and $i = g, e$ is the internal state of the atom (see figure 1).

Two counter-propagating Raman beams with 10 mW power and 2.6 μm waists are used to open the interferometer. This configuration allows for two photons with momentum $\hbar k_{eff} = 2\hbar k_r$ to be transferred from the Raman lasers to the system and allows coupling between neighbouring Wannier-Stark states. By controlling the detuning between the two Raman beams precisely, transitions can be addressed with sufficient selectivity.

The strength of the coupling depends naturally on the laser intensity, but more critically on the depth of the lattice : too deep traps allow for poor spatial overlap of Wannier-Stark states and significantly reduce coupling. The Rabi frequency between two states separated by Δm can

be written as:

$$\Omega_{\Delta m} = \Omega_0 \times \langle m | e^{-ik_{\text{eff}}x} | m + \Delta m \rangle, \quad (3)$$

where Ω_0 is free space coupling between hyperfine states. The wave function, once the interferometer has been opened with the first Raman pulse, is written as :

$$|\Psi(t)\rangle = \frac{1}{\sqrt{2}} (|m, g\rangle + e^{i2\pi\nu t} |m + \Delta m, e\rangle), \quad (4)$$

where $\nu_t = \nu_{\text{HFS}} + \Delta m \nu_B$. After a Ramsey time T , the interferometer is closed with a second Raman pulse, bearing the same characteristics. By detecting populations of atoms in $|g\rangle$ N_g and in $|e\rangle$ N_e , we compute the population ratio $\rho = N_e/(N_e + N_g)$, and obtain Ramsey fringes in frequency space separated by $1/T$. By locating the central fringe and adequately measuring its position, a multiple of the Bloch frequency $\nu_{\Delta m} = \Delta m \times \nu_B$ is retrieved. However, this frequency bears an offset that is imparted to clock shifts, such as second order Zeeman effect or differential light-shifts induced by the confinement beams. In order to remove then, one symmetrically measures the central fringe frequency at Δm and at $-\Delta m$, and computes the half difference $\nu_B = \frac{1}{2\Delta m} (\nu_{\Delta m} - \nu_{-\Delta m})$.

A recap of this methodology can be found on figure 3.

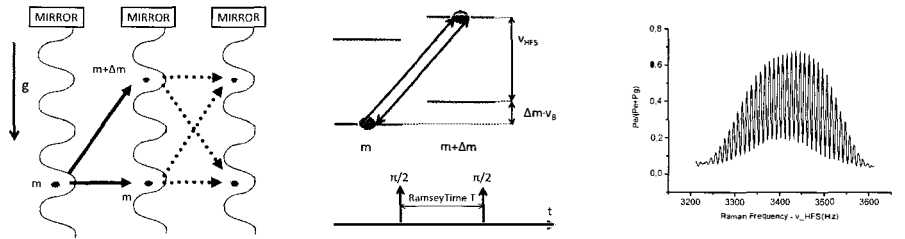


Figure 3 – (left and centre) Wave-functions are spatially separated by a Raman $\pi/2$ pulse, their respective phases evolve during Ramsey time T . They are then recombined with the second Raman $\pi/2$ pulse. (right) Ramsey fringes observed at the output of the interferometer, here $\Delta m = +6$ and $T = 100\text{ms}$.

3.4 Allan standard deviation

In order to quantify stability when measuring such a quantity, we use the Allan deviation¹¹, a 2-sample estimator repeated in time. We measure a stability $\frac{\sigma_\nu}{\nu_B} (@1s) = 1.8 \cdot 10^{-6}$, obtained from the data on figure 4. Since our setup can be seen as a gravimeter, we have $\frac{\sigma_\nu}{\nu_B} = \frac{\sigma_g}{g}$. While modest compared to the best atom interferometry based gravimeters¹⁸ which typically yield a $\sim 5 \cdot 10^{-9}$, our apparatus remains very competitive in the trapped regime¹⁷. This accuracy corresponds to 1 mHz in 1 second and 0.1 mHz in 100 seconds resolution on the Bloch frequency.

We will now address the question of how we can harness this stability to measure short range forces.

4 Short range forces in the μm regime

As mentioned earlier, our experiment's ultimate goal is to measure short range forces with unprecedented accuracy in the micro-meter regime. At the ranges we wish to probe, we expect two forces : gravity and the Casimir-Polder interaction. Our resolution is vastly sufficient to measure these two effects, and we plan at the very least to set new constraints on the existence of a deviation to Newton's law and at best to measure such a deviation.

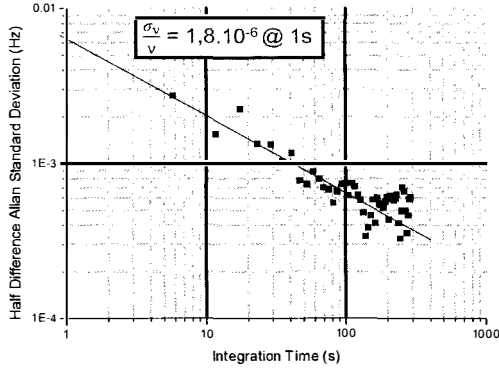


Figure 4 – Allan standard deviation of the Bloch frequency ν_B calculated with the half difference of $\nu_{\Delta m}$ and $\nu_{-\Delta m}$ (here $\Delta m = 6$). The black dashed line is a guide to the eye.

4.1 Casimir-Polder

For two conducting plates, quantification of the vacuum virtual states generates an attractive force that pulls the surfaces together. The Casimir-Polder arises from the same phenomena : instead of two plates, it now takes place between an electric dipole and a conducting surface. An approximate derivation of such a potential gives:

$$U_{CP} = \frac{3\hbar c\alpha_0}{4\pi d^4}, \quad (5)$$

where α_0 is the atomic polarisability, c the Einstein constant and d the distance between the perfectly conducting plate and the dipole.

4.2 Gravitational force and possible deviations

The second force — though orders of magnitude smaller — is the Newtonian potential. Interestingly, in the range we are interested in probing, unifying models predict a deviation to this force. As mentioned earlier, they predict neither range nor magnitude and must be therefore tested. To this effect, we consider a Yukawa type potential to test their bounds :

$$U(r) = \frac{GMm}{r} \left(1 + \alpha e^{-\frac{r}{\lambda}} \right), \quad (6)$$

where α and λ constrains respectively magnitude and range of the deviation. The lower they are constrained, the better. Despite its Yukawa form, it does not contain any physics, but just a mean to parametrise.

5 Paving the way to short range force measurements

The next step in our experiment is to introduce the di-electric mirror — used for the lattice laser back-reflection — in the vacuum cell and move the atoms to its vicinity. As the atoms are moved closer to the surface, they will become affected by the aforementioned short range forces. In practice, this means that to the Bloch frequency ν_B , will be added ν_{CP} for the Casimir-Polder potential and by ν_G for the gravitational pull generated by the mirror on the atom.

The shifts ν_{CP} have been calculated. The precise methodology can be found in^{19,20}. In figure 5, we can observe that at the 12th site, the shift is of 2 Hz. Let it be reminded that this is 3 orders of magnitude larger than our resolution at 1 second, and 4 orders of magnitude at 100 seconds.

However the setup that has been described earlier is not adequate for such measurements...

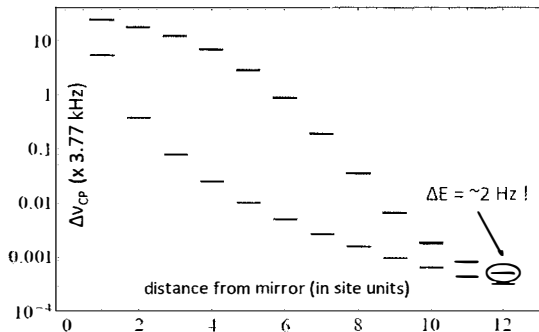


Figure 5 – Energy shift due to the Casimir polder interaction, expressed in units of recoil frequency. The Casimir-Polder potential is calculated for an atom perfectly located on a lattice site (red) and more realistically for an atom described by a wave-function spread on several sites (black). Adapted from¹⁹.

5.1 Achieving higher densities and the added benefits

Loading the atoms from a cold ^{87}Rb cloud is the most straightforward way to populate sites in the MixTrap. However, the size of the cloud is around 1 mm, and the spatial density is low. If loaded from those conditions, the atoms populate 4000 sites, with around 10 atoms per site. While sufficient to perform measurements of the gravitational acceleration constant g , those conditions are not satisfactory for short range force probing : since the Raman transition frequencies will be shifted by the additional forces close to the mirror, only one site can be addressed at a time. One can easily see that making measurements with the signal to noise ratio inherent to 10 atoms per site is far-fetched.

The solution to this difficulty is optical evaporative cooling. For more details on this technique, we refer the curious reader to the rich literature on this subject²¹. To create the required dipolar trap, we cross two 1064 nm laser beams at a 30° angle. The first beam has a maximum of 10W of power and a waist of 30 μm , the second has a maximum power of 30W and a waist of 120 μm . The technique consists of properly ramping their power in order to achieve lower temperature, higher spatial densities and smaller sizes. In practice we obtain around 40000 atoms with a 300 nK temperature, with density of a few 10^{-11} at.cm^{-3} . When loaded in the MixTrap, we estimate that a normal distribution of sites with a scale parameter of 4 sites are populated : this means that less than 20 sites are significantly populated. It is now reasonable to expect that measuring the transition frequency can be achieved when only one site is addressed.

When loading the MixTrap from a dipolar trap, the average density over the trapped atoms is much higher (a few 10^{-11} at.cm^{-3}). When the atoms collide, their spins tend to realign. This phenomenon is called Identical Spin Rotation Effect (ISRE)^{14,15} and protects the coherence of the system over long time scales. We measured coherence times over 3 seconds long (limited only by computer-interfacing difficulties) (figure 6). The subject is still under heavy investigation and at this stage it has not been determined if the frequency offset ISRE yields can be accounted for systematically in the Bloch frequency measurements.

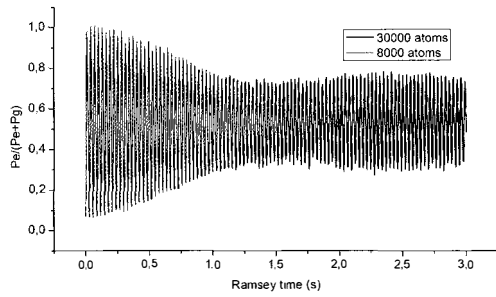


Figure 6 – Long coherence times are observed for high densities. For the highest density (black, $4.0 \times 10^{-11} \text{at.cm}^{-3}$) the observed contrast plateau is higher than for lower densities (red, $1.7 \times 10^{-11} \text{at.cm}^{-3}$). This is a signature of ISRE.

5.2 Elevating the atoms to the mirror

Once the atoms are cooled in the dipolar trap, they need to be brought close to the surface before being loaded in the MixTrap. In order to do so, we have set up a Bloch elevator. It consists of two 780 nm counter-propagating beams, 50 GHz red-detuned, with 100 mW power each and 1 mm waist. By precisely controlling the frequency difference $\Delta\nu$ between the two beams, an accelerated lattice is created. In a classical picture it is easily understood that the atoms can be accelerated upwards if the lattice is moved accordingly. In the quantum picture, the atoms undergo Bloch oscillations^{12,13}. A process through which they gain $2\hbar k_L$ momentum per oscillation. By adequately ramping the power and the frequency, preliminary tests have shown that the atoms can easily go 40 Bloch oscillations (figure 7). We expect to be able to perform the 300 Bloch oscillations that are deemed necessary for our experiment.

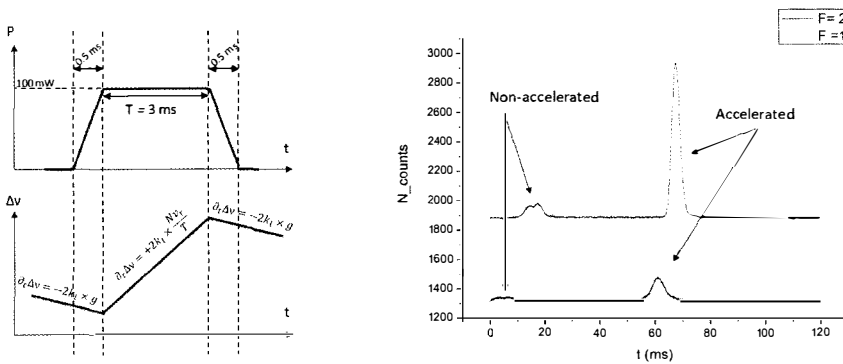


Figure 7 – (left) Power and frequency variations the atoms undergo.(right) Time of flight signals on the two hyperfine levels of ^{87}Rb atoms. Here, the atoms undergo 40 Bloch oscillations in 3 ms to gain $80v_r$ in velocity.

6 Conclusion

We have presented the principle of our experiment and detailed the apparatus. It was also shown that it has the required specifications to perform measurements of the Casimir-Polder interaction in the micro-meter regime with unprecedented accuracy — we expect better than 1% resolution.

Novel phenomena was exhibited in the trapped regime such as ISRE, which may yield some unexpected advantages in probing short range forces. We also gave proof of principle concerning our ability to bring the atoms close to the surface.

We plan in the next year to introduce the mirror in the vacuum and start measuring short range forces.

Acknowledgements

This research is carried on within the iSense project, which acknowledges financial support from the Future and Emerging Technologies (FET) program within the Seventh Framework Program for Research of the European Commission under FET, Open Grant No. 250072. We also acknowledge financial support from the Ville de Paris Emergence(s) Program, IFRAF, the IDEX PSL (ANR-10-IDEX-0001-02 PSL), and ANR (ANR-13-BS04-0003-01). M.K.Z. thanks the FFCSA, CSC, and CNSF (Grant No. 11205064) for financial support. Helpful discussions with all members of the IACI team are gratefully acknowledged.

References

1. E. Fischbach & C. L. Talmadge, *The Search for Non-Newtonian Gravity* (Springer, New York, 1999)
2. S. Dimopoulos & A. A. Geraci, *Phys. Rev. D* **68**, 124021 (2003)
3. N. Arkani-Hamed *et al*, *Phys. Lett. B* **429**, 263 (1998)
4. S. Dimopoulos & G. F. Giudice, *Phys. Lett. B* **379**, 105 (1996)
5. Q. Bailey *et al*, *Phys. Rev. D* **91**, 022006 (2015)
6. P. Wolf *et al*, *Phys. Rev. A* **75**, 063608 (2007)
7. M-K. Zhou *et al*, *Phys. Rev. A* **88**, 013604 (2013)
8. B. Pelle *et al*, *Phys. Rev. A* **87**, 023601 (2013)
9. G. Tackmann *et al*, *Phys. Rev. A* **84**, 063422 (2011)
10. Q. Beaufils *et al*, *Phys. Rev. Lett.* **106**, 231002 (2011)
11. D.W. Allan, *Proceedings of IEEE* **54**, 221-230 (1966)
12. M. Ben Dahan *et al*, *Phys. Rev. Lett.* **76**, 4508 (1996)
13. A.R. Kolovsky & H.J. Korsch, *Int. J. Mod. Phys. B* **18**, 1235 (2004)
14. C. Deutsch *et al*, *Phys. Rev. Lett.* **105**, 020401 (2010)
15. C. Lhuillier & F. Laloe, *J. Phys. (France)* **43**, 197 (1982).
16. J. Nellessen *et al*, *Opt. Comm.* **78**, 300 (1990)
17. G. Ferrari *et al*, *Phys. Rev. Lett.* **97**, 060402 (2006)
18. A. Louchet-Chauvet *et al*, *IEEE Trans. Instrum. Meas.* **60**, 2527 (2011)
19. R. Messina *et. al.*, *Phys. Rev. A* **83**, 069902 (2011)
20. S. Pelisson, *Ph.D. Thesis* <http://hal.upmc.fr/tel-00788325>
21. R. Grimm *et al*, *Adv. At. Mol. Opt. Phys.* **42**, 95 (2000)

The Archimedes experiment

E. Calloni^a, S. Caprara^b, M. De Laurentis^a, G. Esposito^c, M. Grilli^b, E. Majorana^d, G. P. Pepe^e, S. Petrarca^b, P. Puppo^d, F. Ricci^b, L. Rosa^a, C. Rovelli^f, P. Ruggi^g, N. L. Saini^b, C. Stornaiolo^c, F. Tafuri^h

*a: Università di Napoli Federico II, Dipartimento di Fisica and INFN Sezione di Napoli
Complesso Universitario di Monte S. Angelo, Via Cintia Edificio 6, 80126 Napoli, Italy;*

b: Università di Roma "La Sapienza" e INFN Sezione di Roma - P.le A. Moro 2, I-00185, Roma, Italy

*c: INFN Sezione di Napoli Complesso Universitario di Monte S. Angelo, Via Cintia Edificio 6,
80126 Napoli, Italy*

d: INFN Sezione di Roma - P.le A. Moro 2, I-00185, Roma, Italy

*e: Università di Napoli Federico II, Dipartimento di Fisica and INFN Sezione di Napoli
Piazzale Tecchio 80 80126 Napoli, and Complesso Universitario di Monte S. Angelo, Via Cintia Edificio
6, 80126 Napoli, Italy*

*f: Aix Marseille Université CNRS, CPT, UMR 7332, 13288 Marseille, and Université de Toulon,
CNRS, CPT, UMR 7332, 83957 La Garde, France*

g: European Gravitational Observatory (EGO) I-56021 Cascina (Pi), Italy

*h: Dipartimento Ingegneria dell'Informazione, Seconda Università di Napoli, I-81031 Aversa (CE) and
INFN Sezione di Napoli*

Complesso Universitario di Monte S. Angelo, Via Cintia Edificio 6, 80126 Napoli, Italy

Archimedes is a pathfinder to a future experiment to ascertain the interaction of vacuum fluctuations with gravity. The future experiment should measure the force that the earth's gravitational field exerts on a Casimir cavity by using a balance as the small force detector. The Archimedes experiment analyzes the important parameters in view of the final measurement and experimentally explores solutions to the most critical problems

1 Scientific Motivation

One of the profound open question of present physics is the irreconcilability among the quantum mechanical theory of vacuum and the General Relativity. The enormous value of the energy density of vacuum fluctuations as foreseen by quantum mechanics, if inserted in General Relativity theory is not at all compatible with the observed radius of the universe, nor with the acceleration of expansion: a problem known as the cosmological constant problem, as discussed by Weinberg¹ and Ishak². At present, in spite of a detailed and important theoretical work, there is no general consensus on the theoretical solutions proposed, see Rovelli³, Esposito⁴ or Kiefer⁵, and on the fact that vacuum fluctuations do contribute to gravity as discussed by Rovelli⁶ and Padmanabhan⁷. Further, even if the common belief is that this should be the case no experiment has been done to finally verify or discard this assumption.

In a recent paper we⁸ have shown that considering the present technological achievements on small force detectors, on superconductors and on seismic isolation it is possible to foresee an experimental path towards such a measurement.

The principle of the measurement is the weighing of a Casimir cavity. Indeed both our works^{8,9} that other analysis^{10,11,12,13} have shown that if a Casimir cavity is placed in the earth gravita-

tional field and the vacuum energy does interact with gravity it receives a force directed upward equal to :

$$\vec{F} = \mathcal{A} \frac{\pi^2 \hbar}{720 a^3} \frac{\vec{g}}{c} \hat{z} = \frac{E_{\text{cas}}}{c^2} \vec{g}. \quad (1)$$

where \mathcal{A} is the Casimir cavity proper area, a is the Cavity proper distance among the plates, c is the speed of light, \vec{g} is the earth gravitational acceleration (g its modulus), the unit vector \hat{z} is directed upwards, E_{cas} is the Casimir energy and the evaluation is performed to first order with respect to the quantity $\frac{g \cdot \hat{z}}{c^2}$. This force, directed upward, can be interpreted as the lack of weight of the modes that have been removed by the cavity, in similarity with the Archimedes buoyancy of fluid. Notice that, as expected (being assumed in the calculation that the vacuum energy gravitates), the result is in agreement with the equivalence principle and the force can also be interpreted as the effect of the gravitational field on the negative mass associated to the Casimir energy.

1.1 Layered superconductors as Casimir multi-cavities

The smallness of the force to be measured makes it mandatory to exploit the measurement with a modulation of the effect that brings the signal at frequencies within detectors measurement band. Layered superconductors, particularly the cuprates, are natural Casimir cavities, being structured as superconducting planes separated by dielectric planes. Thus, the transition of a layered superconductor can be used to obtain a two-state modulation of the Casimir system that switches from a high (absolute value of) Casimir energy content in the superconducting phase to a low Casimir energy content when the superconductor is in the normal state. An estimation of the variation of Casimir energy in the two states has been carried out in by Kempf⁴ and by Calloni *et al*⁸ assuming that in the superconducting state the Casimir energy can be calculated within the zero-temperature and plasma infinitely thin sheets approximation, while it can be neglected in normal state due to the poor conductivity of the material in this state. In this approximation it can be shown^{15,16} that the Casimir energy $E_c(a)$ of two thin plasma sheets separated by the distance a is equal to

$$E_c(a) = -5 \times 10^{-3} \hbar \frac{cA}{a^{5/2}} \sqrt{\Omega}. \quad (2)$$

The parameter Ω is proportional to the density of the carrier in the plasma sheet as discussed by Barton¹⁵ and Bordag¹⁶:

$$\Omega \equiv \frac{nq^2}{2\pi c^2 \epsilon_0}, \quad (3)$$

where n is the surface density of delocalized particles, q their electric charge, m their mass. In case of layered superconductors, particularly High- T_c cuprates, the particles' density is about $n = 10^{14} \text{ cm}^{-2}$, the charge $q = 2e$, the mass $m = 2\alpha m_e$ with $\alpha = 5$. Inserting these values in Eq. (2), neglecting the Casimir energy in the normal state, considering a layered superconductor with typical distance $a = 1 \text{ nm}$ and total thickness H , the variation of Casimir energy for unit volume is

$$\Delta U_{\text{cas}} \approx \eta(a) \frac{N \pi^2 \hbar c}{720 a^3} \approx 2 \times 10^5 \text{ J/m}^3, \quad (4)$$

where $N \approx 10^9$ is the number of cavities per unit height. Remarkably, this variation is of the same order of magnitude of the total energy variation at the transition: Kempf⁴ hypothesis is here made, according to which the whole transition energy is actually Casimir energy. Nonetheless it is important to remark that, by virtue of the accuracy of the measurement, *even if the contribution of the Casimir energy were only of the order of the percent, its contribution to weight variation could be ascertained.*

Considering a volume of superconductor of the order of ten cm^3 , the corresponding Archimedes force is a weight variation of about $F_A \approx 10^{-16} N$. The force is tiny, but affordable from the

most sensitive macroscopic detectors of small forces, like balances or Gravitational Wave (GW) detectors. In a recent paper⁸ it has been shown that both of these systems could be suitable for detecting the Archimedes force from a sensitivity point of view. In particular, the third generation GW detectors, i.e. the planned Einstein Telescope¹⁷, could reach a sensitivity of about $\tilde{F} = 3 \cdot 10^{-15} \text{N}/\sqrt{\text{Hz}}$ in the low frequency region, corresponding to the detection of the Archimedes force in tens of minutes of integration time. In order to choose the detection system one experimental key point is the modulation of the effect, i.e. the periodical transition from normal to superconducting state. In particular, it must be compatible with the bandwidth of the detectors. The possible modulations of the transition are by temperature or external field. Both are favored in the low frequency region. This motivation leads us to the choice of the balances as the system to be experimentally used for the detection of the force.

1.2 Seismic noise reduction

One of the main problems to be addressed in realizing a balance capable of measuring forces of the order of 10^{-16} N is the lack of an attenuation system in the very low frequency regime of 1-100 mHz. One possible strategy is to hang the balance to a seismic isolation cascade formed by an inverted pendulum and blade-spring attenuator similar to the ones used in the Virgo gravitational wave detector. Whenever these elements are at the best of present technology, they are still not sufficient to assure a sufficient attenuation in the mHz region needed for the Archimedes experiment. A possible solution could be the use of accelerometric sensors, placed on the top of the inverted pendulum, to be used in feed-back with unity gain above the Hz. As shown by Harms *et al*⁹ This will reduce the inverted pendulum motion at the electronic noise floor of the accelerometers $a_s \approx 4 \times 10^{-10} \text{m}^2/\text{s}\sqrt{\text{Hz}}$, corresponding to the displacement noise of $1 \text{nm}/\sqrt{\text{Hz}}$ at 0.1 Hz, and flat for frequency less than 0.1 Hz: if reached, as discussed in Calloni *et al*⁸ this limit would be sufficient for the Archimedes force detection. The realization of such a feed-back system is quite complex and expensive, so that alternative passive solutions can be pursued. Here we present a passive solution based on a mechanical resonator, placed on the top of the Inverted-Pendulum and coupled to the Inverted-Pendulum so as to have the usual pair complex-zero/complex pole tuned so that the complex-zero frequency is the same as the signal modulation frequency. In this way the seismic energy is absorbed by the resonator at that frequency and the suspension motion at the frequency is reduced by the attenuation transfer function of the Inverted-Pendulum and by the quality factor of absorber resonance. This behavior can be appreciated by looking at the transfer function of the seismic noise to the balance suspension point, figure 1 on the right, obtained for the complete system as illustrated on the left of the figure .

To calculate the expected signal and noises at the balance, we have considered a balance having arms of length $L = 0.1$ m, a plate at each arm's end of mass $M = 0.4$ kg, total mass $M_b = 1.25$ kg, moment of inertia $I = 0.01 \text{kg m}^2$. The resonance frequency is placed in the region of low seismic noise: $F_{\text{res}} = \omega_b/2\pi = 40$ mHz, with mechanical internal loss angle $\phi = 10^{-6}$. Setting the resonance frequency in the tens of mHz frequency region makes it possible to relax the constraint on the accuracy of setting the bending point (the point of rotation of the balance arm): in particular, the resonance of 40 mHz corresponds to the setting of the bending point distance from the balance center of mass of about $h_b = 50 \mu\text{m}$. Within this design and quite seism conditions the equivalent noise force due to seismic noise is

$$\tilde{F}_s = M_b \cdot a_s \cdot TF \cdot h_b/L_b = 6 \cdot 10^{-15} \text{N}/\sqrt{\text{Hz}} \quad (5)$$

This value is compatible with the expected thermal noise⁸ and might allow a remarkable simplification of the system, not requiring the active system of accelerometers and control loops. Furthermore, the setting of the bending point in the tens of microns region is an easy task. The

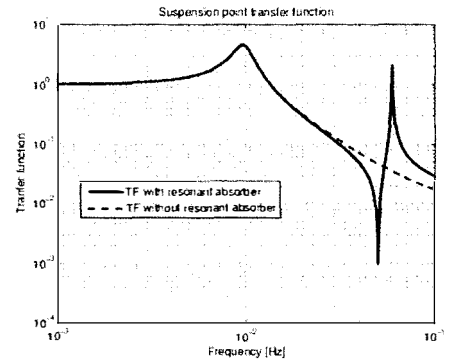


Figure 1 – On the right: Schematic picture of the Archimedes force measurement. On the top of the inverted pendulum there is a second inverted pendulum acting as an absorbing stage. The balance is hanged to the intermediate spring-attenuation element. The signal is read by an optical lever system. On the left: Transfer function of seismic noise to the balance suspension point. The resonant absorber, continuous line, shows the complex zero-poles behavior that, at the complex zero frequency, reduces further the seismic noise for the zero-anti resonance quality factor

investigation of such reduction system, the comparison with the actively controlled inverted pendulum and finally the comparison with a possible push of inverted pendulum resonance frequency in very low frequency is one of the main point of the Archimedes pathfinder. If one of such solutions will prove to be effective it will constitute one a decisive steps towards the realization of the first experiment for the weighing of vacuum fluctuations.

References

1. S. Weinberg *Rev. Mod. Phys.* **61**, 1 (1989)
2. M. Ishak *Found. Phys.* **37**, 1470 (2005)
3. C. Rovelli *Quantum Gravity* (Cambridge: Cambridge University Press)2004.
4. B. S. DeWitt and G. Esposito *Int. J. Geom Methods Mod. Phys.* 51012008
5. C. Kiefer *Quantum Gravity* (Oxford: Clarendon Press) (2012)
6. E. Bianchi E and C. Rovelli *Nature* **466**, 321 (2010)
7. T. Padmanabhan *Int. J. Mod. Phys. D* **15**, 2029 (2006)
8. E. Calloni *et al*, *Phys. Rev. D* **90**, 022002 (2014)
9. E. Calloni *et al*, *Phys. Lett. A* **297**,328 (2002)
10. S. A. Fulling *et al*, *Phys. Rev. D* **76**, 025004 (2007).
11. K. A. Milton *et al*, *J. Phys. A* **41**, 164052 (2008).
12. K. V. Shajesh *et al*, *J. Phys. A* **41**, 164058 (2008).
13. K. A. Milton *et al*, *Phys. Rev. D* **89**, 064027 (2014).
14. A. Kempf *Journal of Physics A: Mathematical and Theoretical* **41**, 164038 (2008)
15. G. Barton *J. Phys. A* **38**, 2997 (2005)
16. Bordag M *J. Phys. A* **39**, 6173 (2006)
17. B. Sathyaprakash *et al*, *Class. Quantum Grav.* **29**, 124013 (2012)
18. P. Poole, H. A. Farach, R. J. Creswick and R. Prozolov *Superconductivity* (second edition) (Academic Press, London) 2007
19. J. Harms *et al*, *Phys. Rev. D* **88**, 122003 (2013)
20. L. Naticchioni *et al*, *Class. Quant. Grav.* **31**, 105016, (2014)

Investigating Dark Energy and Gravitation at cosmological scales with EUCLID

A. BLANCHARD

Université de Toulouse, UPS-OMP, CNRS, IRAP, F-31028 Toulouse, France



The acceleration of the expansion of the universe is now a well demonstrated feature of the universe which is almost impossible to bypassed. This leads to a very surprising question: why is gravity *repulsive* on large scales. By now, it is fair to say that we have no hint about the very reason for the origin of this phenomena (named hereafter “dark energy”) which can be regarded as one of the major surprises in modern physics. Tightening down the properties of dark energy is therefore a major objective of modern science in order to clarify its very nature. The simplest model of dark energy is a cosmological constant, as introduced by Einstein, equivalent to a (quantum) vacuum contribution to the energy budget of the universe. Alternative options are on one side the existence of a scalar field minimally coupled, named quintessence or with more complexity and on the other side the possibility that gravity is actually not driven by general relativity (GR) but by some “modified gravity”, which behaves like GR on small scales, but would be different on large scale. Possible test of such theories relies mainly on the behavior of gravity on large scale, beyond galactic scale. These scales are precisely the target of ongoing project dedicated to dark energy investigation like the ESA space mission EUCLID. Several probes used in combination will allow to constrain dark energy properties with a high accuracy.

1 Introduction: the remarkable successes of the Λ CDM picture

The evidence for an accelerated expansion of the universe coming from the Hubble diagram of type I SNa has gained in robustness with accurate measurements of the fluctuations of the CMB by WMAP, now well reinforced by Planck, and the measurement of the correlation function on large scale by the Sloan telescope : not only the amplitude of the correlation function but also the specific pattern imprinted by the physics of the photon-baryon fluid at recombination time are measured. Both were predicted by Λ CDM picture, with almost no free parameters (except the bias between galaxies and matter) but are the characteristics are almost impossible to reproduce in alternative standard FLRW universes.

1.1 The cosmology precision area

The scientific program which was laid down by Planck twenty years ago, i.e. reaching percent precision on cosmological parameters is now clearly achieved: the latest tables of cosmological

parameters determined solely from CMB or from combination of data provide this precision on the energy contents of the universe as well as on the Hubble constant. Anecdotally, the age of the universe is constrained within 0.2%... An important issue to keep in mind is that those constraints are established within some framework and cannot be interpreted as direct measures (and uncertainties) on the actual characteristics of the universe. One important quantity is however not well known : the equation of state parameter w which describes the relation between energy density and pressure:

$$P = w\rho \quad (1)$$

(with $c = 1$). This quantity is not well constrained by the CMB because dark energy plays a role in the dynamics of the expanding universe only at low redshift and therefore enters mainly through the distance to the last scattering surface located at $z \sim 1100$ i.e. only through an integral. By present day observations, we know that w is close to -1, with an uncertainty of the order of 10%, but we have limited information about its possible variation with time¹³.

2 Tightening down Dark Energy properties

The discovery of dark energy is probably a major upheaval of modern physics that has not yet been completely digested: it means that gravity, the phenomena of nature that Galileo and Newton studied and theorized so well and so successfully largely founding modern physics is at the scale of the universe repulsive with a strength proportional to the distance... something we were not aware of twenty years ago! Furthermore, contrary to how dark matter is generally regarded, dark energy, the standard terminology for the origin of the acceleration of the expansion, does not fit naturally in a framework of modern physics. It is therefore very logical that cosmologists regard the characterization of dark energy and if possible its understanding as the most important scientific program of modern fundamental physics.

The reason why dark energy has escaped detection before its identification at cosmological scales by astrophysical data is due to its weakening on small distance. And there a consequence is that there is little hope for detecting its presence from laboratory experiments. Some specific models lead to a signature that may be looked for in lab^{5,14}, but no generic signal can be foreseen. Solar system tests are providing very accurate tests of gravity and constraints are written in terms of the post newtonian parameters. A cosmological constant is in principle detectable by this means, but the expected signal is much lower than present day limits. In addition the existence of screening mechanisms⁸ implies that the "small scale" test of gravity cannot test modifications of gravity that lead to very different behaviour (compared to GR) on large scale. Galactic scales and cluster scales are dominated by dark matter. Testing gravity on these scales is potentially problematic for two reasons: they are strongly non-linear (in the sense that the contrast density is high) and they are affected by complex hydrodynamic processes during their formation. We are therefore left with large scales. On large scale, beyond ten megaparsecs, fluctuations are in a nearly linear regime and their dynamics should not be affected by complex physics. Therefore they are the most appropriate to provide data on which gravity can be tested (It should be kept in mind however that non-linear physics, in particular physics of galaxy formation, on small scales will affect in some way the properties of the large scale distribution of galaxies compared to that of the dark matter, this difference known as the bias will have to be evaluated to extract meaningful information from the galaxy properties on large scale).

EUCLID was designed precisely to measure the properties of dark energy. It is an optical/near-infrared telescope with both imagery and spectroscopy capabilities. Its detailed properties can be found in the "Euclid red book"¹⁰. Its field of view will be 0.5 deg². It is anticipated to collect the imagery of $\sim 1.5 \cdot 10^9$ galaxies. The high resolution will allow to measure the shape of galaxies and the IR photometry will allow high redshift photometric redshift. Spectroscopic data for

$\sim 310^7$ galaxies will be collected. The universe will be basically mapped up to $z \sim 2$. The chair of the EUCLID consortium board is Yannick Mellier (IAP, France) and the board comprises members from sixteen countries participating to the consortium at the time of writing. Further countries might join in the future. Much more information can be found on the consortium site : <http://www.euclid-ec.org/>

EUCLID primary optimized for investigating dark energy through two probes: weak lensing mapping of the universe and the measures of galaxy distribution in redshift space (including redshift distortion). Other probes will bring additional cosmological information: i) clusters of galaxies, ii) cross correlation with CMB and X-ray sky and iii) strong lensing. Additional legacy science will be produced: studies of the high redshift universe (“primeval universe”), the Galaxy/AGN evolution, the local universe, the Milky Way. Two additional subjects depends on the surveys strategy and are therefore subject to further decisions: exo-planet and supernovae. These various topics are to be prepared and analysed by science working groups.

The full significance of EUCLID observations for fundamental physics is to be handled by the theory science working group. A living review paper is maintained².

3 Astrophysical probes of Dark Energy

Since the discovery of the acceleration of the expansion of the universe, the community has concentrated his scientific activity on investigating the various probes of dark energy and their relevance for accurate characterization¹.

The Hubble diagram of SNIa consists in measuring the luminosity distance against redshift (under the assumption that these objects are standard candles). Cosmological test based on distance measurements are the most common and includes measurements of the transversal baryonic acoustic oscillations and the fluctuations of the cosmological background radiation. A somewhat complementary probes allow measurement of $H(z)$ like the measurements of the longitudinal baryonic acoustic oscillations, the redshift drift, the age against redshift. Weak lensing offers access to both aspects. These probes are essentially probing the background of our Universe, i.e. its geometrical structure and its dynamics.

An other category of tests is able to address the (linear) growth of structure with time. Measurements of the power spectrum of galaxies in redshift space, of tomographic weak lensing and of clusters abundance evolution with redshift are sensitive to the (linear) growth factor $G(z)$:

$$\delta(z) = G(z)\delta_0 \quad (2)$$

In standard FLRW universe a good approximation is:

$$\frac{d \ln(G)}{d \ln(a)} \sim \Omega_m^\gamma(a) \quad (3)$$

with $\gamma \sim 0.55$ in Λ CDM. Weak lensing; redshift space distortion, galaxy clusters abundance are able to constrain γ and thereby to test the standard model at its foundation: a clear departure from $\gamma \sim 0.55$ will be a clear signature of something beyond the standard model, like modified gravity even if this formulation could be improved⁶.

4 Beyond the standard model

4.1 Fiducial models of dark energy

The first class of theories of dark energy are assuming the relevance of general relativity, but includes the existence of a new component. The simplest model in the category is a scalar field with minimal couplings and canonical kinetic energy. This is often call quintessence. This can be specified by its action:

$$S = \int d^4x \sqrt{g} \left[\frac{R}{16\pi G} - \frac{1}{2} g^{\mu\nu} g^{\mu\nu} \partial_\mu \phi \partial_\nu \phi - V(\phi) + \mathcal{L}_m \right] \quad (4)$$

This approach was first introduced by Ratra and Peebles (1988)¹⁵. Pressure (P) and density (ρ) associated to the scalar field can then be deduced. The standard parameter w , the equation of state parameter is then:

$$w = \frac{P}{\rho} = \frac{1/2\dot{\phi}^2 - V(\phi)}{1/2\dot{\phi}^2 + V(\phi)}$$

In the absence of further constraint, the quantity $w(z)$ can be an arbitrary function (which is between -1 and 1 provide the kinetic term and the potential have to remain positive). A popular parametrization is the Chevalier-Polarski-Linder (CPL) on^{6,11}: $w(z) = w_p + (1 - a)w_a$. In such quintessence models the growth index is well approximated by¹²:

$$\gamma = 0.55 + 0.05[1 + w(z = 1)](\text{fitted})$$

The EUCLID forecast on these parameters (w_p, w_a, γ is given in the table 2.2 in the red book¹⁰. Before going one step further in exploring possible models for dark energy it is important to have in mind that EUCLID is a experiment designed to investigate gravity in a specific regime, not investigated by other means and as such is an experiment in fundamental physics. Indeed EUCLID will test gravity in the regime of weak field and weak curvature. This has been nicely summarized in figure 1³.

4.2 The zoology of “dark energy” models

There is a wide variety of explanations for the possible origin of the acceleration of the expansion: more complex fields, with additional couplings or modification of gravity by modifying the Einstein-Hilbert Lagrangian (MG). Beyond the background evolution it is important to address the question of the evolution of perturbations. Assuming that we can describe gravity as a metric theory, it is possible to write the most general perturbed RW metric for scalar mode of the perturbations in the form of :

$$ds^2 = a^2(t)[-(1 + 2\Psi)dt^2 + (1 - 2\Phi)dx^i dx_i]$$

by choosing an appropriate coordinates system. This corresponds to the Newtonian gauge which is generally the most convenient for observational tests. Modifications of the dynamics of scalar perturbations on sub-horizon scales can then represented by two degrees of freedom, Q coming in the Poisson equation (in Fourier space):

$$-k^2 \Phi = 4\pi G Q(a, k) a^2 \rho_m \Delta_m$$

and η entering in the $\Psi - \Phi$ relation:

$$\Phi = \eta(a, k) \Psi$$

For a given DE/MG theory, Q, η can in principle be computed and equations for perturbations can be solved.

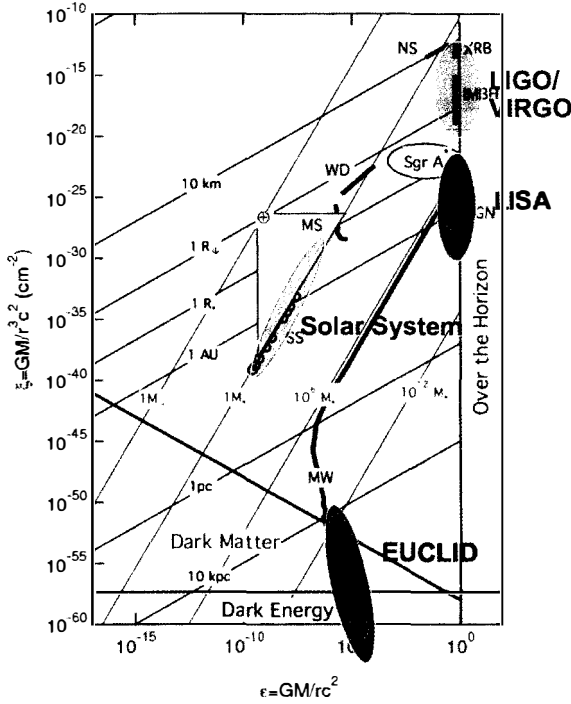


Figure 1 – Testing gravity on different scales and different strength is nicely summarized in this 2 parameter space diagram introduced by Baker et al.³. The axis variables are the gravitational potential and the curvature. Euclid is investigating the low curvature regime.

Redshift space distortions are sensitive to Φ while weak lensing measurements are sensitive to $\Phi + \Psi$. Euclid will therefore not only characterize the energy contents of the universe but provide data to test the underlying theory of gravity. However, in these regimes it should be stated that differences between DE and MG is less clear: a modification to Einstein's equation can be interpreted as standard Einstein gravity with a modified "matter" source (\supset scalars, vectors and tensors). A terminology has therefore been adopted²: *Standard dark energy* refers to models based on standard gravity, canonical kinetic energy, minimal couplings, sound speed $= c$. Beyond this we have *Clustering dark energy* models, for instance allowing non-standard kinetic term, *k-essence*, still keeping $\eta = 1$. *Explicit modified gravity models* are models in which the theory of gravity is explicitly modified from the beginning.

A simple example of such models is the *Coupled dark energy models* in which the Lagrangian includes extra couplings terms between the dark energy field and the matter field(s) ϕ :

$$S = \int d^4x \sqrt{g} \left[\frac{R}{16\pi G} - \frac{1}{2} g^{\mu\nu} \partial_\mu \phi \partial_\nu \phi - V(\phi) + m(\phi) \bar{\psi} \psi + \mathcal{L}_m(\psi) \right]$$

coupling can be with baryons, neutrinos, dark matter... The model leads to a mass varying with the field and thereby with time $m(\phi) = \bar{m} \exp(-\beta(\phi)\phi)$ and to a fifth force term :

$$\tilde{G} = G(1 + 2\beta^2(\phi))$$

Given the wide level of freedom in those theories, one may wish to classify them by identify a limited number of degrees of freedom that can be determined from observations and which are

meaningful in the “space of theories”. Two formalism have been developed in this spirit, the parametrised post Friedmann (PPF) formalism⁷ and the effective field theory (EFT)⁸.

5 Some final comments on the dark sector

5.1 Dark components degeneracy

The standard way to write Friedman-Lemître equation is:

$$\left(\frac{\dot{R}}{R}\right)^2 = \frac{8\pi G\rho_m}{3} + \frac{8\pi G\rho_{DE}}{3} - \frac{kc^2}{R^2}$$

ρ_m and ρ_{DE} always enter together in any equation so the distinction between these two components from cosmological data is not possible. Therefore although the distinction between dark matter and dark energy seems very natural, astrophysical data are unable to distinguish these two components. The description as a single fluid is therefore as adequate, this degeneracy holds as well for perturbations but also for the full energy-momentum tensor! The distinction between matter and dark energy is therefore conventional as long as cosmological observations are concerned⁹.

5.2 Testing general relativity at cosmological scales

The Friedman-Lemître equation in general relativity can be written as:

$$\Omega_k = 1 - \sum \Omega_{contents} \quad (5)$$

Newtonian dynamics would lead to a very similar equation, but with an undertined constant k . So we can define :

$$\Omega_{kgeo} = -\frac{k}{(a_0 H_0)^2} \quad (6)$$

and

$$\Omega_{kdyn} = 1 - \sum \Omega_{contents} \quad (7)$$

Therefore measuring the relation between $\Omega_{contents}$ and Ω_{kgeo} is a test of GR on large scale at the background level. Present day measurements are consistent with GR, see figure2, but the lack of accurate measurements of $H(z)$ does not yet allow to verify this relation accurately without assumption on dark energy¹⁷.

6 Conclusions

The acceleration of the expansion of the universe is one of the most surprising observations in modern fundamental physics. By studying the fall of bodies in the field of terrestrial gravity, it is often said that Galileo founded modern physics. It is somewhat ironic that we now realize that gravitation is repulsive at the scale of the universe and that the actual reason for is essentially unknown. Pining down the properties of dark energy and understanding the properties of gravity at large scale is precisely the aim of EUCLID.

Acknowledgments

I thank Yves Zolnierowski for allowing me to present and use part of the results published in ¹⁷. The author acknowledges the Euclid Collaboration, the European Space Agency and the support of a number of agencies and institutes that have supported the development of Euclid.

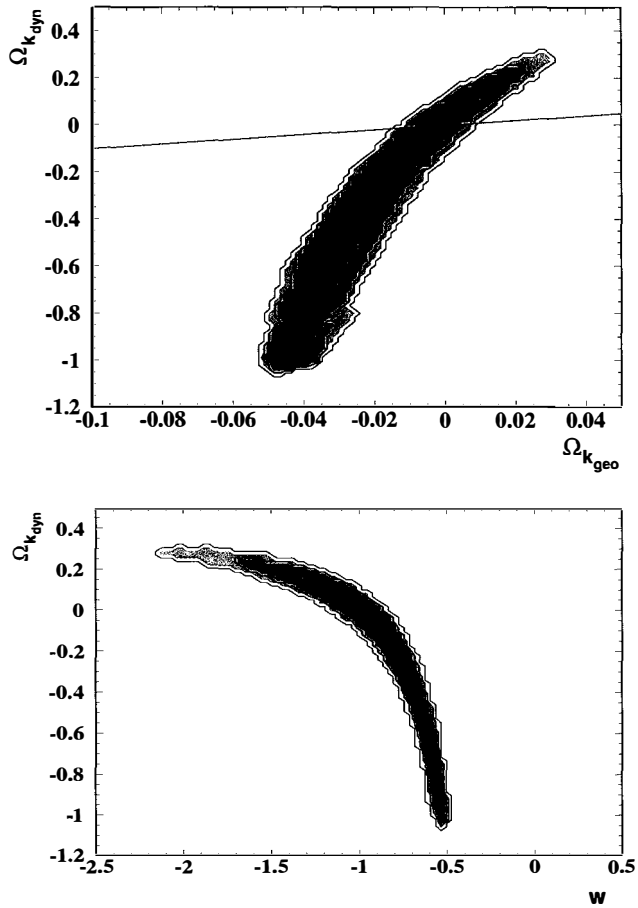


Figure 2 – 1, 2 and 3 σ contours in the $\Omega_{k_{geo}} - \Omega_{k_{dyn}}$ for models having a dark energy component with an arbitrary constant equation of state parameter w . The contours are marginalized for $-2.5 < w < 0.5$. The addition of a new degree of freedom, w , widens the contours revealing a degeneracy between $\Omega_{k_{dyn}}$ and $\Omega_{k_{geo}}$

References

1. Albrecht, A., Bernstein, G., Cahn, R., et al. 2006, arXiv:astro-ph/0609591
2. Amendola, L., Appleby, S., Bacon, D., et al. 2013, *Living Reviews in Relativity*, 16, 6
3. Baker, T., Psaltis, D., & Skordis, C. 2015, *ApJ*, 802, 63
4. Chevallier, M., & Polarski, D. 2001, *International Journal of Modern Physics D*, 10, 213
5. Dupays, A., Lamine, B., & Blanchard, A. 2013, *A&A*, 554, A60
6. Gubitosi, G., Piazza, F., & Vernizzi, F. 2013, *JCAP*, 2, 032
7. Hu, W., & Sawicki, I. 2007, *Phys. Rev. D*, 76, 104043
8. Joyce, A., Jain, B., Khoury, J., & Trodden, M. 2015, *Phys. Rep.*, 568, 1
9. Kunz, M. 2009, *Phys. Rev. D*, 80, 123001
10. Laureijs, R., Amiaux, J., Arduini, S., et al. 2011, arXiv:1110.3193
11. Linder, E. V. 2003, *Physical Review Letters*, 90, 091301
12. Linder, E. V. 2005, *Phys. Rev. D*, 72, 043529
13. Planck Collaboration, Ade, P. A. R., Aghanim, N., et al. 2015, arXiv:1502.01589
14. Pignol, G. 2015, arXiv:1503.03317
15. Ratra, B., & Peebles, P. J. E. 1988, *Phys. Rev. D*, 37, 3406
16. Steigerwald, H., Bel, J., & Marinoni, C. 2014, *JCAP*, 5, 042
17. Zolnierowski, Y., & Blanchard, A. 2015, *Phys. Rev. D*, 91, 083536

Backreaction Effects on the matter side of Einsteins Field Equations

S. Floerchinger¹, N. Tetradis² and U.A.Wiedemann¹

¹ *Physics Department, Theory Unit, CERN, CH-1211 Genève 23, Switzerland*

² *Department of Physics, University of Athens, Zographou 157 84, Greece*



Recently, we have derived a novel and compact expression for how perturbations in the matter fields of the cosmological fluid can lead to deviations from the standard Friedmann equations. Remarkably, the dissipative damping of velocity perturbations by bulk and shear viscosity in the dark sector can modify the expansion history of the universe on arbitrarily large scales. In universes in which this effect is sufficiently sizeable, it could account for the acceleration of the cosmological expansion. But even if dark matter should be less viscous and if the effect would be correspondingly smaller, it may have observable consequences in the era of precision cosmology. Here, we review the origin of this backreaction effect and possibilities to constrain it further.

1 Backreaction effects in cosmology

In the cosmological perturbation theory that is at the basis of the phenomenologically successful Λ CDM model, all fields entering Einstein's field equations are split into a spatially homogeneous and isotropic *background* part and *perturbations* around it. For instance, one writes $g_{\mu\nu}(x) = \bar{g}_{\mu\nu}(\tau) + \delta g_{\mu\nu}(x)$ for the metric, $\epsilon(x) = \bar{\epsilon}(\tau) + \delta\epsilon(x)$ for the energy density, etc., where the background fields are defined as spatial averages of the full fields. Up to first order in perturbations, the spatially averaged Einstein equations reduce then to the well-known Friedmann equations for the background fields. However, Einstein's field equations are non-linear, and, beyond first order in perturbations, a spatial average of Einstein's equations for the full fields differs from Einstein's field equations for the spatially averaged fields. The perturbations *backreact*, that is, the time evolution of the background fields depends on the time evolution of the perturbations.

The possible sources of such backreaction effects, and the question to what extent they may modify Friedmann's equations have been discussed repeatedly. On the one hand, it has been argued that the formation of non-linear structures could affect the average expansion rate of the Universe considerably and that this may even account for the accelerated expansion in late-time cosmology, for a review see Ref. ¹. In sharp contrast to this line of thought, there are also arguments that the phenomenological success of the Λ CDM model is a consequence of its mathematical consistency, in the sense that the evolution of the exactly homogeneous and

isotropic FLRW metric does indeed account with high precision for the evolution of spatially averaged fields in our physically realized Universe with perturbations, for a review see Ref. ². So far, this discussion focussed mainly on backreactions of metric perturbations, that is, terms in Einstein's field equations that are second order or higher in $\delta g_{\mu\nu}$. Instead, we point here to backreaction effects that are second order in matter perturbations and that have a physical interpretation in terms of dissipative processes.

2 Backreaction from matter perturbations and cosmological expansion

Einstein's equation for an exactly homogeneous and isotropic FLRW universe are the first Friedmann equation, that relates $\bar{\epsilon}$ to the Hubble parameter H , and the second Friedmann equation. The only additional information contained in the latter is energy conservation for an expanding system,

$$\frac{1}{a}\dot{\bar{\epsilon}} + 3H(\bar{\epsilon} + \bar{p} - 3\zeta H) = D, \quad (1)$$

where $D = 0$ for the FLRW metric, $H = \dot{a}/a^2$, and the dot denotes a derivative w.r.t. conformal time. We recall these elementary facts to highlight two issues that are important for the following. First, what enters the evolution of the background fields is not the average pressure \bar{p} , but the effective pressure $\bar{p}_{\text{eff}} = \bar{p} - 3\zeta H$ for which a term proportional to the bulk viscosity ζ times expansion scalar is subtracted. Indeed, bulk viscosity is the only dissipative effect that can arise in an exactly homogeneous and isotropic system, and bulk viscous pressure is a negative pressure. The logical possibility that bulk viscosity may therefore account for phenomena normally attributed to dark energy has been explored in several studies^{3,4}. Second, equation (1) illustrates the well-known fact that Einstein's field equations include the conditions for energy momentum conservation, $\nabla_{\mu}T^{\mu\nu} = 0$. In our recent study⁵, we started from energy conservation. Working in the Landau Frame $-u_{\mu}T^{\mu\nu} \equiv \epsilon u^{\nu}$ and keeping shear viscous and bulk viscous effects up to first order in a gradient expansion of the fluid dynamic fields, one finds from $\nabla_{\mu}T^{\mu 0} = 0$

$$u^{\mu}\partial_{\mu}\epsilon + (\epsilon + p)\nabla_{\mu}u^{\mu} - \zeta\Theta^2 - 2\eta\sigma^{\mu\nu}\sigma_{\mu\nu} = 0, \quad (2)$$

where η and ζ denote the shear and bulk viscosity, respectively, $\Delta^{\mu\nu} = g^{\mu\nu} + u^{\mu}u^{\nu}$ and

$$\begin{aligned} \sigma^{\mu\nu} &= \frac{1}{2}\left[\Delta^{\mu\alpha}\Delta^{\nu\beta} + \Delta^{\mu\beta}\Delta^{\nu\alpha} - \frac{2}{3}\Delta^{\mu\nu}\Delta^{\alpha\beta}\right]\nabla_{\alpha}u_{\beta}, \\ \Theta &= \nabla_{\mu}u^{\mu}. \end{aligned} \quad (3)$$

Forming the spatial average of eq. (2), one can determine the dissipative corrections to the time evolution of the average energy density $\bar{\epsilon}$. In general, metric perturbations enter this spatial average via the covariant derivative ∇^{μ} , the projector $\Delta_{\mu\nu}$ and the normalization of the velocity field. For instance, in conformal Newtonian gauge with Newtonian potentials Ψ and Φ , the constraint $u_{\mu}u^{\mu} = -1$ implies $u^{\mu} = (\gamma, \gamma\vec{v})$, where $\gamma = 1/(\alpha\sqrt{1 - \vec{v}^2 + 2\Psi + 2\Phi\vec{v}^2})$. However, in the relevant limit of small gravitational potentials ($\Phi, \Psi \ll 1$), that vary slowly in time, $\dot{\Phi} \sim \frac{\alpha}{a}\Phi$, one finds that the spatial average of (2) is independent of metric perturbations⁵. On the other hand, there are fluid perturbations. In particular, perturbations in the gradients of the velocity field enter the terms Θ^2 and $\sigma^{\mu\nu}\sigma_{\mu\nu}$ in eq. (2) to second order, and thus they do not vanish upon spatial averaging. Since Θ^2 and $\sigma^{\mu\nu}\sigma_{\mu\nu}$ are positive semidefinite, one finds (for small fluid velocity v) that the spatial average of (2) is of the form of (1) with a positive term⁵

$$D = \frac{1}{a^2}\langle\eta\left[\partial_i v_j \partial_i v_j + \partial_i v_j \partial_j v_i - \frac{2}{3}\partial_i v_i \partial_j v_j\right]\rangle + \frac{1}{a^2}\langle\zeta[\vec{\nabla} \cdot \vec{v}]^2\rangle + \frac{1}{a}\langle\vec{v} \cdot \vec{\nabla}(p - 6\zeta H)\rangle. \quad (4)$$

Here, the term D gives an explicit backreaction of fluid perturbations on the time evolution of the average energy density $\bar{\epsilon}$. In Ref. ⁵, we have analyzed the effect of this term on the cosmological expansion. To this end, we combined eq.(1) with an equation for the scale factor a .

For the latter, we used the trace of Einstein's equation since its spatial average does not depend on matter perturbations,

$$R = 8\pi G_N T_\mu^\mu = -8\pi G_N (\bar{\epsilon} - 3\bar{p}_{\text{eff}}) = -6\frac{\ddot{a}}{a^3}. \quad (5)$$

Combining both equations, one finds for the deceleration parameter $q = -1 - \dot{H}/(aH^2)$ the differential equation⁵ (we use the simple equation of state $\bar{p}_{\text{eff}} = \hat{w}\bar{\epsilon}$)

$$-\frac{dq}{d\ln a} + 2(q-1)\left(q - \frac{1}{2}(1+3\hat{w})\right) = \frac{4\pi G_N D(1-3\hat{w})}{3H^3}. \quad (6)$$

The fixed point of this equation is accelerating, i.e. $q < 0$, for $\frac{4\pi G_N D}{3H^3} > \frac{1+3\hat{w}}{1-3\hat{w}}$.

3 An explicit deviation from Friedmann's equation for the (toy) ansatz $D \propto H$

The conclusion of the discussion above is that in a universe in which dissipative effects are sufficiently large, $D \sim O(H^3/G_N)$, dissipation induces accelerated cosmological expansion. Clearly, in a universe in which dissipative effects are smaller, other physical effects need to be invoked to account for an observed accelerated expansion. However, even for small but non-vanishing backreaction D , the cosmic expansion scale factor a will not obey the exact Friedmann equation. We emphasize this point since it is a key assumption of the Λ CDM cosmological concordance model⁶ that a does satisfy the Friedmann equation; this assumption underlies for instance the definition of cosmological distance measures and it is poorly tested at best. Given the precision of modern cosmology, it is thus interesting to explore the sensitivity of distance measures on D by analyzing deviations from Friedmann's equation induced by D .

The term D is calculable once the matter content of the Universe and the dissipative properties of dark matter are specified. D affects the time evolution of the background fields in eq. (1), while the cosmological perturbations needed to determine the spatial average D according to eq. (4) are evolved on top of these background fields. This complicates a dynamical determination of D . In general, since perturbations evolve, D will have a non-trivial dependence on redshift, $D = D(z)$, where $a = \frac{1}{1+z}$. We plan to calculate this evolution of D in future work for different viscous properties of the dark sector. For the purpose of these proceedings, we just examine heuristically one type of z -dependence of D :

Let us consider for a moment a hypothetical universe composed of radiation and viscous dark matter, but without dark energy. What would we have to choose for the dissipative backreaction term D of that hypothetical universe, if we required that its deceleration parameter matches that of the phenomenologically successful Λ CDM universe? To answer this question, we write the scale dependence of the Hubble parameter of the Λ CDM universe, $H(z) = H_0\sqrt{\Omega_\Lambda + \Omega_M(1+z)^3 + \Omega_R(1+z)^4}$, we derive from it the explicit form for the deceleration parameter $q(z)$ in the Λ CDM universe, we insert it into the left hand side of equation (6) and we read off an expression for D . For the case of a pressure-less fluid $\hat{w} = 0$, we find $D = \frac{3}{4\pi G_N} 6\Omega_\Lambda H_0^2 H(z)$. Therefore, if one would aim at exploring the possibility that dissipative properties of dark matter can account for phenomena normally attributed to dark energy, one would seek dark matter with viscous properties that lead to a backreaction $D(z) \approx \text{const.}H(z)$.

We caution that by making the *ad hoc* ansatz $D(z) = \text{const.}H(z)$, we did not check whether this particular scale dependence can arise from a dynamical evolution of perturbations in a fluid with 'realistic' viscous properties. In general, both the size and the scale dependence of $D(z)$ depend on the viscous properties of dark matter. There is no *a priori* reason that the scale dependence satisfies the simple ansatz $D(z) = \text{const.}H(z)$. For a more general form of $D(z)$, the solution of the evolution equations for the background field $\bar{\epsilon}$ will show deviations from Friedmann's equation that involve an integration over the evolution of D . However, for the

ansatz $D(z) = \text{const.}H(z)$, a linear superposition of eqs. (1) and (5) results in

$$\bar{\epsilon} - \frac{D}{4H} = \frac{3}{8\pi G_N} H^2, \quad \text{and} \quad \bar{p}_{\text{eff}} - \frac{D}{12H} = -\frac{1}{8\pi G_N} \left(2\frac{1}{a} \dot{H} + 3H^2 \right). \quad (7)$$

Here, the relation between the Hubble parameter and the total energy density $\bar{\epsilon}$ and total effective pressure differ from the standard Friedmann equations by the terms proportional to D . There is a one-to-one relation between this type of evolution and a Λ CDM model with energy density $\hat{\epsilon} = \bar{\epsilon} - \frac{D}{3H}$ and dark energy density $\frac{D}{12H}$. More precisely, in terms of $\hat{\epsilon}$, the evolution equation (1) for energy density, and the trace (5) of Einstein's equations can be written as

$$\frac{1}{a} \dot{\hat{\epsilon}} + 3H(\hat{\epsilon} + p_{\text{eff}}) = 0, \quad \text{and} \quad R + \frac{8\pi G_N D}{3H} = -8\pi G_N(\hat{\epsilon} - 3\bar{p}_{\text{eff}}). \quad (8)$$

This is of the same form as the corresponding equations in the Λ CDM model if one specializes to a pressureless fluid $p_{\text{eff}} = 0$ and if one identifies $\hat{\epsilon}$ with the energy density in the Λ CDM model and the cosmological constant with

$$\Lambda = \frac{2\pi G_N D}{3H}. \quad (9)$$

4 Outlook

Rather than repeating or anticipating work published in refereed journals, we have made use of this proceedings article to share some simple but heuristic considerations of how dissipative backreaction of matter perturbations may lead to deviations from Friedmann's equation for the scale parameter. Clearly, a more rigorous analysis of these deviations is possible: one can calculate the size and scale dependence of $D(z)$ as a function of the viscous properties of dark matter. This calculation could contribute to a critical appraisal of cosmological distance measures. This line of thought will be presented elsewhere.

We finally remark on a crucial point that was discussed more prominently in the oral presentation of our work in Moriond. The evolution of perturbations and the growth of cosmological structure depends on dissipative properties, and information about structure formation is known to constrain possible dissipative phenomena^{3,4}. To first order in cosmological perturbations, one finds from Einstein equations that the evolution equation of the density contrast $\delta\rho = \delta\epsilon/\bar{\epsilon}$ does not depend explicitly on viscous contributions, while the evolution of fluid velocity perturbations is attenuated by a scale-dependent viscous term. As a consequence, one expects that unlike finite pressure that counteracts the growth of density contrast, finite viscosity will not counteract this growth but it will slow down the growth of velocity gradients and it may thus delay structure formation. We are currently evaluating how the constraints on viscous properties arising from structure formation translate into constraints on the backreaction D .

References

1. T. Buchert and S. Räsänen, *Ann. Rev. Nucl. Part. Sci.* **62** (2012) 57.
2. S. R. Green and R. M. Wald, *Class. Quant. Grav.* **31** (2014) 234003.
3. B. Li and J. D. Barrow, *Phys. Rev. D* **79** (2009) 103521.
4. J. S. Gagnon and J. Lesgourgues, *JCAP* **1109** (2011) 026.
5. S. Floerchinger, N. Tetradis and U. A. Wiedemann, *Phys. Rev. Lett.* **114** (2015) 9, 091301.
6. E. Bertschinger, *Astrophys. J.* **648** (2006) 797 [astro-ph/0604485].

Disformal vectors and anisotropies on a warped brane

Federico R. Urban

*Service de Physique Théorique, Université Libre de Bruxelles,
CP225, Boulevard du Triomphe, B-1050 Brussels, Belgium*

I discuss the cosmological solutions of a system in which the observer, represented in this case by a massive vector field, feels a metric which is *disformally* related to the geometrical one. Hulluilla on Halvat Huvit.

Disformal what?

Imagine a scalar field. Call it, surprise surprise, $\phi(x)$. Imagine there also is no heaven. Well, then there is (almost) certainly a metric: $g_{\mu\nu}(x)$. Now, you want another one: $\mathfrak{g}_{\mu\nu}$, what can you do?

First of all, you take $g_{\mu\nu}$ itself, and generalise it to any function of ϕ , such that you end up with $C(\phi)g_{\mu\nu}$. Now, you can squeeze some indices off ϕ via spacetime derivatives as $\partial_\mu\phi$. Take two of them, and you've just put together something useful, namely $\partial_\mu\phi\partial_\nu\phi$. And why not generalise this term with another function of ϕ ? Well, there is no why, so let's call this object $D(\phi)\partial_\mu\phi\partial_\nu\phi$. Now put it all together and there comes your "disformal" something:

$$\mathfrak{g}_{\mu\nu} = C(\phi)g_{\mu\nu} + D(\phi)\partial_\mu\phi\partial_\nu\phi.$$

Should say, we usually call $C(\phi)$ the Conformal factor, and $D(\phi)$ the Disformal factor: *quelle imagination!* The $\mathfrak{g}_{\mu\nu}$ is, justly, called disformal metric, and if you want your theory to be sane as you are, you would not further generalise this construction including pieces of $\partial_\mu\phi$ into $C(\phi)$ or $D(\phi)$, let alone higher derivatives anywhere: those are bad ideas which lead to plenty nightmares infested by heaps of ghosts. In fact, it has been shown that this is the most general physically consistent theory of two metrics, and a scalar, provided we believe in causality, the weak equivalence principle, and locality or Lorentz symmetry, see¹.

How to lose your audience 101

We've got the disformal metric, so now what? Let me tell you what, but take a big breath^{2,3}.

Consider a warped flux compactification of Type IIB string theory where the 10D higher dimensional generalisations of gauge fields the RR-forms $F_{n+1} = dC_n$ where $n = 2, 4, 6, 8$ as well as the NSNS-form $H_3 = dB_2$ are turned on in the internal space which is six dimensional Calabi-Yau manifold whose fluxes back-react on the geometry warping it and throw in probe Dp-branes embedded in this background which as spatially extended objects they will also break 10D Lorentz symmetry but not Lorentz 4D symmetry and thus will be space-filling in the noncompact dimensions and now specialise to a D3-brane in this setup which due to the potential generated by the RR-forms and the NSNS-form which also stabilises all of the geometric moduli present in the compactification and

now we were talking about the D3-brane and this brane will wander about in search of the bottom of its own valley and ask yourself what happens if you sit on this probe brane and the answer is that life from your point of view would look like $g_{\mu\nu} = h(\phi)^{-1/2}g_{\mu\nu} + h(\phi)^{1/2}\partial_\mu\phi\partial_\nu\phi$ and this includes stepping on a scale and checking your very own weight and where we defined h as the warp factor and ϕ as the compact direction along which the D3 moves but not you.

Got it?

To build an action

Well, now forget it. The point I want to make here is: yes, there are constructions where the disformal metric pops up, and it's good that there are, but before you bang your head on the wall in search of them, just have a look at this action

$$S = \int d^4x \sqrt{-g} \left[\frac{R}{2} + p(\phi, X) \right] - \int d^4x \sqrt{-g} \left[\frac{1}{4} g^{\alpha\beta} g^{\gamma\delta} F_{\alpha\gamma} F_{\beta\delta} + \frac{1}{2} m^2 g^{\mu\nu} A_\mu A_\nu \right].$$

The first piece includes standard Einstein gravity and the scalar with any Lagrangian ($X = -g^{\alpha\beta}\partial_\alpha\phi\partial_\beta\phi/2$ is the kinetic term for ϕ). The second piece is a Proca Lagrangian for the vector A_μ which is coupled to the $g_{\mu\nu}$. The field strength tensor is $F_{\alpha\beta} = A_{\beta,\alpha} - A_{\alpha,\beta}$ as usual.

Isn't it beautiful? In fact, it's the simplest thing you would come up with if you were to—morbidly enough, I admit—to throw in a vector field and ask her/him to feel the disformal metric rather than the regular one. It's also pretty much identical to the action for electromagnetism (truth be told, not quite, but forget the mass) plus a boring real scalar field, except that there are two metrics distributed democratically among the two fields present in the game in the only possible way you can do it.

Cosmology

Is this action any good? If you want the full answer, you can check here:⁴ If you want a different answer, you can also look here:⁵, but that's to a different question. But since you're here, you probably want some answer now, so now and here you have it.

As any action, the first place to check on its wits is^a cosmology, for if this fails, your action is in deep... trouble. So what you've gotta do is to shake it until a good Universe comes out of it. More practically, since there is a vector field, and since we still appear to be living in 4D despite all particle-theoretical efforts in trying to convince us otherwise, we need to accommodate this vector somewhere; somewhere being not everywhere, one direction out of the spatial^b three will be special^c. Technically, we need to employ an anisotropic metric, for example, Bianchi I:

$$ds^2 = -dt^2 + e^{2\alpha(t)} \left[e^{2\sigma(t)} (dx^2 + dy^2) + e^{-4\sigma(t)} dz^2 \right].$$

The variable α is the overall isotropic volume expansion (aka the logarithm of the averaged scale factor of the Universe), and σ describes the anisotropy (take its derivative and you have found the shear); the vector then becomes $A_\mu = (0, 0, 0, A)$.

And with a metric and an action, what comes next? You named it: Euler-Lagrange cosmological equations! Now, if I were a pervert I would write them down here, and since pervert I am, here they are:

Just kidding!

^aIs its wits!

^bOr should it be "spacial"? We do not call it "spate-time" afterall...

^cHmm, yes, "spetial" won't do, never heard of "Spetial Relativity".

Mighty mess, aren't they? Mighty mess notwithstanding, we were brave and courageous, and with some fiddling with rescalings and redefinitions of the variables, we managed to make them look good: convert everything to e-folding number α ; define a generalised Lorentz boost factor as $\gamma \equiv (1 - 2DX/C)^{-1/2} \equiv 1/\tilde{\gamma}$, so that $\tilde{\gamma} \rightarrow 0$ means that our 4D world is rushing headlong at breaknecking speed (a variation on "ultra-relativistic regime"), whereas $\tilde{\gamma} \rightarrow 1$ is turtle-mode (aka "non-relativistic"); specify the scalar action (DBI, for those in the know) $p(X, \phi) = (1 - \tilde{\gamma})/D/C - V$ where $V(\phi)$ is the potential.

And then, change-of-variables' galore! In the end the set of equations comes across as looking pretty much like this:

$$\begin{aligned}
2\tilde{\gamma}^2 x_{,\alpha} &= (1 + 2\tilde{\gamma})(1 - \tilde{\gamma}) [\sqrt{\star}\lambda_h x^2 - \epsilon x] + \Upsilon, \\
y_{,\alpha} &= \sqrt{\star}\lambda_V xy + \epsilon y, \\
u_{,\alpha} &= (2\Sigma - 1)u + \tilde{\gamma}v, \\
v_{,\alpha} &= (\epsilon - 2\Sigma - 2)v - \tilde{\gamma}\mathcal{M}^2 u, \\
\Sigma_{,\alpha} &= (\epsilon - 3)\Sigma + 2\tilde{\gamma}v^2 - 2\tilde{\gamma}\mathcal{M}^2 u^2, \\
\mathcal{M}_{,\alpha} &= \sqrt{\star}\lambda_M \mathcal{M}x + \epsilon \mathcal{M}, \\
1 &= x^2 + y^2 + \mathcal{M}^2 u^2 / \tilde{\gamma} + v^2 / \tilde{\gamma} + \Sigma^2, \\
2\epsilon &= 3(\Sigma^2 + 1) + 3\tilde{\gamma}x^2 - 3y^2 - \tilde{\gamma}\mathcal{M}^2 u^2 + \tilde{\gamma}v^2.
\end{aligned}$$

If you want to know what stands for what, you should probably check⁴ out!

Fixing points

So far so good. We have equations. Now we need solutions. So we set out to find them. We identified all the fixed points of the system and studied their stability by applying Lyapunov's analysis. And off you go scratching your head in bewildered perplexity^d once again: who is this Lyapunov dude? Well, let us just have a look at what he did.

First, linearise the system. Then, call \vec{x}_f one of its fixed points. And then.

- ★ \vec{x}_f is Lyapunov stable if, $\forall \vec{x}(0), \exists \epsilon > 0 : |\vec{x}(t)| < \epsilon, \forall t > 0$. This is realised iff:
 - i. every eigenvalue Λ_i of the linear system has $\Re(\Lambda_i) \leq 0$, and
 - ii. every eigenvalue for which $\Re(\Lambda_i) = 0$ is semisimple.
- ★ \vec{x}_f is semistable if $\forall \vec{x}(0), \exists \lim_{t \rightarrow \infty} \vec{x}(t) < \infty$. This happens iff:
 - i. \vec{x}_f is Lyapunov stable, and
 - ii. $\Im(\Lambda_i) = 0, \forall i$.
- ★ \vec{x}_f is asymptotically stable if $\forall \vec{x}(0), \lim_{t \rightarrow \infty} \vec{x}(t) = \vec{x}_f$. This is true iff:
 - i. $\Re(\Lambda_i) < 0, \forall i$.
- ★ \vec{x}_f is unstable if... you can guess this one!

...alright, \vec{x}_f is unstable if it is not Lyapunov stable. Told you it wasn't hard to guess.

Why do I report all of this here? Because there is much more to stability than asymptotic stability!

Done fixing

So, what are those fixed points? Here comes the list.

Suicidal brane case:

- i. de Sitter expansion with $y = \pm 1$ for any \mathcal{M} driven by the scalar potential;
- ii. kinetic domination with $x = \pm 1$;

^dI could not resist reporting some synonyms to "perplexity": "bafflement", "bamboozlement", "befuddlement", "bewilderment", "discombobulation", "flummoxment"... OK, this last one I made up.

iii. anisotropic solutions with $\Sigma = \pm 1$.

Prudent brane case:

- i. isotropic kinetic solution with $x = \pm 1$;
- ii. isotropic scalar domination solution with $x = -\lambda_V/3$ and any \mathcal{M} ;
- iii. anisotropic solution with zero mass and any Σ ;
- iv. anisotropic stiff solution with non-zero \mathcal{M} and Σ ;
- v. anisotropic vector solution A with $u = \text{any}$ and $\Sigma = 1/2$;
- vi. anisotropic vector solution B where $0 \neq u \neq 0 \neq v \neq 0 \neq \Sigma \neq 0$.

La fin

Out of all the fixed points we found some were stable and some were not, see⁴ for all the details. The bottom line(s) is (are):

1. most of the solutions are not cosmologically viable—no acceleration or the anisotropy is large (make a sad face here);
2. vector fields can be compatible with isotropic expansion—in fact, we found an example of rapidly oscillating non-zero vector vevs, but with zero shear;
3. asymptotic stability is not everything—this is to say, semi-stable points for which a limit does not exist but are still bounded (like a sine or cosine) are perfectly fine and should be looked for when studying stability;
4. our parametrisation for these systems is awesome. Yes, it really is, so if you want to play with disformal vectors you better borrow it. And give us credit: we take citations or craft beers.

Acknowledgements

I wish to thank Tomi Koivisto for general metal awesomeness and for throwing Lagrangians at me whenever he sees a vector field in them. I acknowledge support from the IISN project No. 4.4502.13 and the Belgian Science Policy grant IAP VII/37. And finally, once again, thanks to the organisers and all participants for a most enjoyable workshop!

References

1. Jacob D. Bekenstein. The Relation between physical and gravitational geometry. *Phys.Rev.*, D48:3641–3647, 1993.
2. Tomi Sebastian Koivisto and Danielle Elizabeth Wills. Matters on a moving brane. *Int.J.Mod.Phys.*, D22:1342024, 2013.
3. Tomi Koivisto, Danielle Wills, and Ivonne Zavala. Dark D-brane Cosmology. 2013.
4. Tomi S. Koivisto and Federico R. Urban. Disformal vectors and anisotropies on a warped brane. *JCAP*, 1503(03):003, 2015.
5. Tomi S. Koivisto and Federico R. Urban. Doubly-boosted vector cosmologies from disformal metrics. 2015.

CONSTRAINTS ON STERILE NEUTRINO DARK MATTER CANDIDATE MASS BY THE FERMI GAMMA-RAY BURST MONITOR

ROBERT PREECE

Space Science Department, The University of Alabama in Huntsville, 320 Sparkman Dr., Huntsville AL 35809 USA

KENNY C. Y. NG

Center for Cosmology and AstroParticle Physics (CCAPP), Ohio State University, Columbus, OH 43210 USA

SHUNSAKU HORIUCHI

Center for Neutrino Physics, Department of Physics, Virginia Tech, Blacksburg, VA 24061 USA

JENNIFER GASKINS

GRAPPA, University of Amsterdam, 1098 XH Amsterdam, Netherlands

MILES SMITH

Pennsylvania State University, PA 16802 USA

The Fermi Gamma-Ray Burst Monitor (GBM) is an all-sky gamma-ray detector operating in low-earth orbit since 2008. The 12 individual NaI scintillation detectors have a roughly cosine angular response, which limits the ability to detect point sources to an accuracy of several degrees radius. Still, a diffuse source at the Galactic Center should be detectable. Assuming a sterile neutrino Dark Matter candidate that decays to an active neutrino and a photon, we present search results for a line signal from the Galactic Center in the hard X-ray regime.

1 Motivation

The Gamma-ray Burst Monitor (GBM), on board the *Fermi* Gamma-ray Space Telescope mission, views the entire unoccluded sky in the energies between 8 keV and 40 MeV. The lower energies (below 1 MeV) are observed by 12 Sodium Iodide (NaI) detectors that have modest localization capabilities. The primary science objectives of GBM are the detection and analysis of gamma-ray bursts. However, the instrument's versatility allows the study of other transient sources, such as solar flares, soft gamma-ray repeaters and terrestrial gamma flashes, as well as the continuous monitoring of soft gamma-ray sources in the Galaxy and pulsar timing analyses. We present here an effort to use GBM observations of the Galactic Center as an indirect search for sterile neutrinos as a dark matter candidate.

Massive sterile neutrinos can radiatively decay to active neutrinos, producing a photon line signal at half the sterile neutrino mass^{1,2,3}. Meanwhile, sterile neutrinos produced by neutrino oscillations in the early universe can satisfy the abundance constraints for being a dark matter (DM) candidate, if they have a mass on the order of 1–100 keV range^{4,5,6}. X-ray telescopes have already been searching for spectral lines from keV neutrinos^{7,8,9} and (model-dependent) constraints have been obtained from Lyman alpha measurements (probing clustering in the early universe)¹⁰. However, a window of parameter space remains between 12 and 40 keV, while with

a low-energy cutoff of 8 keV, GBM can put constraints on line emission at half the mass above 16 keV.

2 The Fermi Gamma-Ray Burst Monitor

The GBM was designed to support the Large Area Telescope (LAT) on *Fermi*, which nominally observes in a sky survey mode, resulting in the spacecraft pointing typically within 50° of zenith. GBM NaI detectors 0 and 6 point within $\sim 20^\circ$ of the LAT pointing direction, however, the spacecraft blocks part of their field of view¹¹. For this analysis, we use detector 7, which has good sky coverage (also close to the LAT pointing direction) but has minimal problems with spacecraft blockage. NaI 7 is also not on the Sun-facing side of the spacecraft, so it suffers relatively little soft X-ray contamination from the Sun.

The NaI detectors do not record the arrival direction of each photon; rather, the effective area defines the relevant field of view (FOV). The flat geometry of the NaI crystals, plus attenuation by the housing materials, result in an angular response very similar to the cosine of the detector zenith angle. At low energies, the effective area is close to 0 at incidence angles $\geq 90^\circ$, but note that the response is non-negligible over half the sky. As a function of energy, the effective area increases rapidly from the threshold of 8 keV up to ~ 30 keV. Thus, assuming a line signal from a distribution of DM concentrated at the Galactic Center, it doesn't matter how the DM is distributed, most of it will be contained within 60° , corresponding to the GBM FOV.

2.1 Arrival direction analysis tools for GBM

Since it is not possible to correctly calculate a flux within a limited region-of-interest (ROI), due to lack of individual photon tracking and extremely broad "FOV" of the GBM detectors, we created a suite of tools for directional analysis of GBM data. This includes a tool to calculate the count rate in a specified NaI detector as a function of Galactic pointing direction, based on the actual pointing and livetime history of *Fermi*, which uses public data files (GBM CSPEC files and LAT FT2 files). This is discussed in section 2.2 below. We have also developed a tool to simulate NaI counts data from an input source model, which accounts for the NaI effective area as a function of inclination angle and photon energy. Using this tool, the count rate in a specified NaI detector as a function of Galactic pointing direction can be predicted for a theoretical model.

2.2 The X-ray sky as seen by GBM

Figure 1 is an example of GBM count rate maps as a function of the detector pointing direction of NaI detector 7 in Galactic coordinates for three different energies: 10-11 keV, 16-17 keV and 40-42 keV. Note that this is *not* a flux map, which would require knowledge of the arrival direction of each count. The map is constructed by first dividing the sky into 768 equal-area pixels (using HEALPix^d) and then using the LAT FT2 files to determine the detector zenith pointings that correspond with each pixel. The GBM data set is filtered, excluding data time intervals containing GRBs and other transients, passages through the South Atlantic Anomaly (where the instrument is turned off) and high magnetic latitude regions (to avoid elevated charged particle rates). We also eliminate times when the Earth may be in the field of view. The remaining count rates are then averaged for each sky pixel. The result is a map of the count rates seen by the detector, averaged over the effective area angular response.

Soft X-ray sources centered on the Galactic Center (GC) are clearly detected by this technique, as seen in the top left panel in Figure 1. As expected, no features are significant, due

^d<http://healpix.jpl.nasa.gov>¹²

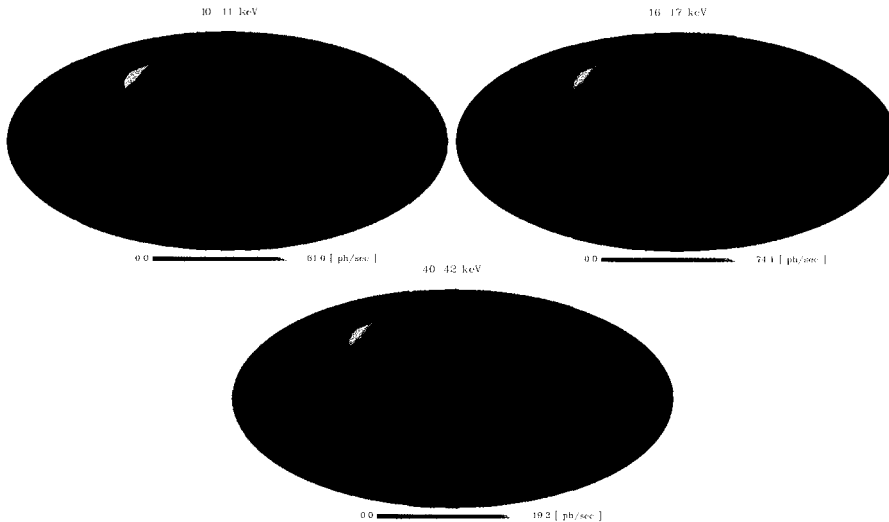


Figure 1 – The final counts rate sample from 4 years of data from NaI detector 7, which corresponds to 4.6 million seconds (~ 53 days) of live time after data cuts. The pixel position corresponds to the pointing direction of the detector normal. The grey pixels are where no observing time is registered after the selection cuts.

to the blurring by the angular response. At higher energies, instrumental backgrounds dominate over astrophysical signals, so the enhancement of count rates at the GC fades into the background.

The counts spectrum (not shown) for the final data sample for both GC ROI ($\psi < 60^\circ$) and anti-GC ROI ($\psi > 120^\circ$) chosen to have the same solid angle, has as its dominant component a power-law plus various background lines. There is an additional excess at low energies towards the GC region that suggests the rise of the astrophysical component.

3 Sterile Neutrino Line Strength Analyses

Two analyses are presented in Figure 2. For the first, we require that the flux from a dark matter signal doesn't exceed the total measured count rate in the energy bin of the line, in the selected ROI. This 'total flux' constraint is quite robust and conservative. For the second analysis, we choose a window around each line energy (larger than expected line signal width) and model the spectrum as a line signal (at fixed energy) plus a power law. The fitted line intensity is the smallest signal to yield a worse fit than the background only hypothesis at the 95% level and thus provides a constraint on the mixing angle between active and sterile neutrinos.

In the mass range shown in Figure 2, the best previous constraints are set by observations of the cosmic X-ray background (CXB) by HEAO-1¹³, the Milky Way (MW) halo from INTEGRAL¹⁴, as well as a model-dependent lower bound based upon DM abundance¹⁵. We show the new limits derived in this work, one derived only from the total flux, and the other derived using spectral line fitting. The spectral analysis is stronger than that from prior studies by about an order of magnitude.

Acknowledgments

We thank Mark Finger (Universities Space Research Association, Huntsville) for providing transient cuts for the GBM data. This work is supported by NASA grant NNX11AO46G. K.C.Y.N.

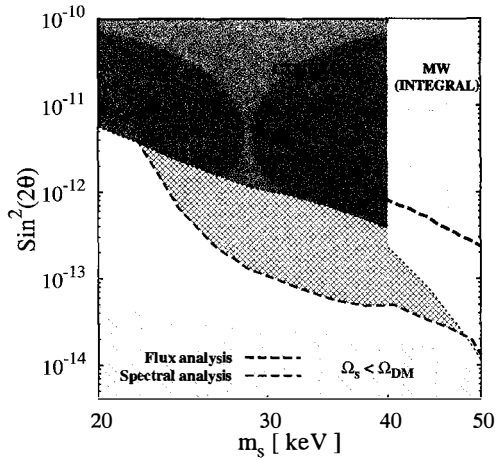


Figure 2 – Constraints from X-ray missions on sterile neutrino dark matter decays, which depends on the mixing angle, $\sin^2(2\theta)$, and the mass, m_s .

was supported by NSF Grants PHY-1101216 and PHY-1404311. J.G. acknowledges support from NASA through Einstein Postdoctoral Fellowship grant PF1-120089 awarded by the Chandra X-ray Center, which is operated by the Smithsonian Astrophysical Observatory for NASA under contract NAS8-03060.

References

1. P. B. Pal and L. Wolfenstein, *Phys. Rev. D* **25**, 766 (1982).
2. V. D. Barger, R. Phillips, and S. Sarkar, *Phys. Lett. B* **352**, 365 (1995), hep-ph/9503295.
3. K. Abazajian, G. M. Fuller, and W. H. Tucker, *Astrophys. J.* **562**, 593 (2001), astro-ph/0106002.
4. S. Dodelson and L. M. Widrow, *Phys. Rev. Lett.* **72**, 17 (1994), hep-ph/9303287.
5. X.-D. Shi and G. M. Fuller, *Phys. Rev. Lett.* **82**, 2832 (1999), astro-ph/9810076.
6. K. Abazajian, G. M. Fuller, and M. Patel, *Phys. Rev. D* **64**, 023501 (2001), astro-ph/0101524.
7. H. Yuksel, J. F. Beacom, and C. R. Watson, *Phys. Rev. Lett.* **101**, 121301 (2008), 0706.4084.
8. A. Boyarsky, O. Ruchayskiy, and M. Markevitch, *Astrophys. J.* **673**, 752 (2008), astro-ph/0611168.
9. M. Loewenstein, A. Kusenko, and P. L. Biermann, *Astrophys. J.* **700**, 426 (2009), 0812.2710.
10. Seljak, U., Slosar, A., & McDonald, P., *J. Cosmol. Astropart. P.* **10**, 014 (2006)
11. C. Meegan *et al.*, *Astrophys. J.* **702**, 791 (2009), 0908.0450.
12. K. Gorski *et al.*, *Astrophys. J.* **622**, 759 (2005), astro-ph/0409513.
13. A. Boyarsky, A. Neronov, O. Ruchayskiy, M. Shaposhnikov, and I. Tkachev, *Phys. Rev. Lett.* **97**, 261302 (2006), astro-ph/0603660.
14. A. Boyarsky, D. Malyshev, A. Neronov, and O. Ruchayskiy, *MNRAS* **387**, 1345 (2008), 0710.4922.
15. A. Boyarsky, O. Ruchayskiy, and M. Shaposhnikov, *Ann. Rev. Nucl. Part. Sci.* **59**, 191 (2009), 0901.0011.

Dark Matter: Connecting LHC searches to direct detection

ANDREAS CRIVELLIN

CERN Theory Division, CH-1211 Geneva 23, Switzerland



In these proceedings we review the interplay between LHC searches for dark matter and direct detection experiments. For this purpose we consider two prime examples: the effective field theory (EFT) approach and the minimal supersymmetric standard model (MSSM). In the EFT scenario we show that for operators which do not enter directly direct detection at tree-level, but only via loop effects, LHC searches give complementary constraints. In the MSSM stop and Higgs exchange contribute to the direct detection amplitude. Therefore, LHC searches for supersymmetric particles and heavy Higgses place constraints on the same parameter space as direct detection.

1 Introduction

Establishing the microscopic nature of Dark Matter (DM) is one of the central, open questions in cosmology and particle physics. In the context of cold nonbaryonic DM, the prevailing paradigm is based on weakly interacting massive particles (WIMPs), and extensive theoretical and experimental resources have been devoted towards identifying viable candidates and developing methods to detect them.

One of the most studied WIMPs scenarios arises in the Minimal Supersymmetric Standard Model (MSSM), where an assumed R -parity ensures that the lightest superpartner (LSP) is a stable neutralino χ composed of bino, wino, and Higgsino eigenstates. The interactions between DM and the SM particles are mainly mediated by squark and Higgses in the case of bino like DM.

However, it is also possible to study DM interactions with the SM particles in a model independent way by using an effective field theory approach in which the particles mediating the interactions are assumed to be heavy and are integrated out. A main strength of this approach is to provide model-independent relations among distinct null DM searches¹. As different search strategies probe different energy scales, this separation of scales can have striking consequences when a connection between direct detection experiments and LHC searches is done.

2 Effective Field Theory

For operators contributing directly to spin independent scattering, direct detection gives in general much better constraints than LHC searches. As was shown in Ref. ^{2,3,4} there are cases in which

operators which do not contribute to spin independent scattering at tree-level, but enter at the one-loop level. As in this case direct detection is loop suppressed, LHC searches can give competitive and complementary constraints.

At dim-6 the operator $O_{qq}^{VA} = \bar{\chi}\gamma^\mu\chi \bar{q}\gamma_\mu\gamma^5q$ mixes into $O_{HHD}^S = \bar{\chi}\Gamma^\mu\chi [H^\dagger\overleftrightarrow{D}^\mu H]$ (H being the SM Higgs doublet and \overleftrightarrow{D} the covariant derivative) which then generates threshold corrections to $\bar{\chi}\gamma^\mu\chi \bar{q}\gamma_\mu q$ entering spin independent direct detection³. The resulting bounds are shown in the left plot of Fig. 1 depicting that even though the contribution is loop suppressed, direct detection gives stronger bound unless DM is very light.

At dimension dim-7 a similar effect occurs for the operators $O_W = \bar{\chi}\chi W_{\mu\nu}W^{\mu\nu}$ involving electroweak field strength tensors. Again, this operator enters direct detection only via mixing and threshold correction⁴. The resulting bounds are shown in the right plot of Fig. 1. In this case the collider bounds are in general stronger⁵, unless dark matter is quite heavy.

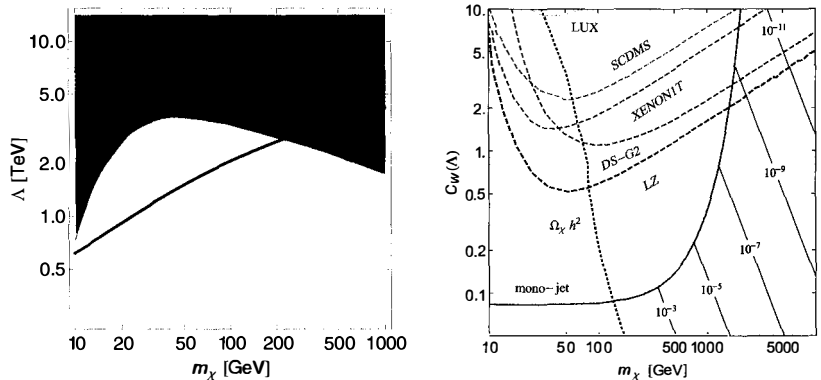


Figure 1 – Left: Allowed regions from LHC searches (yellow) and SI WIMP–nucleon scattering from LUX (green). Projected allowed regions for SCDMS (red) and XENON1T (blue) are also shown, as well as the curve giving the correct thermal relic density (black). Here we set $C_{qq}^{VA} = 1$ while all other Wilson coefficients are assumed to be zero. Right: Restrictions in the m_χ – $C_W(\Lambda)$ plane, assuming DM to be Majorana and setting $\Lambda = 300$ GeV. The green curves illustrate the best limits from missing E_T searches at the LHC, while the black dotted lines correspond to the observed value $\Omega_\chi h^2 = 0.11$ of the relic density. The colored dashed curves mark the bounds from existing and future direct detections experiments. The contour lines denote the fraction of the observed relic density obtained from the operator under consideration.

3 MSSM

Following Ref.⁶, we use naturalness as a guiding principle in order to study neutralino dark matter scattering in the MSSM (see also Ref.⁷ for a recent analysis). In the left plot of Fig. 2 we show four simplified spectra which are increasingly natural (A to D). Interestingly, in all scenarios blind spots^{8,9,10,11} with vanishing scattering cross section can occur. In the proximity of these blind spots isospin violation is enhanced, making a precise determination of the scalar couplings to nucleons crucial^{12,a}.

In the case in which DM interactions are transmitted by the SM Higgs only, a blind spot occurs at $M_1 + \mu s_{2\beta} = 0$ as shown in the right plot of Fig. 2. If we consider in addition the heavy CP-even Higgs H^0 (whose mass is nearly degenerate with the CP-odd Higgs A^0) the situation is more interesting, as we do not only have additional contributions to DM scattering but also get effects in $b \rightarrow s\gamma$ ¹⁴ and obtain bounds from LHC searches for $A^0 \rightarrow \tau^+\tau^-$ ¹⁵ whose interplay is shown in the left plot in Fig. 3. The occurrence of a blind spot where the h^0 and the H^0 contributions

^aThe same scalar couplings to the nucleon are also important for $\mu \rightarrow e$ conversion in nuclei¹³.

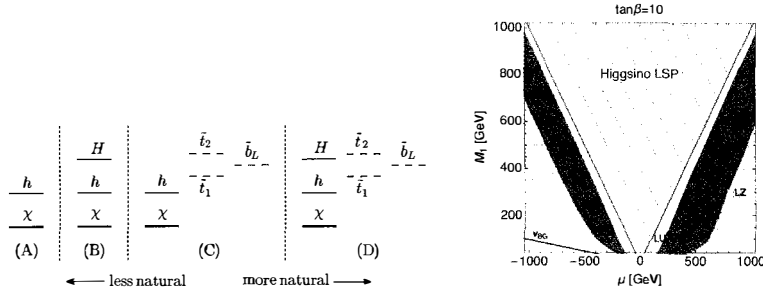


Figure 2 – Left: Spectra of the simplified models for SI χ -nucleus scattering considered in this work. For each model, the SM-like Higgs is denoted by h , while all other states are assumed to lie below 1 TeV, including Higgsinos (not shown). From left-to-right, the spectra become increasingly more natural as one includes the additional CP-even Higgs H and third-generation squarks $\tilde{t}_1, \tilde{t}_2, \tilde{b}_L$. Right: Current and projected limits on SI χ -xenon scattering due to h exchange with $\tan\beta = 10$. The pink band shows the existing constraints from LUX, while projected limits from XENON1T and LZ are given by the blue and orange regions respectively. The blind spot is denoted by the red line and lies within the irreducible neutrino background (ν_{BG}) shown in gray. The triangular, hatched region corresponds to the case where the LSP is Higgsino-like.

cancel is possible. Interestingly, future LHC searches for $A^0 \rightarrow \tau^+\tau^-$ will be able to cover this region in parameter space which cannot be tested with direct detection.

The situation if in addition squarks of the third generation are included (the presence of a left-handed stop requires a left-handed sbottom as well due to $SU(2)_L$ gauge invariance) as dynamical degrees of freedom (scenario D) is shown in the right plot in Fig. 3. Here the complementarity of LHC searches for stops and sbottoms with DM direct detection is illustrated as well as the effect in $B_s \rightarrow \mu^+\mu^-$ which we calculated with SUSY_FLAVOR¹⁶. Again, part of the region in the proximity of the blind spot which cannot be covered by direct detection is already ruled out by LHC searches whose sensitivity to high masses will significantly increase at the 14 TeV run.

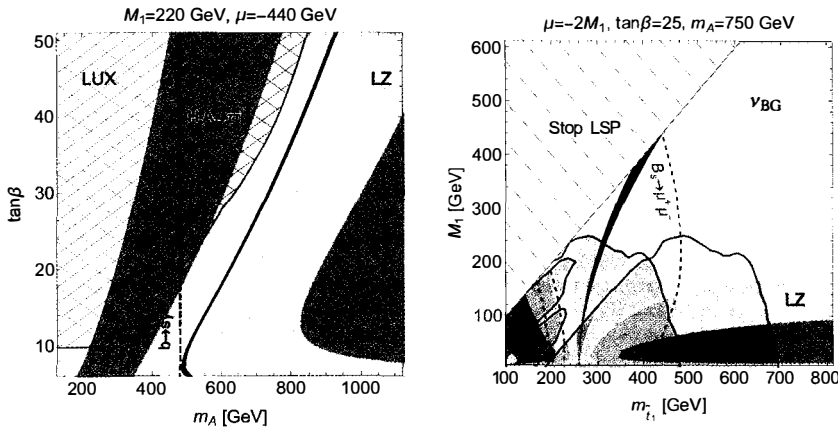


Figure 3 – Left: Current and projected limits on SI χ -xenon scattering due to h, H exchange with different benchmark values for M_1 and μ . The cross-hatched region in dark-blue corresponding to CMS limits on $H, A \rightarrow \tau^+\tau^-$. The region to the left of the dark-red dashed line at $m_A \cong m_{H^+} \simeq 480$ GeV is excluded by $b \rightarrow s\gamma$. Right: Current and projected limits in the $(m_{\tilde{t}_1}, M_1)$ plane from h, H and $\tilde{t}_{1,2}, \tilde{b}_L$ exchange in χ -xenon scattering. In the figures, the value of m_A is increased for fixed $\tan\beta$.

4 Conclusions

In these proceedings we reviewed the interplay between DM direct detection, flavor, and LHC searches by highlighting two prime examples: First we considered the EFT approach. Here LHC searches give complementary constraints on operators which enter spin independent scattering only at the loop level. Second, we considered the MSSM where LHC searches for stops, sbottoms, and heavy Higgses place constraints on the parameter space which are complementary to flavor observables and direct detection. We identify regions in parameter space with blind spots which cannot be covered by direct detection, but can be covered by LHC searches.

Acknowledgments

We thank the organizers of the invitation to *Moriond Gravitation 2015* and for the opportunity to present these results. A.C. is supported by a Marie Curie Intra-European Fellowship of the European Community's 7th Framework Programme under contract number (PIEF-GA-2012-326948).

References

1. Jessica Goodman, Masahiro Ibe, Arvind Rajaraman, William Shepherd, Tim M.P. Tait, et al. Constraints on Light Majorana dark Matter from Colliders. *Phys.Lett.*, B695:185–188, 2011.
2. Mads T. Frandsen, Ulrich Haisch, Felix Kahlhoefer, Philipp Mertsch, and Kai Schmidt-Hoberg. Loop-induced dark matter direct detection signals from gamma-ray lines. *JCAP*, 1210:033, 2012.
3. Andreas Crivellin, Francesco D'Eramo, and Massimiliano Procura. New Constraints on Dark Matter Effective Theories from Standard Model Loops. *Phys.Rev.Lett.*, 112:191304, 2014.
4. Andreas Crivellin and Ulrich Haisch. Dark matter direct detection constraints from gauge bosons loops. *Phys.Rev.*, D90(11):115011, 2014.
5. Andreas Crivellin, Ulrich Haisch, and Anthony Hibbs. LHC constraints on gauge boson couplings to dark matter. *Phys.Rev.*, D91(7):074028, 2015.
6. Andreas Crivellin, Martin Hoferichter, Massimiliano Procura, and Lewis C. Tunstall. Light stops, blind spots, and isospin violation in the MSSM. 2015.
7. Daniele Barducci, Alexander Belyaev, Aoife K. M. Bharucha, Werner Porod, and Veronica Sanz. Uncovering Natural Supersymmetry via the interplay between the LHC and Direct Dark Matter Detection. 2015.
8. Junji Hisano, Koji Ishiwata, and Natsumi Nagata. Direct Search of Dark Matter in High-Scale Supersymmetry. *Phys.Rev.*, D87(3):035020, 2013.
9. Clifford Cheung, Lawrence J. Hall, David Pinner, and Joshua T. Ruderman. Prospects and Blind Spots for Neutralino Dark Matter. *JHEP*, 1305:100, 2013.
10. Peisi Huang and Carlos E. M. Wagner. Blind Spots for neutralino Dark Matter in the MSSM with an intermediate m_A . *Phys.Rev.*, D90(1):015018, 2014.
11. Archana Anandakrishnan, Bibhushan Shakya, and Kuver Sinha. Dark matter at the pseudoscalar Higgs resonance in the phenomenological MSSM and SUSY GUTs. *Phys.Rev.*, D91(3):035029, 2015.
12. Andreas Crivellin, Martin Hoferichter, and Massimiliano Procura. Accurate evaluation of hadronic uncertainties in spin-independent WIMP-nucleon scattering: Disentangling two- and three-flavor effects. *Phys.Rev.*, D89(5):054021, 2014.
13. Andreas Crivellin, Martin Hoferichter, and Massimiliano Procura. Improved predictions for $\mu \rightarrow e$ conversion in nuclei and Higgs-induced lepton flavor violation. *Phys.Rev.*, D89(9):093024, 2014.
14. M. Misiak, H.M. Asatrian, R. Boughezal, M. Czakon, T. Ewerth, et al. Updated NNLO QCD predictions for the weak radiative B-meson decays. 2015.
15. CMS Collaboration. Higgs to tau tau (MSSM). 2013.
16. A. Crivellin, J. Rosiek, P.H. Chankowski, A. Dedes, S. Jaeger, et al. SUSY FLAVOR v2: A Computational tool for FCNC and CP-violating processes in the MSSM. *Comput.Phys.Commun.*, 184:1004–1032, 2013.

4. Gravitational wave detectors

The Status of the Advanced LIGO Gravitational-Wave Detectors

Alexa Staley

On behalf of the LIGO Scientific Collaboration

Department of Physics, Columbia University, New York, NY 10027, USA



The Advanced LIGO gravitational-wave detectors have reached an exciting milestone. Both interferometers have been locked and are being tuned for optimal sensitivity. This proceeding highlights the current status of the two detectors. A brief overview of the design sensitivity goals and configuration of the interferometer is given. Finally, a short explanation of the lock acquisition process for Advanced LIGO is provided.

1 The Advanced LIGO Detectors

The Advanced LIGO detectors consist of two 4km arm ground-based interferometers.¹ The Hanford Observatory is located in Hanford, WA and the Livingston Observatory is located in Livingston, LA. These two detectors are part of a much larger ground-based detector network, including GEO600², Advanced VIRGO³, and KAGRA⁴. This large detector network is important for coincidence testing and source sky localization, for example. The addition of LIGO India will also further improve localizability. Of all these detectors, the Advanced LIGO detectors are the first to come online, and will have the first observation runs.

The simple idea behind the Advanced LIGO detectors is as follows: The main infrared laser beam is split by a beam splitter and travels down two orthogonal arms in vacuum. The light is reflected by end test masses that act as free masses. Nominally, the light at the output port of the interferometer is null. However, in the presence of a gravitational wave, one arm gets shorter, while the other gets longer, changing the light travel time between each arm and the amount of light at the output photodetector. The interferometer acts as a transducer, turning gravitational waves into photocurrent proportional to the strain amplitude, $h = \Delta L/L$. In reality, to reach the designed sensitivity, the detectors are much more complex than this simple Michelson interferometer.

The aim of the detectors' design is to measure gravitational waves with a strain as small as $4 \times 10^{-24}/\sqrt{Hz}$. The advanced detectors have their best sensitivity in the 100 Hz region. The corresponding requirement for length resolution is then $\sim 10^{-19}$ m rms within a 100 Hz bandwidth⁵ This high sensitivity requires multiple optical cavities to enhance the response of the Michelson interferometer. First, Fabry-Perot cavities are added to each Michelson arm to

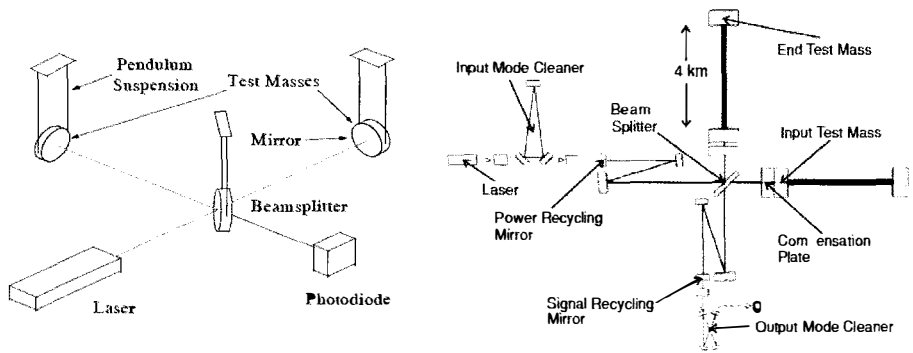


Figure 1 – (Left) A simple Michelson interferometer, showing the proof of concept of Advanced LIGO⁵ (Right) The Advanced LIGO optical layout.⁶

effectively increase the arm length by two orders of magnitude, and increase the interaction time of the main laser light with the gravitational wave signal. Secondly, partially transparent mirrors are added to the symmetric and the anti-symmetric ports of the Michelson interferometer to recycle the laser power and extract the gravitational wave signal, respectively.^{7, 8} And finally, the input and output mode cleaners are added to clean unwanted spatial modes of the beams at the input and output ports of the interferometer, respectively.^{9, 10} The full optical layout of Advanced LIGO is depicted in Figure 1.

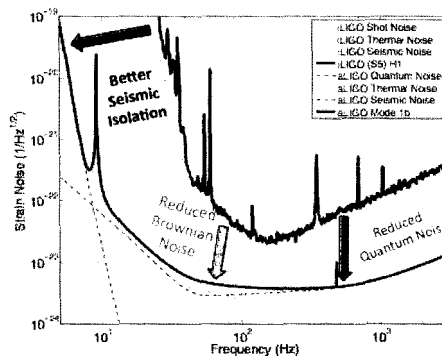


Figure 2 – A comparison of Initial LIGO's 5th science run and Advanced LIGO's design sensitivity curves.

1.1 Advanced LIGO vs. Initial LIGO

Advanced LIGO's design sensitivity goal is at least a factor of 10 greater than the sensitivity reached by Initial LIGO¹¹ throughout the entire gravitational wave frequency band. This implies observing a factor of 1,000 times more volume. Figure 2 compares the final design sensitivity for Advanced LIGO with Initial LIGO's sensitivity curve. Besides the overall sensitivity gain, Advanced LIGO also had a much larger detection bandwidth. To achieve such an improvement, three main contributing noises had to be mitigated. At low frequency, the seismic noise was reduced with the introduction of a seven stage pendulum with passive and active isolation systems. The test mass motion requirement is $< 10^{-19}$ m/rtHz at 10 Hz. Nominally, the ground

motion at 10 Hz is $\sim 10^{-9}$ m/rtHz. Therefore, Advanced LIGO's isolation system must provide 10 orders of magnitude of isolation from ground motion.^{12, 13} At intermediate frequencies, the brownian noise was reduced by using fused silica to suspend the last two stages of the mirrors. For further improvement, the last two stages are also monolithic.¹⁴ Finally, at high frequency, the quantum noise was reduced by increasing the input power to 180 W, and adding the signal extraction cavity.

2 Detection Rates

A common figure of merit used to describe the sensitivity of the detectors is known as the binary inspiral range. This range is the distance to which the gravitational wave signal emitted by a binary neutron star (BNS) coalescence is detectable. The BNS range is defined as the volume- and orientation-averaged distance at which the coalescence of a pair of 1.4-solar mass neutron stars gives a matched filter signal-to-noise ratio of 8 in a single detector¹. Based on the improved sensitivity range, the detection rates for Advanced LIGO are more promising than for Initial LIGO. Figure 3 shows the expected detection rates for Advanced LIGO. The BNS range for Advanced LIGO will be around 60 Mpc for the first observation run and ultimately reach 200 Mpc. Notably, the first observation run will already exceed Initial LIGO's BNS range of ~ 25 Mpc.

| Epoch | Estimated Run Duration | $E_{\text{GW}} = 10^{-2} M_{\odot} c^2$ Burst Range (Mpc) | | BNS Range (Mpc) | | Number of BNS Detections | % BNS Localized within | |
|---------------|------------------------|--|---------|-----------------|----------|--------------------------|------------------------|---------------------|
| | | LIGO | Virgo | LIGO | Virgo | | 5 deg ² | 20 deg ² |
| 2015 | 3 months | 40 - 60 | — | 40 - 80 | — | 0.0004 - 3 | — | — |
| 2016 - 17 | 6 months | 60 - 75 | 20 - 40 | 80 - 120 | 20 - 60 | 0.006 - 20 | 2 | 5 - 12 |
| 2017 - 18 | 9 months | 75 - 90 | 40 - 50 | 120 - 170 | 60 - 85 | 0.04 - 100 | 1 - 2 | 10 - 12 |
| 2019+ | (per year) | 105 | 40 - 80 | 200 | 65 - 130 | 0.2 - 200 | 3 - 8 | 8 - 28 |
| 2022+ (India) | (per year) | 105 | 80 | 200 | 130 | 0.4 - 400 | 17 | 48 |

Figure 3 – This is a table showing the expected detection rates from 2015 to 2022. The estimated run duration listed here are coincidence data taking times for two detectors of equal sensitivity. A binary neutron star detection becomes more promising starting in 2016 as the detector sensitivity is improved. Notably, these expected detections have a large uncertainty stemming from the uncertainty in the number of events present.¹⁵

3 Locking Advanced LIGO

As mentioned in Section 1, the interferometer consists of many optical cavities besides the Michelson interferometer. Since these optical cavities all share the same mirrors, the cavities are highly coupled. This inherently makes locking the detector a nontrivial task.

The interferometer is locked when the main infrared beam is resonating in all the cavities and the five length degrees of freedom are controlled (i. e. the cavity length changes are less than the control bandwidth). The five length degrees of freedom for Advanced LIGO are listed in Figure 4. When the common and differential arms length are locked to the main infrared beam, it is likely that the error signals used to control the Michelson and dual-recycled length are contaminated. This introduces a problem for lock acquisition.

Lock acquisition is further complicated by the fact that Advanced LIGO has a narrow locking range for the arm cavities. As the mirrors swing freely, the main infrared beam will occasionally pass through resonance in the arms. However, they do not resonate for very long, making it difficult to apply a feedback control and maintain resonance. The linear regime of the standard Pound-Drever-Hall locking signal is too small.¹⁷ This is made worse by the fact that Advanced LIGO has intentionally weak actuators on the end test masses, for noise reduction purposes.

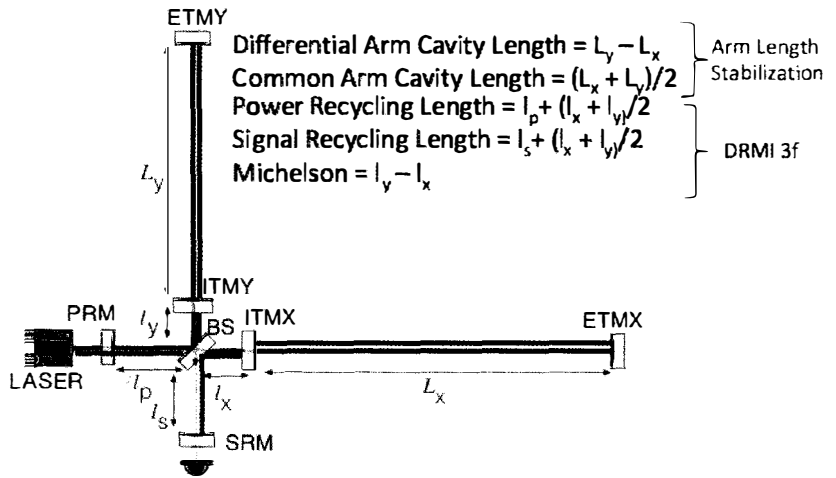


Figure 4 – Cartoon demonstrating the five length degrees of freedom of the interferometer that must be controlled. The Arm Length Stabilization and 3f technique were introduced to decouple the length degrees of freedom and facilitate locking the interferometer.

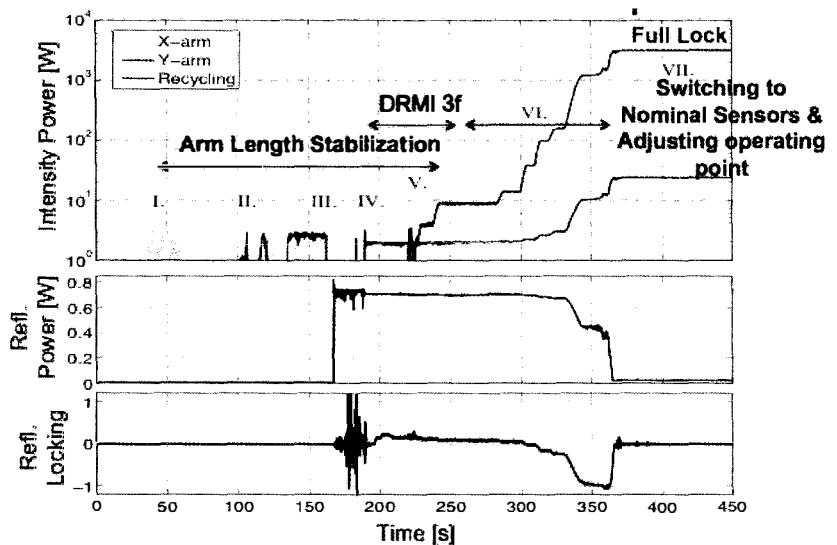


Figure 5 – An example of the Advanced LIGO locking sequence. During this lock the input power was 0.75 W.¹⁶

Extensive commissioning work was required to overcome these challenges. Two techniques are introduced in the lock acquisition process that ultimately make locking faster and more deterministic. These techniques facilitate lock acquisition by decoupling the length degrees of freedom. The first technique is known as the Arm Length Stabilization technique.¹⁶ This scheme introduces two lasers of green light at each end station that are used to independently lock the arm cavities. The green light has a much larger linewidth than the main infrared beam, and

thus resolves the narrow locking range issue. In addition, locking the arm cavities with the green light decouples the arm length degrees of freedom from the rest of the interferometer. Meanwhile, the second technique is known as the 3f-technique.¹⁸ This scheme uses the beat note between the first and second order modulation sidebands of the main infrared beam to lock the Michelson and dual-recycled length degrees of freedom. These RF sidebands are anti-resonant in the arm cavities and thus are further insensitive to the arm cavities. As can be seen by the cartoon in Figure 4, these two techniques split the coupled length degrees of freedom into two more manageable groups.

Both observatories currently employ these schemes and have proven their reliability and robustness. Figure 5 shows an exemplary full lock sequence for the interferometers. In steps I-V, the arm length degrees of freedom are controlled with the Arm Length Stabilization technique. The arms are locked to the green light and stabilized. Using error signals between the green and infrared light and between the green transmitted light of each arm, the infrared light is initially brought onto resonance in the arms, and then intentionally adjusted off-resonance. At point IV, the Michelson and dual-recycled cavities are locked using the 3f-technique, without interference from the arm cavities. Since the 3f signals are insensitive to the arm cavities, and at this stage the arm length degrees of freedom are controlled, at step V the arms can be brought onto resonance without worry of contaminating any other error signal. After step V, the control signals are switched over to the nominal sensors and full lock is achieved. At full lock, the maximal amount of light is in the interferometer, with very little light in reflection.

4 Current Status of Advanced LIGO

The installation timeline for the two Advanced LIGO detectors can be seen in Figure 6. The installation began at the beginning of 2011 for both detectors, and was finished by the end of 2014. The two observatories had staggered installation schedules, with Livingston completed 6 months before Hanford. This timeline also shows the commissioning progress at the two detectors. The Livingston Observatory started from the corner station and worked outward, while the Hanford Observatory followed the opposite trajectory. This was done to ensure that all of the interferometer's components were studied as soon as possible to catch any major issues.

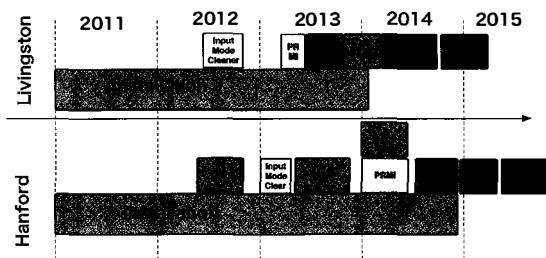


Figure 6 – Advanced LIGO installation and commissioning timeline.

The Livingston Observatory achieved first lock on May 26, 2014 and the Hanford Observatory achieved first lock on February 11, 2015. Both interferometers have been locked for several hours at a time. Figure 7 shows the BNS range of each detector since their first respective locks.

The Livingston detector has an input power of 25 W with a BNS range of ~ 60 Mpc as of April 2015. This instrument is the most sensitive ground-based interferometer to-date. It spans a volume of ~ 50 times greater than Initial LIGO. If it had a $\sim 80\%$ duty cycle and we had two detectors of this sensitivity, we could carry out the 'Initial LIGO one year observing run' in terms of event likelihood in about a week. Under this configuration, the Livingston detector

has already reached the criteria for the first observation run, scheduled for the fall of 2015. Meanwhile, the Hanford detector has a input power of 15 W with a BNS range of ~ 30 Mpc as of April 2015. This sensitivity surpasses Initial LIGO, and will be further improved for the first observation run. The quoted sensitivities have a 15% uncertainty. Figure 8 depicts each of the detectors sensitivity level relative to the sensitivity goals of the project. Both detectors are making astounding progress.

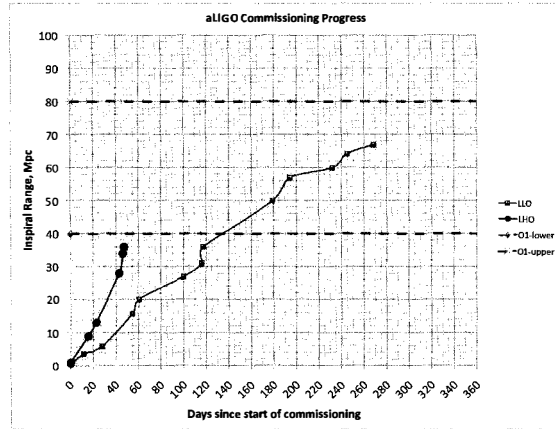


Figure 7 – This plot depicts the sensitivity of each Advanced LIGO detector in terms of the binary neutron star inspiral range as a function of commissioning time. The commissioning time is marked by the first full lock of each interferometer. Additionally, this graph shows the sensitivity range targeted for the first observation run (O1). O1 is scheduled to take place at about day 200 of the Hanford commissioning. Here, LHO is denoted to represent the LIGO Hanford Observatory and LLO represent the LIGO Livingston Observatory.

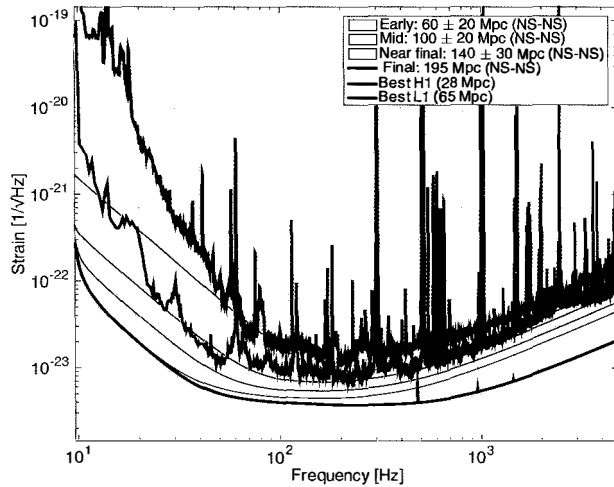


Figure 8 – This plot shows sensitivity curves for the Hanford (H1) and Livingston (L1) detectors as of April 2015.¹⁹ These sensitivity curves are compared to the design sensitivity goals of the detector over the next few years. The quoted “best” inspiral ranges have a 15% uncertainty.

5 Conclusion

The Advanced LIGO detectors have completed installation and have been fully locked. The lock acquisition scheme has proven to be deterministic and reliable at both observatories. The Livingston detector is the most sensitive detector to-date and already meets the criteria for the first observation run. The Hanford detector is close behind and will also be ready for the first observation run.

Over the coming years, the commissioning effort will continue to focus on tuning the sensitivity of each detector. Notably, as the sensitivity improves, commissioning will become more challenging. Foreseen challenges, such as Parametric Instabilities, have already appeared at the Livingston detector.²⁰ Radiation pressure is also expected to play a large role as the input power increases.²¹ Extensive research on squeezing light has been done as either an alternative or to further increase the sensitivity at high frequency.^{22, 23}

There is a lot of work to be done, but the current status of the detectors is promising. There are exciting observation runs to come!

Acknowledgments

LIGO was constructed by the California Institute of Technology and Massachusetts Institute of Technology with funding from the National Science Foundation, and operates under cooperative agreement PHY-0757058. Advanced LIGO was built under award PHY-0823459. AS would like to thank Columbia University in the City of New York for its support. This paper has been assigned LIGO Document No. LIGO-P1500060.

References

1. The LIGO Scientific Collaboration. Advanced LIGO. *Classical and Quantum Gravity*, 32(7):074001, 2015.
2. H. Grote et al. The status of GEO 600. *Classical and Quantum Gravity*, 22(10):S193–W198, April 2005.
3. J. Degallaix et al. Advanced Virgo Status. In *9th LISA Symposium*, volume 467 of *Astronomical Society of the Pacific Conference Series*, page 151, 2012.
4. K. Somiya. Detector configuration of KAGRA - the Japanese cryogenic gravitational-wave detector. *Classical and Quantum Gravity*, 29(12):124007, June 2011.
5. Matthew Pitkin and et. al. Gravitational wave detection by interferometry (ground and space). LIGO-P110004-v3, 2011.
6. G. M. Harry. Advanced LIGO: the next generation of gravitational waves detectors. *Classical and Quantum Gravity*, 27(084006):12, April 2010.
7. R. W. P. Drever. *Fabry-Perot cavity gravity wave detectors*. Cambridge University Press, July 1991.
8. B. J. Meers. Recycling in laser-interferometric gravitational-wave detectors. *Physical Review D*, 38(8):2317–2326, October 1988.
9. Peter Fritschel, Valera Frolov, and David Reitze. Commissioning the Advanced LIGO L1 input mode cleaner. LIGO-T1100201-v2, March 2012.
10. Nicolas Smith. *Techniques for Improving the Readout Sensitivity of Gravitational Wave Antennae*. PhD thesis, Massachusetts Institute of Technology, June 2012.
11. A. Abramovici et al. LIGO: the Laser Interferometer Gravitational-wave Observatory. *Science*, 256(5055):325–333, April 1992.
12. S M Aston, M A Barton, A S Bell, N Beveridge, B Bland, A J Brummitt, G Cagnoli, C A Cantley, L Carbone, A V Cumming, L Cunningham, R M Cutler, R J S Greenhalgh, G D Hammond, K Haughian, T M Hayler, A Heptonstall, J Heefner, D Hoyland, J Hough, R Jones, J S Kissel, R Kumar, N A Lockerbie, D Lodhia, I W Martin, P G Murray, J O'Dell,

- M V Plissi, S Reid, J Romie, N A Robertson, S Rowan, B Shapiro, C C Speake, K A Strain, K V Tokmakov, C Torrie, A A van Veggel, A Vecchio, and I Wilmot. Update on quadruple suspension design for advanced ligo. *Classical and Quantum Gravity*, 29(23):235004, 2012.
13. F. Matichard et al. Seismic isolation of Advanced LIGO gravitational waves detectors: Review of strategy, instrumentation, and performance. *arXiv preprint arXiv:1502.06300*, 2015.
 14. A V Cumming, A S Bell, L Barsotti, M A Barton, G Cagnoli, D Cook, L Cunningham, M Evans, G D Hammond, G M Harry, A Heptonstall, J Hough, R Jones, R Kumar, R Mittleman, N A Robertson, S Rowan, B Shapiro, K A Strain, K Tokmakov, C Torrie, and A A van Veggel. Design and development of the Advanced LIGO monolithic fused silica suspension. *Classical and Quantum Gravity*, 29(3):035003, 2012.
 15. J Abadie et al. Predictions for the rates of compact binary coalescences observable by ground-based gravitational-wave detectors. *Classical and Quantum Gravity*, 27(17):173001, 2010.
 16. A Staley, D Martynov, R Abbott, R X Adhikari, K Arai, S Ballmer, L Barsotti, A F Brooks, R T DeRosa, S Dwyer, A Effler, M Evans, P Fritschel, V V Frolov, C Gray, C J Guido, R Gustafson, M Heintze, D Hoak, K Izumi, K Kawabe, E J King, J S Kissel, K Kokeyama, M Landry, D E McClelland, J Miller, A Mullavey, B O'Reilly, J G Rollins, J R Sanders, R M S Schofield, D Sigg, B J J Slagmolen, N D Smith-Lefebvre, G Vajente, R L Ward, and C Wipf. Achieving resonance in the Advanced LIGO gravitational-wave interferometer. *Classical and Quantum Gravity*, 31(24):245010, 2014.
 17. R.W.P. Drever, J.L. Hall, F.V. Kowalski, J. Hough, G.M. Ford, A.J. Munley, and H. Ward. Laser phase and frequency stabilization using an optical resonator. *Applied Physics B*, 31(2):97–105, 1983.
 18. K. Arai. Sensing and controls for the power-recycling of TAMA300. *Classical and Quantum Gravity*, 19(7):1843, March 2002.
 19. L Barsotti. aLIGO commissioning update. LIGO-G1500414 for LSC-Virgo Collaboration Meeting, March 2015.
 20. M Evans et al. Observation of parametric instability in Advanced LIGO. *Phys. Rev. Lett.*, 114(16):161102, April 2015.
 21. J. A. Sidles and D. Sigg. Optical torques in suspended fabry-perot interferometers. *Physics Letters A*, 354(3):162–172, January 2006.
 22. E. Oelker, L. Barsotti, S. Dwyer, D. Sigg, and N. Mavalvala. Squeezed light for advanced gravitational wave detectors and beyond. *Opt. Express*, 22(17):21106–21121, Aug 2014.
 23. Aasi J. et al. Enhanced sensitivity of the ligo gravitational wave detector by using squeezed states of light. *Nat Photon*, 7(8):613–619, 08 2013.

Advanced LIGO Input Optics

G. Ciani for the LIGO Scientific Collaboration

*Department of Physics, University of Florida, 2001 Museum Rd,
Gainesville, FL-32608, USA*

Critical to the performance of the Advanced LIGO detectors is the Input Optic subsystem, charged with delivering a stable and well-shaped beam across the whole range of possible operating input powers, up to 180 W. This manuscript describes its the overall function and layout, and provides some details on the design and performance of its main components.

1 Introduction

Both Advanced LIGO gravitational wave detectors¹ have now completed the installation phase and reached the milestone of a 2-hour full lock. Commissioning activity is in full swing with the Livingston observatory (LLO) operating routinely at a range of 60+ Mpc, the Hanford observatory (LHO) catching up quickly and the first joint Observation Run planned for the fall of this year². Critical to this success has been the performance of the Input Optics (IO) subsystem, designed and built by the LIGO group at University of Florida. The IO fulfills many different functions, among which are DC power control, injection of side-bands used to control the various degrees of freedom of the interferometer, spatial filtering, frequency stabilization and mode matching of the main laser beam, and separation of the back-reflected light from the main path. Stringent requirements have to be maintained for each of these tasks over the whole range of possible input operating powers, up to 180 W.

The next section briefly describes the IO chain as seen by the laser beam that propagates from the Pre-Stabilized Laser (PSL) to the Power Recycling Cavity, while the following one provides more details on the main components of the IO subsystem, their requirements and performance.

2 Input Optics Overview

Figure 1 shows a schematic representation of the IO chain, largely based on the Enhanced LIGO design³ and upgraded to operate at even higher powers with more stringent requirements. It is located between the PSL subsystem and the Power Recycling Cavity. Most of the main components are distributed among the in-air table shared with the PSL subsystem and two in-vacuum seismically isolated tables; some diagnostics and control components are located on two dedicated in-air IO tables (named IOT2L and IOT2R).

The beam handed off by the PSL to the IO is fed into a manual power control stage and a custom built Electro-Optical Modulator (EOM), which adds phase-modulation sidebands at 9, 24 and 45 MHz. After the EOM, the beam goes through a motorized power control stage (intended for DC power control) and up a periscope that injects it into the vacuum system. Several low power beams are picked-off along the PSL table for diagnostic purposes. Upon

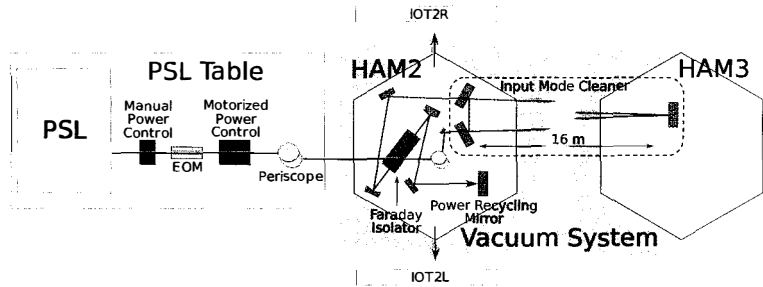


Figure 1 – A schematic layout of the Input Optic chain.

reaching the seismically isolated table inside the HAM2 (Horizontal Access Module 2) chamber, where most of the main IO components are located, the beam is brought down to table height by a periscope; two steering mirrors inject it into the 33 m round-trip length triangular Input Mode Cleaner (IMC) cavity. The beam reflected by the IMC is routed to an out-of-vacuum table where it is used for length and alignment sensing and control of the IMC. The beam transmitted through the IMC is reflected by a steering mirror, then by a mode matching optic, through the Faraday Isolator, onto another mode matching optic, and finally by the last steering mirror that injects it into the Power Recycling Cavity. Forward and backward propagating pick-off beams in transmission of the two steering mirrors are used for active power stabilization of the PSL or routed out-of-vacuum for diagnostic purposes. These four optics are suspended by the HAM Auxiliary Suspensions, single stage suspensions with vertical isolation, actuation capability and active and passive damping. The Faraday Isolator (FI) separates the beam back-reflected by the Power Recycling Mirror Cavity from the main beam path, preventing it from reaching the main laser and making it available for control and diagnostic purposes; the FI is located in vacuum so as to prevent the formation of an uncontrolled optical cavity between the IMC and the Power Recycling Mirror.

3 Main components

3.1 Electro-Optical Modulator

The EOM uses a design already adopted in Enhanced LIGO⁴, with three independent pairs of electrodes installed on a single $4 \times 4 \times 40 \text{ mm}^3$ electro-optical Rubidium Titanyl Phosphate (RTP) crystal. Each pair of electrodes is part of its own RLC circuit tuned to resonate at a specific sideband frequency. RTP was chosen for its low optical absorption, and the single-crystal design reduces the number of interfaces and thus scattering losses. The end faces of the crystal are AR-coated and wedged so as to eliminate the risk of a parasitic interferometer and to help reduce residual unwanted amplitude modulation by separating the two orthogonal polarizations passing through it; the extinction ratio is about 10^5 . Well before the main interferometer control scheme details were worked out, the requirement for the modulation depth of the 9 and 45 MHz sidebands was set at 0.4 to account for ample margins; the 24 MHz sideband has to be adequate to control the IMC. The currently installed EOMs (at the two sites) meet requirement for all but the 45 MHz sidebands, for which the modulation depth is a factor 2-3 too low (see Figure 2). The problem could be solved by employing more powerful drivers and improving the resonant circuit, but the commissioning effort has thus far indicated that the current modulation depth is probably sufficient. The measured residual amplitude modulation to phase modulation ratio is right at the specification level of 10^4 . Although long term observation have shown that thermal drift can slightly compromise this performance, it is not anticipated to be an issue and can be easily mitigated if needed with a dedicated thermal enclosure.

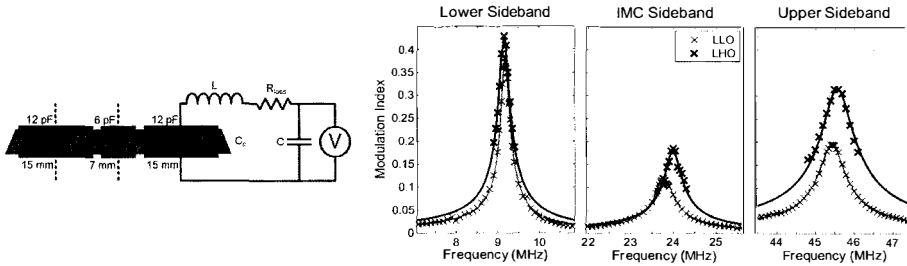


Figure 2 – Left: a schematic representation of the EOM arrangement. Right: the modulation depths for the three sidebands measured at both the Livingston and Hanford observatories.

3.2 Input Mode Cleaner

The IMC (dashed area of Figure 1) is a ~ 33 m round-trip length triangular cavity comprised of 6" diameter mirrors suspended by triple suspensions which are the responsibility of the aLIGO Suspension subsystem. The input and output mirrors are located in HAM2; the third optic is located in HAM3, about 16 m away. The main laser is locked to the IMC using the Pound-Drever-Hall technique; wavefront sensors are employed to control the alignment. Besides filtering and stabilizing the spatial mode and the polarization of the laser, the IMC serves as an intermediate frequency reference for the laser above ~ 15 Hz; the arm cavities are eventually used when the full interferometer is locked. Below 15 Hz, where the seismic isolation performance starts to degrade, the error signal of the locking loop is instead used to control the IMC length actively.

The measured geometrical and optical properties of the two installed IMC satisfy the requirements. As an example, at LHO the cavity pole and finesse have been measured to be 8.72 kHz and 515 respectively, in agreement with the design values (see Figure 3; assuming the transmissivities provided by the vendor, this results in an estimated round trip loss of about 150 ppm. Total and per-mirror absorptions, of particular concern because of possible thermal deformations induced by the absorbed heat, have been measured using a combination of two techniques: cavity Gouy phase tracking⁵ and shift of the individual optics' mechanical resonant modes⁶. The result is a per-mirror absorption between 2 and 4 ppm; the estimated corresponding thermal deformations induce a mode mismatch of less than 0.3% at full power, negligible compared to the 5% maximum higher order mode content required.

An attempt has also been made towards compiling a complete IMC length noise budget, although the final performance depends on many other components and effects in the scope of other subsystems. The budget is reported in Figure 3 and shows that there is an unexplained excess between about 3 and 100 Hz. While at present the excess doesn't represent a limiting factor for the performance of the interferometer, its cause is under ongoing investigation.

3.3 Faraday Isolator

The Faraday Isolator is located after the Input Mode Cleaner and, in addition to the 5% maximum higher order mode content in the transmitted beam, has to satisfy a requirement of at least 30 dB of isolation at all laser powers up to 130 W. To this purpose the Faraday Isolator is based on a special design with particular attention to thermal effects, as shown in Figure 4.

To compensate for thermal depolarization, an arrangement proposed by Snetkov et. al.⁷ has been employed: two Terbium Gallium Garnet (TGG) crystals, each providing 22.5° of rotation in a ≈ 1 T magnetic field, are placed in series, with a 67.5° quartz rotator in between. This allows for thermal induced birefringence effects to be largely compensated between the two crystals. Calcite wedge polarizers with extinction ratio in excess of 10^5 and optical efficiency greater than 99% are used to separate polarization in the input and output beams. A half wave plate placed

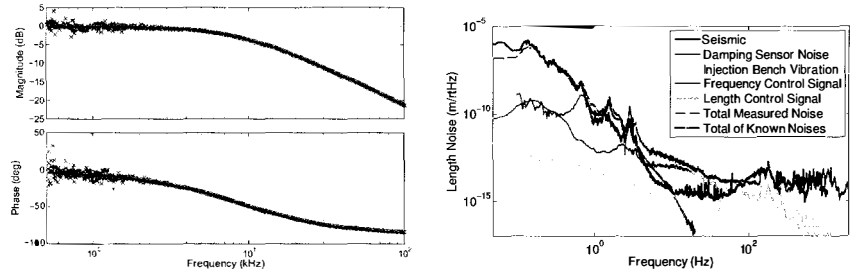


Figure 3 – Left: Measured and fitted cavity pole of the IMC. Right: noise budget of the IMC sensed length noise (or, equivalently, frequency noise of the locked laser). Contributions well below the total noise are not shown.

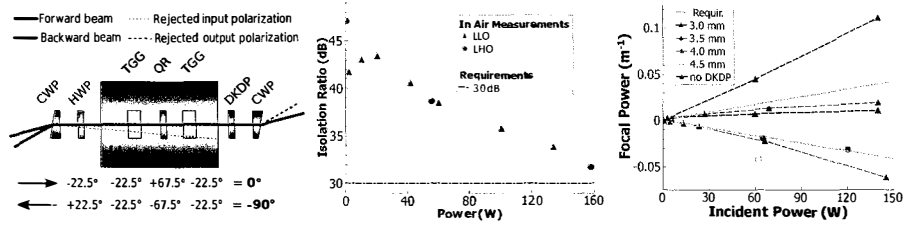


Figure 4 – Left: a schematic representation of the Faraday Isolator. Center: measured in-air isolation ratio of the FI as a function of laser power in the crystals. Right: measured total thermal lensing of the FI as a function of power in the crystals for different DKDP thicknesses. Triangles represent Hanford data, circles Livingston data.

before the Faraday rotator sets the total rotation to 0° and 90° for the forward and backward beams respectively; it is installed on a motorized rotational stage for in-vacuum optimization.

Absorption of laser power creates a thermal gradient inside the TGG crystal. Because of the temperature-dependent index of refraction ($dn/dT > 0$), this translates in a focusing of the beam referred to as “thermal lensing”; to mitigate the effect, a DKDP crystal with negative dn/dT is located right after the Faraday rotator, and its thickness is tuned so that its own thermal lens mostly cancels out that arising inside the TGG crystals.

While the observatories haven’t employed full laser power yet, both isolation ratio and thermal lensing have been successfully tested in air, and the results are shown in Figure 4.

Acknowledgments

The author would like to thank the University of Florida LIGO group and to acknowledge gratefully the support of the National Science Foundation for the construction and operation of the LIGO Laboratory. Research at the University of Florida was supported by NSF grants PHY-0855313, PHY-1205512, and PHY-1306594.

References

1. The LIGO Scientific Collaboration, *Classical and Quantum Gravity* **32**, 074001 (2015)
2. A. N. Staley, *These Proceedings*, (2015)
3. K. L. Dooley et al., *Review of Scientific Instruments* **83**, 033109 (2012)
4. V. Quetschke, *Coherent Optical Technologies and Applications, CMCI* (2008).
5. C. L. Mueller et al., *arXiv:1502.02284* (2015)
6. C. L. Mueller, *PhD thesis, University of Florida* (August 2014)
7. I. Snetkov et al., *Opt. Express* **19**, 6366-6376 (2011)

Large-scale Cryogenic Gravitational wave Telescope: KAGRA

Takayuki TOMARU on behalf of the KAGRA collaboration
*High Energy Accelerator Research Organization,
1-1 Oho, Tsukuba, Ibaraki, 305-0801, Japan,
The Graduate University for Advanced Studies,
1-1 Oho, Tsukuba, Ibaraki, 305-0801, Japan
Institute for Cosmic Ray Research, University of Tokyo
5-1-5, Kashiwanoha, Kashiwa, Chiba, 277-8582, Japan*

Large-scale Cryogenic Gravitational wave Telescope (KAGRA) is a second generation gravitational wave (GW) detector under construction in Japan. KAGRA will have sensitivity of 280 Mpc at the best detector orientation for the GW signal from neutron star binary coalescence, and about 10 events observation is expected every year. This high sensitivity is limited by quantum noises. To realize the quantum noise limited sensitivity, KAGRA uses cryogenic sapphire mirror suspension system and underground site. Cryogenic sapphire mirror and its suspension improves their thermal noises drastically by double effects of low temperature and high mechanical Q of sapphire. This is an original technology and a best feature in KAGRA. It is well known that underground in Kamioka has very small seismic vibration level and has advantage for seismic noise reduction at low frequency range. Seismic vibration of $3 \times 10^{-9} \text{ m} \cdot \text{Hz}^{-1/2}$ at 1 Hz is confirmed in KAGRA tunnel. Tunnel excavation of KAGRA was completed on Mar. 2014, and installation of major devices such like cryostats and vacuum tubes were done until Mar. 2015. Basic operation test of interferometer and data acquisition are planned in the end of 2015, and its preparation is under progress. This paper reports KAGRA and its status.

1 Introduction

Gravitational wave (GW) is one of the remaining pieces to complete verification of general relativity, and it will be a new tool to explore the universe. Strong evidence for the existence of GW was provided by R. A. Hulse and J. H. Taylor Jr. by long term observation of a binary pulsar system¹. The BICEP2 experiment, which is a millimeter-wave telescope to search B-mode polarization of cosmic microwave background, claimed the detection of primordial gravitational wave², however there are also arguments that the result can be contaminated by foreground radiation³.

There is a network of large scale ground based laser interferometers around the world for the direct detection of GW signals. The major sources for GW, which can be detected by ground-based laser interferometer, are compact astronomical objects such like black holes and binary neutron stars. These sources can radiate GW at the frequency range between several dozens Hz and kHz. First serious searches of GWs by interferometric detectors like LIGO⁴, VIRGO⁵, GEO600⁶ and TAMA300⁷, were done in 2000's. Unfortunately, no detection of GWs are reported yet by these first generation GW detectors despite LIGO reached really high sensitivity of $2 \times 10^{-23} \text{ Hz}^{-1/2}$.

In the year 2010, construction of the second generation of GW detectors began. Advance LIGO (aLIGO)⁸ and advanced VIRGO (aVIRGO)⁹ are being upgraded from the first generation LIGO and VIRGO detectors, respectively. GEO-HF¹⁰ is a modified detector from GEO600, which aims to search for high frequency GW signals. Large-scale Cryogenic Gravitational wave

Telescope, which is also named as KAGRA, is a new detector under construction in Japan. These detectors will have almost same sensitivity of the order of $10^{-24} \text{ Hz}^{-1/2}$, and can detect GW signals from neutron-star binary coalescence at 200 – 300 Mpc distance. The GW observation network by aLIGO, aVIRGO and KAGRA realizes 100 % sky coverage with half maximum sensitivity and 82 % duty factor. All of these second generation GW detectors will start observation until 2018.

In this paper, KAGRA project and its status are reported.

2 KAGRA project

KAGRA was funded in 2010, and the construction started soon after. Unlike aLIGO or aVIRGO detector, KAGRA is not an upgrade of other Japanese detectors like TAMA300 or CLIO¹¹. As an international project, the design and concept of KAGRA is unique as compared to other detectors around the world. The leading institution of KAGRA project is Institute for Cosmic Ray Research (ICRR), University of Tokyo, and co-leading institutions are High Energy Accelerator Research Organization (KEK) and National Astronomical Observatory of Japan (NAOJ). At present, 80 international institutions push forward KAGRA project.

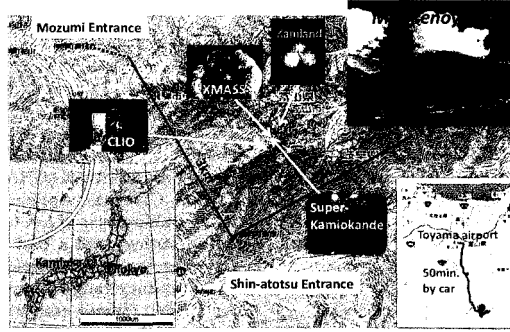


Figure 1 – KAGRA location and layout in Mt. Ikenoyama in Kamioka.

The KAGRA detector is located 200 m underground in Mt. Ikenoyama in Kamioka, Gifu prefecture, Japan. The site is about 250 km away from Tokyo and is 50 mins drive from Toyama airport. Figure 1 shows map and layout of KAGRA. The reason for the detector to be located underground in Mt. Ikenoyama is to reduce seismic vibrations. This underground site is a unique feature in KAGRA.

Another unique feature is the use of cryogenic mirror and suspension system to reduce their thermal noises. This technology has been developed in Japan for 20 years, and can be also applied to future third generation GW detectors.

Fundamental design of KAGRA including these special features are described in following subsections.

2.1 Sensitivity and Science

Figure 2 shows design sensitivity of KAGRA. KAGRA will have two operation modes of interferometer; detuned mode (thick black solid-line) and broadband mode (thick black dashed-line). Unless aiming to observe particular GW sources, broadband mode is fine to search GW signals since its observation band is wider than that in detuned mode. Observation band is between several dozens Hz and kHz. The best sensitivity will be $factor \times 10^{-24} \text{ Hz}^{-1/2}$ at 100 Hz. This sensitivity is limited by quantum noises, that is, radiation pressure noise and photon shot noise. This quantum noise limited condition is realized by suppressing thermal noises of mirror and suspension, which are colored lines in Fig. 2, except for orange line of seismic noise. These noises are

well defined in the reference by P. R. Saulson¹². The suppression of thermal noises are achieved by using semi-monolithic sapphire mirror and suspension cooled to 20K. Sharp peaks at 130 Hz and at 230 Hz are vertical mode and first violin mode of suspension thermal noise, respectively. These peaks arise from the use of thick sapphire fibers of 1.6mm in diameter to cool the mirror against heat generation in mirror by laser power absorption. To remove the vertical mode of suspension thermal noise at 130 Hz from the observation band, introduction of vertical springs made of sapphire (14Hz) in cryogenic payload is planed (see Fig. 6).

KAGRA can detect GW signals from neutron star binary coalescence at 280Mpc distance in the best detector orientation and from 173 Mpc in whole sky average with signal to noise ratio of 8. Estimated event rate within this distance is about 10 per year. For quasi-normal mode of black hole, generated just after merger of neutron star binary, GW signals from about 1 Gpc are detectable. Figure 3 shows detectable range of GW signals from Neutron star binary coalescence (solid lines) and quasi-normal mode of black hole (dashed lines)¹³.

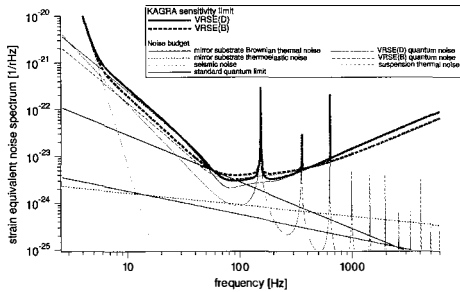


Figure 2 – Design Sensitivities of KAGRA. The thick black solid-line and the thick black dashed-line show the total sensitivities in detuned and broadband mode in interferometer, respectively. Green and blue lines show designed levels of thermal noises, and thin black line shows standard quantum limit.

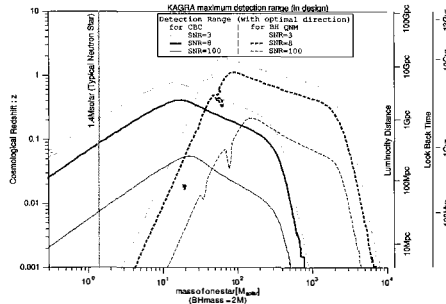


Figure 3 – Detectable range of GW signals from Neutron star binary coalescence (solid lines) and quasi-normal mode of black hole (dashed lines)¹³.

2.2 Interferometer design

Figure 4 shows interferometer design. Dual recycled Fabry-Perot Michelson interferometer with input and output mode cleaners is used. Designed finesse of arm cavity is 1550, and power recycling gain and signal recycling gain are 11 and 15, respectively. One can switch both detuned and broadband mode by changing signal recycling mirror position. In detuned mode, detuning angle of 3.5° is used.

Table 1 lists interferometer and core-optics parameters. Details of the interferometer configuration and parameters are described in references by K. Somiya¹⁴ and Y. Aso¹⁵.

2.3 Underground Site

One of the reason why Mt. Ikenoyama in Kamioka was chosen as KAGRA site is its very small seismic motion. There is also no surface vibration component in KAGRA tunnel since the site is deeper than 200 m from ground surface. Typical seismic vibration level in Mt. Ikenoyama is order of $10^{-9} \text{ m} \cdot \text{Hz}^{-1/2}$ at 1 Hz, which are one or two orders of magnitude smaller than that at other GW sites. This is the principle advantage of KAGRA site, especially to observe GW signals at dozens Hz range.

However, one encounters unexpected amount of underground water in KAGRA tunnel. To drain underground water, KAGRA tunnel has 1/300 slant. There is much water flow in side pits

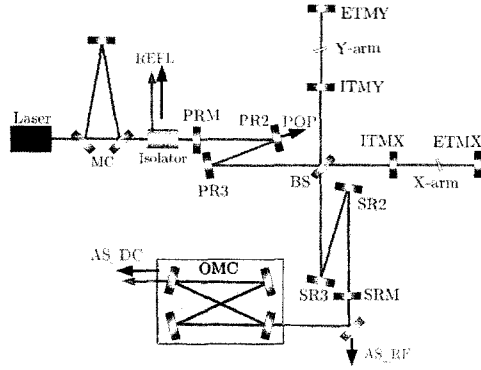


Figure 4 – KAGRA interferometer design. This is dual recycled Fabry-Perot Michelson interferometer configuration with input and output mode cleaners¹⁵.

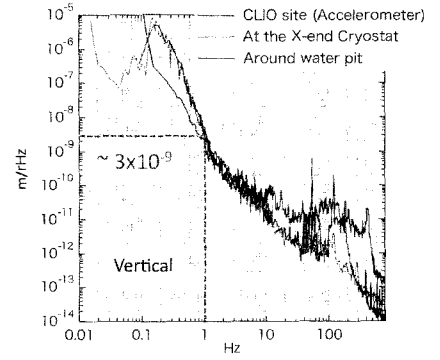


Figure 5 – Measurement result of vertical seismic vibration around main-mirror cryostat in X-end room level in front of water pit (red line). Blue line shows vertical seismic vibration level in front of water pit. Both data were measured by a seismometer, Guralp CMG-3T, which has no sensitivity over 200 Hz. Black line shows vertical seismic vibration measured in CLIO site, where is in same Mt. Ikenoyama, by laser accelerometer, which has no sensitivity below 0.1 Hz.

in tunnel. This water flow can affect seismic vibration, therefore the seismic vibration in KAGRA tunnel was measured after tunnel excavation.

Figure 5 shows measured result of vertical seismic vibration at the main mirror-cryostat location in the X-end. The seismic vibration level is $3 \times 10^{-9} \text{ m} \cdot \text{Hz}^{-1/2}$, which is same level as CLIO site, where is in the same Mt. Ikenoyama. Although we observed large excess over 10 Hz range in front of water pit, we found that there is no affect at cryostat location, where is about 10 m distance from the water pit. And we also found existence of large micro-seismic peak at around 0.2 Hz. It is pointed out that the micro-seismic peak in Mt. Ikenoyama had seasonal variation and this can be almost largest value since the measurement was done in January and the Sea of Japan, where is only 30 km from Mt. Ikenoyama, was rough in winter season. So investigation of seismic vibration at the X-end in long term is under progress.

Very stable temperature in underground should be also mentioned. Only 0.1 degree Celsius temperature variation for a week was observed in Kamioka underground. This is a large advantage for stable interferometer operation.

2.4 Cryogenic Mirror and Suspension

Cryogenic sapphire mirror and suspension are one of the most advanced technology in KAGRA. The power of thermal noise is proportional to temperature and inversely proportional to mechanical Q. So cryogenic mirror and suspension is most straightforward method to reduce thermal noises. Moreover, it is well known that mechanical Q of sapphire increases at cryogenic temperature, which values are 1×10^8 for bulk and 1×10^7 for fiber below 20 K^{16,17}. However, it is also known that mechanical Q of reflective and anti-reflective coatings are small of $10^3 - 10^4$, and it is large issue to suppress the mirror thermal noise. Fortunately, our cryogenic mirror can overcome this issue by cooling down mirror at 20 K.

A practical issue is how we make real semi-monolithic sapphire suspension system like Fig. 6. Sapphire ears are contacted to the side of sapphire mirror substrate by Hydro-Catalysis Bonding (HCB). HCB realizes very thin bonding layer of about 60 nm in spite of large strength, which is sufficient to suspend sapphire mirror of 23 kg. This thin bonding layer gives small contribution to thermal noise even for small mechanical Q, where we assumed Q of 1.0 in a worst case, although

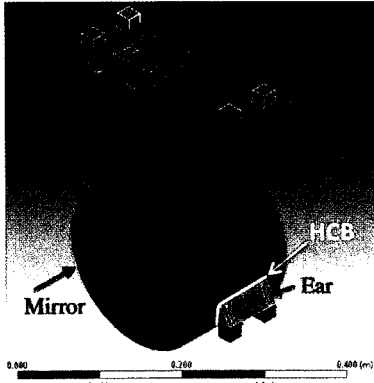


Figure 6 – Sapphire suspension system. HCB: hydro-catalysis bonding. InW: indium welding. HCB is used to contact between two ears and mirror substrate. And InW is used as replaceable contact among blocks at both end of fibers, blades and ears.

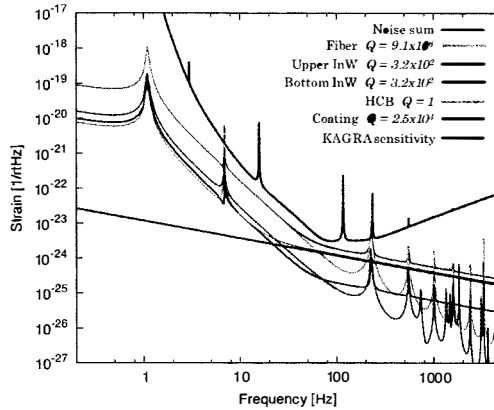


Figure 7 – Estimated thermal noise components with sapphire contacts and coating. Mechanical Q of 1.0 for HCB, 320 for indium welding, 2500 for coating and 9.1×10^6 for fiber are assumed here²⁰.

Q of 10^4 at cryogenic temperature is reported recently¹⁸. But fragile sapphire suspension fibers must be replaced easily when they have trouble. In this reason, we developed indium welding (InW) between sapphire blocks at the both ends of fiber and sapphire ears, and between sapphire blocks and sapphire blades⁹. The mechanical Q of the indium welding is 320 at 20K from our measurement^{20,21}. Figure 7 shows estimated thermal noise contributions to KAGRA sensitivity. Even including small mechanical Q of sapphire contacts and coating, estimated thermal noises are lower than KAGRA sensitivity²⁰.

Figure 8 shows mechanical design of cryogenic payload for sapphire mirror. This cryogenic payload consists of semi-monolithic sapphire suspension, recoil mass, intermediate mass with sapphire vertical blade springs, control stage named Marionette, Marionette recoil mass (not shown) and Geometric Anti-Spring (GAS) filter (not shown). The reason why the Marionette is introduced is to be simple around intermediate mass to keep high Q condition.

The cryogenic payload is suspended by low frequency vibration isolation system (VIS) at room temperature shown in Fig. 9. Steep reduction of seismic noise is achieved by using 14 m long VIS. And this VIS don't need support tower since vertical tunnel is excavated, therefore it is possible to remove structural resonance due to support tower.

An large issue is that heat links for cooling must be connected between cryocoolers and the cryogenic payload. The heat links will be made of the bundle of thin wires of 99.9999 % purity aluminium, which is very soft and very large thermal conductivity material. And ultra-small vibration cryocooler systems developed in CLIO experiment are also used to reduce vibration conduction through heat links²². However, we estimate excess of seismic noise at cryogenic payload by vibration conduction through the heat links. Therefore, we plan to introduce an additional vibration attenuator for heat links²⁰.

Fundamental technologies for cryogenic mirror to reduce thermal noise has been demonstrated in CLIO experiment. It was confirmed that thermal noise of mirror at room temperature around 200Hz decreased after cooling down to 17K¹¹.

3 Present Status

KAGRA tunnel excavation was done at March 2014. The total length of the tunnel is about 7km. The first installed device into the tunnel was a main-mirror cryostat to the Y-end room.

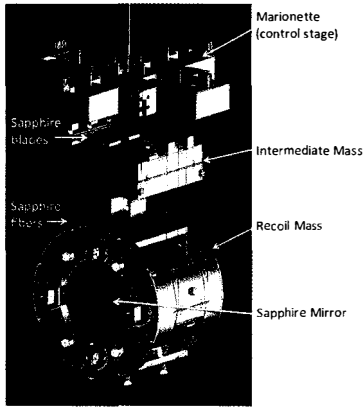


Figure 8 – Mechanical design of cryogenic payload

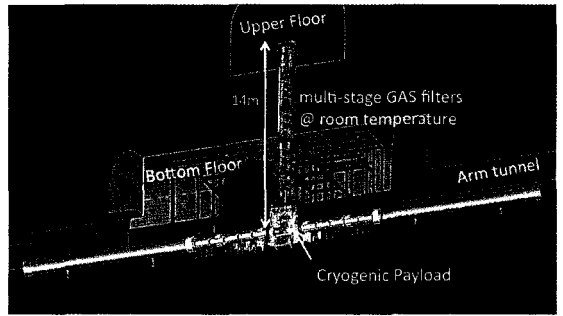


Figure 9 – Vibration isolation system with cryogenic payload.

The size of the cryostat is about 4.3 m in height and 2.6 m in diameter without flanges. This is comparable size with arm tunnel, and it had to be installed in first. The cryostat was transported along 3 km tunnel by using a special cart. We spent about 12 hours for first cryostat installation. Now all of cryostats have been installed and assembled. After cryostat installation to both end rooms, vacuum tubes of 478 in total were installed into arm tunnels. This work was completed at March 2015.

A big issue is much water leakage in tunnel. Maximum water leakage in tunnel was about 1200 ton/hour in this early spring. Vertical drainage holes are constructed and water leakage issue has gradually improved.

Other devices such as input optics, mode cleaners, clean booths, control electronics and data servers are also being installed rapidly.



Figure 10 – Installed vacuum tubes in KAGRA tunnel.

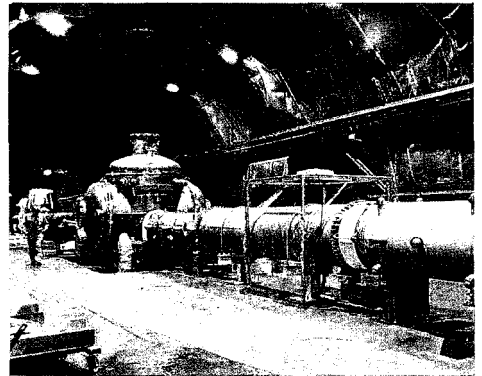


Figure 11 – Cryostat for cryogenic payload and cryogenic thermal radiation shield pipe at Y-front room.

4 Conclusion

KAGRA is a unique second generation GW detector with advanced features of cryogenic mirror system and is located underground. The construction of the detector has rapidly progressed and is as per schedule. Early operation test of interferometer with very simple condition at room temperature, named iKAGRA, is planned at the end of 2015. Construction of baseline KAGRA with advanced systems will be done at the end of 2017 and the observation is to start thereafter.

Acknowledgments

The KAGRA project is funded by the Ministry of Education, Culture, Sports, Science and Technology (MEXT) of Japan under Leading-edge Research Infrastructure Program, and by the Japan Society for the Promotion of Science (JSPS) under Grant-in Aid for Specially Promoted Research. This work is also supported by JSPS Core-to-Core Program, A. Advanced Research Networks, and by the joint research program of the Institute for Cosmic Ray Research, University of Tokyo. Collaborative support for some fundamental studies in KAGRA are given by European groups on the basis of ELiTES program.

References

1. J. M. Weisberg and J. H. Taylor, arXiv:astro-ph/0407149, (2004)
2. BICEP2 collaboration, PRL **112**, 241101 (2014)
3. BICEP2/Keck and Planck Collaborations, Phys. Rev. Lett. **114**, 101301, (2015)
4. A. Abramovici et al., Science **256** 325, (1992)
5. VIRGO collaboration, VIRGO Final Design Report (1997)
6. K. Danzmann et al., Max-Planck Institute fur Quantenoptik Report **190** Garcmjg, Germany (1994)
7. K. Tsubono and the TAMA collaboration, in Proc. TAMA workshop on Gravitational Wave Detection, Universal Academy Press, 183., (1997)
8. G. M. Harry (for the LIGO Scientific Collaboration), Class. Quantum Grav. **27**, 084006 (2010)
9. The Virgo Collaboration, Advanced Virgo Baseline Design: VIR-0027A-09, <https://pub3.ego-gw.it/itf/tds/>
10. B. Willke et al., "The GEO-HF project", Class. Quantum Grav. **23**, S207-S214 (2006)
11. T. Uchiyama et al., PRL **108**, 141101 (2011)
12. P. R. Saulson, "Fundamentals of Interferometric Gravitational Wave Detectors", World Scientific Pub Co Inc. (1994)
13. N. Kanda et al., The 11th Asian-Pacific regional IAU Meeting, NARIT Conference Series **1** (2012); arXiv:astro-ph/1112.3092v1 (2011)
14. K. Somiya et al., Class. Quantum Grav. **29** 124007 (2012)
15. Y. Aso et al., Phys. Rev. D **88**, 043007 (2013)
16. T. Uchiyama et al., Phys. Lett. A **261** 5., (1999)
17. T. Uchiyama et al., Phys. Lett. A **273** 310., (2000)
18. K. Haughian, presentation in ELiTES: 3rd general meeting (2015)
19. A. Khalaidovski et al., Class. Quantum Grav. **31** 105004. (2014)
20. Dan Chen, Ph. D thesis, University of Tokyo (2014)
21. G. Hofmann, et al., in preparation (2015)
22. T. Tomaru et al., Cryocoolers **13**, 695. (2005); T. Tomaru et al., Int. J. Mod. Phys. (Proc. ECRS) **20**, 7063. (2005); Y. Ikushima et al., Cryogenics **48**, 406. (2008)

Table 1: List of interferometer and core-optics parameters^{14,15}. ITM: Input Test Mass, ETM: End Test Mass

| Interferometer | |
|---|--|
| Arm Length | 3000 m |
| Mode cleaner length | 26.639 m |
| Power recycling cavity length | 66.591 |
| Signal recycling cavity length | 66.591 |
| Michelson asymmetry | 3.30 m |
| Modulation Frequency | $f1$: 16.880962 MHz $f2$: 45.015898 MHz $f3$: 56.269873 MHz |
| Arm finesse | 1550 |
| Power recycling gain | 11 |
| Signal recycling gain | 15 |
| Laser wavelength | 1064 nm |
| Laser Power (Input into interferometer) | 180 W (80W) |
| Laser power input into interferometer | 80 W |
| Storage power in arm cavity | 825 W |
| Mode cleaner finesse | 500 |
| Homodyne angle | 132° |
| Detuning angle | 3.5° |
| Test Mass | |
| Size | D220 mm × L150 mm |
| Weight | 22 kg |
| Temperature | 20 K |
| Radius of curvature | 1900 m |
| Transmission at 1064 nm | 0.004 at ITM, 5 - 10 ppm at ETM |
| Optical loss at reflective surface | < 45 ppm |
| Absorption in substrate | 20 - 50 ppm |
| Absorption in coating | 0.5 -1.0 ppm |
| Beam Splitter | |
| Size | D370mm × L80 mm |
| Radius of curvature | Flat |
| Transmission at 1064 nm | 50 % |
| Optical loss at reflective surface | 100 ppm |
| Power Recycling Mirror | |
| Size | D370 mm × L80 mm |
| Radius of curvature | 458.1285 m |
| Transmission at 1064 nm | 0.1 % |
| Optical loss at reflective surface | < 45 ppm |
| Signal Recycling Mirror | |
| Radius of curvature | 458.1285 m |
| Transmission at 1064 nm | 0.1536 % |
| Optical loss at reflective surface | < 45 ppm |

THE CALVA FACILITY FOR GW DETECTOR

D. HUET, N. ARNAUD, M-A BIZOUARD, V. BRISSON, J. CASANUEVA, F. CAVALIER, M. DAVIER, P. HELLO, N. LEROY, V. LORIETTE*, I. MAKSIMOVIC*, F. ROBINET
LAL, Univ Paris-Sud, CNRS/IN2P3, ORSAY, France
**LPEM, UMR8213 CNRS, ESPCI, PARIS, France*

The CALVA facility is a suspended optical system installed in Orsay and designed to test new approaches for cavity control or for optical systems using long cavities¹. The optical scheme is composed by 3 mirrors (2 coupled cavities) which allow to have on the same axis a 50m long cavity and a 5m "recycling" one. The first goal of this facility is to test a technic based on auxiliary lasers to help the lock acquisition of the Advanced Virgo kilometeric gravitational wave detector. With the increase of the cavity finesse in the long cavities and the new signal-recycling mirror, such a technic will ease the transition between mirrors being free to a full resonant device.

1 Aim of the CALVA facility

With the upgrade of the gravitational waves detectors Virgo^{2,3} (Advanced Virgo (AdV)) and LIGO⁴ (Advanced LIGO (AdL)), new difficulties are expected to raise and interfere with the experiment. In particular, two specific points are intended to be studied with the CALVA facility:

- The addition of a fifth cavity with the introduction of the signal recycling mirror will imply the re-coupling of all degrees of freedom error signals. The extraction of each error signal will become more difficult.
- The increase of the finesse (\mathcal{F}) of the Fabry-Perot (FP) cavities (length L) from 150 up to 450 in AdV will reduce the critical velocity from $4\mu\text{m/s}$ down to $0.4\mu\text{m/s}$ ($v_{cr} = \pi c\lambda/4L\mathcal{F}^2$: speed of the resonance crossing above which fields will not have time to build up). This will induce a degradation of the error signal due to the ringing effect⁵.

New locking technics need to be studied in order to solve these concerns and the use of an auxiliary laser to lock the two FP cavities independently is the first scheme we want to test on CALVA. First attempts have already been made on AdL⁶, achieving the lock of the cavities, and we plan to use similar technics in AdV. Other independent studies like thermal deformable mirrors⁷, frequency dependent squeezing and parametric instabilities are intended to be performed.

2 Description of CALVA

2.1 Configuration

In order to meet the challenge and mimic the Advanced Virgo configuration, CALVA is composed of two suspended coupled FP cavities of 5m and 50m (cf. figure 1). The three suspended mirrors are inserted in three vacuum tanks linked by two vacuum pipes. The suspensions are 40cm long leading to a pendulum resonance at 0.8Hz.

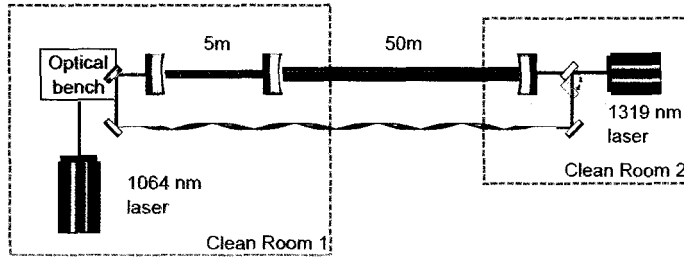


Figure 1: Scheme of CALVA

2.2 Optical systems

CALVA uses three different optical systems:

- The first system is composed of optical levers (red diode/laser with two quadrant photo-diodes) to determine the angular and longitudinal motions of each mirror in the reference of the vacuum tank. It is used in the local control system as the first step for slowing down the mirrors.
- The main system is composed of two lasers and the two FP cavities : the main laser is a Nd-YAG laser at 1064nm with 1W power located in the clean room 1 at one side of the experiment. The auxiliary laser is at 1319nm with 100mW power and is located in the clean room 2 at the other side. The 5m cavity is intended to have a finesse of 15 while the 50m cavity is intended to have a finesse of 620 for the 1064nm laser (it is around 3 for the 1319nm).
- The last system, named reference cavity, is a small triangular silicium monolithic cavity of finesse 50 for the frequency stabilization of the 1064nm laser.

2.3 Control loops

For each optical system, there is a corresponding control loop based on the following architecture which reused as much as possible all the hardware and the software from the Virgo experiment³:

- For the optical levers, the error signals (the pitch θ_x , the yaw θ_y and the longitudinal motion z) are generated with two quadrant photo-diodes per mirror and sent to an ADC. These signals are then treated by the Global Control software⁸ on a real time PC to be transformed into correction signals with an appropriate filtering. Finally they are sent through a DAC to an actuation system composed of four coil-magnet pairs on the back side of each mirror to act on their position.
- For the optical cavities, we use the Pound-Drever-Hall (PDH) technic⁹ to control the cavity or the laser. The error signals are generated by a modulation with an EOM at 2.9MHz for the long cavities and at 80MHz for the reference cavity on the 1064nm laser, and at 4.25MHz for the 1319nm laser. They are obtained by the demodulation - using a home made analog system - of the photo-diode signal in reflection of the cavities and then are sent to an ADC before being filtered with the Global Control. The correction signals are sent either to the mirrors to correct the cavity length or to the piezo actuator and/or the temperature of the laser to adjust the laser frequency.

3 Present situation and results

In order to characterize the limiting factor of the length control accuracy of the 50m cavity, the actual configuration of the experiment is composed of the 5m cavity equipped with the mirrors of the 50m cavity which is not currently used. The expected finesse is then 620 for the 1064nm laser. We also use the auxiliary laser thanks to a fiber that brings the 1319nm laser from clean room 2 into clean room 1 (cf. figure 1).

3.1 Lock acquisition

The first step of the lock is the control of the mirror angular and longitudinal motions with the local controls : they reduce the motion rms by a factor 10 (cf. figure 2). Then the cavity is locked with the 1319nm laser which still reduces the cavity length variations. We search for 1064nm resonances by applying a triangular signal on the 1319nm frequency which leads to a length variation of the cavity. When the 1064nm laser crosses a resonance of the cavity, the final step of the lock can be engaged.

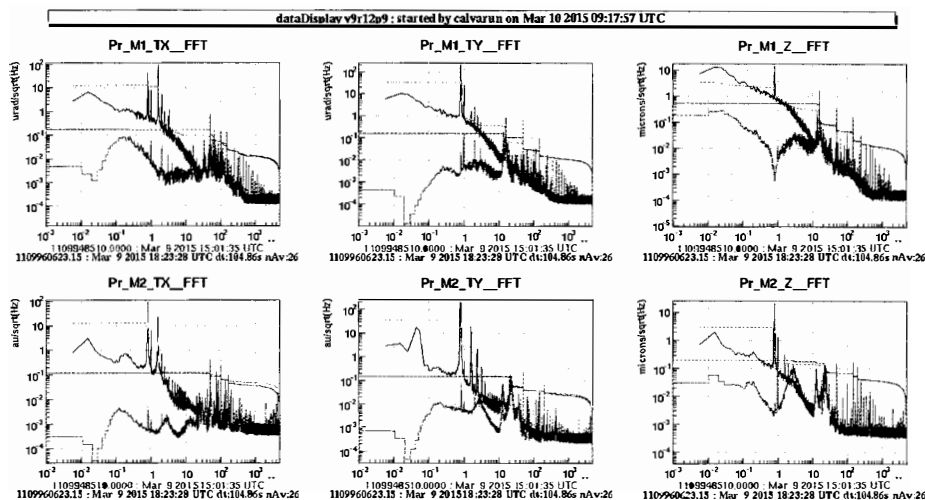
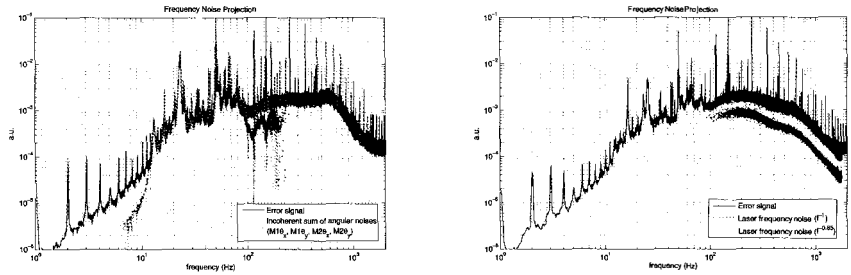


Figure 2: Mirror stabilization by local controls for the 3 dofs, both spectrum and integrated rms are shown when the mirrors are free (black) and under local controls (violet)

3.2 Residual noise on the error signal

The analysis of the error signal while locked tells us what is limiting the length control accuracy. Three main sources of noise have been identified:

- The angular control of the cavity contaminates the length control through the coupling of the degrees of freedom. The contribution of this noise has been evaluated and projected on the error signal (cf. figure 3a). It is the main noise source in the 10-100Hz band.
- The frequency noise of the laser has been evaluated with the usual model in f^{-1} and the calibration of 10kHz @ 1Hz given by the manufacturer. A better projection is with a noise in $f^{-0.85}$ (cf. figure 3b). This noise is the main limitation of the error signal accuracy above 100Hz.
- The DAC noise is known to be the main limitation of the error signal accuracy below 10Hz and shows 1Hz and harmonics peaks



(a) Angular noises projection with the incoherent sum of the 2 angular contributions of each mirror (b) Laser frequency noise projection for 2 different noise shapes f^{-1} in violet and $f^{-0.85}$ in blue

Figure 3: Different noise projections

3.3 Optical characterization

The finesse of the cavity has been estimated by fitting the resonance peak with the Airy function and by measuring the FWHM of the resonance peak. Both methods give coherent results and lead to a finesse $\mathcal{F} = 347 \pm 15$. The difference with the expected value can be explained by a low roughness ($\lambda/10$ instead of the usual $\lambda/20$) and a probable contamination of the mirrors during the installation in the 5m cavity.

4 Present work

As it has been shown previously (cf. 3.2), the frequency noise is the main contribution to residual noise on the error signal. It has been shown by simulation that the lock of the 50m would be impossible with such a high frequency noise. In order to reduce it, the reference cavity has been implemented to control the 1064nm laser frequency. This loop is now operating and we will evaluate the impact of the reference cavity on the accuracy of the control signal.

Acknowledgments

We would like to thank here the European Gravitational Observatory for supporting this work. We would like to thank also the LAPP in Annecy and the LMA in Lyon for their help in the data acquisition system and the cavity mirrors fabrication.

References

1. F. Cavalier *et al.*, *CALVA Conceptual Design*, https://edms.in2p3.fr/file/I-010870/2/Conceptual_Design.pdf
2. The Virgo Collaboration, *Class. Quantum. Grav.* **32**, 2 (2015).
3. The Virgo Collaboration, *Advanced Virgo Technical Design Report*, **VIR-0128A-12**, (2012).
4. The LIGO collaboration, *Class. Quantum. Grav.* **32**, 7 (2015).
5. M.J. Lawrence, B. Willke, M.E. Husman, E.K. Gustafson and R.L. Byer, *J. Opt. Soc. Am. B* **16**, 4 (1999).
6. A. Staley *et al.*, *Class. Quantum. Grav.* **31**, 24 (2014).
7. M. Kasprzak *et al.*, *this proceedings*.
8. F. Cavalier *et al.*, *Nucl. Instrum. Methods A* **550**, 1-2 (2005).
9. E.D. Black, *Am. J. Phys.* **69**, 1 (2001).

THERMALLY DEFORMABLE MIRRORS: A NEW ADAPTIVE OPTICS SCHEME FOR ADVANCED GRAVITATIONAL WAVE INTERFEROMETERS

M. KASPRZACK, F. CAVALIER, P. HELLO, N. LEROY
*Laboratoire de l'Accelérateur Lineaire, Centre scientifique d'Orsay, Batiment 200,
91440 Orsay, France*

R.A. DAY, E. GENIN,
*European Gravitational Observatory, Via E. Amaldi,
56021 Santo Stefano a Macerata - Cascina PI, Italy, Cascina*

The advanced gravitational wave interferometers, currently in development worldwide, are the most promising instruments for a first detection. To reach their target sensitivity, they will use high power lasers. Unfortunately, they will also be very sensitive to thermal effects occurring in the optical components. In particular, the matching of the main beam into the filtering cavities will suffer from these defects, leading to power losses and noise coupling and thus potentially affecting the detector sensitivity. In this talk we present a new system of adaptive optics especially dedicated for correction of optical aberrations in advanced gravitational wave interferometers: the Thermally Deformable Mirror (TDM). To meet the stringent requirements of the noise and optical compatibility, this device is based on thermal actuation. Several TDM prototypes have been built and tested on table-top experiments. They have demonstrated their ability to generate standard optical aberrations, in agreement with thermal simulations. An actuation scheme for reduction of the high order modes produced by the optical aberrations has been proposed. Early experimental tests have shown the possibility to effectively control the high order mode content of a laser beam with a set of TDMs. This opens the way to the implementation of the TDMs for the beam mode matching improvement into a filtering cavity.

1 Motivation

Advanced Virgo is a 3 km-long dual recycling interferometer, located near Cascina in Italy, that aims to detect the gravitational waves produced by some violent events in the Univers. By design, the sensitivity is increased by a factor 10 with respect to Virgo, that produces an equivalent gain of a factor 1000 in the even detection rate. This major improvement is made possible by many innovations and upgrades, in particular by a consequent increase of the laser power, that should eventually reach up to 125 W at the interferometer input. The increase of the circulating laser power will bring the thermal effects occurring in the optical components to the forefront. Then, the control of the resulting aberrations will be one of the major challenges of the advanced gravitational wave interferometer generation.

1.1 Thermal effects

Even at low absorption, a small fraction of the laser power in interaction with an optical element is dissipated into the optical coating and possibly into the substrate if the beam is going through it¹. A non-homogeneous temperature field is established, and the resulting thermal lens and

surface deformation homogeneity depends on the substrate and coating quality. The high spatial frequency components in the heat pattern will lead to the apparition of wavefront aberrations with high spatial frequency. After propagation, the beam will contain high order Gaussian modes. Therefore, the power in the fundamental Gaussian mode will decrease and the high order modes will be a potential source of noise, like for example scattering, at different stages of the interferometer. At the injection of Advanced Virgo, the thermal effects are expected to produce 10% of mismatch of the beam into the main cavities, whereas a mismatch below 1% is required. Moreover, the thermal effects are unlikely predictable and potentially time varying. An adaptive optics system is therefore needed to reach the design sensitivity.

1.2 Requirements

Stringent requirements applied to the adaptive optics system, due to the particular working conditions inside an advanced gravitational wave interferometer: high power laser, high vacuum compatibility (10^{-6} mbar), high optical quality (surface roughness lower than 0.1 nm, flatness better than $\lambda/20$). The relaxed parameter is the time: the actuation is possible at long time scales (min. 10 mHz). All these parameters along with the fact that the noises have to be reduced at the minimum make thermal actuation the best candidate for the corrective system. Some thermal compensation systems have already been developed, but the required high degree of actuation implies the needs of a new system.

We propose the Thermally Deformable Mirror^{2,3} (TDM) for improvement of the cavity matching by correction of the laser beam aberrations.

2 Thermally Deformable Mirror

The principle of the Thermally Deformable Mirror (TDM) is to control the optical path length of a laser beam via the tuning of the substrate temperature of an additional mirror. The optical path length deformation along the transverse direction is expressed with the equation (Eq.1):

$$OPD = \left[\frac{\partial n}{\partial T} + \alpha(1 + \nu)(n - 1) \right] \int_{z=0}^d \Delta T(x, y, z) dz \quad (1)$$

where n is the material refractive index, α is the thermal expansion coefficient, ν is the Poisson coefficient and $T(x, y, z)$ is the temperature field over the substrate. The control is made on the rear side of the mirror, where the beam is reflected back, by adjusting the power dissipated by a set of resistors. We realize a TDM prototype with 61 resistors (500 Ω) organized in a square pattern on a printed circuit board. The Fused Silica substrate is 2" radius and the resistors are 1 mm².

2.1 TDM characterization

A 1064 nm probe beam is sent to the surface of the mirror. The wavefront modifications are observed with a wavefront sensor in the conjugate plane of the TDM rear surface. The amplitude of the phase deformation is checked to be proportional to the dissipated power, with a response time of a few seconds. The stroke of the individual actuators is about 200 nm. Each resistor is switched on to record its influence function.

The correction ability of the TDM is then expressed with respect to its capacity to generate the Zernike polynomials over the active area. We implement a close loop control that is a least square algorithm with boundaries to optimize the dynamic range. We demonstrate that the TDM is able to reproduce the first Zernike polynomials with a very good accuracy, that is with low coupling to other polynomials, and good efficiency up to the 3rd order with 80 nm RMS and up to the 4th order with 30 nm RMS. The 5th order generation is highly limited by the dynamic range of the actuators.

3 Matching control into a resonant cavity

3.1 Suppression of an high order mode

We now explore the possibility to improve the input laser beam matching into a cavity by reducing the high order modes with the help of the TDM. A full description of the input beam is made through a decomposition in Hermite-Gaussian modes. The initial modal content of a beam is preserved along the propagation if no defect is encountered in the system. When thermal effects occur, the generated high order modes are adding a phase dependent term and an amplitude dependent term. Both terms need to be suppressed to recover an ideal Gaussian beam. A corrective device like a TDM is however able to act on the phase dependent term only. With two devices adequately positioned to act in different phase planes, a control of the modal content is possible. For example, if we consider a small correction of the beam phase in two planes, with the two corrective devices separated by a Gouy phase different from π for the Hermite-Gaussian mode to suppress, we can show that the corrective patterns to apply with the TDMs are Hermite polynomial shaped. This analysis highlights the importance of the relative Gouy phase into the conception of a corrective system.

3.2 Mode Matching setup

We implement a mode matching setup at the CALVA facility, with the 1064 nm laser beam frequency locked into a fixed triangular cavity. The laser beam reflects onto three TDMs before reaching the cavity. The first TDM is used to generate additional aberrations in the system. Three telescopes ensure that the beam has the proper dimensions and phases on each of the TDMs and into the triangular cavity. We use Hermite-Gauss polynomials projected onto the TDMs resistance maps to apply the corrective patterns. The amplitude of the actuation is found by scanning the amplitudes of the maps on both TDMs to minimize the power reflected by the cavity. For example, we observe that the mode HG_{11} can be reduced by a factor 3 with respect to its initial power. However, there is also a slight coupling to some other modes, mainly to the defocus, tilt and the mode HG_{30} . This leads to the stop of the algorithm at a pseudo minimum: the correction is found optimal otherwise the tilt and the focus will continue to increase. We are therefore limited by the coupling to the low order modes in this setup configuration.

4 Conclusion

The TDMs have then demonstrated, by simulations and experiments, their ability to correct optical aberrations and to provide mode matching improvement in an adequate system. They will hopefully be helpful devices in the correction of matching for Advanced gravitational interferometers in any place where the systems are sensitive to mismatch losses, like at the injection, the detection or in squeezing systems. The next step toward the completion of the study with these prototypes should be to pursue the implementation of an automatic alignment and focus control, to reduce the mode coupling into these fundamental modes. Then, an iterative method of mode reduction may be tested and a systematic analysis of mode reduction efficiency may be performed.

References

1. P. Hello and J.Y. Vinet, J. Phys. France **51**, 1267-1282 (1990).
2. B. Canuel and R.A. Day and E. Genin and P. La Penna and J. Marque, Classical and Quantum Gravity **29**, 085012 (2012)
3. M. Kasprzack, B. Canuel, F. Cavalier, R.A. Day, E. Genin, J. Marque, D. Sentenac and G. Vajente, Appl. Opt. **52**, 2909-2916 (2013)



DUAL READOUT OF A MICHELSON INTERFEROMETER FOR SUBTRACTION OF STRAY LIGHT INDUCED DISTURBANCES

M. MEINDERS, R. SCHNABEL

*Institut für Laserphysik und Zentrum für Optische Quantentechnologien der Universität Hamburg,
Luruper Chaussee 149, 22761 Hamburg, Germany and
Institut für Gravitationsphysik der Leibniz Universität Hannover and
Max-Planck-Institut für Gravitationsphysik (Albert-Einstein-Institut),
Callinstraße 38, 30167 Hannover, Germany*



Inelastic back-scattering of stray light is a long-standing and fundamental problem in high-sensitivity interferometric measurements and a potential limitation for advanced gravitational-wave detectors. The emerging parasitic interferences cannot be distinguished from a scientific signal via conventional single readout. In this work, we propose the subtraction of inelastic back-scatter signals by employing dual homodyne detection on the output light, and demonstrate it for a table-top Michelson interferometer. The additional readout contains solely parasitic signals and is used to model the scatter source. Subtraction of the scatter signal reduces the noise spectral density and thus improves the measurement sensitivity. Our scheme is qualitatively different from the previously demonstrated vetoing of scatter signals and opens a new path for improving the sensitivity of future gravitational-wave detectors and other back-scatter limited devices.

Scattered light is a long-standing problem in gravitational-wave (GW) detectors. These detectors reach relative strain sensitivities in the order of $10^{-22}/\sqrt{\text{Hz}}$ ¹, employing kilometer scale Michelson interferometers that operate with high-power laser light. Stray light is produced for example by anti-reflection coatings of transmissive optics or micro-roughness of mirror surfaces. Inelastic backscattering from vibrating surfaces in the surrounding causes a frequency shift of the light and recombination with the interferometer mode produces a spurious signal at the interferometer output. Especially frequency up-conversion of light that is back-scattered from sources with large motional amplitudes leads to broadband disturbances that can spoil the sensitivity of a detector over a large frequency range. Observations of these, so called 'scatter shoulders', were described for example for Virgo's second science run². For third generation detectors, which aim for the extension towards lower frequencies (< 10 Hz), significantly improved mitigation schemes against back-scattered light will be required³.

In this work we demonstrate a new readout scheme that enables the subtraction of stray light induced disturbance signals in the post-processing of the measurement data. We employ dual

homodyne detection on the output light of a table-top Michelson interferometer to measure both orthogonal quadratures of the interferometer signal. The amplitude measurement does not contain any scientific signals and provides a reference measurement for the disturbance signal. The additional data is used to calculate a time-dependent phase-space model of the scattered light $\psi_{sc}(t)$ and its projection is subtracted from the scientific phase measurement data $p(t)$. Our approach is qualitatively different from the previously demonstrated vetoing of scatter signals^{4,5} since the subtraction of the scatter signal reduces the noise spectral density and thus improves the measurement sensitivity.

We consider the case of the well understood scatter shoulder^{2,6} that is produced by sources with large motional amplitudes, like already mentioned above. For a simple model we consider a single source that is moving sinusoidally at a constant average distance to the interferometer. We can express the modulated optical path length for the scattered light as

$$s(t) = s_0 + m \sin(2\pi f_m t + \varphi_m) \quad (1)$$

with a constant average path length s_0 , modulation depth m , frequency f_m and phase φ_m . The Doppler shift that the back-scattered light experiences is proportional to the change of the optical path length $f_{ds}(t) = \frac{\dot{s}(t)}{\lambda}$, with λ denoting the laser wavelength. The maximum frequency component, as observed in a single-sided spectrum, is then given by $f_{ds}^{max} = |\frac{2\pi}{\lambda} m f_m|$. For a modulation depth $m > \lambda/2\pi$ this describes frequency up-conversion.

Due to the additional path of the scattered light with respect to the interferometer mode, this frequency shift generally leads to phase *and* amplitude modulations at the interferometer output. The projections of the scatter signal into the phase and amplitude quadratures are given by

$$p_{sc}(t) = A \cos \psi_{sc}(t) \quad \text{and} \quad x_{sc}(t) = A \sin \psi_{sc}(t), \quad (2)$$

where $\psi_{sc}(t) = \frac{2\pi}{\lambda} s(t)$ denotes the time-dependent phase shift with respect to the interferometer mode. The amplitude A of the scatter signal depends for instance on the transfer function of the interferometer and on the intensity of the scattered light but for this simplified model we consider it to be frequency independent and also constant over the time measured.

Since scientific signals, that are produced by differential arm length changes, induce solely phase modulations, the amplitude quadrature serves as an unbiased monitor for the scatter signal. The latter can be evaluated to find an analytical description of the scatter source, which also allows a prediction of how the scattering affects the phase quadrature.

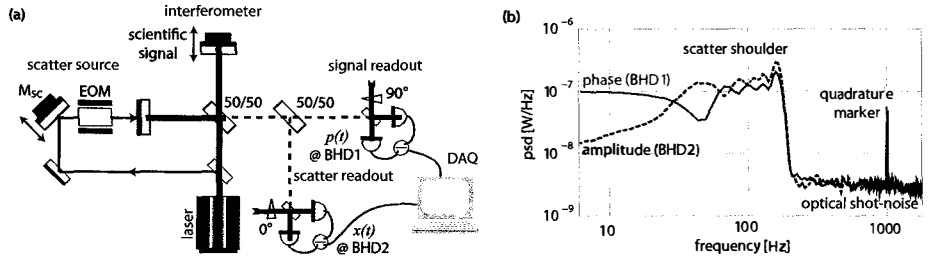


Figure 1 – (a) Schematic of the experimental setup. (b) Dual readout data (demodulated at 5.2 MHz). The averaged power spectral density (psd) was computed with Matlab's 'pwelch' function, using a Hanning window spanning half the oscillation period of the scatter source ($\Delta t = 1/(2f_m)$) and an overlap of 50%. The averaged spectrum shows the scatter shoulder limiting both quadrature measurements over a bandwidth of about 0.2 kHz. Apart from this, the measurements were limited by optical shot noise.

For a proof-of-principle experiment we setup a small table-top Michelson interferometer in which we generated two test signals, figure 1 (a). A GW-like signal (scientific signal) was produced by modulating one piezo actuated interferometer end mirror with a sound file⁷, containing

about 4.5 seconds of a simulated inspiral of two neutron stars with equal masses. The audio frequency signal was shifted by 5.2 MHz with a waveform generator to avoid disturbances, e.g. from acoustics. The second test signal was a scatter shoulder according to equations (1) & (2). An external beam, picked off in front of the interferometer, was sent into the interferometer through the second end mirror. Its optical path was modulated with a piezo actuated mirror at a frequency of 5 Hz and with a modulation depth of a few λ , leading to a maximum frequency shift of $f_{\text{ds}}^{\text{max}} \approx 0.2$ kHz. The scatter signal was also shifted by 5.2 MHz using an electro-optical modulator (EOM). The interferometer used an input power of about 10 mW at 1064 nm and was stabilized to a dark fringe. The output signal was split at a 50/50 beam splitter and two balanced homodyne detectors (BHD1&2) measured the orthogonal quadratures ($p(t), x(t)$), using about 8 mW local oscillator powers. The balanced splitting of our dual readout decreased the scientific signal-to-shot-noise-ratio by a factor of two in power but generally, other splitting ratios can be used. A marker peak at 5.2 MHz+1 kHz was injected to determine the right quadratures. The detected signals were demodulated at 5.2 MHz for data acquisition (DAQ).

The recovered audio-band signals from the phase (solid red) and amplitude (dashed blue) measurements are shown in figure 1 (b). The scatter shoulder clearly limits the sensitivity below the demodulated 0.2 kHz. Above, the measurements were limited by optical shot-noise. The injected GW-signal is not visible, it was completely concealed by the scattering.

In the modeling of the measured scatter signal we allowed for a small contribution of higher harmonics in the modulated optical path of equation 1 to account for a nonlinear response of the piezo:

$$s(t) = \sum_{n=0}^5 m_n \sin(2\pi f_m t + \varphi_{m,n})^n. \quad (3)$$

Figure 2 (a) shows an averaged section of the measured amplitude data (gray) and the resulting fit fit (blue) obtained with equations (2) & (3). As a next step the projection of the scatter signal into the phase quadrature needs to be calculated from equations 2. Here we inserted an additional constant factor in front of the cosine and an additional constant phase shift to compensate e.g. for an imbalanced splitting of the interferometer output and a non-perfect quadrature orientation of the detectors. The new parameters were fitted using the scientific phase data directly, while keeping all other parameters fixed.

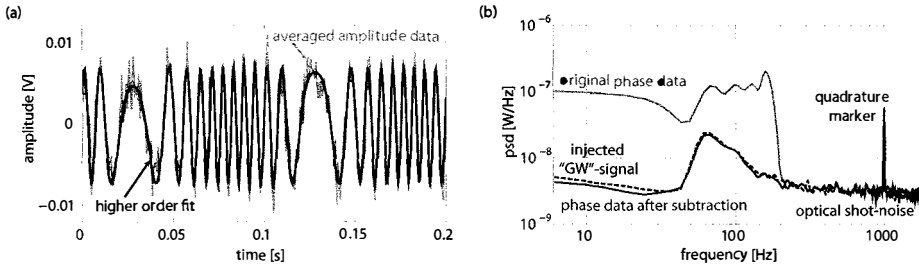


Figure 2 – (a) Original (averaged) time data of BHD2 (gray) with the fitted scatter model (blue). (b) Averaged spectrum showing the recovered GW-signal⁷ after subtraction of the scatter model (solid red) in comparison with the original data (solid gray) and a reference measurement where only the GW-signal was injected and no scattering (dashed black). The frequencies again correspond to the demodulated frequencies from the MHz-range.

In Fig. 2 (b) the phase data after subtraction of the modeled scattering is shown (solid red) in comparison to the original measurement data (solid gray) and a reference measurement (dashed black), recorded while the scattering was blocked and only the simulated GW-signal was being injected. The injected GW-signal could be fully recovered and a sensitivity improvement of more than one order of magnitude was achieved in the scatter limited frequency range below the

demodulated 0.2 kHz. The measurement sensitivity was afterwards limited by optical shot-noise.

In conclusion, we showed in a proof-of-principle experiment that an additional readout of the orthogonal amplitude quadrature of an interferometer signal can be utilized to remove stray light induced disturbances and thereby increase the phase sensitivity of the device. Although the scatter source and model used here are quite simple, they reproduce the basic structure of typical disturbance signals as observed in GW-detectors⁶.

Copyright notice: "Sensitivity improvement of a laser interferometer limited by inelastic back-scattering, employing dual readout" M. Meinders and R. Schnabel, *Class. Quantum Grav.* 32, 195004 (2015). "This article was first published in Classical and Quantum Gravity by IOP Publishing, which maintains the Version of Record."

Acknowledgments

This work was supported by the Deutsche Forschungsgemeinschaft (Sonderforschungsbereich Transregio 7, project C8) and by the International Max Planck Research School for Gravitational Wave Astronomy (IMPRS-GW).

References

1. B. P. Abbott *et al.*, LIGO: the laser interferometer gravitational-wave observatory. *Rep. Prog. Phys.* **72**, 076901 (2009).
2. I. Fiori *et al.*, Noise from scattered light in Virgo's second science run data. *Class. Quantum Gravity* **27**, 194011 (2010)
3. D. J. Ottaway, P. Fritschel and S. J. Waldman, Impact of upconverted scattered light on advanced interferometric gravitational wave detectors, *Opt. Express* **20**, Issue 8, 8329-8336 (2012)
4. T. Ballinger (for the LIGO Scientific Collaboration and the Virgo Collaboration), A powerful veto for gravitational wave searches using data from Virgo's first scientific run. *Class. Quantum Grav.* **26**, 204003 (2009)
5. S. Steinlechner, J. Bauchrowitz, M. Meinders, H. Müller-Ebhardt, K. Danzmann and R. Schnabel, Quantum-dense metrology. *Nat. Phot.* **7**, 626-630 (2013)
6. S. Hild, Beyond the First Generation: Extending the Science Range of the Gravitational Wave Detector GEO600. PhD Thesis, 31-32 (2006)
7. Simulated sound of binary neutron stars from the research group of Professor Scott A. Hughes at MIT, http://gmunu.mit.edu/sounds/comparable_sounds/comparable_sounds.html

NEXT GENERATION NONCLASSICAL LIGHT SOURCES FOR GRAVITATIONAL WAVE DETECTORS

S. AST¹, C. BAUNE¹, J. GNIESMER², R. MOGHADAS NIA², A. SCHÖNBECK¹, C. VOLLMER²,
M. MEHMET², H. VAHLBRUCH², H. GROTE², L. KLEYBOLTE¹, A. KHALAIDOVSKI²
and R. SCHNABEL¹

¹*Institut für Laserphysik und Zentrum für Optische Quantentechnologien
Luruper Chausse 149, 22761 Hamburg, Germany*

²*Institut für Gravitationsphysik der Leibniz Universität Hannover, Max-Planck Institut für
Gravitationsphysik (Albert-Einstein-Institut)
Callinstrasse 38, 30167 Hannover, Germany*



The worldwide network of laser interferometric gravitational-wave detectors is currently in an upgrade phase and will most likely detect gravitational waves within the next few years. Their strain sensitivity will be limited by photon shot noise over a large frequency band. A measurement beyond the shot noise level has already been accomplished via injecting squeezed vacuum states of light into the interferometers. In this proceeding, I review the current status in developments for the next-generation squeezed-light sources for future gravitational-wave detectors. A newly designed doubly-resonant squeezed light source is discussed, as well as squeezed light generated at the wavelengths of 1550 nm and 532 nm. Furthermore, high-efficiency second harmonic generation of laser light for gravitational wave detectors will be presented. The injection of squeezed light as a key technology is well on schedule for improving the sensitivity of future gravitational-wave detectors.

1 Introduction

Einstein's general theory of relativity predicts that accelerating masses generate gravitational waves (GW). Those GWs are small ripples in space-time and are in principle strong enough to be detected on earth, when originating from cataclysmic astrophysical events such as supernovae explosions or the merger of two black holes¹.

There is a worldwide network of five gravitational wave detectors (GWD) consisting of kilometer scale laser interferometers. They aim at detecting gravitational waves by measuring small differential distance changes between their end test masses (mirrors), which will then give rise to a signal at the output ports of these interferometers. The relative gravitational wave strain sensitivity of GWDs nowadays reaches values in the order of $10^{-23}/\sqrt{\text{Hz}}$ and is limited by photon shot noise over a large frequency band².

The injection of squeezed vacuum states of light is a key technology for improving the sensitivity

in the shot noise limited region for future gravitational wave detectors. The technique was first demonstrated in the British-German detector GEO 600³, where it has continuously been used in “science mode” from 2011-2015 with a duty cycle of 85 % and an average nonclassical noise suppression of 3 dB⁴. Squeezed light injection was also already tested in the LIGO Hanford detector⁵ and will, most likely, at some point be implemented in all ground-based gravitational wave detectors. In the following chapters, I will give an overview of new developments in squeezed light sources for future gravitational wave detectors.

2 Potential improvements for the GEO 600 squeezed light source

The laser interferometer GEO 600 is the only GWD currently using squeezed light to enhance the sensitivity in regular science mode. Its squeezed light source consists of one main laser and two auxiliary lasers (Nd:YAG NPRO at 1064nm), phase locked to the main laser of GEO 600. The main laser of the squeezed light source is pumping a second harmonic generation cavity to generate light at 532 nm. This field acts as a pump field for the standing-wave squeezing resonator thus generating the squeezed vacuum.

The squeezing source consists of an external mirror and a periodically-poled potassium titanyl phosphate crystal with one high-reflective end coating acting as the second mirror. The cavity length is stabilized to resonance at 1064nm via one auxiliary laser, which is frequency shifted with respect to the main laser. The second auxiliary laser is also frequency shifted and is used to stabilize the phase of the squeezed field with respect to the GEO 600 laser. Those two auxiliary lasers are necessary in the current setup to allow the so called “coherent control” of the squeezed light source, without destroying the squeezed field in the detection band due to technical laser noise⁶. However, a squeezed light source can in principle also be length stabilized to the second harmonic field at 532 nm. This can be achieved by implementing a squeezing resonator, which is doubly-resonant for both the fundamental and the harmonic field. Thereby, one auxiliary laser would become obsolete and the overall experimental setup is simplified. An additional advantage of the doubly-resonant design is the reduction of necessary external pump power for squeezed light generation.

We realized such a doubly-resonant squeezed light source for a fundamental wavelength of 1550 nm using a PPKTP cavity. It consisted of an external mirror with reflectivities $R_{1550} = 85\%$ and $R_{775} = 97.5\%$ as well as a high-reflective coating for both wavelengths on the end surface of the nonlinear crystal. The squeezing resonator was stabilized via the Pound-Drever-Hall technique using the second harmonic pump field at 775 nm for the squeezed light measurements. First results showed a nonclassical noise suppression of around 10.2 dB at 1 MHz sideband frequency and 7.1 dB at 130 kHz sideband frequency. The decrease in squeezing at kilo Hz was mainly due to the higher dark noise of the homodyne detector measuring the squeezed field at these frequencies. The use of sophisticated electronics, and the reduction of parasitic stray light already employed in the GEO 600 squeezing source, will possibly allow a measurement of 10 dB squeezing in the gravitational-wave detection band using our doubly-resonant squeezer. This design will probably simplify the experimental set-up of the squeezed-light source for future gravitational-wave detectors. Furthermore, the wavelength of 1550 nm is advantageous in a cryogenically-cooled interferometer, which will be discussed in the next chapter.

3 Squeezed light sources at 1550 nm for third generation Gravitational-Wave Detectors

The third generation of gravitational-wave detectors is already in the design phase and aims at performing astronomy via gravitational wave signals. One of the proposed detectors, the Einstein Telescope, is designed to have cryogenically cooled test masses to suppress coating thermal noise in the 50-80 Hz region⁷. This cryogenical cooling demands a change of the test mass material,

which is currently fused-silica, to another material, for example to silicon. This is due to the fact that the mechanical quality factor of fused silica is decreasing at cryogenic temperatures, whereas the quality factor of silicon is increasing at low temperatures. The absorption of silicon at the regularly used wavelength of 1064 nm is, however, much too high for the proposed laser powers in the MW range. This demands the use of a new laser wavelength, for example 1550 nm, for the interferometer. Therefore, the third generation gravitational-wave detectors will need squeezed light sources operating at 1550 nm, which were not yet available with high squeezing factors in the gravitational-wave detection band.

We set up an experiment to generate strongly squeezed light at 1550 nm in the kHz regime using a PPKTP crystal as the nonlinear medium⁸. The squeezing resonator consisted of a piezo-actuated external end mirror with a reflectivity of $R_{1550} = 90\%$ for the squeezed wavelength as well as $R_{775} < 4\%$ for the harmonic pump field and a high-reflective coating on the nonlinear crystal for both wavelengths. A homodyne detector was used to measure the squeezed field with a nonclassical noise suppression of 12.3 dB at 5 MHz sideband frequency. The squeezing strength was limited by around 3.5% of optical loss and about 0.66° of phase noise in the experiment. In the audio frequency band from 1.5-80 kHz a nonclassical noise suppression of around 5 dB at 2 kHz as well as about 11.4 dB from 20-80 kHz was obtained without employing the coherent control scheme typically used in gravitational-wave detectors⁶. This coherent control scheme is compatible with the aforementioned squeezing resonator and will probably enable the detection of 12.3 dB of squeezing over the whole third generation GWD detection band from 1 Hz to 10 kHz at 1550 nm.

4 High-efficiency frequency doubling and squeezed light at visible wavelengths

There are design studies for space-born gravitational-wave detectors, which aim to avoid seismic and newtonian noise currently limiting the sensitivity of ground-based detectors. The Japanese proposal called DECIGO will enable measurements of GWs in the low frequency band from roughly 0.1-100 Hz⁹. Its design is similar to ground-based detectors, although it is meant to use a frequency doubled Nd:YAG laser resulting in a wavelength of 532 nm for the interferometer. Since power consumption is critical in space missions, the reduced wavelength allows the same sensitivity as a 1064 nm laser, but with half the power. This approach relies on a highly efficient frequency doubling of the main laser, which was already realized at 1064 nm with 90% conversion efficiency in a recent experiment¹⁰. We furthermore increased the conversion efficiency to 95% in an experiment using the wavelength of 1550 nm¹¹.

The experiment used a 1550 nm laser which was converted in a hemilithic PPKTP cavity employing an external mirror and a high-reflective coating on one end surface of the crystal. The conversion efficiency was determined by measuring the relative pump depletion of the 1550 nm field in reflection of the cavity. This method showed an external conversion efficiency of 95% with an error as small as 1% mostly consisting of the change in impedance matching of the resonator. A second measurement with a power meter compared the powers of the generated 775 nm light with the initial 1550 nm light. The resulting conversion measurement was consistent with the pump depletion method, but showed a considerably higher error around 6%. The total external conversion efficiency was limited mainly by insufficient pump power for the given cavity design as well as by the non-perfect mode-matching of around 97.5% in the experiment. The experimental realization of a second harmonic generation cavity with an efficiency near unity is an important step towards the frequency doubling for space-born GWDs.

The generation of squeezed light at visible wavelength such as 532 nm for DECIGO is more challenging than generating squeezed light in the infrared regime. The reason is that the pump field for an optical parametric amplifier generating the squeezing at 532 nm would demand a wavelength of 266 nm as a pump field. However, all currently available nonlinear crystals show

a high absorption in the ultra-violet regime. We experimentally realized a squeezed light source at 532 nm by frequency converting a squeezed field from 1550 nm to 532 nm via sum-frequency generation, pumped with a strong coherent field at 810 nm in a nonlinear PPKTP cavity¹². The conversion efficiency of the sum-frequency generation was well above 85 %, which allowed the detection of around 5 dB of nonclassical noise reduction at 532 nm from 2-10 MHz sideband frequency. The squeezing value was limited by a total optical loss of 27 % with the highest loss contribution being the up-conversion efficiency. A sub-shot noise sensitivity was demonstrated with a Mach-Zehnder interferometer which complementarily verifies the compatibility of up-converted squeezed states in quantum metrology.

Acknowledgments

The authors acknowledge support from the Deutsche Forschungsgemeinschaft (DFG), the international Max-Planck research school on gravitational wave astronomy (IMPRS-GW) and the cluster of excellence QUEST.

References

1. B S Sathyaprakash and B F Schutz. Physics, astrophysics and cosmology with gravitational waves. *Living Reviews in Relativity*, 12(2), 2009.
2. The Virgo Collaboration The LIGO Scientific Collaboration. Sensitivity achieved by the ligo and virgo gravitational wave detectors during ligo's sixth and virgo's second and third science runs. *arXiv:1203.2674*, 2012.
3. LIGO Scientific Collaboration. A gravitational wave observatory operating beyond the quantum shot-noise limit. *Nature Physics*, 7(12):962–965, 2011.
4. H Grote, K Danzmann, KL Dooley, R Schnabel, J Slutsky, and H Vahlbruch. First long-term application of squeezed states of light in a gravitational-wave observatory. *Physical review letters*, 110(18):181101, 2013.
5. LIGO Scientific Collaboration. Enhanced sensitivity of the ligo gravitational wave detector by using squeezed states of light. *Nature Photonics*, 7(8):613–619, 2013.
6. H Vahlbruch, S Chelkowski, B Hage, A Franzen, K Danzmann, and R Schnabel. Coherent Control of Vacuum Squeezing in the Gravitational-Wave Detection Band. *Phys. Rev. Lett.*, 97:11101, 2006.
7. M Punturo, M Abernathy, F Acernese, B Allen, Nils Andersson, K Arun, F Barone, B Barr, M Barsuglia, M Beker, et al. The einstein telescope: a third-generation gravitational wave observatory. *Classical and Quantum Gravity*, 27(19):194002, 2010.
8. M Mehmet, S Ast, T Eberle, S Steinlechner, H Vahlbruch, and R Schnabel. Squeezed light at 1550 nm with a quantum noise reduction of 12.3 dB. *Optics express*, 19(25):25763–72, 2011.
9. S Kawamura, N Ando, M Seto, S Sato, T Nakamura, K Tsubono, N Kanda, T Tanaka, J Yokoyama, I Funaki, et al. The japanese space gravitational wave antenna: Decigo. *Classical and Quantum Gravity*, 28(9):094011, 2011.
10. T Meier, B Willke, and K Danzmann. Continuous-wave single-frequency 532 nm laser source emitting 130 W into the fundamental transversal mode. *Optics Letters*, 35:3742–3744, 2010.
11. S Ast, R Moghadas Nia, A Schönbeck, N Lastzka, J Steinlechner, T Eberle, M Mehmet, S Steinlechner, and R Schnabel. High-efficiency frequency doubling of continuous-wave laser light. *Optics letters*, 36(17):3467–9, 2011.
12. C Baune, J Gniesmer, A Schönbeck, C E Vollmer, J Fiurášek, and R Schnabel. Quantum metrology with frequency up-converted squeezed vacuum states. *arXiv:1503.02008*, 2015.

Quantum Sensors in Space - Design Challenges for Spacecraft and Instruments

A. HESKE

*European Space Agency, Keplerlaan 1,
2201 AZ Noordwijk, The Netherlands*

For fundamental physics experiments, such as probing various aspects of Einstein's Equivalence Principle or detection of gravitational waves, space missions offer a number of advantages compared to ground-based laboratory settings. Designing an instrument to fly on a satellite requires particular attention to a number of aspects for the instrument hardware, which are inherent to space missions. To arrive at a viable mission and spacecraft design, the science performance requirements and instrument needs have to be analyzed, drivers for the mission design need to be identified and numerical simulations of measurement performance have to be run. This iterative process of maximizing the science return while optimizing the instrument and spacecraft designs will be illustrated with examples from a study of the fundamental physics mission STE-QUEST - comprising atom interferometry and clock comparisons - carried out at the European Space Agency.

1 Introduction

Quantum sensors, devices which exploit quantum effects, such as entanglement or superposition, achieve highly sensitive measurements of physical parameters. They are employed in accelerometers, gravimeters, atomic clocks and cold atom interferometers. Science applications range from geodesy, time and frequency metrology to fundamental physics experiments. This paper describes the steps required to bring such a fundamental physics experiment employing quantum sensors from a laboratory setting into space.

2 Call for Space

2.1 Advantages of Space

In laboratory settings on ground, experiments are usually easily accessible and fine tuning and modifications can be made to the hardware at virtually any time. Drawbacks for such fundamental physics experiments are the Earth gravity field, the noisy seismic environment and the short interaction times. Space laboratories on the other hand offer a number of advantages, and to exploit the ultimate sensitivity of quantum sensors and to push the measurement accuracy beyond what can be reached on ground, space becomes even a necessity. For fundamental physics experiments space ensures:

- Infinitely long 'free-fall' times and long interaction times
- Large variations of gravitational potential and large velocities and velocity variations
- Huge free-propagation distances and variations in altitude
- Quiet environmental conditions and absence of seismic noise

2.2 Demands on Instruments

Designing and building an experiment to fly on a spacecraft requires particular attention to a number of aspects for the instrument hardware, which are inherent to space missions.

Autonomy and Operability: In orbit, the instrument has to carry out routine measurements and calibrations autonomously, through pre-defined measurement sequences and without frequent intervention from ground.

Radiation Environment: The instrument has to withstand a harsh radiation environment, which severely degrades the performance of the instruments' components with time, if no special measures are taken, e.g. considering appropriate shielding.

Launcher and Accommodation on Spacecraft: Since the spacecraft has to fit on a launcher with given lift capabilities there are limitations for the instruments on mass, volume and power consumption; in addition, the lift capabilities define the range of potential orbits.

Reliability and Redundancy: Once in orbit, the hardware can obviously no longer be accessed or replaced, and the instrument needs to work reliably for the whole mission duration. This requires an appropriate redundancy concept, to render the instrument minimally susceptible to failures.

Model Philosophy, Qualification and Verification: Considering the aspects described above, all instrument functions and its science performance need to be verified and qualified on ground. Building dedicated models of the instrument, these specific aspects are verified by tests thus ensuring that the instrument will work correctly in orbit, and above all, will survive the launch.

Data packages, Standards and Reviews: Data packages have become an essential part of space instrument development. They describe all aspects of the instrument such as justification of the design and plans for development and testing. The contents of these data packages as well as the design, development and testing of an instrument are governed by a wealth of space standards. Regular reviews are held to track progress and identify potential problems early.

3 Mission Assessment - The Theory

The aim of a space mission assessment is to analyze the science performance requirements and instrument needs in order to arrive at a viable spacecraft and overall mission design. Specific science objectives and requirements are derived from the science goals, followed by definition of mission requirements, which address the mission as a whole, including spacecraft and instrument design, orbit and operations. For definition and design of the actual hardware, engineering requirements are derived, further breaking down the description of the mission components. During the assessment of the engineering requirements it can - almost certainly - occur that for technical or technological reasons some of these requirements can not or only partially be fulfilled. The impact on the science objectives is evaluated, model calculations are run and a trade-off is to be found in terms of science output versus mission complexity and feasibility.

During the mission assessment and determining its feasibility the aspects addressed in Section 2.2 are to be considered together with these two related to programmatics and risks:

Technology Maturity: At the end of a mission definition phase, it is required that the critical functions of an instrument have been verified in a relevant environment. This is to reduce the risk that a low technology maturity leads to substantial delays, due to problems during the instrument development.

Management, Schedule and Funding: Spacecraft development is carried out by an industrial partner under an ESA contract, with a fixed budget and a - usually - a tight schedule, to ensure the target launch date. Instrument development is carried out typically by an international consortium funded through national agencies. An appropriate consortium structure needs to be in place and funding to be secured as to align the instrument development schedule with the industry schedule.

Table 1: Measurement Requirements for STE-QUEST

| | |
|---|---|
| <i>Weak Equivalence Principle Tests</i> | Test of the universality of free fall of matter waves to an uncertainty in the Eötvös ratio lower than 2×10^{-15} |
| <i>Gravitational Red-shift Tests</i> | Sun gravitational red-shift measurement to a fractional uncertainty of 2×10^{-6} Moon gravitational red-shift measurement to a fractional uncertainty of 4×10^{-4} |

4 Mission Assessment - The Case Study

In the framework of the call for future medium-size missions issued in 2010 within the Cosmic Vision program of the European Space Agency (ESA) a three-year study was carried out assessing a fundamental physics mission candidate called the Space Time Explorer - Quantum Equivalence Space Test (STE-QUEST) ¹.

The primary science objectives are to test two aspects of Einstein's Equivalence Principle with quantum sensors to unprecedented accuracy: Gravitational red-shift tests in the Sun and Moon field and Weak Equivalence Principle test. The measurement requirements are given in Table 1.

The payload comprises a dual species Rubidium atom interferometer to test the universality of free-fall of matter waves, a microwave link for simultaneous time and frequency comparisons of two atomic clocks on ground and a GNSS receiver for precise orbit determination, needed for the clock comparisons (see Fig. 1). The requirements on measurement accuracies, performances and pointing are given in Table 2.



Figure 1 – STE-QUEST payload: Physics package of the atom interferometer (left), ground clock comparisons via the on-board microwave link (right).

The drivers for the orbit are a low gravity gradient and large gravitational accelerations around perigee for the atom interferometry and long common-views of ground clocks and large variation of the gravitational potential for the clock comparisons. The resulting reference orbit which fulfills the requirements in Table 2 is a highly elliptical with an apogee of about 50000km, a perigee of 700 to 2000km, an inclination of about 63 deg and a period of 16 hours, as illustrated in Figure 2. Numerical simulations demonstrated that with the measurement accuracies given in Table 2 the science performance (see Table 1) can indeed be reached in a four-year mission.

Assessment of the technology maturity of the payload elements concluded that the lowest risk is associated with the commercial GNSS receiver, a medium risk was identified for the upgrade of the microwave link to higher frequency and the largest risk was considered to be the atom interferometer, since for the dual Rubidium source as well as for the laser system critical functions had not yet been verified on full breadboards.

Under two parallel ESA contracts, industrial studies have been carried out to demonstrate a viable mission and spacecraft design, fulfilling the payload's requirements. Figure 3 shows the

Table 2: Performance and Pointing Requirements for STE-QUEST

| | | | |
|----------------------------|-----------------------|--|-----------------------------------|
| Atom Interferometry | | Instability $(13 \times 10^{-12} m/s^2)/\sqrt{\tau}$ Inaccuracy $< 2 \times 10^{-15}$ Gravitational acceleration $> 3m/s^2$ Gravity gradient $< 2.5 \times 10^{-6} s^{-2}$ Rotations $< 10^{-6} rad/s$ | Inertial pointing (see Fig. 2) |
| Clock Comparisons | <i>Microwave Link</i> | Inaccuracy $< 5 \times 10^{-19}$ Frequency instability $< 5.2 \times 10^{-13}(1s)$ to $< 2.8 \times 10^{-18}(16hrs)$ | Nadir pointing (see Fig. 2) |
| | <i>GNSS Receiver</i> | Position error $2m$ Velocity error $2mm/s$ (both in post-processing) | |
| | <i>Ground Clocks</i> | Inaccuracy 10^{-18} Instability $2.5 \times 10^{-16}/\sqrt{\tau}$ | |

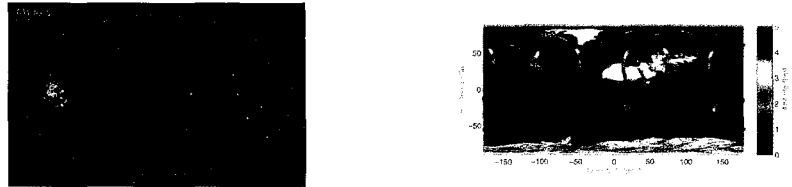


Figure 2 – STE-QUEST orbit and attitude of the spacecraft (left) and the ground track (right).

design solutions from these industrial studies. On the spacecraft side no show-stoppers were identified, and both designs met the required budgets such as mass, power and volume, and with margins, for a launch on a Soyuz rocket.



Figure 3 – STE-QUEST spacecraft. Two design solutions from industrial studies.

5 Outcome and Outlook

The STE-QUEST study showed that such a fundamental physics mission is indeed technically feasible, provided that the technology of the dual species atom interferometer and the upgrades needed for the microwave link can be further pushed to the required maturity needed at the end of a mission definition phase. This in turn requires proper funding for the ongoing experiments to complete bread-boarding and testing of the critical subsystems within the coming years.

References

1. STE-QUEST Team, STE-QUEST Assessment Study Report, ESA/SRE(2013)6, (2013) (<http://sci.esa.int/ste-quest/53445-ste-quest-yellow-book>).

eLISA OPTICAL SENSING DEVELOPMENTS

C.J. KILLOW, M.PERREUR-LLOYD, D.I. ROBERTSON and H. WARD¹
E.D. FITZSIMONS, S. NIKOLOV and D. WEISE²
M. LIESER, S. SCHUSTER, M. TRÖBS, G. HEINZEL and K. DANZMANN³

¹*School of Physics and Astronomy, University of Glasgow, Glasgow, G12 8QQ, UK*

²*Airbus Defence and Space – Space Systems, D-88039, Germany*

³*Max Planck Institute for Gravitational Physics, Albert Einstein Institute, Callinstraße 38, D-30167, Hannover, Germany*



This article summarises an experiment that is underway to demonstrate optical metrology systems that have been identified as being crucial for eLISA. The optical sensing to be used for eLISA metrology is based on that developed for the technology demonstrator mission, LISA Pathfinder. The ground-based experiment described will also benefit from the use of ultra-stable optical benches and will replicate a single link between two spacecraft in a spaceborne gravitational detector. The interferometer will be used to characterise and demonstrate the mitigation of potential noise sources, such as tilt-to-piston coupling.

1 From LISA Pathfinder to a spaceborne gravitational wave detector

The European Space Agency selected “The Gravitational Universe” as the theme for its third ‘L’ class mission¹. eLISA, an evolution of the Laser Interferometer Space Antenna gravitational wave detector, is a mission concept capable of delivering the science for this theme.

The spaceborne gravitational wave detector community now has, based on the development and demonstration of precision optical metrology for LISA Pathfinder^{2,3}, a clear design approach for an eLISA sensing scheme. While this design is now mature a mission such as eLISA requires additional elements due to the increased functionality compared to LISA Pathfinder. This results in a more complex optical topology with, amongst other considerations, flat-top beams and wavefront tilt of the incoming light with respect to the optical benches. A ground-based demonstration of such features is a valuable activity to validate the current design.

The experiment described is being conducted by a team comprising members from the University of Glasgow, Airbus Defence and Space GmbH and the Albert Einstein Institute, Hannover.

2 eLISA interferometry testbed

The experiment will use a testbed to investigate in a representative manner the implications of several metrology design features of eLISA. One key investigation will involve testing of two candidate imaging systems. The relative jitter between a far and receiving spacecraft leads to a variation in the beam angle seen at the receiving spacecraft which results in tilt-to-piston coupling, and this forms a significant part of the eLISA metrology budget. Custom designed imaging systems are part of the proposed solution to suppress this potential noise source to a level of a few picometres/microradian. The testbed will also be capable of performing interferometry tests with: flat-top beams; MHz heterodyne frequencies; active apertures; a range of different photodetectors; and extremely low power (pW) laser beams. These are all situations that will be encountered in spaceborne gravitational wave detector optical metrology.

The strategy being used is to:

- Measure tilt-to-piston coupling factors in a representative interferometer,
- Test the alignment sensitivity and compare the results to predictions, and
- Test different types of imaging system: classical and coherent Gaussian.

The experimental approach is to build two optical benches:

- Construct a Minimal representative eLISA Optical Bench (MOB) and a
- Telescope Simulator (TS) optical bench.

The two optical benches will be coupled using an innovative all-Zerodur® mounting system that has high dimensional stability, with the beams between the two optical benches transmitted and received via periscope optics. This system mimics one link between two eLISA spacecraft. A schematic overview of the optical layout is shown in Figure 1. The precision construction of the optical assemblies was based on the techniques described in⁴ and⁵ and the optomechanical parts are outlined in⁶. Beam angle alignment at the 10's of microradians level is needed, resulting in some optical components having sub-micrometer position tolerances.

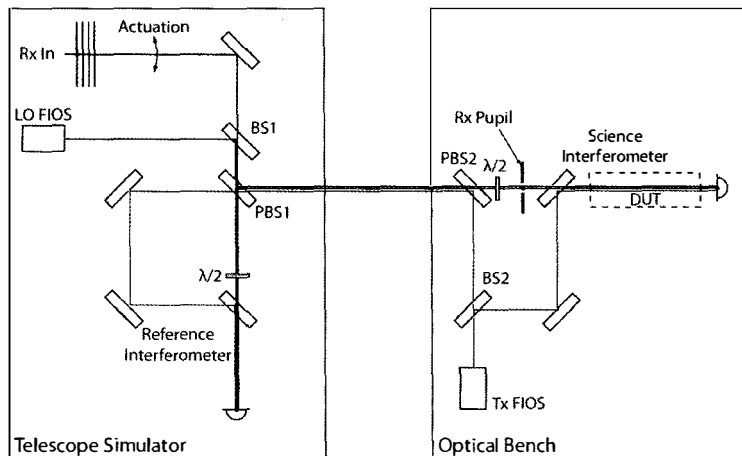


Figure 1 – Schematic optical layout of the Telescope Simulator and the Minimal Optical Bench. 'Rx' is representative of a received beam from a far spacecraft, 'LO' is the local oscillator, 'Tx' represents the beam to be transmitted to the far spacecraft and 'FIOS' is an ultra-stable fibre-coupled input beam. Rx and Tx are phase-locked to LO, with different offset frequencies, at the reference interferometer. Reproduced from⁷.

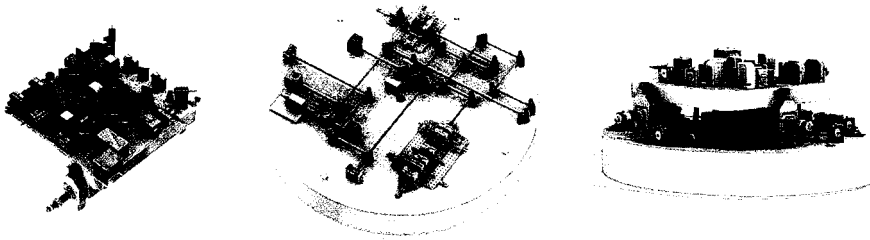


Figure 2 – CAD of Telescope Simulator (left), Minimal Optical Bench (middle) and the benches in their coupled configuration (right). The Minimal Optical Bench baseplate is 580mm diameter for scale.

CAD screenshots of the designed optical benches can be seen in Figure 2 and photographs of a recent state of the benches in Figure 3.

The TS produces a clean ‘top hat’ beam – Rx in – with flat phasefront and intensity profile, as would be the case when a small fraction of the beam from a far eLISA spacecraft is intercepted by the telescope. This top hat beam is directed to the receive aperture on the MOB by two actuated mirrors. The wavefront of this beam can be tilted with a range of $\pm 500 \mu\text{rad}$ around the receive aperture. A second beam which has a Gaussian profile – from LO FIOS – can be used in place of the Rx beam to enable alignment of the two benches. The LO beam path is stable with no actuated components.

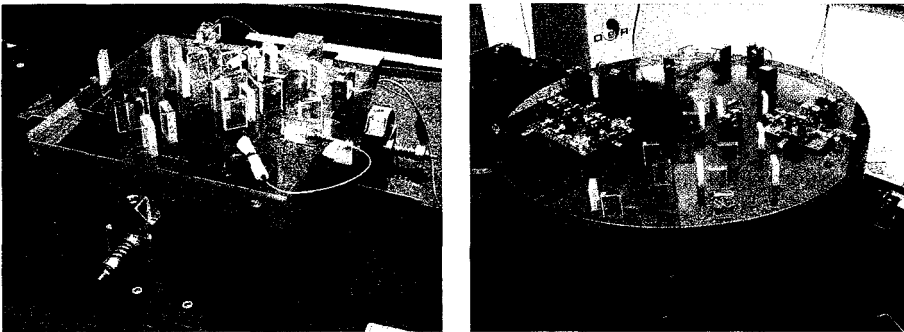


Figure 3 – Photographs of the Telescope Simulator (left) and the Minimal Optical Bench (right) during construction. When these photographs were taken all optical components were in place and the optomechanical hardware integration was in progress.

The MOB is a simplified version of a LISA-type optical bench with one interferometer which can be representative of both the science and test mass readout interferometers. It has an integrated optical alignment reference to aid in the critical co-alignment of the TS and MOB. Its design provides as much space as possible around the imaging systems and internal pupil to maximise the flexibility of the testbed. The imaging systems are interchangeable.

The optical benches are now complete and are currently being installed in a thermally stable vacuum environment ahead of the testing phase.

3 Technology development and transfer

This work is essential for ensuring a successful spaceborne gravitational wave mission, but it also has wider-reaching applicability. Work is ongoing in parallel to make the technologies used in this field accessible to other precision optical measurement fields, *e.g.*:

- Geodesy missions where higher precision monitoring of inter-spacecraft displacements is desirable;
- Spaceborne atom interferometry missions needing stable, complex optical assemblies that are flight worthy, like STE-QUEST⁸;
- Other fundamental science missions requiring space worthy optical benches, like MAQRO⁹;
- Earth observation missions using optical signals;
- Applications, on ground or in space, that require precision optical assemblies that are both stable and robust.

To this end work is ongoing to further refine and improve the optical metrology technologies, for example by mechanising the component placement and joining process.

Acknowledgments

This research was supported through awards from the European Space Agency. Glasgow also acknowledge support from the United Kingdom Space Agency (UKSA) and the University of Glasgow. AEI and Airbus acknowledge support by the German Aerospace Center (DLR). The work is supported by the Federal Ministry for Economic Affairs and Energy based on a resolution of the German Bundestag (FKZ 500Q0601, 500Q1301). CK wishes to acknowledge support from the Scottish Universities Physics Alliance.

References

1. K Danzmann *et al.*, *The Gravitational Universe*. (<http://elisascience.org/whitepaper>, 2014).
2. M Armano *et al.*, *The LISA Pathfinder Mission*. *Journal of Physics: Conference Series* **610**, 012005 (2015).
3. DI Robertson, ED Fitzsimons, CJ Killow, M Perreur-Lloyd, H Ward, J Bryant, AM Cruise, G Dixon, D Hoyland, D Smith and J Bogenstahl, *Construction and testing of the optical bench for LISA Pathfinder*. *Class. Quantum Grav.* **30**, 085006 (2013).
4. CJ Killow, ED Fitzsimons, J Hough, M Perreur-Lloyd, DI Robertson, S Rowan and H Ward, *Construction of rugged, ultra-stable optical assemblies with optical component alignment at the few microradians level*. *Appl. Opt.* **52** (2), pp177-181 (2013).
5. ED Fitzsimons, J Bogenstahl, J Hough, CJ Killow, M Perreur-Lloyd, DI Robertson, and H Ward, *Precision absolute positional measurement of laser beams*. *Appl. Opt.* **52** (12), pp2527-2530 (2013).
6. M Perreur-Lloyd *et al.*, *Sub-system mechanical design for an eLISA optical bench*. *Journal of Physics: Conference Series* **610**, 012032 (2015).
7. E Fitzsimons *et al.*, *Detailed Design of Tilt-to-Piston Investigation*. Project document (unpublished) LOB-TN-14-01-ASD, 24th April 2015.
8. The STE-QUEST Science Study Team, *STE-QUEST Space-Time Explorer and Quantum Equivalence Principle Space Test*. Assessment Study Report ESA/SRE(2013)6.
9. Rainer Kaltenbaek, *et al.*, *Macroscopic quantum resonators (MAQRO): 2015 Update*. arXiv:1503.02640.

MEASUREMENT OF THE GRAVITATIONAL REDSHIFT EFFECT WITH RADIOASTRON SATELLITE

A.V. BIRIUKOV ¹, V.L. KAUTS ^{1,2}, D.A. LITVINOV ³, N.K. PORAYKO ³, V.N. RUDENKO ³

¹ *Astro Space Center, Lebedev Physical Institute, Moscow, Russia*

² *Bauman Moscow State Technical University, Moscow, Russia*

³ *Sternberg Astronomical Institute, Moscow State University, Moscow, Russia*

⁴ *Lomonosov Moscow State University, Sternberg Astronomical Institute, Universitetsky pr. 13, 119991 Moscow, Russia)*

RadioAstron satellite admits in principle a testing the gravitational redshift effect with an accuracy of better than 10^{-5} . It would surpass the result of Gravity Probe A mission at least an order of magnitude. However, RadioAstron's communications and frequency transfer systems are not adapted for a direct application of the non relativistic Doppler and troposphere compensation scheme used in the Gravity Probe A experiment. This leads to degradation of the redshift test accuracy approximately to the level 0.01. We discuss the way to overcome this difficulty and present preliminary results based on data obtained during special observing sessions scheduled for testing the new techniques.

1 Introduction

Phenomenon of the "photon gravitational red shift" was predicted by Einstein in the paper ¹ and then discussed in ², i.e. much before the creation of General Relativity (1916). Further it was involved in the number of three famous effects of GR having been got the experimental confirmation ³. However as it is accepted now the 'photon gravitational red shift' lies in the foundation of GR composing its crucial experimental basis. In particular the red shift effect can be considered as Equivalence Principle Test for photon: i.e. it provides the information concerning the acceleration of photons in gravitational fields ⁴. Thus a precise measurement of this effect with growing accuracy could define limits of GR validity and stimulate a new physics search.

The Einstein's formulation of the phenomenon consists in the statement that "any clock marches slowly in the gravitational field". So the frequency of atomic clock depends on the value of gravitational potential in the place of its location. The terminology "red shift" has historical origin associated with the first observation of the effect⁵ through the measurement of the hydrogen spectral lines in the light coming from the white dwarf Sirius B. On the contrary in the Earth gravity field a clock lifted at some altitude has to show a blue shift. Other interpretation of the "electromagnetic gravitational red shift" effect as a loss of the photon energy while traveling through the gravitational field is not completely correct and could lead to contradictions ⁶.

At present time the most precise test of "red shift" effect was performed in the mission of Gravity Probe A (GP-A) of 1976, in which the frequencies of two hydrogen masers clock were compared-one on the Earth and the other on board of a rocket with a ballistic trajectory of 10^4 km

apogee. The experiment⁷ confirmed the value of frequency shift predicted by GR with accuracy 1.4×10^{-4} . There are several planning experiments aimed at improving the currently achieved accuracy by 2-4 orders of magnitude. The European Space Agency's ACES mission⁸ intends to install two atomic clocks, an H-maser and the cesium fountain clock (complex PHARAO), onto the International Space Station. The active phase of the mission currently is being scheduled for 2016. Because of the ISS's low orbit, the gravitational potential difference between the ground and the on-board clocks will be only 0.1 of that achievable with a spacecraft at a distance of $\sim 10^5$ km from the Earth. Nevertheless, predicted accuracy, which is expected to be reached 10^{-16} in microgravity, provides for measurement accuracy at the level of 10^{-6} .

Another European initiative is STE-QUEST, a candidate mission for the ESA Cosmic Vision M4 program, with a goal to test RS with $10^{-7} - 10^{-8}$ accuracy in the gravitational field of the Earth. Additionally, a special choice of the orbit, which will allow the spacecraft to simultaneously communicate with tracking stations at different continents, will provide opportunities for testing the "red shift" in the field of the Sun. The accuracy of this type of experiment⁹, not requiring a frequency standard on board the spacecraft, is speculated to reach $\sim 10^{-6}$.

Meanwhile the experiment with a potential of testing the "red shift" effect in the field of the Earth with 10^{-6} accuracy is currently being carried out as a part of the mission of the space radio telescope (SRT) "Radioastron" (RA)¹⁰. The possibility for such measurement came with the decision to add a space hydrogen maser (SHM) frequency standard to the scientific payload of the mission's spacecraft.

However the modes of the high-data-rate radio complex (RDC) at this satellite do not allow independent synchronization of the frequencies of the links used for transmission of tone signals, i.e., 7.2 GHz (up) and 8.4 GHz (down), and the 15 GHz carrier of the data downlink (used for observational and telemetry data transmission). It is possible, however, to independently synchronize the carrier (15 GHz) and the modulation (72 or 18 MHz) frequency of the data downlink. This mixed, or "Semi-coherent," mode of synchronization hasn't been used in astronomical observations so far. As our analysis shows, for this mode it is possible to devise a compensation scheme, which is similar to the one used by the GP-A experiment, and which results in the contributions of the non relativistic Doppler effect and the troposphere eliminated in its output signal. The accuracy of the experiment based on this compensation scheme can reach the limit 1.8×10^{-6} part of the total gravitational frequency shift, set by the frequency instability and accuracy of the ground and space H-masers (GHM, SHM)¹¹.

2 Parameters and operational regimes of RA

The RA satellite has a very elliptical orbit which changes under the Moon's gravity influence. Namely: the perigee varies in the region $10^3 - 80 \times 10^3$ km; apogee in $(280 - 350) \times 10^3$ km; the orbital period varies in the range 8 - 10 days; the amplitude modulation of the gravitational frequency shift effect occurs into the interval $(0, 4 - 5.8) \times 10^{-10}$. The satellite and land tracking station (Puschino ASC) have in operation equivalent hydrogen frequency standards (production of the national corporation "Vremya-Che") with the following characteristics: Allan variance under average time 10 - 100 sec is 3×10^{-14} , under $10^3 - 10^4$ sec - 3×10^{-15} ; the frequency drift was estimated as 10^{-15} per day (and 10^{-13} per year). The SHM output signal is transmitted to a TS by the both radio data and radio science complexes (RDC, RSC), which includes two transmitters at 8.4 and 15 GHz, and a 7.2 GHz receiver. The frequencies of the signals used both complexes, can be synthesized either from the reference signal of the SHM or from the 7.2 GHz output of the on-board receiver, which receives the signal transmitted by the TS and locked to the ground H-maser (GHM). The mode of the on-board hardware synchronization significantly affects not only the achievable accuracy but the very possibility of the gravitational redshift experiment.

In order to compare the output frequencies of a ground f_e and a space-borne f_s atomic standards, one needs to transmit any (or both) of these signals by means of radio or optical links. The comparison thus becomes complicated by the necessity of extracting a small gravitational

frequency shift from the mix of accompanying effects, such as resulting from the relative motion of the SC and the TS, also the signal propagation through media with non-uniform and time varying refractive indexes. The total frequency shift of a signal, propagating from the SC to the TS, is given by the following equation:

$$f_{\downarrow s} = f_s + \Delta f_{\text{grav}} + \Delta f_{\text{kin}} + \Delta f_{\text{instr}} + \Delta f_{\text{media}}, \quad (1)$$

where $f_{\downarrow s}$ is the frequency of the signal, as received by and measured at the TS, Δf_{grav} is the gravitational frequency shift, Δf_{kin} is the frequency shift due to the SC and TS relative motion, Δf_{media} is the propagation media contribution (ionospheric, tropospheric, interstellar medium), Δf_{instr} encompasses various instrumental effects, which we will not consider here. The Eq. (1) can be used to determine the gravitational frequency shift Δf_{grav} . Indeed, $f_{\downarrow s}$ is measured at the TS, Δf_{kin} can be evaluated from the orbital data (assuming special relativity is valid), Δf_{media} can be found from multi-frequency measurements (for the ionospheric and interstellar media contributions) and meteorological observations (for the tropospheric one), estimation of Δf_{instr} involves calibration of the hardware and a study of the transmitting, receiving and measuring equipment noise. The value of f_s is unobservable and, therefore, presents a certain difficulty. It is convenient to express it in terms of the frequency of the ground-based standard f_e and an offset Δf_0 :

$$f_s = f_e + \Delta f_0. \quad (2)$$

The problem of f_s (or Δf_0) being not measurable directly has different solutions depending on the type of the frequency standards used and the possibility of varying the gravitational potential difference ΔU between them.

The two principal but typical operation modes were foreseen and realized in ‘‘Radioastron’’ satellite so called ‘‘H-maser’’ and ‘‘Coherent’’.

a) H-maser mode.

This is the main synchronization mode used in radio astronomical observations. In this mode the SHM signal is used to synchronize both the RDC and RSC frequencies. The frequency f_s of the signal, transmitted by the DRC, and frequency $f_{\downarrow s}$ received at a TS are related by the equation (1) where the $\Delta f_{\text{media}} = \Delta f_{\text{trop}} + \Delta f_{\text{ion}}$ presented by sum of troposphere and ionosphere shifts. The kinetic shift having the main contribution from Doppler shift depends on radial velocity of SC in respect of TC $\dot{D}/c = (\mathbf{v}_s - \mathbf{v}_e)\mathbf{n}/c$, where \mathbf{n} - the unit vector of the view line.

The kinematic, gravitational and tropospheric contributions are proportional to the transmitted signal frequency, while the ionospheric contribution is inversely proportional to it. The availability of the 2-frequency link (15 and 8.4 GHz) provides for accurate estimation of the ionospheric term, but the contributions of the other effects cannot be separated from each other and need to be calculated from ballistic data. This causes a large error of the Doppler effect determination and thus degrades the experiment accuracy of the red shift measurement to the value on the order of 1%.

b) Coherent mode.

The ‘‘Coherent’’ mode of the on-board hardware synchronization, also known as the phase-locked loop mode. Here a sinusoidal signal of 7.2 GHz frequency, synchronized to the GHM, is sent to the SC, where it is received by the RDC and used to lock the frequencies of the RSC. All the signals transmitted to the TS by the RDC are also phase-locked to the received 7.2 GHz signal: the 8.4 GHz tone, the 15 GHz carrier of the data transfer link, and, lastly, its 72 (or 18) MHz modulation frequency. The ‘‘Coherent’’ mode alone is of no interest to the redshift experiment, because, it is obvious that the received signal has no information about the gravitational redshift effect. However, in the case of simultaneous operation of the one and two-way communication links, their signals can be combined by means of a special radio engineering compensation scheme⁷, which outputs a signal containing information about the gravitational redshift but, at the same time, free from the 1st-order Doppler and tropospheric contributions. It is also possible to compensate for the ionosphere but only in case of a special selection of the ratios of the up and

down link frequencies. Such compensation scheme, first used in the GP-A mission, cannot be applied directly in the case of “RadioAstron,” because, the mode of independent synchronization of the carrier frequencies of the RDC links is not supported.

Coming back to the “H-maser mode” let’s evaluate a potential sensitivity of the redshift measurement with Radioastron.

During the favorable periods for the gravitational experiment are such that the perigee height is at minimum, (the winter-spring of 2014 and 2016), when it is equal to 1.5×10^3 km, so that $(U_{op} - U_{per})/c^2 = 5.5 \times 10^{-10}$. The frequency drift of used standards is enough small 1×10^{-15} per day – less then its frequency instability under the 10^3 sec of average time 3×10^{-15} . Approximately one day is needed for the RA to travel from perigee to a distance where the gravitation potential is almost equal to its value at apogee. Therefore, the accuracy of a single modulation-type experiment is limited not by the frequency drift of either the SHM or the GHM but by the H-maser frequency instability. Thus supposing the compensation of coherent hindrances (Doppler, troposphere, ionosphere), we obtain the following limit for the total relative accuracy of a single experiment to determine the value of the gravitational redshift modulation in the favorable period of low perigee: 5.5×10^{-6} .

The important advantage of the “RadioAstron” mission, as compared to GP-A, lies in the possibility of conducting the experiment multiple times. Statistical accumulation of measurement results provides reduction of the random error contributions by a factor of \sqrt{N} , where N is the number of measurements performed. For $N = 10$, in particular, the contribution of the frequency instability becomes equal to the one of the frequency drift. Since the drift causes a systematic error, accumulating data any further will not improve the experiment accuracy. Then, we arrive at the following limit for the accuracy of the modulation-type gravitational redshift experiment with “RadioAstron”: 1.8×10^{-6} .

3 Mixed regime “semi-coherent” and preliminary result

The new approach to the compensation scheme for Radioastron specific was proposed in the paper ¹¹. There is the possibility to synchronize the 8.4 and 15 GHz frequencies of the RDC transmitters to the GHM-locked 7.2 GHz tone (the “Coherent” mode) of RDC, while the RSC is synchronized to any of the on-board frequency standards. This “Semi-coherent” mode turns out to be the most suitable for the gravitational experiment. Indeed, just like in the “Coherent” mode, the net gravitational redshift is canceled in the received 8.4 GHz tone and in the carrier of the 15 GHz data link. However, in contrast to the “Coherent” mode, the modulation frequency of the data link is locked not to the 7.2 GHz uplink but to the SHM signal, hence all components of the data link signal spectrum, except for the carrier, are influenced by the gravitational effect. As it is shown in the paper ¹¹, the compensation scheme can be arranged in such a way that all disturbing effects are transferred to the modulation frequency scale too. Moreover, just like in GP-A, it turns out to be possible to eliminate the contributions of the 1st-order Doppler and tropospheric effects as well. The ionospheric effect is cancelled through the two frequency measurement.

Below we present two picture as an illustration of the Radioastron operation in the “semi Coherent” mode.

At the Fig. 1 (a) result of the carrier frequency (8.4 GHz) measurement derived from the data received at the Onsala Radiotelescop (Sweden). The width of the line is estimated as 0.0003 Hz after the complex filtration algorithm used in the radio-astronomical experiments for moving space apparatus ¹². This result provides the accuracy of alone red shift measurement at the level 6×10^{-5} (the absolute magnitude of the red shift is 5 Hz).

At the Fig. 1 (b) the time evolution of the carrier (15 GHz) and two sidebands is presented as it was recorded at the Puschino tracking station. It demonstrates the similar (coherent) time perturbations for central line and sidebands, despite of the fact they were synchronized from different (land and board) standards.

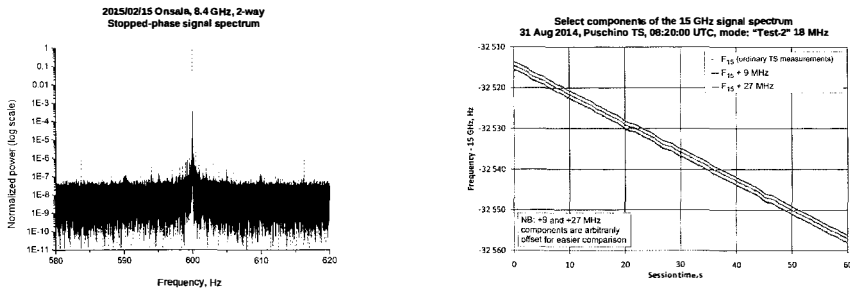


Figure 1 – a) Result of the carrier frequency (8.4 GHz) measurement, b) The time evolution of the carrier (15 GHz) and two sidebands

In the final remark we would like to name the principle Institutions in Russia performing hard work of accompany the Radioastron mission; in that number are: the Astro Space Center of the Lebedev Physical Institute RAS, Sternberg Astronomical Institute MSU, Keldysh Institute for Applied Mathematics RAS and Lavochkin Scientific and Production Association. There are also several world Institutions interested in gravitational program of the mission, they are: the York University (Canada) (N. Bartel, W. Cannon), Joint Institute for VLBI in Europe (Netherlands) (L. Gurvits, S. Pogrebenko, G. Cimo), University of California in Santa-Barbara (USA) (C. Gwinn, M. Johnson), Hartebeesthoek Radio Observatory (South Africa) (M. Bietenholz). Periodically the observational service is carried out by the radio telescope observatories in Green Bank (USA), Effelsberg (Germany), Onsala (Sweden) and others.

Acknowledgments

Authors would like gratitude the main ideologist and leader of the Radioastron mission Nikolai Kardashev (director ASC) for permanent attention and assistance to the gravitational group of the scientific program RA.

References

1. A. Einstein ,Jahrb.Radioaktivitat Elektronik **4**, 411 (1907).
2. A. Einstein ,Ann. Phys. (Leipzig) **35**, 898 (1911).
3. A. Einstein , Ann. Phys. (Leipzig) **49**, 769 (1916).
4. C.Misner, K.Thorne,J.A.Wheeler, *Gravitation*, 7.2 - 7.5, 25.4, 38.5 Freeman and Company, San Francisco 1973.
5. M.G.Adams. Proc.Nat.Acad.Sci.(Wash.) **11**, 382 (1925).
6. L.B. Okun, K.G. Selivanov, V.L. Telegdi,Soviet Physics Uspekhi **42**, 1045 (1999)
7. R.F.C.Vessot, M.W.Levin, E.M.Mattison *et al*, Phys. Rev.Lett. **45**, 2081 (1980).
8. M.P.Hess, L.Stringhetti, B.Hummelsberger *et al*,Acta Astron. **69**, 929 (2011).
9. STE-QUEST *Assesment Study Report 2013* [http:// sci.esa.int/ste-quest/53445-ste-quest-yellow-book](http://sci.esa.int/ste-quest/53445-ste-quest-yellow-book)
10. N.S.Kardashev, V.V.Khartov, V.V.Abramov *et al* Astronomy Report **57**, 153 (2013)
11. A.V.Biriyukov, V.L.Kauts, V.V.Kulagin *et al* Astronomy Report **58 (iss 11)**., 783 (2014)
12. G. Molera Calvés, S. V. Pogrebenko, G. Cimò, et al. A&A **564**, A4 (2014).



5. Search for gravitational waves

GRAVITATIONAL WAVE SEARCHES WITH ADVANCED LIGO AND ADVANCED VIRGO

C. VAN DEN BROECK

for the LIGO Scientific Collaboration and the Virgo Collaboration
*Nikhef – National Institute for Subatomic Physics,
Science Park 105, 1098 XG, Amsterdam, The Netherlands*



Advanced LIGO and Advanced Virgo are expected to make the first direct detections of gravitational waves (GW) in the next several years. Possible types of GW emission include short-duration bursts, signals from the coalescence of compact binaries consisting of neutron stars or black holes, continuous radiation from fast-spinning neutron stars, and stochastic background radiation of a primordial nature or resulting from the superposition of a large number of individually unresolvable sources. We describe the different approaches that have been developed to search for these different types of signals. In this paper we focus on the GW detection methods themselves; multi-messenger searches as well as further science enabled by detections are dealt with in separate contributions to this volume.

1 Introduction

After periods of commissioning as well as scientific observing runs between 2002 and 2011, the two initial LIGO¹ detectors in the US and the Virgo² observatory in Italy reached their design sensitivities, confirming large-scale laser interferometry as a highly promising technique for the direct detection of gravitational waves (GW). The next phase in these projects consists of the upgrades to Advanced LIGO³ and Advanced Virgo⁴, with a gradual improvement in sensitivity of approximately a factor of ten in the course of the next several years, ultimately increasing the volume of space that can be searched by about three orders of magnitude. The Advanced LIGO interferometers will already have a three-month observing run starting in September 2015, to be joined by Advanced Virgo for a six-month run in 2016-17 and a nine-month run in 2017-18, alternated with periods of commissioning; design sensitivity is expected to be reached around 2019. Exactly when these observatories will have their first detections depends on the instruments' duty cycles as well as astrophysical events rates (the latter being highly uncertain), but a GW observation of binary neutron star coalescence before the end of the decade is very plausible⁵. In a few years' time the KAGRA⁶ detector in Japan will join the Advanced LIGO-Virgo network, and LIGO-India⁷ may become active around 2022. The smaller GEO-HF⁸ in Germany is already taking data.

The expected GW signals can be divided into transient signals, whose duration might be anywhere between a millisecond and several hours, and long-duration signals that are continuously emitted. Among the most promising sources of transient GW are *compact binary coalescences* of two neutron stars, a neutron star and a black hole, or two black holes; in this case theoretical predictions of the waveform shapes are available, and coalescence events can be searched for by comparing these with the data. As we shall see, there are many other possible transient sources of GW, called *bursts*, whose emission is much more difficult to predict in detail; the absence of a waveform model then necessitates different ways of searching. Examples of potentially detectable long-duration signals are *continuous waves* from fast-spinning neutron stars, either isolated or accreting matter from a companion star. In this case the emission happens essentially at a single frequency, which however may be changing due to neutron star spin-down and which will be Doppler-modulated due to orbital motion in a binary as well as the motion of the Earth; when searching for unknown stars this leads to a computationally challenging problem. Finally, there will be searches for *stochastic backgrounds* coming from all directions on the sky; these could be of a primordial origin (*e.g.* inflation, or phase transitions in the early Universe), or they could arise from the superposition of a large number of point sources that are not individually resolvable.

Once a GW detection has been made, we will want to characterize the signal and, if possible, reconstruct the source. This involves the development of parameter estimation techniques, which again differ depending on the extent to which the source can be theoretically modeled. We will briefly discuss the methods that are being pursued; what further science this enables is the subject of a separate contribution to these Proceedings.

In this paper we will deal with the detection of the GW signals themselves, but it should be noted that GW searches can be combined with searches for associated electromagnetic and/or neutrino emission; these *multi-messenger* efforts will also be discussed in a separate paper in this volume.

2 Gravitational wave searches

We now discuss in turn the searches that will be performed for compact binary coalescences, unmodeled or poorly modeled burst events, continuous waves from fast-spinning neutron stars, and stochastic backgrounds, along with methods for parameter estimation.

2.1 Compact binary coalescence

Coalescing compact binaries consisting of two neutron stars (NS-NS), a neutron star and a black hole (NS-BH), or two black holes (BH-BH), with typical black hole masses up to a few tens of solar masses (M_{\odot}), are among the most promising sources for the advanced detectors, visible out to hundreds of megaparsecs. The emission of gravitational waves leads to loss of orbital angular momentum as well as orbital energy, causing orbits to circularize as well as shrink. If the component objects do not have intrinsic spins then the GW emission in this quasi-circular *inspiral* regime has a gravitational waveform whose frequency and amplitude both increase steadily as a ‘chirp’; when spins are non-zero then the waveform can get modulated due to precession of the orbital plane caused by spin-orbit and spin-spin interactions⁹. The inspiral continues until some last stable orbit is reached, after which the components plunge towards each other and *merge*, leading to a single black hole (or possibly a hypermassive neutron star). Such a black hole will be highly excited and undergo *ringdown* as it asymptotes to a quiescent, Kerr state. The early inspiral is well-understood in terms of post-Newtonian series expansions in v/c , with v some characteristic velocity¹⁰; similarly, the ringdown signal can be described using black hole perturbation theory¹¹. In recent years, large-scale numerical simulations have aided analytical waveform modeling in the construction of phenomenological models that exhibit a high degree of faithfulness with numerical waveforms also in the late inspiral and merger regimes^{12,13,14,15}.

Thus, the data analyst is increasingly well-equipped with waveform models that can be used to efficiently search for compact binary coalescence signals¹⁶. The main method used is *matched filtering*¹⁷, where one integrates the data against trial waveforms divided by a detector’s noise power spectral density, to give more weight to frequencies where the instruments are the most sensitive; the resulting number is the signal-to-noise ratio (SNR). SNRs are computed for many different choices of the intrinsic parameters (masses and spins), which together comprise a ‘template bank’¹⁸. Candidate detections must have SNRs above a certain threshold in at least two detectors, at consistent parameter values. Since non-stationarities in the noise can mimic GW events, one further performs *e.g.* a χ^2 test¹⁹ to check that the build-up of SNR over frequency is consistent with what one would expect from a real signal. Finally, a noise background distribution is constructed by sliding detector outputs in time with respect to each other and looking for coincident triggers, which are then guaranteed not to be GW events. This background allows one to assign a significance to candidate detections²⁰.

Which waveform approximants are deployed depends on the kind of source one is searching for. In the case of binary neutron star coalescence, the signal terminates at high frequencies and mainly the inspiral part of the waveform is accessible, where post-Newtonian theory is valid to good approximation²¹; moreover, neutron stars in binaries are expected to have small intrinsic spins²², so that at first instance one may choose to neglect them. By contrast, for NS-BH and BH-BH coalescences, all three regimes of inspiral, merger, and ringdown are in the detectors’ sensitive frequency band, and astrophysical black holes are likely to have large spins²³, leading to the abovementioned precession-induced modulation of the signal. Despite significant efforts by the waveform modeling and data analysis communities, template banks that include precession effects are not yet available. Although the use of waveforms with non-zero, aligned spins has been shown to significantly boost the sensitivity of searches compared with non-spinning templates²⁴, some fraction of signals that are in principle detectable will still be missed by not taking precession into account²⁵. Part of the solution may be the use of reduced order modeling, a technique which identifies the essential features of a waveform family and discards the less important information^{26,27}.

When performing matched filtering, the parameter space over which templates need to be placed only comprises intrinsic parameters: the masses of the two component objects, and (if needed) their intrinsic spins; for the purpose of detection, other parameters such as the sky location, the orientation of the inspiral plane with respect to the observer, and the distance to the source can be absorbed into an overall amplitude of the waveform. A rapid determination of the approximate sky position can be performed by looking at the relative phases, amplitudes, and times of arrival of the signal in the different detectors²⁸. However, a full estimation of the source parameters will require the exploration of the complete parameter space; tools that have been developed to this end include MCMC and nested sampling methods²⁹.

2.2 Burst searches

Aside from binary coalescences there is a host of other transient sources with potentially detectable GW signals. Most of these are not well modeled, so that matched filtering is often not an option; moreover, one will also want to search for transient signals of unknown origin, in which case no signal model can be assumed at all. Burst sources include supernovae³⁰, long gamma ray bursts that may be caused by the gravitational collapse of massive stars^{31,32}, and soft gamma-ray repeater giant flares in pulsars³³. These are sources that can be seen if they occur in our near our galaxy; examples of sources that are in principle observable out to cosmological distances are cusps and kinks on cosmic (super)strings^{34,35}. Burst signals potentially span a wide range in frequency (a few Hz to several kHz) and time (milliseconds to hours).

Another target for burst searches are coalescences involving *intermediate mass* black holes with masses up to a few hundred solar masses, which may exist in globular clusters³⁶. Intermediate mass black hole binaries merge at low frequencies ($f < 200$ Hz for total binary mass

$M > 50 M_{\odot}$), so that the part of the signal in band is dominated by the late inspiral and merger, which are poorly modeled; in that case a burst search is advisable to supplement matched-filter searches³⁷. Similarly, binaries whose orbits have significant eccentricity are not well understood theoretically, and here too there will be great benefit in performing a burst search³⁸.

A completely generic burst search requires techniques that can distinguish genuine GW signals from transient noise in the detectors without any prior knowledge of the waveform. In that case one usually first combines data from all detectors in terms of amplitude and phase, such that a GW signal builds up coherently while noise artefacts are removed based on their lack of correlation between detectors. Next the data is decomposed using *e.g.* short Fourier transforms or wavelets, and candidate signals are identified as ‘bright’ pixels in time-frequency maps^{39,40,41,42,43}. Alternative methods first process the data streams separately (‘incoherently’) and then look for coincidences between detectors or trigger a coherent MCMC follow-up^{44,45}.

Also for burst sources, detection will be followed by parameter estimation. In the case of coalescing binaries, this implies measuring the parameters determining the sources (masses, spins, ...). By contrast, for generic burst signals the nature of the source will be *a priori* unknown; what one does in this case is to try and characterize the signal rather than the source, in terms of its time-frequency and polarization content.

For some burst sources a certain amount of theoretical modeling has been done. For example, in the case of supernovae, large-scale numerical simulations have been performed with different underlying assumptions, *e.g.* the neutrino mechanism⁴⁶, the magnetorotational mechanism⁴⁷, or the acoustic mechanism⁴⁸. These lead to waveforms that exhibit qualitative differences. Using a principal component decomposition, the main features can be extracted from sets of numerical relativity waveforms resulting from the different assumptions made in the simulations. By performing Bayesian model selection on detected supernova signals, the different supernova models can be ranked, which will give insight into which mechanism dominates⁴⁹.

At the extreme end, signals from cosmic string cusps and kinks are sufficiently well-understood that template waveforms are available^{34,35}, so that a matched-filter search is in fact possible: in the case of cusps the frequency dependence of the signal is $h \propto f^{-4/3}$, while for kinks one has $h \propto f^{-5/3}$. The amplitudes depend on the string tension, and the intrinsic rate of cusp and kink events depends on the loop size, the string tension, and the reconnection probability, which in the case of superstrings is smaller than one. The non-detection of cosmic string signals with initial LIGO and Virgo has already allowed exclusion of a significant part of parameter space⁵⁰.

2.3 Continuous waves from fast-spinning neutron stars

Fast-spinning neutron stars can be sources of detectable gravitational waves also when not part of a compact binary. GW emission can result from asymmetries due to elastic deformations of the crust^{51,52}, deformations through magnetic fields⁵³, GW-driven unstable oscillation modes (r-modes⁵⁴, and f-mode Chandrasekhar-Friedman-Schutz instabilities⁵⁵), or free precession arising from a misalignment of a neutron star’s symmetry axis and the rotation axis⁵⁶. In cases where the rotation frequency f_{rot} can be established through electromagnetic observations, comparison with the main gravitational wave frequency f_{GW} can reveal the emission mechanism. If $f_{\text{GW}} = 2f_{\text{rot}}$, with no GW emission observed at f_{rot} , then the gravitational radiation is mainly due to non-axisymmetric deformation; on the other hand, if there is appreciable GW emission also at $\simeq f_{\text{rot}}$ then precession probably plays a role. If $f_{\text{GW}} \simeq (4/3)f_{\text{rot}}$ then r-modes are strongly favored, yielding direct information on the interior fluid motion.

In the ‘standard’ scenario of non-axisymmetric deformation ($f_{\text{GW}} = 2f_{\text{rot}}$), the amplitude of the GW emission is proportional to the equatorial ellipticity $\epsilon = (I_{xx} - I_{yy})/I_{zz}$, where the I_{ii} are the moments of inertia of the star, with the spin axis in the z -direction. Estimates of ϵ are highly uncertain⁵², but might be as large as 10^{-6} . Neutron stars in orbit with an ordinary star should be able to maintain axisymmetry due to accretion, and the balancing of accretion torque and GW emission may explain why the spin frequencies of known accreting neutron

stars never approach the break-up limit⁵¹. Depending on the typical size of ϵ , the currently known neutron stars may not yield detectable GW signals, although astrophysically interesting upper bounds have already been put on the percentage of the spin-down energy loss that is due to gravitational radiation⁵⁷. However, the galaxy contains an estimated 10^9 neutron stars, some fraction of which may have eluded electromagnetic detection, yet may be sufficiently close, non-axisymmetric, and fast-spinning to allow for detection with Advanced LIGO and Advanced Virgo.

Though fast-spinning, non-axisymmetric neutron stars are intrinsically quasi-monochromatic, with a frequency that is slowly decreasing, the observed GW signal gets Doppler-modulated due to the motion of the Earth, and by the orbital motion in the case of a binary. GW searches are divided into three categories. *Targeted searches* are those where the neutron star is visible as a pulsar so that its spin frequency (and where applicable, the orbital Doppler frequency) is known from electromagnetic observations^{58,59,60,61}. In *directed searches*, the sky position is known but not the source frequency^{59,62,63,64,65}. Finally, in *all-sky searches* one also looks for neutron stars that have not been discovered by electromagnetic means^{60,63,65,66,67,68}.

In targeted and directed searches, at least some known parameters can be folded into the analysis; in particular, the Doppler modulations can be removed and the search problem reduces to looking for sinusoidal signals; as in the case of compact binary coalescence, intrinsic parameters such as the GW polarization, a reference phase, and the inclination (in the case of binary systems) can be marginalized over. One can then integrate the data over a very long time, in principle the data taking time. By far the most computationally challenging are the all-sky searches. In that case one has to search over all sky positions, frequencies, spin-down parameters, and, in the case of binaries, the orbital parameters. Integration over long periods of time T then becomes difficult, since the resolution in parameter space increases rapidly ($\propto T^5$ even for searches including only leading-order spin-down). In the latter case a hierarchical search must be resorted to in order to keep the problem computationally tractable: one starts with a lower-resolution search that identifies interesting candidates, after which the search is iteratively refined as smaller and smaller parts of parameter space can be studied with increasingly higher resolution.

2.4 Stochastic searches

Omni-directional gravitational wave background radiation could arise from fundamental processes in the early Universe, or from the superposition of a large number of signals with a point-like origin. Examples of the former include parametric amplification of gravitational vacuum fluctuations during the inflationary era^{69,70}, termination of inflation through axion decay⁷¹ or resonant preheating⁷², Pre-Big Bang models inspired by string theory⁷³, and phase transitions in the early Universe⁷⁰; the observation of a primordial background would give access to energy scales of $10^9 - 10^{10}$ GeV, well beyond the reach of particle accelerators on Earth. Astrophysical confusion backgrounds could result from the collective emission of spinning neutron stars in the Galaxy⁷⁴, compact binary coalescences⁷⁵ out to redshifts of $z \sim 5$, or superpositions of cosmic string bursts^{34,35}.

Stochastic backgrounds are conveniently described in terms of the GW energy density ρ_{GW} per logarithmic frequency bin, normalized to the critical density of the Universe, ρ_c :

$$\Omega_{\text{GW}} = \frac{1}{\rho_c} \frac{d\rho_{\text{GW}}}{d \ln f}. \quad (1)$$

The current bound from the initial LIGO-Virgo era is⁷⁶ $\Omega_{\text{GW}} < 6.1 \times 10^{-6}$. Advanced detectors, both through their improved strain sensitivity and their wider frequency sensitivity band, will probe as low as $\Omega_{\text{GW}} \sim 6 \times 10^{-10}$.

Searches for stochastic backgrounds are performed by cross-correlating the output of multiple detectors with an optimal filter that is proportional to an expected form for Ω_{GW} as a function

of frequency^{77,78}. It is reasonable to assume that in the relevant frequency band, stochastic signals can be approximated by a power law: $\Omega_{\text{GW}}(f) = \Omega_0 f^\alpha$. The index α will take on different values depending on the origin of the radiation; in blind searches for cosmological sources one tends to quote upper limits on Ω_{GW} under the assumption of a flat spectrum ($\alpha = 0$), while a superposition of binary inspiral signals corresponds to $\alpha = 2/3$. Although at first instance one may expect stochastic backgrounds to be largely isotropic, we note that non-isotropic backgrounds, arising from *e.g.* random fluctuations in the number of point sources, will be searched for as well⁷⁹.

Like in searches for continuous waves from fast-spinning neutron stars, one can integrate over long times, in this case the length of the data set. In terms of backgrounds due to compact binary coalescences, it turns out that a signal can be seen after one year of operation at design sensitivity, and assuming a rate of a few tens of binary neutron star coalescences per year within a distance of a few hundred megaparsecs⁷⁵. With the latter rate, the dedicated searches for compact binary coalescences are themselves bound to make detections, but since the stochastic background includes sources out to redshifts of several, its measurement can give valuable information about the evolution of star formation rates.

Finally, one can search for stochastic backgrounds with non-standard polarizations, such as longitudinal modes, ‘breathing’ modes, and vector modes, which are predicted by various alternative theories of gravity⁸⁰. This can be done with a relatively straightforward extension of the existing methods, taking into account the different coherence structure of signals across detectors.

3 Conclusions

There exists a wide variety of sources whose GW emission can potentially be detected with second-generation interferometric observatories, within our galaxy (*e.g.* fast-spinning neutron stars and a range of burst sources), at distances of hundreds of megaparsecs (such as coalescing compact binaries), and at cosmological scales (*e.g.* primordial GW backgrounds), promising rich scientific returns. For all these, tailored and robust data analysis techniques are in place, which are continually being improved even further. With the construction of Advanced LIGO and Advanced Virgo well underway, we can look forward to the first direct detections of gravitational waves in the next several years.

Acknowledgments

The authors gratefully acknowledge the support of the United States National Science Foundation (NSF) for the construction and operation of the LIGO Laboratory, the Science and Technology Facilities Council (STFC) of the United Kingdom, the Max-Planck-Society (MPS), and the State of Niedersachsen/Germany for support of the construction and operation of the GEO600 detector, the Italian Istituto Nazionale di Fisica Nucleare (INFN) and the French Centre National de la Recherche Scientifique (CNRS) for the construction and operation of the Virgo detector. The authors also gratefully acknowledge research support from these agencies as well as by the Australian Research Council, the International Science Linkages program of the Commonwealth of Australia, the Council of Scientific and Industrial Research of India, Department of Science and Technology, India, Science & Engineering Research Board (SERB), India, Ministry of Human Resource Development, India, the Spanish Ministerio de Economía y Competitividad, the Conselleria d’Economia i Competitivitat and Conselleria d’Educació, Cultura i Universitats of the Govern de les Illes Balears, the Foundation for Fundamental Research on Matter supported by the Netherlands Organisation for Scientific Research, the Polish Ministry of Science and Higher Education, the FOCUS Programme of Foundation for Polish Science, the European Union, the Royal Society, the Scottish Funding Council, the Scottish Universities

Physics Alliance, the National Aeronautics and Space Administration, the Hungarian Scientific Research Fund (OTKA), the Lyon Institute of Origins (LIO), the National Research Foundation of Korea, Industry Canada and the Province of Ontario through the Ministry of Economic Development and Innovation, the National Science and Engineering Research Council Canada, the Brazilian Ministry of Science, Technology, and Innovation, the Carnegie Trust, the Leverhulme Trust, the David and Lucile Packard Foundation, the Research Corporation, and the Alfred P. Sloan Foundation. The authors gratefully acknowledge the support of the NSF, STFC, MPS, INFN, CNRS and the State of Niedersachsen/Germany for provision of computational resources. This research has made use of the SIMBAD database, operated at CDS, Strasbourg, France.

References

1. B. Abbot *et al.*, *Rep. Prog. Phys.* **72**, 076901 (2009).
2. F. Acernese *et al.*, *Class. Quantum Grav.* **25**, 114045 (2009).
3. J. Aasi *et al.*, *Class. Quantum Grav.* **32**, 074001 (2015).
4. F. Acernese *et al.*, *Class. Quantum Grav.* **32**, 024001 (2015).
5. J. Aasi *et al.*, arXiv:1304.0670 (2013).
6. K. Somiya (KAGRA Collaboration), *Class. Quantum Grav.* **29**, 124007 (2012).
7. B. Iyer *et al.*, LIGO-India Tech. Rep. (2011), <https://dcc.ligo.org/LIGO-M1100296/public>.
8. C. Affeldt *et al.*, *Class. Quantum Grav.* **31**, 224002 (2014).
9. T.A. Apostolatos, C. Cutler, G.J. Sussman, and K.S. Thorne, *Phys. Rev. D* **49**, 6274 (1994).
10. L. Blanchet, *Living. Rev. Rel.* **17**, 2 (2014).
11. K. Kokkotas, *Living. Rev. Rel.* **2**, 2 (1999).
12. L. Santamaria *et al.*, *Phys. Rev. D* **82**, 064016 (2010).
13. R. Sturani *et al.*, in Proceedings of CAPRA and NRDA 2010, Waterloo, Canada, June 20-26, 2010.
14. A. Taracchini *et al.*, *Phys. Rev. D* **89**, 061502 (2014).
15. P. Schmidt, F. Ohme, and M. Hannam, *Phys. Rev. D* **91**, 024043 (2015).
16. J. Aasi *et al.*, *Class. Quantum Grav.* **31**, 115004 (2014).
17. L.A. Wainstein and V.D. Zubakov, *Extraction of signals from noise*, Prentice-Hall, Englewood Cliffs, NJ, 1962.
18. B.S. Sathyaprakash and S.V. Dhurandhar, *Phys. Rev. D* **44**, 3819 (1991).
19. B. Allen, *Phys. Rev. D* **71**, 062001 (2005).
20. S. Babak *et al.*, *Phys. Rev. D* **87**, 024033 (2013).
21. A. Buonanno, B.R. Iyer, E. Ochsner, Y. Pan, and B.S. Sathyaprakash, *Phys. Rev. D* **80**, 084043 (2009).
22. M. Kramer and N. Wex, *Class. Quantum Grav.* **26**, 073001 (2009).
23. V. Kalogera, *Astrophys. J.* **541**, 319 (2000).
24. I.W. Harry, A.H. Nitz, D.A. Brown, A. Lundgren, E. Ochsner, and D. Keppel, *Phys. Rev. D* **89**, 024010 (2014).
25. T. Dal Canton, A.P. Lundgren, and A.B. Nielsen, *Phys. Rev. D* **91**, 062010 (2015).
26. S.E. Field *et al.*, *Phys. Rev. Lett.* **106**, 22110 (2011).
27. M. Pürrer, *Class. Quantum Grav.* **31**, 195010 (2014).
28. L.P. Singer *et al.*, *Astrophys. J.* **795**, 105 (2014).
29. J. Veitch *et al.*, *Phys. Rev. D* **91**, 042003 (2015).
30. C. Ott, *Class. Quantum Grav.* **26**, 204015 (2009).
31. C.L. Freyer, S.E. Woosley, and D.H. Hartmann, *Astrophys. J.* **526**, 152 (1999).
32. B. Metzger *et al.*, *MNRAS* **413**, 2031 (2011).
33. S. Mereghetti, *Astron. Astrophys. Rev.* **15**, 225 (2008).

34. T. Damour and A. Vilenkin, *Phys. Rev. D* **71**, 063510 (2005).
35. S. Olmez, V. Mandic, and X. Siemens, *Phys. Rev. D* **81**, 104028 (2010).
36. M.C. Miller and E.J.M. Colbert, *Int. J. Mod. Phys.* **13**, 1 (2004).
37. J. Aasi *et al.*, *Phys. Rev. D* **89**, 122003 (2014).
38. E. Huerta and D.A. Brown, *Phys. Rev. D* **87**, 127501 (2013).
39. S. Klimenko, S. Mohanty, M. Rakhmanov, and G. Mitselmakher, *Phys. Rev. D* **72**, 122002 (2005).
40. S. Klimenko *et al.*, *CQG* **25**, 114029 (2008).
41. S. Klimenko *et al.*, *PRD* **83**, 102001 (2011).
42. P. Sutton *et al.*, *NJP* **12**, 053034 (2010).
43. E. Thrane and M. Coughlin, *PRD* **89**, 063012 (2014).
44. S. Chatterji, L. Blackburn, G. Martin, and E. Katsavounidis, *CQG* **21**, S1809 (2004).
45. T.B. Littenberg and N.J. Cornish, *Phys. Rev. D* **82**, 103007 (2010).
46. H.A. Bethe and J.R. Wilson, *Astrophys. J.* **295**, 14 (1985).
47. A. Burrows, L. Dessart, E. Livne, C.D. Ott, and J. Murphy, *Astrophys. J.* **664**, 416 (2007).
48. C.D. Ott, A. Burrows, L. Dessart, and E. Livne, *Phys. Rev. Lett.* **96**, 201102 (2006).
49. J. Logue *et al.*, *Phys. Rev. D* **86**, 044023 (2012).
50. J. Aasi *et al.*, *Phys. Rev. Lett.* **112**, 131101 (2014).
51. L. Bildsten, *Astrophys. J.* **501**, L89 (1998).
52. G. Ushomirsky, C. Cutler, and L. Bildsten, *Mon. Not. R. Astron. Soc.* **319**, 902 (2000).
53. C. Cutler, *Phys. Rev. D* **66**, 084025 (2002).
54. N. Andersson, *Astrophys. J.* **502**, 708 (1998).
55. J. Friedman and B.F. Schutz, *Astrophys. J.* **222**, 81 (1978).
56. D.I. Jones and N. Andersson, *Mon. Not. R. Astron. Soc.* **331**, 203 (2002).
57. J. Aasi *et al.*, *Astrophys. J.* **785**, 119 (2014).
58. R.J. Dupuis, PhD thesis, University of Glasgow, 2004.
59. P. Jaranowski, A. Krolak, and B.F. Schutz, *Phys. Rev. D* **58**, 063001 (1998).
60. P. Jaranowski and A. Krolak, *Class. Quantum Grav.* **27**, 194015 (2010).
61. P. Astone *et al.*, *Class. Quantum Grav.* **27**, 194016 (2010).
62. L. Sammut, C. Messenger, A. Melatos, and B.J. Owen, *PRD* **89**, 043001 (2014).
63. E. Goetz and K. Riles, *CQG* **28**, 215006 (2011).
64. S. Dhurandhar, B. Krishnan, H. Mukhopadhyay, and J.T. Whelan, *Phys. Rev. D* **77**, 082001 (2008).
65. S. van der Putten, PhD thesis, VU University Amsterdam, 2011
66. B. Krishnan *et al.*, *Phys. Rev. D* **70**, 082001 (2004).
67. P. Astone *et al.*, *Phys. Rev. D* **90**, 042002 (2014).
68. P.R. Brady and T. Creighton, *Phys. Rev. D* **61**, 082001 (2000).
69. L.P. Grishchuk, *Sov. J. Exp. Theor. Phys.* **40**, 409 (1975).
70. A.A. Starobinsky, *Zh. Eksp. Theor. Fiz. Pisma Red.* **30**, 719 (1979).
71. N. Barnaby, E. Pajer, and M. Peloso, *Phys. Rev. D* **85**, 023525 (2012).
72. R. Easther and E.A. Lim, *JCAP* **0604**, 010 (2006).
73. V. Mandic and A. Buonanno, *Phys. Rev. D* **73**, 06300 (2006).
74. T. Regimbau and J.A. de Freitas Pacheco, *Astron. Astrophys.* **376**, 381 (2001).
75. C. Wu, V. Mandic, and T. Regimbau, *Phys. Rev. D* **85**, 104024 (2012).
76. J. Aasi *et al.*, *Phys. Rev. Lett.* **113**, 231101 (2014).
77. N. Christensen, *Phys. Rev. D* **46**, 5250 (1992).
78. B. Allen and J.D. Romano, *Phys. Rev. D* **59**, 102001 (1999).
79. B. Abbott *et al.*, *Phys. Rev. Lett.* **107**, 271102 (2011).
80. C.M. Will, *Living. Rev. Rel.* **9**, 3 (2006).

MULTI-MESSENGER SEARCHES: PAST RESULTS AND FUTURE PROGRAMS

G. STRATTA

on behalf of the LIGO Scientific Collaboration and the Virgo Collaboration

Università degli studi di Urbino, DiSBF, Piazza della Repubblica 13, 61029, Urbino, PU, Italy
INFN, Sezione di Firenze, I-50019 Sesto Fiorentino

Second generation gravitational wave (GW) detectors LIGO and Virgo are entering in their operative phase by the end of 2015 and expected to improve past sensitivities by one order of magnitudes by 2019. Transient astrophysical sources as binary compact object coalescence, supernovae or bursting magnetars, are among the most promising targets in the GW frequency range covered by LIGO and Virgo (1 Hz - 10kHz). These sources are well known in the electromagnetic spectrum and are expected to emit neutrinos, thus are ideal test benches for the nascent multi-messenger astrophysics. This review presents some of the main properties of these sources, the results obtained so far from past multi-messenger searches with the first generation GW interferometer observatories, and the programs for the era of the second generation GW observatories.

1 Introduction

The two Laser Interferometer Gravitational wave Observatory (LIGO) based in the USA at Livingston, Louisiana, and Hanford, Washington¹, and the Virgo interferometer based in Cascina, Italy², are undergoing deep hardware and software upgrade that will increase their GW strain sensitivity by one order of magnitude around the most sensitive frequency (~ 100 Hz), giving birth to the second generation GW detectors. The nominal sensitivity is expected to be reached by 2019: by that time GW are expected to be detected routinely opening a new era for astronomy in the gravitational wave domain. Transient astrophysical sources such as bursting stars or stars undergoing catastrophic phases, are among the best candidates in the high frequency GW range covered by the advanced LIGO (aLIGO) and Advanced Virgo (1 Hz - 10 kHz).

The most promising transient sources of GWs are binary systems of compact objects, as two neutron stars (NS) or a neutron star and a stellar-mass black hole (BH) or even two BHs. The maximum GW strain is expected to be detected by aLIGO and Advanced Virgo during the final stages of the inspiral phase, just before the merging of the two stars. These systems are often called in the literature as "compact binary coalescence" systems, CBC, or "mergers". The theoretically predicted GW energy from these systems is of the order of $E_{GW} \sim 4.2 \times 10^{-2} M_{\odot} c^2 \left(\frac{M_{chirp}}{1.22 M_{\odot}}\right)^{5/3} \left(\frac{f_{max}}{1 \text{ kHz}}\right)^{2/3}$, where M_{chirp} is the chirp mass and f_{max} is the GW frequency at the end of the inspiral phase³. The expected waveforms from CBCs are fairly well known and a large number of templates are typically used as "matching filters" in the GW data analysis. Another class of transient GW events that may be observed by the 2nd generation of GW detectors are the core collapsing stars, or core-collapse supernovae (SNII, SNIbc). These astrophysical objects are expected to release a certain amount of GW energy due a supposed degree of asymmetry in the stellar envelope ejection phase. However, the large uncertainties affecting our knowledge on the collapsing phase of these objects makes highly uncertain the GW released energy (for which the present estimates^{5,6} range from $10^{-2} M_{\odot} c^2$ to $10^{-8} M_{\odot} c^2$) and, as a consequence, the distance up to which these sources maybe detected is very uncertain too. Another issue for these type of objects it that the waveform is much less defined

than for the CBC case. For this reason, burst search methods, largely independent of the waveform, are used. The third class of transient GW sources is populated by rotating NSs with very intense magnetic fields, of the order of 10^{15} G (magnetars). Theoretical studies predict that when such stars undergo a starquake, asymmetric strains can temporally alterate the geometry of the star and GW are expected to be produced (see also Dall’Osso proceeding, this volume). The expected amplitude however is highly uncertain, with possible estimates that goes from 2 down to 8 orders of magnitude fainter than for CBC systems⁷.

The three above mentioned classes of sources are well known in the electromagnetic spectrum and are expected to emit high-energy neutrinos (HEN), thus are ideal test benches for the nascent multi-messenger astrophysics. In the coming era of "gravitational astronomy", multi-messenger study will be a main tool to gain insights on the physics of several astrophysical phenomena. Joint GW, electromagnetic (EM) and neutrino observations are expected to provide a wealth of information on the source nature that would be unaccessible from the EM observations alone. For example, both GW and HEN can travel almost unaffected from the region of their production to the observer, while photons are highly scattered before escaping from the innermost regions. Therefore, both GW and HEN can provide crucial information on the processes taking place in the innermost engine of the source⁸. At the same time, the only way to localize and therefore to individuate a GW and/or neutrino emitting source is through multi-wavelength EM observations and, if extragalactic, this will ultimately enable to identify the hosting galaxy and the distance of the source can thus be estimated accurately by measuring the cosmological redshift of the galaxy spectral line systems. Both accurate position in the sky and distance, in turn, provide useful priors in the GW data analysis parameter space, refining unique information on the bulk motion and the dynamics of the source central regions⁹.

This review presents some of the main properties of these three classes of sources in Section 2, the results obtained so far from past multi-messenger searches with the first generation GW interferometer observatories in section 3 while in section 4 the future observational scenario with the advent of the second generation observatories is discussed.

2 The electromagnetic and neutrino counterparts of GW transient sources

A key role in multi-messenger astronomy will be played by Gamma-Ray Bursts (GRBs) for which GW and neutrinos are expected to accompany the well known electromagnetic emission. Theoretical models, supported by hydrodynamical relativistic simulations, are generally in agreement by interpreting both long and short GRBs as produced by an accreting stellar mass black hole. However, the central BH is originated through two different channels: from the coalescence of two NSs or a NS and a BH in the case of short GRBs, and from the core collapse of a massive star in the case of long GRBs. This scenario is in line with the experimental properties of GRBs. In particular, the origin of long GRBs from the core collapse of massive stars has been proved by their positional and temporal association with SNIb/c, while for short GRBs there are several indirect evidence as the consistency with older star population than for long GRBs, but the definitive proof will be the coincident detection of GWs. The matter accretion onto the BH is expected to produce relativistic ejecta. Each ejecta, by expanding into the interstellar matter, forms a shock wave that slowly converts the outflow kinetic energy into EM radiation via synchrotron emission¹⁰. A big conundrum still affecting our knowledge on GRBs is the degree of collimation of their ejecta: this has prevented so far precise burst energetics and event rate estimates that indeed are known unless a factor of $(1 - \cos(\theta_{jet}))$. The jet opening angle has been measured only for a small subsample of GRBs with large multi-wavelength data set and known distance and the obtained distribution goes from few degrees up to several tens of degrees¹¹.

The EM emission from GRBs (both long and short) appears as a bright flash of gamma-rays (from keV up to GeV energy range) of various durations (from less than few seconds for short GRBs up to hundreds of seconds for long GRBs) and it further develops at late times with the "afterglow" emission. Afterglows are thought to be produced when the ejecta starts to decelerate while expanding into the external medium. Afterglow emission peaks after minutes/hours from the

burst onset in the X-ray regime (0.1-10 keV), with typical fluxes in the range $10^{-10} - 10^{-12}$ erg $\text{cm}^{-2} \text{s}^{-1}$ and in the optical and near infrared (NIR), with observed magnitude on average comprised between 15 and 25 mag¹². After some days, the afterglow emission shifts in the radio frequencies with fluxes typically below the mJy level, up to weeks-months. The flux temporal decay at late time is on average described by power laws with decay index of about -1.5. Photon spectrum is typically non thermal and well represented by synchrotron emission. The EM energies released during the burst, assuming an isotropic geometry (not collimated) is of the order of 10^{52-54} erg for long GRBs and on average 2 orders of magnitude less for short GRBs.

All the afterglows observed so far were associated with a prompt gamma-ray emission, that is, with a GRB ejecta collimated towards the Earth. However, a non-negligible EM afterglow emission is expected also from GRBs "off-axis" (i.e. not pointing towards the Earth). In particular, both for short and long GRBs, off-axis afterglow emission (also called "orphan afterglow" because no gamma-ray burst is anticipating it) will enter in the observer line of sight when the ejecta starts to spread laterally as it decelerates and expands into the interstellar medium. Off-axis afterglow emission is fainter and peaks at later times than the "on-axis" counterpart. So far, only in one case a possible "orphan afterglow" has been detected with the Palomar Transient Factor Telescope (PTF). However, the detected source (PTF11agg) showed multi-wavelength properties more typical of an "on-axis" afterglow and its origin is still debated¹³.

Coalescing NS-NS systems are theoretically predicted to isotropically eject a small quantity of neutron rich matter, the radioactive decay of which produces optical/NIR transients ("kilonova") with typical thermal spectrum¹⁴. The peak of kilonova emission is predicted at 1 to few days after the merger. Interestingly, the main kilonova emission may be preceded by a moderately bright precursor in the U-band few hours after the merging that can potentially better mark the time of the associated GW event¹⁵. So far only one possible evidence of a kilonova was found for the short GRB 130604B for which a detection about one week after the burst was found to be inconsistent with the expected optical/NIR afterglow fluxes at the same epoch¹⁶. It is thought that the small detection rate of kilonova so far, is mainly due to its intrinsic faintness that is likely dominated by the afterglow emission for on-axis GRBs.

Core-collapse SNe are typically detected in the electromagnetic spectrum at optical frequencies after tens of days from the collapse. Only in very few cases, an early "SN shock break-out" (SBO) was observed in X-rays and UV-optical wavelengths, marking the very first leak of radiation from a collapsing star experiencing its SN phase^{17,18}. Despite its challenging detection, SBO emission is extremely important to mark the time of explosion since it is expected after much shorter time (few hours on average) than the typical optical signature weeks later.

Events such as X-ray flares and bursts from neutron stars are well known phenomena¹⁹ that go under the name of Soft Gamma Repeters (SGR) and Anomalous X-ray Pulsars (AXP). In particular, SGRs were discovered in 1979 as transient sources of hard X-ray bursts and giant flares, while AXPs were identified in late '90s as a class of persistent X-ray pulsars with no evidence of binary companion and with an X-ray luminosity much higher than the expected luminosity from magnetic dipole radiation only. Today, both SGRs and AXPs are largely believed to be associated to a single astrophysical source, that is a highly magnetized neutron star (magnetar), experiencing starquakes and consequent crust disruption. Magnetars emission is characterized by a persistent X-ray emission with luminosity $L_x = 10^{35-36}$ erg s^{-1} (in the 0.2-200 keV energy range) and episodic short bursts of duration of about 0.1-1 s of soft gamma-rays (thermal peak energy at $KT=30-40$ keV and luminosity of $L_x = 10^{39-41}$ erg s^{-1}). In very few cases (3 over 30 years so far) giant flares are emitted by these objects which an X-ray luminosity that can reach values of $L_x > 10^{44}$ erg s^{-1} and an X-ray released energy of the order of 10^{46} erg.

The above mentioned astrophysical sources, and in particular GRBs, are expected to produce relativistic outflows in which hadrons are accelerated and produce high-energy neutrinos by interacting with the surrounding medium and radiation. MeV neutrinos have been detected with SuperKamiokande and the IMB neutrino detectors on 23 February 1987 several hours before the optical discovery of the supernova SN 1987A in the Large Magellanic Cloud^{20,21}. These observations confirmed not only the expected neutrino emission from ccSNe, but also revealed the huge

Table 1: Initial LIGO and Virgo past science runs during which multi-messenger searches were performed.

| LIGO | Virgo |
|-----------------------|--|
| S5: Nov 2005-Aug 2007 | VSR1: May 2007-Oct 2007 |
| S6: Jun 2009-Oct 2010 | VSR2: Jul 2009-Jan 2010 "Winter run" 29 Dec 2009-7 Jan 2010 |
| | VSR3: Aug 2010-Oct 2010 "Autumn run" 16 Sept 2010-3 Oct 2010 |

importance of neutrino detection in the multi-messenger astronomy since it can better mark the time of GW emission. However, in no other case of cosmic neutrino detection an astrophysical source could be associated.

A particular interesting case for joining GW and neutrino detection are the so called "low-luminosity GRB" (or "choked GRBs"). These are a small subset of long GRBs that show fainter and typically softer emission during the burst. The spatial distribution of low luminosity GRBs is on average skewed towards nearby distances with respect to long GRBs. It has been suggested that the peculiar low luminosity of this type of long GRBs is due to mildly relativistic outflows that nearly fail to cross the stellar envelope, thus producing fainter EM emission²².

3 Results from multi-messenger past searches

In this section, some of the results from past multi-messenger searches during the LIGO and Virgo observational runs performed before their upgrade are summarized together with their literature references. Table 1 shows the temporal windows during which LIGO and Virgo performed their past science runs. During LS6 and VSR2 and VSR3 epochs, GW candidate triggers were released to the astronomical facilities that signed the Memorandum of Understanding (MoU) at that time. These were typically large field of view (FOV) optical telescopes (see next section). The candidate triggers were the most significant events of the science runs, but they were low signal to noise ratio events with amplitude corresponding to high False Alarm Rate (FAR). For GRBs and flares from NS that happened during these epochs, off-line GW data analysis was also performed using as priors the time and the sky localization of the astrophysical event.

In the following we summarize some of the results from coincident GW plus electromagnetic (EM) and neutrinos searches during initial LIGO and Virgo science runs. Note that the detector sensitivities during LS6 and VSR3 corresponded to a maximum distance of $D_h = 40, 80, 90$ Mpc for a NS-NS, NS-BH of and BH-BH systems, respectively^a, by assuming $1.35 M_\odot$ for NS mass and $5.0 M_\odot$ for BH mass²³.

3.1 From GW candidate event triggers to EM follow-up

An important issue in the search for multi-messenger counterpart of GW candidate events is the fact that GW observatories are non-imaging detectors. Localization of GW source is based on the triangulation method, that is, on the temporal delay of a GW detection between two or more detectors due to the finite travel velocity of GW. Thus, to localize a GW source, multiple detector network is needed. Localization uncertainty is driven by: 1) amplitude of the signal; 2) time delay between detectors. Therefore, localization strongly benefits of detector network with similar sensitivities and far apart one with the other. For example, the sky localization precision for the second generation GW detectors with the advent of LIGO India²⁴ and KAGRA²⁵ in addition to the aLIGO and Advanced Virgo, is expected to improve of about one order of magnitude the present values (see next section). At the time of the first-generation LIGO and Virgo science runs, the achieved localization precision was not better than hundreds of square degrees.

^awhere with D_h we indicate the horizon distance, that is the maximum distance at which a binary system can be detected in optimal condition (e.g. face-on and at a position in the sky that maximizes the GW detector sensitivity)

During the so called "Winter run" and "Autumn run" observational periods of LIGO and Virgo (see Tab.1), 8 GW trigger alerts were sent to the MoU partners and a multi-wavelength follow-up observational campaign was performed for each trigger. The FAR of these events ranged from 4.5 to 0.02 per day. At that time, the activated large field of view (FOV) facilities were the optical telescopes QUEST, TAROT, ROTSE, PTF, Liverpool-SkyCamZ and Pi Of The Sky and the radio telescope array LOFAR. Small FOV optical telescopes also were pointed, namely Zadko, Liverpool-RATCam, and the UV-Optical (UVOT) and X-ray (XRT) Telescopes on board the Swift satellite.

For each trigger, the date and time of the event, the FAR associated with that event, and the sky probability map, were provided to the astronomers. Several exposures were taken with large FOV telescopes in order to cover the sky regions with maximum probability to detect a GW source indicated by the probability skymaps obtained from GW data analysis and prioritized taking into account of the galaxies within the GW detectors range.

No credible EM counterparts for any of the GW triggers was found. Several papers describe in details the results from the observational campaigns with optical facilities^{26,27}, with Swift-XRT and UVOT²⁸, and at the radio wavelengths²⁹.

Interestingly, during the "Autumn run", one of the GW triggers was labelled as "Big Dog" due to the low FAR with which it was associated ($FAR < 0.01$). However, this event resulted to be a blind injection, that is a simulated signal secretly added to the data to test the end- to-end system. The "Big Dog" injection was not announced until a full analysis has been performed and approved, results gathered in a paper and presented at the LIGO-Virgo meeting on 14th March 2011.

3.2 From EM to GW using GRBs

Using Gamma Ray Bursts as indicators in terms of time and position in the sky, GW signals have been searched at the epoch of 196 long GRBs and 27 short GRBs detected with the high energy satellite network (IPN) during the LIGO-Virgo science run periods quoted in Table 1. Almost all the GRBs were at unknown distances. Indeed, for IPN-discovered GRBs, the time delay in announcing the discovery of a GRB, that is a function of the downlink times of the various missions and the computational time to produce an error-box, is of the order of several hours up to days from the trigger. Such time delays, typically prevent the possibility to detect the GRB afterglow counterpart in the degree-scale sky IPN error boxes, since the emission has already faded below the detection threshold. For all the analyzed IPN GRBs, no significant coincident GW event was found. From the lack of any coincident GW event, the 90 % confidence level lower limits on the distance of each GRB ("exclusion distance") were computed. The obtained values (median exclusion distance) range from 12 to 22 Mpc for short GRBs by assuming face-on NS-NS and a NH-BH system waveforms, respectively, and from 4.9 Mpc to 13 Mpc for long GRBs by assuming unmodeled waveform at 150 Hz and 300 Hz, respectively³⁰.

During LS5 and VSR1 science runs, GW data around the time^b of the burst onset of 22 short GRBs were analyzed. The search for GW signals did not make any assumption on the GW polarization and expected signals from binary coalescence systems. From the lack of any significant detection, the presence of a NS-BH or NS-NS progenitor for these short GRBs was excluded at 90% confidence within a distance of 6.7 Mpc and 3.3 Mpc, respectively⁴³. In the same GW data set a similar search was performed⁴ by looking for GW bursts associated with 137 long and short GRBs. This time, a circularly polarized 1-s long waveform at the detector most sensitive frequencies (about 150 Hz) was assumed. Exclusion distances for each GRB were computed by assuming that $0.01 M_{\odot}$ is converted into isotropically emitted gravitational waves, finding a median of 12 Mpc. With the same assumption on GW emitted energies around the most sensitive frequencies, LS6 and VSR2 and VSR3 GW data were analyzed in coincidence with 154 GRBs detected mostly with Swift and Fermi²⁶. Two search methods were applied: one based on unmodeled GW and the other assuming a NS-NS or NS-BH expected waveforms. Computed median exclusion distance for all bursts was 17 Mpc, while for short GRBs, assuming a NS-NS or NS-BH progenitor, computed values were 16 Mpc and 28 Mpc, respectively. Finally, using data from LS5 and long GRB triggers from Swift,

^bwithin -5 and +1 s from the burst trigger time

a search for unmodeled long-lived (10-1000 s) GW transients was performed⁴¹ and an exclusion distance was obtained at 33 Mpc.

All the exclusion distance values obtained in the above described searches, are well below the typical GRB distances. Indeed, the average distance of short GRBs for which the cosmological redshift has been measured, that is for about 20 short GRBs so far, is $z=0.5$ (3 Gpc) and the most nearby short GRB is at 500 Mpc (Fig.1). Long GRBs have an average redshift around 2.2 although the most nearby (GRB 980425) is at 40 Mpc, a distance within the range of the second-generation GW detectors. Thus, in general, the lack of any GW signal coincident with a GRB is consistent with the observed low rate of these events in the local Universe.

Two interesting cases where the two short GRBs 070201 and 051103 for which the distances could be inferred by their positional coincidence with two known galaxies. For GRB 070201, the IPN sky error box was found to overlap with Andromeda galaxy³¹ at 770 kpc. For the short GRB 051103, the IPN sky error box overlaps³² with M81 at 3.6 Mpc. If these two short GRBs were associated with a NS-NS or NS-BH binary system progenitor, at such distances GWs should had been detected confidently. The lack of any GW counterpart may imply a different nature of these two sources, possibly associated with two Soft Gamma Repeaters. Indeed, the energetics of these two bursts, in terms of isotropically-equivalent released energy in the keV-MeV photon range, are $E_{iso} \sim 10^{45}$ erg and $E_{iso} \sim 10^{46}$ erg for GRB 070201 and 051103 respectively, that is, 2 to 3 orders of magnitude lower than the typical E_{iso} inferred for short GRBs, thus supporting the SGR hypothesis. Another possibility is that these short GRBs are indeed much further away and just by chance their positions, that is the IPN degree-level error boxes, coincide with the two nearby large galaxies.

3.3 From EM to GW using flaring NSs

During the period between November 2006 and June 2009 (science runs S5 and VSR1), 5 SGRs and one AXP phenomena were observed from 6 NSs in their bursting and flaring phase, with a total of 1279 electromagnetic triggers. Using the position and the epoch of the main X-ray activity of each source as priors for the analysis, GW data were analyzed by testing 12 different waveforms for each source³³. From the lack of any signal, stringent 90% model-dependent upper limits on the GW energy E_{GW} released during each event were obtained. The most stringent model dependent E_{GW} value of $< 3 \times 10^{44}$ erg was obtained for the newly discovered SGR0501+4516 at the closeby distance of $d < 1$ kpc, that is one order of magnitude closer than other discovered magnetars. For this source, $E_{GW} < 3 \times 10^{44}$ erg, that is about one order of magnitude lower than past SGR upper limits. More interestingly, for the first time GW energy upper limits are almost comparable with electromagnetic energies from giant flares.

3.4 Neutrinos and GW coincident searches

Neutrino detectors, as the GW detectors, are "all-sky" observatories and cannot provide accurate localization. However, the time of neutrino detection can provide an optimal constraint for GW search since neutrino emission is expected to be nearly simultaneous to GW. Therefore, search for coincident signals from LIGO and Virgo and the two high energy neutrino detectors IceCube, a cubic-kilometer detector at the South Pole³⁴, and ANTARES in the Mediterranean sea³⁵, were performed during the epochs quoted in Table 1. ANTARES is more sensitive to TeV neutrinos while IceCube can detect also MeV neutrinos. Details on the state of the neutrino detectors at that time and on the performed data acquisition and data analysis have been published in the literature for IceCube observations⁴², and for ANTARES observations³⁶ (see also Baret proceeding, this volume).

No temporally coincident detection was found. Assuming the most favorable case of a release of energy of $E_{GW} = 0.01 M_{\odot}c^2$ and a neutrino released energy of $E_{\nu} = 10^{51}$ erg, source rate upper limit was estimated as $R < 1.6 \times 10^{-2} \text{ Mpc}^{-3} \text{ yr}^{-1}$. This value is still too high with respect to astrophysical expected rates and could not constrain any current astrophysical model.

4 Future programs

Second generation of GW detectors will start taking data by Fall 2015 with the two aLIGO at Hanford and Livingston (HL and LL), and by 2016 with the network formed by HL and LL plus Advanced Virgo in Italy. During the next three years, thus up to 2019, the instrumental sensitivities will gradually improve eventually reaching their nominal values.

While for SNe the expected range distance^c for GW detection is of the order of a few to a few dozens of Mpc and for bursting NSs possible detections outside our galaxy is predicted only in the most closely neighborhood, CBC systems are expected to be detected up to 200 Mpc for NS-NS, 400 Mpc for NS-BH and 900 Mpc for BH-BH. Within such distances, the astrophysical rate density estimated for CBC systems, despite large uncertainties, are consistent with a highly plausible detection^{37,38}.

For simultaneous GW and EM plus possibly neutrino detection from short GRBs, the binary system is expected to be face-on. In this configuration, by averaging over all the possible positions in the sky where one can find the source, the range distance of GW detectors increases by a factor of about 1.5, thus reaching values of 300 Mpc for NS-NS and 750 Mpc for NS-BH systems. Within such distances, for an "all-sky" instrument (not limited by its field of view) and by assuming that all short GRB emit GW that can be detected by AdvLIGO and AdvVirgo, if all short GRBs were NS-NS, the expected GRB-GW rate is of 0.1-2 yr⁻¹ and 0.4-15 yr⁻¹ if they all were NS-BH³⁹.

The GW interferometer KAGRA, in Japan, is expected to start taking data by 2018, and the other planned GW interferometer LIGO India, by 2022. The 5 GW detector network will provide significant improvements in sky localization, reaching values down to few degrees sky ellipse regions^{40,41}, that is a factor of more than 10 more precise than the present localization uncertainties. Within such sky errorbox it will be possible to perform transient search with much larger chances of detection than in the past searches. Follow-up campaigns of GW triggers by aLIGO and Advanced Virgo will be performed by more than 150 observatories from 19 countries who signed the LIGO and Virgo Collaboration MoU^d (more than 10 times the MoU partners during the last science run), covering the the entire EM spectrum from radio to gamma-rays. "External trigger" as GRBs will be provided by the Swift and Fermi satellites for which operative life-time has been guaranteed^e up to 2016 and it has been proposed for extension up to 2018 (possible further extensions up to 2020 and beyond are expected). In addition, the GRB dedicated mission SVOM⁴⁴ is expected to be launched for 2021, that is when the 5 detectors network will be in operation.

Starting from then end of 2017, neutrino detections will be performed by the IceCube detector in its final configuration and by the KM3neT, an evolution of ANTARES into a multi-cubic-kilometer detector. The expected detection of GeV up to PeV neutrinos as well as MeV ones from IceCube from several sources of GWs will ensure this important piece of information in the multi-messenger astronomy⁸.

5 Summary

By 2019 the second generation GW detectors will reach their nominal sensitivity and by that time GWs detection is largely plausible. Best astrophysical candidates of high frequency GW (1Hz-10kHz) are the following transient sources: 1) coalescing binary systems of compact objects (Short GRBs); 2) core collapsing rotating stars (SNe, Long GRBs); 3) bursting/flaring magnetars (AXPs and SGRs). These sources are well known in the EM spectrum and neutrinos emission is also expected, therefore are ideal targets for multi-messenger studies. Past results from multi-messenger searches provided upper limits on the energetics in GW and source rate density still consistent

^c"range" is the maximum distance up to which one can detect the source, averaged over all the possible positions in the sky of the source (in terms of latitude and longitude) and over all the possible orientations of the system from which the GW amplitude depends (e.g. from a face-on case, where the maximum GW strain is expected, to a edge-on case)

^dThe list of MoU partners is published at https://gw-astronomy.org/wiki/LV_EM/PublicParticipatingGroups

^ehttp://swift.gsfc.nasa.gov/news/2014/sr_review.html

with current astrophysical models. According to theoretical modelling of ccSNe and flaring NSs, the strain sensitivity of the second generation GW detectors may be enough to enable a detection of nearby sources in the next years. At the same time, the probed distances for CBC systems will contain a number of sources consistent with a significant GW detection rate. The constantly improving localization capabilities of GW detectors network will enable the > 150 MoU partners to ensure EM counterpart detection and monitoring of the newly discovered GW sources.

Acknowledgments

G. Stratta is supported by the Italian Ministry of Education, University and Research via grant FIRB 2012- RBFR12PM1F and acknowledge M. Branchesi and P. Hello for useful discussions.

References

1. J. Abbott *et al*, Rep. Prog. Phys. **72**, 076901 (2009).
2. T. Accadia *et al*, Classical Quantum Gravity **28**, 114002 (2011).
3. A. Viceré, Astrophysics and Space Science Library **404**, 21 (2014).
4. J. Abbott *et al*, Astrophy. Journal. **715**, 1438 (2010).
5. C.L. Fryer and C.B. New, Living Reviews in Relativity **14**, 1 (2011).
6. C. D. Ott, Classical and Quantum Gravity **26**, 6 (2009)
7. J. Abadie *et al*, Astrophy. Journal **734**, 35 (2011).
8. A. Ando, *et al*, arxiv:1203.5192v2 , (2012)
9. M. Branchesi, *et al*, Journ. of Phys. Conf. Ser. **375**, 062004 (2014)
10. P. Mészáros, Rept.Prog.Phys. **69**, 2259L (2006).
11. W. Fong *et al*, Astrophy. Journal **780**, 118 (2014).
12. A.D. Kann *et al*, Astrophy. Journal **720**, 1513 (2010).
13. S.B. Cenko *et al*, apj **769**, 130 (2013).
14. B. D. Metzger and E. Berger, Astrophy. Journal **746**, 48 (2012).
15. B. D. Metzger *et al*, Month. Not. Roy. Astron. Soc. **446**, 1115 (2015).
16. N. R. Tanvir *et al*, Nature **500**, 547 (2013).
17. S. Campana *et al*, Nature **442**, 1008 (2006).
18. A. Soderberg *et al*, Nature **453**, 469 (2008).
19. S. Mereghetti, The Astronomy and Astrophysics Review **15**, 4 (2008).
20. K. Hirata *et al*, Phys. Rev. Lett. **58**, 1490 (1987).
21. R. M. Bionta *et al*, Phys. Rev. Lett. **58**, 1494 (1987).
22. P. Mészáros and E. Waxman, PRL **87**, 171102 (2001).
23. A. Buonanno and B.S. Sathyaprakash, arXiv:1410.7832v2 , (2014).
24. B. Iyer *et al*, LIGO-M1100296 , (2011).
25. K. Somiya, Classical and Quantum Gravity **29**, 124007 (2012)
26. J. Abadie *et al*, Astrophy. Journal **760**, 12 (2012a).
27. J. Aasi *et al*, PRD **90**, 2010 (2014a).
28. P. Evans *et al*, Astrophy. Journal. Suppl. **203**, 28 (2012)
29. Lazio *et al*,IAUS **285**, 65L (2012).
30. J. Aasi *et al*, PRL **113**, 011102 (2014b).
31. J. Abbott *et al*, Astrophy. Journal **681**, 1419 (2008).
32. J. Abadie *et al*, Astrophy. Journal **755**, 2 (2012b).
33. J. Abadie *et al*, Astrophy. Journal **734**, 35 (2012c).
34. R. Abbasi *et al*, Nuc. Instrum. and Meth. in Phys. Res. **A618**, 139 (2010).
35. M. Ageron *et al*, *et al*, Nuc. Instrum. and Meth. in Phys. Res. **A656**, 11 (2011).
36. S. Adrián-Martínez *et al*, JCAP **06**, 008 (2013).
37. J. Abadie *et al*, arxiv:1003.2480v2 , (2010a).
38. J. Aasi *et al*, arxiv1304.0670 , (2013b).
39. J. Clark *et al*, Astrophy. Journal , in press (2015).
40. Fairhurst *et al* , (2012)
41. J. Aasi *et al*, Phys. Rev. D **88**, 122004 (2013a).
42. Aartsen *et al*, PRD **90**, 102002 (2014).
43. J. Abadie *et al*, Astrophy. Journal **715**, 1453 (2010b).
44. S. Schanne *et al*, arXiv:1005.5008 , (2010)

Observational perspectives with advanced gravitational wave detectors

Andrea Viceré

on behalf of the LIGO Scientific Collaboration and of the Virgo Collaboration
*Dipartimento di Scienze di Base e Fondamenti, Università di Urbino "Carlo Bo",
Via S. Chiara 27, I-61029 Urbino (PU), Italy
Istituto Nazionale di Fisica Nucleare, Sezione di Firenze*



The installation and commissioning of 2nd generation, advanced gravitational wave detectors is progressing on schedule, and observations will start in the second half of 2015, beginning with the two LIGO detectors, whereas Virgo will join in 2016. The instruments will gradually lower their noise floor, eventually achieving a tenfold increase in amplitude sensitivity, which translates for some impulsive sources in a thousandfold increase in event rate. In this talk we will review the main science objectives and expected observational perspectives of the advanced detectors network.

1 Introduction

A second generation of interferometric, large gravitational wave detectors is about to start its observations: in the second half of 2015 the two Advanced LIGO (aLIGO) detectors¹ will carry out their first observational run O1, at a sensitivity that promises to be already significantly better than iLIGO. Then in the second half of 2016, after several further improvements, a O2 run will be carried out with the participation also of Advanced Virgo (AdV)².

The evolution of advanced detectors' sensitivity is anticipated in the official LIGO and Virgo plans³; a useful benchmark is the BNS range of the instrument, which is the distance at which a pair of neutron stars with $m_{1,2} = 1.4 M_{\odot}$ will yield an SNR of 8, after averaging over source direction and polarization^a.

In the Early phase (2nd half of 2015) aLIGO will have a range in the 40 – 80 Mpc range; in the Mid phase (2016-17) the range will ramp up to 80 – 120 Mpc, and in the Late phase (2017-18) to 120 – 170 Mpc. Similarly, AdV in the Early phase (2016-17) will have a range in 20 – 60 Mpc, in the Mid phase (2017-18) the range will increase to 60 – 85 Mpc and in the Late phase (2018-20) the range will lie in 85 – 115 Mpc. It is notable that AdV lags aLIGO by about 2 years; this is just the result of a later start of the Advanced Virgo project.

^aAt the same distance, an optimally located and polarized source would yield an SNR exceeding 18; this is why the "horizon distance", namely the distance at which an optimal source yields an SNR 8, is significantly larger than the range.

Eventually, the advanced detectors are expected to achieve their design sensitivity: for aLIGO, in 2019, with a range of 200 Mpc, for AdV in 2021, with a range of 130 Mpc. These figures of merit are about 10 times better than first generation instruments, thanks to the sensitivity improvements shown in Fig. 1; note that also the bandwidth will be widened, particularly at low frequencies for aLIGO.

In addition to LIGO and Virgo instruments, in 2016 it is expected to start its operation the KAGRA detector⁶, which may join the network around 2018 with comparable sensitivity.

Which science will the advanced detectors harvest thanks to these improvements? It is the purpose of this short note to summarize the expected scientific outcomes, focusing on topics which are best known, with no attempt at any generality.

2 Binary coalescences

The one source of gravitational waves (GW) we have several certainties about is the coalescence of binary neutron stars (BNS); thanks to the observation of binary pulsars, we know that these sources do exist⁷. Furthermore, their dynamics is computable and allows predicting the resulting GW signal with accuracies good enough to grant applying matched filtering techniques, which potentially yield optimal sensitivity in the analysis⁸. And finally, a number of studies based both on the observed binary systems and on the simulation of stellar evolution allow to predict the abundance of these sources, as summarized in⁹. Similar studies allow to predict the abundance of pairs of black holes (BH) or of BH and NS, although with lesser certainty for lack of observed systems.

The advanced detectors at design sensitivity will be able to monitor about 10^5 galaxies for the occurrence of BNS coalescences, in a volume of space 1000 times larger than the one monitored by first generation instruments. In such a volume, the number of detectable BNS events is still pretty uncertain: realistic values of 40 events/year are reported, but these could be significantly higher or smaller, down to less than 1 event/year in the pessimistic case, or up to 400 events/year in a more optimistic scenario. The volume accessible when looking for BH-NS or BH-BH events is potentially much larger, but the abundance in a given galaxy is expected to be much smaller, so that the predicted event rates are similar to those for BNS.

Assuming that nature provides us with a significant number of observations, what will we learn from them?

2.1 Constraining the evolution of massive stars

Advanced detectors will *measure* the rate of binary coalescences, and this will help constraining the formation and evolution of massive stars, and shed light on the mechanisms that lead to binary systems sufficiently tight to coalesce in less than a Hubble time.

This is particularly interesting for pairs of massive black holes, say of $O(100) M_{\odot}$, whose coalescence would yield GW events detectable out to $z \sim 2$, and for which the models are highly uncertain¹⁰, to the point that some mechanisms predict no binaries at all.

For binary black holes, the shape of the signal received can provide information about the relative configuration of the BH spins and of the orbital angular momentum of the system; actually, two configurations characterized by different spin-orbit resonances exist, and they carry an imprint of the formation scenario of the binary, which might therefore be accessible by measuring with advanced detectors the fraction of systems in each configuration¹¹.

2.2 BNS as standard sirens

It is well known that binary neutron stars can provide information about the Hubble constant¹²; the basic idea is that the *shape* of the BNS signal gives access to the mass of the stars involved,

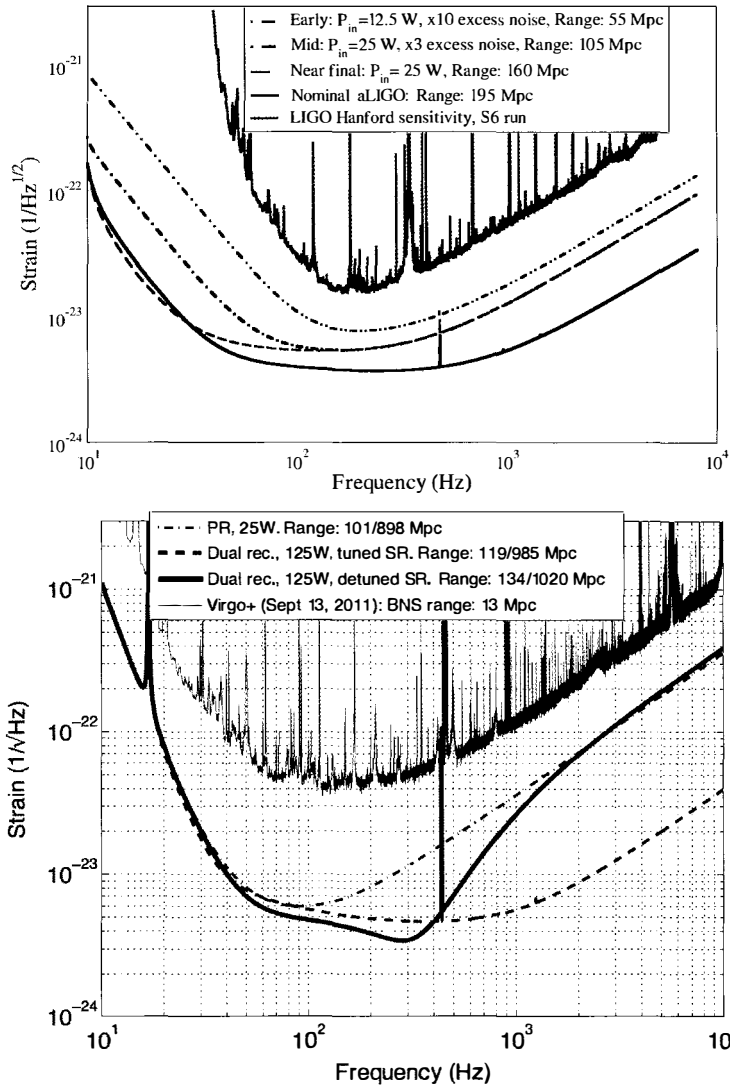


Figure 1 – Up: expected sensitivity of Advanced LIGO (aLIGO) in different configurations⁴, compared with the best sensitivity achieved during run S6⁵. Down: expected sensitivity of Advanced Virgo (AdV) in different configurations², compared with the sensitivity achieved in September 2011; where the “Range” reports two figures, the first one is the range for BNS sources, the second one for BBH sources of $10+10M_{\odot}$.

and therefore allows predicting the expected amplitude of the GW signal. The measured amplitude depends on the distance of the system, but also on the relative orientation of the detector and of the source system; a network of instruments allows to deconvolve the effect of the antenna patterns and therefore to extract the distance information.

At this point, if one has access to an electromagnetic counterpart, and is therefore able to identify the host galaxy, its recession speed can be correlated with its measured distance, thus providing a sample measurement of the Hubble constant H_0 ; already 10 sample measurements within 100 Mpc would yield a 3% accuracy.

Recently it has been shown that it is not mandatory to identify the host galaxy by detecting an electromagnetic counterpart: combining the sky localization information made possible by the network of interferometric detectors with a catalogue of potential host galaxies, it is still possible to perform a reasonable association¹³, using a larger number of events, say 30, in order to achieve a comparable accuracy. It is worth underlining that the electromagnetic signal may not be accessible for a large part of GW events because of short GRB beaming effects, hence this method is expected to be competitive. The drawback is that a fairly complete catalogue of galaxies is required, whereas out to $z \sim 0.1$ such catalogues are known to be still incomplete, though surveys have been proposed¹⁴ which could raise their completeness above 50%.

2.3 Equation of state of neutron stars

The two-body dynamics, albeit complex to calculate, is relatively straightforward even in General Relativity, as far as the masses can be considered points; things get much more complicated, but also more interesting, when the NS starts to be deformed by the tidal forces. The equation of state (EOS) of the nuclear matter that is supposed to constitute these objects becomes relevant, and this affects the last stages of the coalescence before the merger, which reflects in the shape of the signal. Basically, if the EOS is "soft", namely if a change of density yields a smaller pressure increase, the star is easier to compress and the collapse to a black hole is prompt, yielding a waveform which terminates more abruptly. Conversely, if the EOS is "stiff", even a small density change yields a large pressure change, and the star resists to compression; hence during the merger a structure may form, like a bar mode, which lasts for some orbits before the collapse. As a result, the merger waveform is more complicated, with oscillations relating with the rotation of the bar.

It has been shown that these effects can be visible already in second generation detectors^{15,16,17}, and the observation of a realistic number of events would allow measuring parameters like the NS radius or its tidal deformability with interesting accuracies.

2.4 The BNS - GRB connection

A BNS coalescence is long proposed to be the origin of the short GRBs¹⁸, but this association will not be confirmed until we are able to observe a temporal and spatial coincidence between the e.m. energy emitted by the GRB and a GW signals consistent with a coalescence.

Even though first generation detectors have searched for such associations¹⁹, the chances to find any were dim, since less than 7% of the observed GRB have redshift smaller than 10^{-1} , whereas LIGO and Virgo could exclude events only up to a redshift about 10 times smaller. The situation, as shown in the same paper, changes with advanced detectors: referring particularly to Fig. 8 in¹⁹, the population of observed GRB becomes comparable with the projected exclusion curves in the advanced detectors era, which means that an observed association is possible or an exclusion will be highly significant.

2.5 Tests of General Relativity

The good theoretical knowledge of the GW signal emitted by a BNS coalescence, along with the possibility of detecting a fair number of events, will allow performing also tests of General

Relativity, for instance to probe the 1.5 Post-Newtonian contribution to the phase of the signal at the 10% level²⁰, an accomplishment which is not possible for instance using data from binary pulsars or electromagnetic observations. Analysis methodologies exist to this end which have been shown to be robust against poorly modeled effects of an instrumental, astrophysical, and fundamental nature²¹.

3 Supernovae

Supernovae events are a potential source of short GW signals. Their rate is known with reasonable accuracy, particularly thanks to the observation by the INTEGRAL satellite²² of the γ -rays emitted by the isotope ²⁶Al, copiously produced by supernovae; we expect about 1 event/century in our own Milky Way, whereas we observe several events/year in the Virgo Cluster.

Of the different kinds of supernovae, we expect an emission of GW from the so-called *core-collapse* ones, in which the nucleus undergoes a rapid implosion. However, the waveform emitted depends on how asymmetric the implosion is, which remains a matter of modeling. As of today, the energy emitted in GWs by supernovae is highly uncertain, with different models predicting values in the $10^{-11} - 10^{-7} M_{\odot} c^2$ range²³.

In addition to the uncertainty in the emitted energy, also the details of the waveforms are not fully known, even though the simulations allow to predict some general characteristics about their duration. For such signals, a convenient figure of merit is the root square mean signal

$$h_{rss} \equiv \sqrt{\int \left[|h_+(t)|^2 + |h_{\times}(t)|^2 \right] dt} . \quad (1)$$

Advanced detectors will be able to probe values of $h_{rss} \leq 10^{-23} \text{Hz}^{-1/2}$, however the translation into an energy is distance and model dependent. For signals close to the frequency range where the detectors have their best sensitivity, such h_{rss} value translates into $E_{GW} \leq 10^{-9} M_{\odot} c^2$, for a source at 10 kpc²⁴.

It is clear from these considerations that the detection of the next galactic supernova is possible, but not certain: apart from the possibility that the signal is emitted according to pessimistic models, and therefore falls below the analysis threshold, the duty cycle of the detector network, particularly in double coincident mode^b, will certainly not be 100%.

The detection of non-galactic supernovae will be limited, assuming optimistic emission models, to a range of few Mpc, therefore to the galaxies of the Local Group.

Despite the uncertain prospects, even the detection of a single supernova could yield very important scientific results. For instance there are good reasons to believe that the neutrino flash and the gravitational signal are emitted almost simultaneously, therefore any delay among the two signals received should be due to the propagation itself. Assuming that GW propagate at the speed of light, the delay could be due to the neutrino mass²⁵:

$$\delta t_{prop} = 5 \text{ms} \frac{d}{10 \text{kpc}} \left(\frac{m_{\nu}}{1 \text{eV}} \right)^2 \left(\frac{10 \text{MeV}}{E_{\nu}} \right)^2 \quad (2)$$

on which stringent limits could be placed.

The collapse of very large stars has been proposed as a mechanism to explain the class of long γ -ray bursts. Again signal models are quite uncertain; under optimistic assumptions the advanced instruments could detect transient GW in coincidence with long GRBs as far away as 300 Mpc, a distance at which such events are not infrequent (a few/year)^{26,27}.

^bA double or triple coincidence will be probably needed in order to reject false alarms, which in absence of a signal model could be unacceptably frequent.

4 Periodic signals

The detection of continuous signals emitted by rotating NS has long been one of the main objectives of interferometric detectors, and the sensitivity improvement granted by advanced detectors will translate directly in improved upper limits on the signal amplitude, constraining the parameters of the emitter. The signal has the characteristic amplitude

$$h \simeq 3 \times 10^{-27} \left(\frac{10 \text{ kpc}}{r} \right) \left(\frac{I}{10^{45} \text{ g cm}^2} \right) \left(\frac{f}{100 \text{ Hz}} \right)^2 \left(\frac{\epsilon}{10^{-6}} \right) \quad (3)$$

which tells that the detection is necessarily limited to galactic NS. Nevertheless, even focusing just on the known pulsars, for several tens of objects it will be possible to place relevant upper limits on the amplitude²⁸, which will translate linearly into better limits on the oblateness parameter ϵ , thus providing information about the deformability of the star and its EOS.

5 Stochastic background

The first generation detectors have been able to place upper limits on the logarithmic energy spectrum in gravitational waves, defined as

$$\Omega(f) = \frac{f}{\rho_c} \frac{d\rho_{GW}(f)}{df} ; \quad (4)$$

for instance, assuming a flat spectrum $\Omega(f) = \Omega_0$, a limit $\Omega_0 < 6.9 \times 10^{-6}$ has been placed²⁹.

The advanced detectors will improve significantly over this limit, achieving $\Omega_0 < 10^{-9} - 10^{-10}$. This is at first sight not obvious, since as commonly stated the advanced detectors will achieve a tenfold improvement in *amplitude* sensitivity, hence a limit on *energy* should be "just" 100 times better. Actually, as shown in Fig. 1, the bandwidth is going to be significantly widened towards low frequencies, and this results in a further factor 10 – 100 in sensitivity to Ω , depending on the configuration.

Will these sensitivities grant a significant breakthrough in the search for a cosmological stochastic background? Not for the cosmological background due (for instance) to slow-roll inflation, which is predicted³⁰ to scale as

$$\Omega(f) \sim 10^{-16} \left(\frac{\mathcal{V}}{10^{16} \text{ GeV}} \right)^2 \quad (5)$$

as a function of the unknown energy scale of inflation \mathcal{V} , and is expected to be several orders of magnitude weaker than the range accessible to advanced detectors.

But other sources of stochastic background will be constrained, for instance most of the parameter space for cosmic (super) string models will become accessible³¹.

6 Conclusions

Advanced detectors are about to start their operation, and we have good reasons to expect that several sources will become accessible, thanks to the improved detectors' sensitivity.

Are we going to witness the birth of observational gravitational astronomy? Time will, soon, tell!

Acknowledgments

The authors gratefully acknowledge the support of the United States National Science Foundation (NSF) for the construction and operation of the LIGO Laboratory, the Science and Technology Facilities Council (STFC) of the United Kingdom, the Max-Planck-Society (MPS),

and the State of Niedersachsen/Germany for support of the construction and operation of the GEO600 detector, the Italian Istituto Nazionale di Fisica Nucleare (INFN) and the French Centre National de la Recherche Scientifique (CNRS) for the construction and operation of the Virgo detector and the creation and support of the EGO consortium. The authors also gratefully acknowledge research support from these agencies as well as by the Australian Research Council, the International Science Linkages program of the Commonwealth of Australia, the Council of Scientific and Industrial Research of India, Department of Science and Technology, India, Science & Engineering Research Board (SERB), India, Ministry of Human Resource Development, India, the Spanish Ministerio de Economía y Competitividad, the Conselleria d'Economia i Competitivitat and Conselleria d'Educació, Cultura i Universitats of the Govern de les Illes Balears, the Foundation for Fundamental Research on Matter supported by the Netherlands Organisation for Scientific Research, the Polish Ministry of Science and Higher Education, the FOCUS Programme of Foundation for Polish Science, the European Union, the Royal Society, the Scottish Funding Council, the Scottish Universities Physics Alliance, the National Aeronautics and Space Administration, the Hungarian Scientific Research Fund (OTKA), the Lyon Institute of Origins (LIO), the National Research Foundation of Korea, Industry Canada and the Province of Ontario through the Ministry of Economic Development and Innovation, the National Science and Engineering Research Council Canada, the Brazilian Ministry of Science, Technology, and Innovation, the Carnegie Trust, the Leverhulme Trust, the David and Lucile Packard Foundation, the Research Corporation, and the Alfred P. Sloan Foundation. The authors gratefully acknowledge the support of the NSF, STFC, MPS, INFN, CNRS and the State of Niedersachsen/Germany for provision of computational resources.

This document has been assigned LIGO Laboratory document number LIGO-P1500092.

References

1. J. Abadie *et al.*, *Class. Quantum Grav.* **32**, 074001 (2015)
2. F. Acernese *et al.*, *Class. Quantum Grav.* **32**, 024001 (2015)
3. J. Aasi *et al.*, arXiv:1304.0670 [gr-qc]
4. L. Barsotti and P. Fritschel, *Early aLIGO Configurations: example scenarios toward design sensitivity*, LIGO-T1200307-v4, <https://dcc.ligo.org/LIGO-T1200307/public>
5. LSC and Virgo Collaborations, *Sensitivity Achieved by the LIGO and Virgo Gravitational Wave Detectors during LIGOs Sixth and Virgos Second and Third Science Runs*, LIGO-T1100338-v13, <https://dcc.ligo.org/LIGO-T1100338/public>
6. T. Akutsu (for the KAGRA collaboration), *J. Phys.: Conf. Ser.* **610**, 012016 (2015)
7. D. Lorimer, *Living Rev. Rel.* **11**, 8 (2008)
8. L. Blanchet, *Living Rev. Rel.* **17**, 2 (2014)
9. J. Abadie *et al.*, *Class. Quantum Grav.* **27**, 173001 (2010)
10. K. Belczynski *et al.*, *ApJ* **789**, 2014 (120)
11. D. Gerosa *et al.*, *Phys. Rev. D* **89**, 2014 (124025)
12. B.F. Schutz, *Nature* **323**, 310 (1986)
13. W. Del Pozzo, *Phys. Rev. D* **86**, 043011 (2012)
14. B.D. Metzger *et al.* *ApJ* **764**, 2013 (149)
15. W. Del Pozzo *et al.*, *Phys. Rev. Lett.* **111**, 071101 (2013)
16. B.D. Lackey and L. Wade, *Phys. Rev. D* **91**, 043002 (2015)
17. M. Agathos *et al.*, arXiv:1503.05405 (Phys. Rev. D, to appear)
18. D. Eichler *et al.*, *Nature* **340**, 126 (1989)
19. J. Abadie *et al.*, *ApJ* **760**, 12 (2012)
20. T.G.F. Li *et al.*, *Phys. Rev. D* **85**, 082003 (2012)
21. M. Agathos *et al.*, *Phys. Rev. D* **89**, 082001 (2014)
22. R. Diehl *et al.* (INTEGRAL), *Nature* **439**, 45 (2006)

23. C. L. Fryer and K. C. B. New, *Living Rev. Rel.* **14**, 1 (2011)
24. J. Abadie *et al.*, *Phys. Rev. D* **85**, 122007 (2012)
25. N. Arnaud *et al.*, *Phys. Rev. D* **65**, 033010 (2002)
26. J. Aasi *et al.* *Phys. Rev. D* **88**, 122004 (2013)
27. J. Aasi *et al.* *Phys. Rev. Lett.* **113**, 011102 (2014)
28. J. Aasi *et al.*, *ApJ* **785**, 119 (2014)
29. J. Aasi *et al.* *Phys. Rev. Lett.* **113**, 231101 (2014)
30. A. Cooray, *Mod. Phys. Lett. A* **20**, 2005 (2503)
31. X. Siemens *et al.*, *Phys. Rev. Lett.* **98**, 111101 (2007)

PLANNED SEARCH FOR LIGO/GBM COINCIDENCE IN THE LIGO O1 DATA RUN

Jordan Camp¹, Lindy Blackburn², Michael S. Briggs³, Nelson Christensen⁴,
Valerie Connaughton³, Leo Singer¹, Peter Shawhan⁵, John Veitch⁶

¹*Astrophysics Science Division, Goddard Space Flight Center, Greenbelt, Md 20771*

²*Harvard-Smithsonian Center for Astrophysics, Cambridge, Mass 02138*

³*CSPAR, University of Alabama, Huntsville, Al 35899*

⁴*Physics Department, Carleton University, Northfield, Minn. 55057*

⁵*Physics Department, University of Maryland, College Park, Md 20742*

⁶*Physics Department, Cardiff University, Cardiff, UK*

In the fall of 2015 the first scientific observing run (O1) of the advanced LIGO detectors will be conducted. Based on the recent commissioning progress at the LIGO Hanford and Livingston sites, the gravitational wave detector range for a neutron star binary inspiral is expected to be of order 60 Mpc. We describe here our planning for an O1 search for coincidence between a LIGO gravitational wave detection and a gamma-ray signal from the Fermi Gamma-ray Burst Monitor. Such a coincidence would constitute measurement of an electromagnetic counterpart to a gravitational wave signal, with significant corresponding scientific benefits, including revealing the central engine powering the gamma-ray burst, enhanced confidence in the event as a genuine astrophysical detection, and a determination of the relative speed of the photon and graviton.

1. LIGO

The remaining years of this decade are likely to see a direct detection of a gravitational wave (GW). A passing gravitational wave produces a differential strain (ratio of change in distance to distance between two points at rest) in space-time along orthogonal directions transverse to the direction of propagation, and can be observed through the relative timing of the passage of light waves along these directions. Because gravity is a very weak force, the strain expected at the earth from the gravitational waves of even the strongest astrophysical sources is very small, of order 10^{-21} .

The general design of the Laser Interferometer Gravitational Wave Observatory (LIGO) gravitational wave detector is shown in Fig. 1, and is based on the principle of laser interferometry¹. A very high level of displacement sensitivity, of order 10^{-18} m rms, is achieved through careful attention to the frequency and amplitude stability of the laser light, the losses of the interferometer optics, the seismic isolation system which decouples the interferometer from motions of the earth, and the suspension system which stabilizes and positions the optics. Kilometer scale detectors are required to enable sufficient strain sensitivity for gravitational wave detection.

The LIGO detectors in Hanford, Washington (Fig. 2) and Livingston, Louisiana have recently undergone an upgrade² to enhance their range for observation of the GW from a neutron star binary inspiral. Compared to the initial LIGO configuration (disassembled in 2010), the range will ultimately be increased by a factor of 10, from 20 Mpc to 200 Mpc. At the full 200 Mpc sensitivity, the detection rate of NS binary inspirals will be of order 40/yr.³

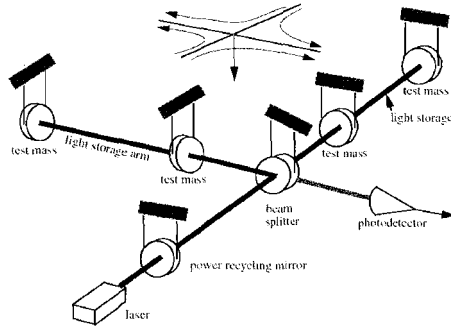


Figure 1. Gravitational wave interferometric detector

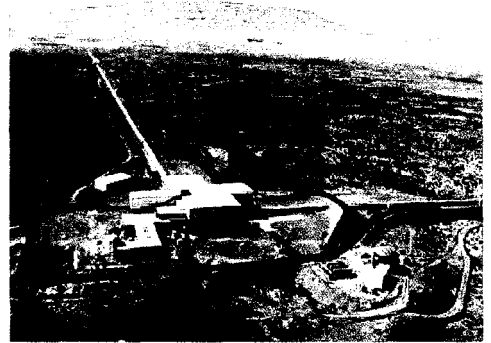


Figure 2. Aerial view of LIGO site at Hanford, Washington

At the time of this writing, the LIGO detector ranges were 35 Mpc and 69 Mpc for Hanford and Livingston, respectively. By the time of the first 3-month advanced LIGO observing run (O1, fall 2015), chances are good that both detectors will be operating in the range of ~ 60 Mpc. Subsequent planned runs include O2 (6 months, fall 2016, ~ 100 Mpc) and O3 (9 months, fall 2017, ~ 150 Mpc)⁴.

2. Fermi GBM

The Fermi mission⁵ (Fig. 3) was launched by NASA in 2008. Designed to survey the gamma-ray sky, it consists of two instruments: the imaging Large Area Telescope (LAT), designed to observe gamma-rays in the energy range of 20 MeV–300 GeV, and the Gamma-ray Burst Monitor (GBM)⁶, sensitive to lower energy gamma-rays from 8 keV to 40 MeV.

GBM (Fig. 4) consists of 11 NaI detectors which have an energy range of up to 1 MeV, and 2 denser BGO detectors which have sensitivity up to 40 MeV. These detectors are affixed to the Fermi spacecraft in varying orientations, as shown in Figure 3. The NaI detectors have a $\cos \theta$ response relative to angle of incidence, providing a position sensitivity to a gamma-ray source of ~ 5 degree by using the relative rates of differently-oriented detectors. GBM has a field of view (FoV) of 63% of the sky, ensuring that a gamma-ray source within the LIGO range that is beamed at the earth will have a good chance of detection.

3. Short Gamma-ray Bursts and GW Gamma-Ray Counterparts

The detection of a gamma-ray counterpart to a gravitational wave signal from an NS-NS or NS-BH merger will powerfully enhance the science of the compact merger event. In brief, the detection of a

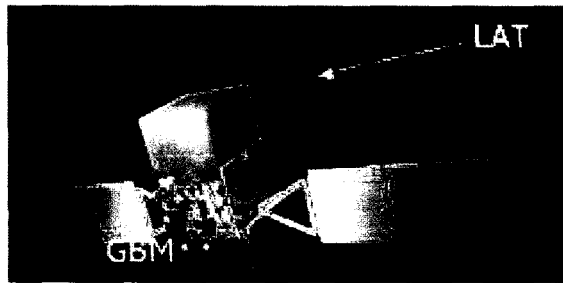


Figure 3. Fermi spacecraft showing LAT and GBM instruments

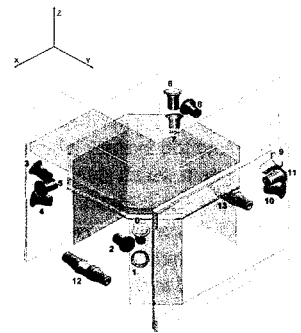


Figure 4. GBM detector array. Detectors 1–11 are NaI, 12–13 are BGO

counterpart will: 1) test predictions of General Relativity, including the speed and polarizations of gravitational waves; 2) raise the confidence level of a GW detection by reducing false alarms; and 3) determine the engine of the sGRB (NS-NS or NS-BH) through the analysis of the GW.

The short gamma-ray burst⁷ (sGRB) is an extremely energetic event powered by accretion onto a central compact object, which produces a jet of gamma-rays lasting less than two seconds. Strong circumstantial evidence identifies the sGRB engine as an NS-NS or NS-BH merger, whose inspiral is also the main anticipated source of gravitational waves for LIGO. The sGRB, observed with a rate density of $\sim 10 \text{ Gpc}^{-3}\text{yr}^{-1}$ (ref. 8), is thus an excellent candidate for a GW/gamma-ray coincidence. Given an expected NS-NS horizon for the LIGO O1, O2, and O3 runs of 60 Mpc, 100 Mpc, and 150 Mpc, respectively, and including a range enhancement factor of ~ 2 from the gamma-ray coincidence⁹, the number of GW/gamma-ray coincidences detected in these runs will be of order 0.02, 0.1, and 0.5 respectively. If the engine includes a BH (mass $\sim 10 M_{\odot}$), the horizon is doubled and the rates increase by a factor of 8.

A further interesting possibility for a gamma-ray counterpart is the production of a so-called sGRB precursor through the resonant cracking of a NS crust¹⁰. In this model, seconds before the NS merger of a binary inspiral, tidal deformation of a NS causes crust disruption by resonant excitation of a bulk-crust interface mode. The crust cracking then couples to the NS magnetic field to produce near-isotropic gamma-rays. Observation of a precursor in coincidence with a GW could determine the crust resonant frequency and provide information on the NS equation of state.

4. LIGO-GBM coincidence search: Detection Pipeline

The detection pipeline¹¹ for the LIGO-GBM coincident search is outlined in the flowchart of Figure 5. It consists of four steps: i) the identification of a GW trigger using a template-based analysis of the LIGO time-series data; ii) the extraction of the sky location of the GW event using a fast parameter estimation code BAYESTAR¹²; iii) the coherent analysis of the GBM detector data to determine consistency with the time and sky location of the LIGO trigger; and iv) the final output of the LIGO-GBM coincident events.

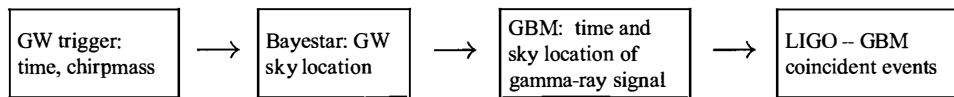


Figure 5. Flowchart of LIGO-GBM analysis pipeline

The initial step in the detection pipeline is the identification of a GW trigger. This is done primarily through the use of matched filtering, correlating the GW data in each detector against a bank of theoretical templates composed of model inspiral chirp signals with various component masses and possibly spin¹³. For the filter corresponding to a frequency domain signal $\tilde{h}(f)$, the matched filter produces an expected single-detector S/N of

$$\rho^2 = \int_0^{\infty} 4 \frac{|\tilde{h}(f)|^2}{S_n(f)} df \quad (1)$$

where $S_n(f)$ is the power spectral density of the stationary noise. When the event has a ρ value above a predetermined threshold (e.g., one false alarm per 10^3 yr), the event is considered a GW candidate.

Once a GW trigger has been generated, the algorithm BAYESTAR¹² is used for sky localization. BAYESTAR is a rapid Bayesian position reconstruction code that produces accurate sky maps less than a minute after a BNS merger detection, by using the times, phases, and amplitudes of the GW coincident signals. This allows the delivery of real-time alerts to the astronomical community.

The gamma-ray signal is determined using a coherent offline analysis of the 14 GBM detectors, allowing the possibility of sub-threshold detection¹¹ with respect to the on-board two-detector coincidence. This involves the maximum likelihood $\Lambda_{GBM}(d, H)$, which is calculated as the probability

of measuring the observed GBM data d in the presence of a model signal H relative to the probability from background fluctuations alone:

$$\Lambda_{GBM} \sim \prod_i \frac{\sigma_{n_i}}{\sigma_{d_i}} \exp\left(\frac{(d_i - n_i)^2}{2\sigma_{n_i}^2} - \frac{(d_i - n_i - r_i s)^2}{2\sigma_{d_i}^2}\right) \quad (2)$$

where for a given model (time, duration, spectrum, sky location) d_i is the data and n_i is the expected contribution from background; σ_{d_i} is the expected standard deviation of the total measured counts and σ_{n_i} is the standard deviation from background alone. The instrumental response r_i is a function of source spectrum and location and when multiplied by source amplitude at the earth, $r_i s$ gives the expected contribution to each of the measured counts from the presence of the model signal.

The final probability of a GW / gamma-ray coincidence is then given by

$$\Lambda_{GW-GBM} = \int P_{GW}(\Omega) \Lambda_{GBM}(\Omega) d\Omega \quad (3)$$

where $P_{GW}(\Omega)$ is the GW probability distribution over the sky, derived from BAYESTAR.

The GW-triggered approach presented here will be able to provide an automated characterization of the high-energy sky during the time of known NS/NS mergers seen by Advanced LIGO. An alternate strategy to search for GW's associated with GRB's involves triggering a deep search in GW data using the time and sky location of known GRB's¹⁴. Finally, this LIGO-GBM search also complements related efforts with ground-based optical telescopes.¹⁵

5. Summary

We have presented our plan for the upcoming LIGO O1 science run, which involves a search for a GW / gamma-ray coincidence. At the expected O1 detector ranges in fall 2015, a detection of a coincidence is not likely. However the search will allow us to implement and test the detection pipeline, and be ready for the future O2 and O3 runs where a GW / gamma-ray coincidence becomes increasingly plausible.

References

1. Abbott, BP et al, 2009, Reports on Progress in Physics **72**, 076901
2. Aasi, J et al, 2015, Classical and Quantum Gravity **32**, 074001
3. Abadie J et al, 2010, Classical and Quantum Gravity **27**, 173001
4. Aasi, J et al, 2013, arXiv:1304.0670
5. www.fermi.gsfc.nasa.gov
6. Meegan, C et al., 2009 Astrophysical Journal **702**, 791
7. Nakar, E, 2007, Physics Reports 442, 166
8. Guetta, D et al, 2006, Astronomy and Astrophysics **453**, 823
9. Camp, J et al, 2013, Experimental Astronomy **36**, 505
10. Tsang, D et al, 2012, Physical Review Letters **108**, 011102
11. Blackburn, L et al, 2015, The Astrophysical Journal Supplement **217**, 8
12. Singer, L et al, 2014 Astrophysical Journal **795**, 105
13. Abadie, J et al, 2012, Phys. Rev. D **85**, 082002
14. Abadie, J et al, 2012, The Astrophysical Journal **760**, 12
15. Abadie, J et al, 2012, Astronomy & Astrophysics **541**, A155

Search for Joint sources of gravitationnal waves and high energy neutrinos with the LIGO-Virgo and ANTARES Detectors

Bruny Baret for the ANTARES and LIGO and Virgo collaborations.

*Astroparticule et Cosmologie , 10 rue Alice Domon et Lonie Duquet,
75013 Paris, France*

Cataclysmic cosmic events can be plausible sources of both gravitational waves (GW) and high energy neutrinos (HEN), alternative cosmic messengers carrying information from the innermost regions of the astrophysical engines. Possible sources include long and short gamma-ray bursts (GRBs) but also low-luminosity or choked GRBs, with no or low gamma-ray emissions. The ANTARES Neutrino Telescope can determine accurately the time and direction of high energy neutrino events, and the Virgo/LIGO network of gravitational wave interferometers can provide timing/directional information for gravitational wave bursts. Combining these informations through GW+HEN coincidences provides a novel way of constraining the processes at play in the sources, and also enables to improve the sensitivity of both channels relying on the independence of backgrounds of each experiment. We will describe the joint GW+HEN search performed using data taken with the ANTARES telescope in 2009-2010 (with the full ANTARES) combined with data from the Virgo/LIGO interferometers during the VSR1/S5 and VSR2-3/S6 (with improved sensitivities) science runs. The first 2007 search had allowed to place the first upper limits on the density of joint GW+HEN emitters, and the 2009-2010 analysis will allow a significant improvement in sensitivity.

1 Introduction

Multimessenger astronomy is at a turning point. With the first cosmic High Energy Neutrinos (HEN) detection by the IceCube experiment¹ and the very probable detection of Gravitational Waves (GW) with the advanced generation of the LIGO² and Virgo³ detectors a new window opens on the Universe with new messengers conserving timing and directionality in complement to electromagnetic observations. In particular, beside enabling to decrease detection threshold of corresponding GW and HEN detectors, the search for a coincident signal can give access to electromagnetically dark sources like the so called "choked GRBs"⁴ which could constitute the missing link between core collapse supernovae and GRBs. Building on the experience of the first pioneer search in 2007 concomitant data of ANTARES and LIGO-Virgo⁵ which was performing a GW search with triggers constituted by neutrino candidates used for the search of HEN point sources, and following the common 2009 IceCube-LIGO-Virgo analysis⁶ which introduced a more complete and symmetrical characterisation⁷ of the events taking into account information from both HEN and GW sides to better discriminate signal from background, we performed an optimisation of the HEN trigger list in order to maximise the number of sources detectable by the search.

2 Detectors and associated datasets

2.1 The ANTARES neutrino telescope

Neutrino telescopes rely on the detection of the Cherenkov light generated by the products of the interaction of a high energy neutrino in the vicinity of the detector or inside it. They consists of a tridimensionnal array of photomultipliers in a very large volume of transparent medium like glacier ice or deep sea. The reconstruction of the direction of the impinging neutrino is done from the timing of the signal recorded by the photomultipliers and its energy can be estimated thanks to the amount of light detected by the triggered photomultipliers. The ANTARES telescope⁸ is located at a depth of 2400m in the french Mediterranean Sea off the coast of Toulon, at $42^{\circ}48' N, 6^{\circ}10' E$. It comprises 885 optical modules housing with $10''$ photomultipliers in $17''$ glass spheres installed on 12 strings representing an instrumented volume of 0.02 km^3 . The data used in this analysis cover the period from July 7th 2009 to October 20th 2010 for a total observation time of 266 days. The most suited event sample to this search, due to its good pointing angular resolution (below the degree) is the one coming from charge current interactions from muon neutrinos producing a track-like signal in the detector.

2.2 The LIGO and Virgo Gravitational wave interferometers and associated data set

LIGO² and Virgo³ gravitationnal wave detectors rely on perpendicular km-size Fabry-Perrot cavities forming a Michelson interferometers tuned to the dark fringe. Any gravitationnal wave passing through the detector would induce a difference of path length in the two arms thus changing the interference pattern. The direction of an event is reconstructed by time of flight techniques which implies the use of at least two detectors. The GW data used in this search are the S6-VSR2/3 LIGO-Virgo data. Three detectors participated to this data taking namely LIGO-Livingston and LIGO-Hanford in the US and Virgo near Pisa in Italy. These data were collected between July 07, 2009 and October 21, 2010.

Common dataset

The concomitant data taking period between S6VSR2/3 and ANTARES goes from July 7th, 2009 up to October 20th 2010 with some in between periods where one or no interferometer was in science mode. In this period, the observation time for each interferometer network configuration (two or three interferometers taking data at the same time) is $\tau \equiv 128.7$ days.

3 Joint optimisation of the common data-set

Definition of the joint Figure-of-merit

The approach adopted here is to optimise the HEN and GW selection cuts to maximize the number $\mathcal{N}_{\text{GWHEN}}$ of detectable sources emitting both GW and HEN. A trade off should be found between on the one hand the fact that relaxing cuts on the HEN side will enhance efficiency to HEN signal, making the number of candidates grow, and on the other hand the fact that this makes necessary to apply harder GW cuts in order to maintain the False Alarm Rate (FAR) below a fixed value. Let us assume that the sources are all identical and radiate E_{GW} in GW and emit a fluence φ_{ν} in HEN. Let us further assume that their population is isotropic so their density per unit time and volume R is a constant. The number of detectable sources is

$$\mathcal{N}_{\text{GWHEN}}(\text{cuts}) = \int dt d^3\Omega \mathcal{R}(r, t) \epsilon_{\nu}(\text{cuts}) \epsilon_{\text{GW}}(\text{cuts}; E_{\text{GW}}, r) \quad (1)$$

where $\mathcal{R}(r, t) = R \mathcal{P}(N_{\nu} > 0 | \varphi_{\nu} / (4\pi r^2))$ is the density of detectable sources. From Poisson statistics, we get $\mathcal{P}(N_{\nu} > 0 | \varphi_{\nu} / (4\pi r^2)) \propto 1/r^2$ in the limit of small fluxes. We optimize over

the cut thresholds applied to the two following parameters: the quality of the muon track reconstruction Λ and a proxy to the signal-to-noise ratio ρ for the HEN and GW, respectively. We obtain

$$\mathcal{N}_{\text{GWHEN}}(\Lambda, \rho_{\text{threshold}}) \propto \int_0^\infty 4\pi r^2 dr \frac{1}{r^2} \epsilon_\nu(\Lambda) \epsilon_{\text{GW}}(\rho_{\text{threshold}}; E_{\text{GW}}, r) \quad (2)$$

where $\epsilon_i \in \{\text{GW}, \text{HEN}\}$ are the detector efficiencies to signal. ϵ_{GW} can be reasonably well approximated by a step-like function with the edge placed at the maximum distance $D(\rho_{\text{threshold}})$ at which a GW source is detectable, i.e., the GW *horizon*, therefore :

$$\mathcal{N}_{\text{GWHEN}}(\Lambda, \rho_{\text{threshold}}) \propto \epsilon_\nu(\Lambda) \int_0^{D(\rho_{\text{threshold}})} dr \quad (3)$$

For a GW “standard candle”, $\rho_{\text{threshold}}$ is inversely proportional to $D(\rho_{\text{threshold}})$. Therefore, we get

$$\mathcal{N}_{\text{GWHEN}}(\Lambda, \rho_{\text{threshold}}) \propto \epsilon_\nu(\Lambda) / \rho_{\text{threshold}} \quad (4)$$

As a conclusion, our aim is to tune the neutrino selection cuts in order to maximize the figure-of-merit given by the ratio $\epsilon_\nu(\Lambda) / \rho_{\text{threshold}}$.

List of neutrino candidates

Applying this optimal cut leads to 1986 neutrino candidates each of them characterized by its arrival time, sky direction, energy and associated error box. The energy estimator is the number of hits (or n^{hit}) used in the track fit and the error box ASW90% is defined as the 90% percentile of the distribution of space angles ψ between the reconstructed muon and the in-pinging neutrino direction estimated from Monte Carlo simulations. To each neutrino candidate i will be attached a p-value p_i^{HEN} i.e. the probability that the atmospheric background would produce an event with at least the number of hits of the considered event.

3.1 Associated GW reconstructed events

For each of the selected neutrino events, the adapted pipeline skymask coherent WavBurst (s-cWB)⁹ performs a search for GW around the neutrino time. The whole sky is not scanned but only the region corresponding to ASW90% centered on the reconstructed arrival direction of the neutrino \vec{d}_0 . For each candidate, s-cWB will provide the GW skymap labeled hereafter $\mathcal{F}_i^{\text{GW}}(\vec{d})$ within ASW90%. These ”sky-maps” are made of pixels of $0.4^\circ \times 0.4^\circ$ each associated with the probability that a GW is coming from it. The reconstruction pipeline also provides the value of ρ for each GW candidates. This latter will correspond to a false alarm rate $\text{FAR}_i(\rho_i)$ which in turn can be associated to a GW p-value indicating what is the probability that coherently combined GW interferometers background produces an event with at least this value of ρ_i , defined as:

$$p_i^{\text{GW}} = 1 - P(0 | \tau_i \times \text{FAR}_i(\rho_i)) \quad (5)$$

where τ_i is the duration of the GW interferometers run in a certain configuration (i.e. combination of active detectors) during which event i was recorded. The distributions are computed using $O(10^3)$ background realisations obtained with time shifts of the data stream.

3.2 Statistical characterisation of the joint candidates

The direction of the joint candidate event can be defined as the one maximizing the convolution of the GW skymaps and HEN point spread function $\mathcal{F}_i^{\text{GW}}$ and $\mathcal{F}_i^{\text{HEN}}$.

The joint directional test statistic will rely on the marginalized likelihood of the joint event which is defined as:

$$\ln(\mathcal{L}_i) = \ln \left(\int \mathcal{F}_i^{\text{GW}}(\vec{x}) \times \mathcal{F}_i^{\text{HEN}}(\vec{x}) d\vec{x} \right) \quad (6)$$

The p-value corresponding to the combined PSF-likelihood will be defined as:

$$p_i^{sky} = \int_{\mathcal{L}_i}^{\infty} P_{bg}(\ln(\mathcal{L}))d\mathcal{L} \quad (7)$$

3.3 Final test statistic

The three obtained p-values can be combined using Fisher's method¹⁰ to construct a test statistic for each event i :

$$X_i^2 = -2 \ln(p_i^{sky} \times p_i^{GW} \times p_i^{HEN}) \quad (8)$$

The final result of the search is the p-value of its most significant event i defined as:

$$p^{GWHEN} = \int_{Max(X_i^2)}^{\infty} P_{bg}(max(X^2))dX^2 \quad (9)$$

The background probability density function $P_{bg}(max(X^2))$ is estimated by a Monte Carlo simulation of 10^4 pseudo-experiments of 773 joint triggers (the remaining of the 1986 neutrinos coincident with data taking periods of GW interferometers) obtained by applying the analysis on time shifted gravitational wave data. It will determine the significance of the loudest event once the non time shifted data will be looked at.

4 Expected sensitivity

The global improvement gain expected on the upper limit of population density of common HEN and GW emitters with respect to the 2007 comes from two main improvements. A gain of a factor 1.4 arises from the observation time (91.36 days and 128.7 days for 2007 and 2009-2010 joint data respectively). Another factor ~ 6 comes from the increase of the neutrino effective area multiplied by a bit more than 3 since the 2007 because of the number of lines going from 5 to 12.

This implies a net improvement by a factor ~ 8 with respect to what was achieved in the 2007 search. For instance this search should be able to constrain the core collapse type event's density population at the order of 10^{-4} Mpc $^{-3}$ yr $^{-1}$ which is the observed rate of core collapse supernovae. It also opens the path for the future with the advanced version of GW interferometers aLIGO and aVirgo which will have ten-fold sensitivity and will be operated at the same time as kilometric scale neutrino detectors IceCube and KM3NeT¹¹.

References

1. Aartsen M. G. et al. *Science* **342**, (2013)
2. B. P. Abbott et al., *Rep. Prog. Phys.* **72**, 076901 (2009).
3. T. Accadia et al., *Class. Quant. Grav.* **28**, 114002 (2011).
4. S. Ando et al. *Rev. Mod. Phys.* **85**, 1401 (2013)
5. The ANTARES collaboration, the LIGO Collaboration and the Virgo Collaboration *J. of Cosm. and Astrop. Phys.* **06**, 008 (2013)
6. The IceCube Collaboration, the LIGO Collaboration and the Virgo Collaboration *Phys. Rev. D* **90**, 102002 (2014)
7. B. Baret et al. *Phys. Rev. D* **85**, 103004 (2012)
8. M. Ageron et al. , *Nucl. Instrum. Methods A* **656**, 11 (2011)
9. B. Bouhou, PhD of Université P. et M. Curie Paris VI (2012) <https://tel.archives-ouvertes.fr/tel-00819985>
10. R. A. FISHER, *Statistical Methods for Research Workers*, Oliver and Boyd (Edinburgh), (1925).
11. KM3NeT Technical Design Report ISBN-978-90-6488-033-9

LOW LATENCY SEARCH FOR COMPACT BINARY COALESCENCES USING MBTA

T. ADAMS

on behalf of the LIGO Scientific Collaboration and the Virgo Collaboration
*Laboratoire d'Annecy-le-Vieux de Physique des Particules (LAPP), Université de Savoie,
CNRS/IN2P3, F-74941 Annecy-le-Vieux, France*

The Multi-Band Template Analysis is a low-latency analysis pipeline for the detection of gravitational waves to triggering electromagnetic follow up observations. Coincident observation of gravitational waves and an electromagnetic counterpart will allow us to develop a complete picture of energetic astronomical events. We give an outline of the MBTA pipeline, as well as the procedure for distributing gravitational wave candidate events to our astronomical partners. We give some details of the recent work that has been done to improve the MBTA pipeline and are now making preparations for the advanced detector era.

1 Introduction

Currently the LIGO¹ and Virgo² detectors are being brought back into operation after an extended period of upgrades and commissioning. This is an extremely exciting time in the gravitational wave (GW) community as we prepare for the beginning of the advanced detector era, when advanced LIGO³ and advanced Virgo⁴ come online. The advanced detectors will have a sensitive range for binary neutron stars (BNS) source a factor of 10 better than the initial detectors, which corresponds to an increase in the observable volume by three orders of magnitude. This will improve the “realistic” BNS detector rates from 0.02yr^{-1} in the initial detector era to 40yr^{-1} in the advanced detector era⁵.

The first scheduled observing run in the advanced detector era will be a three month run starting in September 2015 which will only include the two LIGO detectors while the Virgo detector finishes its upgrades and commissioning. Virgo will join the detector network for the first three detector observing run in 2016-2017 for six month.

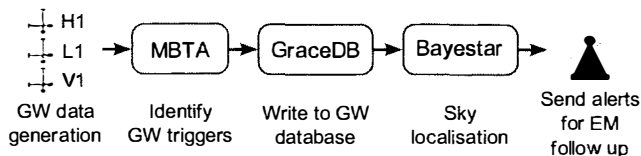


Figure 1 – Overview of the joint GW-EM observation pipeline.

In this paper we will outline the key elements of the Multi-Band Template Analysis (MBTA) pipeline and the procedure for distributing GW candidate events for electromagnetic (EM) follow up observations, as shown in figure 1. In section 2.1 we explain how GW signals are extracted from the GW channel data of each detector. In section 2.2 we explain the criteria for selecting

GW candidate events. In section 2.3 we give details of the post-MBTA event processing and explain how GW candidate events are distributed to our astronomical partners. In section 2.4 we give details of some of the improvements recently implemented in MBTA. In section 3 we summarise the status of the MBTA pipeline in preparation for the advanced detector era.

2 The Multi-Band Template Analysis

MBTA⁶ is a low-latency coincidence analysis pipeline used to detect GWs from compact binary coalescences (CBCs). Some of the best understood and strongest sources of GWs for the LIGO and Virgo detectors are CBCs consisting of two neutron stars (NS-NS), or a neutron star and a black hole (NS-BH). These systems have many possible mechanisms for producing EM counterparts⁷. The possibility of a strong GW signal and EM counterpart make these sources the focus of the MBTA pipeline, which aims to detect GW candidate events with low enough latency to trigger EM follow up observations by our astronomical partners⁸.

2.1 Single detector analysis

Each detector in the network is analysed independently, before the results are later combined to find GW candidate events. We obtain the calibrated GW channel data from each of the detectors, as well as basic data quality information, informing us of the status of the detectors. MBTA uses the standard matched filter⁹ to extract CBC signals from the GW channel data of each detector. To do this a bank of search templates is used to cover the parameter space of expected signals, this is generated at initialisation to keep the analysis latency as low as possible. This template bank is referred to as the “virtual” template bank, and covers the parameter space we are interested in.

To reduce the computational cost of the matched filtering, which is the most computationally expensive element of the analysis, MBTA splits the matched filter across two (or more) frequency bands. The boundary frequency between the low and high frequency bands is selected so that the signal-to-noise ratio (SNR) is roughly equally shared between the two bands. This multi-band analysis procedure gives a reduction in the computational cost and we lose negligible SNR compared to a matched filter performed with a single band analysis. The reduction in computational cost comes from the fact that in each frequency band we can use shorter templates and so the phase of the signal is tracked over fewer cycles, this reduces the number of templates that is required to cover the equivalent mass space of a single band analysis. We also benefit from being able to use a reduced sampling rate for the low frequency band, which reduces the computational cost of the fast Fourier transforms involved in the filtering.

Each frequency band requires a separate “real” template bank, which is actually used to filter the data. For each template in the virtual template bank, a template from the low and high frequency real template banks are combined to reconstruct the result from a single band analysis. The real template banks and the parameters for combination and association with the virtual template bank are produced during initialisation to keep the analysis latency low.

To further reduce the computational cost of the filtering, the template banks are split across multiple jobs and run in parallel across the parameter space. Once we have the results from each band across the full parameter space the results are coherently combined between the bands. Triggers are extracted from the match filter output in each band when $SNR > 5$, and a computationally inexpensive χ^2 test is used to check the SNR distribution across the frequency bands is consistent with the expected signal SNR evolution.

2.2 Coincidence events

The trigger lists from the individual detectors are combined to find coincidence events. Time coincidence is checked using a simple time of flight consistency test between triggers in detector

pairs. In the past we also used a mass coincidence criterion, but this has now been superseded by the exact match requirement. The exact match requires that triggers are found in all detectors with the same template parameters; the component masses and spins. The significance of each event is estimated by calculating the false alarm rate (FAR), the expected rate of coincidence triggers from noise only that have an equal or large SNR than the event.

2.3 Event follow up

GW candidate events found by the MBTA pipeline are sent to the Gravitational Wave Candidate Event Database (GraCEDb)¹⁰, an automated archive for GW candidate events. When MBTA uploads a new event to GraCEDb rapid sky localisation is performed with Bayestar¹¹, a rapid Bayesian position reconstruction code, using the time, amplitude, and phase information reported by MBTA. Bayestar returns a probability skymap that is appended to the GraCEDb event and can be used to plan follow up observations around the most probably sky positions of the source. As well as sky localisation, any additional data quality vetoes can be applied to remove events that are associated with detector noise.

In previous analysis runs⁶ GW candidate events have then undergone verification by a human monitor. The purpose of this human monitor was to review the events, consult the detector control rooms about the status of the detectors, and verify the data quality. In the past the entire pipeline, from data collection distributing GW candidate events to our astronomical partners, had a latency of 20-40 minutes; where the human monitor step gave the largest contribution to the latency. We give an example of a GW candidate event skymap⁶ in figure 2. This event was distributed to our astronomical partners with a latency of 39 minutes and follow up observations were performed by Quest, ROTSE, SkyMapper, TAROT and Zadko.

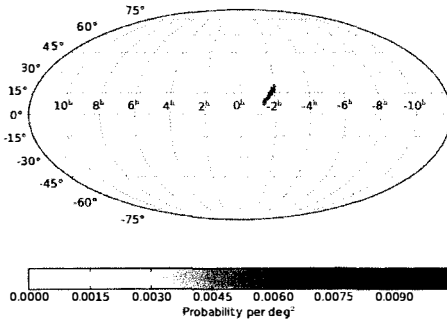


Figure 2 – Skymap of GW candidate event G20190

2.4 Recent improvements

In preparation for the first observing run in the advanced detector era we have implemented a number of improvements to the MBTA pipeline. We are now able to run MBTA using spinning template banks, this was achieved by changing the interface for generating the template banks. Now that we are using the exact match, we can provide the coalescence phase of events for improved sky localisation with Bayestar. Finally, to remove noise events we have added a signal based consistency test. This uses the fact that a real CBC signal should produce a single loud peak in the matched filter output, whereas a noise trigger could possibly produce multiple loud peaks. Comparing the peak SNR of an event to the surrounding level we can veto events that do not behave like real CBC signals.

3 Conclusion

In this paper we have outlined the MBTA pipeline, and how the GW candidate events produced by MBTA are distributed to our astronomical partners for EM follow up observations. As was shown in previous observing runs, we are ready to perform this task and are now focusing on implementing improvements in preparation for the first advanced era observing run in September 2015. We expect that as the detectors sensitivities are improved, we will soon be making the first GW detections and can begin to do real GW astronomy in coalition with our astronomical partners.

Acknowledgements

The authors gratefully acknowledge the support of the United States National Science Foundation (NSF) for the construction and operation of the LIGO Laboratory, the Science and Technology Facilities Council (STFC) of the United Kingdom, the Max-Planck-Society (MPS), and the State of Niedersachsen/Germany for support of the construction and operation of the GEO600 detector, the Italian Istituto Nazionale di Fisica Nucleare (INFN) and the French Centre National de la Recherche Scientifique (CNRS) for the construction and operation of the Virgo detector. The authors also gratefully acknowledge research support from these agencies as well as by the Australian Research Council, the International Science Linkages program of the Commonwealth of Australia, the Council of Scientific and Industrial Research of India, Department of Science and Technology, India, Science & Engineering Research Board (SERB), India, Ministry of Human Resource Development, India, the Spanish Ministerio de Economía y Competitividad, the Conselleria d'Economia i Competitivitat and Conselleria d'Educació, Cultura i Universitats of the Govern de les Illes Balears, the Foundation for Fundamental Research on Matter supported by the Netherlands Organisation for Scientific Research, the Polish Ministry of Science and Higher Education, the FOCUS Programme of Foundation for Polish Science, the European Union, the Royal Society, the Scottish Funding Council, the Scottish Universities Physics Alliance, the National Aeronautics and Space Administration, the Hungarian Scientific Research Fund (OTKA), the Lyon Institute of Origins (LIO), the National Research Foundation of Korea, Industry Canada and the Province of Ontario through the Ministry of Economic Development and Innovation, the National Science and Engineering Research Council Canada, the Brazilian Ministry of Science, Technology, and Innovation, the Carnegie Trust, the Leverhulme Trust, the David and Lucile Packard Foundation, the Research Corporation, and the Alfred P. Sloan Foundation. The authors gratefully acknowledge the support of the NSF, STFC, MPS, INFN, CNRS and the State of Niedersachsen/Germany for provision of computational resources. This research has made use of the SIMBAD database, operated at CDS, Strasbourg, France.

References

1. B. Abbott *et al*, Rep. Prog. Phys. **7**, 076901 (2009)
2. T. Accadia *et al*, Journal of Instr. **3**, 03012 (2012)
3. J. Aasi *et al*, *Class. Quantum Grav.* **32**, 074001 (2015)
4. F. Acernese *et al*, *Class. Quantum Grav.* **32**, 024001 (2015)
5. J. Abadie *et al*, *Class. Quantum Grav.* **27**, 173001 (2010)
6. J. Abadie *et al*, *Astro. & Astrophys.* **541**, A155 (2012)
7. B.D. Metzger & E. Berger *Astrophys. J.* **746**, 48 (2012)
8. J. Aasi *et al* <http://arxiv.org/abs/1304.0670> 2013
9. L.A. Wainstein and V.D. Zubakov, Extraction of signals from noise, Prentice-Hall, 1962
10. <https://gracedb.ligo.org>
11. L. Singer *et al*, APJ **795**, 105 (2014)

On the possibility of GRB forecasting algorithm and alert system for future gravitational wave detectors

G. DEBRECZENI

*Wigner Research Centre for Physics, 29-33 Konkoly-Thege M. u,
1121, Budapest, Hungary*

Modern gravitational wave (GW) detectors are hunting for GWs originating from various sources. It is assumed that in some cases it is the coalescence (merging) of binary neutron stars (BNS) which is responsible for gamma-ray burst (GRB). Since already well before their merging, during the inspiral phase the BNS system emits GWs, these signals could be used to predict, in advance the time and sky location of a GRB and set up constraints on the physical parameters of the system. There exists no such prediction algorithm, as of today. Despite the fact that it is not yet feasible to use this new method with the current GW detectors, it will be of utmost importance in the late-Advanced LIGO/Virgo era and definitely for Einstein Telescope. The very goal of the research presented in this paper is to develop the above described zero-latency, BNS coalescence forecasting method and design the associated alert system to be used by next generation of GW detectors and collaborating EM observatories.

1 Introduction

Gravitational waves originating from inspiraling binary black holes or binary neutron stars are the most widely believed candidates for the first direct detection of gravitational waves predicted by Einstein's theory of General Relativity. In the following couple of years, the current and next generation of ground-based interferometric gravitational wave detectors (the advanced detectors) will have non-negligible chance to perform the first direct observation of such inspiraling events. It is believed that in some cases it is the inspiraling (merger) of such binary neutron star system which is responsible for the production of (a class of) GRBs - routinely observed by electromagnetic observatories.

1.1 About Gamma Ray Bursts and gravitational waves

GRBs are unrepeatable astrophysical events happening at quasi random distances and sky locations. As a consequence their observation is performed on a probabilistic basis. A network of ground based detector and space borned satellites is watching the sky with the biggest possible coverage in 24/7 waiting for events. Despite all this effort a fraction of GRBs remains undetected due to various reasons (for example incomplete sky coverage). Even with this approach we have already detected a lot of events and extracted meaningful physics from it, but there are important cases (for example in observing the early light curve of afterglows) when the prior knowledge of the exact or approximate time and sky location of a GRB would tremendously help us performing much more precise, prepared and targeted observations.

A class of GRB is produced by the merger of BNS which is producing gravitational waves in its inspiraling phase. Being able to observe these GWs in advance the electromagnetic burst would allow us not only to reposition our electromagnetic detectors to point to correct sky

locations, but to determine several of the properties of the GRB in advance the electromagnetic observation and examine the dependency of burst properties on BNS system parameters.

1.2 Feasibility

When such a GW based GRB forecasting alert system is in operation, it is important not to send too many false alarm to the telescopes, since their preparation and/or repositioning needs time and could be expensive. Since this prediction algorithm is intended to be a generic solution - not only restricted to the GRB mass range - it is important to examine which are those parameter spaces where the algorithm can accumulate enough confidence sufficient time before the merger to generate a trigger and send out an alert. A gravitational wave signal is considered to be detected - apart from many other kind of condition - if its SNR is larger than 8.0. The accumulation of SNR over time depends on the shape and duration (Figure 1 b., Eq. 1) of the GW signal, the lower frequency cutoff (10 Hz in this analysis), and on the sensitivity curve of the detector¹ (Figure 1 a.).

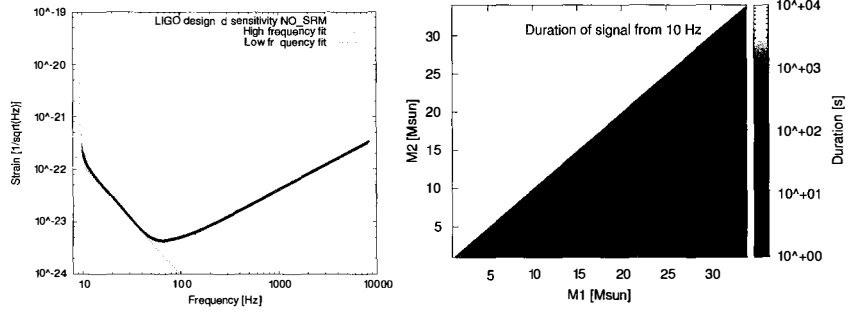


Figure 1 – a.) The designed sensitivity of the advanced LIGO detector without the signal recycling mirror applied. The straight lines represents the analytically fitted approximations used in this analysis. b.) Duration of gravitational wave signal from 10 Hz to f_{ISCO} emitted by a non-spinning, circular binary neutron star system.

The duration of a gravitational wave emitted by a circular, non-spinning binary from f_{low} to f_{isco} can be approximated by

$$T(f_{low}) = \frac{5}{256\eta} \frac{GM}{c^3} \left[v_{low}^{-8} + \left(\frac{743}{252} + \frac{11}{3}\eta \right) v_{low}^{-6} - \frac{32\pi}{5} v_{low}^{-5} + \left(\frac{3058673}{508032} + \frac{5429}{504}\eta + \frac{617}{72}\eta^2 \right) v_{low}^{-4} \right], \quad (1)$$

where

$$v_{low} = \left(\frac{GM}{c^3} \pi f_{low} \right)^{1/3}, \quad (2)$$

However what does really matter is the accumulation of the SNR over time. Figure 2 a. shows the accumulation of SNR over time for a typical 1.4 - 1.4 solar mass BNS. It is visible that despite the very long duration of this signal from the nominal 10 Hz lower frequency cut-off it is only the last (few) hundreds of seconds when significant signal accumulation does indeed happen. If we EM telescopes needs in the order of 100 second for preparation for observations, than it follows that since at time $t=-100$ only the 0.2 of the total SNR is available the algorithm requires strong signals with total SNR in the order of $SNR_{Tot} = 8 / 0.2 = 40$ to ensure low false alarm probability.

Having determined the above constraints we can now focus on the details of the forecasting algorithm presented in the next section.

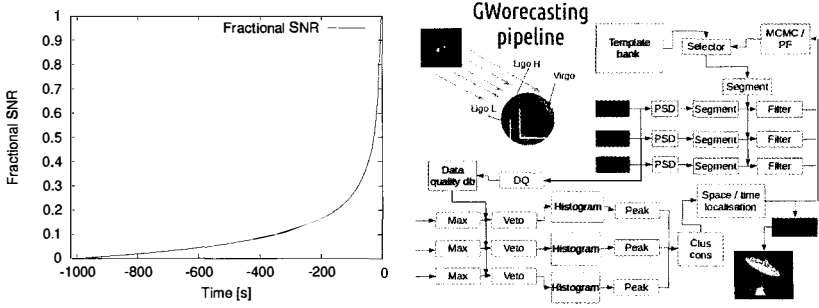


Figure 2 – Accumulation of the SNR (in units of total SNR of the waveform) as a function of time-to-coalescence for a typical 1.4 - 1.4 solar mass binary neutron star system. b.) The bird-eye view of the architecture of the forecasting pipeline.

2 The forecasting algorithm

One could imagine many different implementation of a forecasting algorithm in question. Our goal here is not to develop a unique implementation but instead, to determine the general characteristics and limitations of such a pipeline.

We choose the usual template bank based matched-filter with the necessary modifications. As a prototype algorithm one could think of the following solution:

1. Generate a template bank in the usual way for a specific parameter space.
2. a.) Split all the templates of the template bank into equal-time chunks, chunk duration corresponds to a pre-fixed time window size, to be optimized later.

b.) Split all the template of a template bank into different size chunks the time duration of which corresponds to integer multiples of the above mention window size.
3. Match the template chunks of the template bank against the data strain using matched-filter.
4. From the parameters of the template chunks the SNR of which exceeded a given threshold build an N dimensional histogram. One of the simplest - in case of non-spinning, circular binaries - would be a 3 dimensional m_1 , m_2 , t_{coal} histogram, where m_1 and m_2 are the parameters of template chunk and t_{coal} is the estimated coalescence time calculated from the position of the maximum match of the chunk with the data and from the position of the chunk relative to its 'parent' template.
5. Perform continuous clustering and max finding on the resulted histogram, and whenever a consistent accumulation of peak for specific parameter set is observed generate a trigger.

2.1 Estimation of coalescence time

Let's examine how accurately the coalescence time of a binary neutron star merger can be predicted in advance and how the accuracy of the prediction improves over time using the above described algorithm. For this purpose we inject a gravitational wave signal ($m_1 = 1.4$, $m_2 = 1.4$) into a simulated gaussian noise with various amplitudes. After that we apply the algorithm and determine the mean and variance of the time parameter of any peak accumulated in the constructed histogram at various times prior to the known coalescence of the injected signal. The estimates are shown on Figure 3.

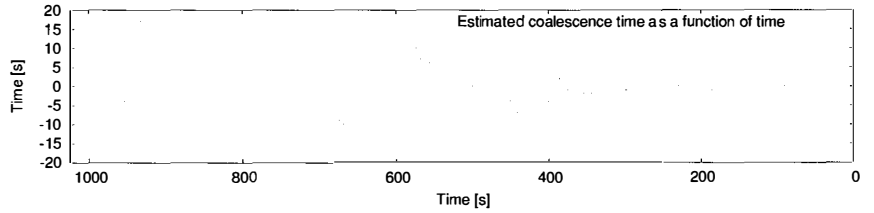


Figure 3 – Improvement of arrival time estimation as a function of time-to-coalescence of injected signals.

2.2 Estimation of sky location

Sky location can be derived using the simple triangulation formula. For the case of the two LIGO detector the theoretical maximum precision of sky localization (Figure 4 a.) and the precision of sky localization in presence of timing inaccuracies (Figure 4 b.) are shown. It is immediately visible that very good coalescence time estimation is necessary for usable sky location estimates some ten or hundred sec before the merger.

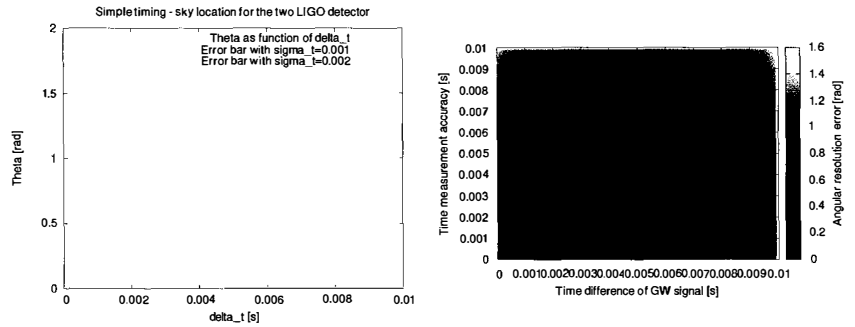


Figure 4 – a.) Theoretical maximum precision of sky localization (θ angle estimate) as a function of arrival time difference for the two LIGO detectors using the simple triangulation. b.) Precision of sky localization as a function of arrival time difference and timing accuracy.

3 Summary and future plans

A novel GRB forecasting algorithm has been presented. The algorithm will be usable when relatively strong GW signals will be seen by GW detectors. It is capable of predicting the estimated coalescence time and sky location of such events, however the precision and early availability of accurate sky location estimates still need to be improved which is the subject of our future research.

Acknowledgements

This research was supported by the GPU Laboratory of Wigner Research Centre.

References

1. LIGO sensitivity curves: <https://dcc.ligo.org/LIGO-T0900288/public>

GRAVITATIONAL WAVES FROM THREE-DIMENSIONAL CORE COLLAPSE SUPERNOVA SIMULATIONS

H. ANDRESEN, E. MÜLLER, H.T. JANKA.

*Max Planck Institut für Astrophysik, Karl-Schwarzschild-Str. 1
85748 Garching, Germany*

In this work we present the gravitational wave signals from sophisticated three-dimensional supernova core collapse simulations of three progenitors, of 11.2, 20 and 27 solar masses. In the two most massive models large scale shock deformation develops. This is reflected in the gravitational wave signals as a strong emission component below ~ 250 Hz.

1 Introduction

Exactly how a core-collapse supernova comes about is still shrouded in mystery. The prevailing theory is the delayed neutrino explosion mechanism¹: A shock wave forms when the contracting iron core reaches nuclear densities and the equation of state stiffens. This halts the collapse and infalling stellar matter bounces off the proto-neutron star (PNS). As the shock wave propagates outwards, through the dense stellar matter, it loses energy and stalls after some hundreds of kilometres. The energy needed to revive the shock wave, ensuring a successful explosion, is thought to be provided by neutrinos streaming out of the PNS. Neutrinos captured in post-shock matter deposit energy. After ~ 100 milliseconds (ms) neutrino heating can be sufficient to revive the shock and successfully launch the supernova. Hydrodynamical instabilities operating behind the stalled shock front have been found to be crucial for the success of this scenario, in particular large scale convection in the neutrino heated post-shock region and the standing accretion shock instability (SASI). See for example Ott² for a review of the history of the subject.

Presently we are witnessing the emergence of exploding stars in 3D modelling. Melson *et al*³ present a successful 3D simulation of a neutrino driven supernova explosion, for a $9.6 M_{\odot}$ progenitor. Observations of a supernova core could complement the theoretical work and provide much needed insight about the explosion mechanism. Unfortunately in the electromagnetic regime the core is quite literally shrouded by the surrounding stellar material. Gravitational waves (GW) and neutrinos, however, propagate unhindered through the outer layers of the star and can provide us with direct observations of the core. Here we present the GW arising from the three first 3D core-collapse simulations with sophisticated neutrino physics. The two most massive progenitors (27 and $20 M_{\odot}$) develop SASI activity, while the third and least massive star ($11.2 M_{\odot}$) shows no signs of SASI activity.

2 Numerical set-up

Our analysis is based on 3D simulations of three solar metallicity progenitors with masses $27 M_{\odot}$, $20 M_{\odot}$ and $11.2 M_{\odot}$. These models have been evolved until the onset of iron core collapse^{4,5}. Then the 3D core collapses were simulated with PROMETHEUS-VERTEX, a hydro code including

the neutrino transport module VERTEX. PROMETHEUS⁶ implements a dimensionally split piecewise parabolic method⁷ and VERTEX is a “ray-by-ray-plus” neutrino transport module. VERTEX⁸ solves the neutrino momentum, energy and Boltzmann equations based on a variable Eddington-factor technique. The equation of state is that of Lattimer & Swesty⁹ with a nuclear incompressibility $K = 220$ MeV. We use an initial grid resolution of $400 \times 88 \times 176$ grid cells in r , θ and ϕ , respectively. During the simulations grid adjustments were made to maintain sufficient resolution around the PNS surface.

3 Gravitational wave extraction

In order to extract the GW signal from the hydrodynamical simulations a post-processing step is necessary. A concise description of the formalism used to determine the GW signal arising from matter flow is given below¹⁰.

When expressing the gravitational radiation as a multi-pole expansion one finds that the leading term is given by the quadrupole, this is a consequence of mass and momentum conservation. In the transverse traceless(TT) gauge the gravitational quadrupole radiation tensor, at a distance D from the source, is given by,

$$\mathbf{h}^{TT}(\mathbf{X}, t) = \frac{1}{D} [A_+ \mathbf{e}_+ + A_\times \mathbf{e}_\times]. \quad (1)$$

Here \mathbf{e}_\times and \mathbf{e}_+ are the unit linear-polarization tensor given by

$$\mathbf{e}_+ = \mathbf{e}_\theta \otimes \mathbf{e}_\theta - \mathbf{e}_\phi \otimes \mathbf{e}_\phi, \quad (2)$$

$$\mathbf{e}_\times = \mathbf{e}_\theta \otimes \mathbf{e}_\phi + \mathbf{e}_\phi \otimes \mathbf{e}_\theta. \quad (3)$$

\mathbf{e}_θ and \mathbf{e}_ϕ are the unit polarization vectors in spherical coordinates. A_\times and A_+ are the two independent wave amplitudes of the TT gauge, given in the slow-motion limit by

$$A_+ = \ddot{Q}_{\theta\theta} - \ddot{Q}_{\phi\phi}, \quad (4)$$

$$A_\times = 2\ddot{Q}_{\theta\phi}. \quad (5)$$

Here \ddot{Q} is second time derivative of the symmetric trace-free(STF) mass quadrupole tensor¹¹. In Cartesian coordinates this quantity can be written as,

$$\ddot{Q}_{ij} = \text{STF} \left[\frac{G}{c^4} \int d^3x (v_i v_j - x_i \partial_j \Phi) \right]. \quad (6)$$

Here G is Newtons gravitational constant, c the speed of light, v_i and x_i refer to the Cartesian velocity and position ($i = 1, 2, 3$), respectively. The gravitational potential, Φ , refers to the gravitational potential with post-Newtonian corrections taken into account. The advantage of this form is that the second-order time derivatives are transformed in to first-order spatial derivatives, thus circumventing problems associated with the numerical evaluation of second-order time derivatives. Using standard coordinate transformations, between Cartesian and spherical coordinates, we find

$$\begin{aligned} \ddot{Q}_{\theta\phi} &= (\ddot{Q}_{22} - \ddot{Q}_{11}) \cos \theta \sin \phi \cos \phi \\ &+ \ddot{Q}_{12} \cos \theta (\cos^2 \phi - \sin^2 \phi) \\ &+ \ddot{Q}_{13} \sin \theta \sin \phi - \ddot{Q}_{23} \sin \theta \cos \phi, \end{aligned} \quad (7)$$

$$\ddot{Q}_{\phi\phi} = \ddot{Q}_{11} \sin^2 \phi + \ddot{Q}_{22} \cos^2 \phi - 2\ddot{Q}_{12} \sin \phi \cos \phi \quad (8)$$

and

$$\begin{aligned} \ddot{Q}_{\theta\theta} = & \left(\ddot{Q}_{11} \cos^2 \phi + \ddot{Q}_{22} \sin^2 \phi + 2\ddot{Q}_{12} \sin \phi \cos \phi \right) \cos^2 \theta \\ & + \ddot{Q}_{33} \sin^2 \theta - 2 \left(\ddot{Q}_{13} \cos \phi + \ddot{Q}_{23} \sin \phi \right) \sin \theta \cos \theta. \end{aligned} \quad (9)$$

4 Signal description

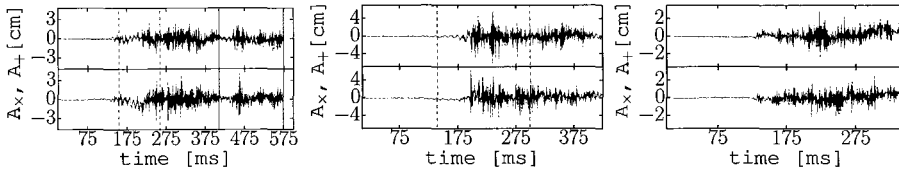


Figure 1 – GW amplitudes as seen by an observer at the pole, normalized by the distance to the source. Left, middle and right panel: 27, 20 and 11.2 M_{\odot} . The top and bottom row represents the cross and plus polarized amplitudes, respectively. Vertical lines indicate periods with SASI activity.

Amplitudes for GW generated by asymmetric mass motions are shown in Figure 1. For each progenitor we show two panels representing the cross and plus polarization. The waveforms are in general characterised by an initial quiescent phase, which is followed by a rather stochastic phase with amplitudes of a few cm. Besides from the fact that we see slightly stronger amplitudes in the 27 and 20 M_{\odot} models there is little apparent difference in the waveforms, between the models with and without SASI activity. In order to dissect the signal further we apply the standard Short-time Fourier transform (STFT) to our waveforms. We calculate the STFT for the cross and plus polarization separately before adding them together. Using a time window of 50 ms and shift it 5 ms forward in time each iteration, the resulting spectrograms are shown in Figure 2. Inspecting the spectrograms it is clear that the 11.2 M_{\odot} model stands out, lacking the strong emission below 250 Hz seen in the two SASI models. One can also clearly see that this signal component varies greatly between the 20 and 27 M_{\odot} model. In the former we see a broad and noisy emission component, while we see a clean and narrow emission band in the signal from the more massive progenitor. Common to both models is the fact that the low frequency emission is strongest during the SASI episodes and that the signal is weak after the SASI has died out. A second component of the signal has frequencies above 350 Hz. While this

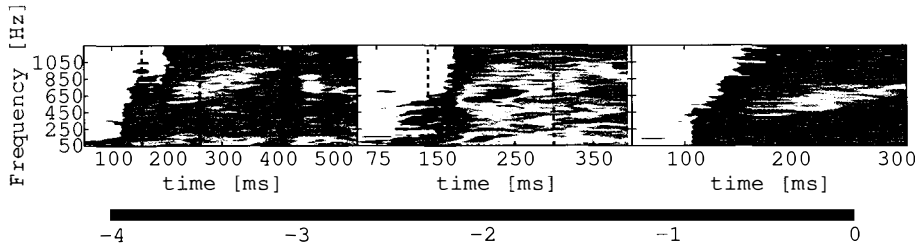


Figure 2 – Normalized spectrogram, summed over the two polarization modes ($|\mathcal{F}(h_+)|^2 + |\mathcal{F}(h_{\times})|^2$). From left to right: the 27, 20 and 11.2 M_{\odot} model. Colours in log scale. All plots have been normalized by the same factor. Vertical lines indicate periods with SASI activity.

component is present in all models, it varies strongly from model to model. The $20 M_{\odot}$ model initially emits in a broad frequency range. As time passes the model slowly develops a narrow emission band. In contrast the more massive $27 M_{\odot}$ model radiates high frequency GWs in a thin strip. Similarly the $11.2 M_{\odot}$ progenitor produces a narrow high frequency emission band. In all three models the peak-frequency of this component increases linearly with time.

Acknowledgments

This project was supported by the SFB/TR 7 “Gravitational Wave Astronomy” and ERC-AdG No. 341157-COCO2CASA. The simulations this work is based on could only be achieved with the assistance of high performance computing resources (Tier-0) provided by PRACE on CURIE TN (GENCI@CEA, France) and SuperMUC (GCS@LRZ, Germany).

References

1. H.-T. Janka. Explosion Mechanisms of Core-Collapse Supernovae. *Annual Review of Nuclear and Particle Science*, 62:407–451, November 2012.
2. C. D Ott. TOPICAL REVIEW: The gravitational-wave signature of core-collapse supernovae. *Classical and Quantum Gravity*, 26(6):063001, March 2009.
3. T. Melson, H.-T. Janka, and A. Marek. Neutrino-driven Supernova of a Low-mass Iron-core Progenitor Boosted by Three-dimensional Turbulent Convection. *ApJL*, 801:L24, March 2015.
4. S. E. Woosley and A. Heger. Nucleosynthesis and remnants in massive stars of solar metallicity. *Phys. Rep.*, 442:269–283, April 2007.
5. S. E. Woosley, A. Heger, and T. A. Weaver. The evolution and explosion of massive stars. *Reviews of Modern Physics*, 74:1015–1071, November 2002.
6. B. A Fryxell, E. Müller, and D. Arnett. Preprint0. *Max-Planck-Institut für Astrophysik*, 449, 1989.
7. P. Colella and P. R. Woodward. The Piecewise Parabolic Method (PPM) for Gas-Dynamical Simulations. *Journal of Computational Physics*, 54:174–201, September 1984.
8. M. Rampp and H.-T. Janka. Radiation hydrodynamics with neutrinos. Variable Eddington factor method for core-collapse supernova simulations. *A&A*, 396:361–392, December 2002.
9. J. M. Lattimer and F. D Swesty. A generalized equation of state for hot, dense matter. *Nuclear Physics A*, 535:331–376, December 1991.
10. Müller, E., H.-T. Janka, and A. Wongwathanarat. Parametrized 3D models of neutrino-driven supernova explosions. Neutrino emission asymmetries and gravitational-wave signals. *A&A*, 537:A63, January 2012.
11. L. Blanchet, T. Damour, and G. Schafer. Post-Newtonian hydrodynamics and post-Newtonian gravitational wave generation for numerical relativity. *MNRAS*, 242:289–305, January 1990.

POST-NEWTONIAN HIGHER ORDER ORDER SPIN EFFECTS IN INSPIRALING COMPACT BINARIES

S. MARSAT

*Maryland Center for Fundamental Physics & Joint Space-Science Center,
Department of Physics, University of Maryland, College Park, MD 20742, USA
Gravitational Astrophysics Laboratory, NASA Goddard Space Flight Center, Greenbelt, MD 20771*



We report recent results for the effects of the spins in binary systems of compact objects (black holes and/or neutron stars), obtained in the post-Newtonian framework at quadratic and cubic order in the spins. The new contributions enter at the third and third-and-a-half post-Newtonian order respectively, and further complete existing theoretical predictions for the gravitational wave signals expected from these binaries. The treatment of higher orders in spins required an extension of the Lagrangian formalism for spinning point particles to the quadrupolar and octupolar orders.

1 Introduction

With the advent of a new generation of ground-based gravitational waves detectors such as LIGO, VIRGO and KAGRA, gravitational waves astronomy is expected to enter a new observational era. The most promising sources for these detectors are binary systems of compact objects, neutron stars and/or black holes. Among the different approaches to the joint problems of the dynamics and gravitational waves emission by such systems, the post-Newtonian theory provides analytical predictions, in the form of formal series, covering the long inspiraling phase of the system. Extending this framework to include the effects of the angular momentum (or spin) of the compact bodies has driven a lot of effort in the past few years, as they are expected to be significant for binaries containing black holes.

Beyond the linear order in spin (or spin-orbit, SO), the terms quadratic in the spins (SS) enter at the second post-Newtonian order (2PN), and the cubic terms at the 3.5PN order. Recent results for the dynamics, derived by other authors, cover the 3PN (and partially 4PN) SS contributions^{2,3,4,5,6,7} and the 3.5PN SSS⁸ (as well as 4PN SSSS) terms. In the work we are reporting^{9,10}, using the multipolar post-Newtonian method¹, which provides a comprehensive treatment of both the dynamics and the gravitational waves generation, we confirmed these results for the dynamics and extended them to compute the energy flux emitted in gravitational waves, thus predicting the phasing of the binary for circular orbits. These results will be useful to further improve post-Newtonian waveform templates used in the data analysis of the detectors.

2 Lagrangian formalism for spinning point particles

2.1 Definitions

The representation of the effects of the spins requires an extension of the point particle approximation. The approach we use here is based on a Lagrangian formalism, first introduced by Hanson&Regge¹¹ and Bailey&Israel¹². To represent the rotational degrees of freedom, an orthonormal tetrad ϵ_A^μ is introduced, and the antisymmetric rotation coefficients are defined as (with ^a τ the proper time, u^μ the 4-velocity, and $D/d\tau = u^\mu \nabla_\mu$)

$$\Omega^{\mu\nu} \equiv \epsilon^{A\mu} \frac{D\epsilon_A^\nu}{d\tau}. \quad (1)$$

We make then the following ansatz for the action describing the particle's dynamics:

$$S = \int d\tau L [w^\mu, \Omega^{\mu\nu}, g_{\mu\nu}, R_{\mu\nu\rho\sigma}, \nabla_\lambda R_{\mu\nu\rho\sigma}]. \quad (2)$$

The couplings to the Riemann tensor and its derivative are included here to represent spin-induced finite-size effects up to the octupolar order. From this general form of the Lagrangian, the linear momentum p_μ and the spin tensor $S_{\mu\nu}$ are defined as conjugate momenta for the positional and rotational degrees of freedom, and the quadrupolar and octupolar moments $J^{\mu\nu\rho\sigma}$ and $J^{\lambda\mu\nu\rho\sigma}$ as partial derivatives with respect to the curvature tensor, according to

$$p_\mu \equiv \frac{\partial L}{\partial w^\mu}, \quad S_{\mu\nu} \equiv 2 \frac{\partial L}{\partial \Omega^{\mu\nu}}, \quad J^{\mu\nu\rho\sigma} \equiv -6 \frac{\partial L}{\partial R_{\mu\nu\rho\sigma}}, \quad J^{\lambda\mu\nu\rho\sigma} \equiv -12 \frac{\partial L}{\partial \nabla_\lambda R_{\mu\nu\rho\sigma}}. \quad (3)$$

2.2 Equations of motion and stress-energy tensor

The equations of motion governing the dynamics are derived by varying the action with respect to the worldline and to the rotational degrees of freedom, and read

$$\begin{aligned} \frac{Dp_\mu}{d\tau} &= -\frac{1}{2} R_{\mu\nu\rho\sigma} u^\nu S^{\rho\sigma} - \frac{1}{6} J^{\lambda\nu\rho\sigma} \nabla_\mu R_{\lambda\nu\rho\sigma} - \frac{1}{12} J^{\tau\lambda\nu\rho\sigma} \nabla_\mu \nabla_\tau R_{\lambda\nu\rho\sigma}, \\ \frac{DS^{\mu\nu}}{d\tau} &= 2p^{[\mu} u^{\nu]} + \frac{4}{3} R^{[\mu}{}_{\lambda\rho\sigma} J^{\nu]\lambda\rho\sigma} + \frac{2}{3} \nabla^\lambda R^{[\mu}{}_{\tau\rho\sigma} J_{\lambda}{}^{\nu]\tau\rho\sigma} + \frac{1}{6} \nabla^{[\mu} R_{\lambda\tau\rho\sigma} J^{\nu]\lambda\tau\rho\sigma}. \end{aligned} \quad (4)$$

Introducing the number density $n(x) = \int d\tau \delta^4(x-z)/\sqrt{-g}$, with z^μ the trajectory of the particle, the stress-energy tensor is obtained with a variation with respect to the metric as

$$\begin{aligned} T_{\text{pole-dipole}}^{\mu\nu} &= p^{(\mu} u^{\nu)} n - \nabla_\rho [S^{\rho(\mu} u^{\nu)} n], \\ T_{\text{quad}}^{\mu\nu} &= \frac{1}{3} R^{(\mu}{}_{\lambda\rho\sigma} J^{\nu)\lambda\rho\sigma} n - \nabla_\rho \nabla_\sigma \left[\frac{2}{3} J^{\rho(\mu\nu)\sigma} n \right], \\ T_{\text{oct}}^{\mu\nu} &= \left(\frac{1}{6} \nabla^\lambda R^{(\mu}{}_{\xi\rho\sigma} J_{\lambda}{}^{\nu)\xi\rho\sigma} + \frac{1}{12} \nabla^{(\mu} R_{\xi\tau\rho\sigma} J^{\nu)\xi\tau\rho\sigma} \right) n \\ &\quad + \nabla_\rho \left[\left(-\frac{1}{6} R^{(\mu}{}_{\xi\lambda\sigma} J^{|\rho|\nu)\xi\lambda\sigma} - \frac{1}{3} R^{(\mu}{}_{\xi\lambda\sigma} J^{\nu)\rho\xi\lambda\sigma} + \frac{1}{3} R^\rho{}_{\xi\lambda\sigma} J^{(\mu\nu)\xi\lambda\sigma} \right) n \right] \\ &\quad + \nabla_\lambda \nabla_\rho \nabla_\sigma \left[\frac{1}{3} J^{\sigma\rho(\mu\nu)\lambda} n \right], \end{aligned} \quad (5)$$

where we separated the pole-dipole, quadrupolar and octupolar contributions.

^aSee the original papers^{9,10} for more details on the conventions.

2.3 Spin-induced multipolar moments and conserved norm spin vector

In the case of interest for us, where the extended-size structure of the compact bodies is only induced by their spin, it is possible to derive a unique structure for the quadrupolar and octupolar moments, given by

$$\begin{aligned} J^{\mu\nu\rho\sigma} &= \frac{3\kappa}{m} u^{[\mu} S^{\nu]\lambda} S_{\lambda}{}^{[\rho} u^{\sigma]} \\ J^{\lambda\mu\nu\rho\sigma} &= \frac{\lambda}{4m^2} \left[\Theta^{\lambda[\mu} u^{\nu]} S^{\rho\sigma} + \Theta^{\lambda[\rho} u^{\sigma]} S^{\mu\nu} - \Theta^{\lambda[\mu} S^{\nu][\rho} u^{\sigma]} - \Theta^{\lambda[\rho} S^{\sigma][\mu} u^{\nu]} \right. \\ &\quad \left. - S^{\lambda[\mu} \Theta^{\nu][\rho} u^{\sigma]} - S^{\lambda[\rho} \Theta^{\sigma][\mu} u^{\nu]} \right]. \end{aligned} \quad (6)$$

Here $\Theta^{\mu\nu} = S^{\mu}{}_{\rho} S^{\nu\rho}$, and κ, λ are polarizability constants describing the structure of the compact object. Their value is 1 for black holes and must be determined numerically for neutron stars.

An important feature of the formalism is the requirement of a supplementary spin condition, corresponding to fixing the worldline inside the rotating body. We choose the covariant condition $p_{\nu} S^{\mu\nu} = 0$, which allows the definition of a spin covector as

$$\tilde{S}_{\mu} = -\frac{1}{2} \epsilon_{\mu\nu\rho\sigma} \frac{p^{\nu}}{m} S^{\rho\sigma}. \quad (7)$$

By introducing a tetrad $(u^{\mu}, e_a{}^{\mu})$, one can then define a spin vector of conserved Euclidean norm $S_a = e_a{}^{\mu} \tilde{S}_{\mu}$, which will obey a precession equation of the form $\dot{\mathbf{S}} = \mathbf{\Omega} \times \mathbf{S}$.

3 Post-Newtonian dynamics and emission of gravitational waves

3.1 Multipolar post-Newtonian formalism

Equipped with the multipolar point particle representation of spinning extended objects described above, we were able to use the general framework of the multipolar post-Newtonian formalism (MPN)¹ to derive new results at the SS 3PN and SSS 3.5PN orders. Introducing the metric perturbation $h^{\mu\nu} = \sqrt{-g} g^{\mu\nu} - \eta^{\mu\nu}$, with $\eta^{\mu\nu}$ the background Minkowski metric, in the harmonic gauge $\partial_{\nu} h^{\mu\nu} = 0$, the gravitational field equations take the form

$$\square h^{\mu\nu} = \frac{16\pi G}{c^4} |g| T^{\mu\nu} + \Lambda^{\mu\nu} [h] \equiv \frac{16\pi G}{c^4} \tau^{\mu\nu}, \quad (8)$$

where $\Lambda^{\mu\nu}$ contains the non-linearities in h , and $T^{\mu\nu}$ is the multipolar stress-energy tensor (5).

The MPN formalism contains (i) a near-zone iteration of the Einstein equation (8), where the full metric is parametrized by a set of potentials which are iteratively solved for, and then plugged in the equations of motion (4); (ii) a vacuum iteration of (8) outside the source, allowing the calculation of the radiative moments U_L, V_L , parametrizing the waveform at infinity, in terms of source moments I_L, J_L containing both the matter source and the gravitational field.

When iterating the near-zone metric, we use the Hadamard regularization to give sense to distributional sources such as (5). The conserved energy can then be deduced from the results for the dynamics obtained in (i), and the emitted energy flux is computed from the radiative moments obtained in (ii) as (where L stands for a multi-index $i_1 \dots i_{\ell}$)

$$\mathcal{F} = \sum_{\ell=2}^{+\infty} \frac{G}{c^{2\ell+1}} \left[\frac{(\ell+1)(\ell+2)}{(\ell-1)\ell!(2\ell+1)!!} \dot{U}_L \dot{U}_L + \frac{4\ell(\ell+2)}{c^2(\ell-1)(\ell+1)!(2\ell+1)!!} \dot{V}_L \dot{V}_L \right]. \quad (9)$$

3.2 Results

After reduction in the center-of-mass frame, and specialization to the case of circular orbits with no eccentricity nor precession, the results for the conserved energy E and the flux \mathcal{F} can be

written as series in the PN expansion parameter $x = (Gm\omega/c^3)^{2/3}$, with ω the orbital frequency:

$$\begin{aligned} E &= -\frac{1}{2}m\nu c^2 x \left[1 + x e_{\text{NS}} + x^{3/2} \frac{e_{\text{SO}}}{Gm^2} + x^2 \frac{e_{\text{SS}}}{G^2 m^4} + x^{7/2} \frac{e_{\text{SSS}}}{G^3 m^6} + \mathcal{O}(8) \right], \\ \mathcal{F} &= \frac{32\nu^2}{5G} c^5 x^5 \left[1 + x f_{\text{NS}} + x^{3/2} \frac{f_{\text{SO}}}{Gm^2} + x^2 \frac{f_{\text{SS}}}{G^2 m^4} + x^{7/2} \frac{f_{\text{SSS}}}{G^3 m^6} + \mathcal{O}(8) \right]. \end{aligned} \quad (10)$$

The complete expressions for the new coefficients are too long to be displayed here and can be found for e_{SSS} and f_{SSS} in eqs. (6.17) and (6.19) of⁹, and for e_{SS} and f_{SS} in eqs. (3.33) and (4.14) of¹⁰. The balance equation $\mathcal{F} = -dE/dt$ can then be used to derive the frequency evolution of the binary with time, and ultimately the expected phasing of the gravitational wave signal. Table 1 gives an illustration of the contribution of each PN term in this phasing.

| LIGO/Virgo | $10M_{\odot} + 1.4M_{\odot}$ | $10M_{\odot} + 10M_{\odot}$ |
|------------|---|--|
| Newtonian | 3558.9 | 598.8 |
| 1PN | 212.4 | 59.1 |
| 1.5PN | $-180.9 + 114.0\chi_1 + 11.7\chi_2$ | $-51.2 + 16.0\chi_1 + 16.0\chi_2$ |
| 2PN | $9.8 - 10.5\chi_1^2 - 2.9\chi_1\chi_2$ | $4.0 - 1.1\chi_1^2 - 2.2\chi_1\chi_2 - 1.1\chi_2^2$ |
| 2.5PN | $-20.0 + 33.8\chi_1 + 2.9\chi_2$ | $-7.1 + 5.7\chi_1 + 5.7\chi_2$ |
| 3PN | $2.3 - 13.2\chi_1 - 1.3\chi_2$ $-1.2\chi_1^2 - 0.2\chi_1\chi_2$ | $2.2 - 2.6\chi_1 - 2.6\chi_2$ $-0.1\chi_1^2 - 0.2\chi_1\chi_2 - 0.1\chi_2^2$ |
| 3.5PN | $-1.8 + 11.1\chi_1 + 0.8\chi_2 + (\text{SS})$ $-0.7\chi_1^3 - 0.3\chi_1^2\chi_2$ | $-0.8 + 1.7\chi_1 + 1.7\chi_2 + (\text{SS})$ $-0.05\chi_1^3 - 0.2\chi_1^2\chi_2 - 0.2\chi_1\chi_2^2 - 0.05\chi_2^3$ |
| 4PN | $(\text{NS}) - 8.0\chi_1 - 0.7\chi_2 + (\text{SS})$ | $(\text{NS}) - 1.5\chi_1 - 1.5\chi_2 + (\text{SS})$ |

Table 1: Contribution of each PN order to the number of cycles of a gravitational wave signal for typical neutron star/black hole and black hole/black hole systems, between an entry frequency in the detector band of 10Hz and the Schwarzschild ISCO $r = 6M$. We assume circular orbits and aligned spins, and χ_A stands for the dimensionless Kerr parameter. All contributions known to date are included (except absorption terms across the horizon).

Acknowledgments

This work was supported by the NASA grant 11-ATP-046, as well as the NASA grant NNX12AN10G at the University of Maryland College Park. Some of our computations were done using Mathematica[®] and the symbolic tensor calculus package xAct¹³.

References

1. L. Blanchet, *Living Rev. Rel.* **9**, 4 (2012)
2. S. Hergt *et al*, *Class. Quant. Grav.* **27**, 135007 (2010)
3. J. Hartung and J. Steinhoff, *Annalen der Physik* **523**, 919 (2011)
4. R. Porto and I. Rothstein, *Phys. Rev. D* **78**, 044012 (2008)
5. R. Porto and I. Rothstein, *Phys. Rev. D* **78**, 044013 (2008)
6. M. Levi, *Phys. Rev. D* **82**, 064029 (2010)
7. M. Levi, *Phys. Rev. D* **85**, 064043 (2012)
8. M. Levi and J. Steinhoff, *JHEP* **1506**, 059 (2015)
9. S. Marsat, *Class. Quant. Grav.* **32**, 085008 (2015)
10. A. Bohé *et al*, Accepted for publication in *Class. Quant. Grav.*, arXiv:gr-qc/1501.01529 (2015)
11. A. J. Hanson and T. Regge, *Annals of Physics* **87**, 498 (1974)
12. I. Bailey and W. Israel, *Commun. Math. Phys.* **42**, 65 (1975)
13. J.M. Martín-García, <http://metric.iem.csic.es/Martin-Garcia/xAct> (2002)

HIGH-ORDER COMPARISONS BETWEEN POST-NEWTONIAN AND PERTURBATIVE SELF FORCES

Luc BLANCHET and Guillaume FAYE

*GRεCO Institut d'Astrophysique de Paris, UMR 7095, CNRS,
Sorbonne Universités & UPMC Univ Paris 6, 98^{bis} boulevard Arago, 75014 Paris, France*

Bernard F. WHITING

*Institute for Fundamental Theory, Department of Physics,
University of Florida, Gainesville, FL 32611, USA*

Recent numerical and analytic computations based on the self-force (SF) formalism in general relativity showed that half-integral post-Newtonian (PN) terms, i.e. terms involving odd powers of $1/c$, arise in the redshift factor of small mass-ratio black-hole binaries on exact circular orbits. Although those contributions might seem puzzling at first sight for conservative systems that are invariant under time-reversal, they are in fact associated with the so-called non-linear tail-of-tail effect. We shall describe here how the next-to-next-to-leading order contributions beyond the first half-integral 5.5PN conservative effect (i.e. up to order 7.5PN included) have been obtained by means of the standard PN formalism applied to binary systems of point-like objects. The resulting redshift factor in the small mass-ratio limit fully agrees with that of the SF approach.

1 Introduction

Stellar-mass compact objects inspiraling gradually about super-massive black holes may produce gravitational waves detectable by future space missions such as eLISA¹. These systems, referred to as Extreme Mass Ratio Inspirals (EMRIs), can probe the strong gravity field regime, but proper data analysis of the resulting signal will require accurate waveform templates built from theoretical models. This has motivated, over the past ten years, numerous studies on the dynamics of point-like objects on a curved background^{2,3,4}. Due to the metric perturbations generated by its own mass-energy, the point mass effectively feels a self-force (SF) that induces deviations from the geodesic worldline followed by a test particle on the background. When the background is a black-hole spacetime, the acceleration may be sought in the form of an asymptotic expansion in powers of the mass ratio $q = m_1/m_2 \ll 1$.

In the SF approach, the first order perturbation $\delta g_{\mu\nu}$ of the background metric $g_{\mu\nu}^{(0)}$ is obtained by convolving over the stress-energy tensor $T^{\mu\nu}$ the regularized (R) Green function $G_{\text{R}}^{\mu\nu}{}_{\alpha'\beta'}(x, x')$ that solves the linearized homogeneous Einstein equations in harmonic gauge and has the property that it coincides with the retarded Green function when x lies in the chronological future of x' , while vanishing when x is in the chronological past of x' ⁵. The trajectory of the particle is then precisely that of a geodesic for the perturbed metric $g_{\mu\nu}^{(0)} + \delta g_{\mu\nu}$.

By contrast, the post-Newtonian (PN) approach is based on the formal expansion, on a flat background spacetime, of all quantities of interest, in powers of v/c , where v is the largest typical velocity of the problem. The standard PN approach is first defined for general extended PN sources with compact support and then specialized to compact binary systems⁶. In that case,

v is taken to be the relative coordinate velocity v_{12} . Moreover, when the bodies are compact, they may be effectively represented as point particles. Ultra-violet (UV) divergences at the particle positions are tackled by means of dimensional regularization^{7,8}. The PN expressions are valid at a given coordinate time in a spatial region, referred to as the near zone, that entirely contains the matter source and whose radius is much smaller than the gravitational wavelength. Because SF and PN methods are so radically different from each other, notably regarding the regularization schemes, comparing PN expansions of observable quantities truncated at linear order in q to their SF counterparts expanded in power of $1/c$ allows for non-trivial cross-checks that strengthen our confidence in both perturbative techniques.

After the first comparison between PN and gravitational SF calculations⁹, rapid progress has been made over the last six years, mainly due to both high precision numerical computations from a SF perspective and extensive analytical PN computations^{10,11}. Recently, after the possibility for this comparison had been dramatically extended from the SF side¹², it was realized that observable quantities could contain half-integral $\frac{n}{2}$ PN terms that are nevertheless conservative, starting at the order 5.5PN¹². Here, we shall explain how those terms can arise within the PN framework¹³ and sketch their calculation at the next-to-next-to-leading order^{13,14}. As we shall see, they are closely related to the so-called tail-of-tail effects in general relativity. The success of this SF/PN comparison actually provides an excellent test of the intricate PN machinery for computing non-linear tail-of-tail effects — these being relevant for template waveform generation of comparable mass compact binaries to be analyzed in ground and space based detectors.

2 Comparing post-Newtonian and self-force results

2.1 The Detweiler variable

We shall focus on the Detweiler variable⁹, which represents physically the inverse of the redshift of a photon emitted by a particle moving on an exact circular orbit around a Schwarzschild black hole and detected by an infinitely far-away observer along the rotation axis. The ensuing spacetime is helically symmetric, with a helical Killing vector K^α tangent to the four-velocity u_1^α on the particle worldline. Alternatively, the redshift variable is defined geometrically as the conserved quantity associated with the helical Killing symmetry relevant to spacetimes with exactly circular orbits. In an appropriate class of coordinate systems, the redshift factor u_1^T reduces to the t component of the particle's four-velocity,

$$u_1^T = \frac{1}{\sqrt{-g_{\alpha\beta}(y_1)v_1^\alpha v_1^\beta/c^2}}, \quad (1)$$

where $g_{\alpha\beta}(y_1)$ denotes the metric evaluated at the particle's location $y_1^\alpha = (ct, y_1^i)$ by means of dimensional regularization, and $v_1^\alpha \equiv dy_1^\alpha/dt = (c, v_1^i)$ is the coordinate velocity.

The Detweiler variable (1) has been computed to high-order using on the one hand standard PN theory supplemented with dimensional regularization, valid in weak field^{10,11}, and on the other hand both numerical and analytical SF approaches, valid in the limit $q = m_1/m_2 \ll 1$. Over the last two years, its accuracy has improved drastically on the SF side due to the new application of methods to represent analytic solutions for metric perturbations of black-hole spacetimes. In a first stage, based on some exact solutions of the Teukolsky equation¹⁵, the PN coefficients of the redshift factor were obtained numerically to 10.5PN order¹². Analytic expressions were even found for a subset of coefficients, specifically those that are either rational, or made of the product of π with a rational, or a sum of commonly occurring transcendentals. An alternative SF approach¹⁶, based on the post-Minkowskian expansion of the Regge-Wheeler-Zerilli equation¹⁷, has also reached PN coefficients analytically up to 8.5PN order. Most recently, both methods have been extended to extremely high orders, typically 21.5PN for the redshift factor^{18,19}.

The appearance of *half-integral* PN coefficients (of type $\frac{n}{2}$ PN with n being an odd integer) in the conservative dynamics of two particles on circular orbits is a feature of high-order PN

expansion. Resorting to standard PN methods, we shall show now that the leading half-integral PN terms originate from non-linear integrals depending on the past history of the source — so-called hereditary type integrals.

2.2 Dimensionality argument

The fact that terms at half-integral PN orders cannot stem from the source variables evaluated at the current time follows from the general structure of “instantaneous” terms entering the redshift factor (1) in the center-of-mass frame. After replacing all accelerations by the lower-order equations of motion, u_1^T takes the form (with usual Euclidean notation)

$$(u_1^T)_{\text{inst}} \sim \sum_{\substack{j,k,n,p \\ \text{integers}}} \nu^j \left(\frac{Gm}{r_{12}c^2} \right)^k \left(\frac{v_{12}^2}{c^2} \right)^n \left(\frac{\mathbf{n}_{12} \cdot \mathbf{v}_{12}}{c} \right)^p, \quad (2)$$

where $m = m_1 + m_2$, $\nu = m_1 m_2 / m^2$, while $\mathbf{n}_{12} = (\mathbf{y}_1 - \mathbf{y}_2) / r_{12}$ stands for the relative direction of the two particles. We have taken the expansion when the mass ratio $\nu \rightarrow 0$.

The counting of the $1/c$ powers shows that the PN order of the generic term in Eq. (2) can be half-integral only if p is odd, in which case it vanishes for circular orbits, when the velocity \mathbf{v}_{12} and unit direction \mathbf{n}_{12} are evaluated at the same current time t . However, integration over some intermediate time extending from the infinite past up to t could allow a coupling between these vectors at different times. Of course, in general relativity, this type of “hereditary” dependence over the past of the system does occur, due, in particular, to wave tails produced by the backscatter of linear waves on the spacetime curvature.

3 Post-Newtonian computation of half-integral order contributions

3.1 Structure of the tail contributions

The tail effects, associated with non-linear wave propagation, are best investigated by constructing the (multipolar-)post-Minkowskian expansion of the metric $g_{\mu\nu}$ in powers of the gravitational constant G , outside the matter source⁶. We start from the Einstein field equations in vacuum, written in terms of the field perturbation variable $h^{\mu\nu} \equiv \sqrt{-g} g^{\mu\nu} - \eta^{\mu\nu}$ on the flat background $\eta^{\mu\nu}$ in Cartesian coordinates $\{x^i\}$, with g representing the determinant of $g_{\mu\nu}$. Adopting the harmonic-gauge condition $\partial_\nu h^{\mu\nu} = 0$, the relaxed Einstein equations for $h^{\mu\nu}$ reduce to the wave-like equations $\square h^{\mu\nu} = \Lambda^{\mu\nu}$, with $\square \equiv \eta^{\alpha\beta} \partial_\alpha \partial_\beta$. The non-linear source term $\Lambda^{\mu\nu}$ is an expression of second-order (at least) in $h^{\alpha\beta}$. At linear order in G , the most general solution depends on six sets of source multipole moments: the mass-type moments, $I_L \equiv I_{i_1 \dots i_\ell}$ (ℓ being the multipole order), the current-type moments $J_L \equiv J_{i_1 \dots i_\ell}$, and four sets of so-called gauge moments, irrelevant for the present discussion. The higher order solutions are obtained iteratively by applying the flat retarded integral operator $\square_{\text{ret}}^{-1}$ on the source term, after multiplication by a regularization factor r^B to cope with the divergence of the multipole expansion when $r \equiv |\mathbf{x}| \rightarrow 0$. Analytic continuation in $B \in \mathbb{C}$ is invoked and the finite part (FP) when $B \rightarrow 0$ provides a certain particular solution. To ensure that the harmonic coordinate condition is satisfied at each step, we must add to the latter solution a specific homogeneous retarded solution, which does not generate tail integrals and can be safely ignored here.

Since, ultimately, we shall be interested in the metric at the location of one of the particles, our goal is to compute the near-zone expansion, indicated below by an overline, of the general solution initially defined in the exterior of the source, when $r \rightarrow 0$. It is obtained directly at a given order from the near-zone expansion of the corresponding source, without need to control the full solution, from the formula²⁰:

$$\overline{\text{FP}_{B=0} \square_{\text{ret}}^{-1} [\hat{n}_L S(r, t - r/c)]} = \hat{\delta}_L \left\{ \frac{\overline{\mathcal{G}(t - r/c) - \mathcal{G}(t + r/c)}}{r} \right\} + \text{FP}_{B=0} \square_{\text{inst}}^{-1} [\hat{n}_L \overline{S}(r, t - r/c)], \quad (3)$$

where \hat{n}_L denotes the symmetric trace-free part of $n_L \equiv x^i \dots x^i / r^\ell$ ($\ell \in \mathbb{N}$). The first term is a homogeneous solution of the wave equation which is of retarded-minus-advanced type and regular at $r = 0$. It may be directly expanded in the near-zone, where it is valid by virtue of a matching argument. The second term in Eq. (3) is a particular solution of the inhomogeneous equation that is defined by means of the “instantaneous” inverse box operator, $\square_{\text{inst}}^{-1}$, representing the PN expansion of the symmetric integral operator supplemented with a regulator r^B multiplying the source and a finite part as $B \rightarrow 0$. This term diverges when $r \rightarrow 0$ and should be matched to a full-fledge solution of the field equations inside the source. However, we proved¹³ (see the appendix there) that it cannot actually contribute at half-integral PN orders, so that the effect we are looking for comes only from the term containing $\mathcal{G}(u)$. The latter function is given by a specific double integral over the source piece $S(r, t)$, and regularized by the finite part as $B \rightarrow 0$,

$$\mathcal{G}(u) = \text{FP}_{B=0} \int_{-\infty}^u ds R_B \left(\frac{u-s}{2}, s \right), \quad (4)$$

$$\text{where } R_B(\rho, s) = 2^{\ell-1} \rho^\ell \int_0^\rho d\lambda \frac{(r-\lambda)^\ell}{\ell!} \lambda^{B-\ell+1} S(\lambda, s). \quad (5)$$

This function is the crucial object to investigate for the purpose here.

At linear order in the mass ratio, we may disregard any hereditary term involving the product of more than two moments other than the mass monopole M , since each such multipole is proportional to ν . General results on the structure of the gravitational field in harmonic gauge tell us that hereditary contributions of type $M \times \dots \times M \times \mathcal{M}_P$, with $\mathcal{M}_P = I_P$ or J_P , read⁶

$$h_{M \times \dots \times M \times \mathcal{M}_P}^{\mu\nu} \sim \sum_{\substack{k,p,\ell,i \\ \text{integers}}} \frac{G^k M^{k-1}}{c^{3k+p}} \hat{n}_L \left(\frac{r}{c} \right)^{\ell+2i} \int_{-\infty}^{+\infty} du \kappa_{LP}^{\mu\nu}(t, u) \mathcal{M}_P^{(a)}(u), \quad (6)$$

where the upper sign (a) refers to time derivatives and the tensor function $\kappa_{LP}^{\mu\nu}(t, u)$ is a dimensionless kernel. Using dimensional analysis combined with “angular-momentum” selection rules, it is straightforward to show that only interactions with $k \geq 3$ can produce the half-integral PN terms of interest, starting at the leading 5.5PN order. In fact, at the next-to-next-to-leading order beyond 5.5PN, we can restrict ourselves to hereditary cubic interactions $M \times M \times \mathcal{M}_P$, which may be interpreted physically as gravitational-wave tails of tails. They must be computed at the 5.5PN, 6.5PN and 7.5PN orders for the mass quadrupole, 6.5PN and 7.5PN orders for the mass octupole and current quadrupole, and so on. The leading contributions of current-type moments are 1PN order higher than those of the mass moments.

3.2 Sketch of the calculation of u_1^T

The elementary source terms $\hat{n}_L S(r, t - r/c)$ for the tails of tails can be either instantaneous, with $S(r, t - r/c) = r^k \mathcal{M}_P^{(a)}(t - r/c)$, or hereditary. In the latter case, $S(r, t - r/c)$ is an integral of the type $r^{-k} \int_1^{+\infty} dx Q_m(x) \mathcal{M}_P^{(a)}(t - rx/c)$, with $Q_m(x)$ being a Legendre function of the second kind. After some transformations, the tail-of-tail piece of $\mathcal{G}(u)$ can be written as the finite part at $B = 0$ of some coefficient $C_{\ell km}(B)$, times an integral of the variable τ whose integrand involves the regulator τ^B times derivatives of $\mathcal{M}_P(t - \tau)$. Now, we find that $C_{\ell km}(B)$ may comprise (simple) poles at the order we are working, so that the factor τ^B generates a logarithm kernel $\ln \tau$. Insertion of the former piece of \mathcal{G} into the homogeneous wave entering Eq. (3) yields the form (6), with $\kappa_{LP}^{\mu\nu}(t, u)$ proportional to $\ln(t - u)$ for $t > u$, and zero elsewhere^{13,14}.

At this stage, it is important to realize that this sort of “pure” tail-of-tail contributions can generate another kind of half-integral terms, “mixed” contributions, by coupling to the non-tail part of the PN metric in the source of Einstein’s equations. This part is obtained most conveniently by solving the relaxed field equations in the near zone, where $\Lambda^{\mu\nu}$ is augmented by the matter source $16\pi Gc^{-4}|g|T^{\mu\nu}$. It is usually parametrized by means of appropriate potentials,

such as the Newtonian potential $U = Gm_1/r_1 + Gm_2/r_2$ (with $r_1 = |\mathbf{x} - \mathbf{y}_1|$). The time component h^{00} of the gravitational field, for instance, is composed of “ordinary” PN terms: $-4U/c^2 + \dots$, plus tail terms containing our effect: $h_{\text{tail}}^{00(5.5\text{PN})} + \dots$. Its product with, say, h^{ij} , whose structure is similar, produces couplings that must be crucially taken into account in the calculation. Their number is minimized by moving to an adapted gauge. Quadratic and cubic PN iterations are then required to find the complete half-integral PN part of the metric at the 7.5PN order. The successive solutions are constructed by means of hierarchies of “superpotentials” derived from the potentials that enter $g_{\mu\nu}$ at the 2PN order¹⁴. In the end, we decompose the tail integrals into conservative time symmetric and dissipative time anti-symmetric pieces and simply discard the dissipative piece from our results.

Using the standard stress-energy tensor for point particles to model the binary, all multipole moments, potentials and superpotentials can be evaluated explicitly for circular orbits. The hereditary integrals are derived from standard formulas. This yields for the redshift^{13,14}

$$u_{\text{SF}}^T = -y - 2y^2 - 5y^3 + \dots - \frac{13696}{525}\pi y^{13/2} + \frac{81077}{3675}\pi y^{15/2} + \frac{82561159}{467775}\pi y^{17/2} + \dots, \quad (7)$$

where we have written only the relative 2PN terms relevant to our next-to-next-to-leading order calculation, with all the other terms indicated by ellipsis. The result (7) is in full agreement with those derived by gravitational SF methods, either semi-analytical or purely analytical^{12,16}. We emphasize that it has been achieved from the standard PN approach, which is not tuned to a particular type of source (contrary to various analytical and numerical SF calculations), as it is actually applicable to any extended PN source with compact support. The 7.5PN order reached by the present calculation is perhaps the highest order ever reached by traditional PN methods. Note also that while SF results may be relativistic but with $q \ll 1$, the present method, valid primarily in the PN regime, is in principle applicable for arbitrary mass ratios. The time is now ripe for the SF approach to proceed to second order in q . We look forward to an occasion when high precision SF methods applied at second order may be fruitfully compared with known PN results in the weak field regime.

References

1. eLISA Consortium. The Gravitational Universe. Technical report, May 2013.
2. Y. Mino, M. Sasaki, and T. Tanaka. *Phys. Rev. D*, 55:3457, 1997.
3. T. C. Quinn and R. M. Wald. *Phys. Rev. D*, 56:3381, 1997.
4. E. Poisson, A. Pound, and I. Vega. *Living Rev. Rel.*, 14:7, 2011.
5. S. Detweiler and B. F. Whiting. *Phys. Rev. D*, 67:024025, 2003.
6. L. Blanchet. *Living Rev. Rel.*, 17:2, 2014.
7. G. ’t Hooft and M. Veltman. *Nucl. Phys.*, B44:139, 1972.
8. C. G. Bollini and J. J. Giambiagi. *Phys. Lett. B*, 40:566, 1972.
9. S. Detweiler. *Phys. Rev. D*, 77:124026, 2008.
10. L. Blanchet, S. Detweiler, A. Le Tiec, and B. F. Whiting. *Phys. Rev. D*, 81:064004, 2010.
11. L. Blanchet, S. Detweiler, A. Le Tiec, and B. F. Whiting. *Phys. Rev. D*, 81:084033, 2010.
12. A. G. Shah, J. L. Friedmann, and B. F. Whiting. *Phys. Rev. D*, 89:064042, 2014.
13. L. Blanchet, G. Faye, and B. F. Whiting. *Phys. Rev. D*, 89:064026, 2014.
14. L. Blanchet, G. Faye, and B. F. Whiting. *Phys. Rev. D*, 90(4):044017, Aug 2014.
15. S. Mano, H. Susuki, and E. Takasugi. *Prog. Theor. Phys.*, 95:1079, 1996.
16. D. Bini and T. Damour. *Phys. Rev. D*, 89:104047, 2014.
17. S. Mano, H. Susuki, and E. Takasugi. *Prog. Theor. Phys.*, 96:549, 1996.
18. C. Kavanagh, A. C. Ottewill, and B. Wardell. *ArXiv e-prints*, Mar 2015.
19. Nathan K. Johnson-McDaniel, Abhay G. Shah, and Bernard F. Whiting. *ArXiv e-prints*, Mar 2015.
20. L. Blanchet. *Phys. Rev. D*, 47:4392–4420, 1993.



CONSTRAINING THE DISTANCE TO INSPIRALING NS-NS WITH EINSTEIN TELESCOPE

I. KOWALSKA-LESZCZYNSKA¹, T. BULIK¹

¹*Astronomical Observatory, University of Warsaw, Al Ujazdowskie 4, 00-478 Warsaw, Poland*

1 Introduction

Einstein Telescope (ET) is a planned third generation gravitational waves detector located in Europe¹. Its design will be different from currently build interferometers: First, ET will be located underground in order to reduce the seismic noise. The arms length will be 10 km, and the configuration of arms will be different from all interferometers build so far i.e. there will be three tunnels in a triangular shape. ET will consist of three interferometers rotated by a 60deg with respect to each other in one plane. One of the biggest challenges for ET will be to determine sky position and distance to observed sources. If an object is observed in a few interferometers simultaneously one can estimate the position using traingulation from time delays², but so far there are no plans for a network of third generation detectors. Another possibility to deal with that problem is by using multimessenger approach, because redshift and sky position could be recovered from electromagnetic observations. However, in most cases of ET detection there will be only gravitational signal. In this paper we present a novel method of estimating distance and position in the sky of merging binaries. While our procedure is not as accurate as the multimessenger method, it can be applied to all observations, not just the ones with electromagnetic counterparts.

2 Distance estimation using one interferometer

For simplicity let us consider the case of observation of a double neutron star. In gravitational waves we will be observing directly two quantities: signal to noise ratio (ρ), which is a complicated function of the source properties, as well as the detector characterization, and redshifted chirp mass ($M_z = (1+z)M_{chirp}$, $M_{chirp} = (M_1M_2)^{3/5}(M_1+M_2)^{-1/5}$). In this particular case we consider only binaries consisting of two neutron stars of equal masses $M_1 = M_2 = 1.4 M_\odot$, so $M_{chirp} = 1.2 M_\odot$. The signal to noise ratio in the quadruple approximation for merging double compact objects is well known³:

$$\rho \sim \frac{\Theta}{d_L(z)} (M_z)^{5/6} \sqrt{\xi(z)}, \quad (1)$$

where d_L is the luminosity distance, M_z is the redshifted chirp mass, z is the redshift, Θ is a function of sky position and orientation of the source, and ξ is the function that determines fraction of the sensitivity window filled by a signal (it depends on the chirp mass, and for NSNS

binaries its value is close to unity). For a given binary that will be observed in the detector, we can measure ξ directly, by measuring the cutoff frequency when the inspiral ceases.

The function Θ depends on the sky position of the source $\Omega(\vartheta, \varphi)$ and on the orientation of the orbit with respect to the line of sight $\Omega_p(\Psi, i)$:

$$\begin{aligned}\Theta &= 2\sqrt{(1 + \cos^2 i)(F_+)^2 + 4\cos^2 i(F_x)^2}, \\ F_+ &= 0.5(1 + \cos^2 \vartheta) \cos 2\varphi \cos 2\Psi - \cos \vartheta \sin 2\varphi \sin 2\Psi, \\ F_x &= 0.5(1 + \cos^2 \vartheta) \cos 2\varphi \sin 2\Psi + \cos \vartheta \sin 2\varphi \cos 2\Psi.\end{aligned}\tag{2}$$

The density of sources in a unit volume can be expressed by:

$$\frac{d^2n}{dzd\Omega d\Omega_p} = \frac{n(z)}{1+z} \frac{dV}{dz}.\tag{3}$$

The comoving volume is $\frac{dV}{dz} = 4\pi \frac{c}{H_0} \frac{r^2(z)}{E(\Omega, z)}$, and $E(\Omega, z) = \sqrt{\Omega_\Lambda + \Omega_M(1+z)^3}$. Then we obtain for a single detector

$$\begin{aligned}\frac{dn}{dz} &= \int d\Omega d\Omega_p \frac{n(z)}{1+z} \delta(\rho - \rho_m) \\ &= 4\pi \frac{n(z)}{1+z} \frac{c}{H_0} \frac{r^2(z)}{E(\Omega, z)} \frac{d_L}{8r_0} \left(\frac{1.2}{M_z}\right)^{5/6} \frac{1}{\sqrt{\xi}} \\ &\quad \times P\left(\frac{\rho^m}{8r_0\left(\frac{M_z}{1.2}\right)^{5/6}\sqrt{\xi}} d_L(z)\right),\end{aligned}\tag{4}$$

where $n(z)$ is the merger rate, r_0 is the characteristic distance for a given detector (see Table 1 in paper by Taylor⁴ for more details), ρ^m is the actual signal-to-noise ratio measured in the detector.

3 Distance estimation using three co-located interferometers

Design of the Einstein Telescope assumes three co-located interferometers lying in the same plane, so the methods for distance estimation based on triangulation will not be possible. However, a single source will be observed by each of the interferometer with a different orientation. There will be three different measurements of signal to noise ratio. That will provide additional information about the observed source and it allows to constrain the distributions obtained in previous section.

The density of sources per unit volume given by Eq. 3 has to be integrated taking into account that we have three conditions to satisfy. We assume that each signal to noise ratio is measured with perfect accuracy:

$$\begin{aligned}\frac{dn}{dz} &= \int d\Omega d\Omega_p \frac{n(z)}{1+z} \delta(\rho_1 - \rho_1^m) \delta(\rho_2 - \rho_2^m) \delta(\rho_3 - \rho_3^m) \\ &= \int \frac{d^2n}{dzd\Omega d\Omega_p} 4\pi \frac{n(z)}{1+z} \frac{c}{H_0} \frac{r^2(z)}{E(\Omega, z)} \frac{d_L}{8r_0} \left(\frac{1.2}{M_z}\right)^{5/6} \frac{1}{\sqrt{\xi}(\rho_1^m)^2} \\ &\quad \times \delta\left(\Theta_1 - \frac{\rho_1^m}{8r_0\left(\frac{M_z}{1.2}\right)^{5/6}\sqrt{\xi}} d_L(z)\right) \delta\left(\frac{\Theta_2}{\Theta_1} - \frac{\rho_2^m}{\rho_1^m}\right) \delta\left(\frac{\Theta_3}{\Theta_1} - \frac{\rho_3^m}{\rho_1^m}\right),\end{aligned}\tag{5}$$

For illustration we present four cases of binary neutron stars simulated ET observations. The physical parameters of those sources, as well as the observed quantities are shown in Table 1.

Table 1: Physical parameters and observed quantities of four sources. For first three of them (A, B, C) sky position and orientation were chosen randomly from uniform distributions, while in the last case (D) they were chosen to maximize the obtained signal to noise ratio (the binary is optimally oriented).

| | Physical parameters | | | | | | Observed quantities | | | |
|---|-----------------------|-----|-------------------|--------------|--------------|------------|---------------------|------------|------------|------------|
| | $M_1 = M_2 [M_\odot]$ | z | ϑ [rad] | ϕ [rad] | Ψ [rad] | i [rad] | $M_z [M_\odot]$ | ρ_1^n | ρ_2^n | ρ_3^n |
| A | 1.4 | 0.1 | 0.53π | 0.82π | 1.30π | 0.70π | 1.34 | 44.04 | 94.42 | 55.95 |
| B | | 0.5 | 0.71π | 0.18π | 1.38π | 0.08π | 1.83 | 41.46 | 42.42 | 45.35 |
| C | | 1.0 | 0.34π | 1.61π | 0.64π | 0.66π | 2.44 | 9.99 | 10.57 | 12.69 |
| D | | 1.0 | 0 | π | π | 0 | 2.44 | 36.90 | 36.90 | 36.90 |

The results are shown in Fig. 1. It can be clearly seen that our method can constrain distances to with the accuracy of about 20%.

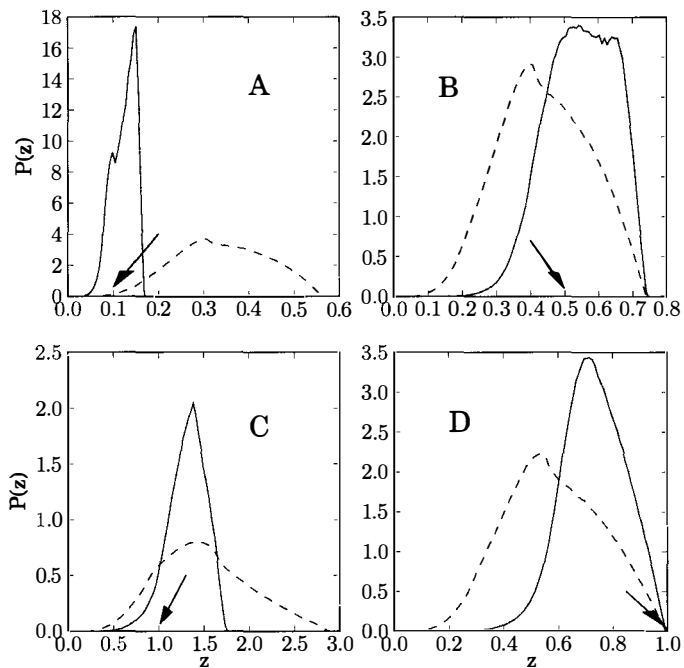


Figure 1 – Normalized redshift distributions for four NSNS system listed in Table 1. Dashed line represent distribution obtained using only one interferometer, while solid line represent distribution taking into account information from all three interferometers. The arrows indicate the position of the source.

4 Summary

Distance measurements to merging binaries will be very challenging in the third generation detectors era. So far, there are no plans for any other detector than Einstein Telescope. In this paper, we presented a method that can be used to constrain distance distribution for a given double neutron star observation. We have shown that it is possible to significantly

improve distance estimates using the measurements of the signal to noise ratio from all three interferometers .

Acknowledgments

This work was supported by the following Polish NCN grants DEC-2011/01/V/ST9/03171 and 2014/15/Z/ST9/00038.

References

1. M. Punturo *et al.*, *Class. Quantum Grav* **27**, 19 (2010).
2. S. Fairhurst, *New J. Phys.* **11**, 123006 (2009)
3. S. R. Taylor *et al.*, *Phys. Rev. D* **85**, 023536 (2012)
4. S. Taylor and J. R. Gair, *Phys. Rev. D* **86**, 023502 (2012)

RELATIVISTIC STELLAR DYNAMICS AROUND A MASSIVE BLACK HOLE IN STEADY STATE

TAL ALEXANDER

Department of Particle Physics and Astrophysics, Weizmann Institute of Science, Rehovot 76100, Israel

I briefly review advances in the understanding and modeling of relativistic stellar dynamics around massive black holes (MBHs) in galactic nuclei, following the inclusion of coherent relaxation and of secular processes in a new formal analytic description of the dynamics.

1 Relaxation in galactic nuclei

The dense, centrally concentrated stellar cluster that exists around most MBHs offers opportunities for strong, possibly destructive interactions between it and stars. These include direct plunges, leading to tidal disruption flares or gravitational waves (GW) flares, inspiral processes leading to quasi-periodic GW emission from extreme mass ratio inspiral events (EMRIs)¹, tidally powered stars (“squeezars”)², strong tidal scattering³ or capture by massive accretion disks. These processes affect MBH growth and may create exotic stellar populations around MBHs³.

This naturally leads to the question “How do stars closely interact with, and fall into a MBH, and at what rates?” This is known as the stellar dynamical “loss-cone problem”. It is a non-trivial problem, in spite of the presence of so many stars so close to the MBH, because the phase space volume of unstable orbits is minute. The few stars initially on such orbits quickly fall into the MBH on the short dynamical timescale, and then the rates would drop to zero, if it were not for dynamical processes that deflect additional stars from stable orbits to those with velocity vectors that point toward the MBH, within the loss-cone (Fig. 1 left). Thus, the loss-cone question is essentially the question: “how do galactic nuclei randomize and relax?”

1.1 Non-coherent 2-body relaxation (NR)

The discreteness of stellar systems leads to non-coherent 2-body relaxation (NR) (Fig. 1 left). This guarantees a minimal relaxation rate, on a timescale $T_{NR} \sim Q^2 P(r)/N_*(r) \log Q$, where $Q = M_\bullet/M_*$ is the MBH/star mass ratio, $P(r)$ is the radial orbital period, and $N_*(r)$ the number of stars inside r . Because the impact parameter b of these *point-point interactions* can be small, NR is boosted by the Coulomb factor $\log(b_{\max}/b_{\min}) = \log Q$. T_{NR} is the timescale for changes of order unity in energy, T_E . It is however easier to drive a star into the MBH by reducing its angular momentum L and making its orbit more radial, than by reducing the orbital energy $E < 0$, and shrinking the orbit. The timescale for changing $j = L/L_c(a) = \sqrt{1 - e^2}$ from j to 0 is $T_L = j^2 T_E$ ($L_c = \sqrt{GM_\bullet a}$ is the circular L , a the sma and e the eccentricity).

In the absence of dissipation, stars with $j \ll 1$ are deflected by L -scattering at nearly constant a to the innermost stable orbit (ISO), at $j_{\text{iso}} = 4\sqrt{r_g/a}$ ($r_g = GM_\bullet/c^2$) and then plunge directly into the MBH⁵ (Fig. 1 center). When a dissipative mechanism is present (e.g. GW), phase space is divided in two (Fig. 1 left). Below some critical sma a_c , all stars eventually cross the

“inspiral line” where E -dissipation is faster than j -scattering, and then inspiral gradually into the MBH as EMRIs. Stars above a_c plunge directly. The respective rates of plunges and inspirals can then be estimated by the ratio of number of stars on the relevant scales (the MBH radius of influence r_h for plunges (e.g tidal disruptions), and a_c for inspirals) over T_{NR} on that scale: $R_p \sim N_*(r_h)/T_{NR} \log(L_c/L_{iso})$ and $R_i \sim N_*(a_c)/T_{NR} \log(L_c/L_{iso})$. Because $N_*(a_c) \ll N_*(r_h)$, the inspiral rate is much lower than the plunge rate⁶, typically $R_i \sim 0.01R_p$.

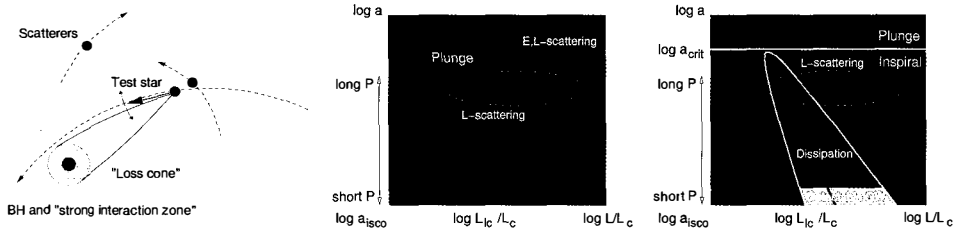


Figure 1 – The 2-body relaxation-driven loss-cone. **Left:** A star is scattered to an orbit in the loss-cone, which takes it close enough to the MBH for a strong (possibly destructive) interaction with it. **Center:** The loss-cone phase space in terms of the normalized angular momentum $j = L/L_c = \sqrt{1-e^2}$ and the semi-major axis a , without dissipation. **Right:** The same, but with a dissipative mechanism (here, the emission of GWs). See text.

1.2 Coherent resonant relaxation (RR) in nearly-spherical systems

Resonant relaxation⁴ is a process of rapid L -relaxation that occurs when the gravitational potential is symmetric enough to restrict the evolution of orbits on timescales much longer than the orbital time (e.g. nearly-fixed Keplerian ellipses in the nearly-Keplerian potential close to a MBH, where the stellar mass is negligible, but far enough so that GR effects are weak). In that case, a test orbit will feel a residual torque from the static, orbit-averaged background of stellar “mass wires”, which persists for a long coherence time T_c , until small deviations from symmetry accumulate and randomize the background. These *orbit-orbit interactions* randomize the angular momentum on a timescale $T_{RR} \sim Q^2 P(r)^2 / N_*(r) T_c$. Unlike NR, these extended objects do not undergo close interactions. Rather, RR is boosted by the long coherence time.

RR is relevant for the loss-cone problem because it is possible to have $T_c \gg P$ in the symmetric potential near a MBH, so that $T_{RR}/T_{NR} \sim (\log Q)P/T_c \ll 1$. That is, angular momentum evolution, and in particular that leading to $j \rightarrow 0$ and strong interactions with the MBH, can be greatly accelerated. Unchecked, RR will completely suppress EMRIs by driving all stars into plunge orbits (Fig. 2 center). However, very eccentric orbits undergo GR in-plane (Schwarzschild) precession, which quenches RR by rapidly alternating the direction of the residual torque on the orbit. This motivated the “fortunate coincidence conjecture”⁷: The $\mathcal{O}(\beta^2 j^{-2})$ GR precession becomes significant before $\mathcal{O}(\beta^5 j^{-7} Q^{-1})$ GW dissipation, and this may allow EMRIs to proceed unperturbed, decoupled from the background stars.

1.3 The Schwarzschild Barrier

The first full PN2.5 N -body simulations⁸ revealed a surprising result: not only does GR precession quench RR before the GW-dominated regime, as conjectured, but there appears to be some kind of barrier in phase space, dubbed the Schwarzschild Barrier (SB), which prevents the orbits from evolving to $j \rightarrow 0$. Instead, they appear to linger for roughly T_c near the SB, where their orbital parameters oscillate at the GR precession frequency, and then they evolve back to $j \rightarrow 1$. An early analysis⁹ suggested that this behavior is related to precession under the influence of a residual dipole-like residual force. However, a full self-consistent explanation of the SB was lacking, and its very existence and nature remained controversial.

I now describe briefly a new formal framework for expressing coherent relaxation and secular processes in galactic nuclei¹⁰, and discuss implications for the steady state phase space structure and loss rates¹¹.

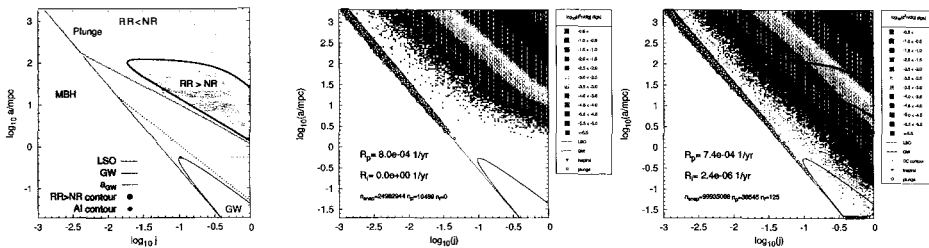


Figure 2 – The loss-cone phase space. **Left:** A schematic for a model of the Milky Way nucleus ($M_\bullet = 4 \times 10^6 M_\odot$, $M_\star = 10 M_\odot$). Orbits are unstable in the gray region left of the ISO line. Dynamics are dominated by GW dissipation inside the GW curve at the bottom right. The horizontal line tangent to the upper tip of the GW line is the critical sma separating plunge and inspiral tracks (one example shown for each). RR dominates over NR in the shaded region in the middle right. RR is ineffective on short timescales below the diagonal AI line just below the RR region. **Center:** The phase space density and loss rates calculated by MC simulations, for an artificial model without GR precession to quench RR, resulting in rapid plunges (circles at ISO line) and complete suppression of EMRIs. **Right:** The same, but with GR precession, which suppresses RR (RR remains strong only inside the $T_{RR} = 0.1$, $1T_{NR}$ contours). This enables EMRIs (triangles at bottom of GW region). See text.

2 Hamiltonian dynamics with correlated background noise

Two key insights inform the new advances in understanding coherent relativistic dynamics, which lie in the difficult-to-treat interface between deterministic Hamiltonian dynamics and stochastic kinetic theory. (1) The effect of the background stars on a test star should be described by a *correlated* noise model $\boldsymbol{\eta}(t)$, whose degree of smoothness (differentiability) determines dynamics on short timescales¹⁰. (2) The long-term steady-state remains (unavoidably) the maximal entropy configuration, irrespective of the details of the nature of the relaxation processes¹¹.

This formal treatment of PN1 dynamics in the presence of correlated (RR) noise $\boldsymbol{\eta}$ (a 3-vector in L -space) allows to write a phase-averaged leading-order ($\ell = 1$) Hamiltonian \mathcal{H}_1 and derive *stochastic* EOMs for the orbital elements of a test star, $\mathbf{x} \equiv (j, \phi, \cos \theta)$ and the argument of periape ψ , which precesses at frequency $\nu_p(j)$,

$$\dot{\mathbf{x}} = \boldsymbol{\nu}_{\tau, \mathbf{x}}(\mathbf{x}, \psi) \cdot \boldsymbol{\eta}, \quad \dot{\psi} = \boldsymbol{\nu}_{\tau, \psi}(\mathbf{x}, \psi) \cdot \boldsymbol{\eta} + \nu_p(j), \quad (1)$$

where ν_τ is the RR torque frequency. This $\boldsymbol{\eta}$ formalism allows to evolve a test star in time for a given realization of the noise. Moreover, even though $\boldsymbol{\eta}$ is time-correlated, it is possible to derive (and validate with the stochastic EOMs) approximate diffusion coefficients (DCs) $D_{1,2}$, which allow to evolve in time the probability density $\rho(j)$ with the Fokker-Planck (FP) equation,

$$\frac{\partial \rho}{\partial t} = \frac{1}{2} \frac{\partial}{\partial j} \left\{ j D_2 \frac{\partial}{\partial j} \left[\frac{\rho}{j} \right] \right\}, \quad \text{where } D_2 = |\boldsymbol{\nu}_{\tau, j}|^2 \mathcal{F}_{C(t)}[\nu_p(j)] \text{ and } D_1 = \frac{1}{2j} \frac{\partial j D_2}{\partial j}. \quad (2)$$

$\mathcal{F}_{C(t)}$ is the Fourier transform of $\boldsymbol{\eta}$'s auto-correlation function (ACF). The explicit dependence of D_2 on the spectral power of the noise at the precession frequency is an expression of *adiabatic invariance* (AI). If, and *only if* the noise has an upper frequency cutoff, as it must if it is smooth (this is physically expected, since the background noise is the superposition of continuous orbital motions), then there is a critical j_0 such that for $j < j_0$ the precession is fast enough so that $D_2(j) \rightarrow 0$, and the star decouples from the background resonant torques (Fig. 3 left, center). This describes the dynamics of the SB: it is not a reflecting boundary, but a locus in phase space where diffusion rapidly drops due to AI. Since diffusion to yet lower j slows further down, while diffusion to higher j speeds further up, orbits statistically seem to bounce away from the SB.

3 The steady state loss-cone

NR is impervious to AI. When $t \rightarrow T_{NR}$, the system approaches the maximal entropy solution ($dN/dj = 2j$, Fig. 3 right). Monte Carlo (MC) simulations of the probability density, branching ratios and loss rates with the η formalism (Fig. 2 right) show that the RR-dominated region in phase space is well separated from the plunge and inspiral loss-lines, so the effect of RR on the loss rates is small ($< \times 2 - 3$). Specifically, we conclude that GR quenching of RR is effective, so the EMRI rates remain largely unaffected by RR. RR can be significant for processes whose loss-line crosses the RR-dominated region, e.g. destruction by interaction with an accretion disk.

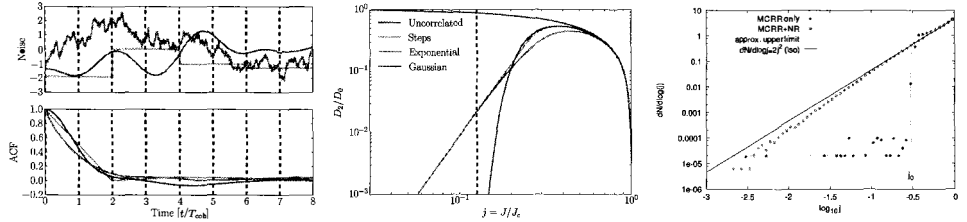


Figure 3 – The smoothness of the noise model and diffusion dynamics. **Left:** Three η models and their ACF: discontinuous steps (C^0), continuous but not continuously differentiable (C^1 with exponential ACF), smooth (C^∞ with Gaussian ACF). **Center:** The corresponding D_2 ; note the steep cutoff at $j < 0.1$ for the smooth noise model. **Right:** The MC simulations of j -only evolution reproduce the AI/SB limit at $j < j_0$ in the absence of NR, but NR erases this feature completely on timescale $t \rightarrow T_{NR}$.

4 Summary

NR, RR, GW dissipation and secular precession can be treated analytically as effective diffusion with correlated noise. The steady state depends mostly on NR, which erases AI. RR can be important in special cases. The η formalism provides stochastic EOMs for evolving test particles and an FP/MC diffusion procedure for evolving the probability density. This makes it possible to model the relativistic loss-cone in galactic nuclei with realistic $N_* \gg 1$, (unlike direct N -body simulations), and obtain the branching ratios, loss rates and steady state stellar distributions.

Acknowledgments

This research was supported by the I-CORE program of the PBC and ISF (grant No 1829/12).

References

1. P. Amaro-Seoane *et al.* *Classical and Quantum Gravity* **24**, 113 (2007).
2. T. Alexander & M. Morris, *Astrophysical Journal* **590**, L25 (2003).
3. T. Alexander & M. Livio, *Astrophysical Journal* **560**, L143 (2001).
4. K. P. Rauch, & S. Tremaine, *New Astronomy* **1**, 149 (1996).
5. A. P. Lightman & S. L. Shapiro, *Astrophysical Journal* **211**, 244 (1977).
6. T. Alexander & C. Hopman, 2003, *Astrophysical Journal* **590**, L29 (2003).
7. C. Hopman & T. Alexander, 2006, *Astrophysical Journal* **645**, 1152 (2006).
8. D. Merritt, T. Alexander, S. Mikkola, & C. M. Will, 2011, *Phys. Rev. D* **84**, 044024 (2011).
9. Alexander, T. 2010, in *GW and EM signatures of MBH binaries and EMRIs*, ed. P. Amaro-Seoane & E. Porter (Laboratoire Astroparticule et Cosmologie, Paris)
10. B. Bar-Or & T. Alexander, *Classical and Quantum Gravity* **31**, 244003 (2014).
11. B. Bar-Or & T. Alexander, 2015, in preparation.

6. Posters

mSTAR: TESTING LORENTZ INVARIANCE IN SPACE USING HIGH PERFORMANCE OPTICAL FREQUENCY REFERENCES

Norman Gürlebeck^{1,*}, Shailendhar Saraf², Alberto Stochino², Klaus Döringshoff³, Sasha Buchman², Grant D. Cutler², John Lipa², Si Tan², John Hanson⁴, Belgacem Jaroux⁴, Claus Braxmaier^{1,6}, Thilo Schuldt⁶, Sven Herrmann¹, Claus Lämmerzahl¹, Achim Peters³, Abdul Alfauwaz⁵, Abdulaziz Alhussien⁵, Badr Alsuwaidan⁵, Turki Al Saud⁵, Hansjörg Dittus⁶, Ulrich Johann⁷, Simon P. Worden⁴, and Robert Byer²

¹ *Center of Applied Space Technology and Microgravity (ZARM), University of Bremen, Germany*

² *Stanford University, Hansen Experimental Physics Laboratory, Stanford, California, USA*

³ *Humboldt University Berlin, Department of Physics, Berlin, Germany*

⁴ *NASA Ames Research Center (ARC), Mountain View, California, USA*

⁵ *King Abdulaziz City for Science and Technology (KACST), Riyadh, Saudi-Arabia*

⁶ *German Aerospace Center (DLR), Institute for Space Systems, Bremen, Germany*

⁷ *Airbus Defence and Space GmbH, Friedrichshafen, Germany*

* email: norman.guerlebeck@zarm.uni-bremen.de

The proposed mini SpaceTime Asymmetry Research (mSTAR) satellite mission will perform a test of special relativity. By comparing an absolute to a length based frequency reference, a Kennedy-Thorndike (KT) type experiment is carried out testing the boost dependency of the speed of light using the large velocity modulation in low Earth orbit (LEO). Using clocks with instabilities below the 10^{-15} level at orbit time, the KT coefficient will be measured with an up to two orders of magnitude higher accuracy than current ground-based experiments. In the baseline design, an absolute frequency reference based on modulation transfer spectroscopy of molecular iodine near 532 nm is compared to a high finesse optical cavity made of ultra-low expansion glass (ULE) as length based frequency reference. Variations between the two references indicate a violation of Lorentz invariance.

Summary of the mSTAR mission

Special Relativity is classically tested by performing three types of experiments investigating the direction-dependence of the speed of light (Michelson-Morley experiment), the boost-dependence of the speed of light (KT experiment), and the effect of time dilation (Ives-Stilwell experiment). The proposed mSTAR mission will perform a KT experiment in space by comparing an absolute iodine-based frequency reference to a length based frequency reference, i.e. a laser frequency stabilized to a cavity – both with frequency instabilities at or below the $1 \cdot 10^{-15}$ level at orbit time. This allows to determine the KT coefficient with an up to two orders of magnitude higher accuracy than current ground-based experiments.¹ Performing the experiment in space has several advantages. For KT experiments on ground, the relevant variation of the velocity of the laboratory comes from Earth's daily rotation (≈ 300 m/s) and for a space-based one from the satellite's velocity (≈ 7.4 km/s). Thus, the putative science signal is 25 times higher in this case. Additionally, the science signal is shifted to a Fourier frequency (≈ 0.2 mHz) where the stability of oscillators is better compared to sidereal frequencies. Moreover, space offers a vibration free environment and the elimination of large DC gravity forces.

In the baseline design, mSTAR employs an absolute frequency reference based on a hyperfine

transition in molecular iodine near 532 nm. A frequency-doubled Nd:YAG laser is foreseen as laser that is stabilized to the iodine reference. Part of the fundamental (1064 nm) stabilized laser light is split off and sideband locked to the resonance frequency of a high finesse optical cavity made of ULE with an electro-optic modulator (EOM). The frequency difference between the two references can be extracted from the EOM sideband frequency, which is then analyzed with respect to variations at the orbit frequency yielding the KT coefficient.

The mSTAR iodine clock is based on a DLR-funded setup on engineering model level realized in a cooperation of Humboldt University Berlin, DLR Bremen, University of Applied Sciences Konstanz, Airbus D&S Friedrichshafen, and ZARM Bremen.² Its optical components are joined to a fused silica baseplate using adhesive bonding technology in combination with a space-qualified two-component epoxy. This technique allows for a high long-term stability of the iodine reference due to a reduced pointing instability. This setup takes space mission related criteria such as compactness, MAIVT (manufacturing, assembly, integration, verification and test), and robustness with respect to shock, vibration, and thermal stress into account. A frequency stability of $7 \cdot 10^{-15}$ and below $5 \cdot 10^{-15}$ at integration times of 1 s and between 10 s and 5000 s, respectively, is reached, which is similar to the best current laboratory setup.⁴

The mSTAR cavity is based on the development of a space qualified setup for the GRACE Follow-On mission carried out by JPL and Ball Aerospace. It foresees a mid-plane mounted cavity with a finesse > 160.000 made of ULE with a coefficient of thermal expansion (CTE) of $\sim 10^{-9}/\text{K}$ within an operating temperature range of 10–30°C and a CTE zero crossing temperature near 15°C. Mirror substrates are made of fused silica in order to reduce thermal noise and ULE compensation rings are planned in order to maintain the CTE zero crossing temperature.⁵ The thermal enclosure of the cavity consists of 4 gold coated aluminum cans with titanium alloy supports, for which thermal simulations show an attenuation factor $> 10^{10}$ so that a 1 K temperature swing at the outer shield, which can be provided by the satellite bus, will have negligible stress effects on the cavity.

The proposed baseline orbit for mSTAR is a circular 6 AM dawn-dusk sun-synchronous LEO with an altitude of 650 km, which provides a natural de-orbiting in 25 years. This altitude minimizes the need for radiation hardness of the components and the sun-synchronous orbit provides a good thermal stability of the payload. The spacecraft bus will be contributed by KACST based on their SaudiSat 4 spacecraft with an envelope size of $672 \times 606 \times 1227 \text{ mm}^3$. It provides $\sim 100 \text{ W}$ of electrical power for a scientific payload with a mass up to 30 kg and a volume up to 140 liters. In an ongoing Phase A study, the feasibility of the payload accommodation within the SaudiSat 4 satellite bus is evaluated.

The mSTAR mission is investigated in an international collaboration including KACST (Saudi Arabia), Stanford University (USA), NASA Ames (USA) and a German Team consisting of the DLR Institute of Space Systems, ZARM, and the Humboldt-University Berlin.

Acknowledgment

Financial support by the German Space Agency DLR with funds provided by the Federal Ministry of Economics and Technology (BMWi) under grant numbers 50 QT 1102, 50 QT 1201, and 50 QT 1401 and by KACST is highly appreciated.

References

1. M.E. Tobar *et al.*, *Phys. Rev. D* **81**, 022003 (2010).
2. T. Schuldt *et al.*, in Proceedings of the 10th International Conference on Space Optics (2014), 2014.
3. W.M. Folkner *et al.*, in Proceedings of the Earth Science Technology Forum (2010), 2010.
4. E.J. Zang *et al.*, *IEEE Transactions on Instruments and Measurement* **56**, p. 673, 2007.
5. T. Legero *et al.*, *J. Opt. Soc. Am. B* **27**, 914 (2010).

Gravity gradiometer using large momentum transfer beamsplitters

M. Langlois, S. Merlet, F. Pereira Dos Santos

SYRTE, Observatoire de Paris, PSL Research University, CNRS, Sorbonne Universités, UPMC Univ. Paris 06, LNE, 61 avenue de l'Observatoire, 75014 Paris, France



We are currently developing a vertical gravity gradiometer. This new experiment will combine ultracold atoms produced on atom chips and large momentum transfer beamsplitters. Two separated atomic clouds will be interrogated simultaneously to measure the vertical gravity gradient. For that purpose high power laser sources will be developed to get a large separation between the two arms of each interferometer and thus a high sensitivity. We expect a shot noise limited sensitivity of $9.10^{-12}g$ at 1s on a single cloud, and a sensitivity of the gravity gradient measurement of $1, 3.10^{-1}E$ at 1s, for a separation of 1m between the two clouds.

1 Principle of our gravity gradiometer

The goal of this experiment is to measure the Earth vertical gravity gradient using atom interferometry with a very high sensitivity. The principle used is similar to the one applied on cold atom gravimeters¹ (CAG).

In a CAG, a cold atom cloud is first prepared and a Bordé-Chu interferometer² is performed while the atoms are free falling thanks to a sequence of laser pulses that split and recombine the atomic wavepackets. In these instruments, the measurement of g is extracted from a frequency chirp applied onto the frequency of the interferometer lasers to compensate the Doppler shift during the interferometer.

An atom gradiometer combines two gravimeters and the gradient is calculated from the difference between the two gravity values obtained on two clouds located at two different heights. As a first step, we will generate the two clouds with a single atom chip, and later a second will be developed. For the two clouds, the same laser beams will drive the two interferometers simultaneously. Subtracting the phases of the two interferometers allows extracting the gravity gradient while efficiently rejecting common mode phase fluctuations, such as arising from vibration noise and laser phase noise.

2 Using of large momentum transfer

Large momentum transfer techniques refer to beamsplitting methods that allow transferring to the atoms much larger momenta than conventional two photon processes, based for instance on two photon stimulated Raman transition. Such transfers are possible using the interaction

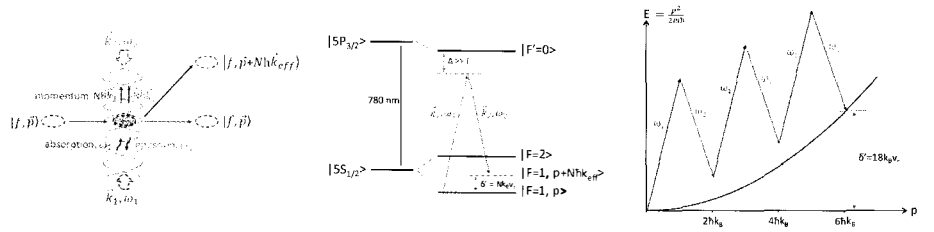


Figure 1 – Left: Trajectories of the atoms after a LMT beamsplitter pulse. Middle: Multiphoton Bragg laser frequency shown on the ^{87}Rb energy levels. Right: Energy-momentum diagram of resonant multiphoton transitions driven by two counter-propagating beams.

of the atoms with standing waves in motion, such as in high order Bragg diffraction or Bloch oscillations. See Fig. 1. Such large momentum transfers increase the separation between the two arms of the interferometer, and hence their sensitivity to inertial forces.

Such techniques require a significantly larger laser intensity than conventional techniques. If using cold atom sample of size of order of a mm, such as produced by standard laser cooling techniques, a laser power of about a watt is required⁴. If using smaller samples, such as produced by evaporative cooling in conservative traps, smaller powers of about 100 mW is enough³.

We propose to combine both ultracold atom sources and high power lasers, to increase the efficiency of the beamsplitters. For that purpose, atoms will be trapped on atom chips, that allow for efficient and fast production of ultracold samples, and eventually Bose-Einstein condensates (BEC). High power laser sources of power in the few W range will be developed using frequency doubling of fibred telecom lasers.

3 Progress and excepted results

The laser system for cooling and detection of the atoms is operational⁵, and work on the generation of the beamsplitting lasers is ongoing. We aim at producing two independent counter-propagating lasers beams, whose relative phase is locked with a high bandwidth of a few MHz via feedback onto a broadband phase modulator, similar to ref⁶. The main vacuum chamber, in which the magneto-optical trap (MOT) will be loaded with a 2D MOT, has been designed and is under construction. Design of the atom chips is underway.

Presently, CAG have demonstrated a best short term sensitivity of $4, 2 \cdot 10^{-9}g$ at $1s$ ⁷, and sensitivity to the gravity gradient of $30E$ at $1s$ ⁸. With our new experiment we expect to produce a $100 \hbar k$ separation, with a cycle time $T_C = 2 s$, a Ramsey time $T_R = 500 ms$ and the two sciences chambers separated by $1 m$. This will give a single accelerometer short term sensitivity limited by quantum projection noise (QPN) at the level of $9.10^{-12}g$ at $1s$, and a gravity gradiometer with a sensitivity of $1, 3 \cdot 10^{-1}E$ at $1s$

References

1. Louchet-Chauvet *et al*, *New J. Phys.* **13**, 065025 (2011).
2. Bordé, *Phys. Lett. A* **140**, 10 (1989).
3. G. D. McDonald *et al*, *Phys. Rev. A* **88**, 053620 (2013).
4. S.-W. Chiow *et al*, *Phys. Rev. Lett.* **107**, 130403 (2011).
5. S. Merlet *et al*, *Appl. Phys. B* **117**, 749 (2014).
6. H. Müller *et al*, *Appl. Phys. B* **84**, 633 (2006).
7. Z.-K. Hu *et al*, *Phys. Rev. A* **88**, 043610 (2013).
8. F. Sorrentino *et al*, *Phys. Rev. A* **89**, 023607 (2014).

Atom interferometry with ultra-cold strontium

N. Poli, T. Mazzone, X. Zhang, L. Salvi, R. P. del Aguila and G. M. Tino

*Dipartimento di Fisica e Astronomia and LENS - Università di Firenze, INFN - Sezione di Firenze,
Via Sansone 1, 50019 Sesto Fiorentino, Italy*



We report on the the first realization of an atom interferometer based on alkali-earth atoms, namely strontium, using Bragg diffraction. The present status of the project and future prospects towards high precision tests in gravitational physics are discussed.

1 Introduction

Strontium atoms have interesting features for atom interferometry. In particular for bosonic ^{88}Sr isotope, atoms in the ground electronic $^1\text{S}_0$ state has zero spin, making them insensitive to external electric and magnetic fields. Moreover, cold collisions among atoms in this state are very rare. The almost negligible scattering cross section ($a=-2a_0$) is particularly favorable in order to preserve coherence of the atomic wave function for long interferometric sequences and Bloch oscillations¹. For these reasons, bosonic ^{88}Sr atoms are considered for testing large momentum transfer (LMT) interferometers by employing two-photon Bragg transitions².

Toward this goal, we are performing first tests of Bragg diffraction on ultra-cold strontium samples. Bragg pulses are applied along the vertical direction on a pre-cooled sample of strontium (about 10^6 atoms at μ K temperatures). The Bragg pulses are produced by a secondary 461 nm blue laser frequency offset locked to the primary cooling laser source with a typical frequency offset of $\Delta = 9$ GHz. Two acousto-optical modulators are used to produce two optical beams with the proper frequency detuning $\delta = \omega_1 - \omega_2$ for the Bragg pulses. The different diffraction order n is then selected by choosing the proper $\delta_n = 4n\omega_r$, where $\omega_r = \hbar k^2/(2M)$ is the recoil frequency ($\omega_r = 2\pi \times 10.6$ kHz for strontium). The two frequency components are then coupled into a single mode fiber with mutually orthogonal polarization and sent to the atomic sample; after the atom chamber, the polarization is changed with a quarter wave plate and the beam is retro-reflected by a suspended mirror.

By choosing the proper Bragg pulses parameters (laser intensity, frequency detuning and pulse duration), it is possible to transfer efficiently the atomic cloud in the first diffracted order (π pulse, as shown by Fig.1) with net momentum of $+2\hbar k$. To ensure high efficiency π pulses³, atoms with lower velocity spread along the vertical direction are selected and launched upward before the subsequent Bragg interaction. About 10^5 atoms are launched upward with an initial

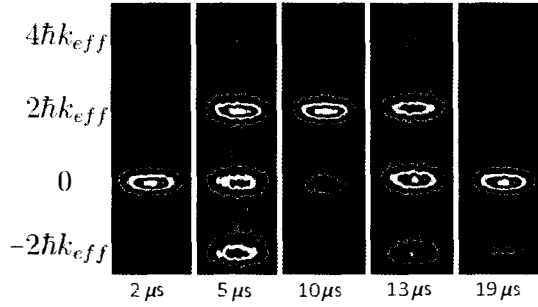


Figure 1 – False colour images of Bragg-diffracted ultra-cold strontium atoms after time of flight $T_{tof} = 20$ ms. On the bottom of each picture is reported the corresponding Bragg pulse duration.

momentum $p_0 \sim 24\hbar k$ and a velocity spread of $\Delta p \sim 0.1\hbar k$. In this condition, the maximum diffraction efficiency we reached for a π -pulse is nearly 90%.

We have also performed first tests on Mach-Zehnder $\pi/2$ - π - $\pi/2$ interferometer, obtaining fringes with a contrast $C \sim 50\%$ for an interferometer time $T = 30$ ms. While the total interferometer time is currently limited by the vertical size of the vacuum system, in this configuration, we could perform precision measurements of the local gravitational acceleration g . A detailed study of the sensitivity of the strontium gravimeter, $\Delta g/g < 10^{-7}$ for an integration time $\tau = 400$ s, is currently under study. Meanwhile, to overcome some of the limitation imposed by the current experimental setup, a feasibility study for a 10 m strontium fountain is under way. In conclusion, ultra-cold strontium atoms might represent a valid choice for precision gravimeter and gravity gradiometer, with possible future application to stringent tests of fundamental physics theories⁴.

Acknowledgments

We acknowledge support from INFN, LENS, EU and MIUR.

References

1. N. Poli, F.-Y. Wang, M. G. Tarallo, A. Alberti, M. Prevedelli, G. M. Tino, “Precision measurement of gravity with cold atoms in an optical lattice and comparison with a classical gravimeter”, *Phys. Rev. Lett.* **106**, 038501 (2011)
2. G. M. Tino, “Testing gravity with atom interferometry” in *Atom Interferometry*, Proceedings of the International School of Physics “Enrico Fermi”, Course CLXXXVIII, Varenna 2013, p. 457-491, Editor G. M. Tino and M. A. Kasevich, Società Italiana di Fisica and IOS, (2014)
3. S. S. Szigeti, J. E. Debs, J. J. Hope, N. P. Robins, J. D. Close, “Why momentum width matters for atom interferometry with Bragg pulses”, *New J. Phys.* **14**, 023009 (2012)
4. M. G. Tarallo, T. Mazzoni, N. Poli, D. V. Sutyryn, X. Zhang, and G. M. Tino, “Test of Einstein Equivalence Principle for 0-spin and half-integer-spin atoms: Search for spin-gravity coupling effects”, *Phys. Rev. Lett.* **113**, 023005 (2014)

Gravitational Wave Recoils in Non-head-on Collisions of Black Holes

R. F. Aranha¹, I. Damião Soares¹ and E. V. Tonini²

¹ *Centro Brasileiro de Pesquisas Físicas, Rio de Janeiro 22290-180, Brazil,*

² *Instituto Federal do Espírito Santo, Vitória 29040-780, Brazil.*

We examine the gravitational wave recoil in the non-head-on collisions of two black holes. We make a numerical study of the kick distributions for an extended range of the incidence angle ρ_0 in the initial data. The kicks V_k fit accurately an empirically modified Fitchett law, with a parameter C that accounts for the non-zero gravitational wave momentum flux in the equal-mass case, with a normalized rms error $\leq 0.3\%$ for the whole range of ρ_0 . The maximum kick velocity obtained is $\simeq 190\text{km/s}$ for $\rho_0 \simeq 55^\circ$ and equal mass. We construct the surface $V_k(\rho_0, \eta)$ in the parameter space of the initial data, giving an overall view of the behavior of V_k as the parameters change.

This communication reports part of the results of Aranha et al.¹ where we examined the production of kicks by gravitational wave recoils in the post-merger phase of two colliding black holes in non-head-on collisions. Our treatment is made in the realm of Robinson-Trautman (RT) spacetimes² with initial data given by

$$P(u_0, \theta, \phi) = \left(\frac{1}{\sqrt{\cosh \gamma + \cos \theta \sinh \gamma}} + \frac{\alpha}{\sqrt{\cosh \gamma - (\cos \rho_0 \cos \theta + \sin \rho_0 \sin \theta \cos \phi) \sinh \gamma}} \right)^{-2}, \quad (1)$$

which can be interpreted³ as two instantaneously colliding Schwarzschild black holes with mass-ratio α and boosted with initial velocity $v = \tanh \gamma$ respectively along the positive direction of the z -axis and along the direction defined by the unit vector $\hat{\mathbf{n}} = (-\sin \rho_0, 0, -\cos \rho_0)$ with respect to an asymptotic Lorentz frame. The data (1) is evolved from the initial data characteristic surface $u = u_0$ via the RT dynamics; the final configuration is a boosted Schwarzschild black hole^a. The momentum extraction and associated recoils are given by the Bondi-Sachs conservation laws^{4,5} for the momentum and impulse, respectively $d\mathbf{P}(u)/du = \mathbf{P}_W(u)$ and $\mathbf{P}(u) - \mathbf{P}(u_0) = \mathbf{I}_W$, where

$$\mathbf{P}_W(u) = \frac{1}{4\pi} \int_0^{2\pi} \int_0^\pi \frac{\mathbf{n}}{P} (c_u^{(1)2} + c_u^{(2)2}) \sin \theta d\theta, \quad \mathbf{I}_W(u) = \int_{u_0}^u \mathbf{P}_W(u') du', \quad (2)$$

are the net momentum flux and net impulse of the gravitational waves emitted. The functions $(c_u^{(i)}, i = 1, 2)$ are the *news functions* connected to the two polarization modes of the radiation and $\mathbf{n} = (-\sin \theta \cos \phi, \sin \theta \sin \phi, \cos \theta)$. We define (restoring universal constants) the net kick velocities $\mathbf{V}_k = c \mathbf{I}_W(u_f)/M_{\text{rem}}$ as proportional to the total net momentum imparted to the system by the gravitational waves, in a zero-initial-Bondi-momentum frame, which can then be compared with the results of the literature. M_{rem} is the mass of the remnant black hole.

For the initial data (1) we evaluated numerically V_k contemplating an extended range of parameters α and ρ_0 with fixed $\gamma = 0.5$. In Figs. 1 we display the distribution curves of V_k versus the symmetric mass parameter $\eta = \alpha/(1 + \alpha)^2$. The continuous curves are the best fit of the points to the analytical formula

$$V_k(\eta) = A\eta^2(1 - 4C\eta)^{1/2}(1 + B\eta) \times 10^3 \text{km/s}, \quad (3)$$

^aOur numerical code is based on the Galerkin method; for details see Aranha et al.³ and references therein.

with best fit parameters given in Table 3 of Aranha et al.¹. The parameter $C > 1$ is needed to account for the nonzero gravitational wave net momentum flux in the equal-mass case.

Our main results are displayed in Figs. 1.

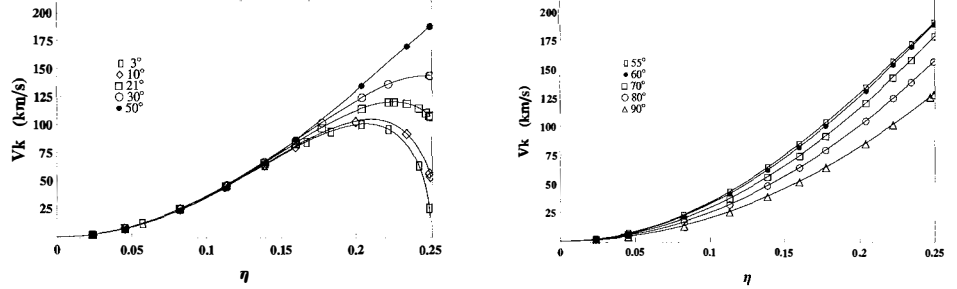


Figure 1 – Plot of the numerical points (V_k, η) where V_k is due to the total impulse imparted to the merged system by the gravitational waves emitted, for incidence angles ρ_0 varying from 3° to 90° . The continuous curves are the best fit of the points to the analytical form (3) with a normalized rms error of the order of, or smaller than 0.3%. For $C = 1$ eq. (3) reduces to the Fitchett law, which corresponds to the $\rho_0 = 0^\circ$ case, when the net gravitational wave momentum flux is zero for the equal mass case $\alpha = 1$.

In Fig. 2 (left) we plot the parameters A , B and C (associated with the best fit of the law (3) to the numerical RT data) versus ρ_0 as given in Table 3 of Aranha et al.¹. The continuous curves are the best fit of the points through an eighth order polynomial least-squares method. By using the best fit curves $A(\rho_0)$, $B(\rho_0)$ and $C(\rho_0)$ of Fig. 2 (left) and the kick velocity distributions we construct the surface $V_k(\eta, \rho_0)$ in the parameter space of RT initial data (1) as shown in Fig. 2 (right). This gives a global view of the behavior of V_k as the mass-ratio and the incidence angle vary, e.g., the absolute maximum of V_k for $(\eta = 0.25, \rho_0 \simeq 55^\circ)$.

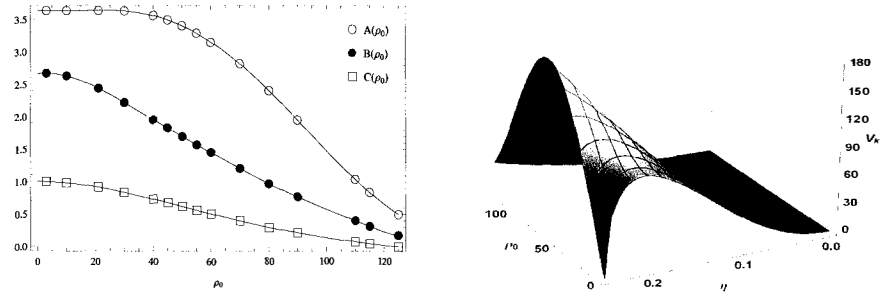


Figure 2 – (left) Plots of the parameters A , B and C (associated with the best fit of the the law (3) to the numerical RT data) versus ρ_0 . (right) The kick velocity surface $V_k(\eta, \rho_0)$ in the parameter space of the initial data.

Acknowledgments

The authors acknowledge the partial support of CNPq/MCTI-Brazil and CAPES-Brazil.

References

1. R.F. Aranha, I. Damião Soares and E.V. Tonini, *Eur. Phys. J. C* **74**, 3097 (2014).
2. I. Robinson and A. Trautman, *Proc. R. Soc. Lond. A* **265**, 463 (1962).
3. R.F. Aranha, I. Damião Soares and E.V. Tonini, *Phys. Rev. D* **81**, 104005 (2010).
4. H. Bondi, M. G. J. van der Berg and A. W. K. Metzner, *Proc. R. Soc. Lond. A* **269**, 21 (1962); R. K. Sachs *Proc. R. Soc. Lond. A* **270**, 103 (1962).
5. R.F. Aranha, I. Damião Soares and E.V. Tonini, *Class. Quantum Grav.* **30**, 025014 (2013).

MULTIMESSENGERS FROM 3D CORE-COLLAPSE SUPERNOVAE

K. N. YAKUNIN^{ab}, P. MARRONETTI^c, A. MEZZACAPPA^{ab}, O. E. B. MESSER^{ade}, E. LENTZ^{abe},
S. BRUENN^f, W. RAPHAEL HIX^{ac}, J. A. HARRIS^a

^a*Department of Physics and Astronomy, University of Tennessee, Knoxville, TN 37996 USA*

^b*Joint Institute for Computational Sciences, ORNL, Oak Ridge, TN 37831 USA*

^c*Physics Division, National Science Foundation, Arlington, VA 22230 USA*

^d*National Center for Computational Sciences, ORNL, Oak Ridge, TN 37831 USA*

^e*Physics Division, ORNL, Oak Ridge, TN 37831, USA*

^f*Department of Physics, Florida Atlantic University, Boca Raton, FL 33431, USA*

We present gravitational wave and neutrino signatures obtained in our *ab initio* 3D core-collapse supernova simulation of a $15 M_{\odot}$ non-rotating progenitor with the CHIMERA code. Observations of neutrinos emitted by the forming neutron star and the gravitational waves produced by hydrodynamic instabilities are the most promising channel of direct information about the supernova engine. Both signals show different phases of the supernova evolution.

The era of multimessenger astronomy is about to begin as an advanced generation of gravitational wave detectors will come on-line this year. Core-Collapse Supernovae (CCSN) are among the most promising sources for multi-messenger astronomy due to strong electromagnetic and neutrino signals, as well as powerful gravitational wave (GW) bursts. Multimessenger observations could help resolve a number of open questions concerning the physics of CCSN such as: 1) What collapse mechanisms can we confirm or reject? 2) Can GW detectors provide an early warning to EM observers? 3) What happens in CCSN before light and neutrinos break free?

In order to address these questions, we study the GW emission in a 3D model performed with the neutrino-hydrodynamics code CHIMERA¹, which is composed of five major modules: hydrodynamics, neutrino transport, self-gravity, a nuclear equation of state, and a nuclear reaction network. We evolve a non-rotating model corresponding to a zero-age main sequence progenitor of $15 M_{\odot}$ ², on an adaptive spherical-polar mesh with resolution $512(r) \times 180(\theta) \times 180(\phi)$. This model was simulated using the Lattimer–Swesty equation of state (EoS) with $K = 220$ MeV for $\rho > 10^{11} \text{g cm}^{-3}$, and an enhanced version of the Cooperstein EoS for $\rho < 10^{11} \text{g cm}^{-3}$. The simulation exhibits shock revival and the development of neutrino-driven explosions, a unique feature for first-principle simulations from progenitors with canonical CCSN masses (Fig. 1 left). All the main phases of supernova dynamics can be seen in the gravitational waveforms (Fig. 1 right): prompt convection, standing accretion shock instability (SASI), neutrino-driven convection, and formation of accretion downflows impinging on the surface of the proto-neutron star. The frequency of the gravitational wave signals tends to increase during the first 500 ms of post-bounce evolution.

Low-energy neutrinos (LENs) will be an important multi-messenger partner to GWs from CCSN. A CCSN produces 10–160 MeV neutrinos (all flavors) over a few tens of seconds. The estimation of antineutrino rate detection in IceCube³ presented in Fig. 2 was done using Eq. (1) of Lund *et al.*⁴.

The SASI, with characteristic frequencies of 50–100 Hz, strongly imprints the neutrino signals observable by large Cherenkov detectors for Galactic CCSN. If neutrino-driven convection dominates, the pre-explosion time variations of the neutrino flux are expected to exhibit smaller

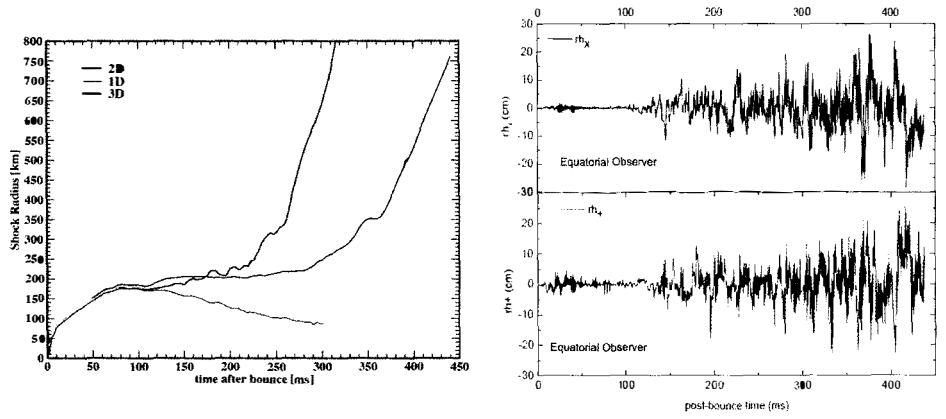


Figure 1 – Evolution of the shock trajectory from our 1D model and the angle-averaged shock trajectories from our 2D and 3D models, all for the same $15M_{\odot}$ progenitor (left). Gravitational wave polarizations rh_+ and rh_x as a function of post-bounce time seen by an observer on the equator (right).

amplitude and higher frequency variations. Hence, the neutrino signal of the next Galactic CCSN may observationally constrain the contribution of neutrino-driven convection and SASI⁵.

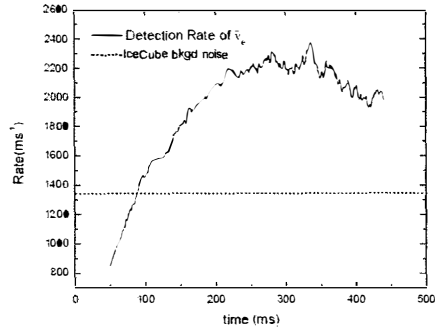


Figure 2 – Detection rate of $\bar{\nu}_e$ in IceCube for Galactic CCSN.

Acknowledgments

This research was supported by the U.S. Department of Energy Offices of Nuclear Physics and Advanced Scientific Computing Research and the NASA Astrophysics Theory and Fundamental Physics Program (NNH11AQ72I). PM is supported by the National Science Foundation through its employee IR/D program. The opinions and conclusions expressed herein are those of the authors and do not represent the National Science Foundation.

References

1. S. W. Bruenn *et al.*, ArXiv1409.5779 (2014)
2. S. E. Woosley and A. Heger, *Physics Reports* **442**, 269 (2007)
3. <https://icecube.wisc.edu/>
4. T. Lund *et al.* *Phys. Rev. D* **86**, 105031 (2012)
5. C. D. Ott *et al.*, *Proceedings of the Neutrino 2012 Conference*, (2012)

STUDY OF A NEW GENERATION SPATIO-TEMPORAL REFERENCE SYSTEM BASED ON INTER-SATELLITE LINKS

E. RICHARD, P. DELVA AND P. WOLF

SYRTE, Observatoire de Paris, PSL Research University, CNRS, Sorbonne Universités, UPMC Univ. Paris 06, LNE, 61 avenue de l'Observatoire, 75014 Paris, France

The main aim of this study is to compare the quantitative error budgets of the Galileo classical system and of a Galileo system augmented by inter-satellite links. We will determine if this new technology could improve the actual system for high precision positioning, and for different users : stationary or moving on Earth, LEO satellite and planes. For this purpose, we simulate pseudo-range observables which are analyzed in both configurations, with and without inter-satellite links, in order to compare the merits of each system.

1 Introduction

The Galileo system will reach its full capability around 2020. Then the first launched satellites will be replaced with a second generation of Galileo satellites, for which the design has already begun. When thinking about the next generation of Galileo, we have to consider the present limits of standard GNSS, such as tropospheric delay, poor observation geometry and issues coming from tracking stations. Those three limits could be partly overcome by adding links between satellites. Several studies have shown the interest of such links and their feasibility^{1,2,3,4}. They improve the geometry knowledge: the amount of data from the relative positioning of one satellite to another will result in a better knowledge of the constellation position and dynamics. Moreover, the need for ground stations is reduced. The reliability, integrity and robustness of the constellation message are improved^{5,6} and near real time ephemeris and clock determination can be performed^{7,8}. Inter-satellite links (ISLs) allow to directly synchronize the satellite clocks in space, and determine orbits using ISLs pseudo-ranges.

Our on-going study will show, at the end, if adding ISLs in a GNSS constellation is a real improvement for high precision space-time positioning. In these proceedings we present the methodology of the ongoing work and we briefly detail the software needed to answer our problematic.

2 Methodology

We compare a *classical* GNSS configuration which contains only Satellite to Ground (SG) observables, and configurations augmented by ISLs, which can contain both Satellite to Satellite (SS) and SG observables (*hybrid* configuration), or just SS observables (*autonomous* configuration). A way to implement the SS observables into the constellations has been designed by ESA studies^{4,5}. Our aim is to establish a quantitative error budget taking into account leading sources of errors (coming from both instruments and used models), in order to do a differential study between the three configurations. Note that, contrary to other studies, here we aim primarily at a determination of the relative merit of the two configurations (with and without ISLs) and not at the determination of the performance of one individual configuration. As a result inaccuracies in

the introduced models for the error sources are not critical as they will be largely common mode between the two systems and thus will only play a minor role. Therefore, in our application, it is sufficient to capture the leading error terms.

3 Software

In order to do this comparison, we are writing a software made of two distinct parts : the simulation calculates the pseudo-range observables, while the analysis takes as input the simulated observables with the aim of getting back the simulation initial parameters. The resulting difference will help to build a quantitative error budget, depending on the different error sources introduced in the system, and will permit to compare the merits of the different configurations.

The simulation computes the SG and SS pseudo-ranges. It is written in FORTRAN 90 and takes as input station and satellite initial coordinates. Trajectories of stations and satellites are calculated in the Geocentric Celestial Reference System (GCRS). The pseudo-ranges are calculated by solving numerically the time transfer problem. For the moment we assume a ionospheric-free signal and the tropospheric delay is computed by using the Saastamoinen model⁹. Satellite and station clocks include realistic phase bias, drift coefficient and drift rate coefficient, as well as random noise (white and flicker frequency noise)

The analysis software takes as input the simulated pseudo-ranges. It uses a non linear adjustment procedure in order to recover the initial parameters of the simulation. In order to ensure robustness of the whole process, the analysis is written in a different language (MATLAB) from the simulation. We are currently implementing potential error sources affecting the satellite to ground observables in order to compare the merits of the different system configurations. In particular we study the effect of a mismodelling of the tropospheric delay.

4 Conclusion

The implementation of Inter-Satellite Links is a strongly considered option for the next generation of Galileo satellites. In addition of a high scientific interest, we expect an improvement of the space-time positioning. Our study will give a quantitative comparison between different configurations of the system, giving clear conclusions on the interest of implementing ISLs in GNSS constellations.

References

1. L. Arona, J.A. Pulido, F. Soualle, A.J. Fernández, and M. Sánchez-Nogales. GNSSPLUS, Final Report. GNSSPLUS-DMS-TEC-FIR01-11-E-R. Technical report, DEIMOS Space S.L., 2006.
2. F. Amarillo Fernández. Inter-satellite ranging and inter-satellite communication links for enhancing GNSS satellite broadcast navigation data. *Adv. Space Res.*, 47:786–801, 2011.
3. R. Wolf. Onboard Autonomous Integrity Monitoring using Intersatellite Links. 2000.
4. F. Amarillo Fernández, J. L. Gerner, and J. Dow. ESA ADVISE Project. New Developments on Inter-Satellite Ranging for Orbit and Clock Determination.
5. I. Rodríguez-Pérez, C. García-Serrano, C. Catalán Catalán, A. M. García, P. Tavella, L. Galleani, and F. Amarillo. Inter-satellite links for satellite autonomous integrity monitoring. *Advances in Space Research*, 47:197–212, 2011.
6. X. Zhao, S. Liu, and C. Han. Performance analysis of autonomous navigation of constellation based on inter satellite range measurement. *Procedia Engineering*, 15:4094–4098, 2011.
7. H. Xu, J. Wang, and X. Zhan. Autonomous broadcast ephemeris improvement for GNSS using inter-satellite ranging measurements. *Advances in Space Research*, 49:1034–1044, 2012.
8. Li Hai-sheng, Wang Hai-hong, and Xu Bo NOM. An efficient algorithm for autonomous orbit determination of navigation constellation based on cross-link range. 2009.
9. J. Saastamoinen. Atmospheric Correction for Troposphere and Stratosphere in Radio Ranging of Satellites. In S. W. Henriksen, A. Mancini, and B. H. Chovitz, editors, *The Use of Artificial Satellites for Geodesy*, volume 15 of *Washington DC American Geophysical Union Geophysical Monograph Series*, page 247, 1972.

STRONG-FIELD TESTS OF $f(R)$ -GRAVITY IN BINARY PULSARS

P.I. DYADINA, S.O. ALEXEYEV, K.A. RANNU

*Sternberg Astronomical Institute, Lomonosov Moscow State University, Universitetsky Prospekt, 13,
Moscow 119991, Russia*

In this work we develop the PPK approach for a class of analytic $f(R)$ -models of gravity. We use data from the double binary pulsar system PSR J0737-3039. We obtain restrictions on parameters of this class of $f(R)$ -models and show that $f(R)$ -gravity is not ruled out by the observations in strong field regime.

1 Introduction

General relativity (GR) is a very beautiful theory which allows to go beyond the Newtonian picture of the world and explains many unaccounted phenomena. However our understanding of fundamental laws still has several shortcomings. The accelerated expansion of the Universe (i.e., dark energy) has been found from cosmological observations recently¹. Moreover already in 1930s the problem of galactic rotation curves arose². One way to unriddle these puzzles is to add yet unknown particles and look for them on LHC³ and in cosmic rays. Another way is to expand GR by including additional corrections in terms of the Ricci scalar in the Lagrangian. This method underlies $f(R)$ -gravity^{4,5}.

2 $f(R)$ -gravity

$f(R)$ -gravity is actually a family of theories, each of them is defined by a different function of the Ricci scalar. In the simplest case the function equals to the scalar; that is GR. We can explain dark matter, dark energy and inflation⁴ by different models of $f(R)$ -gravity. The action of $f(R)$ -gravity has the following form^{6,7}:

$$S = \int d^4x \sqrt{-g} [f(R) + \kappa L_m], \quad (1)$$

where $\kappa = 16\pi G/c^4$ is the coupling coefficient, g is the determinant of the metric tensor, L_m is the standard matter Lagrangian, $f(R)$ is an analytical function of the general form. This function can be expanded in a series in terms of the Ricci scalar⁶:

$$f(R) = \sum_n \frac{f^n(R_0)}{n!} (R - R_0)^n \simeq f_0 + f'_0 R + \frac{1}{2} f''_0 R^2 + \dots, \quad (2)$$

where

$$f_0 = \text{const}, \quad f'_0 = \left. \frac{df(R)}{dR} \right|_{R=R_0}, \quad f''_0 = \left. \frac{d^2f(R)}{dR^2} \right|_{R=R_0}. \quad (3)$$

Table 1: Post-Newtonian parameters

| PPN parameter | Physical meaning | Experimental value |
|---------------|---|----------------------------|
| γ | space-curvature produced by unit restmass | $1 \pm 2.3 \times 10^{-5}$ |
| β | nonlinearity in the superposition law for gravity | $1 \pm 8 \times 10^{-5}$ |

The flat Minkowskian background is recovered for $R = R_0 \simeq 0$. GR is recovered in the limit $f_0 = 0$, $f'_0 = 4/3$, $f''_0 = 0$ ⁷. Hereafter we assume $f_0 = 0$, $f'_0 = 4/3$ whereas f''_0 is a free parameter. Our purpose is to restrict the possible value of this free parameter f''_0 .

However any theory of gravity should be verifiable. Naturally, there are many other ways for testing theories of gravity but in this work we applied only PPN and PPK formalisms to $f(R)$ -gravity.

3 Parametrized post-Newtonian formalism

Parametrized post-Newtonian formalism was originally developed to compare various metric theories with each other and GR^{8,9}. The post-Newtonian limit (PPN) is established in the framework of the asymptotically flat space-time background and small velocities. Motion of matter should obey the hydrodynamics equations for the perfect fluid. Distinctions between GR and other theories of gravity are reflected via the set of 10 post-Newtonian parameters. Each parameter is responsible for its effect. However, the considered $f(R)$ gravity model is the conservative theory and, in this case, only two parameters (γ , β) are not equal to zero (see table 1)¹⁰.

Drawing an analogy between the scalar-tensor gravity and the higher order theories of gravity, Capozziello and Troisi⁶ developed the PPN formalism for $f(R)$ -gravity. The similarity between the non-minimally coupled scalar models (Lagrangian of Brans-Dicke type^{11,12}) and the models of gravity with higher order curvature corrections have been discussed since 1983¹³. Basing on this similarity Capozziello and Troisi⁶ obtained the Eddington's parameters for $f(R)$ -gravity in analytical form:

$$\gamma_R^{PPN} - 1 = - \frac{f''(R)^2}{f'(R) + 2f''(R)^2}, \quad \beta_R^{PPN} - 1 = \frac{1}{4} \frac{f'(R)f''(R)}{2f'(R)^2 + 3f''(R)^2} \frac{d\gamma_R^{PPN}}{d\phi}, \quad (4)$$

where $f(R)$ is an arbitrary function of R . Using the expansion (2), we carried out the Eddington's parameters for the considered model of $f(R)$ -gravity:

$$\gamma_R^{PPN} - 1 = - \frac{(f''_0)^2}{f'_0 + 2(f''_0)^2}, \quad \beta_R^{PPN} - 1 = \frac{1}{4} \frac{f'_0(f''_0)^3}{2(f'_0)^3 + 20f'_0(f''_0)^4 + 11(f''_0)^2(f''_0)^2 + 6(f''_0)^4}. \quad (5)$$

Using the fact that $f(R)$ -gravity recovers GR at $f'_0 = 4/3$ ⁷ and the observational values of parameters γ^{PPN} and β^{PPN} ¹⁰ (see. table 1), we can impose restrictions on the value of f''_0 by solving the system of equations (5):

$$\gamma^{PPN} : \quad -0.0055 \leq f''_0 \leq 0, \quad \beta^{PPN} : \quad -7 \leq f''_0 \leq 0, \quad (6)$$

4 Parametrized post-Keplerian formalism

Parametrized post-Keplerian formalism (PPK) was created to link the arrival time of the pulses and their time of radiation in the frame of a pulsar^{14,15}. PPK is a strong-field analogue of

Table 2: Parameters of PSR 0737-3039

| Parameters PSR J0737-3039 | | |
|---|--|------------------------------|
| Parameter | Physical meaning | Experimental value |
| $P_b(\text{day})$ | orbital period | 0.10225156248(5) |
| e | eccentricity | 0.0877775(9) |
| $x(s)$ | projected semimajor axis of the pulsar orbit | 1.415032(1) |
| $\dot{\omega}(\text{deg/yr})$ | secular advance of the periastron | 16.89947(68) |
| $\tilde{\gamma}(ms)$ | time dilation parameter | 0.3856(26) |
| \dot{P}_b | secular change of the orbital period | $-1.252(17) \times 10^{-12}$ |
| s | Shapiro delay parameter | 0.99974(-39, +16) |
| $r(\mu s)$ | Shapiro delay parameter | 6.21(33) |
| $R = \frac{m_1}{m_2} = \frac{x_2}{x_1}$ | mass ratio | 1.0714(11) |

the PPN formalism. It includes such effects as the Einstein time delay, Römer time delay, Shapiro time delay and the effects of aberration. The general form of these corrections is model-independent, therefore all possible manifestations of the extended gravity model can be expressed through the 8 post-Keplerian parameters $\dot{\omega}$, γ , \dot{P}_b , r , s , δ_θ , \dot{e} , \dot{x} . However, in this work we considered only those parameters that have the most accurate measurements, so we didn't take into account the last three of them.

It should be noted that different theories of gravity can give different predictions for PPK parameters. We should compare predictions of the theory and the values of these parameters obtained from observations. Thus we have powerful instrument for testing extended gravity models in the strong field limit^{9,16}.

The analytical form of the first derivative of the orbital period for considered model of f(R) gravity was obtained by De Laurentis and Capozziello⁷. And other PPK parameters were obtained for the first time in our work for this model of f(R) gravity.

$$\begin{aligned}
\dot{\omega} &= \left(\frac{2\pi}{P_b}\right)^{5/3} \frac{G^{2/3} M_\odot^{2/3} (m_1 + m_2)^{2/3}}{c^2(1 - e^2)} \times \left(\frac{2(f'_0) + 4(f''_0)^2}{2(f'_0) + 3(f''_0)^2}\right)^{2/3} \times \\
&\times \left(\frac{24(f'_0)^3 + 130(f'_0)^2(f''_0)^2 - (f'_0)(f''_0)^3 + 232(f'_0)(f''_0)^4 + 136(f''_0)^6}{8(f'_0)^3 + 48(f'_0)^2(f''_0)^2 + 96(f'_0)(f''_0)^4 + 64(f''_0)^6}\right), \\
\gamma &= e \left(\frac{2\pi}{P_b}\right)^{-1/3} \frac{G^{2/3} M_\odot^{2/3} m_2}{c^2(m_1 + m_2)^{4/3}} \times \left(m_1 + m_2 \left[2 + \frac{(f''_0)^2}{2f'_0 + 3(f''_0)^2}\right]\right) \times \left(1 + \frac{(f''_0)^2}{2f'_0 + 3(f''_0)^2}\right)^{2/3}, \\
r &= \frac{1}{4c^3} GM_\odot m_2, \\
s &= \left(\frac{2\pi}{P_b}\right)^{-2/3} \frac{cx(m_1 + m_2)^{2/3}}{(GM_\odot)^{1/3} m_2} \left(1 + \frac{(f''_0)^2}{2f'_0 + 3(f''_0)^2}\right)^{-1/3}, \\
\dot{P}_b &= -\frac{6\pi}{20} \left(\frac{2\pi}{P_b}\right)^{-5/3} \frac{(GM_\odot)^{5/3}}{c^5(1 - e^2)^{7/2}} \frac{m_1 m_2}{(m_1 + m_2)^{1/3}} \times \left((f'_0)(37e^4 + 292e^2 + 96) - \frac{f''_0 \pi^2}{2P_b(1 + e^2)^3} \times \right. \\
&\times \left. (891e^8 + 28016e^6 + 82736e^4 + 43520e^2 + 3072)\right). \tag{7}
\end{aligned}$$

These parameters depend only on the orbit eccentricity, projection of the semi-major axis of the pulsar orbit, orbital period, masses of the pulsar and its companion and also the parameter f''_0 of the f(R) gravity model. All of them, except the parameter and masses of the model,

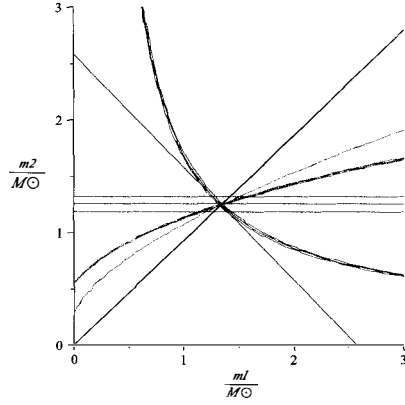


Figure 1 – Dependence of the companion mass of the pulsar mass, $f_0'' = 0$. Colors indicate: curve $\dot{\omega}(m_1, m_2)$ – blue, curve $\gamma(m_1, m_2)$ – brown, curve $\dot{P}_b(m_1, m_2)$ – red, curve $s(m_1, m_2)$ – pink, curve $r(m_1, m_2)$ – green, curve $R(m_1, m_2)$ – black.

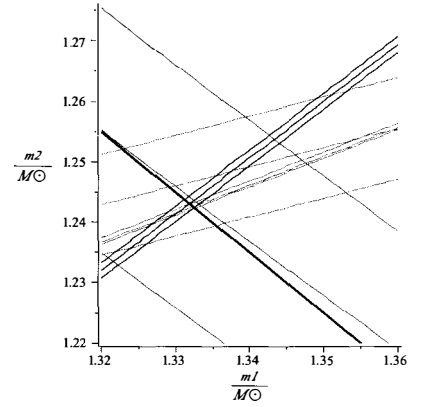


Figure 2 – Dependence of the companion mass of the pulsar mass, $f_0'' = -0.03$. Colors indicate: curve $\dot{\omega}(m_1, m_2)$ – blue, curve $\gamma(m_1, m_2)$ – brown, curve $\dot{P}_b(m_1, m_2)$ – red, curve $s(m_1, m_2)$ – pink, curve $r(m_1, m_2)$ – green, curve $R(m_1, m_2)$ – black. The graph shows that $s(m_1, m_2)$, $R(m_1, m_2)$ and $\dot{\omega}(m_1, m_2)$ shift in different directions.

can be obtained from observations. In our work we used the data for binary pulsar J0737-3039 which was presented in the article by Kramer and his colleagues¹⁷. It is the only known double binary pulsar. It is the smallest period that the known systems of this type may have. The extraordinary closeness of system components, small orbital period and also the fact that we see almost edge-on system allow to investigate the manifestation of relativistic effects with the highest precision. Also it is possible to measure semi-major axis of the orbit for each of components of the system J0737-3039 and hence their ratio is equals:

$$\frac{a_2}{a_1} = \frac{m_2}{m_1} = R, \quad (8)$$

i.e. the ratio of the masses can be measured directly!

5 Test of f(R)-gravity

And now we proceed directly to the method of testing models of gravity¹⁵. We constructed curves on the plane, where the ordinate displays the possible values of the companion masses m_2 , and the abscissa displays possible values of the masses of the pulsar m_1 . Each parameter specifies the curve. The point of intersection of all curves on this plane within the measurement accuracy will display the values of the pulsar and companion masses. However, if curves diverge within some model of gravity, it does not speak in favor of the model.

All the results are presented in the corresponding figures. For GR all the curves intersect within the measurement accuracy (see fig. 1)¹⁷. Let us to recall that GR is recovered in the limit $f_0 = 0, f_0' = 4/3, f_0'' = 0$. Then we begin to change f_0'' and we can see that at some point $f_0'' = 0.05772$ the curves start to diverge (see fig. 1, fig. 2, fig. 3). That is the limitation that we receive for this parameter from the binary pulsar data:

$$-0.05772 \leq f_0'' \leq 0. \quad (9)$$

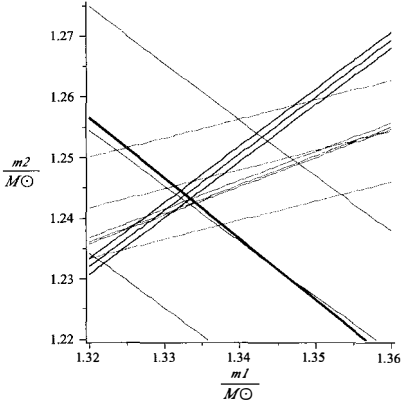


Figure 3 – Dependence of the companion mass of the pulsar mass, $f_0'' = -0.05772$. Colors indicate: curve $\dot{\omega}(m_1, m_2)$ — blue, curve $\gamma(m_1, m_2)$ — brown, curve $\dot{P}_b(m_1, m_2)$ — red, curve $s(m_1, m_2)$ — pink, curve $r(m_1, m_2)$ — green, curve $R(m_1, m_2)$ — black. The last point of intersection $s(m_1, m_2)$, $R(m_1, m_2)$ $\dot{\omega}(m_1, m_2)$ within the measurement accuracy.

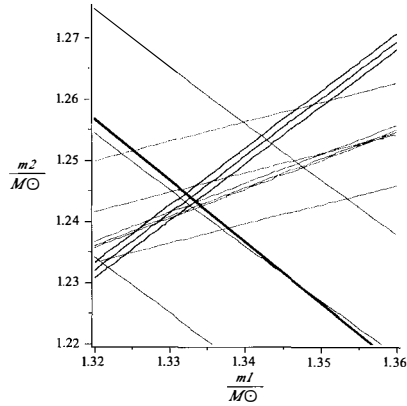


Figure 4 – Dependence of the companion mass of the pulsar mass, $f_0'' = -0.06$. Colors indicate: curve $\dot{\omega}(m_1, m_2)$ — blue, curve $\gamma(m_1, m_2)$ — brown, curve $\dot{P}_b(m_1, m_2)$ — red, curve $s(m_1, m_2)$ — pink, curve $r(m_1, m_2)$ — green, curve $R(m_1, m_2)$ — black. Curves $s(m_1, m_2)$, $R(m_1, m_2)$ $\dot{\omega}(m_1, m_2)$ diverge.

6 Conclusions

In this work we impose restrictions on the considered model of $f(R)$ -gravity from the observations in the strong and weak field limits. For our aims we used the data of double binary pulsar system and accurate measurements of the PPN parameters in the Solar System, respectively. We show that the observational data of double pulsar system give the following limit on a value of parameter f_0'' :

$$-0.05772 \leq f_0'' \leq 0. \quad (10)$$

This parameter characterizes the contribution of the quadratic curvature correction in the action of $f(R)$ -gravity. It is important to note that the obtained restriction on the possible values of f_0'' is small but at the same time it can not be considered negligible even within the measurement accuracy. This result allows the realization of GR as well as its extensions, including quadratic curvature corrections.

At the same time it is possible to receive the limitations on the value f_0'' from Eddington parameters measurements in the Solar system. The parameter γ^{PPN} gives a better limit than the parameter β^{PPN} :

$$\gamma^{PPN} : -0.0055 \leq f_0'' \leq 0, \quad \beta^{PPN} : -7 \leq f_0'' \leq 0, \quad (11)$$

Thus, more strict limitation on the model parameters follows from the experiments in the solar system than from the data of binary pulsar systems. On the one hand, it can be connected with the fact that measurement accuracy in the Solar system is much better than in the systems with the pulsar. On the other hand, in a system with a compact object gravity is much stronger ($2GM/(c^2R)_{PSR} \simeq 0.2$), than in the solar system ($2GM/(c^2R)_{SUN} \simeq 10^{-6}$), therefore, the contribution of corrections type R^2 should be more prominent.

Since $f(R)$ -gravity is one of the ways to describe dark energy and dark matter, then obtaining the experimental constraints on the parameters of such models is an important step in solving these fundamental problems.

Acknowledgments

I would like to thank the organizers for the possibility to participate in this very interesting conference!

References

1. A.G. Riess et al., *Astron. J.*, **116**, 1009 (1999),
A.G. Riess et al., *Astroph. Journ.*, **607**, 665 (2004),
S. Perlmutter et al., *Astrophys. J.*, **517**, 565 (1999),
D.N. Spergel et al., *Astrophysical Journal Supplement Seriest* **170**, 377 (2007);
2. F. Zwicky, *Helvetica Physica Acta* **6**, 110 (1933);
J.H. Oort, *Bull. Astron. Inst. Netherlands* **6**, 249 (1932);
3. J. Goodman, M. Ibe, A. Rajaraman, W. Shepherd, T. M.P. Tait, H.-B. Yu, *Phys. Rev.* **D82**, 116010 (2010),
P. J. Fox, R.i Harnik, J. Kopp, Y. Tsai *Phys. Rev.* **D85**, 056011 (2012),
V. Khachatryan et al. (CMS Collaboration), (2014), arXiv:1408.3583 [hep-ex],
V. Khachatryan et al. (CMS Collaboration), (2015), arXiv:1504.03198 [hep-ex];
4. A. A. Starobinsky *Phys. Lett* **B91**, 99 (1980);
5. S. Capozziello, R.de Ritis, *Class. Quantum Grav.* **11**, 107 (1994),
S. Capozziello, R.de Ritis, *Phys.Lett.* **A177**, 1 (1993),
S. Capozziello, R.de Ritis, C. Rubano, *Phys.Lett.* **A177**, 8 (1993),
S. Capozziello, M. Demianski, R.de Ritis, C. Rubano, *Phys. Rev* **D52** (1995);
6. S. Capozziello, A. Troisi, *Phys. Rev.* **D72**, 044022 (2005),
S. Capozziello, A. Stabile, A. Troisi, *Mod.Phys.Lett.* **A21**, 2291 (2006),
S. Capozziello, A. Stabile, A. Troisi, *Phys.Rev.* **D76**, 104019 (2007),
S. Capozziello, A. Stabile, A. Troisi, *Class.Quant.Grav.* **25**, 085004 (2008),
S. Capozziello, A. Stabile, A. Troisi, *Mod.Phys.Lett* **A24**, 659 (2009),
S. Capozziello, A. Stabile, A. Troisi, *Int. Jour. of Theor. Phys* **49**, 1251 (2010);
7. M. De Laurentis , S. Capozziello , *Astrop. Phys.* **35**, 257 (2011),
M. De Laurentis , I. de Martino *MNRAS* **741D**, 431 (2013),
M. De Laurentis , I. de Martino *International Journal of Geometric Methods in Modern Physics* [http:// arXiv.org/pdf/1310.0711.pdf](http://arXiv.org/pdf/1310.0711.pdf);
8. A.S. Eddington, *The Mathematical Theory of Relativity Cambridge University Press, London, (1922)*,
K. Nordtvedt, *Phys. Rev.* **169**, 1017 (1968),
C.M. Will, *Astrophys. J.* **163**, 611 (1971),
C.M. Will and K. Nordtvedt, *Astrophys. J.* **177**, 757 (1972);
9. C.M. Will, *Theory and Experiment in Gravitational Physics, Cambridge University Press, (1981)*,
C.M. Will, *Living Rev. Relativity* **17**, 4 (2014);
10. S. G. Turyshev, *Ann. Rev. Nucl. Part. Sci* **58**, 207 (2008);
11. C. Brans, H. Dicke , *Phys. Rev.* **124**, 925 (1961);
12. D.A.Tretyakova, A.A.Shatskiy, I.D.Novikov, S.O.Alexeyev, *Phys. Rev.* **D85**, 124059 (2012);
13. Teyssandier P., Tourranc P., *J. Math. Phys.* **24**, 2793 (1983);
14. T. Damour, N. Deruelle, *Ann. Inst. Henri Poincare* **A43**, 107 (1985),
T. Damour, N. Deruelle, *Ann. Inst. Henri Poincare* **A44**, 263 (1986);
15. T. Damour, J.H. Taylor, *Phys.Rev.* **D45**, 1840 (1992);
16. D.M. Eardley, *Astrophys. J. Lett.* **196**, L59 (1975);
17. M. Burgay, et al, *Nature* **426**, 531 (2003),
M. Kramer, et al., *Science* **341**, 97 (2006).

INFLATIONARY AND LATE UNIVERSE TESTS FOR $\Lambda(H)$ COSMOLOGIES

E.L.D. PERICO and J.A.S. LIMA
Universidade de São Paulo - Instituto de Física
São Paulo, SP, Brazil

The aim of this work is to analyze a model with a dark energy density that grows with the Hubble parameter, generating not only the current acceleration, but also it dominating the universe during the inflationary period. In the context of an FRW flat universe the model has two new free parameters, n and ν , which characterize separately the two accelerated stages. Regarding the inflationary period, we are interested in to estimate the power spectrum of scalar perturbations as a function of the first free parameter of the model. Already during the recent universe we restrict the second free parameter using observational data of supernovae, BAO/CMB, $H(z)$ and linear growth function of scalar perturbations.

1 Introduction

One of the major strands on modern theoretical cosmology is to find a physical component capable of generating the acceleration of the universe, currently observed^{1,2}. Assuming the validity of general relativity, the observed acceleration can be only generated by introducing an energetic component with negative pressure and whose fraction is of the order of 70% of the critical density, it is known as dark energy. The simplest way of model the dark energy, and further fits very well to observable cosmological results, is considered as a constant energy density with negative pressure equal to its density, known as the cosmological constant. The present work aims to study the compatibility of phenomenological models with a greater freedom for the dark energy. Specifically we assume that its pressure is equal to the negative of its density, $p_\Lambda = -\rho_\Lambda$, but allowing its variation throughout cosmic history $\rho_\Lambda = \rho_\Lambda(t)$.

2 The Model to be Tested

The model we are testing in this work parametrize the dark energy evolution as a function of the Hubble parameter H as follows³:

$$\Lambda = \Lambda_c + 3\nu H^2 + 3\lambda H^{2+n}, \quad (1)$$

where $\lambda^{-1/2}$ sets the Hubble scale during inflation. Any power $n > 0$ causes the universe to be dominated by dark energy when the energy density is very high, generating the inflationary stage. On the other hand, the constant term allows the universe to become again dominated by the dark energy density for a low energy universe, generating the current acceleration. Regardless of the values of the parameters $n > 0$ and $\Lambda_c > 0$, the universe has a natural exit of the accelerated initial period, with a sharp increase in the relativistic fluid density (r), which leads it to dominate the evolution of a hot universe after inflation. The background solutions for both early and late universe can be seen in³.

Solving the perturbed Einstein equations for sub-horizon scales we can estimate the ζ gauge invariant when a given Fourier mode k cross the horizon during inflation. Since ζ is constant outside the horizon (over the approximation of adiabatic evolution and vanish the anisotropic stress⁴), we can express the matter over-density δ_m in terms of ζ when the scale k enters in the horizon during the radiation dominated era as shown:

$$\frac{3}{2}\phi \xrightarrow[\text{inflation}]{k=aH} \zeta \xrightarrow[\zeta=0]{k \gg aH} \zeta \xrightarrow[\text{radiation era}]{k=aH} -\frac{2\pi G a^2 \rho_\gamma}{k^2} \delta_m \xrightarrow[\rho_r \gg \rho_m]{} -\frac{3}{4} \delta_m. \quad (2)$$

allowing us estimate the matter power spectrum around the pivot scale⁵ in order to constrain the parameter n . ϕ is the gravitational potential, ρ_r and ρ_m are the background densities of radiation and matter, a is the scale factor of the FRW metric, and the over-dot means time derivative.

In order to find the values of the free parameters of the model during the late universe, in this case ν , and test its feasibility, we use a set of recent observations: (i) the Hubble parameter data as a function of z reported by⁶, (ii) the growth function of the linear perturbations, using the same data that used by⁷, (iii) the magnitudes of supernovae compilation Union2.1⁸, and (iv) the quantity:

$$f_z \equiv \frac{d_A(z_*)}{D_V(z)}, \quad \text{where} \quad D_V(z) \equiv \left[\frac{z d_A^2(z)}{H(z)} \right]^{1/3}, \quad (3)$$

z_* is the redshift at recombination, d_A is the comoving angular diameter distance, and $D_V(z_{BAO})$ is the scale of dilation of the Baryon Acoustic Oscillations. The observational value of f_z used in this work was reported by⁹.

3 Results

It is possible, making a fine-tuning on the parameter $n \approx 2 \times 10^{-2}$, drawn a primordial spectrum (scalar index around the pivot scale) that is compatible with the observed values⁵. For this it was assumed that the perturbations of radiation dominate over any perturbation of dark energy, even when the density of the radiation is sub-dominant during inflation. Regarding the fit of the model to the observations in the low redshift universe, we find that the free parameter ν is of the order of $\nu = 0.03 \pm 0.01$, $\Omega_m = 0.285 \pm 0.022$, $h = 0.692 \pm 0.018$ and $\sigma_8 = 0.873 \pm 0.045$ for 68% of CL.

Acknowledgments

ELDP and JASL acknowledge CNPq (Brazilian Research Foundation) for partial support.

References

1. Riess, A. G. et al., *Astron. J.* **116** (1998) 1009.
2. Amanullah, R. et al., *Astrophys. J.* **716** (2010) 712.
3. Perico, E. L. D., Lima, J. A. S., Basilakos, S., & Solà, J., *Phys. Rev. D* **88** (2013) 1.
4. Mukhanov, V. F., Feldman, H. A., & Brandenberger, F. H., *Phys. Rept.* **215** (1992) 203.
5. Planck Collaboration, *A & A* (2013).
6. Farooq, O. and Ratra, B., *Astrophys. J.* **766** (2013).
7. Ramos, R. O., Santos, M. V., & Waga, I., *Phys. Rev. D* **89** (2014) 1.
8. Suzuki, N. et al., *Astrophys. J.* **746** (2012) 24pp.
9. <http://lambda.gsfc.nasa.gov/product/map/current/parameters.cfm>.

ENSEMBLE OF GALACTIC ROTATING NEUTRON STARS AS A SOURCE OF GRAVITATIONAL BACKGROUND FOR ADVANCED VIRGO, ADVANCED LIGO AND EINSTEIN TELESCOPE DETECTORS

M. KUCABA¹, D. GONDEK-ROSIŃSKA¹, T. BULIK², M. CIEŚLAR²

¹*Institute of Astronomy, University of Zielona Góra, ul. Szafrana 2, 65-516 Zielona Góra, Poland*

²*Astronomical Observatory, University of Warsaw, Al Ujazdowskie 4, 00-478 Warsaw, Poland*

A spinning neutron star is a source of continuous gravitational waves, if its mass distribution is non-axisymmetric. Such asymmetry can be caused by various instabilities and deformations (e.g. Andersson, 2003, Gondek-Rosińska et al. 2003). We have performed calculations of the gravitational waves background produced by the ensemble of rotating neutron stars in the Milky Way. In our calculations we use a model of population of neutron stars which takes into account the distribution of birth places, kicks, and evolution of pulsars. We analyze the spatial shape and the spectrum of such background. We find that the signal is detectable above 20 Hz with a one year Einstein Telescope observations and above 40 Hz with a one year Advanced VIRGO/LIGO observations if the mean asymmetry is as high as 10^{-6} .

1 Introduction and assumptions

It is estimated that 10^8 neutron stars (NSs) exist in the Galaxy. They are considered to be likely sources for 2nd generation interferometer gravitational waves (GWs) detectors: Advanced LIGO and Advanced Virgo and 3rd generation underground detector – Einstein Telescope (ET). Advanced detectors are designed to improve the sensitivity of initial Virgo/LIGO by more than a factor of 10 boosting the rate of observable events by a factor of 1000. They will start collecting data at limited sensitivity in 2015 and 2016 respectively. They should reach design sensitivity in 2019. Einstein Telescope would have the limiting sensitivity better than one order of magnitude than advanced detectors. It will enable to observe $\sim 10^6$ more events per year than first generation detectors. ET has passed the design readiness phase. Currently work on ET concentrates on developing the right technologies for the observatory as well as some site characterization work.

The simplified model of GWs signal from population of NSs in the Galaxy was studied by Giazotto, Bonazzola and Gourgoulhon (1997). Regimbau and de Freitas Pacheco (2000) estimated the probability of the detection of GWs from galactic radio pulsars by the 1st generation Virgo detector. In this contribution we report a study of the GW signal from a population of NSs using a realistic model of their distribution in the Galaxy (Cieślár, Bulik and Osłowski, 2015).

In this work the assumptions for the population of NSs are as follows: a neutron star is born every 100 yrs, the initial positions of NSs follows the shape of the spiral arms of the Galaxy and the evolution of the positions of the objects is calculated taking into account the initial velocities and propagation in the gravitational potential of the Galaxy (Cieślár, Bulik and Osłowski, 2015, Faucher-Giguère and Kaspi, 2006). The gravitational potential includes a halo, a disc and bulge components. We neglect objects further than 30 kpc from the center of the Galaxy. With these

assumptions we obtain a population of about 6.5 million objects with age below 1 Gyr. It is less than the estimated number of NSs but sufficient for reasonable results. We set the position of the Earth at 8.5 kpc from the Galactic center.

For each neutron star we assume: the initial spin period $1/f_{\text{rot}} = P_0 = 0.01$ s, the initial magnetic field $B = 10^{12.5}$ G, the breaking index $n = 3$, the moment of inertia $I = 10^{45}$ g/cm², the distortion level $\frac{I_3 - I_1}{I_1} = \epsilon = 10^{-6}$ (we do not specify any mechanism causing it, but only that it occurs). The angle between the distortion axis and the rotation axis is in the range $\alpha = \langle 0^\circ - 90^\circ \rangle$, and so is the inclination of the rotation axis on the sky $i = \langle 0^\circ - 90^\circ \rangle$.

2 Calculations and results

Given the population and properties for each neutron star, we performed calculation of the signal. In the calculations we used the location of the Virgo detector near Pisa. First we determined the characteristic amplitude of the signal $h_0 = \frac{16\pi^2 G}{c^4} \frac{I\epsilon}{P^2 r}$ for each neutron star, where P, r, G, c are a spin of a neutron star, the distance to NS, gravitational constants and speed of light respectively. Each neutron star emits at two frequencies f_{rot} and $2f_{\text{rot}}$. We took into account rotation of the Earth and change of the relative position of each object and the detector as a function of time.

Given h_0, α and the inclination for each object we calculated the signal from each neutron star depending on these values and on the relative position of the object and the detector and on rotational phase at a given moment (for more details see Bonazzola & Gourgoulhon, 1996). Such signals are not coherent so we take sum of square of these signals from each NS to obtain the total signal for the entire population.

We analyzed the results by dividing them into sub-populations coming from NSs at different distance intervals and gravitational waves frequency bins. This procedure allowed us to determine the contribution of each component on the total signal.

We find that close and most rapidly rotating NSs would dominate the total signal. The signal profile is robust for sub-populations with at least a hundred of objects. For sub-populations with low number of NSs the signal may change significantly depending on a particular model. The signal will be detectable at frequencies above 20Hz for one year of the Einstein Telescope observations, while for Advanced detectors above 40Hz assuming that the mean deformation is at least 10^{-6} . For more details see the forthcoming paper (Kucaba, Gondek-Rosińska, Bulik, Cieřlar, 2015).

Acknowledgments

This work was partially supported by UMO-2013/01/ASPERA/ST9/00001, by POMOST/2012-6/11 Program of Foundation for Polish Science co-financed by the European Union within the European Regional Development Fund and by Polish Science Foundation "Master2013" Subsidy. Calculations were performed on PIRXGW computer cluster funded by Foundation for Polish Science within FOCUS program.

References

1. N. Andersson, *Classical and Quantum Gravity* **20**, R105 (2003)
2. S. Bonazzola, E. Gourgoulhon, *A&A* **312**, 675 (1996)
3. M. Cieřlar, T. Bulik, S. Osłowski *in preparation*, (2015)
4. C-A. Faucher-Giguère, V. M. Kaspi, *ApJ* **643**, 332 (2006)
5. A. Giazotto, S. Bonazzola, E. Gourgoulhon, *Phys. Rev. D* **55**, 2014 (1997)
6. D. Gondek-Rosińska, E. Gourgoulhon, P. Haensel, *A&A* **412**, 777 (2003)
7. M. Kucaba, D Gondek-Rosińska, T. Bulik, M. Cieřlar *in preparation*, (2015)
8. T. Regimbau, J. A. de Freitas Pacheco, *A&A* **359**, 242 (2000)

PURE FIELD PHYSICS OF CONTINUOUS CHARGES WITHOUT SINGULARITIES

I.E. BULYZHENKOV

*Moscow Institute of Physics and Technology, 9 Institutskiy Bystreet,
Dolgoprudny, Moscow Region, 141700, Russia*

“A coherent field theory requires that all elements be continuous And from this requirement arises the fact that the material particle has no place as a basic concept in a field theory. Thus, even apart from the fact that it does not include gravitation, Maxwell’s theory cannot be considered as a complete theory” - A. Einstein.

Einstein’s metric theory of gravitational fields is to be redesigned in a self-contained form in order to avoid the conceptual shortage of the Newton attraction of spatially separated point masses. While Newton employed the formal model of point masses in empty space, material sources in the Einstein Equation are tensor energy densities but not scalar mass invariants. The energy density of source is more suitable for a continuous distribution of the extended elementary mass rather than for a point mass singularity. In other words, Newtonian empty-space references cannot be accepted in principle (or by default) by Einstein’s metric gravitation of overlapping mass-energy distributions associated with extended particles or sources.

It is essential to employ metric references in General Relativity (GR) not on the basis of the Newton empty space theory with degenerated (point) particle, but on a self-contained basis like the Special Relativity (SR) limit for GR energy of a probe body. In favor of such coherent self-references, Einstein’s metric formalism¹ uniquely relates the fourth component,

$$P_o \equiv mcg_{o\mu} \frac{dx^\mu}{ds} \equiv mc(g_{oo}V^o + g_{oi}V^i) \equiv \frac{mc\sqrt{g_{oo}}}{\sqrt{1-v^2c^{-2}}} \equiv \frac{(K+U)}{c}, \quad (1)$$

of the covariant four-momentum $P_\mu \equiv mcg_{\mu\nu}dx^\nu/ds$ of the probe scalar mass m to its full relativistic energy $E = K + U$ containing positive kinetic energy $K = mc^2/\sqrt{1-v^2c^{-2}}$ and negative potential energy U in gravitational fields. One can use the GR energy definition $E \equiv cP_o > 0$ in order to rewrite the metric component g_{oo} in terms of the negative gravitational potential U/cP_o for GR energy E , which is the only measure of inertia (and gravity) of the moving probe mass m ,

$$\sqrt{g_{oo}} \equiv (K+U) \frac{\sqrt{1-v^2c^{-2}}}{mc^2} \equiv 1 + \frac{U\sqrt{g_{oo}}}{E} \equiv \frac{1}{[1-(U/E)]}. \quad (2)$$

Basing on identical algebra operations in (2), one can formulate the following g_{oo} -theorem: “Time-time component of the pseudo-Riemann metric tensor in Einstein’s GR is defined by a gravitational field potential $\varphi = U/E$ exactly as $g_{oo} = (1 - \varphi)^{-2}$, which has no peculiarities for $-\infty < \varphi \leq 0$ ”. Notice that the Schwarzschild metric² of empty space, where $g_{oo} = 1 - (2GM/c^2r)$ was optimistically used for strong fields from the Newton weak-field references, does not match the g_{oo} -theorem and the strict equalities (2). In fact, Newton’s point mass gravitation is not a true limit even for weak-field gravitation of overlapping extended sources which are continuously distributed within spatial structures of their own fields, both strong and weak.

The Newtonian superposition of weak-field potentials is based on the strong-field logarithmic potential, $W \propto \ln g_{oo}^{-1/2}$, in the many body system^{3,4}. Masses in this static metric potential can be represented by real Schwarzschild-type scales, while electric charges by imagine numbers,

$$W(\mathbf{x}) = \varphi_o \ln \left(1 + \frac{z_1}{|\mathbf{x}-\mathbf{a}_1|} + \frac{z_2}{|\mathbf{x}-\mathbf{a}_2|} + \dots + \frac{z_n}{|\mathbf{x}-\mathbf{a}_n|} \right). \quad (3)$$

Here the complex scale z_k of each continuous carrier of real mass $m = |m|$ and imaginary electric charge $q_e \equiv ie = i|e|$ is related in (3) to the complex energy $E = E_m + iE_e$ through the universal self potential $\varphi_o = -c^2/\sqrt{G}$ of complex charges $q_k \equiv i(e + i\sqrt{G}m)_k$,

$$z_k \equiv \frac{q_k}{\varphi_o} = \frac{(E_m + iE_e)_k}{\varphi_o^2} = \frac{G(E_m)_k}{c^4} - \frac{ie_k\sqrt{G}}{c^2} \equiv r_m + ir_e. \quad (4)$$

This scale always takes the positive real part, $r_m > 0$ due to $E_m \Rightarrow mc^2 > 0$, despite the negative gravitational charge definition $q_m \equiv E_m/\varphi_o \Rightarrow -\sqrt{G}m < 0$. Summary charged densities of interaction fields and their continuous particles,

$$\rho_f(\mathbf{x}) \equiv \frac{[-\nabla W(\mathbf{x})]^2}{4\pi\varphi_o} = -\frac{\nabla^2 W(\mathbf{x})}{4\pi} \equiv \rho_p(\mathbf{x}), \quad (5)$$

within joint nonempty (material) space are defined by the same complex potential (3). Electric field and electric charge densities are equal in (5) in the very line of the Einstein Principle of Equivalence for real inertial and gravitational densities of extended masses^{3,4}.

A total complex charge of the many body system with paired Newton/Coulomb interactions can be found by integration of net charge densities (5) over the spatial 3-volume⁵,

$$\begin{aligned} \int \frac{(\rho_f + \rho_p)}{2} d^3x &= \varphi_o \int \left(\frac{\frac{(x-a_1)z_1}{|x-a_1|^3} + \frac{(x-a_2)z_2}{|x-a_2|^3} + \dots + \frac{(x-a_n)z_n}{|x-a_n|^3}}{1 + \frac{z_1}{|x-a_1|} + \frac{z_2}{|x-a_2|} + \dots + \frac{z_n}{|x-a_n|}} \right)^2 \frac{d^3x}{4\pi} \\ &= \varphi_o \oint \left(\frac{\frac{(x-a_1)z_1}{|x-a_1|^3} + \frac{(x-a_2)z_2}{|x-a_2|^3} + \dots + \frac{(x-a_n)z_n}{|x-a_n|^3}}{1 + \frac{z_1}{|x-a_1|} + \frac{z_2}{|x-a_2|} + \dots + \frac{z_n}{|x-a_n|}} \right) \frac{d\mathbf{S}}{4\pi} = i \sum_k (e_k + i\sqrt{G}m_k) = const. \end{aligned} \quad (6)$$

Electron's electric scale, $|i(-e_o)/\varphi_o| = 1.38 \times 10^{-36}m$, highly exceeds its gravitational scale, $\sqrt{G}m_o/|\varphi_o| = 6.77 \times 10^{-58}m$, because elementary electric energy $|e_o\varphi_o| = 1.67 \times 10^{15}erg = 1.04 \times 10^{21}MeV$ highly exceeds electron's real, mechanical energy $m_o c^2 = 0.511MeV$.

If we would like to integrate charged densities of one radial charge, $q = i(e + i\sqrt{G}m)$ and $z_q = q/\varphi_o$, distributed around its center of the spherical symmetry at a point \mathbf{a} (far from centers \mathbf{a}_k of other radial particles, $|\mathbf{a} - \mathbf{a}_k|/|z_q| \rightarrow \infty$) then mechanical (real) and imaginary (electric) self-energies of such a 'secluded' infinite system with negligible interactions with 'the rest of the Universe' could be found directly from (5):

$$E_q = \int \frac{\varphi_o^2 z_q^2 d^3x}{4\pi(\mathbf{x} - \mathbf{a})^2 [|\mathbf{x} - \mathbf{a}| + z_q]^2} = \varphi_o^2 z_q \int_o^\infty \frac{d(r/z_q)}{[1 + (r/z_q)]^2} = mc^2 + \frac{ec^2}{\sqrt{-G}}. \quad (7)$$

This complex energy of electrically charged masses is an analog of the celebrated Einstein formula for relativistic energy of uncharged masses.

References

1. A. Einstein, *Annalen der Physik* **49**, 769 (1916).
2. K. Schwarzschild, *Sitzungsber. K. Preuss. Akad. Wiss., Phys.-Math. Kl.* 189 (1916).
3. I.E. Bulzhenkov, *Int. Jour. of Theor. Phys.* **47**, 1261 (2008).
4. I.E. Bulzhenkov, *Jour. Supercond. and Novel Magn.* **22**, 723 (2009).
5. I.E. Bulzhenkov, *Pure Field Electrodynamics of Continuous Complex Charges* (MIPT, Moscow, 2015), ISBN 978-5-7417-0554-4.

REVIEWING GRISHCHUK GW GENERATOR VIA TOKAMAK PHYSICS

A.W. BECKWITH

Chongqing University Department of Physics, Chongqing, P.R.China, 400014

We generalize Grishchuk and Sazhin's¹ amplitude for GW generation due to plasma in a toroid for Tokamak physics, obtaining central strain values up to $h_{2nd-term} \sim 10^{-25}$ - 10^{-26} . This value may allow detection of GW. The critical breakthrough is in utilizing a burning plasma drift current, which relies upon a thermal contribution to an electric field. The gravitational wave amplitude would be detectable in part also due to the Tokamak reaching the threshold for plasma fusion burning, when $T_{temp} \geq 100$ keV, which is how one could detect GW of amplitude so low five meters above the Tokamak center.

1 Introduction

We update Grishchuk and Sazhin¹ with plasma fusion burning. Consult the author's vixra.org article² and Mazzucato³ for a good heuristic overview of the E-M wave problem and nuclear fusion, which gives a good grounding as to E and M waves, plasmas and fusion processes. Finally, the work if completed experimentally involves connections to a Tokamak in Hefei, PRC.⁴ Russian physicists Grishchuk and Sazhin¹ obtained the amplitude of a gravitational wave (GW) in a plasma as

$$A(\text{amplitude} - \text{GW}) = h \sim \frac{G}{c^4} \cdot E^2 \cdot \lambda_{\text{GW}}^2. \quad (1)$$

Compare with Beckwith,² and we can diagram the situation.⁴ Here, E is the electric field and λ_{GW} is the wavelength for the GW generated by the Tokamak in our model. The original Grishchuk model has very small strain values, defining the relationship between GW wavelength and frequency: If $\omega_{\text{GW}} \sim 10^6$ Hz, $\lambda_{\text{GW}} \sim 300$ m. We assume setting $\omega_{\text{GW}} \sim 10^9$ Hz ($\lambda_{\text{GW}} \sim 0.3$ m) as a baseline measurement for GW detection above the Tokamak. Dr. Li has recently suggested considering an even higher frequency: $\omega_{\text{GW}} \sim 10^{10}$ Hz ($\lambda_{\text{GW}} \sim 0.03$ m). Furthermore, we will write the strain introduced by (massive) gravitons⁴ from an Ohm's law treatment of current and electric field, by first-principles comparison of the terms' magnitude.^{2,5}

$$A(\text{amplitude} - \text{GW}) \sim h \sim \frac{G \cdot W_E \cdot V_{\text{volume}}}{c^4 \cdot a} \quad (2)$$

where W_E is average energy density, V_{volume} is toroid volume, and a is the inner toroid radius.

2 Phenomenology to Confirm

Eq. (2) is due to the first term of a two-part composition of the strain, with the second term of the strain value significantly larger than the first term and due to ignition of the plasma in the Tokamak. The first term of strain is largely due to what was calculated by Grishchuk.¹ The second term is due to plasma fusion burning. This plasma fusion burning contribution is due to

nonequilibrium contributions to plasma ignition, which will be elaborated on in this document. The first term is given by Eq. (3) below and the all important second term is given by Eq. (4).

$$h_{1\text{st-term}} \sim \frac{G}{c^4} \cdot E^2 \cdot \lambda_{\text{GW}}^2 \sim \frac{G}{c^4} \cdot \left[\frac{J}{\sigma} \right]^2 \cdot \lambda_{\text{GW}}^2 \quad (3)$$

$$h_{2\text{nd-term}} \sim \frac{G}{c^4} \cdot B_{\theta}^2 \cdot \left(\frac{j_b}{n_j \cdot e_j} \right)^2 \cdot \lambda_{\text{GW}}^2 \sim \frac{G}{c^4} \cdot \frac{\xi^{\frac{1}{4}} a^2 T_{\text{Temp}}^2}{e_j^2} \cdot \lambda_{\text{GW}}^2 \sim 10^{-25} \quad (4)$$

Eq. (4) is about five orders of magnitude larger than Eq. (3), with the temperature given by Wesson in Figure 1. Note that $h_{1\text{st-term}}$ is due to the electric field within the toroid, not plasma fusion burning. In use of the facility,⁴ Chongqing University researchers will need an experimental protocol to read Eq. (4) for plasma fusion burning situations, which will be aided by the fact that the Hefei Tokamak has an unusually long stable-fusion period, corresponding to about the low point of Figure 1 and lasting for up to 100 s. We state that this will aid in obtaining a suitable value of Eq. (4), above which in turn will be affected that the one rule we have is that the strain drops in detectability an order of two above the Tokamak center.

$$h_{2\text{nd-term}} |_{5\text{m-above-Tokamak}} \sim O(T_{\text{Temp}}^2 \cdot \lambda_{\text{GW}}^2 10^{-25} \otimes 10^{-2} \propto 10^{-27}) \quad (5)$$

Researchers in Chongqing University will have to measure this to confirm GW and gravitons.

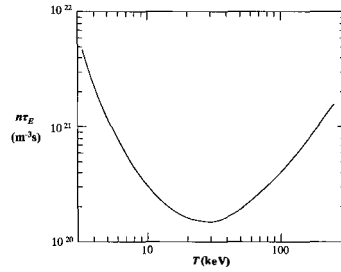


(Figure reproduced from Wesson.⁶)

Figure 1 – The value of $n\tau_E$ required to obtain ignition, as a function of temperature.

3 Conclusion: GW Generation Due to the Thermal Output of Plasma Burning

$h \sim 10^{-27}$ for a GW five meters above a Tokamak represents the extreme limits of what could be detected, but it is within the design specifications.⁷ The challenge, as frankly brought up in discussions in Chongqing University is to push development of GW detection hardware to its limits, and use the Hefei Tokamak configuration as a test bed for the new technology embodied in the plasma fusion burning generation of gravitation waves.

References

1. L.P. Grishchuk and M.V. Sazhin, *Zh. Eksp. Theor. Fiz* **68**, 1569 (1975).
2. A.W. Beckwith, <http://vixra.org/abs/1502.0011>.
3. E. Mazzucato, *Electromagnetic Waves for Thermonuclear Fusion Research*, (World Scientific, Singapore, 2014).
4. J. Li, et al., *Nat. Phys.* **9**, 817 (2013).
5. F. Li, L.M. Tang, J. Luo, and Y.-C. Li, *Phys. Rev. D* **62**, 44018 (2000).
6. J. Wesson, *Tokamaks*, 4th ed. Vol. 149 (Oxford Science, Oxford, 2011).
7. F.Y. Li et al., *Phys. Rev. D* **80**, 064013 (2009).

Authors index

| | | |
|-----------------|--|-----|
| Abele, H. | Gravity experiments with ultracold neutrons and the q BOUNCE experiment | 115 |
| Adams, T. | Low latency search for compact binary coalescences using MBTA | 327 |
| del Aguila, R.. | Atom interferometry with ultra-cold strontium | 363 |
| Albers, H. | Ground Tests of Einstein's Equivalence Principle: From Lab-based to 10-m Atomic Fountains | 153 |
| Alexander, T. | Relativistic stellar dynamics around a massive black hole in steady state | 353 |
| Alexyev, S. | Strong-field tests of $f(R)$ -gravity in binary pulsars | 371 |
| Alfauwaz, A. | mSTAR: Testing Lorentz Invariance in Space Using High Performance Optical Frequency References | 359 |
| Alhussien, A. | mSTAR: Testing Lorentz Invariance in Space Using High Performance Optical Frequency References | 359 |
| Alsuwaidan, N. | mSTAR: Testing Lorentz Invariance in Space Using High Performance Optical Frequency References | 359 |
| Al Saud, T. | mSTAR: Testing Lorentz Invariance in Space Using High Performance Optical Frequency References | 359 |
| Amand, L. | Matter-wave laser Interferometric Gravitation Antenna (MIGA): New perspectives for fundamental physics and geosciences | 163 |
| Andresen, H. | Gravitational waves three-dimensional core collapse supernova simulations | 335 |
| Aranha, R. | Gravitational Wave Recoils in Non-head-on Collisions of Black Holes | 365 |
| Arnaud, N. | The Calva facility for GW detector | 263 |
| Ast, S. | Next generation nonclassical light sources for gravitational wave detectors | 275 |
| Baghi, Q. | An Equivalence Principle test in space on the way to launch | 131 |
| Bailey, Q. | What do we know about Lorentz Symmetry? | 3 |
| Baret, B. | Search for Joint sources of gravitational waves and high energy neutrinos with the LIGO-Virgo and ANTARES Detectors | 323 |
| Barnes, V. | Weak equivalence principle, Lorentz noninvariance, and nuclear decays | 173 |
| Baune, C. | Next generation nonclassical light sources for gravitational wave detectors | 275 |
| Bawaj, M. | Probing deformed commutators with macroscopic harmonic oscillators | 97 |
| Beckwith, A. | Reviewing Grishchuk GW generator via Tokamak physics | 383 |
| Bernard, L. | Consistent massive graviton on arbitrary background | 23 |
| | Bimetric gravity and dark matter | 43 |
| Bertoldi, A. | Matter-wave laser Interferometric Gravitation Antenna (MIGA): New perspectives for fundamental physics and geosciences | 163 |
| Bertone, S. | Test of the gravitational redshift using Galileo satellites 5 and 6 | 89 |
| Biancofiore, C. | Probing deformed commutators with macroscopic harmonic oscillators | 97 |
| Billon, A. | Ground Tests of Einstein's Equivalence Principle: From Lab-based to 10-m Atomic Fountains | 153 |
| Biriukov, A. | Measurement of the Gravitational Redshift Effect with the RadioAstron satellite | 287 |
| Bizouard, M-A. | The Calva facility for GW detector | 263 |
| Blackburn, L. | Planned search for LIGO/GBM coincidence in the LIGO O1 data run | 319 |
| Blanchard, A. | Investigating Dark Energy and Gravitation at cosmological scales with EUCLID | 217 |
| Blanchet, L. | Bimetric gravity and dark matter | 43 |
| | High-order comparisons between post-Newtonian and perturbative self forces | 343 |
| Blas, D. | Lorentz violation in gravity | 11 |
| Bohinec, J. | An Autonomous Relativistic Positioning System | 81 |
| Bonaldi, M. | Probing deformed commutators with macroscopic harmonic oscillators | 97 |
| Bonfigli, F. | Probing deformed commutators with macroscopic harmonic oscillators | 97 |
| Bongs, K. | The STE-QUEST M4 proposal | 137 |
| Borrielli, A. | Probing deformed commutators with macroscopic harmonic oscillators | 97 |
| Bouyer, P. | The STE-QUEST M4 proposal | 137 |
| | Matter-wave laser Interferometric Gravitation Antenna (MIGA): New perspectives for fundamental physics and geosciences | 163 |
| Braxmaier, C. | mSTAR: Testing Lorentz Invariance in Space Using High Performance Optical Frequency References | 359 |
| Briggs, M. | Planned search for LIGO/GBM coincidence in the LIGO O1 data run | 319 |
| Brisson, V. | The Calva facility for GW detector | 263 |
| Bruenn, S. | Multimessengers from 3D Core-Collapse Supernovae | 367 |
| Buchman, S. | mSTAR: Testing Lorentz Invariance in Space Using High Performance Optical Frequency References | 359 |

| | | |
|------------------|--|-----|
| Bulik, T. | Constraining the distance to inspiralling NS-NS with Einstein Telescope | 349 |
| | Ensemble of galactic rotating neutron stars as a source of gravitational background for advanced Virgo, advanced Ligo and Einstein telescope detectors | 379 |
| Bulyzhenkov, I. | Pure field physics of continuous charges without singularities | 381 |
| Byer, Robert. | mSTAR: Testing Lorentz Invariance in Space Using High Performance Optical Frequency References | 359 |
| Cacciapuoti, L. | Testing Fundamental Physics with Clocks in Space: the ACES Mission: | 103 |
| Calloni, E. | The Archimedes Experiment | 213 |
| Calonico, D. | The STE-QUEST M4 proposal | 137 |
| Camp, J. | Planned search for LIGO/GBM coincidence in the LIGO O1 data run | 319 |
| Canuel, B. | Matter-wave laser Interferometric Gravitation Antenna (MIGA): New perspectives for fundamental physics and geosciences | 163 |
| Caprara, S. | The Archimedes Experiment | 213 |
| Casanueva, J. | The Calva facility for GW detector | 263 |
| Cavalier, F. | The Calva facility for GW detector | 263 |
| | Thermally Deformable Mirrors: a new Adaptive Optics scheme for Advanced Gravitational Wave Interferometers | 267 |
| Chaibi, W. | Matter-wave laser Interferometric Gravitation Antenna (MIGA): New perspectives for fundamental physics and geosciences | 163 |
| Chhun, R. | An Equivalence Principle test in space on the way to launch | 131 |
| Christensen, N. | Planned search for LIGO/GBM coincidence in the LIGO O1 data run | 319 |
| Ciani, G. | Advanced LIGO Input Optics | 251 |
| Cieřlar, M. | Ensemble of galactic rotating neutron stars as a source of gravitational background for advanced Virgo, advanced Ligo and Einstein telescope detectors | 379 |
| Connaughton, V. | Planned search for LIGO/GBM coincidence in the LIGO O1 data run | 319 |
| Crivellin, A. | Dark Matter: Connecting LHC searches to direct detection | 237 |
| Cronenberg, C. | Gravity experiments with ultracold neutrons and the g BOUNCE experiment | 115 |
| Cruise, M. | The STE-QUEST M4 proposal | 137 |
| Cutler, G. | mSTAR: Testing Lorentz Invariance in Space Using High Performance Optical Frequency References | 359 |
| Danquigny, C. | Matter-wave laser Interferometric Gravitation Antenna (MIGA): New perspectives for fundamental physics and geosciences | 163 |
| Danzmann, K. | eLISA Optical Sensing Developments | 283 |
| Davier, M. | The Calva facility for GW detector | 263 |
| Day, R. | Thermally Deformable Mirrors: a new Adaptive Optics scheme for Advanced Gravitational Wave Interferometers | 267 |
| De Laurentis, M. | The Archimedes Experiment | 213 |
| Debrecezeni, G. | On the possibility of GRB forecasting algorithm and alert system for future gravitational wave detectors | 331 |
| Delva, P. | Test of the gravitational redshift using Galileo satellites 5 and 6 | 89 |
| | ACES MWL data analysis preparation status | 111 |
| | Study of a new generation spatio-temporal reference system based on inter-satellite links | 369 |
| Di Giuseppe, G. | Probing deformed commutators with macroscopic harmonic oscillators | 97 |
| Dittus, H. | mSTAR: Testing Lorentz Invariance in Space Using High Performance Optical Frequency References | 359 |
| Döringshoff, K. | mSTAR: Testing Lorentz Invariance in Space Using High Performance Optical Frequency References | 359 |
| Dufour, G. | Casimir effect and quantum reflection | 197 |
| Dutta, I. | Matter-wave laser Interferometric Gravitation Antenna (MIGA): New perspectives for fundamental physics and geosciences | 163 |
| Dyadina, P. | Strong-field tests of $f(R)$ -gravity in binary pulsars | 371 |
| Ertmer, W. | Ground Tests of Einstein's Equivalence Principle: From Lab-based to 10-m Atomic Fountains | 153 |
| Esposito, G. | The Archimedes Experiment | 213 |
| Exertier, P. | INPOP planetary ephemerides: Recent results in testing gravity | 73 |

| | | |
|-------------------|--|-----|
| Fang, B. | Matter-wave laser Interferometric Gravitation Antenna (MIGA): New perspectives for fundamental physics and geosciences | 163 |
| Faye, G. | High-order comparisons between post-Newtonian and perturbative self forces | 343 |
| Ferreira, M. C. | From precision spectroscopy to fundamental cosmology | 123 |
| Fienga, A. | INPOP planetary ephemerides: Recent results in testing gravity | 73 |
| Fischbach, E. | Weak equivalence principle, Lorentz noninvariance, and nuclear decays | 173 |
| Fitzsimins, E. D. | eLISA Optical Sensing Developments | 283 |
| Floerchinger, S. | Backreaction Effects on the matter side of Einsteins Field Equations | 225 |
| Gaaloul, N. | The STE-QUEST M4 proposal | 137 |
| | Ground Tests of Einstein's Equivalence Principle: From Lab-based to 10-m Atomic Fountains | 153 |
| Gaffet, S. | Matter-wave laser Interferometric Gravitation Antenna (MIGA): New perspectives for fundamental physics and geosciences | 163 |
| Galli, S. | A Joint Analysis of BICEP2/Keck Array and Planck Data | 181 |
| Gaskins, J. | Constraints on Sterile Neutrino Dark Matter Candidate Mass by the Fermi Gamma-Ray Burst Monitor | 233 |
| Gastineau, M. | INPOP planetary ephemerides: Recent results in testing gravity | 73 |
| Geiger, R. | Matter-wave laser Interferometric Gravitation Antenna (MIGA): New perspectives for fundamental physics and geosciences | 163 |
| Geltenbort, P. | Gravity experiments with ultracold neutrons and the q BOUNCE experiment | 115 |
| Genin, E. | Thermally Deformable Mirrors: a new Adaptive Optics scheme for Advanced Gravitational Wave Interferometers | 267 |
| Gillot, J. | Matter-wave laser Interferometric Gravitation Antenna (MIGA): New perspectives for fundamental physics and geosciences | 163 |
| Gniesmer, J. | Next generation nonclassical light sources for gravitational wave detectors | 275 |
| Gomboc, A. | An Autonomous Relativistic Positioning System | 81 |
| Grilli, M. | The Archimedes Experiment | 213 |
| Grote, H. | Next generation nonclassical light sources for gravitational wave detectors | 275 |
| Guerlin, C. | ACES MWL data analysis preparation status | 111 |
| Guérou, R. | Casimir effect and quantum reflection | 197 |
| Gurlebeck, N. | mSTAR: Testing Lorentz Invariance in Space Using High Performance Optical Frequency References | 359 |
| Hanson, J. | mSTAR: Testing Lorentz Invariance in Space Using High Performance Optical Frequency References | 359 |
| Harris, J. | Multimessengers from 3D Core-Collapse Supernovae | 367 |
| Hartwig, J. | Ground Tests of Einstein's Equivalence Principle: From Lab-based to 10-m Atomic Fountains | 153 |
| Hees, A. | Some cosmological consequences of a breaking of the Einstein equivalence principle | 149 |
| | Basics of the Pressuron | 31 |
| | Test of the gravitational redshift using Galileo satellites 5 and 6 | 89 |
| Heim, J. | Weak equivalence principle, Lorentz noninvariance, and nuclear decays | 173 |
| Heine, H. | Ground Tests of Einstein's Equivalence Principle: From Lab-based to 10-m Atomic Fountains | 153 |
| Heinzel, G. | eLISA Optical Sensing Developments | 283 |
| Heisenberg, L. | Bimetric gravity and dark matter | 43 |
| Hello, P. | The Calva facility for GW detector | 263 |
| | Thermally Deformable Mirrors: a new Adaptive Optics scheme for Advanced Gravitational Wave Interferometers | 267 |
| Herrmann, S. | mSTAR: Testing Lorentz Invariance in Space Using High Performance Optical Frequency References | 359 |
| Heske, A. | Quantum Sensors in Space - Design Challenges for Spacecraft and Instruments | 279 |
| Holleville, D. | Matter-wave laser Interferometric Gravitation Antenna (MIGA): New perspectives for fundamental physics and geosciences | 163 |
| Horiuchi, S. | Constraints on Sterile Neutrino Dark Matter Candidate Mass by the Fermi Gamma-Ray Burst Monitor | 233 |
| Horvat, M. | An Autonomous Relativistic Positioning System | 81 |
| Huet, D. | The Calva facility for GW detector | 263 |

| | | |
|------------------------------|---|------------|
| Iess, L. | The STE-QUEST M4 proposal | 137 |
| Janka, H. | Gravitational waves three-dimensional core collapse supernova simulations | 335 |
| Jaroux, B. | mSTAR: Testing Lorentz Invariance in Space Using High Performance Optical Frequency References | 359 |
| Jenke, T. | Gravity experiments with ultracold neutrons and the <i>qBOUNCE</i> experiment | 115 |
| Jetzer, P. | The STE-QUEST M4 proposal | 137 |
| Johann, U. | mSTAR: Testing Lorentz Invariance in Space Using High Performance Optical Frequency References | 359 |
| João, S. | From precision spectroscopy to fundamental cosmology | 123 |
| Kaltenbaek, R. | Testing quantum physics in space using high-mass matter-wave interferometry | 141 |
| Kasprzack, M. | Thermally Deformable Mirrors: a new Adaptive Optics scheme for Advanced Gravitational Wave Interferometers | 267 |
| Kauts, V. | Measurement of the Gravitational Redshift Effect with the RadioAstron satellite | 287 |
| Khalaidovski, A. | Next generation nonclassical light sources for gravitational wave detectors | 275 |
| Khoury, J. | A dark matter superfluid | 35 |
| Killow, C. | eLISA Optical Sensing Developments | 283 |
| Kleybolte, L. | Next generation nonclassical light sources for gravitational wave detectors | 275 |
| von Klitzing, W. | The STE-QUEST M4 proposal | 137 |
| Klioner, S. | Gaia: astrometry and gravitation | 65 |
| Koštić, U. | An Autonomous Relativistic Positioning System | 81 |
| Kowalska- Leszczynska, I. | Constraining the distance to inspiralling NS-NS with Einstein Telescope | 349 |
| Krause, D. | Weak equivalence principle, Lorentz noninvariance, and nuclear decays | 173 |
| Kucaba, M. | Ensemble of galactic rotating neutron stars as a source of gravitational background for advanced Virgo, advanced Ligo and Einstein telescope detectors | 379 |
| Lambrecht, A. | Casimir effect and quantum reflection | 197 |
| Lämmerzahl, C. | mSTAR: Testing Lorentz Invariance in Space Using High Performance Optical Frequency References | 359 |
| Landragin, A. | Matter-wave laser Interferometric Gravitation Antenna (MIGA): New perspectives for fundamental physics and geosciences | 163 |
| Langlois, M. | Gravity gradiometer using large momentum transfer beamsplitters | 361 |
| Larena, J. | Some cosmological consequences of a breaking of the Einstein equivalence principle | 149 |
| Laskar, J. | INPOP planetary ephemerides: Recent results in testing gravity | 73 |
| Laurent, P. | Testing Fundamental Physics with Clocks in Space: the ACES Mission: ACES MWL data analysis preparation status | 103 111 |
| LePoncin-Lafitte, C. | ACES MWL data analysis preparation status | 111 |
| Leal, P. | From precision spectroscopy to fundamental cosmology | 123 |
| Lecomte, S. | The STE-QUEST M4 proposal | 137 |
| Leite, A. | Optimization of ESPRESSO Fundamental Physics Tests From precision spectroscopy to fundamental cosmology | 127 123 |
| Lentz, E. | Multimessengers from 3D Core-Collapse Supernovae | 367 |
| Leroy, N. | The Calva facility for GW detector Thermally Deformable Mirrors: a new Adaptive Optics scheme for Advanced Gravitational Wave Interferometers | 263 267 |
| Lieser, D. | eLISA Optical Sensing Developments | 283 |
| Lima, J. | Inflationary and late universe tests for $\Lambda(H)$ cosmologies | 377 |
| Lipa, J. | mSTAR: Testing Lorentz Invariance in Space Using High Performance Optical Frequency References | 359 |
| Litvinov, D. | Measurement of the Gravitational Redshift Effect with the RadioAstron satellite | 287 |
| Lopez, M. | Atom interferometry test of short range gravity: recent progress in the FORCA-G experiment | 205 |
| Loriette, V. | The Calva facility for GW detector | 263 |

| | | |
|------------------------|--|-----|
| Majorana, E. | The Archimedes Experiment | 213 |
| Maskimovic, I. | The Calva facility for GW detector | 263 |
| Manche, H. | INPOP planetary ephemerides: Recent results in testing gravity | 73 |
| Marconi, L. | Probing deformed commutators with macroscopic harmonic oscillators | 97 |
| Marin, F. | Probing deformed commutators with macroscopic harmonic oscillators | 97 |
| Marino, F. | Probing deformed commutators with macroscopic harmonic oscillators | 97 |
| Marronetti, P. | Multimessengers from 3D Core-Collapse Supernovae | 367 |
| Marsat, S. | Post-Newtonian higher-order spin effects in inspiraling compact binaries | 339 |
| Martins, C. | COrE+: mapping our cosmic origins | 185 |
| | From precision spectroscopy to fundamental cosmology | 123 |
| | Optimization of ESPRESSO Fundamental Physics Tests | 127 |
| Massonnet, D. | Testing Fundamental Physics with Clocks in Space: the ACES Mission: | 103 |
| Mazzoni, T. | Atom interferometry with ultra-cold strontium | 363 |
| Mehmet, M. | Next generation nonclassical light sources for gravitational wave detectors | 275 |
| Meinders, M. | Dual readout of a Michelson interferometer for subtraction of stray light induced disturbances | 271 |
| Meiners, C. | Ground Tests of Einstein's Equivalence Principle: From Lab-based to 10-m Atomic Fountains | 153 |
| Merlet, S. | Gravity gradiometer using large momentum transfer beamsplitters | 361 |
| Merzougui, M. | Matter-wave laser Interferometric Gravitation Antenna (MIGA): New perspectives for fundamental physics and geosciences | 163 |
| Messer, E. | Multimessengers from 3D Core-Collapse Supernovae | 367 |
| Meynadier, F. | ACES MWL data analysis preparation status | 111 |
| Mezzacappa, A. | Multimessengers from 3D Core-Collapse Supernovae | 367 |
| Minazzoli, O. | Basics of the Pressuron | 31 |
| | Some cosmological consequences of a breaking of the Einstein equivalence principle | 149 |
| Moghadas Nia, R. | Next generation nonclassical light sources for gravitational wave detectors | 275 |
| Mota, D. | Nonlinear Cosmological Probes of Screening Mechanism in Modified Gravity | 27 |
| Mota, I. | From precision spectroscopy to fundamental cosmology | 123 |
| Müller, E. | Gravitational waves three-dimensional core collapse supernova simulations | 335 |
| Natali, R. | Probing deformed commutators with macroscopic harmonic oscillators | 97 |
| Nath, D. | Ground Tests of Einstein's Equivalence Principle: From Lab-based to 10-m Atomic Fountains | 153 |
| Nedelec, P. | AEgIS experiment: goals and status | 59 |
| Nesvizhevsky, V. | Neutrons and Gravity | 191 |
| Ng, K. | Constraints on Sterile Neutrino Dark Matter Candidate Mass by the Fermi Gamma-Ray Burst Monitor | 233 |
| Nikolov, S. | eLISA Optical Sensing Developments | 283 |
| Nistor, J. | Weak equivalence principle, Lorentz noninvariance, and nuclear decays | 173 |
| Pepe, G. P. | The Archimedes Experiment | 213 |
| Pereira, F. | Atom interferometry test of short range gravity: recent progress in the FORCA-G experiment | 205 |
| Pereira dos Santos, F. | Gravity gradiometer using large momentum transfer beamsplitters | 361 |
| Perez, P. | GBAR status and goals | 53 |
| Perreux-Lloyd, M. | eLISA Optical Sensing Developments | 283 |
| Perico, L. | Inflationary and late universe tests for $\Lambda(H)$ cosmologies | 377 |
| Peters, A. | mSTAR: Testing Lorentz Invariance in Space Using High Performance Optical Frequency References | 359 |
| Petrarca, S. | The Archimedes Experiment | 213 |
| Pinho, A. | From precision spectroscopy to fundamental cosmology | 123 |
| Poli, N. | Atom interferometry with ultra-cold strontium | 363 |
| Pontin, A. | Probing deformed commutators with macroscopic harmonic oscillators | 97 |
| Porayko, N. | Measurement of the Gravitational Redshift Effect with the RadioAstron satellite | 287 |
| Preece, R. | Constraints on Sterile Neutrino Dark Matter Candidate Mass by the Fermi Gamma-Ray Burst Monitor | 233 |
| Prodi, G. A. | Probing deformed commutators with macroscopic harmonic oscillators | 97 |
| Puppo, P. | The Archimedes Experiment | 213 |

| | | |
|-------------------|--|-----|
| Rannu, K. | Strong-field tests of $f(R)$ -gravity in binary pulsars | 371 |
| Raphael, H. | Multimessengers from 3D Core-Collapse Supernovae | 367 |
| Rasel, E. | Ground Tests of Einstein's Equivalence Principle: From Lab-based to 10-m Atomic Fountains | 153 |
| | The STE-QUEST M4 proposal | 137 |
| Rechberger, T. | Gravity experiments with ultracold neutrons and the g BOUNCE experiment | 115 |
| Renaux-Petel, S. | Aspects of massive gravity | 19 |
| Reynaud, S. | Casimir effect and quantum reflection | 197 |
| Ricci, F. | The Archimedes Experiment | 213 |
| Richard, E. | Study of a new generation spatio-temporal reference system based on inter-satellite links | 369 |
| | Test of the gravitational redshift using Galileo satellites 5 and 6 | 89 |
| Richardson, L. L. | Ground Tests of Einstein's Equivalence Principle: From Lab-based to 10-m Atomic Fountains | 153 |
| Riou, I. | Matter-wave laser Interferometric Gravitation Antenna (MIGA): New perspectives for fundamental physics and geosciences | 163 |
| Robertson, D.I. | eLISA Optical Sensing Developments | 283 |
| Robinet, F. | The Calva facility for GW detector | 263 |
| Rodrigues, M. | An Equivalence Principle test in space on the way to launch | 131 |
| Rosa, L. | The Archimedes Experiment | 213 |
| Rosinska, D. | Ensemble of galactic rotating neutron stars as a source of gravitational background for advanced Virgo, advanced Ligo and Einstein telescope detectors | 379 |
| Rothacher, M. | The STE-QUEST M4 proposal | 137 |
| Rovelli, C. | The Archimedes Experiment | 213 |
| Rudenko, V. | Measurement of the Gravitational Redshift Effect with the RadioAstron satellite | 287 |
| Ruggi, P. | The Archimedes Experiment | 213 |
| Saini, N. L. | The Archimedes Experiment | 213 |
| Salomon, C. | Testing Fundamental Physics with Clocks in Space: the ACES Mission: | 103 |
| Salvi, L. | Atom interferometry with ultra-cold strontium | 363 |
| Saraf, S. | mSTAR: Testing Lorentz Invariance in Space Using High Performance Optical Frequency References | 359 |
| Savoie, D. | Matter-wave laser Interferometric Gravitation Antenna (MIGA): New perspectives for fundamental physics and geosciences | 163 |
| Schiller, S. | The STE-QUEST M4 proposal | 137 |
| Schlippert, D. | Ground Tests of Einstein's Equivalence Principle: From Lab-based to 10-m Atomic Fountains | 153 |
| Schnabel, R. | Dual readout of a Michelson interferometer for subtraction of stray light induced disturbances | 271 |
| | Next generation nonclassical light sources for gravitational wave detectors | 275 |
| Schönbeck, A. | Next generation nonclassical light sources for gravitational wave detectors | 275 |
| Schubert, C. | Ground Tests of Einstein's Equivalence Principle: From Lab-based to 10-m Atomic Fountains | 153 |
| Schuldt, T. | mSTAR: Testing Lorentz Invariance in Space Using High Performance Optical Frequency References | 359 |
| Schuster, S. | eLISA Optical Sensing Developments | 283 |
| Serra, E. | Probing deformed commutators with macroscopic harmonic oscillators | 97 |
| Shawhan, P. | Planned search for LIGO/GBM coincidence in the LIGO O1 data run | 319 |
| Singer, L. | Planned search for LIGO/GBM coincidence in the LIGO O1 data run | 319 |
| Smith, M. | Constraints on Sterile Neutrino Dark Matter Candidate Mass by the Fermi Gamma-Ray Burst Monitor | 233 |
| Soares, I. D. | Gravitational Wave Recoils in Non-head-on Collisions of Black Holes | 365 |
| Solaro, C. | Atom interferometry test of short range gravity: recent progress in the FORCA-G experiment | 205 |
| Sopuerta, C. | The STE-QUEST M4 proposal | 137 |
| Staley, A. | The Status of the Advanced LIGO Gravitational-Wave Detectors | 243 |
| Stochino, A. | mSTAR: Testing Lorentz Invariance in Space Using High Performance Optical Frequency References | 359 |
| Stornaiolo, C. | The Archimedes Experiment | 213 |
| Stratta, G. | Multi-messenger searches: past results and future programs | 303 |

| | | |
|--------------------|---|-----|
| Tafari, F. | The Archimedes Experiment | 213 |
| Tan, S. | mSTAR: Testing Lorentz Invariance in Space Using High Performance Optical Frequency References | 359 |
| Tartaglia, A. | GINGER - A terrestrial experiment to verify the Lense-Thirring effect or possible deviations from General Relativity | 15 |
| Tetradis, N. | Backreaction Effects on the matter side of Einsteins Field Equations | 225 |
| Thalhammer, M. | Gravity experiments with ultracold neutrons and the q BOUNCE experiment | 115 |
| Tino, G. | The STE-QUEST M4 proposal | 137 |
| | Atom interferometry with ultra-cold strontium | 363 |
| Tobar, M. | Precision oscillator technology with application to testing fundamental physics, detecting high frequency gravitational waves, and quantum measurement | 145 |
| Tomaru, T. | Large-scale Cryogenic Gravitational wave Telescope: KAGRA | 255 |
| Tonini, E. | Gravitational Wave Recoils in Non-head-on Collisions of Black Holes | 365 |
| Touboul, P. | An Equivalence Principle test in space on the way to launch | 131 |
| Tröbs, M. | eLISA Optical Sensing Developments | 283 |
| Tuckey, P. | The STE-QUEST M4 proposal | 137 |
| Unnikrishnan, C. | Dynamics, Relativity and the Equivalence Principle in the 'once-given' Universe | 177 |
| Urban, F. | Disformal vectors and anisotropies on a warped brane | 229 |
| Vahlbruch, H. | Next generation nonclassical light sources for gravitational wave detectors | 275 |
| Van Den Broeck, C. | Gravitational Waves searches with advanced Ligo and advanced Virgo | 295 |
| Veitch, J. | Planned search for LIGO/GBM coincidence in the LIGO O1 data run | 319 |
| Ventura, L. | From precision spectroscopy to fundamental cosmology | 123 |
| Vianez, P. | From precision spectroscopy to fundamental cosmology | 123 |
| Viceré, A. | Observational perspectives with advanced gravitational wave detectors | 311 |
| Vielzeuf, P. | From precision spectroscopy to fundamental cosmology | 123 |
| Vitali, D. | Probing deformed commutators with macroscopic harmonic oscillators | 97 |
| Vollmer, C. | Next generation nonclassical light sources for gravitational wave detectors | 275 |
| Ward, H. | eLISA Optical Sensing Developments | 283 |
| Weise, D. | eLISA Optical Sensing Developments | 283 |
| Whiting, B. | High-order comparisons between post-Newtonian and perturbative self forces | 343 |
| Wiedemann, U. | Backreaction Effects on the matter side of Einsteins Field Equations | 225 |
| Wodey, E. | Ground Tests of Einstein's Equivalence Principle: From Lab-based to 10-m Atomic Fountains | 153 |
| Wolf, P. | The STE-QUEST M4 proposal | 137 |
| | Test of the gravitational redshift using Galileo satellites 5 and 6 | 89 |
| | ACES MWL data analysis preparation status | 111 |
| | Study of a new generation spatio-temporal reference system based on inter-satellite links | 369 |
| Worden, S. | mSTAR: Testing Lorentz Invariance in Space Using High Performance Optical Frequency References | 359 |
| Yakunin, K. | Multimessengers from 3D Core-Collapse Supernovae | 367 |
| Zelan, M. | The STE-QUEST M4 proposal | 137 |
| Zhang, X. | Atom interferometry with ultra-cold strontium | 363 |

List of Participants

| Family name | First name | Institution | Country | Email address |
|-------------|----------------------|---|-----------------|--------------------------------------|
| | Abele Hartmut | TU Wien | Austria | abele@ati.ac.at |
| | Adams Thomas | LAPP | France | thomas.adams@ligo.org |
| | Alexander Tal | Weizmann Institute | Israel | tal.alexander@weizmann.ac.il |
| | Andresen Haakon | MPI Astrophysik | Germany | haakoan@mpa-garching.mpg.de |
| | Angonin Marie-Ch. | SYRTE | France | m-c.angonin@obspm.fr |
| | Ast Stefan | Institute for Gravitational Physics | Germany | stefan.ast@aei.mpg.de |
| | Babichev Eugeny | LPT | France | eugeny.babichev@th.u-psud.fr |
| | Bailey Quentin | Embry-Riddle Aeronautical University | USA | baileyq@erau.edu |
| | Baret Bruny | APC | France | baret@in2p3.fr |
| | Beckwith Andrew | Chongqing University | China | rwill9955b@gmail.com |
| | Belczynski Krzysztof | Astronomical Observatory | Poland | chrisbelczynski@gmail.com |
| | Bernard Laura | IAP | France | bernard@iap.fr |
| | Biancale Richard | CNES | France | richard.biancale@cnes.fr |
| | Bize Sébastien | LNE - SYRTE | France | sebastien.bize@obspm.fr |
| | Blanchard Alain | IRAP | France | alain.blanchard@irap.omp.eu |
| | Blanchet Luc | IAP | France | blanchet@iap.fr |
| | Blas Diego | CERN - TH Division | Switzerland | blas.diego@gmail.com |
| | Bohe Alejandro | Albert Einstein Institute - MPI | Germany | alejandro.bohe@aei.mpg.de |
| | Bourgoin Adrien | SYRTE | France | adrien.bourgoin@obspm.fr |
| | Bulzhenkov Igor | Moscow Inst. Physics and Technology | Russia | bulyzhenkov.ie@mipt.ru |
| | Burde Georgy | Ben-Gurion University of the Negev | Israel | georg@bgu.ac.il |
| | Cacciapuoti Luigi | European Space Agency | The Netherlands | Luigi.Cacciapuoti@esa.int |
| | Calloni Enrico | Università Federico II | Italy | enrico.calloni@na.infn.it |
| | Camp Jordan | NASA - GSFC | USA | jordan.b.camp@nasa.gov |
| | Ciani Giacomo | University of Florida | USA | ciani@phys.ufl.edu |
| | Coleman Jon | University of Liverpool | UK | coleman@liv.ac.uk |
| | Cronenberg Gunther | TU Wien | Austria | cronenberg@ati.ac.at |
| | Curir Anna | Osservatorio Astrofisico di Torino | Italy | curir@oato.inaf.it |
| | Dall'Osso Simone | Universität Tübingen - Th. Astrophysics | Germany | simone.dallosso@uni-tuebingen.de |
| | Debreczeni Gergely | Wigner Research Centre for Physics | Hungary | Debreczeni.Gergely@wigner.mta.hu |
| | Delva Pacôme | SYRTE | France | pacome.delva@obspm.fr |
| | Dibi Salomé | Radboud University | The Netherlands | s.dibi@astro.ru.nl |
| | Dolesi Rita | Università di Trento - INFN - TIFPA | Italy | dolesi@science.unitn.it |
| | Duarte Leonardo | Universidade de São Paulo | Brazil | elduarte@usp.br |
| | Dufour Gabriel | Lab. Kastler Brossel | France | gabriel.dufour@upmc.fr |
| | Dumarchez Jacques | LPNHE | France | jacques.dumarchez@cern.ch |
| | Dyadina Polina | Sternberg Astronomical Institute | Russia | guldur.anwo@gmail.com |
| | Famaey Benoit | Observatoire Astronomique | France | benoit.famaey@astro.unistra.fr |
| | Fave Guillaume | IAP | France | fave@iap.fr |
| | Fienga Agnes | GEOAZUR | France | agnes.fienga@oca.eu |
| | Fischbach Ephraim | Purdue University | USA | ephraim@purdue.edu |
| | Freire Paulo | MPI Radio Astronomy | Germany | pfreire@mpifr-bonn.mpg.de |
| | Galli Silvia | University of Chicago - KICP | USA | galli@kicp.uchicago.edu |
| | Geiger Remi | Observatoire de Paris - SYRTE | France | remi.geiger@obspm.fr |
| | Gouaty Romain | LAPP | France | gouaty@lapp.in2p3.fr |
| | Gürlebeck Norman | University of Bremen - ZARM | Germany | norman.guerlebeck@zarm.uni-bremen.de |
| | Hamilton Paul | UC Berkeley | USA | paul.hamilton@berkeley.edu |
| | Harms Jan | Università degli Studi "Carlo Bo" | Italy | ian.harms@uniurb.it |
| | Haslinger Philipp | UC Berkeley | USA | haslinger@berkeley.edu |
| | Hedgès Morgan | Princeton University | USA | mhedges@princeton.edu |
| | Hees Aurélien | Rhodes University | South Africa | aurelien.hees@gmail.com |
| | Heske Astrid | ESA - ESTEC | The Netherlands | astrid.heske@esa.int |
| | Huet Dominique | LAL | France | huet@lal.in2p3.fr |
| | Ivanov Andrey | Institute of Atomic and Subatomic Physics | Austria | ivanov@kph.tuwien.ac.at |
| | Jaekel Marc-Thierry | LPT - ENS | France | jaekel@lpt.ens.fr |
| | Jaffe Matthew | UC Berkeley | USA | miaffe@berkeley.edu |
| | Jenke Tobias | TU Wien - Atominstüt | Austria | tienke@ati.ac.at |
| | Kaltenbaek Rainer | University of Vienna | Austria | rainer.kaltenbaek@univie.ac.at |
| | Kasprzack Marie | Louisiana State University | USA | mkasprzack@lsu.edu |
| | Khoury Justin | University of Pennsylvania | USA | ikhoury@sas.upenn.edu |
| | Killow Christian | University of Glasgow | UK | christian.killow@glasgow.ac.uk |
| | Klioner Sergei | TU Dresden - Lohrmann Observ. | Germany | Sergei.Klioner@tu-dresden.de |
| | Koshelev Alexey | VUB | Belgium | alexey.koshelev@vub.ac.be |

| | | |
|------------------------|---|---------------------------------|
| Kostić Uroš | University of Ljubljana Slovenia | uros.kostic@fmf.uni-lj.si |
| Kowalska Izabela | University of Warsaw Poland | ikowalska@astrouw.edu.pl |
| Langlois David | APC France | langlois@apc.univ-paris7.fr |
| Langlois Mehdi | Observatoire de Paris France | mehdi.langlois@obspm.fr |
| Le Goff Jean-Marc | CEA Saclay France | jmlegoff@cea.fr |
| Le Tiec Alexandre | Observatoire de Paris France | letiec@obspm.fr |
| Leite Ana Catarina | CAUP Portugal | Ana.Leite@astro.up.pt |
| Lion Guillaume | Observatoire de Paris - SYRTE France | Guillaume.Lion@obspm.fr |
| Lisdat Christian | Physikalisch-Technische Bundesanstalt Germany | christian.lisdat@ptb.de |
| Lopez Matthias | SYRTE France | Matthias.lopez@obspm.fr |
| Maggiore Michele | Université de Genève Switzerland | michele.maggiore@unige.ch |
| Marchand Tanguy | École Polytechnique France | tanguy.marchand@polytechnique.e |
| Marin Francesco | Università di Firenze Italy | marin@fi.infn.it |
| Marronetti Pedro | National Science Foundation USA | pmarrone@nsf.gov |
| Marsat Sylvain | University of Maryland USA | smarsat@umd.edu |
| Martins Carlos | CAUP Portugal | Carlos.Martins@astro.up.pt |
| Meinders Melanie | Institute for Gravitational Physics Germany | melanie.meinders@aei.mpg.de |
| Meynadier Frédéric | SYRTE France | Frederic.Meynadier@obspm.fr |
| Minazzoli Olivier | Centre Sc. de Monaco & ARTEMIS France | ominazzoli@gmail.com |
| Mota David | Institute of Theoretical Astrophysics Norway | d.f.mota@astro.uio.no |
| Mozaffari Ali | Imperial College UK | ali.mozaffari@imperial.ac.uk |
| Nardini Germano | DESY Germany | germano.nardini@desy.de |
| Nedelec Patrick | IPN Lyon France | p.nedelec@ipnl.in2p3.fr |
| Nesvizhevsky Valery | Institut Laue - Langevin France | nesvizhevsky@ill.eu |
| Niggebaum Alexander | University of Birmingham UK | axn136@bham.ac.uk |
| Nobili Anna M. | Università di Pisa - Dpt. E. Fermi Italy | nobili@dm.unipi.it |
| Perez Patrice | CEA Saclay - IRFU/SPP France | patrice.perez@cea.fr |
| Pitschmann Mario | Vienna University of Technology Austria | pitschmann@hotmail.com |
| Poli Nicola | INFN Firenze Italy | nicola.poli@unifi.it |
| Porter Edward | APC France | porter@apc.in2p3.fr |
| Preece Robert | University of Alabama USA | Rob.Preece@nasa.gov |
| Rasel Ernst | Leibnitz University - Ins. Quantum Optics Germany | rasel@iqo.uni-hannover.de |
| Renaux-Petel Sébastien | IAP France | renaux@iap.fr |
| Richard Edouard | SYRTE France | edouard.richard@obspm.fr |
| Rodrigues Manuel | ONERA France | manuel.rodrigues@onera.fr |
| Rosinska Dorota | Kepler Institute of Astronomy Poland | dorota@astro.ia.uz.zgora.pl |
| Rudenko Valentin | Sternberg Astronomical Institute Russia | rvn@sai.msu.ru |
| Sadovyan Avetis Abel | Yerevan State University Armenia | asadovyan@gmail.com |
| Soares Ivano D. | Centro Brasileiro de Pesquisas Físicas Brazil | ivano@cbpf.br |
| Staley Alexa | Columbia University USA | alexa.n.staley@gmail.com |
| Stratta Giulia | Università di Urbino Italy | giulia.stratta@gmail.com |
| Tartaglia Angelo | Politecnico di Torino - INFN Italy | angelo.tartaglia@polito.it |
| Tino Guglielmo M. | Università di Firenze / LENS Italy | tino@fi.infn.it |
| Tobar Michael | The University of Western Australia Australia | michael.tobar@uwa.edu.au |
| Tomaru Takayuki | KEK Japan | tomaru@post.kek.ip |
| Unnikrishnan CS | Tata Institute India | unni@tifr.res.in |
| Urban Federico | ULB Belgium | urban@ulb.ac.be |
| Van Den Broeck Chris | NIKHEF The Netherlands | vdbroeck@nikhef.nl |
| Vardanyan Mihran | Yerevan State University Armenia | mva@astro.ox.ac.uk |
| Viceré Andrea | Università degli Studi "Carlo Bo" Italy | andrea.vicere@uniurb.it |
| Vieira José | CAUP Portugal | J.Pinto-Vieira@sussex.ac.uk |
| Vikman Alexander | LMU Germany | vikman@cern.ch |
| Viswanathan Vishnu | Observatoire de Paris France | viswanat@geoazur.unice.fr |
| Wiedemann Urs Achim | CERN Switzerland | Urs.Wiedemann@cern.ch |
| Wintergerst Nico | Oskar Klein center for Cosmoparticle Ph. Sweden | nico.wintergerst@fvsik.su.se |
| Wolf Peter | LNE-SYRTE France | peter.wolf@obspm.fr |